AJNR

AMERICAN JOURNAL OF NEURORADIOLOGY

NOVEMBER 2013
VOLUME 34
NUMBER 11
WWW.AJNR.ORG

THE JOURNAL OF DIAGNOSTIC AND INTERVENTIONAL NEURORADIOLOGY

Use of off-label drugs and devices in neurointervention

Endovascular magnetically navigated catheter under MR guidance

Abnormalities in insular and peri-insular epilepsy

Official Journal ASNR • ASFNR • ASHNR • ASPNR • ASSR

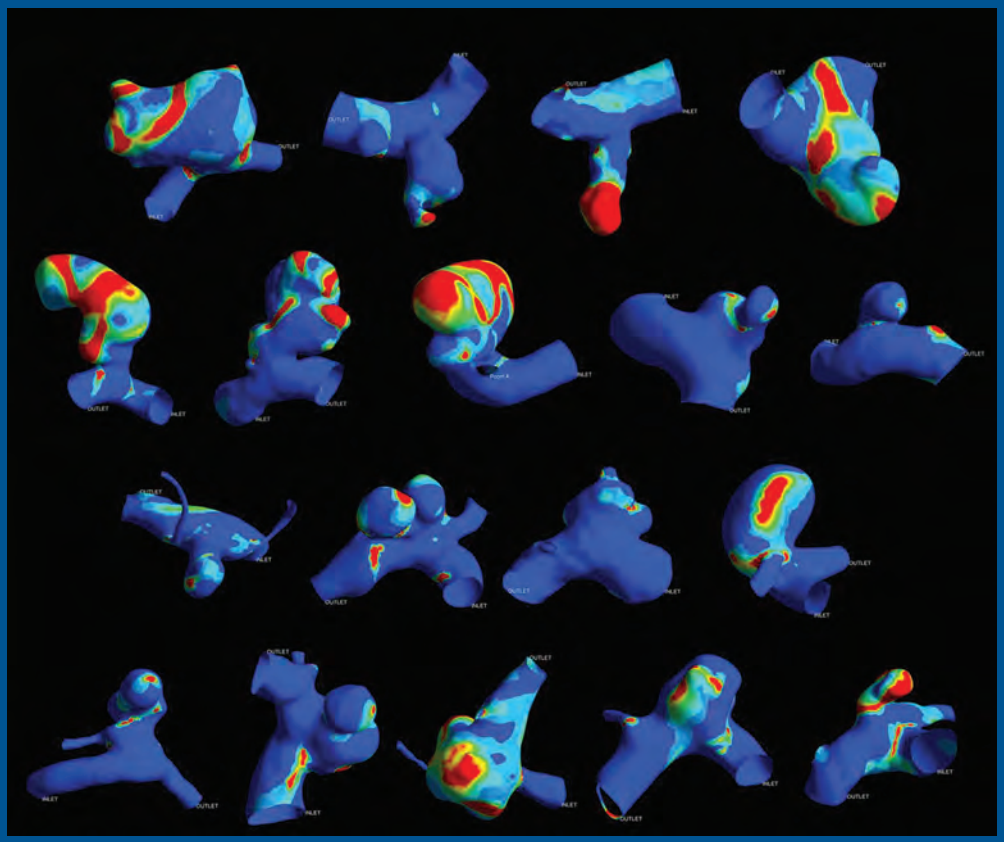

Scepter C®

Occlusion Balloon Catheter

The New Standard of Excellence, Redefining

Compliant balloon designed for reliable vessel occlusion yet conforms to vessel anatomy

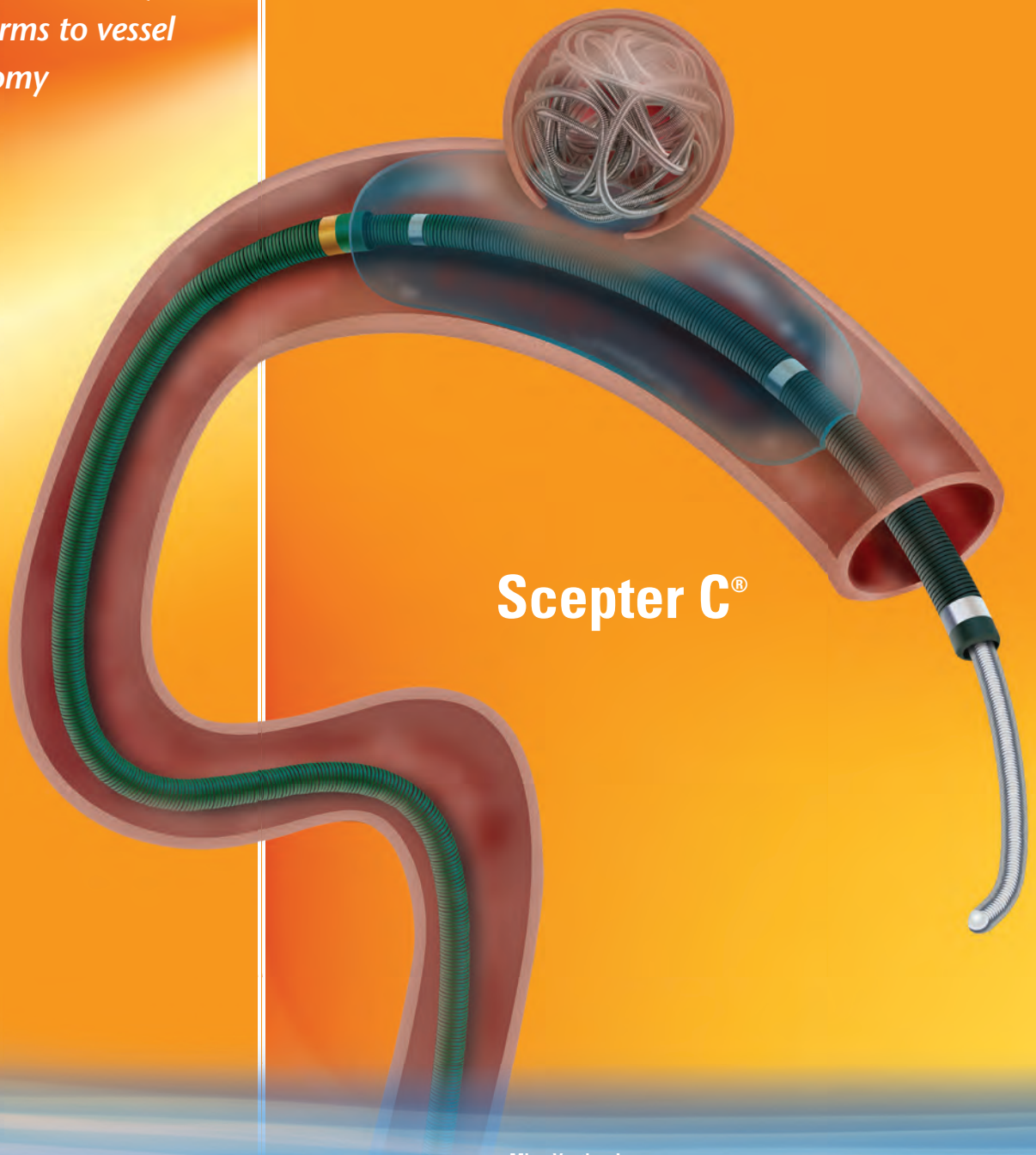

Scepter C®

For more information or a product demonstration, contact your local MicroVention representative:

MicroVention, Inc.
Worldwide Headquarters PH +1.714.247.8000
1311 Valencia Avenue
Tustin, CA 92780 USA
MicroVention United Kingdom PH +44 (0) 191 258 6777
MicroVention Europe, S.A.R.L. PH +33 (1) 39 21 77 46
MicroVention Deutschland GmbH PH +49 211 210 798-0
Web **microvention.com**

Deliverability Versatility and Control

Scepter XC®

Occlusion Balloon Catheter

Occlusion Balloon with .014" Guidewire Compatibility

– *Maximizing the utility of a unique coaxial shaft, Scepter Occlusion Balloon Catheter incorporates many new product features*

– *Balloon diameters range from 2mm to 6mm*

Key Compatible Agents

– *Compatible for use with dimethyl sulfoxide (DMSO)*

– *Compatible for use with diagnostic agents and liquid embolic agents such as Onyx® Liquid Embolic System (FDA and CE approved)*

Xtra Compliant balloon conforms to extremely complex anatomies where neck coverage is more challenging

Scepter XC®

Compatible with Traxcess® Docking Wire

CE 0297

MicroVention® TERUMO

BARRICADE COIL SYSTEM™

COILING SIMPLIFIED, PERFORMANCE DELIVERED

BLOCKADE
MEDICAL

18 TECHNOLOGY DRIVE #169, IRVINE CA 92618 | **P** 949.788.1443
WWW.BLOCKADEMEDICAL.COM

MADE IN AMERICA

CE
0297

MKTG-020 REV. A

AJNR

AMERICAN JOURNAL OF NEURORADIOLOGY

NOVEMBER 2013
VOLUME 34
NUMBER 11
WWW.AJNR.ORG

Publication Preview at www.ajnr.org features articles released in advance of print. Visit www.ajnrblog.org to comment on AJNR content and chat with colleagues and AJNR's News Digest at http://ajnrdigest.org to read the stories behind the latest research in neuroimaging.

Indicates Editor's Choices selection

Indicates Fellows' Journal Club selection

Indicates open access to non-subscribers at www.ajnr.org

Indicates article with supplemental on-line table

Indicates article with supplemental on-line photo

Indicates article with supplemental on-line video

Indicates Evidence-Based Medicine Level 1

Indicates Evidence-Based Medicine Level 2

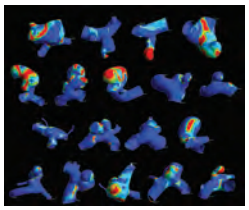

Posterior communicating artery aneurysms with third cranial nerve palsy show high oscillatory shear indices that may contribute to rupture.

ASNR 52ND ANNUAL MEETING & THE FOUNDATION OF THE ASNR SYMPOSIUM 2014

MAY 17-22 | **Montreal** ■ Palais des congrés de Montreal

ASNR 2014 PROGRAM CHAIR/PRESIDENT-ELECT - Gordon K. Sze, MD, FACR

THE FOUNDATION OF THE ASNR

The Foundation of the ASNR Symposium 2014: Inflammatory and Infectious Diseases of the CNS

SYMPOSIUM 2014:

- The Role of Inflammation and Infections in Stroke, Seizures, White Matter Diseases, etc.
- Advanced Imaging Techniques in the Evaluation of Inflammatory CNS Diseases
- Infectious Agents for Human Good: Oncolytic Viruses, Viral Vector Gene Therapy and Advanced Imaging

ADDITIONAL NEW EDUCATIONAL COURSE PROGRAM IN 2014 (concurrent program with the Symposium 2014)

EDUCATIONAL COURSE 2014: with world class speakers including

- Anne G. Osborn, MD, Thomas P. Naidich, MD, Donald Resnick, MD, James G. Smirniotopoulos, MD, Jeffrey S. Ross, MD, Howard A. Rowley, MD, David M. Yousem, MD, MBA, Laurie A. Loevner, MD, Peter M. Som, MD, Patricia A. Hudgins, MD, Robert D. Zimmerman MD, FACR, Hugh D. Curtin, MD, M. Judith Donovan Post, MD, FACR, and More...

ANNUAL MEETING:

- One-day **MINI SYMPOSIUM** on **STROKE** - Organized by Pina C. Sanelli, MD, MPH and Max Wintermark, MD
- One-day **MINI SYMPOSIUM** on **TUMORS** - Organized by Girish M. Fatterpekar, MD, MBBS, DNB, Whitney B. Pope, MD, PhD and Gordon K. Sze, MD, FACR
- **Nobel Prize Laureate, Stanley Prusiner, MD, Keynote Speaker, on Prions and Alzheimer's Disease, Parkinson's Disease, and Other Neurodegenerative Disorders**
- **More "Hands-On" Experience Applicable to Your Practices**
- **Young Professionals Programming**
- **Expanded Self-Assessment Module (SAM) Session Programming Throughout the Week**

ASNR MONTREAL 2014

ASFNR ASHNR ASPNR ASSR SNIS

PROGRAMMING DEVELOPED IN COOPERATION WITH THE...

- American Society of Functional Neuroradiology (ASFNR) David J. Mikulis, MD
- American Society of Head and Neck Radiology (ASHNR) Yoshimi Anzai, MD, MPH
- American Society of Pediatric Neuroradiology (ASPNR) Richard L. Robertson, MD
- American Society of Spine Radiology (ASSR) Meng Law, MD, MBBS, FRACR
- Society of NeuroInterventional Surgery (SNIS) Peter A. Rasmussen, MD

Abstract Deadline:
Friday, December 13, 2013!

Abstract submission site is available. Please visit www.asnr.org/2014 for more information.

TO REQUEST PROGRAMMING AND REGISTRATION MATERIALS FOR THE ASNR 52ND ANNUAL MEETING, CONTACT:

ASNR 52ND ANNUAL MEETING
c/o American Society of Neuroradiology
800 Enterprise Drive, Suite 205
Oak Brook, Illinois 60523-4216

Phone: 630-574-0220
Fax: 630-574-0661
Email: meetings@asnr.org
Website: www.asnr.org/2014

Scan Now
to visit our website

Call for *AJNR* Editorial Fellowship Candidates

ASNR and *AJNR* are pleased once again in 2014 to join efforts with other imaging-related journals that have training programs on editorial aspects of publishing for trainees or junior staff (3–5 years after training) such as *Radiology* (Olmsted fellowship), *AJR* (Figley and Rogers fellowships [USA and international respectively]), and *Radiologia* (from Spain).

Goals:

1. Increase interest in "editorial" and publication-related activities in younger individuals.
2. Increase understanding and participation in the *AJNR* review process.
3. Incorporate into *AJNR's* Editorial Board younger individuals who have previous experience in the review and publication process.
4. Fill a specific need in neuroradiology not offered by other similar fellowships.
5. Increase the relationship between "newer" generations of neuroradiologists and more established individuals.
6. Increase visibility of *AJNR* among younger neuroradiologists.

Activities of the Fellowship:

1. Serve as "Editorial Fellow" for one year. This individual will be listed on the masthead as such and will receive a certificate stating his/her activities at the end of the service period.
2. Review at least one manuscript per month for 12 months. Evaluate all review articles submitted to *AJNR*. Access to our electronic manuscript review system will be granted so that the candidate can learn how these systems work.
3. Be involved in the final decision of selected manuscripts together with the EIC.
4. Participate in all monthly telephone Senior Editor conference calls.
5. Participate in all meetings of the Editors and Publications Committee during the annual meetings of ASNR and RSNA as per candidate's availability. *AJNR*/ASNR will not provide funding for this activity but may offer a discounted fee for its annual meeting.
6. Evaluate progress and adjust program to specific needs in biannual meeting or telephone conference with the EIC.
7. Write at least one editorial for *AJNR*.
8. Embark on an editorial scientific or bibliometric project that will lead to the submission of an article to *AJNR* or another appropriate journal as determined by *AJNR's* EIC. This project can be done in conjunction with the EIC or one of the Senior Editors.
9. Serve as liaison between *AJNR* and ASNR's Young Professionals Network and the 3 YPs appointed to *AJNR* as special consultants. Participate in meetings and telephone calls with this group. Design one electronic survey/year polling the group regarding readership attitudes and wishes.
10. Recruit trainees as reviewers as determined by the EIC.
11. Participate in Web improvement projects.
12. Potentially become a member of *AJNR's* Editorial Board at the end of the fellowship.
13. Invite Guest Editors for *AJNR's* News Digest to cover a variety of timely topics.

Qualifications:

1. Be a fellow in neuroradiology from North America, including Canada (this may be extended to include other countries).
2. Be a junior faculty neuroradiology member (<3 years) in either an academic and private environment.
3. Provide an "end" of fellowship report to *AJNR's* EIC and ASNR's Publications Committee.
4. Be an "in-training" or member of ASNR in any other category.

Application:

1. Include a short letter of intent with statement of goals and desired research project. CV must be included.
2. Include a letter of recommendation from the Division Chief or fellowship program director. A statement of protected time to perform the functions outlined is desirable.
3. Applications will be evaluated by *AJNR's* Senior Editors and the Chair of the Publications Committee prior to the ASNR meeting. The name of the selected individual will be announced at the meeting.
4. Applications should be received by March 3, 2014 and sent to Ms. Karen Halm, *AJNR* Managing Editor, electronically at khalm@asnr.org.

CALL FOR APPLICATIONS

ARRS/ASNR Scholarship in Neuroradiology

Applications are being accepted in any area of research related to neuroradiology. Applications should describe the unique nature of the research effort independent of existing research efforts, and should have well-defined goals for the funding period of the grant.

The two-year scholarship will provide $150,000 ($75,000 per year); it requires a minimum 50 percent time commitment.

Application Deadline: January 15

Eligibility

- Applicant must be a member of both ARRS and ASNR at the time of application and for the duration of the award.
- Applicant must hold a full-time faculty position in a department of radiology, radiation oncology, or nuclear medicine within a North American educational institution at the time of application.
- Applicant must be within 5 years of initial faculty appointment with an academic rank of instructor or assistant professor, (or equivalent).
- Applicant must have completed advanced training and be certified by the American Board of Radiology (ABR) or on track for certification.
- Applicant must have completed neuroradiology training in an accredited ACGME neuroradiology fellowship program.

The deadline for receipt of applications is **January 15, 2014.**

Log onto **www.arrs.org/RoentgenFund/Scholarships/ARRS_ASNR.aspx** or **foundation.asnr.org** for more information.

This scholarship is funded by The Foundation of the American Society of Neuroradiology in conjunction with The Roentgen Fund.® To support neuroradiology research and education with a generous tax-deductible contribution, visit **foundation.asnr.org**.

www.asnr.org

FOUNDATION OF THE ASNR

AJNR

AMERICAN JOURNAL OF NEURORADIOLOGY

Publication Preview at www.ajnr.org features articles released in advance of print. Visit www.ajnrblog.org to comment on AJNR content and chat with colleagues and AJNR's News Digest at http://ajnrdigest.org to read the stories behind the latest research in neuroimaging.

NOVEMBER 2013 • VOLUME 34 • NUMBER 11 • WWW.AJNR.ORG

AJNR (Am J Neuroradiol ISSN 0195–6108) is a journal published monthly, owned and published by the American Society of Neuroradiology (ASNR), 800 Enterprise Drive, Suite 205, Oak Brook, IL 60523. Annual dues for the ASNR include $170.00 for journal subscription. The journal is printed by Cadmus Journal Services, 5457 Twin Knolls Road, Suite 200, Columbia, MD 21045; Periodicals postage paid at Oak Brook, IL and additional mailing offices. Printed in the U.S.A. POSTMASTER: Please send address changes to American Journal of Neuroradiology, P.O. Box 3000, Denville, NJ 07834, U.S.A. Subscription rates: nonmember $370 ($440 foreign) print and online, $300 online only; institutions $430 ($495 foreign) print and basic online, $850 ($915 foreign) print and extended online, $355 online only (basic), extended online $770; single copies are $35 each ($40 foreign). Indexed by PubMed/Medline, BIOSIS Previews, Current Contents (Clinical Medicine and Life Sciences), EMBASE, Google Scholar, HighWire Press, Q-Sensei, RefSeek, Science Citation Index, and SCI Expanded.

Simplify
the MOC Process

Manage
your CME Credits Online

CMEgateway.org

It's Easy and Free!

Log on to CME Gateway to:

- View or print reports of your CME credits from multiple societies from a single access point.
- Print an aggregated report or certificate from each participating organization.
- Link to SAMs and other tools to help with maintenance of certification.

American Board of Radiology (ABR) participation!

By activating ABR in your organizational profile, your MOC–fulfilling CME and SAM credits can be transferred to your own personalized database on the ABR Web site.

Sign Up Today!

go to CMEgateway.org

Available to Members of Participating Societies

- American Board of Radiology (ABR)
- American College of Radiology (ACR)
- American Roentgen Ray Society (ARRS)
- American Society of Neuroradiology (ASNR)
- Commission on Accreditation of Medical Physics Educational Programs, Inc. (CAMPEP)
- Radiological Society of North America (RSNA)
- Society of Interventional Radiology (SIR)
- SNM
- The Society for Pediatric Radiology (SPR)

Predators and Cranks

M. Castillo, *Editor-in-Chief*

A few years ago I received an e-mail invitation to write a review article on MR spectroscopy from a journal I did not know. Thinking that it was a good project for one of my visiting research fellows, I accepted. It took us about 3 months to write and illustrate the article, and when we submitted it, we signed, as is commonly done, their copyright agreement. Much to my surprise, we shortly thereafter received an invoice for US $2700 because this journal operated under the "open access" model. Paying that much would have used much of my "book and travel" allowance, so we retracted the publication only to find that retractions were impossible! After much back and forth and threatening to get the University's lawyers involved, they returned the article to us (it was later published in the *Neuroimaging Clinics*, a bona fide journal, not open access). While there is nothing wrong with open access and the *American Journal of Neuroradiology* (*AJNR*) supports it as long as our current financial model remains stable, it is a system ripe for abuse by many.

In April 2013, the *New York Times* (*NYT*) published a piece on "predatory" medical journals and scientific meetings.[1] It described how a group of scientists were duped into participating at a meeting that initially seemed legitimate (see below). Welcome to the world of "pseudoacademia," where newly created outfits recruit speakers and authors strictly for profit in activities that are not linked to any respectable scientific society, group, or journal.

There are currently hundreds of companies that "sponsor" meetings and journals under the rubric of "open access." The open access movement arose from the need to share information with all of those who are interested in it while trying to avoid paying for subscriptions or buying individual articles, especially if these sprang from investigations financed by public funds. Although controversial, open access makes articles easier to find and quote and is thus beneficial to authors and readers alike. There are legitimate, prestigious open access journals such as ones published by the *Public Library of Science*, which rightly demand a fee for publication. Predatory publishers take advantage of the open access movement and of our never-ending hunger to fill our resumes and be promoted and have developed journals that closely resemble genuine ones. In September these fraudulent activities hit home when many of us received an e-mail message from Ivy Union Publishing Company (a well-known publisher of predatory journals) recruiting editorial board members for the new *AJNR* (*American Journal of Neuroscience Research*). The e-mail was designed in blue tones similar to those used by our *AJNR*, and even the font used was exactly the same as the one in our previous cover design. Immediately we contacted our lawyers, who sent a letter to Ivy Union Publishing demanding that they cease to use our trademark, to which, not surprisingly, we have yet to receive a response.

http://dx.doi.org/10.3174/ajnr.A3774

Jeffrey Beall, an academic librarian at the University of Colorado, has created a list of predatory journals (commonly known as "Beall's list") and their publishers.[2] Mr Beall divides these publications into those questionable publishers that have portfolios of up to hundreds of journals (the Ivy Union Publishing Web site had 131 pages of journal titles when I looked at it) and individual journals published outside traditional platforms. Before submitting an article to a new journal, Mr Beall suggests that one checks his list of criteria for determining predatory open access journals and publishers found at http://scholarlyoa.com/2012/11/30/criteria-for-determining-predatory-open-access-publishers-2nd-edition. Briefly, any of the following should steer one away from submitting articles to a journal:

1) The name of the journal is incompatible with its scope.
2) Its national base is not clear.
3) Submission-to-publication periods are incompatible with traditional peer review (my comment: less than 21 days is suspicious).
4) No clear editor and no editorial board.
5) No Impact Factor listed.
6) Unprofessional, hastily put together Web site.
7) No mention of fees until an article has been accepted.

Today, there are more than 4000 predatory journals that publish 10%–15% of all open access articles. Not only are they tricking authors into submitting and paying for their articles, they offer members of their editorial boards as much as 20% of the author fees. Once you become a member of one of these editorial boards, it is basically impossible to be removed as several anecdotes in the *NYT* article recount.[1] Needless to say, Mr Beall is being sued by several of these publishers, has been a victim of vicious on-line comments, and is the subject of Internet campaigns to discredit him.[3]

Because rapidly developing economies are generating a significant number of new researchers, most "open access" publishers are springing up there, but their Web sites manipulate the truth to appear as if they are headquartered in the United States, United Kingdom, Australia, or Canada (though no contact information is found on the Ivy Union Publishing Web site, our investigation led to an address in Delaware, which then led us to an address in Boston). The geographic bases of predatory journals can be found on Semantico.com. Data there show that by plugging the IP addresses of 192 predatory journals and 321 predatory publishers into a geolocator, one finds that 65% of such journals and 67% of publishers were registered in the United States. Because one can never be sure whether the locations linked to the addresses are real or fake, it is always possible that indeed these publications actually started in the United States.

Predatory journals care little about the quality of science and are known to sometimes publish plagiarized work.[4] Their articles receive little professional formatting to save costs, and they are never listed in the larger citation databases such as PubMed, Web of Science, or Scopus; a fact that nullifies their open access spirit because they are very hard to find and quote. Sometimes, predatory journals even publish articles without the author's permis-

sion. Many of these journals offer to translate their articles into 50 different languages, when, in reality, this feature only directs the readers to use the free Google Translate service for this purpose.

A glaring example of types of peer review and acceptances carried out by predatory journals is illustrated by the following hoax. Two well-regarded professionals utilized SCIgen (http://pdos.csail.mit.edu/scigen), a computer program that generates nonsensical articles dealing with computer science, to create an article that was submitted to a predatory journal called *The Open Information Science Journal*.[5] The authors even gave their affiliation as the Center for Research in Applied Phrenology (CRAP)! After the article was accepted, they received a bill for US $800 to be sent to a PO Box located in the United Arab Emirates. However, to be fair, SCIgen was also used to generate a similar article that was submitted and accepted by a reputable journal published by Elsevier.

The problem gets worse, and the lines, blurrier. Between 2000 and 2005, publishing giant Elsevier published 6 fake medical journals, all sponsored by pharmaceutical companies, and as if that was not bad enough, these journals often contained reprinted articles that were favorable to products manufactured by the sponsoring companies.[6] Immediately after this was publicly disclosed, the CEO of Elsevier's Health Sciences Division issued an apology and a reassurance that this would not occur any more.

All of the above also extends to congresses and meetings. In the previously mentioned *NYT* article,[1] researchers were tricked into presenting at a meeting called "Entomology-2013" when they thought they were presenting at the well-recognized and prestigious "Entomology 2013" (do you see the difference in the titles?). Later they were charged for participating at the meeting. Last month I received an invitation to participate in the 1st International Conference of Radiology to be held in Raleigh, North Carolina (just 30 miles away from where I live). The invitation that came from some outfit located in China promised me time at the podium, dinners, "mingling" with the best researchers, and a name badge that would clearly identify me as a prominent participant and world expert. When I did not respond, I was bombarded with spamlike e-mail messages asking me to confirm my participation.

These so-called "crank" meetings promise luminary speakers who often do not have enough valid publications to support this denomination or simply have not published their research.[7] To me, it is not clear who attends and who lectures; I do not know anyone who has.

One of the best known crank meetings is Autism One (which is held in Canada and the United States).[7] In it, researchers of dubious integrity give talks, and the main speaker is generally Jenny McCarthy. Ms McCarthy, a former *Playboy* Playmate, is a popular television show host and author of books on parenting, alternative medicine, and autism. Other guest speakers generally have published their results in blogs and popular media and, at best, in predatory journals. Unfortunately, serious institutions such as the University of Toronto, the Sick Kids Foundation, and even the American Academy of Pediatrics have been suckered into debacles stirred by presentations at these autism meetings.

I urge you to look in your own backyard for predators. Many institutional libraries, when choosing journal subscriptions, have rules that force them to buy those under the categories of "Gold or Green Open Access" (one archives the articles for the authors; in the other, the authors themselves archive the articles) or those that adhere to the Creative Commons license agreement. Gold or green has nothing to do with paying to get published, just with access. Most predatory journals claim to be gold or green to make themselves attractive to libraries. Like true predators, these journals stay around just while there is prey. Anecdotally, I heard that a predatory publisher abruptly closed its doors (and Web site) once its profits reached US $100 million. Beware, because predatory journals will take away not only your money but, more important, your prestige, reputation, and self-respect.

REFERENCES

1. Kolata G. **Scientific articles accepted (personal checks, too).** *New York Times.* April 7, 2013. http://www.nytimes.com/2013/04/08/health/for-scientists-an-exploding-world-of-pseudo-academia.html?pagewanted=all&_r=0. Accessed September 16, 2013
2. Beall's list of predatory, open-access publishers. http://www.academia.edu/1151857/Bealls_List_of_Predatory_Open-Access_Publishers. Accessed September 16, 2013
3. Butler D. **Investigating journals: the dark side of publishing.** *Nature* 2013;445. http://www.nature.com/news/investigating-journals-the-dark-side-of-publishing-1.12666. Accessed September 16, 2013
4. Sanchez J. **Predatory publishers are corrupting open access.** *Nature* 2012;489. http://www.nature.com/news/predatory-publishers-are-corrupting-open-access-1.11385. Accessed September 16, 2013
5. Aldhous P. **CRAP paper accepted by journal.** *New Scientist* 2009. http://www.newscientist.com/article/dn17288-crap-paper-accepted-by-journal.html#.Ujc7HD-Jnq5. Accessed September 16, 2013
6. Grant B. **Elsevier published 6 fake journals.** *The Scientist* 2009. http://www.the-scientist.com/?articles.view/articleNo/27383/title/Elsevier-published-6-fake-journals. Accessed September 16, 2013
7. Gorski D. **Crank "scientific" conferences: a parody of science-based medicine that can deceive even reputable scientists and institutions**. *Science-Based Medicine* 2009. http://www.sciencebasedmedicine.org/crank-conferences-a-parody-of-science-based-medicine-that-can-suck-in-even-reputable-scientists-and-institutions. Accessed September 16, 2013

Stroke Imaging: Diffusion, Perfusion, but No More Confusion!

M. Wintermark, P. Sanelli, and C.C. Meltzer

After attending numerous sessions dedicated to stroke imaging at national conferences, one cannot help but leave confused with unanswered questions because the presentations consist of diametrically opposed positions regarding the imaging of patients with acute stroke. For example, some presenters advocate for the use of advanced imaging techniques, while others maintain that noncontrast CT alone is indicated to guide treatment decisions. Perfusion imaging is praised by some yet criticized by others regarding its added value in the management and treatment of patients with acute stroke. Additionally, there is no consensus regarding the preferred use of CT or MR imaging in the acute stroke setting. Therefore, it has become challenging to standardize and optimize the imaging evaluation of patients with suspected acute stroke across sites.

A wide variety of imaging techniques has become available to assess vascular lesions and brain tissue status in patients with acute stroke. In addition to scientific evidence of effectiveness, important variables that influence imaging choices include constraints of time, cost, access to imaging modalities, preferences of treating physicians, availability of expertise, and availability of endovascular therapy.

In the article entitled, "Imaging Recommendations for Acute Stroke and Transient Ischemic Attack Patients: A Joint Statement by the American Society of Neuroradiology, the American College of Radiology, and the Society of NeuroInterventional Surgery,"[1] we are proposing a simple, pragmatic approach that will allow the reader to develop an optimal imaging algorithm for patients with stroke at their institution.

The key elements of this consensus article can be summarized as follows:

- The primary goal of imaging patients with acute stroke symptoms is to distinguish between hemorrhagic and ischemic stroke. In patients with ischemic stroke, secondary goals of imaging before initiating revascularization interventions with intravenous thrombolysis or endovascular therapies include identification of the location and extent of intravascular clot and the presence and extent of infarct (irreversibly damaged tissue) and ischemic penumbra (hypoperfused tissue at risk for infarction).
- Early identification of the stroke etiology or mechanism (carotid atherosclerotic disease or other treatable causes) is critical to treatment decisions and long-term management.
- There is strong evidence supporting the use of IV tissue plasminogen activator as a recanalization therapy to improve clinical outcomes during the 0- to 3-hour time window and during the 3- to 4.5-hour time window following symptom onset. This benefit is despite an increased risk of symptomatic intracranial hemorrhage after infusion. The timely use of imaging of the brain to exclude hemorrhage in patients with the clinical diagnosis of stroke and before initiating IV thrombolytic therapy is supported by strong evidence and FDA guidelines. In patients with acute stroke who are candidates for IV thrombolysis (0- to 4.5-hour time window), either noncontrast CT or MR imaging of the brain is recommended to exclude intracranial hemorrhage and determine the extent of ischemic changes. Most important, imaging in patients who are potential candidates for IV thrombolysis should not delay administration of IV thrombolysis, because "time is brain."
- There is limited evidence supporting the use of intra-arterial thrombolytic agents up to 6 hours after symptom onset. Also, the evidence supporting improved clinical outcomes with first-generation mechanical embolectomy devices up to 8 hours following symptom onset, compared with standard medical care, has been challenged by the results of the Mechanical Retrieval and Recanalization of Stroke Clots Using Embolectomy (MR RESCUE),[2] Interventional Management of Stroke (IMS III),[3] and Intra-arterial Versus Systemic Thrombolysis for Acute Ischemic Stroke (SYNTHESIS EXP)[4] trials. Although the next generation of mechanical embolectomy devices (stent–retrievers) has received FDA approval, their clinical efficacy has not yet been established. In patients with acute stroke who are candidates for endovascular therapy, vascular imaging (CTA, MRA, conventional angiography) is strongly recommended during the initial imaging evaluation. Perfusion imaging may be considered to assess the target tissue "at risk" for reperfusion therapy. However, the accuracy and usefulness of perfusion imaging to identify and differentiate viable tissue have not been well-established.
- In patients with acute stroke, vascular imaging of the head and neck should be performed to evaluate the mechanism of stroke and assess the risk of future stroke.

These recommendations are detailed in our article. The strength of the available evidence supporting various imaging options is presented as well as considerations of available resources. It is our intention that this review and its recommendations will provide a foundation for optimizing the value of imaging in patients with acute stroke.

http://dx.doi.org/10.3174/ajnr.A3691

REFERENCES

1. Wintermark M, Sanelli P, Albers GW, et al. **Imaging recommendations for acute stroke and transient ischemic attack patients: a joint statement by the American Society of Neuroradiology, the American College of Radiology, and the Society of NeuroInterventional Surgery.** *AJNR Am J Neuroradiol* 2013;34:E117–E27
2. Kidwell CS, Jahan R, Gornbein J, et al. **A trial of imaging selection and endovascular treatment for ischemic stroke.** *N Engl J Med* 2013;368:914–23
3. Broderick JP, Palesch YY, Demchuk AM, et al. **Endovascular therapy after intravenous T-PA versus T-PA alone for stroke.** *N Engl J Med* 2013;368:893–903
4. Ciccone A, Valvassori L, Nichelatti M, et al, for the SYNTHESIS Expansion Investigators. **Endovascular treatment for acute ischemic stroke.** *N Engl J Med* 2013;368:904–13

Off-Label Use of Drugs and Devices in the Neuroendovascular Suite

M.M. Abdihalim, A.E. Hassan, and A.I. Qureshi

ABSTRACT

SUMMARY: The off-label use of drugs and devices in neuroendovascular procedures is common. Neurointerventionalists should be well aware of the level of evidence available in support of the off-label use of drugs and devices in their practice and some of the potential adverse events associated with them. These uses are categorized as I or II if they have been evaluated as primary or ancillary interventions in prospective trials/registries of neuroendovascular procedures and III if they were evaluated in case series. Category IV use is based on evaluation as primary or ancillary interventions in prospective trials/registries of non-neuroendovascular procedures. Physicians are allowed to use off-label drugs and procedures if there is strong evidence that they are beneficial for the patient. The neurointerventional professional societies agree that off-label use of drugs and devices is an important part of the specialty, but practicing providers should base their decisions on sound evidence when using such drugs and devices.

ABBREVIATIONS: GDC = Guglielmi detachable coil; IA = intra-arterial; ICH = intracerebral hemorrhage; PROACT = Prolyse in Acute Cerebral Thromboembolism; UK = urokinase

Off-label[1] use for prescription drugs, biologics, and approved medical devices is any use that is not specified in the labeling approved by the US Food and Drug Administration. Labeling includes any written material that accompanies, supplements, or explains the product. In neuroendovascular procedures practice, this use is relatively common.[1] However, the knowledge among practicing neuroradiologists, endovascular neurosurgeons, and interventional neurologists regarding the principles and consequences of using off-label products in their practice is lacking.

If physicians use a product for an indication not in the approved or cleared labeling, they have the responsibility to be well-informed about the product, to base its use on firm scientific rationale and on sound medical evidence, and to maintain awareness of the use and effects of the product. FDA regulations allow the exchange and dissemination of scientific information on the unapproved uses of a product in response to unsolicited requests from physicians, continuing medical education programs, and peer-reviewed scientific and medical journals.[1]

This Review Article provides data with the following objectives: 1) allowing physicians to recognize off-label use of products within the scope of their practice, 2) identifying instances when the off-label use of medical products is recognized as a generally accepted medical standard within the physician community, 3) summarizing our experience using off-label products in our practice, and 4) providing recommendations from professional organizations on off-label use of drugs and medical devices.

OFF-LABEL USE OF DRUGS IN THE NEUROENDOVASCULAR SUITE

The following summarizes the most common drugs used off-label within the neuroendovascular suite.

Intra-Arterial Use of Thrombolytics

Approved Use of Thrombolytics. For acute ischemic stroke, intravenous administration within 3 hours of symptom onset; massive pulmonary embolus; and acute myocardial infarction.

Off-Label Use. Intra-arterial administration for acute ischemic stroke up to 9 hours after symptom onset (category I). The only FDA-approved thrombolytic for acute ischemic stroke treatment is IV alteplase (Activase; Genentech, South San Francisco, California).[2] Treatment should only be initiated within 3 hours after the onset of stroke symptoms and after exclusion of intracranial hemorrhage by a cranial CT scan. A subgroup of patients with ischemic stroke is treated by using intra-arterial thrombolytics with various criteria either alone or in combination with IV

From the Zeenat Qureshi Stroke Research Center (M.M.A., A.E.H., A.I.Q.) and Department of Radiology (M.M.A.), University of Minnesota, Minneapolis, Minnesota.

Please address correspondence to Mohamed Abdilhalim, MD, Department of Radiology, University of Minnesota, Diagnostic Radiology MMC 292, 420 Delaware St SE, Minneapolis, MN 55455; e-mail: abdi0018@umn.edu

Indicates open access to non-subscribers at www.ajnr.org

Indicates article with supplemental on-line table

http://dx.doi.org/10.3174/ajnr.A3447

thrombolytics and/or mechanical thrombectomy.[3,4] Intra-arterial urokinase (Abbokinase; Abbott Laboratories, Chicago, Illinois) was the most commonly used intra-arterial thrombolytic for acute ischemic stroke before 1999.[5] However, an FDA action resulted in withdrawal of urokinase from the market for 4 years. FDA inspectors found that Abbott was not taking adequate steps to test for infection in or prevent contamination of the kidney cells used to manufacture the drug.[6]

This withdrawal led to use of other thrombolytic medications including prourokinase, reteplase, tenecteplase, and alteplase as part of endovascular treatment for acute ischemic stroke.[5] Prourokinase was the only thrombolytic that was considered for FDA approval on the basis of the results of PROACT I and II trials.[7,8] In both of those trials, patients were given intra-arterial (IA) prourokinase within 6 hours of symptoms onset. These trials demonstrated an increased rate of recanalization, 57.7% and 67% (treatment group) versus 14.3% and 18% (controls).[7,8] Moreover, a recent meta-analysis of 5 randomized controlled trials of IA thrombolysis of acute ischemic stroke with 395 participants showed IA thrombolysis by using pro-UK, UK, or recombinant tissue plasminogen activator substantially increased the rates of recanalization and had excellent clinical outcomes. The increased hemorrhage frequencies were not associated with any increase in mortality.[9] The off-label use of thrombolytics is recognized as a generally accepted medical standard within the physician community (category I). The formulation of thrombolytics (more concentrated compared with IV-use formulation) and the maximum dose used require sound principles or previous studies that have reported on these issues.[10] Third-generation thrombolytics, tenecteplase (17 ± 7 minutes), and reteplase (15–18 minutes), have longer half-lives and greater penetration in the thrombus matrix than alteplase (5 minutes).[11]

Platelet Glycoprotein IIb/IIIa Inhibitors

Approved Use. Patients with acute coronary syndrome who are treated medically only and those undergoing percutaneous coronary intervention; and patients undergoing percutaneous coronary intervention including stent placement.

Off-Label Use. Intraprocedural thrombosis and ischemic events following endovascular procedures (category III). The experience of using platelet glycoprotein IIb/IIIa inhibitors abciximab (Reopro; Johnson and Johnson, Malvern, Pennsylvania), eptifibatide (Integrillin; Merck, Whitehouse Station, New Jersey), and tirofiban (Aggrasat; Merck, West Point, Pennsylvania) in neurointerventional procedures is limited. These agents are effective in reducing ischemic complications of acute myocardial infarctions and thrombotic complications associated with percutaneous coronary interventions.[12-14] The FDA-approved indications of glycoprotein IIb/IIIa inhibitors are in acute coronary syndromes and as an adjunct to percutaneous coronary interventions. The off-label use of glycoprotein IIb/IIIa inhibitors was evaluated in several case series and clinical trials focusing on patients undergoing endovascular treatment for acute ischemic stroke or those undergoing carotid artery stent placement.[15-17] The use of platelet glycoprotein IIb/IIIa inhibitors in both of these applications was discontinued for the most part. The premature discontinuation of the Abciximab in Emergency Treatment of Stroke Trial II after 808 patients with acute ischemia were enrolled due to high rates of intracranial hemorrhage associated with IV abciximab (IV bolus followed by IV infusion) limited the enthusiasm for further evaluation in ischemic stroke.[18] The routine use in carotid artery stent placement was discontinued after a randomized trial, and 2 single-center comparisons with historical controls did not demonstrate any reduction in periprocedural ischemic events.[19-21] The relatively high rate of fatal intracerebral hemorrhages (ICHs) observed in studies also reduced the enthusiasm for using these agents.[22] Some local institutional review boards may require that planned use of these agents involve informing patients or relatives regarding such complications. The current use in neuroendovascular procedures is limited to intraprocedural thrombosis and ischemic events (category III).[16,23,24] Glycoprotein IIb/IIIa inhibitors are approved only for IV administration but are usually administered by IV infusion, IA bolus followed by IV infusion, or IV bolus followed by IV infusion.[15]

Physicians administering these agents should be well aware of the principle of dose conversion of any agent requiring special formulation, reversal half-lives, and monitoring for thrombocytopenia. Abciximab requires filtration, while eptifibatide and tirofiban do not, before administration. Dosing of both eptifibatide and tirofiban should be adjusted in patients with renal failure (renal elimination) but this is not necessary with abciximab (eliminated by the reticuloendothelial system).[25] Although rare, thrombocytopenia can occur within 1–24 hours after infusion.[26] When these agents are infused, platelets should be monitored 1–2 hours after infusion and again 24 hours after infusion. Platelets should recover rapidly after discontinuation.[27] The off-label use of platelet glycoprotein IIb/IIIa inhibitors is recognized as a generally accepted medical standard within the physician community in certain situations such as intraprocedural thrombosis.

Calcium Channel Blockers

Approved Use. Cerebral vasospasm (nimodipine), hypertension, angina, atrial arrhythmia, and paroxysmal supraventricular tachycardia.

Off-Label Use. Intra-arterial administration for improving arterial luminal narrowing in patients with symptomatic cerebral vasospasm due to subarachnoid hemorrhage in native intracranial arteries (category III).

Randomized controlled trials have shown that oral nimodipine (Nimotop; Bayer, West Haven, Connecticut) is effective in reducing delayed ischemic neurologic deficits caused by cerebral vasospasm following subarachnoid hemorrhage.[28-30] Nimodipine, 60 mg orally every 4 hours for 21 consecutive days started within 96 hours of subarachnoid hemorrhage, is FDA-approved to prevent cerebral vasospasm.[31]

Intra-arterial or intravenous use of verapamil, nimodipine (Nimotop), and nicardipine (Cardene; Baxter Healthcare, Deerfield, Illinois) have all been reported to be effective and safe in the treatment of cerebral vasospasm (category III).[10,32-35] The off-label use of calcium channel blockers in treating cerebral vasospasm is recognized as a generally accepted medical practice within the physician community; however, the treating physician

must ensure that adequate hemodynamic monitoring is performed on patients receiving these agents. Low doses of intra-arterial calcium channel blockers were not associated with significant hemodynamic changes, but high-dose nicardipine was associated with hypotension.[34] The duration of monitoring must be adequate on the basis of the half-life of the agent: verapamil (4 minutes), nimodipine (7 minutes), and nicardipine (3 minutes). Physicians must also be familiar with and prepared to address commonly observed adverse events of hypotension and bradycardia. These agents are all category C medications during pregnancy.

Magnesium Sulfate

Approved Use. Atrial paroxysmal tachycardia, eclampsia, cerebral edema, barium poisoning, seizures associated with epilepsy, glomerulonephritis, or hypothyroidism.

Off-Label Use. Intra-arterial administration for improving arterial luminal narrowing in patients with symptomatic cerebral vasospasm due to subarachnoid hemorrhage in native intracranial arteries (category III).

Magnesium sulfate is a noncompetitive calcium channel blocker.[36] Suarez et al[37] reviewed 17 studies including a single phase III randomized controlled trial and 6 phase II randomized controlled trials on the effects of magnesium sulfate on cerebral vasospasm. They reported that the studies suggested either no net benefit or uncertain trade-offs.[37] Shah et al[38] reported that a combination of IA magnesium (0.25–1 g) and nicardipine (2.5–20 mg) was well-tolerated in a small case series of patients with cerebral vasospasm.

Heparin, Low-Molecular-Weight Heparin, and Direct Thrombin Inhibitors

Approved Use. Multiple indications including venous thrombosis or thromboembolism, pulmonary embolism, cardiac surgery, and heparin-induced thrombocytopenia requiring anticoagulation (direct thrombin inhibitors).

Off-Label Use. Continuous infusion or intermittent boluses during neuroendovascular procedures (category II). Heparin is primarily used in neurointerventional procedures to reduce the risk of perioperative and immediate postoperative ischemia.[39] Measurement of the activated coagulation time is the preferred method for evaluation of responses to heparin because the activated coagulation time demonstrates a linear heparin dose-response curve, even at the higher doses used during interventional procedures.[5] The target activated coagulation time in neurointerventional procedures is 250–350 seconds.[39] Vance et al[40] found that the administration of heparin is safe during the first 24 hours after endovascular treatment of ruptured intracranial aneurysms. The measurement of the intensity of anticoagulation by activated coagulation time requires understanding of the methods and instruments used for such measurements.[41]

Unlike unfractionated heparin and low-molecular-weight heparin, direct thrombin inhibitors such as bivalirudin (Angiomax; The Medicines Company, Parsippany, New Jersey), lepirudin (Refludan; Bayer), or argatroban (Argatroban; GlaxoSmithKline, Research Triangle Park, North Carolina) are antithrombin III–independent inhibitors of thrombin that are effective against thrombin even after it binds to fibrin. Direct thrombin inhibitors are not associated with heparin-induced thrombocytopenia.[5] Direct thrombin inhibitors are primarily used for the anticoagulation of patients with heparin-induced thrombocytopenia or those who are at risk for heparin-induced thrombocytopenia.[42] A recent small retrospective study showed that a bivalirudin bolus of 0.6 mg/kg followed by an infusion of 1.25 mg/kg/h until the target activated coagulation time was achieved was a safe alternative to heparin infusion for anticoagulation during neuroendovascular procedures.[43]

Aspirin and Clopidogrel

Approved Use. Aspirin: anesthesia, antipyretic, anti-inflammatory, myocardial infarction, prophylaxis for myocardial infarction, and cerebrovascular accident. Clopidogrel: percutaneous coronary intervention for non-ST elevation myocardial infarction, prophylaxis for cerebrovascular accident, myocardial infarction, and peripheral arterial disease.

Off-Label Use. Combined aspirin and clopidogrel after intracranial or craniocervical angioplasty and/or stent placement to prevent thrombosis and ischemic complications (category II). Aspirin leads to: irreversible inhibition of platelet cyclooxygenase-1 and production of thromboxane A_2, resulting in platelet inhibition.[5] Aspirin is commonly used in the prevention of thromboembolic events during or following neurointerventional procedures such as aneurysm embolization or carotid and intracranial stent placement.[44] van den Bergh et al[45] showed that the use of antiplatelets during or after aneurysm embolization improved outcome in patients with SAH in the International Subarachnoid Aneurysm Trial. Several retrospective case series showed that antiplatelet therapy with aspirin and/or clopidogrel reduced thromboembolic events of coil embolization for unruptured intracranial aneurysms.[46,47] Clopidogrel (Plavix; Sanofi Aventis, Bridgewater, New Jersey) inhibits the binding of adenosine diphosphate to its platelet receptor, leading to inhibition of platelet aggregation.[5] It is approved for the prevention of stroke in patients with recent history of stroke, myocardial infraction, or established peripheral arterial disease.[48,49]

Dual antiplatelet therapy is routinely used after intracranial angioplasty and intracranial or extracranial stent placement. However, the duration of dual antiplatelet therapy is not well-defined.[50] Most of the data regarding periprocedural antiplatelet management are derived from the coronary interventional literature.[51] A retrospective case series recently did not show increased adverse events from dual antiplatelet therapy beyond 1 month of the endovascular procedure.[51] Several large prospective multicenter trials (category II) have used aspirin and clopidogrel at least 3 days before the procedure and continued to 1–3 months after carotid artery stent placement (Carotid Revascularization Endarterectomy vs. Stenting Trial [CREST]/ Stenting and Angioplasty with Protection in Patients at High Risk for Endarterectomy [SAPPHIRE]/International Carotid Stenting Study [ICSS]/ Stent-Protected Angioplasty vs. Carotid Endarterectomy in Symptomatic Patients [SPACE]) and intracranial stent placement (Stenting vs. Aggressive Medical Management for Preventing Recur-

rent stroke in Intracranial Stenosis [SAMMPRIS]).[52-56] The safety and tolerability of these medications for a month following the procedure has been ascertained in 3121 patients with a very low rate of ICH (1.6%).[52-56] Two of the above trials (CREST and SAMMPRIS) permitted a bolus dose of clopidogrel (450 or 600 mg) if it could not be administered at least 3 days before the procedure.[44] Physicians should be aware of the risk of thrombotic thrombocytopenia purpura and bone marrow suppression with clopidogrel, which occurs in 1 case per 8500–26,000 patients treated with clopidogrel.

MEDICAL DEVICES

Intracranial and Extracranial Stent Placement

Drug-eluting balloon-expandable, bare-metal balloon-expandable, and self-expanding stents have all been used to treat medically refractory intracranial stenosis.[52,57-67] These case series suggested that intracranial stent placement can be performed safely and with high technical success.

Drug-Eluting Stents

Approved Use. Improving coronary luminal narrowing in patients with symptomatic ischemic disease due to de novo lesions in native coronary arteries.

Off-Label Use. Improving arterial luminal narrowing in patients with symptomatic ischemic disease due to de novo lesions in native intracranial arteries (category III). Drug-eluting stents indicated for coronary artery disease have significantly reduced restenosis rates.[68] Common drug-eluting stents include the Taxus Express (Boston Scientific, Natick, Massachusetts), which elutes paclitaxel; Cypher (Cordis, Miami Lakes, Florida), which elutes sirolimus; and Endeavor (Medtronic, Minneapolis, Minnesota), which elutes zotarolimus. There are no large trials evaluating the safety and efficacy of drug-eluting stents in the intracranial circulation, to our knowledge. Case series report on the use of Cypher and Taxus stents for intracranial stenosis and more frequently vertebral artery–origin stenosis (category III). Intracranial application of drug-eluting stents has been limited by their inflexibility, the tortuous nature of intracranial vessels, and the high rate of late stent thrombosis requiring prolonged dual antiplatelet use.[69,70] The benefit demonstrated in prevention of restenosis is less obvious in neurovascular applications. Fields et al[65] reported a restenosis rate of 21% with drug-eluting stents at the vertebral origin (3/14) and 38% (3/8) with intracranial use. Overall, restenosis rates were comparable with restenosis rates of bare metal stents. The off-label use must be performed with the understanding of the current guidelines for antiplatelet treatment with drug-eluting stents, which require 12 months of dual antiplatelet therapy and low-dose aspirin continued indefinitely.[71]

Balloon-Expandable Stents

Approved Use. Improving coronary luminal narrowing in patients with symptomatic ischemic disease due to de novo lesions in native coronary arteries.

Off-Label Use. Improving arterial luminal narrowing in patients with symptomatic ischemic disease due to de novo lesions in native intracranial arteries (category III).

The nonrandomized multicenter Stenting of Symptomatic Atherosclerotic Lesions in the Vertebral or Intracranial Arteries trial, which tested the Neurolink system (Guidant, St. Paul, Minnesota), showed 30-day and 1-year stroke rates of 7.2% and 10.9%, respectively. Recurrent stenosis occurred in 35% at 6 months.[67] The Neurolink stent was approved on the basis of that result on a Human Device Exemption approval; however, that stent is no longer being manufactured. Cruz-Flores and Diamond[72] reported a systematic review of 79 studies (1999 cases) on the efficacy and safety of intracranial artery angioplasty and stent placement for intracranial artery stenosis. The rate for perioperative stroke was 8%; perioperative death, 3%; perioperative stroke or death, 10%; and other perioperative complications (such as groin hematoma and arterial dissection), 10%. Additionally, in those studies with follow-up of at least 1 year, the risk of stroke or death was 6%.[73]

Qureshi et al[73] reported on the complications following angioplasty and/or stent placement in 92 patients in 3 medical centers. They found a nonsignificantly higher rate of periprocedural adverse events with balloon-expandable stents. However, Kurre et al[74] analyzed the large INTRASTENT registry, a European multicenter registry, and found no statistically significant difference in complications between 254 lesions treated with balloon-expandable stents and 155 lesions treated with self-expanding stents. Some examples of balloon-expandable stents include AVE S660 (Medtronic), BX sonic (Cordis), and Multi-Link (Abbott Vascular, Redwood, California). The off-label use of balloon-expandable stents for intracranial stenosis is category III. The unique technical challenges in placement with long intracranial lesions must be recognized.

The Apollo Stent for Symptomatic Atherosclerotic Intracranial Stenosis (ASSIST) study reported that stent-delivery failure was more frequent in lesions of >10 mm compared with those of <10 mm (25% versus 3%), though no relationship could be demonstrated with periprocedural stroke and death. The presence of tortuous proximal vessels (≥2 acute curves requiring traversing, judged by experience or trial), limited vessel length available distal to the lesion to allow stable placement of microwire, or the inability to place a guide catheter in the distal vertebral artery or internal carotid artery resulted in a higher technical failure rate than that reported for "on-label" indications.[75] The operator must be familiar with the inflation and deployment profiles of balloon-expandable stents to avoid excessive distention of the arterial wall and difficulties with deployment in contiguous arterial segments with major differences in diameter such as the vertebral-basilar junction.

Coronary Angioplasty Balloons for Intracranial Angioplasty

Approved Use. Improving coronary luminal narrowing in patients with symptomatic ischemic disease due to de novo lesions in native coronary arteries.

Off-Label Use. Improving arterial luminal narrowing in patients with symptomatic ischemic disease due to de novo lesions in native intracranial arteries (category III).

In a systematic review of 69 studies (33 primary angioplasty studies with coronary angioplasty balloons with a total of 1027

patients and 36 stent-placement studies with a total of 1291 patients), there were 91 strokes and deaths reported in the angioplasty-treated group compared with 104 in the stent-treated group during a 1-month period ($P = .5$). The 1-year stroke and death rate in patients treated with angioplasty was 20% compared with 14% in the stent-treated patients ($P = .009$). The pooled restenosis rate was 14% in the angioplasty-treated group compared with 11% in the stent-treated group ($P = .04$). No effect of the publication year of the studies was seen on the risk of stroke and death.[76] Common balloon catheters used for intracranial angioplasty included the Maverick (Boston Scientific), Ninja (Cordis), and Gemini (Guidant). New generations of semicompliant balloon catheters such as Gateway (Boston Scientific) with hydrophilic coating designed for low-pressure inflations and high navigability have been introduced recently, specifically for intracranial use. No clear data support the superiority of such angioplasty catheters over the existing coronary angioplasty catheters.

Self-Expanding Stents for Intracranial or Extracranial Dissections

Approved Use. Intracranial stenosis (Wingspan; Boston Scientific) and stent-assisted embolization of aneurysms (Neuroform; Boston Scientific).

Off-Label Use. Improving arterial luminal narrowing and reducing irregularity in patients with symptomatic ischemic disease due to arterial dissections in native intracranial or extracranial arteries (category III).

The Wingspan self-expandable stent and Gateway balloon (Boston Scientific) are currently an FDA-approved intracranial stent and angioplasty balloon system for intracranial atherosclerotic stenosis; and the Neuroform self-expandable stent (Boston Scientific) is currently approved for stent-assisted embolization of wide-neck intracranial aneurysms that are not candidates for surgical treatment. Both stents have been used for treatment of intracranial dissections. Other self-expandable stents used in extracranial and vertebral artery dissections include the X-pert Self-Expanding Stent System (Abbott Vascular), approved for palliation of malignant strictures in the biliary system, and the Fluency Plus (Bard Peripheral Vascular, Tempe, Arizona); and carotid artery stents are approved for atherosclerotic stenosis of the ICA.[76-79] Both the Wingspan and Neuroform stents have been used for treatment of extracranial dissections. There are some data that support a high technical success rate and long-term patency of these stents in intracranial or extracranial dissections (category III).[80] However, the operator must be aware that there are limited data on the comparative efficacy with medical treatment alone and long-term angiographic patency following the procedure.

Carotid Balloon Angioplasty

Approved Use. Aviator Plus and Savvy (Cordis) and Symmetry (Boston Scientific) in improving coronary or peripheral artery luminal narrowing in patients with symptomatic coronary artery or peripheral arterial disease.

Off-Label Use. Improving carotid artery luminal narrowing (category III). Carotid atherosclerotic disease is implicated in 15%–30% of all ischemic strokes.[81] Multiple studies have shown that carotid artery angioplasty and stent placement have long-term outcomes similar to those in carotid artery endarterectomy for patients with carotid artery disease.[49,53-56] Currently, the Aviator Plus and Viatrac 14 Plus are the only 2 angioplasty balloon catheters approved for carotid angioplasty. However, many different types of angioplasty balloons with unique properties approved for coronary artery or peripheral artery angioplasty have been used off-label for carotid artery angioplasty.[82,83] Understanding of the differences in angioplasty balloon properties is essential. Angioplasty balloon catheters can be grouped into 5 categories, as follows: standard (0.035-inch) balloon catheters (eg, Ultra-Thin Diamond; Boston Scientific), small-vessel (0.014/0.018-inch) balloon catheters (eg, Coyote, Sterling SL, and Symmetry; Boston Scientific and SLEEK and SAVVY; Cordis), high-pressure balloon catheters (eg, Mustang; Boston Scientific and Dorado and Conquest; Bard Peripheral Vascular, Tempe, Arizona), large-vessel balloon catheters (eg, XXL; Boston Scientific and Atlas; Bard Peripheral Vascular, Tempe Arizona), and special angioplasty balloon catheters (eg, Cutting Balloon and PolarCath; Boston Scientific).[84]

Balloon Angioplasty for Cerebral Vasospasm

Approved Use. Improving coronary luminal narrowing in patients with symptomatic ischemic disease due to de novo lesions in native coronary arteries.

Off-Label Use. Improving arterial luminal narrowing in patients with symptomatic cerebral vasospasm due to subarachnoid hemorrhage in native intracranial arteries (category III).

Balloon angioplasty for symptomatic or angiographic cerebral vasospasm has been shown to improve clinical outcomes (category III).[85-87] Angioplasty provides the most improvement in reducing vasospasm in patients with subarachnoid hemorrhage presenting with low Hunt and Hess scale SAH (I or II) and if performed within 12 hours of symptom onset.[86,87] In a recent small series of 30 patients, no difference was noted between compliant and noncompliant balloons for the angioplasty of cerebral vasospasm.[88] This group compared compliant balloons (HyperGlide or HyperForm; ev3, Irvine, California) or noncompliant balloons (Maverick or Gateway, Boston Scientific; Sprinter, Medtronic; and Voyager, Abbott Vascular). Achieving normal or supranormal vessel-lumen diameter after the first angioplasty was associated with significant reduction in future angioplasties.[88] The main complications of balloon angioplasty are rare but include rupture or occlusion of the vessel.[85,89-91] In addition, balloon angioplasty proximal to an unsecured aneurysm may result in aneurysmal rupture.[90,91]

Intravascular Sonography

Approved Use. Diagnostic sonography of the peripheral and coronary vasculature.

Off-Label Use. Sonography of the carotid and intracranial vasculature (category III). Intravascular sonography has many potential applications in neurointerventional practice.[92] It can be used in the determination of the morphology and composition of ath-

erosclerotic plaque within the extracranial and intracranial circulation, mural thrombus, plaque ulceration, and aneurysm and vessel dissection; it allows evaluation of correct stent diameter required and the amount of balloon-inflation pressure needed during angioplasty; and it enables visualization of stent apposition and expansion. Currently there are no FDA-approved intravascular sonographic devices for intracranial application. Several studies have shown that intravascular sonography is safe in the intracranial circulation.[93-96] Clark et al[93] prospectively evaluated the safety of intravascular sonography in carotid stent placement in 98 patients. They had an acceptable 30-day stroke rate and combined stroke and death rates of 5% and 6%, respectively (category III).

Embolic Agents for Aneurysms, Tumors, and Epistaxis

Approved Use. Vascular malformations.

Off-Label Use. Aneurysms, tumors, and epistaxis (category III). Onyx (ev3), *n*-butyl cyanoacrylic acid (*n*-BCA) (Trufills; Cordis), and polyvinyl alcohol particles have all been approved for treating cerebral arteriovenous malformations.[97] However, they have also been used in treating intracranial aneurysms, epistaxis, tumors, and dissecting vertebral artery aneurysms.[98-106] The FDA approved a high-viscosity type of Onyx (Onyx HD500) as a Humanitarian Use Device for wide-neck aneurysms (>4 mm or dome-neck ratio of <2) that are not amenable to surgical treatment.[107] Onyx HD500 is safe and effective for treating wide-neck aneurysms that are not amenable to other techniques. Piske et al[107] reported complete aneurysm occlusion of 65.5% (postprocedure), 84.6% (6 months), and 90.3% (18 months) in 84 aneurysms treated with Onyx HD500 with a peri-procedural mortality rate of 2.9%. Small case series have shown that *n*-BCA is safe and effective for the embolization of distal small intracranial aneurysms.[105,106] In experimental models, polyvinyl alcohol has been shown to be effective in the embolization of aneurysms.[108,109]

Polyvinyl alcohol, gelatin sponge pledgets (Gelfoam; Pfizer, New York, New York), and trisacryl gelatin microspheres (Embosphere; BioSphere Medical, Rockland, Massachusetts) are used in the treatment of epistaxis (category III).[110,111] The complication rates and success of embolization or surgical ligation are similar, though embolization is associated with more major complications when embolic agents inadvertently enter the internal carotid or ophthalmic artery.[111]

Preoperative embolization of intracranial tumors with embolic agents before surgical resection is performed in selected cases. Most often these are hypervascular skull base tumors, including meningiomas, paragangliomas, and juvenile nasopharyngeal angiofibromas (category III).[112-114] These procedures are associated with low complications mostly related to thromboembolic events.[113]

Coils for Parent Artery or Venous Sinus Occlusion

Approved Use. Embolization of intracranial aneurysms.

Off-Label Use. Embolization of the parent artery or venous sinus for achieving therapeutic occlusion (category III).

Coil embolization (HydroCoil; MicroVention Terumo, Aliso Viejo, California and GDC and Complex Helical; Boston Scientific) of intracranial aneurysms is a proved and effective treatment. However, occlusion of the parent vessel may be necessary in certain situations when treating intracranial aneurysms. Most commonly, it is used when treating distal small intracranial aneurysms that cannot be accessed (category III).[115-118] In a small series of 9 patients, Eckard et al[118] found that parent vessel occlusion was safe and effective in treating distal aneurysms that were not amenable to surgical treatment or intra-aneurysmal coil placement. The main risk of parent vessel occlusion is brain ischemia. Temporarily inflating a balloon to occlude the parent vessel and evaluating the effects on brain function and hemodynamics can be used to predict the risk of ischemia.[119] Ischemic sequelae may still occur even in those who tolerate a test occlusion, which has a 3.3%–10% false-negative rate.[119]

Embolization of the venous sinus is sometimes used to treat dural arteriovenous fistulas.[120-122] Kirsch et al[120] reported no complications related to transvenous coiling of the affected sinus in 21 patients with dural arteriovenous fistulas. Complete occlusion of the dural arteriovenous fistulas can be obtained in most cases with only transvenous coil placement (category III).[120,122] In addition, the use of coils before liquid embolic agents slows and decreases flow in the fistula and provides secure anchoring to the Onyx or glue cast.[123]

Amplatzer for Intracranial Parent Vessel Occlusion

Approved Use. Cardiopulmonary and peripheral vascular occlusions.

Off-Label Use. Parent artery deployment for achieving therapeutic occlusion of cervical arteries (category IV).

The Amplatzer Vascular Plug (St. Jude Medical, St Paul, Minnesota) is approved for vessel occlusion in the cardiopulmonary and peripheral vasculature that would have required many coils. However, experience in the intracranial vasculature is limited. Common indications for parent vessel occlusion might include treating carotid cavernous fistulas and aneurysms and preoperative embolization of skull base tumors. Several small case series have reported good technical outcome and safety when the Amplatzer Vascular Plug was used in the intracranial vasculature (category IV).[124,125]

SINGLE-CENTER EXPERIENCE

We retrospectively reviewed the medical records and angiographic images of 100 consecutive cases of endovascular interventions at 2 institutions. The patients were identified by using local registries maintained by the cerebrovascular/endovascular programs that track all patients who undergo endovascular treatment. The patients reviewed were treated at the University of Minnesota Medical Center, Minneapolis, Minnesota, from June 2010 –August 2010. The protocol for collecting data was reviewed and approved by the institutional review boards.

In the 100 cases reviewed, the indications for the procedures were the following: cerebral vasospasm following SAH (31%), coil embolization of intracranial aneurysms (16%), carotid artery stenosis (15%), IA thrombolytics for ischemic stroke (13%), intracranial angioplasty and/or stent placement for intracranial stenosis (7%), preoperative tumor embolization (8%), intracranial vascular malformation (5%), carotid or vertebral artery dissections (3%), and facial trauma/epistaxis (2%).

Principles of label use of medication and/or devices in neuroendovascular procedures

Principles
1. Identify off-label use and understand the use according to label/indications
2. Categorize the off-label use according to categories presented in the On-line Table
3. Category III requires informed consent for medication/device use with a description of adverse events observed in neurovascular procedures
4. Category IV requires informed consent for medication/device use with a description of adverse events observed in non-neurovascular procedures and acknowledgment of paucity of data from neurovascular procedures

Following the classification scheme in the On-line Table, all the procedures were performed under heparin infusion (category II): IA nicardipine or verapamil (category III) in 31 cases; dual antiplatelet therapy (category II) in 24 cases; IA thrombolytics (category I) in 13 cases; stent-assisted embolization of intracranial aneurysms (category I) in 3 cases; stent placement of intracranial stenosis (category I) in 4 cases; angioplasty alone of intracranial stenosis (category III) in 3 cases; stent placement of carotid or vertebral dissections (category III) in 5 cases; the intravasular ultrasound catheter system in 3 cases (category III); and polyvinyl alcohol embolization of the internal maxillary artery (category III) in 2 cases.

RECOMMENDATIONS FROM PROFESSIONAL SOCIETIES

The FDA states, "Good medical practice and the best interests of the patient require that physicians use legally available drugs, biologics and devices according to their best knowledge and judgment."[1] The FDA recommends that if a physician uses an off-label drug or medical device, he or she should base judgment on sound medical evidence and should maintain a record of the products used and effects.[1] A proposed scheme to categorize the off-label use of medications and devices is summarized in the On-line Table.

The position of the Society of Interventional Radiology supports the lawful use by a physician of an FDA-approved medical device or drug product for an unlabeled indication when such use is based on sound scientific evidence and/or sound medical opinion.[126] Off-label use of drugs and devices is an important part of the specialty but practicing providers should base their decisions on sound evidence when using them.

Disclosures: Adnan I. Qureshi—*RELATED*: *Grant*: Dr Qureshi received funding from the National Institutes of Health RO1-NS44976–01A2 (medication provided by Export Service Parma), American Heart Association Established Investigator Award 0840053N, National Institutes of Health U01-NS062091–01A2, and the Minnesota Medical Foundation, Minneapolis, Minnesota. Ameer E. Hassan—*UNRELATED*: *Payment for Lectures (including service on Speakers Bureaus)*: MicroVention, *Comments*: lecture on new Versatile range fill coils.

REFERENCES

1. FDA. "Off-Label" and Investigational Use of Marketed Drugs, Biologics, and Medical Devices: Information Sheet. August 10, 2011. http://www.fda.gov/RegulatoryInformation/Guidances/ucm126486.htm. Accessed April 10, 2012
2. Parsons M. Spratt N. Bivard A. et al. **A randomized trial of tenecteplase versus alteplase for acute ischemic stroke.** *N Engl J Med* 2012;366:1099–107
3. Chaudhary N. Pandey AS. Gemmete JJ. **Intervention in acute cerebral ischemic stroke: a review of the role of pharmacological therapies and intra-arterial mechanical thrombectomy devices.** *Postgrad Med J* 2011;87:714–23
4. Lee M, Hong KS, Saver JL. **Efficacy of intra-arterial fibrinolysis for acute ischemic stroke: meta-analysis of randomized controlled trials.** *Stroke* 20102:41:932–37
5. Qureshi A. Luft A, Sharma M, et al. **Prevention and treatment of thromboembolic and ischemic complications associated with endovascular procedures: part I. Pathophysiological and pharmacological features.** *Neurosurgery* 2000;46:1344–59
6. Castelluci L. FDA reapproves urokinase. October 11, 2002. The heart.org. http://www.theheart.org/article/266091.do. Accessed July 10, 2012
7. Furlan A, Higashida R, Wechsler L, et al. **Intra-arterial prourokinase for acute ischemic stroke: the PROACT II study—a randomized controlled trial. Prolyse in Acute Cerebral Thromboembolism.** *JAMA* 1999;282:2003–11
8. del Zoppo GJ, Higashida RT, Furlan AJ., et al. **PROACT: a phase II randomized trial of recombinant pro-urokinase by direct arterial delivery in acute middle cerebral artery stroke.** *Stroke* 1998;29:4–11
9. Lee M. Hon, KS. Saver J. **Efficacy of intra-arterial fibrinolysis for acute ischemic stroke meta-analysis of randomized controlled trials.** *Stroke* 2010;41:932–37
10. Biondi A, Ricciardi GK, Puybasset L, et al. **Intra-arterial nimodipine for the treatment of symptomatic cerebral vasospasm after aneurysmal subarachnoid hemorrhage: preliminary results.** *AJNR Am J Neuroradiol* 2004;25:1067–76
11. Qureshi AI, Pande R, Kim S, et al. **Third generation thrombolytics for the treatment of ischemic stroke.** *Curr Opin Investig Drugs* 2002;3:1729–32
12. Topol EJ. **Reperfusion therapy for acute myocardial infarction with fibrinolytic therapy or combination reduced fibrinolytic therapy and platelet glycoprotein IIb/IIIa inhibition: the GUSTO V randomised trial.** *Lancet* 2001;357:1905–14
13. The EPISTENT Investigators. **Randomised placebo-controlled and balloon-angioplasty-controlled trial to assess safety of coronary stenting with use of platelet glycoprotein-IIb/IIIa blockade.** *Lancet* 1998;352:87–92
14. The CAPTURE Investigators. **Randomised placebo-controlled trial of abciximab before and during coronary intervention in refractory unstable angina: the CAPTURE study.** *Lancet* 1997;349:1429–35
15. Walsh R, Barrett K, Aguilar M, et al. **Intracranial hemorrhage following neuroendovascular procedures with abciximab is associated with high mortality: a multicenter series**. *Neurocrit Care* 2011;15:85–95
16. Memon M, Natarajan S, Sharma J, et al. **Safety and feasibility of intraarterial eptifibatide as a revascularization tool in acute ischemic stroke.** *J Neurosurg* 2011;114:1008–13
17. Ries T, Siemonsen S, Grzyska U, et al. **Abciximab is a safe rescue therapy in thromboembolic events complicating cerebral aneurysm coil embolization: single center experience in 42 cases and review of the literature.** *Stroke* 2009;40:1750–57
18. Adams HP Jr, Effron MB, Torner J, et al, for the AbESTT-II Investigators**. Emergency administration of abciximab for treatment of patients with acute ischemic stroke: results of an international phase III trial: Abciximab in Emergency Treatment of Stroke Trial (AbESTT-II).** *Stroke* 2008;39:87–99
19. Hofmann R, Kerschner K, Steinwender C, et al. **Abciximab bolus injection does not reduce cerebral ischemic complications of elective carotid artery stenting: a randomized study.** *Stroke* 2002;33:725–27
20. Chan AW, Yadav JS, Bhatt DL, et al. **Comparison of the safety and efficacy of emboli prevention devices versus platelet glycoprotein IIb/IIIa inhibition during carotid stenting.** *Am J Cardiol* 2005;95:791–95

21. Wholey MH, Wholey MH, Eles G, et al. **Evaluation of glycoprotein IIb/IIIa inhibitors in carotid angioplasty and stenting.** *J Endovasc Ther* 2003;10:33–41
22. Qureshi AI, Saad M, Zaidat OO, et al. **Intracerebral hemorrhages associated with neurointerventional procedures using a combination of antithrombotic agents including abciximab.** *Stroke* 2002;33:1916–19
23. Katsaridis V, Papagiannaki C, Skoulios N, et al. **Local intra-arterial eptifibatide for intraoperative vessel thrombosis during aneurysm coiling.** *AJNR Am J Neuroradiol* 2008;29:1414–17
24. Park JH, Kim JE. Sheen SH, et al. **Intraarterial abciximab for treatment of thromboembolism during coil embolization of intracranial aneurysms: outcome and fatal hemorrhagic complications.** *J Neurosurg* 2008;108:450–57
25. Chun R, Orser B, Madan M. **Platelet glycoprotein IIb/IIIa inhibitors: overview and implications for the anesthesiologist.** *Anesth Analg* 2002;95:879–88
26. Lincoff AM, Topol EJ, eds. *Platelet Glycoprotein IIb/IIIa Inhibitors in Cardiovascular Disease.* Totowa, New Jersey: Humana Press; 1999:169–97
27. Bhatt D, Topol E. **Current role of platelet glycoprotein IIb/IIIa inhibitors in acute coronary syndromes.** *JAMA* 2000;284:1549–58
28. Dorhout Mees SM, Rinkel G, Feigin V, et al. **Calcium antagonists for aneurysmal subarachnoid hemorrhage.** *Cochrane Database Syst Rev* 2007:CD000277
29. Pickard JD, Murray GD, Illingworth R, et al. **Effect of oral nimodipine on cerebral infraction and outcome after subarachnoid haemorrhage: British aneurysm nimodipine trial.** *BMJ* 1989;298:636–42
30. Barker F, Ogilvy C. **Efficacy of prophylactic nimodipine for delayed ischemic deficit after subarachnoid hemorrhage: a meta-analysis.** *J Neurosurg* 1996:84:405–14
31. FDA Labeling Text. Nimtop (nimodipine) capsules for oral use. January 20, 2006. http://www.accessdata.fda.gov/drugsatfda_docs/label/2006/018869s014lbl.pdf. Accessed June 7, 2012
32. Kronvall E, Undren P, Romner B, et al. **Nimodipine in aneurysmal subarachnoid hemorrhage: a randomized study of intravenous or peroral administration.** *J Neurosurg* 2009;110:58–63
33. Jan M, Buchneit F, Tremoulet M. **Therapeutic trial of intravenous nimodipine in patients with established cerebral vasospasm after rupture of intracranial aneurysms.** *Neurosurgery* 1988;23:154–57
34. Rosenberg N, Lazzaro MA, Lopes DK, et al. **High-dose intra-arterial nicardipine results in hypotension following vasospasm treatment in subarachnoid hemorrhage.** *Neurocrit Care* 2011;15:400–04
35. Keuskamp J, Murali R, Chao K. **High-dose intraarterial verapamil in the treatment of cerebral vasospasm after aneurysmal subarachnoid hemorrhage.** *J Neurosurg* 2008;108:458–63
36. Taccone FS. **Vasodilation and neuroprotection: the magnesium saga in subarachnoid hemorrhage.** *Crit Care Med* 2010;38:1382–84
37. Suarez JI, for Participants in the International Multidisciplinary Consensus Conference on the Critical Care Management of Subarachnoid Hemorrhage. **Magnesium sulfate administration in subarachnoid hemorrhage.** *Neurocrit Care* 2011;15:302–07
38. Shah Q, Memom M, Suri MF, et al. **Super-selective intra-arterial magnesium sulfate in combination with nicardipine for the treatment of cerebral vasospasm in patients with subarachnoid hemorrhage.** *Neurocrit Care* 2009;11:190–98
39. Zaidat O. **Periprocedural management of patients with endovascular treatment of intracranial atherosclerotic disease**. *J Neuroimaging* 2009;19:35S–38S
40. Vance AZ, Jayaraman MV, Dubel GJ, et al. **Safety of intravenous heparin administration after endovascular treatment of ruptured intracranial aneurysms.** *J Neurointervent Surg* 2009;1:136–41
41. Hussein HM, Geordiadis AL, Qureshi AI. **Point of care testing of anticoagulation monitoring in neuroendovascular procedures.** *AJNR Am J Neuroradiol* 2012;33:1211–20
42. Di Nisio M, Middeldorp S, Büller, H. **Direct thrombin inhibitors.** *N Engl J Med* 2005;353:1028–40
43. Hassan AE, Memon M, Georgiadis A, et al. **Safety and tolerability of high-intensity anticoagulation with bivalirudin during neuroendovascular procedures.** *Neurocrit Care* 2011;15:96–100
44. Pandya DJ, Fitzsimmons BF, Wolfe TJ, et al. **Measurement of antiplatelet inhibition during neurointerventional procedures: the effect of antithrombotic duration and loading dose.** *J Neuroimaging* 2010;20:64–69
45. van den Bergh WM, Kerr RS, Algra A, et al, for the International Subarachnoid Aneurysm Trial (ISAT) Collaborative Group. **Effect of antiplatelet therapy for endovascular coiling in aneurysmal subarachnoid hemorrhage.** *Stroke* 2009;40:1969–72
46. Yamada NK, Cross DT 3rd, Pilgram TK, et al. **Effect of antiplatelet therapy on thromboembolic complications of elective coil embolization of cerebral aneurysms.** *AJNR Am J Neuroradiol* 2007;28:1778–82
47. Kang HS, Han M, Kwon, B, et al. **Is clopidogrel premedication useful to reduce thromboembolic events during coil embolization for unruptured intracranial aneurysms?** *Neurosurgery* 2010;67:1371–76
48. Bristol-Myers Squibb/Sanofi Pharmaceuticals Partnership. Highlights of Prescribing Information. December 2011, 2012. http://www.accessdata.fda.gov/drugsatfda_docs/label/2011/020839s055lbl.pdf. Accessed July 3, 2012
49. Mas JL, Trinquart L, Leys D, et al. **Endarterectomy Versus Angioplasty in Patients with Symptomatic Severe Carotid Stenosis (EVA-3S) trial: results up to 4 years from a randomised, multicentre trial.** *Lancet Neurol* 2008;7:885–92
50. Hassan AE, Zacharatos H, Vazquez G, et al. **Low risk of intracranial and systemic hemorrhages in patients on dual antiplatelet treatment beyond 1 month following neuroendovascular angioplasty and/or stent placement.** *J Neuroimaging* 2012;22:67–73
51. Qureshi AI, Feldmann E, Gomez CR, et al. **Consensus conference on intracranial atherosclerotic disease: rationale, methodology, and results.** *J Neuroimaging* 2009;19(suppl 1):1S–10S
52. Chimowitz MI, Lynn MJ, Derdeyn CP, for the SAMMPRIS Trial Investigators. **Stenting versus aggressive medical therapy for intracranial arterial stenosis.** *N Engl J Med* 2011;365:993–1003
53. Brott TG, Hobson RW II, Howard G, et al for the CREST Investigators. **Stenting versus Endarterectomy for Treatment of Carotid-Artery Stenosis.** *N Engl J Med* 2010;363:11–23
54. Yadav JS, Wholey MH, Kuntz RE, et al for the Stenting and Angioplasty with Protection in Patients at High Risk for Endarterectomy Investigators. **Protected carotid-artery stenting versus endarterectomy in high-risk patients.** *N Engl J Med* 2004;351:1493–501
55. Ederle J, Dobson J, Featherstone RL, et al for the International Carotid Stenting Study investigators. **Carotid artery stenting compared with endarterectomy in patients with symptomatic carotid stenosis (International Carotid Stenting Study): an interim analysis of a randomised controlled trial.** *Lancet* 2010;375:985–997
56. Ringleb PA, Allenberg J, Brückmann H, et al for the SPACE Collaborative Group. **30 day results from the SPACE trial of stent-protected angioplasty versus carotid endarterectomy in symptomatic patients: a randomised non-inferiority trial.** *Lancet* 2006;368;1239–47
57. Costalat V, Maldonado IL, Zerlauth JB, et al. **Endovascular treatment of symptomatic intracranial arterial stenosis: six-year experience in a single-center series of 42 consecutive patients with acute and mid-term results.** *Neurosurgery* 2010;67:1505–13
58. Jiang WJ, Wang YJ, Du B, et al. **Stenting of symptomatic M1 stenosis of middle cerebral artery: an initial experience of 40 patients.** *Stroke* 2004;35:1375–80
59. Lylyk P, Vila JF, Miranda C, et al. **Endovascular reconstruction by means of stent placement in symptomatic intracranial atherosclerotic stenosis.** *Neurol Res* 2005;27(suppl 1):S84–88
60. Mori T, Kazita K, Chokyu K, et al. **Short-term arteriographic and clinical outcome after cerebral angioplasty and stenting for intracranial vertebrobasilar and carotid atherosclerotic occlusive disease.** *AJNR J Neuroradiol* 2000;21:249–54
61. Fiorella D, Chow MM, Anderson M, et al. **A 7-year experience with**

balloon-mounted coronary stents for the treatment of symptomatic vertebrobasilar intracranial atheromatous disease. *Neurosurgery* 2007;61:236–42
62. Gupta R, Al-Ali F, Thomas AJ, et al. **Safety, feasibility, and short-term follow-up of drug-eluting stent placement in the intracranial and extracranial circulation.** *Stroke* 2006;37:2562–66
63. Abou-Chebl A, Bashir Q, Yadav JS. **Drug-eluting stents for the treatment of intracranial atherosclerosis: initial experience and midterm angiographic follow-up.** *Stroke* 2005;36:e165–68
64. Vajda Z, Guthe T, Perez MA. **Neurovascular in-stent stenoses: treatment with conventional and drug-eluting balloons.** *AJNR Am J Neuroradiol* 2011;32:1942–47
65. Fields JD, Petersen BD, Lutsep HL, et al. **Drug eluting stents for symptomatic intracranial and vertebral artery stenosis.** *Interv Neuroradiol* 2011;17:241–47
66. Siddiq F, Vasquez G, Memon M, et al. **Comparison of primary angioplasty with stent placement for treating symptomatic intracranial atherosclerotic diseases a multicenter study.** *Stroke* 2008;39:2505–10
67. The SSYLVIA Study Investigators. **Stenting of Symptomatic Atherosclerotic Lesions in the Vertebral or Intracranial Arteries (SSYLVIA).** *Stroke* 2004;35:1388–92
68. Takayama T, Hiro T, Hirayama A. **Stent thrombosis and drug-eluting stents.** *J Cardiol* 2011;58:92–98
69. Derdeyn C, Chimowitz M. **Angioplasty and stenting for atherosclerotic intracranial stenosis: rationale for a randomized clinical trial.** *Neuroimaging Clin N Am* 2007;17:355–63, viii-ix
70. Ding D, Liu KC. **Applications of stenting for intracranial atherosclerosis.** *Neurosurg Focus* 2011;30:E15
71. King SB 3rd, Smith SC Jr, Hirshfeld JW Jr, et al. **2007 Focused update of the ACC/AHA/SCAI 2005 Guideline Update for Percutaneous Coronary Intervention: a report of the American College of Cardiology/American Heart Association Task Force on Practice Guidelines—2007 writing group to review new evidence and update the ACC/AHA/SCAI 2005 Guideline Update for Percutaneous Coronary, Writing on Behalf of the 2005 Writing Committee.** *Circulation* 2008;117:261–295
72. Cruz-Flores S, Diamond AL. **Angioplasty for intracranial artery stenosis.** *Cochrane Database Syst Rev* 2006;CD004133
73. Qureshi AI, Tariq N, Hassan AE, et al. **Predictors and timing of neurological complications following intracranial angioplasty and/or stent placement.** *Neurosurgery* 2011;68:53–60
74. Kurre W, Brassel F, Bruning R, et al, for the INTRASTENT study group. **Complication rates using balloon-expandable and self-expanding stents for the treatment of intracranial atherosclerotic stenoses: analysis of the INTRASTENT multicentric registry.** *Neuroradiology* 2012;54:43–50
75. Jiang W, Xu X, Jin M, et al. **Apollo stent for symptomatic atherosclerotic intracranial stenosis: study results.** *AJNR Am J Neuroradiol* 2007;28:830–34
76. Siddiq F, Memon M, Vazquez G, et al. **Comparison between primary angioplasty and stent placement for symptomatic intracranial atherosclerotic disease: meta-analysis of case series.** *Neurosurgery* 2009;65:1024–33
77. Hauck E. Natarajan S. Horvathy D, et al. **Stent-assisted basilar reconstruction for a traumatic vertebral dissection with a large basilar artery thrombosis.** *J Neurointerv Surg* 2011;3:47–49
78. Yi A, Palmer E, Luh G, et al. **Endovascular treatment of carotid and vertebral pseudoaneurysms with covered stents.** *AJNR Am J Neuroradiol* 2008;29:983–87
79. Kadkhodayan Y, Jeck D, Moran, C, et al. **Angioplasty and stenting in carotid dissection with or without associated pseudoaneurysm.** *AJNR Am J Neuroradiol* 2005;26:2328–35
80. Hassan AE, Zacharatos H, Souslian F, et al. **Long-term clinical and angiographic outcomes in patients with cervico-cranial dissections treated with stent placement: a meta-analysis of case series.** *J Neurotrauma* 2012;29:1342–53
81. Kan P, Mokin M, Dumont T, et al. **Cervical carotid artery stenosis: latest update on diagnosis and management.** *Curr Probl Cardiol* 2012;37:127–69
82. Brooks W, McClure R, Jones M, et al. **Carotid angioplasty and stenting versus carotid endarterectomy: randomized trial in a community hospital.** *J Am Coll Cardiol* 2001;38:1589–95
83. Parodi J, La Mura R, Ferreira, L, et al. **Initial evaluation of carotid angioplasty and stenting with three different cerebral protection devices**. *J Vasc Surg* 2000;32:1127–36
84. Wichman HJ, Rowe VL. Percutaneous transluminal angioplasty balloons. Medscape. February 15, 2012. http://emedicine.medscape.com/article/2035433-overview#aw2aab6b2. Accessed July 13, 2012
85. Terry A, Zipfel G, Milner E, et al. **Safety and technical efficacy of over-the-wire balloons for the treatment of subarachnoid hemorrhage-induced cerebral vasospasm.** *Neurosurg Focus* 2006;21:E14
86. Eskridge JM, McAuliffe W, Song JK, et al. **Balloon angioplasty for the treatment of vasospasm: results of first 50 cases.** N*eurosurgery* 1998;42:510–16, discussion 516–17
87. Zubkov YN, Alexander LF, Smith RR, et al. **Angioplasty of vasospasm: is it reasonable?** *Neurol Res* 1994;16:9–11
88. Miley J, Tariq N, Souslian F, et al. **Comparison between angioplasty using compliant and noncompliant balloons for treatment of cerebral vasospasm associated with subarachnoid hemorrhage.** *Neurosurgery* 2011;69(2 suppl operative):ons161–68, discussion ons168
89. Newell DW, Eskridge J, Mayberg M, et al. **Endovascular treatment of intracranial aneurysms and cerebral vasospasm.** *Clin Neurosurg* 1992;39:348–60
90. Eskridge JM Newell, DW, Pendleton, GA. **Transluminal angioplasty for treatment of vasospasm.** *Neurosurg Clin N Am* 1990;1:387–99
91. Takahashi A, Yoshoto T, Mizou K, et al. **Transluminal balloon angioplasty for cerebral vasospasm after subarachnoid hemorrhage.** In: Sano K, Takakura K, Kassell N, et al. (eds). *Cerebral Vasospasm,* Tokyo: University of Tokyo Press; 1990, pp. 429–32
92. Zacharatos H, Hassan AE, Qureshi, AI. **Intravascular ultrasound: principles and cerebrovascular applications.** *AJNR Am J Neuroradiol* 2010;31:586–97
93. Clark DJ, Lessio S, O'Donoghue M, et al. **Safety and utility of intravascular ultrasound guided carotid artery stenting.** *Catheter Cardiovasc Interv* 2004;63:355–62
94. Weissman N, Canos M, Mintz G, et al. **Carotid artery intravascular ultrasound: safety and morphologic observations during carotid stenting in 102 patients.** *J Am Coll Cardiol* 2000;35(2 supple 1):10A
95. Manninen HI, Räsänen H, Vanninen RL, et al. **Human carotid arteries: correlation of intravascular US with angiographic and histopathologic findings.** *Radiology* 1998;206:65–74
96. Kan P, Mokin M, Abla AA, et al. **Utility of intravascular ultrasound in intracranial and extracranial neurointerventions: experience at University at Buffalo Neurosurgery-Millard Fillmore Gates Circle Hospital.** *Neurosurg Focus* 2012;2:E6
97. Strozyk D, Baccin CE, Pryor JC, et al. **Intracranial arteriovenous malformations**. In: Quershi AI, ed. *Textbook of Interventional Neurology*. New York: Cambridge University Press; 2011:255
98. Oh D, Hirsch J, Yoo, A. **Novel use of Onyx for treatment of intracranial vertebral artery dissection.** *J Neurointerv Surg* 2012;4:31–33
99. Tevah J, Senf R, Cruz J, et al. **Endovascular treatment of complex cerebral aneurysms with Onyx HD-500 in 38 patients.** *J Neuroradiol* 2011;38:283–90
100. Simon SD, Lopes DK, Mericle RA. **Use of intracranial stenting to secure unstable liquid embolic casts in wide-neck sidewall intracranial aneurysms.** *Neurosurgery* 2010;66(3 suppl operative):92–97, discussion 97–98
101. Medel R, Crowley RW, Hamilton DK, et al. **Endovascular obliteration of an intracranial pseudoaneurysm: the utility of Onyx.** *J Neurosurg Pediatr* 2009;4:445–48
102. Eddleman CS, Surdell D, DiPatri A Jr, et al. **Infectious intracranial aneurysms in the pediatric population: endovascular treatment with Onyx.** *Childs Nerv Syst* 2008;24:909–15

103. Isokangas JM, Siniluoto T, Tikkakoski T, et al. **Endovascular treatment of peripheral aneurysms of the posterior inferior cerebellar artery.** *AJNR Am J Neuroradiol* 2008;29:1783–88
104. Choulakian A, Drazin D, Alexander MJ. **NBCA embolization of a ruptured intraventricular distal anterior choroidal artery aneurysm in a patient with Moyamoya disease.** *J Neurointerv Surg* 2010;2:368–70
105. Larrazabal R, Pelz D, Findlay JM. **Endovascular treatment of a lenticulostriate artery aneurysm with N-butyl cyanoacrylate.** *Can J Neurol Sci* 2001;28:256–59
106. Kim SH, Kwon O-Ki, Jung CK, et al. **Endovascular treatment of ruptured aneurysms of pseudoaneurysms on the collateral vessels in patients with Moyamoya disease.** *Neurosurgery* 2009;65: 1000–04
107. Piske RL, Kanashiro LH, Paschoal E, et al. **Evaluation of Onyx HD-500 embolic system in the treatment of 84 wide-neck intracranial aneurysms.** *Neurosurgery* 2009;64:E865–75
108. Dudeck O, Jordan O. Hoffmann KT, et al. **Embolization of experimental wide-necked aneurysms with iodine-containing polyvinyl alcohol solubilized in a low-angiotoxicity solvent.** *AJNR Am J Neuroradiol* 2006;27:1849–55
109. Ohta M, Handa A, Iwata H, et al. **Poly-vinyl alcohol hydrogel vascular models for in vitro aneurysm simulations: the key to low friction surfaces.** *Technol Health Care* 2004;12:225–33
110. Andersen P, Kjeldsen, A, Nepper-Rasmussen J. **Selective embolization in the treatment of intractable epistaxis.** *Acta Otolaryngol* 2005;125:293–97
111. Willems P, Farb R, Agid R. **Endovascular treatment of epistaxis.** *AJNR Am J Neuroradiol* 2009;30:1637–45
112. Gruber A, Bavinski G, Killer M, et al. **Preoperative embolization of hypervascular skull base tumors.** *Minim Invasive Neurosurg* 2000;43:62–71
113. Manelfe C, Lasjaunias P, Ruscalleda J. **Preoperative embolization of intracranial meningiomas.** *AJNR Am J Neuroradiol* 1986;7:963–72
114. Perry A, Chicione MR, Filiput E, et al. **Clinicopathologic assessment and grading of embolized meningiomas: a correlative study of 64 patients.** *Cancer* 2001;92:701–11
115. Liu L, He H, Jiang C, et al. **Deliberate parent artery occlusion for non-saccular posterior cerebral artery aneurysms.** *Interv Neuroradiol* 2011;17:159–68
116. Lv X, Li Y, Jiang C, et al. **Parent vessel occlusion for P2 dissecting aneurysms of the posterior cerebral artery.** *Surg Neurol* 2009;71: 319–25, discussion 325
117. Pierot L, Boulin A, Castaings L, et al. **The endovascular approach in the management of patients with multiple intracranial aneurysms.** *Neuroradiology* 1997;39:361–66
118. Eckard D, O'Boynick P, McPherson C, et al. **Coil occlusion of the parent artery for treatment of symptomatic peripheral intracranial aneurysms.** *AJNR Am J Neuroradiol* 2000;21:137–42
119. Linskey ME, Jungreis CA, Yonas H, et al. **Stroke risk after abrupt internal carotid artery sacrifice: accuracy of preoperative assessment with balloon test occlusion and stable xenon-enhanced CT.** *AJNR Am J Neuroradiol* 1994;15:829–43
120. Kirsch M, Liebig T, Kühne D, et al. **Endovascular management of dural arteriovenous fistulas of the transverse and sigmoid sinus in 150 patients.** *Neuroradiology* 2009;51:477–83
121. Shi Z, Loh Y, Gonzalez, N, et al. **Flow control techniques for Onyx embolization of intracranial dural arteriovenous fistulae.** *J Neurointervent Surg* 2013;5:311–16
122. Quiñones D, Duckwiler G, Gobin PY, et al. **Embolization of dural cavernous fistulas via superior ophthalmic vein approach.** *AJNR Am J Neuroradiol* 1997;18:921–28
123. Gupta AK, Periakaruppan AL. **Intracranial dural arteriovenous fistulas: a review.** *Indian J Radiol Imaging* 2009;19:43–48
124. Ong CK, Lam DV, Ong MT, et al. **Neuroapplication of Amplatzer Vascular Plug for therapeutic sacrifice of major craniocerebral arteries: an initial clinical experience.** *Ann Acad Med Singapore* 2009;38:763–68
125. Gralla J, Schroth G, Kickuth R, et al. **Closing the gap between coil and balloon in the neurointerventional armamentarium? Initial clinical experience with a nitinol vascular occlusion plug.** *Neuroradiology* 2008;50:709–14
126. Society of Interventional Radiology Executive Council. SIR Policy on Off-Label Use. November 18, 2007. http://sirweb.org/clinical/cpg/SIR_Off-label_use_statement11–18-07.pdf. Accessed July 12, 2012

A Decade of DTI in Traumatic Brain Injury: 10 Years and 100 Articles Later

M.B. Hulkower, D.B. Poliak, S.B. Rosenbaum, M.E. Zimmerman, and M.L. Lipton

ABSTRACT

SUMMARY: The past decade has seen an increase in the number of articles reporting the use of DTI to detect brain abnormalities in patients with traumatic brain injury. DTI is well-suited to the interrogation of white matter microstructure, the most important location of pathology in TBI. Additionally, studies in animal models have demonstrated the correlation of DTI findings and TBI pathology. One hundred articles met the inclusion criteria for this quantitative literature review. Despite significant variability in sample characteristics, technical aspects of imaging, and analysis approaches, the consensus is that DTI effectively differentiates patients with TBI and controls, regardless of the severity and timeframe following injury. Furthermore, many have established a relationship between DTI measures and TBI outcomes. However, the heterogeneity of specific outcome measures used limits interpretation of the literature. Similarly, few longitudinal studies have been performed, limiting inferences regarding the long-term predictive utility of DTI. Larger longitudinal studies, using standardized imaging, analysis approaches, and outcome measures will help realize the promise of DTI as a prognostic tool in the care of patients with TBI.

ABBREVIATIONS: FA = fractional anisotropy; GCS = Glasgow Coma Scale; MD = mean diffusivity; TAI = traumatic axonal injury; TBI = traumatic brain injury; TBSS = tract-based spatial statistics

The clinical pathology underlying TBI-related impairment is traumatic axonal injury.[1] TAI, referred to as diffuse axonal injury when damage is extensive, is a microscopic injury that occurs even in the absence of frank tissue disruption. Therefore, patients may experience significant impairment despite the absence of abnormal findings on conventional CT and MR imaging. Moreover, focal imaging abnormalities that can be detected by using CT and MR imaging are poor predictors of outcome.[1] Diagnostic tests that can discriminate significant TAI are needed to effectively allocate patients to follow-up and treatment, to accurately assess injury severity and safety in sports and military settings, and to guide clinical trials of novel therapeutic agents. DTI is a relatively new MR imaging technique that measures the directional coherence of water diffusion in vivo. Because of the highly uniform collinear structure of normal white matter, DTI is uniquely able to probe its microscopic structure and is, therefore, particularly well-suited for the assessment of TAI. Although gross abnormalities can be identified in some cases of TAI by using CT and conventional MR imaging, DTI can both qualitatively and quantitatively (Fig 1) demonstrate pathology not detected by other modalities and is, therefore, an important tool not only in the research setting but in the clinical setting as well.

Most studies of TBI report fractional anisotropy, a summary measure derived from DTI, which describes the directional coherence (anisotropy) of water diffusion within tissue. However, mean diffusivity, axial diffusivity, and radial diffusivity may more specifically describe the direction and magnitude of tissue water diffusion. Animal studies have shown a direct correspondence between even very subtle TAI pathology and decreases in white matter anisotropy that can be imaged in vivo by using DTI (eg, Mac Donald et al[2]). Numerous clinical studies have assessed TBI by using DTI. Since the earliest research article reporting DTI applied to TBI was published in 2002,[3] there has been an overall exponential increase in the number of articles published on this topic (Fig 2).

The purpose of this review was to systematically summarize and detail the landscape of DTI applied to the study of TBI and to highlight both the salient conclusions to be drawn from this large literature and its limitations, which can serve as important considerations for future research. We summarize a number of different aspects of the articles, including the demo-

From the Gruss Magnetic Resonance Research Center (M.L.L.) and Saul R. Korey Department of Neurology (M.E.Z.), Albert Einstein College of Medicine (M.B.H., D.B.P., S.B.R.), Bronx, New York.

Please address correspondence to Michael Lipton, MD, PhD, The Gruss Magnetic Resonance Research Center, Albert Einstein College of Medicine, 1300 Morris Park Ave, Bronx, NY 10461; e-mail: michael.lipton@einstein.yu.edu

Indicates open access to non-subscribers at www.ajnr.org

Indicates article with supplemental on-line tables

http://dx.doi.org/10.3174/ajnr.A3395

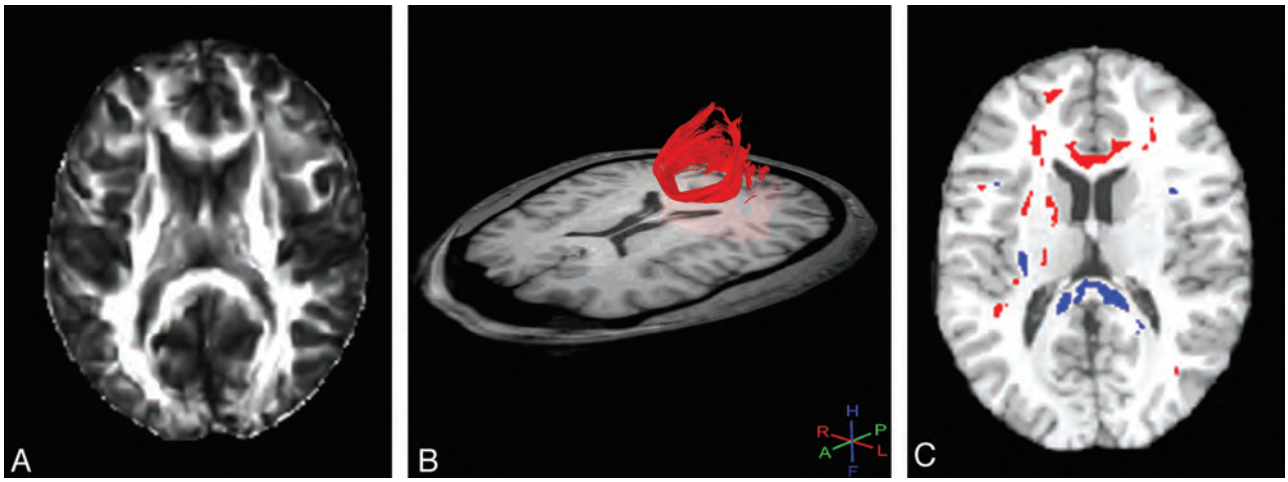

FIG 1. FA image (*A*) reveals no abnormality in a patient with TBI. Tractography (*B*) can be used to delineate a region of interest for analysis. In this case, the forceps major (red) appears normal, but quantitative analysis of FA within this tract showed lower FA in the TBI group compared with controls. Whole-brain voxelwise analysis (*C*) reveals areas of low (blue) and high (red) FA. Low FA, consistent with TAI, is present within the forceps major at the splenium of the corpus callosum, as well as elsewhere.

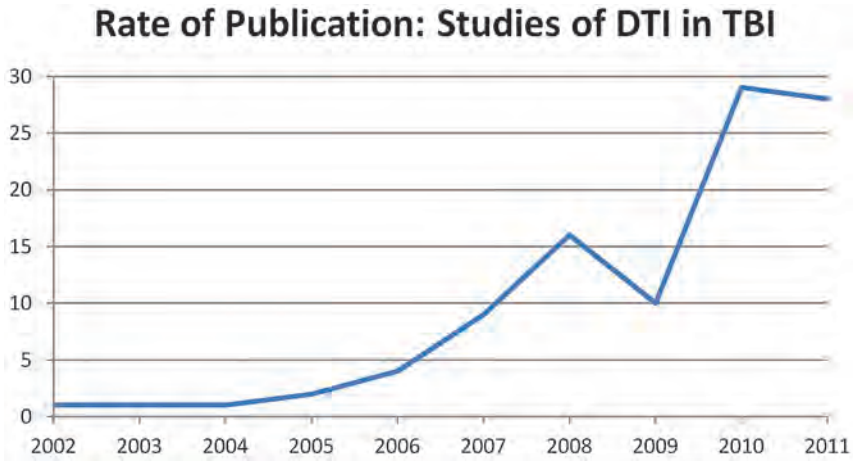

FIG 2. The number of publications per year reporting DTI in TBI.

graphics of TBI subjects and controls, the timing and severity of TBI, technical factors related to image acquisition and analysis, the nature and location of abnormalities, and findings relating DTI to outcome measures. We also note that a valid meta-analysis of this literature is not feasible due to the great diversity in study design and measurement approaches used across the articles.

A structured search was performed by using PubMed to include all relevant articles through 2011. The search used the following key word combinations: "diffusion tensor imaging and traumatic brain injury," "DTI and TBI," and "DTI and concussion." The total results included 391 articles with 293 unique articles. We further examined the references cited by these articles to identify additional relevant articles. After we eliminated articles on the basis of our exclusion criteria (below), 100 articles[3-102] remained and were systematically analyzed and included in this review. Exclusion criteria included the following: language other than English ($n = 7$); animal or in vitro studies ($n = 30$); studies of diseases other than TBI (eg, spinal cord injury, brain tumors) ($n = 57$); case reports ($n = 37$), reviews ($n = 48$), editorials ($n = 3$), posters ($n = 1$), or abstracts ($n = 1$); and use of diffusion-weighted imaging or other MR imaging measures, but not DTI ($n = 8$).

SUBJECTS WITH TBI

The population studied or substrate of injury is perhaps as important as the TBI itself in determining the nature and extent of consequent pathology.[103] An important consideration in the study of TBI is thus the choice of the study sample and the feasibility of attaining a homogeneous cohort. A total of 2337 subjects was studied across all 100 articles. The average number of patients per study was 23 (range, 5–83 subjects). Our review identified several articles that described patient samples with extremely similar or identical demographic characteristics (eg, McCauley et al[55] and Wilde et al,[87,88,90]) but reported either different abnormal brain regions or different analyses of DTI in relation to outcome. Thus, some of the subjects may have been reported in multiple studies published by the same group of researchers. Our best estimate is that the number of subjects reported in multiple studies may be up to 140 individuals. All except 8 articles reported sex breakdown; 65% of reported subjects were male.[6,30,41,46,52,77,81,83]

Most commonly, abnormalities on DTI are defined on the basis of comparison with a control group because universal thresholds for abnormality have not yet been established. All studies, except 5, compared subjects with TBI with a control group.[17,18,24,83,85] Three of these exceptions used a longitudinal within-subjects design.[24,83,85] In all except 7 studies, control subjects were healthy individuals.[28,43,49,53,55,81,90] In 3 of the studies

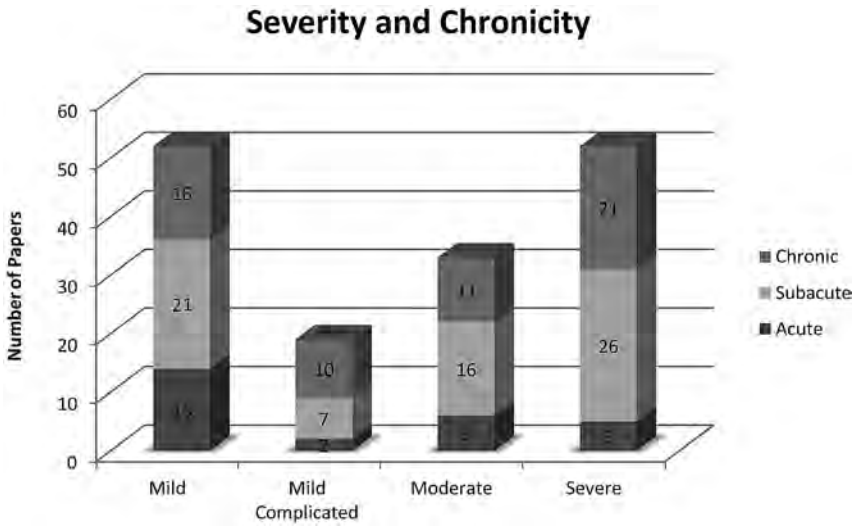

FIG 3. The number of articles that studied patients at each timeframe and level of injury severity. Articles were only included if there was sufficient information to determine both the severity and the chronicity of individual patient injuries. Articles may be included multiple times if they studied subjects with multiple severities and/or multiple chronicities. A fully referenced version of this figure is available in On-line Table I.

that did not use healthy individuals as control subjects, 2 groups of subjects with TBI were compared (eg, with and without major depressive disorders[53]). In 3 pediatric studies, the control groups were children who were hospitalized for orthopedic injury but had no evidence of head injury.[43,55,90] The average number of control subjects per study was 18 (range, 6–47). Several articles, in addition to comparing patients with TBI with controls by using DTI, looked at subgroups of patients with TBI, including patients with TBI with major depressive disorders,[53,99] with raised intracranial pressures,[81] with spinal cord injuries,[86] or veterans with blast injuries.[41,49,53,79,99] An important consideration in the selection of control subjects, particularly when studying symptom endorsement, is that comparison of subjects with TBI with healthy controls fails to eliminate the potential confound of morbidity due to the experience of trauma itself, rather than adverse outcomes specifically due to physical injury to the brain. At the same time, it is unclear whether a purportedly non-head-injured patient sustained neurologic trauma during the course of an injury, even if not reported by the patient or witnesses of the event or detected by clinical assessment of the patient.

The ages of subjects studied across all articles ranged from 2 through 70 years, with each individual article reporting on a more limited age range. Children were studied exclusively in 29 of 72 articles.[4,5,11-14,17,19-22,25,27,42,43,55,66,75,81,87-94,96,98] The total number of children studied across all 29 articles was 564. In addition, 20 studies included adults and children (younger than 19 years).[8-11,26,31,49,50,56,59,60,62,64,65,67,70,83,84,97,99] However, varied age thresholds were used to define the pediatric population. Most studies defined the pediatric population as individuals younger than 17 years of age, but other studies included children up to 18 years,[4,5,92] 19 years,[75] 20 years,[12-14] or 22.5 years of age.[81] White matter changes associated with normal development might confound detection of white matter injury; moreover, because developmental changes can occur at different rates even in children of the same chronologic age, use of DTI in the pediatric population is a challenging undertaking.

Many studies reported the mechanism of injury of patients with TBI such as motor vehicle collisions, falls, and assaults. However, because patients with different mechanisms were almost always consolidated into a single patient group, it is impossible to draw conclusions about imaging findings as they relate to different mechanisms of injury.

Because age, sex, anthropometrics, and injury mechanism can greatly influence outcomes, it is important that these issues be considered in study design and interpretation of results. Two major issues therefore emerge in consideration of the demographics of a TBI population. First, it is important to frame the comparison of results from multiple studies in the context of demographic differences between the studied samples. Second, within a single study, a group analysis involving a demographically diverse sample might mask important findings unique to a particular demographic subset or lead to spurious group differences.

SEVERITY, CHRONICITY, AND STUDY DESIGN

Traumatic injury to the brain can result in a spectrum of injuries. There is a lack of consensus regarding whether they represent subsets of a single-entity or distinct pathologic processes. We found a wide variation in the injury severity studied, ranging from mild, in which there is a complete absence of abnormalities on conventional imaging, to severe, in which subjects remain in a vegetative state. While some studies were restricted to patients of a specific injury severity, many studies included patients of varying severities. For studies reporting the GCS, we defined severity as mild (GCS, 13–15), moderate (GCS, 9–12), or severe (GCS, 3–8). For articles that did not report the GCS but characterized severity as mild, moderate, or severe, we accepted the authors' report of severity. Four studies did not report injury severity.[26,33,53,60] Several articles distinguished between mild-complicated and mild-uncomplicated TBI. While both groups of patients exhibited GCS in the mild range (>13), patients with mild-complicated TBI had findings of TBI on conventional imaging (CT and structural MR imaging), whereas patients with "true" mild or mild-uncomplicated TBI did not. Some articles specifically reported a distinction between patients with mild-complicated and mild-uncomplicated TBI. Many articles, though not making the mild-complicated versus mild-uncomplicated distinction, specifically noted that subjects with mild TBI lacked significant findings on conventional imaging. However, other articles simply reported "mild" severity without mentioning the results of conventional brain imaging. There has been an increasing trend toward differentiating mild-complicated versus mild-uncomplicated injury beginning in 2009. The earlier literature did not make the distinction, referring to the injury as "mild" without

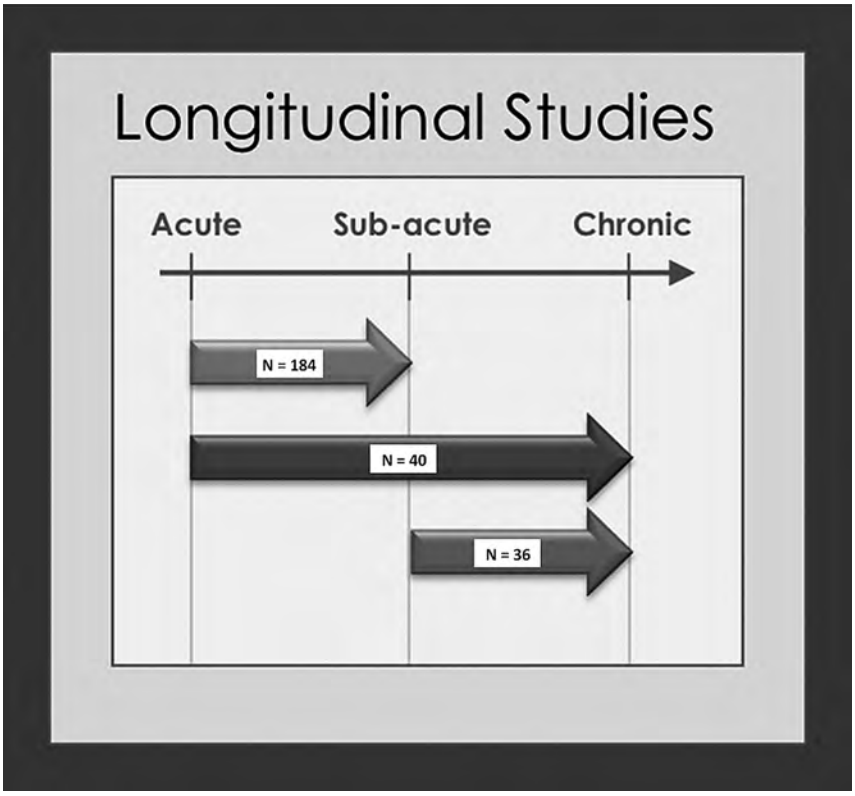

FIG 4. Thirteen studies used a longitudinal design. Numbers represent patients from all studies imaged at 2 time points. Nine studies assessed patients at both acute and subacute time points.[3,29,39,47,54,56,67,83,85] One study assessed patients at both acute and chronic time points.[102] Two studies assessed patients at both subacute and chronic time points.[24,93] One study ($n = 47$) assessed patients twice during the subacute period and, therefore, was omitted from the figure.[49]

qualification. This likely represents an increasing awareness of the distinction between mild-complicated and mild-uncomplicated, because studies have demonstrated that the clinical features of mild-complicated injuries often bear closer resemblance to those of moderate TBI than they do to mild-uncomplicated TBI.[104] Finally, some articles did not differentiate moderate and severe TBI but, rather, grouped all such patients into 1 category.

Similar to severity, chronicity (Fig 3) is an important factor in the development of the study design. Primary injury and secondary injury play different roles in the evolution of pathology as a function of time postinjury. Similarly, microstructural pathology, as detected with DTI, may change with time. We found a wide variation among studies as to the timing of DTI relative to TBI, ranging from days to years. To systematically assess the timing of DTI after injury, which we termed "injury chronicity," we divided subjects into 3 generally accepted categories. Acute injury included patients imaged within 2 weeks of TBI, while chronic injury included patients imaged at least 1 year following injury. The subacute period included imaging performed between 2 weeks and 1 year after TBI. All articles reported the timing of DTI after TBI.

Figure 3 details the total number of articles reporting DTI for the study of TBI within a given timeframe and of a particular injury severity and includes articles that report mixed severities, mixed chronicities, or both. Most subjects were studied in the subacute setting (Fig 3), most commonly having severe TBI followed by mild TBI. This trend might be attributable to the greater ease of subject enrollment during the subacute period, rather than to the clinical importance of this timeframe for the study. Patients are more easily enrolled from rehabilitation centers, where they were actively seeking treatment for their injuries. In the acute setting, patients with mild TBI might not even seek medical treatment and patients with severe TBI were too involved in urgent treatment to participate in a research study. Unless identified retrospectively, patients are easily lost to follow-up at chronic time points. When categorized according to severity, independent of chronicity, the total number of patients with moderate TBI represented approximately half the total number of patients with mild TBI and half the total number of patients with severe TBI (Fig 3). Although the minority of patients studied across all severities was examined in the acute setting, use of DTI as a prognostic tool is dependent on the identification of early biomarkers; therefore, the acute setting is an important area for future research, as are longitudinal studies examining patients at both the acute and chronic time points.

Most articles used cross-sectional designs. Eighteen articles reported multiple groups of subjects who were imaged at various times postinjury,[3,5,8,24,25,31,32,34,39,54,56,65,68,72,76,85,93,102] whereas 79 articles reported a single homogeneous group of patients all within a 1-injury chronicity timeframe. Only 13 articles, reporting a total of 283 patients, used longitudinal designs and imaged the same group of patients at 2 different time points (Fig 4).[3,24,29,39,47,49,54,56,67,83,85,93,102] One additional article reported imaging of the same group of patients acutely and again at least 1 year following injury but used a cross-sectional analysis at each of these time points and did not report change with time within subjects.[85]

A prospective study of patients with TBI is difficult; attrition during follow-up is a significant challenge. Of those studies that used a longitudinal design, only 8 reported attrition. The average attrition rate across these studies was 0.32 (range, 0.11–0.60).[3,24,29,49,54,56,83,85] Despite the challenge of attrition, longitudinal studies are integral to the understanding the natural history of TBI and for early prognostication.

DATA ACQUISITION PARAMETERS

Important considerations in the use of DTI are the strength of the magnetic field, the number of diffusion-sensitizing gradient magnetic field directions, and the choice of b-values. Use of greater magnetic field strengths has advantages and disadvantages; greater signal-to-noise ratio, improved spatial resolution, and

faster scanning times commonly achieved at stronger magnetic field strengths come at the cost of increased magnetic field inhomogeneity. In the setting of clinical DTI, most facilities will choose a b-value between 750 and 1000, whereas b-values of up to 3000 are used experimentally.[105,106] Increasing the b-value increases the sensitivity to diffusion, but with a decrease in signal-to-noise ratio. Encoding the direction of diffusion requires a minimum of 6 diffusion-sensitizing directions; greater resolution can be achieved by introducing additional directions, but this adds time to image acquisition. We summarize the acquisition parameters used in DTI studies of TBI as follows.

Nearly equal numbers of articles reported performing DTI at 1.5T and 3T (48[3-5,8,15-18,24,26-28,30-34,38,39,42-44,47-49,52,55-58,66-68,70,72,73,76,77,79,80,82,87,88,91,93,97,101,102] and 52,[6,7,9-14,19-23,25,29,35-37,40,41,45,46,50,51,53,54,59-65,69,71,74,75,78,81,83-86,89,90,92,94-96,98-100] respectively). The number of diffusion-sensitizing directions used ranged from 6 to 64, with an average of 27 but a mode of 12. In 2011 alone, the mode increased to 64. The b-value was reported in all except 6 articles.[24,53,74,96,99,100] All articles except 7 used a single b-value in addition to zero.[25,59-63,81] The 7 articles using multiple b-values each used 5 unique b-values. The average b-value was 947, the range of b-values was 300–1590, and the median and the mode were 1000.

Spatial resolution is an additional important consideration. Assessments of anisotropy, which are central to studies of TBI, measure the aggregate range of diffusivities across the tissues composing the voxel. Partial volume effects that may spuriously reduce anisotropy will be more likely when larger voxel volumes are examined. Voxel sizes varied among the articles we reviewed, with an average voxel size of 11.3 mL^3 (range, 1.83–31.25 mL^3). Average section thickness was 3.08 mm (range, 1.72–6 mm).

DATA ANALYSIS METHODS

DTI can be used to study brain structure either on a regional or a whole-brain level. Regional analyses include both those in which an a priori region of interest is chosen for study and tractography, in which an a priori region of interest is used to define a white matter tract for study. In both approaches, average diffusion values such as FA are extracted from voxels within the ROIs or tracts for subsequent analysis. Whole-brain analyses include voxelwise analyses, tract-based spatial statistics, a specialized type of voxelwise analysis, and histogram analyses of all brain or all white matter voxels.

In our review of the literature, we found that among those studies using regional analyses, 60 studies[3-6,10,12-19,22-28,30,33-35,37-41,43,46,48,49,51,52,54,55,57-66,76,81,82,86,92,93,95-100,102] used a region-of-interest approach and 30 studies[9,11,17-19,21,31,41,42,46,47,50,55,58,63,67,69,72,73,75,77,79,80,83,84,87,88,91,95,101] used tractography. Fewer studies used whole-brain analyses, of which 17 studies[7,11,20,21,29,44,45,50,53,56,58,71,74,80,95,98,101] were based on a voxelwise approach, 7 studies[14,32,36,68,78,86,100] used TBSS, and 4 studies[8,34,44,50] used histogram analysis. Cross-validation of approaches can be achieved by using multiple analytic strategies. For instance, 1 article that used both a voxelwise analysis and TBSS found abnormalities in the same areas by using both techniques.[70] In our review of the literature, we found that 18 articles reported using >1 type of analysis.[6,14,17-19,27,34,41,46,50,55,58,63,80,86,95,98,100]

Table 1: Most common locations of abnormal FA by ROI analysis[a]

Locations	Findings
Corpus callosum, anterior/genu	22[b]/30
Corpus callosum, posterior/splenium	21[b]/32
Posterior limb of the internal capsule	11/22
Corpus callosum, body	10/18
Frontal lobe	7/10
Corona radiata	6[b]/10
Cingulum bundle	7/8
Centrum semiovale	6/11
Brain stem	5/8
Cerebral peduncle	5/7

[a] Values indicate the number of articles reporting abnormally low FA. Denominators represent the number of studies that assessed FA at these locations, including those that did not find abnormal FA.
[b] Includes articles reporting abnormally high FA. A fully referenced version of this Table is available in On-line Table 2.

Table 2: Most common locations of abnormal FA by tractography[a]

Locations	Findings
Corpus callosum, total	10[b]/11
Corpus callosum, anterior/genu	8/8
Corpus callosum, posterior/splenium	7/8
Cingulum bundle	6/10
Fornix	5/7
Corpus callosum, body	4/6
Fronto-occipital fasciculus	4/5
Inferior longitudinal fasciculus	4/5
Uncinate fasciculus	4/5
Hippocampus	3/3

[a] Values indicate the number of articles reporting abnormally low FA. Denominators represent the number of studies that assessed FA at these locations, including those that did not find abnormal FA.
[b] Includes articles reporting abnormally high FA. A fully referenced version of this Table is available in On-line Table 3.

Table 3: Most common locations of abnormal FA by whole-brain analysis[a]

Locations	Findings
Superior longitudinal fasciculus	7/25
Corpus callosum, anterior/genu	7/25
Inferior longitudinal fasciculus	7/25
Posterior limb of the internal capsule	6/25
Fronto-occipital fasciculus	6/25
Cingulum bundle	5/25
Corona radiata	5/25
Corpus callosum, overall	5/25
Corpus callosum, body	5/25
Fornix	5/25
Frontal lobe	5/25
Temporal lobe	5/25

[a] Values indicate the number of articles reporting low FA in these locations. Twenty-five articles used voxelwise analysis to assess FA throughout the entire brain. Because whole-brain analyses examine all brain regions, denominators are identical for all brain regions. A fully referenced version of this Table is available in On-line Table 4.

Tables 1–3 show the most commonly identified areas of abnormal FA in region-of-interest, tractography, and whole-brain analyses; the most commonly implicated regions are generally similar across approaches. However, they are not entirely consistent. For example, the centrum semiovale and the brain stem are locations where abnormal FA has commonly been identified by using region-of-interest analysis, but these locations are not commonly identified by using either tractography or whole-brain analysis. Additionally, the superior longitudinal fasciculus is the most commonly identified location with abnormal FA by using whole-

Table 4: Most common locations of abnormal mean diffusivity by ROI analysis[a]

Locations	Findings
Corpus callosum, posterior/splenium	10[b]/20
Corpus callosum, anterior/genu	10/16
Frontal lobe	9/10
White matter	7/7
Thalamus	4/6

[a] Values indicate the number of articles reporting abnormally low MD. Denominators represent the number of studies that assessed MD at these locations, including those that did not find abnormal MD.
[b] Includes articles reporting abnormally high MD. A fully referenced version of this Table is available in On-line Table 5.

Table 5: Most common locations of abnormal mean diffusivity by tractography analysis[a]

Locations	Findings
Corpus callosum, anterior/genu	4/4
Fronto-occipital fasciculus	4/5
Inferior longitudinal fasciculus	4/5
Uncinate fasciculus	4/4
Cingulum bundle	3[b]/7

[a] Values indicate the number of articles reporting abnormally low MD. Denominators represent the number of studies that assessed MD at these locations, including those that did not find abnormal MD.
[b] Includes articles reporting abnormally high MD. A fully referenced version of this Table is available in On-line Table 6.

Table 6: Most common locations of abnormal mean diffusivity by whole-brain analysis[a]

Locations	Findings
Cingulum bundle	6/13
Corpus callosum, total	5/13
Superior longitudinal fasciculus	4/13
Posterior limb of the internal capsule	4/13
Fronto-occipital fasciculus	4/13
Frontal lobe	4/13

[a] Values indicate the number of articles reporting abnormally increased MD in these locations. Thirteen articles used whole-brain analysis to assess MD throughout the entire brain. Because whole-brain analyses examine all brain regions, denominators are identical for all brain regions. A fully referenced version of this Table is available in On-line Table 7.

brain analysis, but this region does not appear as a common location by using either region-of-interest analysis or tractography. This discrepancy may be due to the fact that the superior longitudinal fasciculus was examined infrequently and does not necessarily indicate that it is an uncommon site of TAI. Tables 4–6 show the most commonly identified areas of abnormal MD in each of the region-of-interest, tractography, and whole-brain analyses. The corpus callosum is the most commonly identified region of abnormal FA and MD, perhaps because it is the largest white matter tract in the brain and an important site of TBI pathology. For both reasons, the corpus callosum is commonly chosen as a target of regional analyses, a choice that may bias the net findings of the literature.

The reliability of regional analyses depends on accurate and reproducible spatial localization of ROIs or tracts across subjects. Approaches to ensuring reliability may include specific reliability and reproducibility testing when expert observers perform placement of ROIs. Alternatively, subject images may be spatially normalized to a standard template, with placement of ROIs based on the template. This latter approach ensures that region-of-interest placement is consistent among subjects; however, it depends on the robustness of the registration of the subject brains to a standard space. Fourteen articles used spatial normalization to ensure standardization of region-of-interest/tract location.[5,13,14,35,54,61-63,72,73,77,86,92,100] Sixty-three articles used expert manual placement of regions of interest.[3,4,6,9-11,15,16,19,22-28,30,31,33,34,37-43,46-51,55,57,59,60,63-67,69,72,75,76,80-85,87-89,91,93-95,97-99,102] However, only 35 of 63 studies reported that they performed reliability assessments, such as inter-/intraobserver reliability.[6,9-11,19,25,40-43,46,47,49,53,55,59,60, 64-67,75,76,81,83-85,87-89,91,93,94,98,99] The studies that did report reliability testing included 63% (18/30) of articles using tractography[9,11,19,41,42,46,47,55,67,75,83-85,87-89,91,94] but only 31% (19/61) of articles using region-of-interest analyses.[6,10,19,25,40,41,43,46,55,59,60,64-66,76,81,93,98,99]

In comparing articles using whole-brain approaches, 5/8 of the TBSS studies found significant abnormalities,[14,32,36,68,78] whereas all of the articles using voxelwise approaches identified significant differences. The greater likelihood of identifying abnormalities through voxelwise approaches as opposed to TBSS might be indicative of spurious group differences between patients and controls due to misalignment between subjects and the standard template, an issue that may be minimized by the TBSS approach.[107] On the other hand, TBSS may be inherently less sensitive because the analyses are restricted to a limited white matter skeleton.

SPECIFIC DIFFUSION MEASURES STUDIED

Diffusion tensor imaging yields multiple measures at each voxel. FA describes the directional coherence of water diffusion in tissue. MD is the scalar measure of the total direction-independent diffusion within a voxel. Axial diffusivity describes diffusion along the principal axis of the diffusion ellipsoid, while radial diffusivity is an average of diffusion along its 2 minor axes. FA was the most commonly studied parameter across the studies we reviewed. Abnormally low FA is widely held to represent alterations of white matter microstructure consistent with TAI.[108] Elevations of FA have been much less frequently reported (see below). Although some authors have hypothesized that abnormally high FA represents cytotoxic edema,[54] the mechanistic basis of abnormally high FA remains uncertain.

FA was examined in all studies. All 100 articles, except for 4[6,54,89,96] (which showed elevated FA), described findings of low FA in subjects with TBI, regardless of the time of injury and across the spectrum of injury severity. MD is the next most commonly reported parameter ($n = 51$).[3,9,10,13-17,19,21,22,25,28,29,33-40,42,43,48-50,55,56,59-63,66,67,69,71,72,76,77,81,83,90,91,93,95,96,100-102] Articles that examined parameters other than FA almost always identified areas of abnormal FA and then assessed other parameters within these regions. One article initially identified loci of abnormal MD and then assessed FA in the regions of abnormal MD.[20] Axial diffusivity and radial diffusivity were much less commonly assessed ($n = 18$).[3,8,11,13,14,20,22,36-38,49,54,56,63,66,76,81,89] Only 2 articles reported radial diffusivity and not axial diffusivity.[29,66] One article used a predictive model in which all 4 measures were incorporated.[65]

While FA is a useful summary measure, more detailed information regarding diffusional uniformity, potentially obtainable through study of eigenvalue measures, may be important for diagnosis and outcome prediction and especially for understanding

Table 7: Relationship of DTI metrics to cognitive outcome measures[a]

DTI Measure	Correlation	Attention	Executive Function	Memory	Motor	Psychomotor/ Processing Speed	Visuospatial	IQ
FA	Positive correlation	11	9	14	4	5	4	2
	Negative correlation	6	5	2	0	2	0	0
	No correlation	2	6	6	1	1	0	6
MD	Positive correlation	3	2	2	0	0	1	0
	Negative correlation	4	6	7	0	1	3	0
	No correlation	1	4	3	1	2	0	0

Note:—IQ indicates intelligence quotient.

[a] Total number of articles assessing relationships between DTI measures and cognitive outcomes. Cognitive-outcome measures have been categorized as 7 domains (top row). Articles are classified as reporting positive correlation, negative correlation, or no correlation. Positive correlation indicates a correlation coefficient greater than zero. Negative correlation indicates a correlation coefficient less than zero. No correlation includes articles that reported analyzing relationships between the DTI measures and cognitive outcomes within a domain but either reported finding no correlation (correlation coefficient equal to zero) or a correlation with a *P* value > .05. A fully referenced version of this Table is available in On-line Table 8.

pathologic mechanisms of TBI in humans. Eigenvalue measures implicate specific pathologic mechanisms in animal models of TBI and other types of brain injury.[2] Including eigenvalue measures in a future study would facilitate a transitional bridge from animal to human studies and enable more informed targeting of novel interventions in a patient group with few therapeutic options.

BRAIN REGIONS

Brain regions examined varied greatly among the articles. We systematically tabulated the location of abnormal DTI measures (FA and MD separately) across all articles (Tables 1–6). To effectively summarize a large number of regions, we list only the top 10 most commonly identified regions of abnormal FA and the top 5 most commonly identified regions of abnormal MD via region-of-interest, tractography, and whole-brain analyses. When tabulating abnormal regions, it is important to recognize the relationship between study design and detection—that is, regional analyses can only detect a region as abnormal if the study design specifically examines that region. Whole-brain analyses, on the other hand, are positioned to detect all abnormal areas in the brain. Thus, the number of studies reporting an area as abnormal is influenced by the study design. Nonetheless, overall we found a large degree of consistency between studies regardless of the method of analysis. The corpus callosum, frontal lobe, internal capsule, and cingulum are among the most commonly identified regions of abnormality in DTI studies of TBI, perhaps because these structures are particularly vulnerable to injury due to their anatomic relationship to the skull and other structures such as the falx cerebri. These findings are almost entirely based on group comparisons and, therefore, do not necessarily reflect the distribution of injuries in the individual.

FUNCTIONAL OUTCOMES AFTER TBI

Seventy-two of 100 articles examined outcomes associated with TBI in addition to the imaging findings,[4-9,11,13,14,16-23,25,27,30,33,36-43,45-47,49-59,61,62,64-68,70,71,74-76,78,80-82,84,87-94,96,98,101,102] and almost all of these 72 articles reported specifically on the association of DTI findings with the outcomes. Most surprising however, 3 articles, though they reported outcomes, did not report analysis of the relationship between the outcome measures and DTI.[27,35,56] Fifty-one of the 72 articles assessed neuropsychological outcomes.[5-7,9-14,16-19,22,23,25,27,30,36-39,41-43,45,46,50-52,54,57-60,64,65,67,68,74,75,80,81,88,90-94,96,102] Eighteen of 72 used a global outcome measure (eg, Glasgow Outcomes Scale, Coma Recovery Scale, Mini-Mental Status Examination),[4,16,22,33,42,50,57-59,63,66,70,76,80-82,84,88] 14 articles reported correlation with the GCS,[4,5,7,8,22,33,38,42,61,62,66,87,91,98] 8 articles correlated FA with intelligence quotient ,[5,14,16,22,54,58,80,92] and 12 articles examined the relationship between DTI and postconcussive symptoms (eg, headaches, visual disturbances, cognitive symptoms) and/or mood disorders.[6,20,23,40,53,54,78,80,81,89,92,99] Several articles reported the association of DTI with other patient assessments as surrogate outcome measures. These measures included electroencephalography,[79] fMRI,[10,63,69,75,90,100] MR spectroscopy,[5,82] regional brain volumes,[85] and motor-evoked potentials.[97]

Table 8: Relationship of DTI metrics to general clinical assessments[a]

DTI Measure	Correlation	Global Outcome Measures	GCS	Postconcussion Symptoms
FA	Positive correlation	11	5	3
	Negative correlation	4	1	3
	No correlation	3	8	6
MD	Positive correlation	1	1	1
	Negative correlation	5	4	2
	No correlation	0	0	1

[a] Total number of articles assessing relationships between DTI measures and global outcome measures (see "Functional Outcomes after TBI"), GCS, or postconcussive symptoms. Articles are classified as reporting positive correlation, negative correlation, or no correlation. Positive correlation indicates a correlation coefficient greater than zero. Negative correlation indicates a correlation coefficient less than zero. No correlation includes articles that reported analyzing relationships between the DTI measure and cognitive outcomes within a domain but either reported finding no correlation (correlation coefficient equal to zero) or a correlation with a *P* value >.05. A fully referenced version of this Table is available in On-line Table 9.

Of the articles that correlated DTI metrics with outcome, we found considerable heterogeneity among studies with respect to the specific outcome measures used. Choice of specific neuropsychological tests was most variable, with only a few articles reporting the same measure (range, 1–19; mean, 1.8; median, 1.5). To summarize the data from these studies, we divided the various outcome measures into domains, including the following: attention, executive function, memory, motor function, psychomotor/processing speed, visuospatial function, global outcome, GCS, intelligence quotient, and postconcussive symptoms. Tables 7 and 8 summarize the significant associations reported between DTI metrics and these outcome categories.

In addition to heterogeneity of the outcome measures used, additional variability (eg, brain region examined, analysis type, and DTI metric assessed) among studies examining the same out-

come domain further complicated summary of the literature. The average number of studies examining the same outcome domain was 15 (range, 6–29; Tables 7 and 8). However, even among articles examining the same domain, results are inconsistent.

Discordance in the results of outcome studies can, perhaps, be attributed to several issues. Although studies may examine the same domain, they typically vary in the choice of the specific measure/instrument used. Because the sensitivity and specificity of any 2 measures, though designed to test the same cognitive domain, for instance, will differ,[109] results of studies relating imaging to these differing outcome measures will potentially differ between the 2 studies as well. Moreover, the severity of TBI might determine the extent to which a patient experiences impairment in cognition or other adverse outcomes. As a result, comparison between studies including different injury severities might not be appropriate. Finally, impairment secondary to TBI, particularly mild TBI, can be subtle and, therefore, escape detection by using some formal testing tools. Perhaps the most salient message to be derived from this segment of the literature is that standardization of outcome measures and study design is essential to future meaningful study of TBI.[110]

ASSESSMENT OF INDIVIDUAL PATIENTS WITH TBI

The heterogeneity of injury mechanisms that cause TBI is likely best captured in studies assessing individual patients with TBI; group comparisons are inherently insensitive to interindividual variation, which is a hallmark of TBI. All of the articles included in this review report group analyses of patients with TBI. However, >35 additional articles report the use of DTI in individual TBI cases (eg, Gold and Lipton[111]). Several of the articles included in this review reported assessment of individual patients in addition to their group analyses. Two articles examined whole-brain white matter histograms of individual patients,[8,50] but only 1 reported results at the single-subject level, finding the distribution of FA in patients with TBI to be skewed toward lower FA in comparison with controls.[8] Three articles applied a tractography approach to individual subjects,[31,58,63] while 2 articles applied the whole-brain approach to individuals.[44,50] Assessment of individual patients with TBI is important to the characterization of outliers, who might differ from the group in terms of extent and spatial distribution of injury, and is a prerequisite to clinical use of DTI in evaluating patients with TBI.

IMPLICATIONS, LIMITATIONS, AND POSSIBILITIES

DTI has been studied extensively as a tool for identification of brain abnormalities related to TBI and to understand the relationship of these brain abnormalities to other clinical features of the disorder. During the past decade, the number of such studies has risen exponentially and continues to increase with no sign of abatement. A unifying theme can be deduced from this large body of research: DTI is an extremely useful and robust tool for the detection of TBI-related brain abnormalities. The overwhelming consensus of these studies is that low white matter FA is characteristic of TBI. This finding is consistent across almost all the articles we reviewed, despite significant variability in patient demographics, modest differences in data acquisition parameters, and a multiplicity of data analysis techniques. This consistency across studies attests to the robustness of DTI as a measure of brain injury in TBI. The finding of significant differences in FA histograms that pool all white matter voxels across the whole brain is particularly compelling, indicating that a substantial portion of the hundreds of thousands of voxels in the image datasets are abnormal.

We also found an overwhelming consensus that imaging abnormalities detected with DTI are associated with important clinical outcomes. This further validates DTI as a meaningful measure of clinically important brain injury. However, heterogeneity among the outcome measures that have been reported limits our ability to draw direct generalizable connections between DTI abnormalities at specific brain locations and specific outcomes. The greatest degree of variability among the studies we reviewed was in the choice of outcome measures. As others have suggested, an important priority for future studies of TBI should be the use of standardized approaches, particularly standardization of outcome measures.[112] Additionally, more high-quality longitudinal studies are needed to extend the power of DTI, from identifying patients with TBI at cross-section to accurately predicting future clinical status.

By far, FA was the DTI measure used most commonly across the studies we reviewed. Too few articles reported analyses of eigenvalues to permit meaningful inferences regarding the role of eigenvalue findings in the assessment of TBI at this time. This is an important area of deficiency because preclinical studies indicate that differential effects on eigenvalue measures can separate pathologic mechanisms. Thus, more detailed study of the full palette of metrics available from DTI is a great area for future study.

The variety of data analysis approaches applied across the studies we reviewed presents a significant obstacle to summary of the data and limits the inferences that can be made on the basis of the literature as a whole. It is primarily on the basis of this factor that we determined that meta-analysis methods would not be appropriate for assessment of this literature. Studies reporting regional analyses might be considered comparable on the basis of similarity of brain regions tested across multiple studies. However, the precise spatial location represented by a given region-of-interest, tract, or brain structure descriptors may vary significantly among studies on the basis of the methods, criteria, and raters used to define ROIs. Intra- and inter-rater variability can confound inferences based on these studies. While reliability testing can and should be performed to verify the reproducibility of region-of-interest placement, only a minority of studies did so.

Whole-brain analyses perhaps offer the greatest promise for pooling of results across studies, provided that the studies normalize their image data to the same brain template. Variability in the brain atlases used for spatial normalization and inconsistent reporting of coordinates for abnormalities in the studies we reviewed limit such cross-study comparison at this time.

All articles captured by our review used group analyses, though several also incorporated assessments of individual patients with TBI. Group-analysis approaches are powerful means for improving statistical power. However, the use of a group analysis limits the study to detection of abnormalities that occur in the same location in all patients. The fact that robust group effects have been reproduced in studies of DTI in patients with TBI is consistent with long-standing concepts that identify certain brain regions as particularly susceptible to TAI. Intersubject differences in the mechanism of injury as well as other biomechanical factors

such as head and body composition make it highly probable that despite some commonalities, many areas of injury will differ among patients. Further application of individualized assessments of regional brain injury is thus needed to realize the full potential of DTI as a research and clinical tool.

On the basis of our analysis of the current literature, we suggest that important focus areas for future study should include larger longitudinal studies, incorporation of multiple outcome measures in statistical models that account for the complexity inherent in TBI populations, and assessment of interindividual differences. Standardization across centers, specifically with regard to data acquisition parameters, data analysis techniques, and the specific outcome measures assessed, promises to greatly increase the yield of such studies.

In summary, DTI provides a robust measure of clinically important TAI at cross-section, despite the variability inherent in characteristics of patients with TBI and injury mechanisms as well as study differences in data acquisition and analysis methods. Larger longitudinal studies will be essential for the evaluation of DTI as a prognostic biomarker in TBI. More detailed assessment of DTI metrics and translational imaging studies should be undertaken to link pathophysiologic mechanisms in animal models to important clinical outcomes in patients. Together, these approaches promise to realize the full potential of DTI to improve diagnosis and treatment of patients with TBI.

ACKNOWLEDGMENTS

We thank Tova M. Gardin for graphic arts assistance.

Disclosures: Molly E. Zimmerman—*UNRELATED*: *Grants/Grants Pending*: National Institutes of Health (NIH)/National Institute on Aging,* Alzheimer's Association,* Bristol-Myers Squibb.* Michael L. Lipton—*UNRELATED*: *Grants/Grants Pending*: NIH,* Dana Foundation,* Resurrecting Lives Foundation,* *Patents (planned, pending, or issued)*: Einstein patent pending,* *Comments*: for data analysis techniques. *Money paid to the institution.

REFERENCES

1. Niogi SN, Mukherjee P. **Diffusion tensor imaging of mild traumatic brain injury.** *J Head Trauma Rehabil* 2010;25:241–55
2. Mac Donald CL, Dikranian K, Bayly P, et al. **Diffusion tensor imaging reliably detects experimental traumatic axonal injury and indicates approximate time of injury.** *J Neurosci* 2007;27:11869–76
3. Arfanakis K, Haughton VM, Carew JD, et al. **Diffusion tensor MR imaging in diffuse axonal injury.** *AJNR Am J Neuroradiol* 2002;23:794–802
4. Akpinar E, Koroglu M, Ptak T. **Diffusion tensor MR imaging in pediatric head trauma.** *J Comput Assist Tomogr* 2007;31:657–61
5. Babikian T, Marion SD, Copeland S, et al. **Metabolic levels in the corpus callosum and their structural and behavioral correlates after moderate to severe pediatric TBI.** *J Neurotrauma* 2010;27:473–81
6. Bazarian JJ, Zhong J, Blyth B, et al. **Diffusion tensor imaging detects clinically important axonal damage after mild traumatic brain injury: a pilot study.** *J Neurotrauma* 2007;24:1447–59
7. Bendlin BB, Ries ML, Lazar M, et al. **Longitudinal changes in patients with traumatic brain injury assessed with diffusion-tensor and volumetric imaging.** *Neuroimage* 2008;42:503–14
8. Benson RR, Meda SA, Vasudevan S, et al. **Global white matter analysis of diffusion tensor images is predictive of injury severity in traumatic brain injury.** *J Neurotrauma* 2007;24:446–59
9. Bigler ED, McCauley SR, Wu TC, et al. **The temporal stem in traumatic brain injury: preliminary findings.** *Brain Imaging Behav* 2010;4:270–82
10. Bonnelle V, Leech R, Kinnunen KM, et al. **Default mode network connectivity predicts sustained attention deficits after traumatic brain injury.** *J Neurosci* 2011;31:13442–51
11. Caeyenberghs K, Leemans A, Coxon J, et al. **Bimanual coordination and corpus callosum microstructure in young adults with traumatic brain injury: a diffusion tensor imaging study.** *J Neurotrauma* 2011;28:897–913
12. Caeyenberghs K, Leemans A, Geurts M, et al. **Correlations between white matter integrity and motor function in traumatic brain injury patients.** *Neurorehabil Neural Repair* 2011;25:492–502
13. Caeyenberghs K, Leemans A, Geurts M, et al. **Brain-behavior relationships in young traumatic brain injury patients: DTI metrics are highly correlated with postural control.** *Hum Brain Mapp* 2010;31:992–1002
14. Caeyenberghs K, Leemans A, Geurts M, et al. **Brain-behavior relationships in young traumatic brain injury patients: fractional anisotropy measures are highly correlated with dynamic visuomotor tracking performance.** *Neuropsychologia* 2010;48:1472–82
15. Chang MC, Jang SH. **Corpus callosum injury in patients with diffuse axonal injury: a diffusion tensor imaging study.** *NeuroRehabilitation* 2010;26:339–45
16. Chang MC, Kim SH, Kim OL, et al. **The relation between fornix injury and memory impairment in patients with diffuse axonal injury: a diffusion tensor imaging study.** *NeuroRehabilitation* 2010;26:347–53
17. Cho HK, Hong JH, Kim SH, et al. **Clinical usefulness of diffusion tensor imaging in patients with transtentorial herniation following traumatic brain injury.** *Brain Inj* 2011;25:1005–09
18. Choi GS, Kim OL, Kim SH, et al. **Classification of cause of motor weakness in traumatic brain injury using diffusion tensor imaging.** *Arch Neurol* 2012;69:363–67
19. Christidi F, Bigler ED, McCauley SR, et al. **Diffusion tensor imaging of the perforant pathway zone and its relation to memory function in patients with severe traumatic brain injury.** *J Neurotrauma* 2011;28:711–25
20. Chu Z, Wilde EA, Hunter JV, et al. **Voxel-based analysis of diffusion tensor imaging in mild traumatic brain injury in adolescents.** *AJNR Am J Neuroradiol* 2010;31:340–46
21. Cubon VA, Putukian M, Boyer C, et al. **A diffusion tensor imaging study on the white matter skeleton in individuals with sports-related concussion.** *J Neurotrauma* 2011;28:189–201
22. Ewing-Cobbs L, Prasad MR, Swank P, et al. **Arrested development and disrupted callosal microstructure following pediatric traumatic brain injury: relation to neurobehavioral outcomes.** *Neuroimage* 2008;42:1305–15
23. Geary EK, Kraus MF, Pliskin NH, et al. **Verbal learning differences in chronic mild traumatic brain injury.** *J Int Neuropsychol Soc* 2010;16:506–16
24. Greenberg G, Mikulis DJ, Ng K, et al. **Use of diffusion tensor imaging to examine subacute white matter injury progression in moderate to severe traumatic brain injury.** *Arch Phys Med Rehabil* 2008;89:S45–50
25. Grossman EJ, Ge Y, Jensen JH, et al. **Thalamus and cognitive impairment in mild traumatic brain injury: a diffusional kurtosis imaging study.** *J Neurotrauma* 2012;29:2318–27
26. Gupta RK, Saksena S, Agarwal A, et al. **Diffusion tensor imaging in late posttraumatic epilepsy.** *Epilepsia* 2005;46:1465–71
27. Hanten G, Wilde EA, Menefee DS, et al. **Correlates of social problem solving during the first year after traumatic brain injury in children.** *Neuropsychology* 2008;22:357–70
28. Hartikainen KM, Waljas M, Isoviita T, et al. **Persistent symptoms in mild to moderate traumatic brain injury associated with executive dysfunction.** *J Clin Exp Neuropsychol* 2010;32:767–74
29. Henry LC, Tremblay J, Tremblay S, et al. **Acute and chronic changes in diffusivity measures after sports concussion.** *J Neurotrauma* 2011;28:2049–59
30. Holli KK, Waljas M, Harrison L, et al. **Mild traumatic brain injury**

tissue texture analysis correlated to neuropsychological and DTI findings. *Acad Radiol* 2010;17:1096–102
31. Hong JH, Kim OL, Kim SH, et al. **Cerebellar peduncle injury in patients with ataxia following diffuse axonal injury.** *Brain Res Bull* 2009;80:30–35
32. Huang MX, Theilmann RJ, Robb A, et al. **Integrated imaging approach with MEG and DTI to detect mild traumatic brain injury in military and civilian patients.** *J Neurotrauma* 2009;26:1213–26
33. Huisman TA, Schwamm LH, Schaefer PW, et al. **Diffusion tensor imaging as potential biomarker of white matter injury in diffuse axonal injury.** *AJNR Am J Neuroradiol* 2004;25:370–76
34. Inglese M, Makani S, Johnson G, et al. **Diffuse axonal injury in mild traumatic brain injury: a diffusion tensor imaging study.** *J Neurosurg* 2005;103:298–303
35. Kennedy MR, Wozniak JR, Muetzel RL, et al. **White matter and neurocognitive changes in adults with chronic traumatic brain injury.** *J Int Neuropsychol Soc* 2009;15:130–36
36. Kinnunen KM, Greenwood R, Powell JH, et al. **White matter damage and cognitive impairment after traumatic brain injury.** *Brain* 2011;134:449–63
37. Kraus MF, Susmaras T, Caughlin BP, et al. **White matter integrity and cognition in chronic traumatic brain injury: a diffusion tensor imaging study.** *Brain* 2007;130:2508–19
38. Kumar R, Gupta RK, Husain M, et al. **Comparative evaluation of corpus callosum DTI metrics in acute mild and moderate traumatic brain injury: its correlation with neuropsychometric tests.** *Brain Inj* 2009;23:675–85
39. Kumar R, Husain M, Gupta RK, et al. **Serial changes in the white matter diffusion tensor imaging metrics in moderate traumatic brain injury and correlation with neuro-cognitive function.** *J Neurotrauma* 2009;26:481–95
40. Lange RT, Iverson GL, Brubacher JR, et al. **Diffusion tensor imaging findings are not strongly associated with postconcussional disorder 2 months following mild traumatic brain injury.** *J Head Trauma Rehabil* 2012;27:188–98
41. Levin HS, Wilde E, Troyanskaya M, et al. **Diffusion tensor imaging of mild to moderate blast-related traumatic brain injury and its sequelae.** *J Neurotrauma* 2010;27:683–94
42. Levin HS, Wilde EA, Chu Z, et al. **Diffusion tensor imaging in relation to cognitive and functional outcome of traumatic brain injury in children.** *J Head Trauma Rehabil* 2008;23:197–208
43. Levin HS, Wilde EA, Hanten G, et al. **Mental state attributions and diffusion tensor imaging after traumatic brain injury in children.** *Dev Neuropsychol* 2011;36:273–87
44. Lipton ML, Gellella E, Lo C, et al. **Multifocal white matter ultrastructural abnormalities in mild traumatic brain injury with cognitive disability: a voxel-wise analysis of diffusion tensor imaging.** *J Neurotrauma* 2008;25:1335–42
45. Lipton ML, Gulko E, Zimmerman ME, et al. **Diffusion tensor imaging implicates prefrontal axonal injury in executive function impairment following mild traumatic brain injury.** *Radiology* 2009;252:816–24
46. Little DM, Kraus MF, Joseph J, et al. **Thalamic integrity underlies executive dysfunction in traumatic brain injury.** *Neurology* 2010;74:558–64
47. Ljungqvist J, Nilsson D, Ljungberg M, et al. **Longitudinal study of the diffusion tensor imaging properties of the corpus callosum in acute and chronic diffuse axonal injury.** *Brain Inj* 2011;25:370–78
48. Lo C, Shifteh K, Gold T, et al. **Diffusion tensor imaging abnormalities in patients with mild traumatic brain injury and neurocognitive impairment**. *J Comput Assist Tomogr* 2009;33:293–97
49. Mac Donald CL, Johnson AM, Cooper D, et al. **Detection of blast-related traumatic brain injury in U.S. military personnel.** *N Engl J Med* 2011;364:2091–100
50. Marquez de la Plata CD, Yang FG, Wang JY, et al. **Diffusion tensor imaging biomarkers for traumatic axonal injury: analysis of three analytic methods.** *J Int Neuropsychol Soc* 2011;17:24–35
51. Maruta J, Suh M, Niogi SN, et al. **Visual tracking synchronization as a metric for concussion screening.** *J Head Trauma Rehabil* 2010;25:293–305
52. Matsushita M, Hosoda K, Naitoh Y, et al. **Utility of diffusion tensor imaging in the acute stage of mild to moderate traumatic brain injury for detecting white matter lesions and predicting long-term cognitive function in adults.** *J Neurosurg* 2011;115:130–39
53. Matthews SC, Strigo IA, Simmons AN, et al. **A multimodal imaging study in U.S. veterans of Operations Iraqi and Enduring Freedom with and without major depression after blast-related concussion.** *Neuroimage* 2011;54(suppl 1):S69–75
54. Mayer AR, Ling J, Mannell MV, et al. **A prospective diffusion tensor imaging study in mild traumatic brain injury.** *Neurology* 2010;74:643–50
55. McCauley SR, Wilde EA, Bigler ED, et al. **Diffusion tensor imaging of incentive effects in prospective memory after pediatric traumatic brain injury.** *J Neurotrauma* 2011;28:503–16
56. Messé A, Caplain S, Paradot G, et al. **Diffusion tensor imaging and white matter lesions at the subacute stage in mild traumatic brain injury with persistent neurobehavioral impairment.** *Hum Brain Mapp* 2011;32:999–1011
57. Miles L, Grossman RI, Johnson G, et al. **Short-term DTI predictors of cognitive dysfunction in mild traumatic brain injury.** *Brain Inj* 2008;22:115–22
58. Nakayama N, Okumura A, Shinoda J, et al. **Evidence for white matter disruption in traumatic brain injury without macroscopic lesions.** *J Neurol Neurosurg Psychiatry* 2006;77:850–55
59. Newcombe V, Chatfield D, Outtrim J, et al. **Mapping traumatic axonal injury using diffusion tensor imaging: correlations with functional outcome.** *PloS One* 2011;6:e19214
60. Newcombe VF, Outtrim JG, Chatfield DA, et al. **Parcellating the neuroanatomical basis of impaired decision-making in traumatic brain injury.** *Brain* 2011;134:759–68
61. Newcombe VF, Williams GB, Nortje J, et al. **Concordant biology underlies discordant imaging findings: diffusivity behaves differently in grey and white matter post acute neurotrauma.** *Acta Neurochir Suppl* 2008;102:247–51
62. Newcombe VF, Williams GB, Nortje J, et al. **Analysis of acute traumatic axonal injury using diffusion tensor imaging.** *Br J Neurosurg* 2007;21:340–48
63. Newcombe VF, Williams GB, Scoffings D, et al. **Aetiological differences in neuroanatomy of the vegetative state: insights from diffusion tensor imaging and functional implications.** *J Neurol Neurosurg Psychiatry* 2010;81:552–61
64. Niogi SN, Mukherjee P, Ghajar J, et al. **Extent of microstructural white matter injury in postconcussive syndrome correlates with impaired cognitive reaction time: a 3T diffusion tensor imaging study of mild traumatic brain injury.** *AJNR Am J Neuroradiol* 2008;29:967–73
65. Niogi SN, Mukherjee P, Ghajar J, et al. **Structural dissociation of attentional control and memory in adults with and without mild traumatic brain injury.** *Brain* 2008;131:3209–21
66. Oni MB, Wilde EA, Bigler ED, et al. **Diffusion tensor imaging analysis of frontal lobes in pediatric traumatic brain injury.** *J Child Neurol* 2010;25:976–84
67. Pal D, Gupta RK, Agarwal S, et al. **Diffusion tensor tractography indices in patients with frontal lobe injury and its correlation with neuropsychological tests.** *Clin Neurol Neurosurg* 2012;114:564–71
68. Palacios EM, Fernandez-Espejo D, Junque C, et al. **Diffusion tensor imaging differences relate to memory deficits in diffuse traumatic brain injury.** *BMC Neurol* 2011;11:24
69. Palmer HS, Garzon B, Xu J, et al. **Reduced fractional anisotropy does not change the shape of the hemodynamic response in survivors of severe traumatic brain injury.** *J Neurotrauma* 2010;27:853–62
70. Perlbarg V, Puybasset L, Tollard E, et al. **Relation between brain lesion location and clinical outcome in patients with severe traumatic brain injury: a diffusion tensor imaging study using voxel-based approaches.** *Hum Brain Mapp* 2009;30:3924–33

71. Porto L, Jurcoane A, Margerkurth J, et al. **Morphometry and diffusion MR imaging years after childhood traumatic brain injury.** *Eur J Paediatr Neurol* 2011;15:493–501
72. Rutgers DR, Fillard P, Paradot G, et al. **Diffusion tensor imaging characteristics of the corpus callosum in mild, moderate, and severe traumatic brain injury.** *AJNR Am J Neuroradiol* 2008;29:1730–35
73. Rutgers DR, Toulgoat F, Cazejust J, et al. **White matter abnormalities in mild traumatic brain injury: a diffusion tensor imaging study.** *AJNR Am J Neuroradiol* 2008;29:514–19
74. Salmond CH, Menon DK, Chatfield DA, et al. **Diffusion tensor imaging in chronic head injury survivors: correlations with learning and memory indices.** *Neuroimage* 2006;29:117–24
75. Scheibel RS, Newsome MR, Wilde EA, et al. **Brain activation during a social attribution task in adolescents with moderate to severe traumatic brain injury.** *Soc Neurosci* 2011;6:582–98
76. Sidaros A, Engberg AW, Sidaros K, et al. **Diffusion tensor imaging during recovery from severe traumatic brain injury and relation to clinical outcome: a longitudinal study.** *Brain* 2008;131:559–72
77. Singh M, Jeong J, Hwang D, et al. **Novel diffusion tensor imaging methodology to detect and quantify injured regions and affected brain pathways in traumatic brain injury.** *Magn Reson Imaging* 2010;28:22–40
78. Smits M, Houston GC, Dippel DW, et al. **Microstructural brain injury in post-concussion syndrome after minor head injury.** *Neuroradiology* 2011;53:553–63
79. Sponheim SR, McGuire KA, Kang SS, et al. **Evidence of disrupted functional connectivity in the brain after combat-related blast injury.** *Neuroimage* 2011;54(suppl 1):S21–29
80. Sugiyama K, Kondo T, Oouchida Y, et al. **Clinical utility of diffusion tensor imaging for evaluating patients with diffuse axonal injury and cognitive disorders in the chronic stage.** *J Neurotrauma* 2009;26:1879–90
81. Tasker RC, Gunn Westland A, White DK, et al. **Corpus callosum and inferior forebrain white matter microstructure are related to functional outcome from raised intracranial pressure in child traumatic brain injury.** *Dev Neurosci* 2010;32:374–84
82. Tollard E, Galanaud D, Perlbarg V, et al. **Experience of diffusion tensor imaging and 1H spectroscopy for outcome prediction in severe traumatic brain injury: preliminary results.** *Crit Care Med* 2009;37:1448–55
83. Wang JY, Bakhadirov K, Abdi H, et al. **Longitudinal changes of structural connectivity in traumatic axonal injury.** *Neurology* 2011;77:818–26
84. Wang JY, Bakhadirov K, Devous MD, Sr., et al. **Diffusion tensor tractography of traumatic diffuse axonal injury.** *Arch Neurol* 2008;65:619–26
85. Warner MA, Marquez de la Plata C, Spence J, et al. **Assessing spatial relationships between axonal integrity, regional brain volumes, and neuropsychological outcomes after traumatic axonal injury.** *J Neurotrauma* 2010;27:2121–30
86. Wei CW, Tharmakulasingam J, Crawley A, et al. **Use of diffusion-tensor imaging in traumatic spinal cord injury to identify concomitant traumatic brain injury.** *Arch Phys Med Rehabil* 2008;89:S85–91
87. Wilde EA, Bigler ED, Haider JM, et al. **Vulnerability of the anterior commissure in moderate to severe pediatric traumatic brain injury.** *J Child Neurol* 2006;21:769–76
88. Wilde EA, Chu Z, Bigler ED, et al. **Diffusion tensor imaging in the corpus callosum in children after moderate to severe traumatic brain injury.** *J Neurotrauma* 2006;23:1412–26
89. Wilde EA, McCauley SR, Hunter JV, et al. **Diffusion tensor imaging of acute mild traumatic brain injury in adolescents.** *Neurology* 2008;70:948–55
90. Wilde EA, Newsome MR, Bigler ED, et al. **Brain imaging correlates of verbal working memory in children following traumatic brain injury.** *Int J Psychophysiol* 2011;82:86–96
91. Wilde EA, Ramos MA, Yallampalli R, et al. **Diffusion tensor imaging of the cingulum bundle in children after traumatic brain injury.** *Dev Neuropsychol* 2010;35:333–51
92. Wozniak JR, Krach L, Ward E, et al. **Neurocognitive and neuroimaging correlates of pediatric traumatic brain injury: a diffusion tensor imaging (DTI) study.** *Arch Clin Neuropsychol* 2007;22:555–68
93. Wu TC, Wilde EA, Bigler ED, et al. **Longitudinal changes in the corpus callosum following pediatric traumatic brain injury.** *Dev Neurosci* 2010;32:361–73
94. Wu TC, Wilde EA, Bigler ED, et al. **Evaluating the relationship between memory functioning and cingulum bundles in acute mild traumatic brain injury using diffusion tensor imaging.** *J Neurotrauma* 2010;27:303–07
95. Xu J, Rasmussen IA, Lagopoulos J, et al. **Diffuse axonal injury in severe traumatic brain injury visualized using high-resolution diffusion tensor imaging.** *J Neurotrauma* 2007;24:753–65
96. Yallampalli R, Wilde EA, Bigler ED, et al. **Acute white matter differences in the fornix following mild traumatic brain injury using diffusion tensor imaging.** *J Neuroimaging* 2013;23:224–27
97. Yasokawa YT, Shinoda J, Okumura A, et al. **Correlation between diffusion-tensor magnetic resonance imaging and motor-evoked potential in chronic severe diffuse axonal injury.** *J Neurotrauma* 2007;24:163–73
98. Yuan W, Holland SK, Schmithorst VJ, et al. **Diffusion tensor MR imaging reveals persistent white matter alteration after traumatic brain injury experienced during early childhood.** *AJNR Am J Neuroradiol* 2007;28:1919–25
99. Yurgelun-Todd DA, Bueler CE, McGlade EC, et al. **Neuroimaging correlates of traumatic brain injury and suicidal behavior.** *J Head Trauma Rehabil* 2011;26:276–89
100. Zhang K, Johnson B, Pennell D, et al. **Are functional deficits in concussed individuals consistent with white matter structural alterations: combined FMRI & DTI study.** *Exp Brain Res* 2010;204:57–70
101. Hong JH, Jang SH, Kim OL, et al. **Neuronal loss in the medial cholinergic pathway from the nucleus basalis of Meynert in patients with traumatic axonal injury: a preliminary diffusion tensor imaging study.** *J Head Trauma Rehabil* 2012;27:172–76
102. Kumar R, Saksena S, Husain M, et al. **Serial changes in diffusion tensor imaging metrics of corpus callosum in moderate traumatic brain injury patients and their correlation with neuropsychometric tests: a 2-year follow-up study.** *J Head Trauma Rehabil* 2010;25:31–42
103. Rosenbaum SB, Lipton ML. **Embracing chaos: the scope and importance of clinical and pathological heterogeneity in mTBI.** *Brain Imaging Behav* 2012;6:255–82
104. Kashluba S, Hanks RA, Casey JE, et al. **Neuropsychologic and functional outcome after complicated mild traumatic brain injury.** *Arch Phys Med Rehabil* 2008;89:904–11
105. Burdette JH, Durden DD, Elster AD, et al. **High b-value diffusion-weighted MRI of normal brain.** *J Comput Assist Tomogr* 2001;25:515–19
106. Dudink J, Larkman DJ, Kapellou O, et al. **High b-value diffusion tensor imaging of the neonatal brain at 3T.** *AJNR Am J Neuroradiol* 2008;29:1966–72
107. Smith SM, Jenkinson M, Johansen-Berg H, et al. **Tract-based spatial statistics: voxelwise analysis of multi-subject diffusion data.** *Neuroimage* 2006;31:1487–505
108. Shenton ME, Hamoda HM, Schneiderman JS, et al. **A review of magnetic resonance imaging and diffusion tensor imaging findings in mild traumatic brain injury.** *Brain Imaging Behav* 2012;6:137–92
109. Cicerone KD, Azulay J. **Diagnostic utility of attention measures in postconcussion syndrome.** *Clin Neuropsychol* 2002;16:280–89
110. Duhaime AC, Holshouser B, Hunter JV, et al. **Common data elements for neuroimaging of traumatic brain injury: pediatric considerations.** *J Neurotrauma* 2012;29:629–33
111. Gold MM, Lipton ML. **Neurological picture: diffusion tractography of axonal degeneration following shear injury.** *J Neurol Neurosurg Psychiatry* 2008;79:1374–75
112. Duhaime AC, Gean AD, Haacke EM, et al. **Common data elements in radiologic imaging of traumatic brain injury.** *Arch Phys Med Rehabil* 2010;91:1661–66

An Expanded Role for Neuroimaging in the Evaluation of Memory Impairment

R.S. Desikan, M.S. Rafii, J.B. Brewer, and C.P. Hess

ABSTRACT

SUMMARY: Alzheimer disease affects millions of people worldwide. The neuropathologic process underlying this disease begins years, if not decades, before the onset of memory decline. Recent advances in neuroimaging suggest that it is now possible to detect Alzheimer-associated neuropathologic changes well before dementia onset. Here, we evaluate the role of recently developed in vivo biomarkers in the clinical evaluation of Alzheimer disease. We discuss how assessment strategies might incorporate neuroimaging markers to better inform patients, families, and clinicians when memory impairment prompts a search for diagnosis and management options.

ABBREVIATIONS: AD = Alzheimer disease; *APOE* ε4 = *apolipoprotein* ε4; FTD = frontotemporal dementia; MCI = mild cognitive impairment; NFTs = neurofibrillary tangles; PIB = Pittsburgh Compound-B; vMRI = volume-based MR imaging; amyloid-β = Aβ

Late-onset Alzheimer disease (AD) is the most common form of dementia with an estimated prevalence of 30 million people worldwide, a number that is expected to quadruple in 40 years. With increasing awareness that symptoms develop over many years, there is a growing need to identify nondemented older people at risk for AD. Mild cognitive impairment (MCI) represents a transitional state between normal aging and dementia. Clinical features of amnestic MCI are presented in Table 1 and are reviewed by Petersen et al[1] and again by Petersen.[2] In this piece, we focus on recent advances in biomarker development for the predictive prognosis of MCI and suggest that a neuroimaging-based evaluation strategy can help guide clinical management decisions in older people with memory impairment.

Received April 20, 2013; accepted after revision April 22.

From the Departments of Radiology (R.S.D., J.B.B.) and Neurosciences (M.S.R., J.B.B.), University of California, San Diego, La Jolla, California; and Neuroradiology Section, Department of Radiology and Biomedical Imaging (C.P.H.), University of California, San Francisco, San Francisco, California.

Grant Support: Research support was provided by NIH grants NINDS K02 NS067427 (J.B.B.), NIA U01 AG10483 (J.B.B.), NIA P50 AG005131 (J.B.B.), NIA R01AG034062 (J.B.B.), NIH R01 HD072074–01 (C.P.H.), T32 EB005970 (R.S.D.), and General Electric Medical Foundation (J.B.B.).

All authors contributed equally to this study.

Please address correspondence to Dr. Rahul S. Desikan, Department of Radiology, University of California, San Diego, 8950 Villa La Jolla Dr, Suite C101, La Jolla, CA 92037-0841; e-mail: rdesikan@ucsd.edu


Indicates open access to non-subscribers at www.ajnr.org


Indicates article with supplemental on-line table.

http://dx.doi.org/10.3174/ajnr.A3644

AD Pathobiology

Since their first description by Alois Alzheimer in 1907,[3] amyloid-containing plaques and tau-associated neurofibrillary tangles (NFTs) have remained the 2 hallmark pathologic lesions of AD. Senile and neuritic plaques are composed of amyloid-beta (Aβ), a 38–43 amino acid peptide that derives from the much larger cell membrane–associated amyloid precursor protein and gradually accumulates over time in the extracellular spaces of the brain.[4] Within plaques, Aβ is present in aggregated/insoluble forms such as fibrils and soluble forms such as oligomers.[5] In animal models, Aβ initiates downstream loss of dendrites and synapses[5] and functional disruption of neuronal networks.[6] Genetic evidence indicates that *apolipoprotein* ε4 (*APOE* ε4), the most important known genetic risk factor for late-onset AD, accelerates the onset of Aβ deposition into plaques and decreases the transport of Aβ across the blood-brain barrier.[7] Furthermore, a recently discovered mutation in Aβ-precursor protein protects against AD,[8] providing additional evidence regarding the central role of Aβ in AD pathogenesis. However, neocortical Aβ plaques are present not only in cognitively impaired patients but also in cognitively normal older adults.[9] Poor correlations between Aβ deposition and memory decline,[10] together with the observation that immunotherapy-induced Aβ plaque removal may not prevent neurodegeneration,[11] suggest that additional entities besides Aβ are required for AD-associated degeneration.

NFTs, primarily found in neuronal cell bodies, are composed of the hyperphosphorylated, aggregated form of the microtubule-binding protein, tau. Unlike Aβ plaques, tau-associated NFTs correlate strongly with clinical severity[10] and follow a defined temporal topographic pattern in which medial temporal lobe re-

Table 1: Clinical features in amnestic patients with MCI

Clinical Characteristics	
Memory Impairment	**Episodic Memory Dysfunction**
Nonmemory cognitive impairment	Executive dysfunction, apraxia, aphasia, and/or visuospatial dysfunction may be present in amnestic MCI multidomain
Functional impairment	No change in ability to perform activities of daily living
Behavioral impairment	Depression and anxiety may be present
Annual rate of progression to dementia	Variable (range, 3%–15%)

gions underlying memory function are affected in the earliest stages of the disease.[12] Recent work in animal models[13,14] and in humans[15,16] points to a synergistic relationship between Aβ and tau whereby Aβ-associated neurodegeneration occurs only in the presence of tau. Intriguingly, evidence from animal models indicates that reducing tau levels rescues mice from premature mortality and memory deficits without altering Aβ levels or plaque burden.[13] These findings, along with other biochemical and experimental evidence, support a 2-stage disease process where Aβ deposition initiates the neurodegenerative cascade (including tau hyperphosphorylation and aggregation), which in turn becomes increasingly independent of the initiating Aβ.[17]

Imaging and Fluid Biomarkers for Assessment of AD Pathology

Neuropathologic findings indicate that Aβ accumulation and tau pathology begins years or even decades before the onset of clinical symptoms.[18] Neuroimaging and CSF markers can detect the earliest pathology associated with AD, enabling identification of clinically normal patients in the presymptomatic or preclinical stage of AD.[19] In the sections below, we review the most extensively validated in vivo biomarkers of amyloid pathology and AD-related neurodegeneration. For simplicity, we do not review the putative markers of synaptic injury, such as FDG-PET or functional MR imaging, which may prove useful in distinguishing among certain neurodegenerative disorders.

Volumetric Structural MR Imaging

Structural MR imaging is a convenient first imaging technique to assess AD neurodegeneration because current practice guidelines include its use during the routine evaluation of patients with cognitive complaints, primarily to exclude structural abnormalities such as infarction, brain tumors, or hydrocephalus.[20] Brain atrophy on structural MR imaging reflects the loss of dendrites, synapses, and neurons.[21] Although atrophy is not specific to AD, a strong association exists between the severity of atrophy and cognitive decline along the aging continuum, and the degree of atrophy correlates with Braak pathologic staging at autopsy.[21] It is important to note that the topographic distribution of MR imaging–based atrophy in AD maps well onto the distribution of NFT pathologic features, with the entorhinal cortex and hippocampus demonstrating the largest magnitude of gray matter loss in patients with a high tau burden.[22]

A number of methodologies, ranging from whole-brain or voxel-based techniques to region-of-interest–based methods, have been proposed to quantitatively evaluate brain atrophy on MR imaging. Within the last decade, the routine acquisition of high-quality 3D T1-weighted images and rapid advances in image analysis algorithms have led to the availability of volumetric MR imaging–based (vMRI) software tools capable of automatically subdividing the brain into neuroanatomic regions and quantifying tissue loss within each region for a single patient.[23-25] Fully automated quantitative vMRI-based neuroanatomic assessments can detect AD-associated volume loss, predict disease progression, and be used as an outcome measure in therapeutic trials.[26,27] Recently, the FDA has approved one such vMRI technology[28] that can assist in the clinical work-up of memory decline (Fig 1). In the On-line Table, we review recent (from 2009–2012) prospective studies using vMRI methods to predict clinical progression from MCI to AD.

However, structural MR imaging has limitations. vMRI does not directly evaluate Aβ and tau but, rather, provides an indirect assessment of neurodegeneration that occurs downstream from molecular pathology. Another limitation is that although certain patterns of volume loss are characteristic of different diseases (eg, entorhinal cortex atrophy in AD), the finding of medial temporal lobe atrophy by itself is nonspecific and can also be seen in other neurologic and psychiatric disorders. Therefore, vMRI of the medial temporal lobe structures, in isolation, cannot distinguish AD from hippocampal sclerosis or other neurodegenerative diseases such as frontotemporal dementia (FTD). Moreover, neuropathologic evidence demonstrates the presence of uncommon AD subtypes that spare the medial temporal lobes, especially in younger patients.[29] Despite these weaknesses, given its capability for precise anatomic description with high reliability, analysis of MR imaging data across a wide range of scanner types/manufacturers, and the ability to efficiently generate normative databases from multicenter data, vMRI will undoubtedly play a significant role in decision making during the clinical evaluation of dementia. The optimal diagnostic and prognostic value of vMRI will be obtained when combined with clinical/cognitive testing and other markers including CSF and imaging measures of AD pathology.

Molecular Imaging and Fluid Biomarkers of Aβ Deposition

Within the last decade, a number of PET-based radiotracers have been developed to noninvasively assess for the presence of Aβ, of which the most extensively examined is ^{11}C-labeled [*N*-methyl]-2-(4′-methylaminophenyl)-6-hydroxybenzothiazole (Pittsburgh Compound-B, PIB). Studies with transgenic mouse models and human brain sections indicate that PIB selectively binds to the fibrillar form of Aβ in neuritic plaques and cerebral amyloid angiopathy.[30,31] In vivo, ante mortem PIB retention strongly correlates with in vitro, postmortem measures of fibrillar Aβ pathology in autopsy-confirmed AD but does not associate with NFTs, Lewy bodies, or other protein aggregates.[32,33] In humans, the overall pattern of increased PIB retention mirrors the distribution of fibrillar Aβ plaques found at autopsy and involves the prefrontal, parietal, and lateral temporal cortices.[34] A recent review suggests that the overwhelming majority of patients with AD and cognitively impaired patients who progress to AD are amyloid "positive."[35] Furthermore, approximately 24% of cognitively normal older adults older than 60 years also show increased cerebral PIB

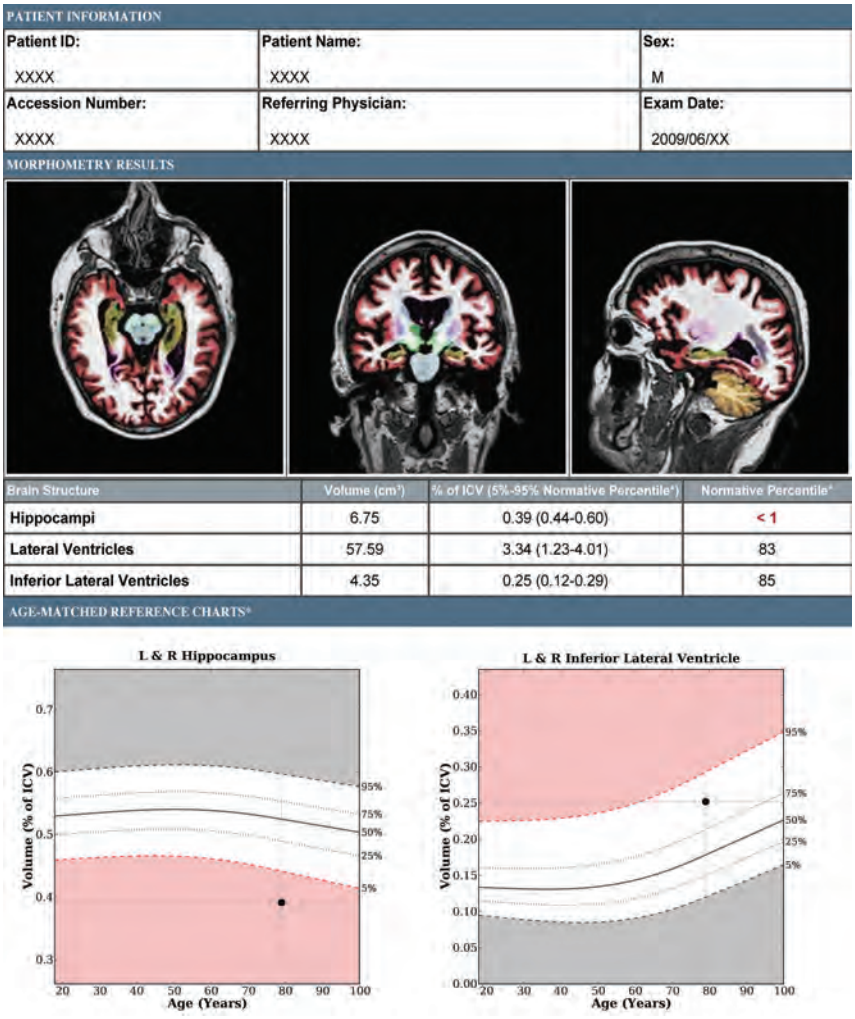

FIG 1. Brain MR imaging evaluation of a patient with amnestic MCI by use of a volumetric technique (NeuroQuant, http://www.cortechslabs.com). The top panel illustrates subcortical regions, such as the hippocampus (*dark yellow*), automatically classified on axial, coronal, and sagittal T1-weighted MR images. The middle and bottom panel demonstrate volumes and normative percentiles for the hippocampus and ventricles. Analyses of the baseline MR imaging scan demonstrated hippocampal volumes that were at the < 1 normative percentile, lending objective support to an impression of medial temporal lobe atrophy. At the time of volumetric assessment, the patient's Mini-Mental Status Examination score was 29 of 30, yet memory impairment was suggested by more detailed neuropsychological testing. Three years later, his Mini-Mental Status Examination score was 22 of 30, and he had clinically progressed to dementia with high biomarker probability of AD, as supported by evidence of neuronal injury on structural MR imaging and elevated amyloid levels on a florbetapir scan (Fig 3).

retention, and the prevalence of amyloid positivity is closely related to age and *APOE* ε4 carrier status.[35] Together, these findings raise the possibility that amyloid imaging may yield positive results long before the appearance of cognitive symptoms, which, as discussed below, has both positive and negative consequences.

As either an alternative or adjunct to amyloid PET imaging, CSF sampling can also detect Aβ pathologic detail. Although most Aβ is produced in the brain and is secreted into the extracellular spaces of the brain, a fraction of central nervous system–produced Aβ diffuses into the CSF and is present in modest concentrations (approximately 10–15 ng/mL).[36] CSF assessments measure the monomeric form of Aβ. Low CSF Aβ levels correlate strongly with increased PIB binding, intracranial plaque deposition, and total Aβ load, demonstrating the value of these CSF measurements as a marker of fibrillar Aβ pathologic findings.[36] However, an important clinical consideration with CSF sampling is the need for lumbar puncture, an uncomfortable procedure that carries a small risk for morbidity.

Imaging Evaluation Strategy for MCI and AD

Clinical assessment of the elderly patient with a memory complaint usually begins with a mental status evaluation to objectively confirm the presence of the cognitive deficit. If the degree of cognitive decline is greater than expected for healthy aging and further information is needed to guide management, the determination of whether a neurodegenerative process underlies the cognitive complaint can help determine which further diagnostic method to use. Above and beyond exclusion of other conditions to explain cognitive deficits (eg, brain tumor, traumatic brain injury, infarctions, chronic hemorrhage, hydrocephalus, or encephalitis), structural MR imaging by use of vMRI techniques at this stage can be useful to document objective evidence of atrophy. As illustrated in Fig 2, vMRI can assist in supporting or contradicting a putative clinical diagnosis while providing an informative assessment of disease risk. The presence of reduced hippocampal volume provides support to the clinical impression that a neurodegenerative process contributes to the cognitive deficit but does not exclude the possibility of a congenitally small hippocampus or hippocampal damage from a prior insult. It is important to note that low hippocampal volumes do not specify whether the underlying cause is AD or other diseases such as FTD, dementia with Lewy bodies, or hippocampal sclerosis (Fig 2). Nevertheless, once a neurodegenerative cause is supported through clinical and radiologic evaluation, distinguishing among neurodegenerative disorders may benefit from supplemental testing for amyloid. This would likely be reserved for cases where additional tailoring of education or management is required and may be limited, as the more clinically relevant distinction is between benign or curable causes vs those with a near-term dire prognosis (Fig 2). It is important to note that in light of prior[11] and recent[37] clinical trial evidence that removing Aβ plaques by using immunotherapeutic methods may not halt the neurodegenerative process, amyloid testing to confirm AD as the underlying cause may prove most useful when therapies preventing downstream neurodegeneration become clinically available (Fig 2).

Challenges remain regarding the clinical application of vMRI in the patient with cognitive impairment. The difficulty in estab-

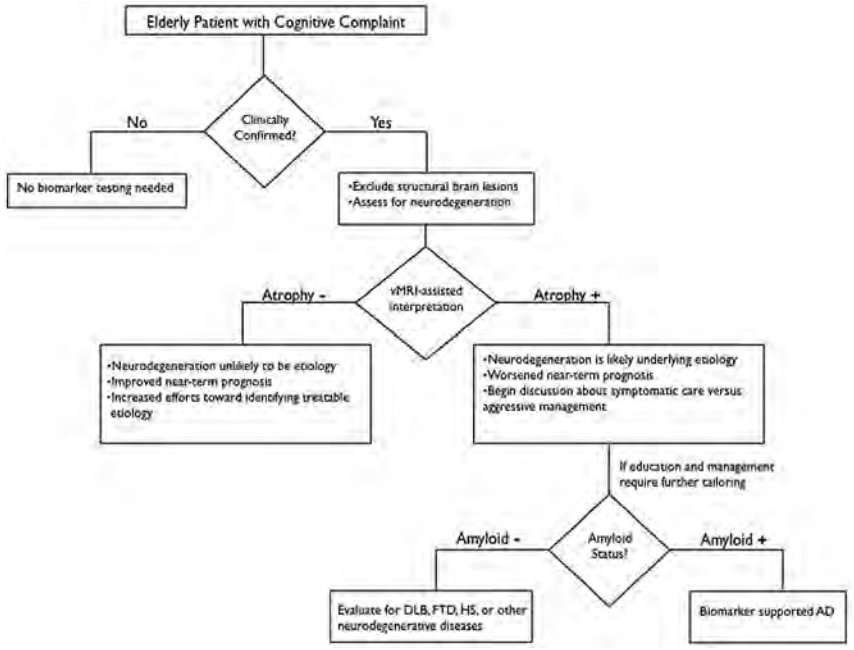

FIG 2. Recommended decision tree for evaluating the elderly patient with a cognitive complaint. DLB = Dementia with Lewy bodies; HS = hippocampal sclerosis. Figure adapted from McEvoy and Brewer.[48]

lishing normative ranges across a broad population of patients is a significant obstacle, but one that can be overcome by the availability of large data bases of images in cognitively normal elderly patients and patients with both MCI and AD enrolled in multisite, multinational initiatives such as the Alzheimer Disease Neuroimaging Initiative (ADNI) in North America and the AddNeuroMed Consortium in Europe (On-line Table). Because atrophy is not diagnostic of AD neuropathologically and because the hippocampus is affected by a broad array of disorders, the diagnosis of AD cannot rely on simple "cut points" or "thresholds" in hippocampal volume[38,39] derived from studies of progression to AD dementia. Furthermore, the degree of abnormality, along with other radiologic features, including ex vacuo dilation of adjacent temporal horn and qualitative assessment of sulcal widening and cortical volume loss, will yield the impression of the presence or absence of neurodegeneration. It is important to note that the diagnosis of AD cannot be established by imaging alone; radiologic input serves to *inform,* rather than establish, an overall clinical impression.

Recommendations to use medial temporal atrophy on structural MR imaging among cognitively impaired patients have already been proposed by an international AD working group,[40] and vMRI is one of the biomarkers recently incorporated into revised diagnostic criteria for AD, which noted that such biomarkers could serve "as optional clinical tools for use where available and when deemed appropriate by the clinician."[41] Consistent with these recently revised diagnostic guidelines for AD[41] and MCI,[42] by supporting the presence or absence of neurodegeneration, vMRI-based methods can also inform the likelihood of whether a patient with clinically confirmed memory loss will progress to dementia. The absence of vMRI-based brain atrophy diminishes the likelihood of neurodegeneration and increases the likelihood that a nonneurodegenerative, and potentially treatable, cause underlies the memory complaint. It is important to note that normal brain volumes for age, though not excluding the possibility of future neurodegeneration, can also be helpful to guide clinical management while providing a more accurate predictive prognosis. Normal hippocampal volumes confer a better near-term prognosis and can foster increased efforts toward finding a treatable cause for the memory impairment while providing needed, albeit cautious, reassurance to the patient and caregivers who will be anxious about being given a dire prognosis.

Amyloid Biomarkers in MCI and AD

The ability to specifically assess fibrillar Aβ pathology in vivo has generated considerable clinical excitement. Recently, the FDA has approved the fluorine-based amyloid tracer [F-18]florbetapir (Amyvid; Eli Lilly, Indianapolis, Indiana) for use in patients being evaluated for AD and other causes of cognitive decline (Fig 3). Furthermore, commercial CSF Aβ assays with established normative ranges for amyloid status are now clinically available (http://www.athenadiagnostics.com). However, as noted by the FDA, although a negative florbetapir (amyloid) scan result is inconsistent with a neuropathologic diagnosis of AD at the time of image acquisition, a positive florbetapir scan result does not establish a diagnosis of AD.[43] Furthermore, elevated deposition of amyloid may occur in other neurologic conditions and is often present in healthy older adults with normal cognition. Recently, it has become increasingly evident that Aβ oligomers (eg, dimers, trimers, tetramers, and higher oligomers), rather than fibrillar Aβ plaques, represent the principal synaptotoxic form of amyloid that initiate the neurodegenerative process underlying AD. Insoluble Aβ fibrils, though serving as a reservoir for the neurotoxic oligomers, might themselves be relatively inactive.[44] It is important to realize that neither CSF analytes nor amyloid imaging can detect the oligomeric form of Aβ.[36] In a similar fashion, in cognitively normal older patients, although some studies have found a relationship between Aβ plaque deposition and neurodegeneration,[45,46] recent studies have suggested that tau and other "downstream" markers of neuronal injury modulate the effect of Aβ on cognitive decline and brain atrophy.[15-16,47] In addition, recent clinical trials with monoclonal antibodies (solanezumab and bapineuzumab) that target Aβ and promote its clearance from the brain demonstrate a minimal effect on disease trajectory modification in patients with mild or moderate AD: solanezumab showed marginal improvement in cognitive and functional decline, and bapineuzumab, though affecting fibrillar Aβ and tau levels, did not modify the disease trajectory.[37] Taken collectively, this indicates that Aβ deposition precedes neurodegeneration and, in the absence of cognitive decline or brain atrophy, represents an elevated risk state in much the same fashion that hypercholesterolemia serves as a

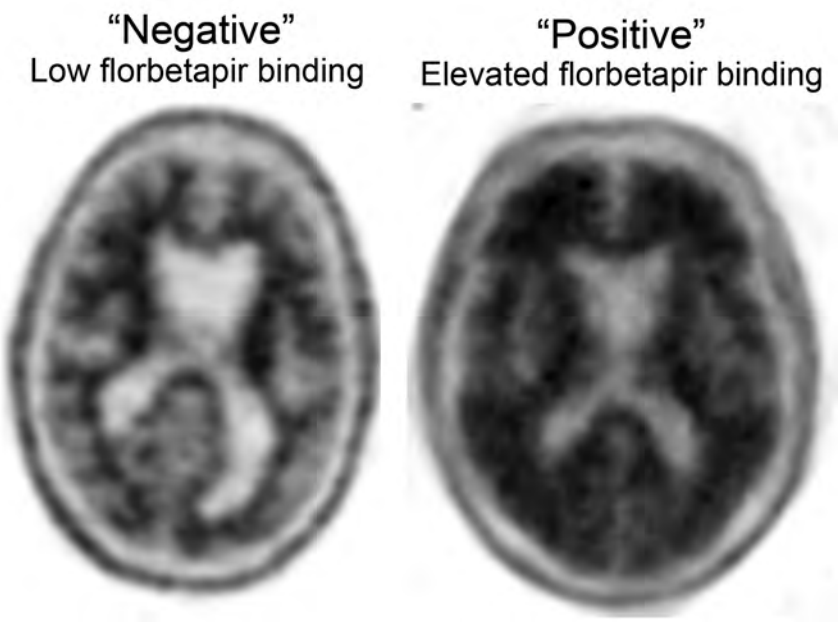

FIG 3. Assessment of amyloid deposition by use of florbetapir (Amyvid). The axial PET image on the left shows normal preserved gray-white contrast with the cortical radioactivity less than the adjacent white matter (amyloid-"negative" scan). The axial PET image on the right demonstrates areas of decreased gray-white contrast with increased cortical radioactivity that is comparable to the radioactivity in the adjacent white matter (amyloid-"positive" scan). The florbetapir scan on the right was acquired on a patient with MCI who clinically progressed to dementia with a high biomarker probability of AD, as supported by this amyloid-positive scan and evidence of neuronal injury on structural MR imaging (Fig 1).

risk factor for heart disease in the absence of myocardial damage. Just as cholesterol levels would not be used to diagnose a myocardial infarction in the setting of chest pain, detecting amyloid deposition may be less valuable than markers of neuronal damage when determining the cause of ongoing memory impairment. Nevertheless, it is hoped that a future contribution of Aβ testing, from diagnostic and therapeutic perspectives, may be among cognitively normal adults *before* the onset of neurodegeneration.

Role of Biomarkers in Guiding Clinical Management

Biomarker testing can help inform near-term prognosis by providing an objective assessment as to whether neurodegeneration is likely to be present. Whereas cognitive testing validates the patient or caregiver complaint that initiated the clinical visit, vMRI provides an orthogonal measure that is less overlapping with the patient complaint, thereby guarding against circularity in concluding that the cognitive problem is the result of AD. The presence of brain atrophy on vMRI, together with documented memory impairment confirmed by cognitive testing, suggests a prognosis of near-term decline and can prompt a discussion on evaluating the risk/benefit ratio for considering aggressive disease management vs symptomatic care (Fig 2). For patients and family members, these findings can help initiate a dialogue on future planning including determining the need for residential and driving support, involvement of a geriatric case manager, and financial decisions.

Evaluation with amyloid testing can prove useful once a neurodegenerative cause for cognitive decline has been established, especially in younger patients and in patients presenting with complaints atypical for AD. An amyloid test may be helpful for making a more informative dementia diagnosis (eg, AD vs FTD) in these patients, and can help guide the selection of medications for symptomatic management. As with vMRI, amyloid testing may also be of benefit to refine and tailor expectations while providing additional education to patients and caregivers.

The absence of brain atrophy on vMRI confers a better near-term prognosis and can provide cautious, but increased, optimism to physicians, patients, and caregivers. Although not excluding the possibility of future neurodegeneration, normal brain volumes can guide clinical management by prompting the physician to intensify efforts toward detecting a treatable cause for the patient's memory impairment (Fig 2). Such physician optimism is not lost on patients and may serve as needed reassurance to those patients with an inappropriately debilitating fear about progressing to dementia. Importantly, the intensified physician effort on behalf of patients whose complaints and cognitive impairments are incongruous with vMRI findings may lead to an improved likelihood of successful treatment and subsequent return of patients to normal cognitive function.

Potential Pitfalls with Biomarker Testing

In addition to valid concerns of added expense (Table 2), it is our opinion that biomarker assessment of patients without objective evidence of memory impairment could cause potential harm, as described by McEvoy and Brewer.[48] For example, given the high frequency of nonspecific memory complaints in the general population and the high prevalence of amyloid positivity among the cognitively normal population, there is a significant chance that a patient's memory complaint is unrelated to intracranial Aβ deposition. A finding of elevated amyloid or low hippocampal volume might lead to inappropriate attribution of memory complaints to AD, circumventing a thorough work-up for other potentially treatable causes while exacerbating the debilitating worry that initially brought the patient to the clinic. Even in those patients where memory impairment is clinically confirmed, elevated amyloid levels do not assure that the cause of the impairment is AD. Amyloid positivity, in patients with objective memory decline, might lead to an overly simplistic attribution of memory complaints to AD and incomplete evaluations for modifiable causes of cognitive impairment. Finally, a negative amyloid test result is not necessarily a result to be celebrated because other neurodegenerative disorders should remain under consideration.

Future Directions: Preclinical AD

Currently, there are no effective treatments that delay the onset or halt the progression from MCI to AD. There is increasing recog-

Table 2: Disease progression markers in amnestic patients with MCI

Markers of Disease Progression	Characteristics	Procedure(s)[a]	Approximate Cost (in US dollars)[b]
Structural neuroimaging with vMRI	Medial temporal lobe and/or neocortical atrophy; white matter abnormalities may also be present	1) Noncontrast MRI brain CPT 70551 2) 3D quantitative segmental volume reporting and assessment[c] CPT 76377	1) 437.20 (365.75[f]+71.45[g]) 2) 82.68 (44.57[f]+38.11[g])
FDG-PET	Temporoparietal hypometabolism	Brain imaging (PET) metabolic evaluation CPT 78608	1266.40 (1041.99[f]+150[i]+74.41[g])
Amyloid imaging	Increased uptake in frontal, parietal, and/or temporal regions	PET imaging limited area CPT 78811	2721.83 (1041.99[f]+1600[i]+79.84[g])
CSF amyloid CSF tau (total tau)	Decreased Increased	1) CSF lumbar puncture CPT 62270 2) CSF analysis and interpretation[d] CPT 83520	1) 242.58 (78.93[h]+163.65[g]) 2) 1080
APOE ϵ4 carrier status	Dose-dependent effect (risk for AD: ϵ4/ϵ4 > ϵ3/ϵ4 > ϵ3/ϵ3 > ϵ3/ϵ2 > ϵ2/ϵ2)	1) Buccal swab or routine venipuncture CPT 36415 2) *APOE* genotype analysis and interpretation[e] CPT 81401	1) 3 2) 500

Note:—APOE ϵ4 indicates apolipoprotein E4; CPT, Current Procedural Terminology; vMRI, volumetric-based MR imaging.

[a] Determined using data from the Centers for Medicare and Medicaid Services (www.cms.gov). For informational purposes only. Selected CPT code may vary.

[b] Determined, when possible, using National Payment Amount data from the Centers for Medicare and Medicaid Services (www.cms.gov). For informational purposes only. Payment amount varies by location.

[c] Using NeuroQuant (http://www.cortechs.net/products/neuroquant.php).

[d] Using the ADmark Phospho-Tau/Total-Tau/Ab42 CSF Analysis & Interpretation (Symptomatic) test (http://www.athenadiagnostics.com/content/test-catalog/find-test/service-detail/q/id/311).

[e] Using the ADmark ApoE Genotype Analysis & Interpretation (Symptomatic) (http://www.athenadiagnostics.com/content/test-catalog/find-test/service-detail/q/id/35).

[f] Approximate technical charge.

[g] Approximate professional charge.

[h] Approximate facility price.

[i] Approximate ligand price.

nition that early intervention before the onset of neurodegeneration or clinical symptoms may represent the most effective treatment against AD,[19] and a number of secondary prevention trials in preclinical older patients are currently underway. We believe that a screening strategy to assess dementia risk in cognitively normal adults could be useful if a meaningful therapy with minimal adverse effects becomes clinically available. Biomarker testing in asymptomatic patients is inherently controversial; therefore, we note that this evaluation strategy, though not currently applicable, may become relevant when or if meaningful preventive interventions are available.

Genetic, biochemical, and imaging evidence indicates that fibrillar Aβ pathologic change begins at least 15 years before the onset of clinical symptoms.[49] Increasing levels of Aβ oligomers that progressively lead to plaque deposition are likely present at an even earlier age.[50] These observations suggest that screening for the presence of amyloid should start in cognitively normal older adults (> 60 years old), similar to the current screening strategies for hypercholesterolemia or common cancers such as breast, colon, or prostate carcinoma. Although CSF concentrations of Aβ may become aberrant before amyloid imaging,[49] additional factors such as the need to assess therapeutic response with time, clinical availability, and patient comfort should also be considered when determining whether to use fluid or imaging markers for amyloid status screening.

In cognitively normal older adults, a negative amyloid test result indicates a significantly lower risk for the development of AD. Because increased amyloid tracer uptake can also be seen with other conditions, such as cerebral amyloid angiopathy,[32] a positive amyloid test result could be further evaluated with cognitive testing and, possibly, vMRI. Positive amyloid status along with the presence of progressive medial temporal lobe atrophy would suggest that the patient has entered the neurodegenerative phase of the disease process, which would change the risk/benefit calculation in considering more aggressive, less-benign medications that may become available. Although neuropathology remains the only way to definitively diagnose AD, available fluid and imaging markers supplement the physician toolbox for treating and educating patients and families worried about AD. As disease-modifying therapies are developed, this physician toolbox will likely evolve to further address the need for improved predictive prognosis and disease management in preclinical AD.

ACKNOWLEDGMENTS

We thank Drs. Linda McEvoy, Dominic Holland, Gil Rabinovici, John Morris, Brad Hyman, Marilyn Albert, William Dillon, Bruce Fischl, Reisa Sperling, Keith Johnson, Clifford Jack, William Bradley, John Hesselink, Ole Andreassen, and Anders Dale for helpful input on an earlier draft of this manuscript. This study was supported by a grant from the National Institutes of Health (T32 EB005970).

ICMJE Disclosures: Christopher Hess—*RELATED: Grant:* General Electric,* Comments: Research support; *UNRELATED: Board Membership:* General Electric,* Comments: Research support for projects related to dementia and ultrahigh-field MRI; *Expert Testimony:* Medicolegal consulting, Comments: occasional; *Grants/Grants Pending:* NIH.* James Brewer—*UNRELATED: Consultancy:* Lilly Biomarker Business Unit (Amyvid), Bristol-Myers Squibb, Avanir Pharmaceuticals, Comments: Advisory boards; *Grants/Grants Pending:* Janssen Alzheimer Immunotherapy,* General Electric Medical Foundation,* Comments: Support as Site PI of clinical trials- Janssen; Support for investigator initiated studies—General Electric; *Payment for Lectures (including service on speaker bureaus):* Lilly Biomarker Business Unit, Comments: Two lectures; *Stock/Stock Options:* Cortechs Laboratories, (NeuroQuant), Comments: Stock options less than 5%. **Money paid to institution.*

REFERENCES

1. Petersen RC, Roberts RO, Knopman DS, et al. **Mild cognitive impairment: ten years later.** *Arch Neurol* 2009;66:1447–55
2. Petersen RC. **Clinical practice. Mild cognitive impairment.** *N Eng J Med* 2011;364:2227–34
3. Alzheimer A. **Über eine eigenartige Erkrankung der Hirnrinde.** *Allg Z Psychiatr* 1907;64:146–48
4. Holtzman DM, Morris JC, Goate AM. **Alzheimer's disease: the challenge of the second century.** *Sci Transl Med* 2011;6:3:77sr1
5. Koffie RM, Meyer-Luehmann M, Hashimoto T, et al. **Oligomeric amyloid beta associates with postsynaptic densities and correlates with excitatory synapse loss near senile plaques.** *Proc Natl Acad Sci U S A* 2009;106:4012–17
6. Kuchibhotla KV, Goldman ST, Lattarulo CR, et al. **Abeta plaques lead to aberrant regulation of calcium homeostasis in vivo resulting in structural and functional disruption of neuronal networks.** *Neuron* 2008;59:214–25
7. Kim J, Basak JM, Holtzman DM. **The role of apolipoprotein E in Alzheimer's disease.** *Neuron* 2009;64:632–44
8. Jonsson T, Atwal JK, Steinberg S, et al. **A mutation in APP protects against Alzheimer's disease and age-related cognitive decline.** *Nature* 2012;488:96–99
9. Crystal H, Dickson D, Fuld P, et al. **Clinico-pathologic studies in dementia: nondemented subjects with pathologically confirmed Alzheimer's disease.** *Neurology* 1988;38:1682–87
10. Arriagada PV, Growdon JH, Hedley-Whyte ET, et al. **Neurofibrillary tangles but not senile plaques parallel duration and severity of Alzheimer's disease.** *Neurology* 1992;42:631–39
11. Holmes C, Boche D, Wilkinson D, et al. **Long-term effects of Abeta42 immunisation in Alzheimer's disease: follow-up of a randomised, placebo-controlled phase I trial.** *Lancet* 2008;372:216–23
12. Braak H, Braak E. **Neuropathological stageing of Alzheimer-related changes.** *Acta Neuropathol* 1991;82:239–59
13. Roberson ED, Scearce-Levie K, Palop JJ, et al. **Reducing endogenous tau ameliorates amyloid beta-induced deficits in an Alzheimer's disease mouse model.** *Science* 2007;316:750–54
14. Ittner LM, Ke YD, Delerue F, et al. **Dendritic function of tau mediates amyloid-beta toxicity in Alzheimer's disease mouse models.** *Cell* 2010;142:387–97
15. Desikan RS, McEvoy LK, Thompson WK, et al. **Amyloid-β associated volume loss occurs only in the presence of phospho-tau.** *Ann Neurol* 2011;70:657–61
16. Desikan RS, McEvoy LK, Thompson WK, et al. **Amyloid-β-associated clinical decline occurs only in the presence of elevated P-tau.** *Arch Neurol* 2012;69:709–13
17. Hyman BT. **Amyloid-dependent and amyloid-independent stages of Alzheimer disease.** *Arch Neurol* 2011;68:1062–64
18. Morris JC, Price JL. **Pathologic correlates of nondemented aging, mild cognitive impairment, and early-stage Alzheimer's disease.** *J Mol Neurosci* 2001;17:101–18
19. Sperling RA, Aisen PS, Beckett LA. **Toward defining the preclinical stages of Alzheimer's disease: recommendations from the National Institute on Aging-Alzheimer's Association workgroups on diagnostic guidelines for Alzheimer's disease.** *Alzheimers Dement* 2011;7:280–92
20. Knopman DS, DeKosky ST, Cummings JL. **Practice parameter: diagnosis of dementia (an evidence-based review). Report of the Quality Standards Subcommittee of the American Academy of Neurology.** *Neurology* 2001;56:1143–53
21. Vemuri P, Jack CR Jr. **Role of structural MRI in Alzheimer's disease.** *Alzheimers Res Ther* 2010;2:23
22. Whitwell JL, Josephs KA, Murray ME, et al. **MRI correlates of neurofibrillary tangle pathology at autopsy: a voxel-based morphometry study.** *Neurology* 2008;71:743–49
23. Fischl B, Salat DH, Busa E, et al. **Whole brain segmentation: automated labeling of neuroanatomical structures in the human brain.** *Neuron* 2002;33:341–55
24. Fischl B, van der Kouwe A, Destrieux C, et al. **Automatically parcellating the human cerebral cortex.** *Cereb Cortex* 2004;14:11–22
25. Desikan RS, Ségonne F, Fischl B, et al. **An automated labeling system for subdividing the human cerebral cortex on MRI scans into gyral based regions of interest.** *Neuroimage* 2006;31:968–80
26. McEvoy LK, Brewer JB. **Quantitative structural MRI for early detection of Alzheimer's disease.** *Expert Rev Neurother* 2010;10:1675–88
27. Holland D, McEvoy LK, Dale AM, et al. **Unbiased comparison of sample size estimates from longitudinal structural measures in ADNI.** *Hum Brain Mapp* 2011;33:2586–602
28. Brewer JB, Magda S, Airriess C, et al. **Fully-automated quantification of regional brain volumes for improved detection of focal atrophy in Alzheimer disease.** *AJNR Am J Neuroradiol* 2009;30:578–80
29. Murray ME, Graff-Radford NR, Ross OA, et al. **Neuropathologically defined subtypes of Alzheimer's disease with distinct clinical characteristics: a retrospective study.** *Lancet Neurol* 2011;10:785–96
30. Bacskai BJ, Hickey GA, Skoch J, et al. **Four-dimensional multiphoton imaging of brain entry, amyloid binding, and clearance of an amyloid-beta ligand in transgenic mice.** *Proc Natl Acad Sci U S A* 2003;100:12462–67
31. Klunk WE, Wang Y, Huang GF, et al. **The binding of 2-(4′-methylaminophenyl)benzothiazole to postmortem brain homogenates is dominated by the amyloid component.** *J Neurosci* 2003;23:2086–92
32. Bacskai BJ, Frosch MP, Freeman SH, et al. **Molecular imaging with Pittsburgh Compound B confirmed at autopsy: a case report.** *Arch Neurol* 2007;64:431–44
33. Ikonomovic MD, Klunk WE, Abrahamson EE, et al. **Post-mortem correlates of in vivo PiB-PET amyloid imaging in a typical case of Alzheimer's disease.** *Brain* 2008;131:1630–45
34. Rabinovici GD, Jagust WJ. **Amyloid imaging in aging and dementia: testing the amyloid hypothesis in vivo.** *Behav Neurol* 2009;21:117–28
35. Johnson KA, Fox NC, Sperling RA, et al. **Brain imaging in Alzheimer disease.** *Cold Spring Harb Perspect Med* 2012;2:a006213
36. Holtzman DM. **CSF biomarkers for Alzheimer's disease: current utility and potential future use.** *Neurobiol Aging* 2011;32 Suppl 1:S4–9
37. Laino C. **News from the American Neurological Association Annual Meeting: anti-amyloid-beta drug modestly slows cognitive decline in mild to moderate AD.** *Neurol Today* 2012;12:34–38
38. Jack CR Jr, Barkhof F, Bernstein MA, et al. **Steps to standardization and validation of hippocampal volumetry as a biomarker in clinical trials and diagnostic criterion for Alzheimer's disease.** *Alzheimers Dement* 2011;7:474–85.e4
39. Jack CR Jr. **Alzheimer disease: new concepts on its neurobiology and the clinical role imaging will play.** *Radiology* 2012;263:344–61
40. Dubois B, Feldman HH, Jacova C, et al. **Revising the definition of Alzheimer's disease: a new lexicon.** *Lancet Neurol* 2010;9:1118–27
41. McKhann GM, Knopman DS, Chertkow H, et al. **The diagnosis of dementia due to Alzheimer's disease: recommendations from the National Institute on Aging-Alzheimer's Association workgroups on diagnostic guidelines for Alzheimer's disease.** *Alzheimers Dement* 2011;7:263–69
42. Albert MS, DeKosky ST, Dickson D, et al. **The diagnosis of mild cognitive impairment due to Alzheimer's disease: recommendations from the National Institute on Aging-Alzheimer's Association workgroups on diagnostic guidelines for Alzheimer's disease.** *Alzheimers Dement* 2011;7:270–79
43. Highlights of prescribing information: Amyvid (florbetapir F18 injection). Silver Spring, MD: Food and Drug Administration (http://www.accessdata.fda.gov/drugsatfda_docs/label/2012/202008s000lbl.pdf)
44. Mucke L, Selkoe DJ. **Neurotoxicity of amyloid β-protein: synaptic and network dysfunction.** *Cold Spring Harb Perspect Med* 2012;2:a006338
45. Storandt M, Mintun MA, Head D, et al. **Cognitive decline and brain volume loss as signatures of cerebral amyloid-beta peptide deposi-**

tion identified with Pittsburgh compound B: cognitive decline associated with Abeta deposition. *Arch Neurol* 2009;66:1476–81
46. Schott JM, Bartlett JW, Fox NC, et al. **Increased brain atrophy rates in cognitively normal older adults with low cerebrospinal fluid Aβ 1–42.** *Ann Neurol* 2010;68:825–34
47. Tarawneh R, D'Angelo G, Macy E, et al. **Visinin-like protein-1: diagnostic and prognostic biomarker in Alzheimer disease.** *Ann Neurol* 2011;70:274–85
48. McEvoy LK, Brewer JB. **Biomarkers for the clinical evaluation of the cognitively impaired elderly: amyloid is not enough.** *Imaging Med* 2012;4:343–57
49. Bateman RJ, Xiong C, Benzinger TL, et al. **Clinical and biomarker changes in dominantly inherited Alzheimer's disease.** *N Engl J Med* 2012;367:795–804
50. Selkoe DJ. **Resolving controversies on the path to Alzheimer's therapeutics.** *Nat Med* 2011;17:1060–65
51. Bakkour A, Morris JC, Dickerson BC. **The cortical signature of prodromal AD: regional thinning predicts mild AD dementia.** *Neurology* 2009;72:1048–55
52. Costafreda SG, Dinov ID, Tu Z, et al. **Automated hippocampal shape analysis predicts the onset of dementia in mild cognitive impairment.** *Neuroimage* 2011;56:212–19
53. den Heijer T, van der Lijn F, Koudstaal PJ, et al. **A 10-year follow-up of hippocampal volume on magnetic resonance imaging in early dementia and cognitive decline.** *Brain* 2010;133:1163–72
54. Desikan RS, Cabral HJ, Fischl B, et al. **Temporoparietal MR imaging measures of atrophy in subjects with mild cognitive impairment that predict subsequent diagnosis of Alzheimer disease.** *AJNR Am J Neuroradiol* 2009;30:532–38
55. Heister D, Brewer JB, Magda S, et al. **Predicting MCI outcome with clinically available MRI and CSF biomarkers.** *Neurology* 2011;77:1619–28
56. Jack CR Jr, Wiste HJ, Vemuri P, et al. **Brain beta-amyloid measures and magnetic resonance imaging atrophy both predict time-to-progression from mild cognitive impairment to Alzheimer's disease.** *Brain* 2010;133:3336–48
57. Kovacevic S, Rafii MS, Brewer JB, et al. **High-throughput, fully automated volumetry for prediction of MMSE and CDR decline in mild cognitive impairment.** *Alzheimer Dis Assoc Disord* 2009;23:139–45
58. Sluimer JD, van der Flier WM, Karas GB, et al. **Accelerating regional atrophy rates in the progression from normal aging to Alzheimer's disease.** *Eur Radiol* 2009;19:2826–33
59. Vemuri P, Wiste HJ, Weigand SD, et al. **MRI and CSF biomarkers in normal, MCI, and AD subjects: predicting future clinical change.** *Neurology* 2009;73:294–301
60. Westman E, Cavallin L, Muehlboeck JS, et al. **Sensitivity and specificity of medial temporal lobe visual ratings and multivariate regional MRI classification in Alzheimer's disease.** *PLoS One* 2011;6:e22506
61. Dickerson BC, Stoub TR, Shah RC, et al. **Alzheimer-signature MRI biomarker predicts AD dementia in cognitively normal adults.** *Neurology* 2011;76:1395–402
62. Dickerson BC, Wolk DA. **Alzheimer's Disease Neuroimaging Initiative. MRI cortical thickness biomarker predicts AD-like CSF and cognitive decline in normal adults.** *Neurology* 2012;78:84–90
63. Adams HP Jr, del Zoppo G, Alberts MJ, et al. **Guidelines for the early management of adults with ischemic stroke: a guideline from the American Heart Association/American Stroke Association Stroke Council, Clinical Cardiology Council, Cardiovascular Radiology and Intervention Council, and the Atherosclerotic Peripheral Vascular Disease and Quality of Care Outcomes in Research Interdisciplinary Working Groups: the American Academy of Neurology affirms the value of this guideline as an educational tool for neurologists.** *Stroke* 2007;38:1655–711

Endovascular Catheter for Magnetic Navigation under MR Imaging Guidance: Evaluation of Safety In Vivo at 1.5T

S.W. Hetts, M. Saeed, A.J. Martin, L. Evans, A.F. Bernhardt, V. Malba, F. Settecase, L. Do, E.J. Yee, A. Losey, R. Sincic, P. Lillaney, S. Roy, R.L. Arenson, and M.W. Wilson

ABSTRACT

BACKGROUND AND PURPOSE: Endovascular navigation under MR imaging guidance can be facilitated by a catheter with steerable microcoils on the tip. Not only do microcoils create visible artifacts allowing catheter tracking, but also they create a small magnetic moment permitting remote-controlled catheter tip deflection. A side product of catheter tip electrical currents, however, is the heat that might damage blood vessels. We sought to determine the upper boundary of electrical currents safely usable at 1.5T in a coil-tipped microcatheter system.

MATERIALS AND METHODS: Alumina tubes with solenoid copper coils were attached to neurovascular microcatheters with heat shrink-wrap. Catheters were tested in carotid arteries of 8 pigs. The catheters were advanced under x-ray fluoroscopy and MR imaging. Currents from 0 mA to 700 mA were applied to test heating and potential vascular damage. Postmortem histologic analysis was the primary endpoint.

RESULTS: Several heat-mitigation strategies demonstrated negligible vascular damage compared with control arteries. Coil currents ≤300 mA resulted in no damage (0/58 samples) compared with 9 (25%) of 36 samples for > 300-mA activations ($P = .0001$). Tip coil activation ≤1 minute and a proximal carotid guide catheter saline drip > 2 mL/minute also had a nonsignificantly lower likelihood of vascular damage. For catheter tip coil activations ≤300 mA for ≤1 minute in normal carotid flow, 0 of 43 samples had tissue damage.

CONCLUSIONS: Activations of copper coils at the tip of microcatheters at low currents in 1.5T MR scanners can be achieved without significant damage to blood vessel walls in a controlled experimental setting. Further optimization of catheter design and procedure protocols is necessary for safe remote control magnetic catheter guidance.

ABBREVIATIONS: CCA = common carotid artery; ECA = external carotid artery; iMRI = interventional MR imaging; MARC = magnetically assisted remote control; RF = radio-frequency; SSFP = steady-state free precession.

MR imaging offers soft tissue contrast and physiologic parameter measurement (eg, diffusion and perfusion) that make it an ideal technique to monitor the effect of endovascular interventions in real time. Previously, low spatial and temporal resolution of MR imaging compared with x-ray fluoroscopy have made navigation of endovascular catheters from an access point to a point of therapy delivery unattractive. In the past decade, improvements in MR imaging spatial and temporal resolution—particularly the advent of near-real-time SSFP sequences—have renewed interest in the development of endovascular iMRI applications.[1]

A fundamental barrier to performing endovascular interventions under real-time MR imaging guidance is the steering of catheter tips. Compared with the myriad catheters and guidewires available for endovascular navigation under x-ray fluoroscopy guidance, iMRI has a relative lack of compatible, safe tools for endovascular interventions in the main B0 magnetic field (1.5T or 3T) of the MR imaging scanner.[2] The strong magnetic environment of the MR imaging scanner does, however, provide an op-

Received September 5, 2012; accepted after revision December 27, 2012.

From the Departments of Radiology and Biomedical Imaging (S.W.H., M.S., A.J.M., F.S., L.D., E.J.Y., R.S., P.L., R.L.A., M.W.W.), and Bioengineering (S.R.), and School of Medicine (A.L.), University of California, San Francisco; and Lawrence Livermore National Laboratory (L.E., A.F.B., V.M.), Livermore, California.

This study was supported by American Society of Neuroradiology Research and Education Foundation Scholar Award 2010 and 2011 (S.W.H.), National Heart Lung Blood Institute, National Institutes of Health (NIH), through M. Wilson Grant Number 1R01HL076486, National Institute of Biomedical Imaging and Bioengineering, NIH, through Grant Number 1R01EB012031-01A1 (S.W.H.), and National Center for Research Resources and the National Center for Advancing Translational Sciences, NIH, through UCSF-CTSI Grant Number UL1 RR024131, National Institute of on Minority Health and Health Disparities, NIH, through Grant Number R25MD006832. Its contents are solely the responsibility of the authors and do not necessarily represent the official views of the American Society of Neuroradiology or the NIH.

Paper previously presented in part at: Annual Meeting of the American Society of Neuroradiology, April 23, 2012; New York, New York.

Please address correspondence to Steven W. Hetts, MD, Interventional Neuroradiology, UCSF Medical Center, 505 Parnassus Ave, L-352, San Francisco, CA 94143-0628; e-mail: steven.hetts@ucsf.edu

Indicates open access to non-subscribers at www.ajnr.org

Indicates article with supplemental on-line tables.

http://dx.doi.org/10.3174/ajnr.A3530

Table 1: Microcatheter constructs

Experimental Catheter No.	Substrate Microcatheter	Catheter Length (cm)	Solenoid Coil (no. of turns)	Resistance (ohms)	Thermocouple
I	2.3F RapidTransit	170	30	2	None
II	2.7F Tracker-18	150	75	5.5	None
III	2.3F RapidTransit	170	30	2.5	Copper/constantan type T
IV	2.3F RapidTransit	170	30	2.5	Copper/constantan type T

portunity to use magnetic forces to steer catheters by remote control.[3-6]

We have developed a system for MARC catheter tip navigation for iMRI.[3,4,7-9] The system consists of a microcatheter with copper microcoils wound around the catheter tip, copper current-carrying wires through the catheter lumen (or embedded in the catheter wall), and a wired connection to a current controller and a power source located outside of the MR imaging scanner room. Small amounts of electric current delivered to the catheter tip coils create a magnetic moment at the catheter tip that seeks to align with the main B0 magnetic field of the MR imaging scanner. Depending on coil geometry, navigation in 3D can be achieved with catheter tip currents of $\leq$150 mA applied for $<$ 30 seconds per activation.[3,4,10]

Heat is a side product of the electrical currents needed to create magnetic moments on the tips of catheters. Miniaturization of the microcoils requires small wire dimensions, which are associated with relatively high resistivity. Early versions of our catheter system experienced significant heating in vitro, such that they would result in damaged blood vessels or coagulated blood if used in vivo. Catheter tip heating has been largely mitigated in vitro through a selection of new catheter tip materials and the use of room-temperature catheter luminal saline drips.[7,8] In the experiments presented, we sought to determine the upper boundary of electrical currents safely useable at 1.5T in a coil-tipped microcatheter system in vivo. We hypothesized that catheter tip coil current activations of up to 300 mA for $\leq$1 minute would not result in definite arterial wall damage.

MATERIALS AND METHODS

Magnetic Catheter Construction

Previous in vitro experiments in which copper microcoils were placed on aluminum oxide (alumina) tubes demonstrated substantial heat flow radially outwards into the surrounding fluid.[7] Instead, by transferring heat generated by the microcoils to saline coolant flowing through the catheter lumen, microcoils were wound onto alumina tubes. Efficient heat removal by the saline coolant allowed an insulating layer to be placed between the copper coil on the outer surface of the alumina tube and the blood.

Several 2.3F RapidTransit (Codman Neurovascular, Raynham, Massachusetts) and Tracker-18 (Boston Scientific, Natick, Massachusetts) microcatheters were used as substrates for microcoils (Table 1). Copper wire (0.0015-inch) was wrapped around the outer surface of a 99.8% pure 1.3-mm outer diameter tube (Ortech Advanced Ceramics, Sacramento, California) to create solenoid coils of 30 to 75 turns (Table 1 and Fig 1*A*). The copper wire was wound into thermal epoxy to ensure adherence to the tube. Additional layers of epoxy and heat shrink-wrap were placed over the solenoid, resulting in a final outer diameter of approximately 2.0 mm. The heat shrink-wrap also attached the alumina tube–copper coil assembly to the distal tip of the microcatheter (Fig 1*B*).

Two 0.005-inch copper H-polyinsulated wires were run through the lumen of each microcatheter. Lead wires were attached to microcoil leads located proximal to the catheter tip. Microcoil leads were made of copper wire 0.0015 inch in diameter. Coil lead wires were 2.5 and 3.25 inches long. Coil lead wires allowed separation of the electrical connection point from the tip while maintaining a patent central catheter lumen. The leads were drawn through a modified Thuoy-Borst Y-adaptor (Abbott Vascular, Abbott Park, Illinois) at the microcatheter hub and were subsequently attached to the catheter. Power leads from the center 2 leads of a phone jack power adaptor were placed through the center bore of the Y-adaptor (Fig 1*B, -C*). The design enabled saline drip delivery through the Thuoy-Borst side port. The resistance of coils on alumina tubes ranged from 2.0 to 5.5 ω (Table 1), and the total resistance of the assembled catheter with coil tips was between 6.0 and 9.0 ω.

Microcatheter Thermocouple Construction

Two of the microcatheter constructs were designed with built-in Type T copper-constantan thermocouples (OMEGA Engineering, Stamford, Connecticut) to allow direct temperature measurement at the solenoid (Fig 1*C*, *-D* and Table 1). Three copper-coated 99.9% pure wires (0.004-inch diameter) and one 0.004-inch-diameter constantan wire were pulled through the microcatheter. One copper wire and the constantan wire were used to form the Type T thermocouple (welded ball, Fig 1*B*). The lead ends were attached to a Type T thermocouple jack. The catheter thermocouple was plugged into a copper/constantan lead of 0.025-inch wires 0.91 meter long.

In vitro heating experiments were performed with a microcatheter containing 2 thermocouples. The first thermocouple was buried into the far end of the alumina tube. A slot was machined in to the alumina, and the ball of the thermocouple was wedged into it approximately 0.025 inch from the end of the solenoid coil (Fig 1*B*). This allowed the temperature of the coil tip to be measured. The second thermocouple was mounted on the surface of heat shrink-wrap over the top of the coil area on the same radial axis as the first thermocouple. This external thermocouple allowed temperature measurement outside of the heat shrink-wrap of the microcatheter construct. A HH66U hand-held thermocouple thermometer (OMEGA Engineering) was used for temperature measurements.

In Vitro Heating Experiments

To examine the heating properties of copper solenoids on alumina tubes, we performed several benchtop-heating experiments. Hand-wound copper coils (30 turns of 1-mm copper wire) with a resistance of 0.25 ω were wound onto the alumina tube (1.26-mm

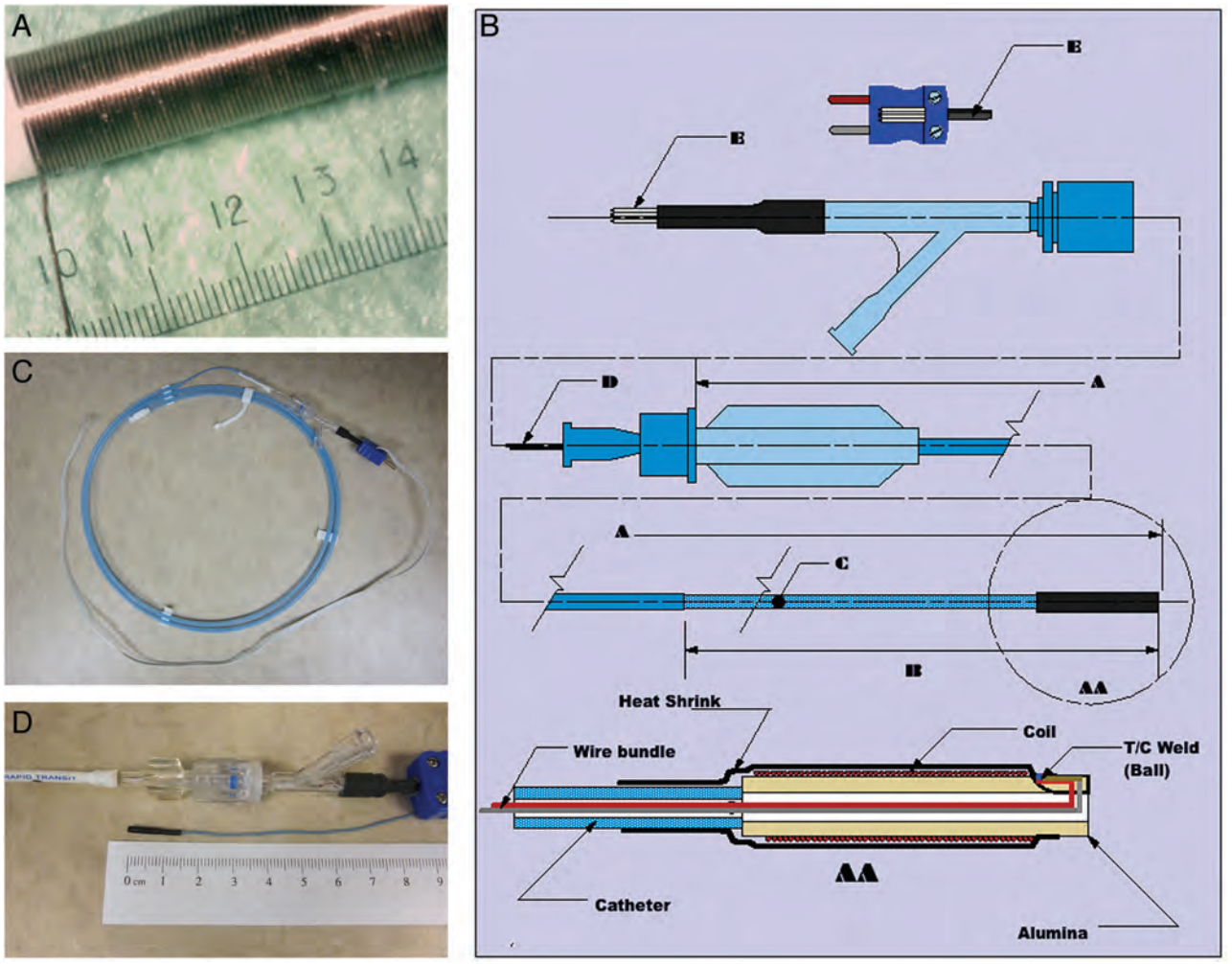

FIG 1. MARC catheter system. *A*, Hand-wound copper coil solenoid on an alumina substrate tube. *B*, Catheter diagram with thermocouple**.** A. Catheter length. B. Catheter tip. C. Coil feedwire. D. Power lead E. Power phone jack lead AA. Catheter tip. *C*, Magnetic microcatheter III with thermocouple**.** A light blue Rapid Transit microcatheter (Cordis, Miami Lakes, Florida) with a 2.3F distal tip has been used as a substrate. A 30-turn copper solenoid coil mounted on an alumina tube is attached to the distal tip of the microcatheter with brown shrink-wrap. A copper-constantan thermocouple terminates adjacent to the coils within the shrink-wrap. Current-carrying copper wires to the solenoid coil run down the catheter lumen and are attached to a phone jack adaptor that, itself, can be plugged into a power source for activation experiments. The dark blue thermocouple plug at the catheter hub can be attached to a data logger for temperature measurements. *D*, Distal tip of magnetic microcatheter III. A 30-turn copper solenoid coil mounted on an alumina tube is attached to the distal tip of the microcatheter. Brown shrink-wrap attaches the alumina tube–copper coil assembly to the distal tip of the microcatheter. The final outer diameter is approximately 2 mm.

outer diameter and wall thickness of 0.45 mm) substrates. Black heat shrink-wrap was placed over the solenoid tip, resulting in approximately 0.31 mm of insulation after shrinking. The 2 thermocouples were then assembled as discussed above.

Three sets of experiments were conducted, each involving temperature measurements at the coil and outside the heat shrink-wrap at current levels ranging from 10 mA to 700 mA. In a single set of experiments, water (2 mL/minute) flowed through the catheter lumen and through the alumina tube. Two other sets of experiments were performed with no flow, but the coil was immersed in water at 25°C and 37°C.

In Vivo Testing at 1.5T

Eight 30-kg farm pigs were used to investigate potential thermal damage from resistive or RF heating related to use of the microcoil-tipped catheter, under a protocol approved by the University of California, San Francisco Institutional Committee on Animal Care and Research. Each pig fasted for 12 hours before the experiment and before being premedicated with acepromazine (1.1 mg/kg IV) and ketamine (20–30 mg/kg); intubated; and anesthetized with 1.5%–2.5% isoflurane, 2%–3% nitrous oxide, and 100% oxygen throughout the study.

A 9F vascular sheath was inserted into the femoral artery percutaneously under aseptic conditions. Immediately afterward, heparin (50 IU/kg IV) was administered. Under x-ray guidance (Philips V5000; Best, the Netherlands, or OEC Medical Systems 9600; GE Healthcare, Milwaukee, Wisconsin), either a 9F balloon guide catheter (Concentric Medical, Mountain View, California) or an 8F MPC Envoy guide catheter (Codman) was navigated coaxially over a 5F vertebral artery catheter (Cook Medical, Bloomington, Indiana) and a 0.035-inch Bentson guidewire (Boston Scientific) to the proximal left or right CCA. The inner catheter and guidewire were removed, and the guide catheter was

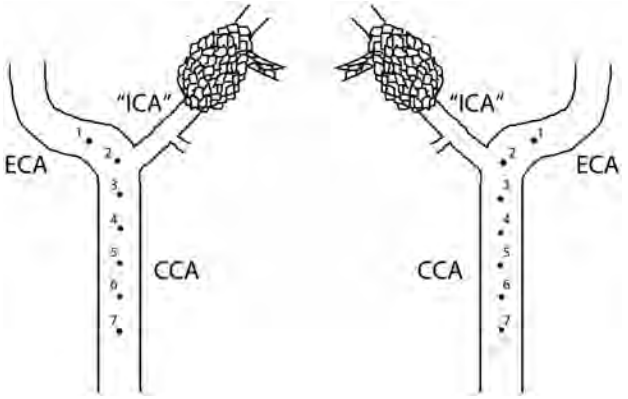

FIG 2. Schematic diagram depicting coil-tipped microcatheter heating activation points in vivo (*swine right and left common carotid arteries, respectively*). The first activation point is 1 cm distal to the origin of the internal carotid artery (ascending pharyngeal artery). Each subsequent activation point is separated by a 1-cm manual pullback of the catheter, confirmed by imaging. This ensures adequate spacing between points in case of potential thermal damage to the arterial wall at any given point.

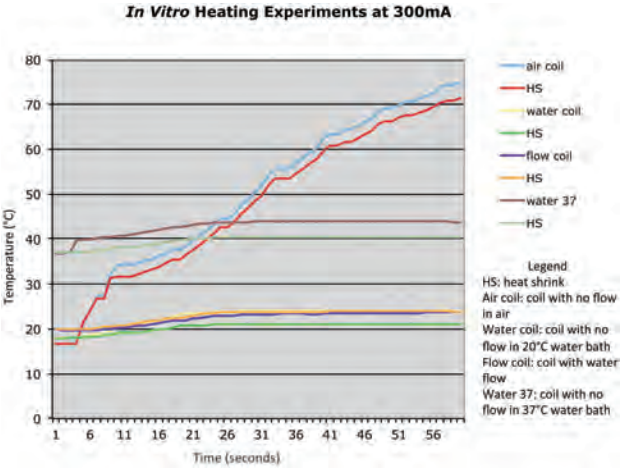

FIG 3. In vitro heating data for alumina tube construct tested at 300 mA in air, in a 25°C water bath, and in a 37°C water bath.

double-flushed and perfused with room-temperature normal saline solution at a variable drip rate depending on the desired experimental conditions (On-line Tables). Next, the coil-tipped microcatheter construct was inserted through the guide catheter and was advanced to the proximal ECA under x-ray fluoroscopic road-mapping by use of iohexol contrast (Omnipaque 300; GE Healthcare), diluted 1:1 with normal saline. The animal was moved to the 1.5T MR imaging scanner (Achieva; Philips) along a single sliding table in the University of California, San Francisco's combined x-ray/MR imaging suite. Imaging and catheter-heating experiments were then performed under MR imaging guidance in the ECA and CCA as outlined below.

After the procedures were performed in 1 carotid artery, the pig was moved to the x-ray angiography suite for catheterization of the contralateral proximal CCA with the guide catheter as above. The coil-tipped microcatheter was reinserted through the guide catheter and was advanced to the proximal ECA. In 4 animals, the CCA was then occluded at the tip of the guide catheter (several centimeters proximal to the microcoil-tipped catheter) either via guide catheter balloon inflation or surgical silk suture ligature. The animal was then transported to the MR imaging scanner in preparation for repeated imaging and heating experiments as outlined below.

In Vivo Imaging and Heating Experiments

Microcatheters were activated at 6–7 positions in each carotid artery, with the most distal test-point in the proximal ECA (1 cm distal to the origin of the ascending pharyngeal artery, which is the equivalent of the internal carotid artery in pigs) and subsequent test-points more proximal in the CCA (Fig 2). Microcatheters were manually pulled back 1 cm (confirmed by imaging) between each successive activation point in the carotid artery. This was performed to ensure adequate spacing between points if thermal or mechanical damage occurred at any given point. Activations with up to 700 mA of catheter-tip current for various durations of time were directed at testing resistive heating caused by running current through the catheter coils during imaging. In contrast, sham activation points that were performed with no current (0 mA for 0.5, 1, or 5 minutes) were directed at investigating potential radio frequency heating from imaging alone, as well as assessing potential mechanical damage to the vessel walls from catheterization. Imaging was performed with an SSFP sequence (TR, 5.5 ms; TE, 1.6 ms; flip angle, 30°; matrix, 128 × 128; section thickness, 5–6 mm; specific absorption rate, 3.7 W/kg), with real-time imaging at 3–5 frames per second.

Euthanasia and Postmortem Gross and Histologic Analyses

On completion of imaging, both the guide and the microcoil-tipped catheters were carefully withdrawn from the femoral access site and were examined for blood clots. Animals were permitted to remain under anesthesia for 4 to 5 additional hours to provide sufficient time for evolution of vascular changes related to thermal or mechanical damage. Euthanasia was performed by injection of saturated potassium chloride (1 mL/kg IV), and bilateral thoracotomy. The carotid arteries were isolated, excised en bloc, and opened longitudinally for gross examination. They were then fixed in 10% buffered formalin and embedded in paraffin in preparation for histologic staining. Arteries were sectioned into 5-μm-thick cross-sections and were subsequently stained with hematoxylin-eosin, Masson trichrome, and cleaved caspase 3 stain. Microscopic analyses were performed on all sections to evaluate any thermal or mechanical damage to the arterial walls. Composite gross and histologic damage scoring of samples was separated into 3 levels: 0 = normal arterial wall and lumen, 1 = questionable damage (endothelial denudation, subtle changes to vessel wall, small amount of luminal thrombus adherent to endothelial surface), and 2 = definite thermal damage (infiltration of inflammatory cells into vessel wall, mural hemorrhage, endothelial disruption). Histologic damage data were analyzed with STATA SE version 10 (StataCorp, College Station, Texas), by use of a case-control odds ratio calculator, 2-sided Fisher exact tests, and Wilcoxon log-rank sum tests.

RESULTS

In Vitro Testing

Benchtop heating experiments demonstrated temperatures at thermocouple 2 outside of the heat shrink-wrap were significantly

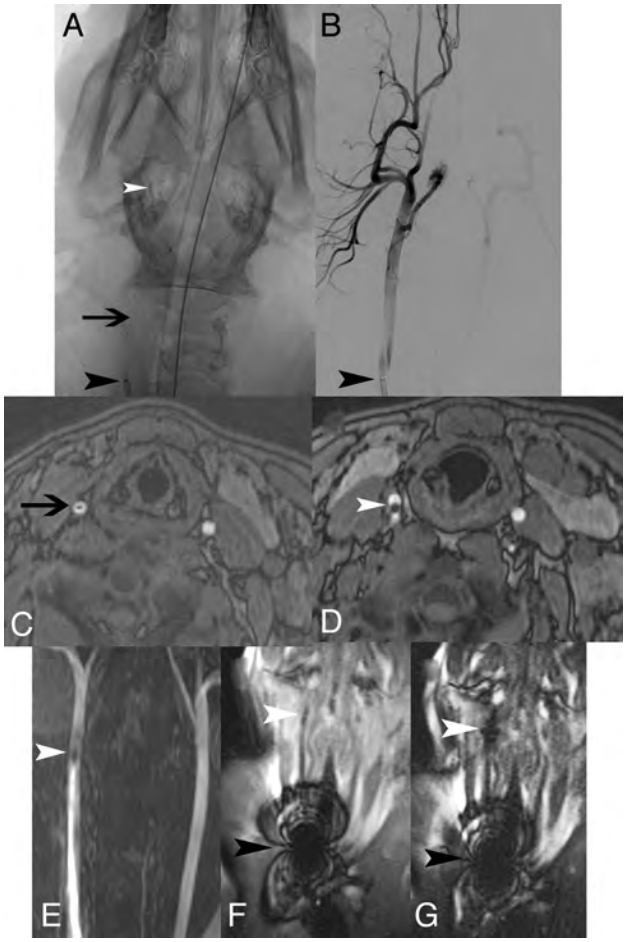

FIG 4. In vivo x-ray, DSA, axial MRA, coronal MRA MIP, and coronal SSFP. Unsubtracted x-ray image (*A*) demonstrates MARC catheter tip coils (*white arrowhead*), microcatheter shaft with lead wires (*black arrow*), and guiding catheter (*black arrowhead*) in the right CCA. Only the guiding catheter tip marker is readily evident on the equivalent DSA image (*B*). Susceptibility from the catheter shaft lead wires (*black arrow*) and catheter tip (*white arrowhead*) is seen on axial MRA (*C* and *D*), coronal MRA MIP (*E*), and coronal SSFP (*F*). With a 300-mA current applied (*G*), the catheter tip coils are more apparent (*white arrowhead*). Guide catheter tip artifacts resulting from a metallic marker band are very prominent on the SSFP sequence (*F* and *G*).

lower than temperatures at thermocouple 1 at the coil because of the insulating effect of the heat shrink-wrap (Fig 3). For example, in experiments at 500 mA without luminal flow, the increase in temperature at the outer surface of the catheter tip was roughly 10°C less than it would be in the absence of shrink-wrap. Higher currents correlated with higher temperatures at both thermocouples but also a larger temperature difference between thermocouple 1 and thermocouple 2.

With the addition of 2-mL/minute water flow through the catheter lumen, temperature rise at both thermocouples was significantly decreased. At 500 mA of current, the coil was 18°C without flow and 11°C with flow. There was also a much smaller temperature decrease across the heat shrink-wrap with flow than without, indicating that most of the heat from the coils flows inward rather than outward.

Coils made of insulated copper wire result in large increases in temperature at high currents. Thermal resistance between the coil and alumina substrate accounted for a temperature increase of the coil of > 10°C with luminal saline flow at 2 mL/minute. For coils fabricated directly on the alumina, the thermal barrier of the wire insulation is absent and much lower temperature increases are observed.[7]

In Vivo Catheter Visualization

It was possible to visualize the MARC in vivo in porcine carotid arteries under x-ray fluoroscopic, time-of-flight MRA, and SSFP MR imaging (Fig 4). The MARC tip was visible on unsubtracted x-ray fluoroscopy (Fig 4*A*) but was difficult to see on x-ray angiography (Fig 4*B*). The MARC shaft (Fig 4*C*) and tip (Fig 4*D*) were clearly evident on axial MRA, and the MARC tip was easily visible on coronally reformatted MRA MIP (Fig 4*E*). Whereas the guiding catheter used to reach the proximal CCA demonstrated extensive MR imaging artifacts because of a metallic marker band at the catheter tip (Fig 4*F*, -*G*), the MARC tip was barely visible without current activation on SSFP (Fig 4*F*) and was easily visible when current was running through the catheter tip coils (Fig 4*G*). MR imaging, MRA, and x-ray were used to confirm MARC positioning before each tip coil current activation experiment. MR imaging, MRA, and x-ray angiography did not demonstrate

Table 2: Definite vs no or questionable histologic damage to carotid arteries under various conditions of catheter testing in vivo

Condition Tested	Definite Damage (%)	No/Questionable Damage (%)	Odds Ratio	95% CI	*P* Value*
Arterial stasis ($n = 24$)	4	96	3.0	0.36–137	.44
Normal flow ($n = 70$)	11	89			
Current ≤300 mA ($n = 58$)	0	100	0	0–0.21	.0001
Current > 300 mA ($n = 36$)	25	75			
Activations ≤1 min ($n = 52$)	6	94	0.37	0.056–1.9	.29
Activations > 1 min ($n = 42$)	14	86			
Work ≤100 J ($n = 68$)	3	97	0.082	0.008–0.5	.0015
Work >100 J ($n = 26$)	27	73			
Saline drip ≤2 mL/min ($n = 39$)	15	85	3.2	0.61–21	.16
Saline drip > 2 mL/min ($n = 55$)	5	95			
≤5°C catheter tip coil temperature rise ($n = 36$)	0	100	0	0–0.36	.0022
> 5°C temperature rise ($n = 29$)	24	76			
MR and x-ray guidance ($n = 45$)	11	88	1.9	0.35–13	.47
X-ray guidance only ($n = 49$)	6	94			

CI indicates confidence interval; J, Joules; mA, milliamperes.

Note:—Definite damage denotes a histologic score of 2; questionable damage, histologic score of 1; and no damage, histologic score of 0.

**P* value = 2-tailed Fisher exact test.

Table 3: Definite or questionable vs no histologic damage to carotid arteries under various conditions of catheter testing in vivo

Condition Tested	Definite/Questionable Damage (%)	No Damage (%)	Odds Ratio	95% CI	*P* Value*
Arterial stasis ($n = 24$)	21	79	0.87	0.25–3.5	.77
Normal flow ($n = 57$)	23	77			
Current ≤300 mA ($n = 51$)	14	86	0.31	0.092–1.020	.034
Current > 300 mA ($n = 36$)	31	69			
Activations ≤1 minute ($n = 52$)	8	92	0.17	0.037–0.61	.003
Activations > 1 min ($n = 42$)	33	67			
Work ≤100 J ($n = 68$)	13	87	0.29	0.018–1	.037
Work > 100 J ($n = 26$)	35	65			
Saline drip ≤2 mL/min ($n = 39$)	21	79	1.2	0.35–3.7	.80
Saline drip >2 mL/min ($n = 55$)	18	82			
≤5°C catheter tip coil temperature rise ($n = 36$)	8	92	0.17	0.028–0.80	.013
> 5°C temperature rise ($n = 29$)	34	68			
MR and x-ray guidance ($n = 45$)	16	84	0.64	0.19–2.0	.44
X-ray guidance only ($n = 49$)	22	78			

* *P* value = 2-tailed Fisher exact test.

changes in vessel caliber or macroscopic luminal thrombus after the activation experiments.

In Vivo Catheter Activation–Related Heating

A total of 94 current activation experiments were performed in 8 pigs (16 carotid arteries). The principal variables examined for pair-wise comparisons on the likelihood of vessel wall damage include normal carotid arterial flow vs arterial stasis, amount of current applied to the MARC tip (≤300 mA vs > 300 mA), duration of MARC tip current activation (≤1 minute vs > 1 minute), estimated energy dissipation, rate of guide catheter saline drip, catheter tip coil temperature measured within the MARC tip shrink-wrap, and guidance under MR imaging and x-ray vs x-ray alone (Tables 2 and 3).

Three sets of conditions demonstrated significant differences in the likelihood of vascular damage both by use of the criterion of definite histologic damage or the more conservative criterion of definite or questionable histologic damage: ≤300-mA catheter tip current activations vs > 300mA (less damage with less current), ≤100 J of energy delivered vs > 100 J (less damage with less energy), and ≤5°C MARC catheter tip coil temperature increase (measured at the thermocouple immediately adjacent to the coil within the shrink-wrap at the tip of the catheter) vs > 5°C (less damage with less temperature increase). As energy (work) equals the square of current × resistance × duration of activation, the relevant parameters were multiplied for each catheter system activation by use of the resistances measured in Table 1. This calculation assumes that the resistance of the catheter system does not change with temperature. Temperature increases measured at the MARC coils ranged from 0°C for zero current to 16°C for 600-mA current (On-line Tables). MARC coil activations of ≤1 minute vs > 1 minute did not differ in the likelihood of definite histologic damage (OR, 0.37; 95% CI, 0.056–1.9; $P = .29$), but by use of the more conservative criterion of definite or questionable histologic damage, shorter activations were less likely to be associated with histologic changes (OR, 0.17; 95% CI, 0.037–0.61; $P = .003$).

Of 70 activations performed under normal arterial flow conditions, more samples had histologic changes than those under carotid artery stasis by use of both the definite damage criterion (Table 2) and the more conservative definite or questionable histologic changes criterion (Table 3). This is counterintuitive but may relate to the ability of inflammatory cells to access the vascular wall after arterial stasis, though carotid arteries were reperfused after catheter tip activations.

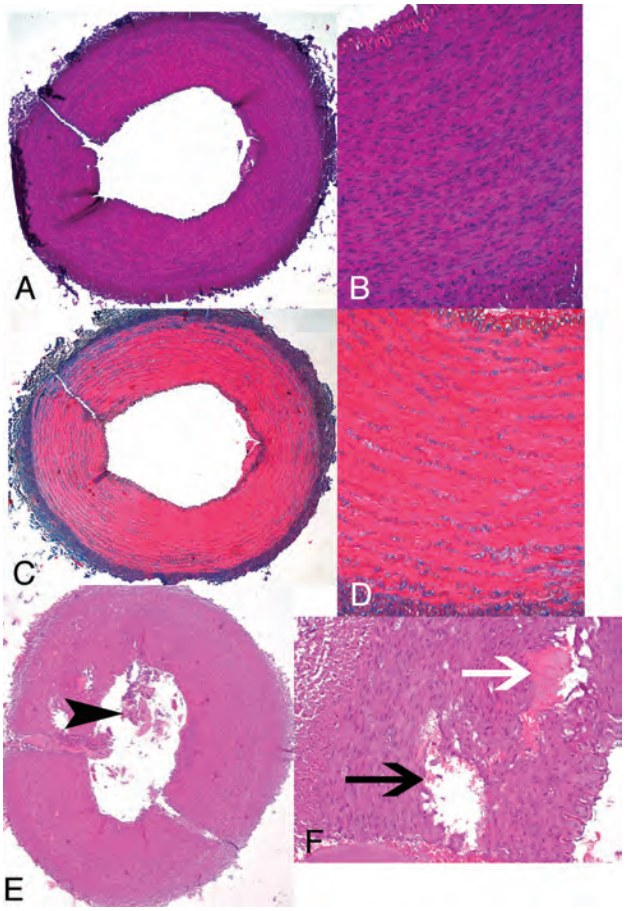

FIG 5. Porcine carotid artery wall histologic appearance after use of endovascular catheter tip coils at a 300-mA tip current for 1 minute at normal flow (*A-D*) or a 600-mA tip current for 2 minutes at zero flow (*E* and *F*). There is no evidence of vessel wall damage on hematoxylin-eosin (*A* and *B*) or Masson trichrome (*C* and *D*) at 300 mA. At 600 mA, however, luminal thrombus (*E*, *black arrowhead*), extensive medial vacuolization (*F*, *black arrow*), and medial hemorrhage (*G*, *white arrow*) all indicate thermal damage to the arterial wall.

In vivo vascular heating experiments were performed both in the MR imaging scanner and under x-ray guidance alone, to assess

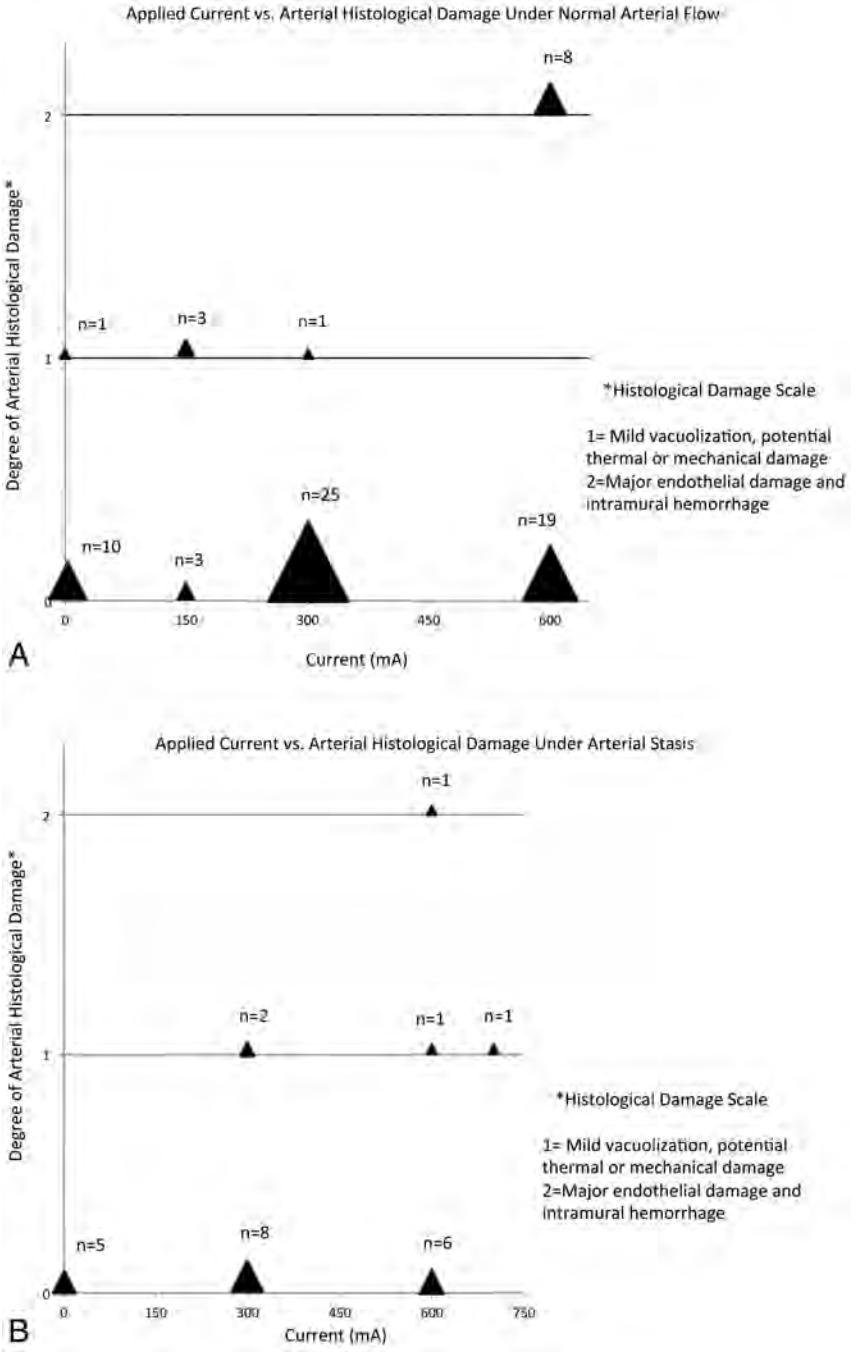

FIG 6. Plot of applied current vs degree of histologic damage for catheter activation experiments in vivo ($n=94$) in porcine carotid arteries. *A*, Normal arterial flow. *B*, Arterial stasis.

potential effect of the MR environment (strong magnetic field and SSFP imaging sequence with concomitant RF energy deposition) on tissue heating. No significant differences in the odds of histologic changes or definite damage were evident between the group receiving x-ray only and the group receiving x-ray plus MR imaging (Tables 2 and 3).

Subset Analysis

The degree of histologic damage identified at various current levels under normal carotid flow vs carotid stasis is displayed in Fig 5 and categorized in Fig 6. Under normal carotid arterial flow, with 0 (0%) of 43 activations with ≤300-mA MARC tip current resulted in definite histologic damage, whereas 8 (30%) of 27 activations with > 300 mA resulted in definite histologic damage (OR, 0; 95% CI, 0–0.23; $P = .0002$). With use of the more conservative criterion of definite or questionable histologic damage, under normal carotid arterial flow, with ≤300-mA tip current 5 (12%) of 43 had definite or questionable damage vs 8 (30%) of 27 with > 300 mA (OR, 0.31; 95% CI, 0.71–1.3; $P = .11$).

DISCUSSION

Preliminary in vivo testing of coil-tipped magnetically remote-controlled catheters at a microcatheter tip current of 0 to 700 mA demonstrated damage to carotid artery walls under several conditions when more than 300 mA of current was applied to the catheter tip. Lesser amounts of current did not result in infiltration of inflammatory cells into the carotid artery wall, but a few samples, even at 0 mA of tip current, did show evidence of endothelial denudation. This was likely the result of the mechanical force of the catheter tip against the blood vessel wall, as can happen with any endovascular device.[11,12]

One of the limitations of our study was its inability to discriminate between endothelial damage caused by heating compared with mechanical forces. Our MARC catheter has various mechanical features that differ from conventional catheters. Conventional neurovascular microcatheters usually contain radiopaque metallic bands (approximately 1 mm long) at the tip (and often 3 cm proximal to the tip) that are used as markers during procedures performed under x-ray. The MARC catheter contains copper microcoils at the tip that produce distinct artifacts during MR imaging that serve as an indicator of catheter tip position. In addition, the MARC catheter tip (approximately 1 cm) is stiffer and of slightly greater diameter than conventional neurovascular microcatheter tips. The present length of the stiff alumina tube at the MARC tip may ultimately impair its ability to have the desirable tight turning radius for navigating small vessels. Rigid devices are also more likely than soft devices to put greater forces on vascular walls, potentially leading to endothelial denudation or mural dissection. These differences warrant consideration of mechanical as well as thermal damage caused by the MARC to evaluate overall safety in vivo.

The potential for mechanical damage to vessel walls was miti-

gated throughout our experiments by use of a solenoid coil whose generated magnetic moment aligns with the bore of the MR imaging scanner (and thus aligns with B0) when the MARC is placed in the carotid artery (which also aligns with the bore of the MR imaging scanner). Thus, current activations, to a first approximation, should not force the catheter into the wall of the carotid artery. Initial placement of the relatively stiff-tipped catheter into the distal carotid artery may scrape the walls of the vessel and cause damage.

As the degree of vascular damage did not differ between tests performed in the MR imaging scanner (in which RF heating during imaging is a potential concern)[8] and those performed solely under x-ray guidance, there is likely a negligible contribution of RF energy absorption to catheter heating under the conditions tested. Instead, reducing resistive heating of the catheter tip coils during navigation current activation remains the primary challenge for developing a functional MARC system for remote-control catheter steering under MR imaging guidance.

Reductions in heat deposited by the MARC tip coils at the brief ($<$ 30-second), low currents ($<$ 300 mA) required for useful tip deflection at 1.5T can be addressed in several ways. First, room temperature or cooled saline irrigation to guide catheters and MARC catheters can reduce heating. This approach is similar to that used in the cooling of electrophysiology catheters used in MR imaging: mitigation of temperature increase (from $>$ 22°C to $<$2°C) with electrophysiology catheters has been achieved with irrigation rates of 2 mL/min at 1W and 10–14 mL/min at 5W.[13] As the MARC catheter has a power output of approximately 1.2W at 300 mA currents, irrigation at rates we have achieved experimentally would be expected to increase the safety of our device. Second, the manufacture of MARC tip coils directly on substrate alumina tubes with laser lithography versus the present use of hand-wound insulated copper wires would be expected to reduce heating, because lithographed coils would have a larger contact surface area with the highly thermally conductive alumina than round insulated wires, which only contact the alumina over a small percentage of their surface. Third, optimizing the catheter design (eg, with coaxial chokes on the catheter shaft current-carrying wires to mitigate potential RF-induced heating during MR imaging) would also contribute to device safety.[14]

Direct intravascular temperature measurements are challenging in MR imaging, thus explaining our choice of histologic features as the endpoint for analysis of potential thermal damage in the experiments presented. MR imaging thermometry typically involves measurements of proton resonance frequency or molecular motion, which are overwhelmed by the flow of blood and the artifacts generated by microcoil activation. Fiberoptic temperature sensors are presently not small enough in caliber to be included as part of a microcatheter system. Thermocouples on our endovascular catheters were able to measure temperatures adjacent to the MARC coils immediately before and after SSFP imaging, but not during imaging, probably because of RF interference. It may be possible to develop an interleaved imaging, navigation, and temperature-sensing strategy in which temperature measurements are taken from a catheter tip thermocouple during short pauses in imaging.

Our experimental design addressed only the simplest MARC tip coil geometry and device and vascular alignment in the MR imaging scanner bore. As the MARC system is developed further, non-solenoid steering coils (such as Helmholz saddle-shaped coils) will be required for navigating in different planes. These different coil geometries—and particularly multilevel designs with solenoids on an outer layer and saddle coils on an inner layer—may have different heating properties and will certainly have different mechanical properties than the conditions tested herein. Blood vessel branches can arise in many orientations relative to parent vessels. Remote-controlled navigation into various vascular branches will require different amounts of electrical current delivered to the MARC catheter depending not only on the angle at which the target vessel arises, but also depending on the orientation of the catheter tip relative to the bore of the MR imaging scanner. Determining in real-time the amount of current that needs to be delivered to the MARC coils for the spectrum of possible vascular configurations is an ongoing challenge that will have to be developed in parallel with new steering coil designs.

CONCLUSIONS

Preliminary in vivo testing of coil-tipped magnetically remote-controlled catheters demonstrated minimal injury to vessel walls when currents of ≤300 mA were applied. As prior experiments have suggested useful catheter tip deflection at similarly low currents, future experiments will evaluate navigation at currents $<$ 300 mA to maximize potential safety.

ACKNOWLEDGMENTS

The authors would like to thank Carol Stillson, Timothy Roberts, Pallav Kolli, Daniel Cooke, Matthew Amans, and Robert Taylor.

Disclosures: Steven Hetts—*RELATED: Grant:* ASNR,* NIH,* Comments: ASNR Foundation Scholar Award; NIH-NIBIB R01 Research Grant; *UNRELATED: Consultancy:* Silk Road Medical, Comments: Consultation on a medical device startup company; not related to the work presented. Alastair Martin—*RELATED: Grant:* NIH.* Anthony Bernhardt—*RELATED: Grant:* NIH.* Fabio Settecase—*RELATED: Grant:* NIH grant R01EB012031–02,* Comments: "Endovascular Magnetic Catheter for Interventional MRI," Principal Investigator: Steven W. Hetts; *UNRELATED: Grants/Grants Pending:* NIH grant R01EB012031–02.* Shuvo Roy—*RELATED: Grant:* NIH,* Comments: Grant to Steven Hetts (PI). Ronald Arenson—*RELATED: Grant:* NIH R01 1R01EB012031–01,* Comments: I am listed as consultant but have not received any payments; *UNRELATED: Board Membership:* Radiological Society of North America (RSNA), Comments: Board of Directors—paid for travel including for spouse and upgrades to business class; *Grants/Grants Pending:* NIH via RSNA;* *Payment for Lectures (including service on speaker bureaus):* Stanford University, Ochsner Clinic, Comments: Honorarium for speaking; *Patents (planned, pending or issued):* Patent for catheter design, Comments: I hold the patent, which is the subject of this manuscript, but I have not received any royalties because it has not been licensed yet; *Stock/Stock Options:* Retirement funds, Comments: All managed by third parties; *Travel/Accommodations/Meeting Expenses Unrelated to Activities Listed:* University of California, San Francisco, Comments: Reimbursement from UCSF for professional travel; *OTHER RELATIONSHIPS:* Some readers could conceivably believe the fact that I hold the patent influenced the work. Mark Wilson—*RELATED: Grant:* NIH.* **Money paid to institution.*

REFERENCES

1. Bock M, Wacker FK. **MR-guided intravascular interventions: techniques and applications.** *J Magn Reson Imaging* 2008;27:326–38
2. Muller L, Saeed M, Wilson MW, et al. **Remote control catheter navigation: options for guidance under MRI.** *J Cardiovasc Magn Reson* 2012;14:33
3. Roberts TP, Hassenzahl WV, Hetts SW, et al. **Remote control of catheter tip deflection: an opportunity for interventional MRI.** *Magn Reson Med* 2002;48:1091–95
4. Hetts SW. **Interventional magnetic resonance imaging: the revolution begins.** *Appl Radiol* 2005;34:84–91
5. Lalande V, Gosselin FP, Martel S. **Catheter steering using a magnetic**

resonance imaging system. *Conf Proc IEEE Eng Med Biol Soc* 2010:1874–77
6. Gosselin FP, Lalande V, Martel S. **Characterization of the deflections of a catheter steered using a magnetic resonance imaging system.** *Med Phys* 2011;38:4994–5002
7. Bernhardt A, Wilson MW, Settecase F, et al. **Steerable catheter microcoils for interventional MRI reducing resistive heating.** *Acad Radiol* 2011;18:270–76
8. Settecase F, Hetts SW, Martin AJ, et al. **RF heating of MRI-assisted catheter steering coils for interventional MRI.** *Acad Radiol* 2011;18:277–85
9. Settecase F, Sussman MS, Wilson MW, et al. **Magnetically-assisted remote control (MARC) steering of endovascular catheters for interventional MRI: a model for deflection and design implications.** *Med Phys* 2007;34:3135–42
10. Wilson MW, Martin AB, Lillaney P, et al. **Magnetic catheter manipulation in the interventional MR imaging environment.** *JVIR* 2013;24:885–91
11. Kalef-Ezra J, Michalis L, Bozios G, et al. **Effects of delayed (24 h postintervention) beta-irradiation therapy after coronary angioplasty and stenting in de novo native coronary artery lesions; results of a randomized clinical and intravascular ultrasound study.** *Cardiovasc Radiat Med* 2003;4:176–81
12. Muller-Hulsbeck S, Stolzmann P, Liess C, et al. **Vessel wall damage caused by cerebral protection devices: ex vivo evaluation in porcine carotid arteries.** *Radiology* 2005;235:454–60
13. Reiter T, Gensler D, Ritter O, et al. **Direct cooling of the catheter tip increases safety for CMR-guided electrophysiological procedures.** *J Cardiovasc Magn Reson* 2012;14:12
14. Ladd ME, Quick HH. **Reduction of resonant RF heating in intravascular catheters using coaxial chokes.** *Magn Reson Med* 2000;43:615–19

Improved T2* Imaging without Increase in Scan Time: SWI Processing of 2D Gradient Echo

S. Soman, S.J. Holdsworth, P.D. Barnes, J. Rosenberg, J.B. Andre, R. Bammer, and K.W. Yeom

ABSTRACT

BACKGROUND AND PURPOSE: 2D gradient-echo imaging is sensitive to T2* lesions (hemorrhages, mineralization, and vascular lesions), and susceptibility-weighted imaging is even more sensitive, but at the cost of additional scan time (SWI: 5–10 minutes; 2D gradient-echo: 2 minutes). The long acquisition time of SWI may pose challenges in motion-prone patients. We hypothesized that 2D SWI/phase unwrapped images processed from 2D gradient-echo imaging could improve T2* lesion detection.

MATERIALS AND METHODS: 2D gradient-echo brain images of 50 consecutive pediatric patients (mean age, 8 years) acquired at 3T were retrospectively processed to generate 2D SWI/phase unwrapped images. The 2D gradient-echo and 2D SWI/phase unwrapped images were compared for various imaging parameters and were scored in a blinded fashion.

RESULTS: Of 50 patients, 2D gradient-echo imaging detected T2* lesions in 29 patients and had normal findings in 21 patients. 2D SWI was more sensitive than standard 2D gradient-echo imaging in detecting T2* lesions ($P < .0001$). 2D SWI/phase unwrapped imaging also improved delineation of normal venous structures and nonpathologic calcifications and helped distinguish calcifications from hemorrhage. A few pitfalls of 2D SWI/phase unwrapped imaging were noted, including worsened motion and dental artifacts and challenges in detecting T2* lesions adjacent to calvaria or robust deoxygenated veins.

CONCLUSIONS: 2D SWI and associated phase unwrapped images processed from standard 2D gradient-echo images were more sensitive in detecting T2* lesions and delineating normal venous structures and nonpathologic mineralization, and they also helped distinguish calcification at no additional scan time. SWI processing of 2D gradient-echo images may be a useful adjunct in cases in which longer scan times of 3D SWI are difficult to implement.

ABBREVIATIONS: 2D SWI = SWI-processed 2D GRE; PU = phase unwrapped; 3D SWI = SWI-processed 3D GRE; GRE = gradient-echo

Gradient-echo (GRE) imaging is a robust MR imaging method for evaluating intracranial hemorrhage, mineralization, and venous structures[1,2] and is routinely used when brain MR imaging is performed. The image contrast in GRE is dependent on T2* relaxation, which refers to decay of transverse magnetization caused by a combination of spin-spin relaxation and magnetic field inhomogeneity. However, an additional form of image contrast can be generated by exploiting the phase information of GRE images. Depending on the TE, substances with different magnetic susceptibilities come out of phase with their surrounding tissue. Thus phase images can contain valuable information about local susceptibility changes among neighboring tissues. Using phase images to either enhance the contrast of T2*-weighted magnitude images or, on their own, as a complementary form of image contrast is called susceptibility-weighted imaging.[3] SWI better accentuates the paramagnetic properties of blood products than 2D GRE imaging and adds the ability to distinguish blood products from calcification. While SWI has shown clinical utility in the evaluation of hemorrhage, arterial venous malformations, small vessel diseases,

Received December 16, 2012; accepted after revision February 21, 2013.

From the Department of Radiology (S.S., P.D.B., K.W.Y.), Lucile Packard Children's Hospital, Stanford University, Palo Alto, California; Department of Radiology (S.J.H., J.R., R.B.), Lucas Center, Stanford University, Stanford, California; and Department of Radiology (J.B.A.), University of Washington, Seattle, Washington.

Paper previously presented in abstract form at: American Society of Neuroradiology 49th Annual Meeting and the Foundation of the ASNR Symposium, June 4–9, 2011; Seattle, Washington.

Please address correspondence to: Kristen W. Yeom, MD, Department of Radiology, Pediatric MRI and CT, Lucile Packard Children's Hospital, Stanford University, Room 0511, 725 Welch Rd, Palo Alto, CA 94304; e-mail: kyeom@stanford.edu

Indicates open access to non-subscribers at www.ajnr.org

Indicates article with supplemental on-line table

EBM 2 Evidence-Based Medicine Level 2.

http://dx.doi.org/10.3174/ajnr.A3595

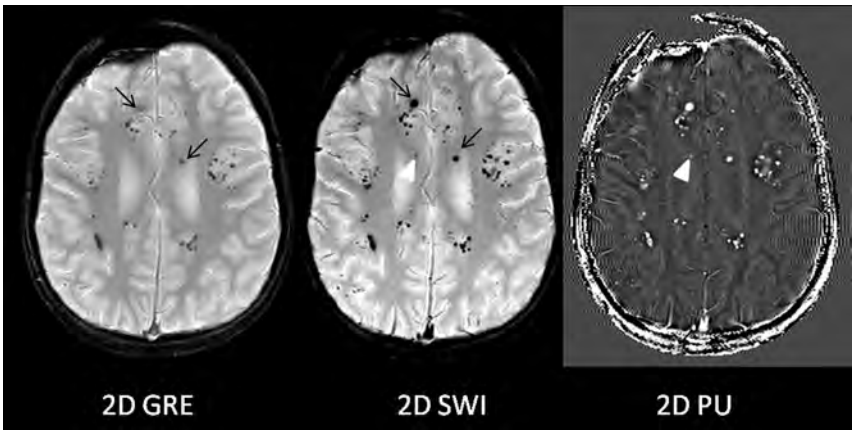

FIG 1. Improved T2* lesion conspicuity on 2D SWI compared with 2D GRE. Multiple T2* lesions are seen throughout the brain of a 14-year-old boy previously irradiated for medulloblastoma and presumed to have radiation-induced cavernous malformations/telangiectasias. Note improved visualization of these lesions (*black arrows*) on 2D SWI compared with corresponding lesions on 2D GRE (*black arrows*). Note a new T2* lesion on 2D SWI and PU images (*arrowheads*) not previously seen on 2D GRE.

amyloid angiopathy, cavernous malformations, multiple sclerosis, trauma, tumors, and hemosiderosis,[3-13] routine clinical implementation may be difficult due to the longer acquisition time (between 5 and 10 minutes[3-5,14-17]), particularly in children who are motion-prone and often require sedation.

Proponents of SWI have suggested that high-resolution 3D GRE images are crucial to optimally visualize cancellation effects between veins and background tissue and to avoid rapid dephasing across voxels that can occur by using a 2D GRE acquisition.[3,4,18] For this reason, vendors typically use 3D GRE sequences with resolutions on the order of 0.5 × 1.0 × 2.0 mm, resulting in acquisition times ranging from 5 to 10 minutes (depending on other imaging parameters and the MR imaging system used). In addition, TEs in SWI are typically optimized to maximize the phase difference between the venous and surrounding parenchymal tissue, usually a TE of ~25 ms at 3T.[3,4,18]

While SWI as derived from 3D GRE images yields excellent contrast among tissues of differing susceptibilities, we questioned whether SWI derived from 2D GRE images could also provide useful image contrast. 2D GRE images are acquired at considerably lower resolution (0.6 × 1.4 × 5 mm) and TE (15 ms) than SWI-processed 3D GRE (3D SWI). However 2D GRE images are also acquired in <2 minutes as part of our routine clinical practice. To the best of our knowledge, whether the phase information can be leveraged to boost image contrast and (if so) whether this additional postprocessing step is clinically useful are not known. Here, we hypothesized that 2D SWI/phase unwrapped (PU) images derived from SWI-processed 2D GRE could improve T2* lesion detection compared with standard 2D GRE.

MATERIALS AND METHODS

Subjects and Equipment

Fifty consecutive patients, mean age 8 years (median, 9 years; range, 2 months to 19 years; 28 males and 22 females), who underwent 2D GRE as part of routine brain MR imaging at 3T (Discovery 750; GE Healthcare, Milwaukee, Wisconsin), were retrospectively evaluated at our children's hospital after institutional review board approval. Axial 2D GRE imaging parameters were: TE = 15 ms, TR = 650 ms, flip angle = 20°, section thickness = 5 mm, 1-mm gap, FOV = 18–24 cm, rectangular FOV = 0.75, matrix = 384 × 168, bandwidth = 15 kHz, with flow compensation enabled, scan time = 1 minute, 50 seconds. An 8-channel head coil was used. Additional MR imaging sequences included T1 FLAIR, T2 FSE, DWI, T2 FLAIR, with or without contrast-enhanced T1 spin-echo images.

SWI Production from 2D GRE Data

SWI was created in line with the approach outlined by Haacke et al and Reichenbach et al.[3,4] A Hanning filter was used to phase unwrap and low-pass filter the complex data to create the 2D PU images. A negative phase mask was then generated from the PU images and was multiplied by the magnitude image $n = 5$ times to generate the 2D SWI. Note that $n = 5$ was considered empirically to be an acceptable trade-off between SNR and susceptibility contrast. The PU images were then inverted for blood products to appear hypointense. The raw data from the 2D GRE acquisition were saved on the scanner and sent to a computer for processing off-line. Postprocessing was performed by using a fully automated in-house-built Matlab code (7.8.0; MathWorks, Natick, Massachusetts), taking 2 minutes to complete per patient, with subsequent 2D SWI/PU images automatically returned to the PACS.

Data Review

Standard 2D GRE images were reviewed for any abnormalities by a blinded board-certified neuroradiologist (P.D.B.) with a Certificate of Added Qualification (>30 years' experience). A second board-certified neuroradiologist (K.W.Y.) with a Certificate of Added Qualification (7 years' experience) independently compared and scored the 2D GRE and 2D SWI in a blinded fashion. The 2D SWI and 2D PU images were subsequently compared side by side to identify any opposite signal intensities that might suggest the presence of calcifications as previously described for 3D SWI[16,17] and were also compared with available CT scans. A first-year neuroradiology fellow (S.S.) was present throughout the study to administer the review process in a randomized and blinded fashion.

Baseline 2D GRE

T2* lesions were defined as hemorrhages, mineralization, abnormal vascularity (AVM, telangiectasias, or tumor vascularity), or other hemosiderin-stained hypointense lesions. The 2D GRE imaging findings of all patients were randomly reviewed and interpreted as either normal in the absence of such lesions or abnormal if such lesions were present. As summarized by Wu et al,[17] calcifications of the pineal gland, choroid plexus, basal ganglia, deep cerebellar nuclei, and dura mater, also referred as "nonpathologic calcifications," are usually not associated with pathology. Hence, examinations that showed nonpathologic calcifications were cat-

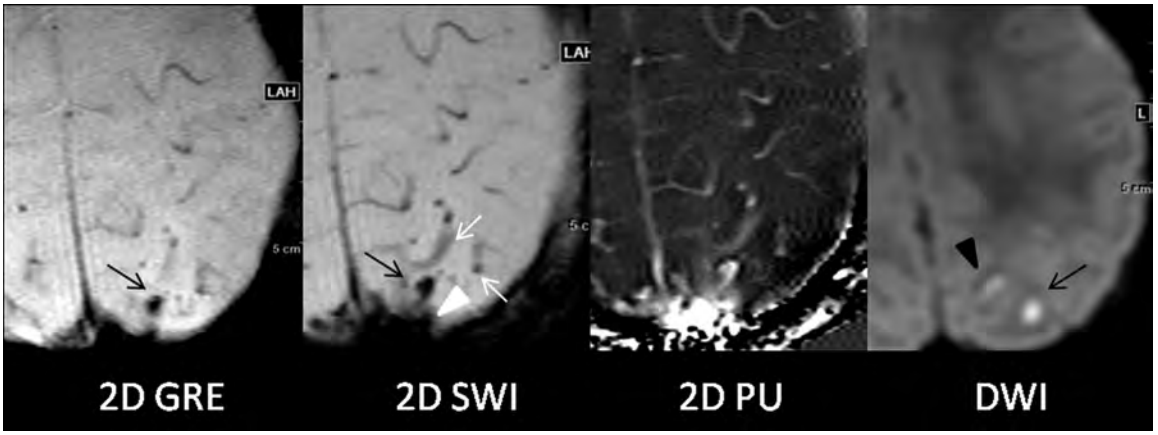

FIG 2. Potential pitfalls of 2D SWI/PU. Focal venous thrombosis (*black arrow*) and an adjacent area suspicious for focal venous ischemia (*black arrowhead*) on DWI are identified in a 5-month-old boy with seizures. The T2* lesion corresponding to the thrombosis is well-visualized on both 2D GRE and 2D SWI (*black arrows*) and is, in fact, even more prominent on 2D SWI images. However, prominent adjacent calvarial bony artifacts (*arrowhead*) and heightened visualization of deoxygenated and slow-flow cortical veins on 2D SWI (*white arrows*) were thought to be distracting.

egorized as having normal findings. In addition, the presence of a developmental venous anomaly was considered normal for this study purpose. Of note, no patients had disorders of calcium/phosphate metabolism. Also, the presence of motion or metal artifacts did not constitute an abnormality.

Comparison of 2D GRE and 2D SWI

For the 2D GRE studies with abnormal findings, conspicuity of the T2* lesions were scored for both 2D GRE and corresponding 2D SWI by using the following 5-point scale: −2, findings were visible on 2D GRE, but not visible on 2D SWI; −1, findings were better seen on 2D GRE compared with 2D SWI; 0, all findings were equally visible on 2D GRE and 2D SWI; +1, findings were better identified on 2D SWI than on 2D GRE; and +2, findings were visible on 2D SWI that were not visible on 2D GRE. If multiple T2* lesions were present in any given patient, scoring was still performed for each T2* lesion but the lowest of the scores was used as the final score.

Among 2D GRE studies with normal findings, any new potential T2* lesion on 2D SWI not previously detected by 2D GRE was also recorded. In such cases, additional MR imaging sequences (T1WI, T2WI, DWI, contrast-enhanced images) and CT were used to exclude potential artifacts and to further define the "new" T2* lesion, with the understanding that without a histologic correlate, lesion verity may not be confirmed.

Other Imaging Features

For all 50 baseline 2D GRE examinations with normal and abnormal findings, additional imaging features on 2D SWI relative to 2D GRE were queried, requiring yes (1) or no (0) responses:

- If present, was T2* of the deep gray nuclei more conspicuous or newly identified?
- If present, were motion/dental artifacts worse?
- Was depiction of normal venous structures and/or developmental venous anomalies more prominent, and were new venous structures seen on 2D SWI not detected by 2D GRE?
- If present, was surgical catheter detail improved?

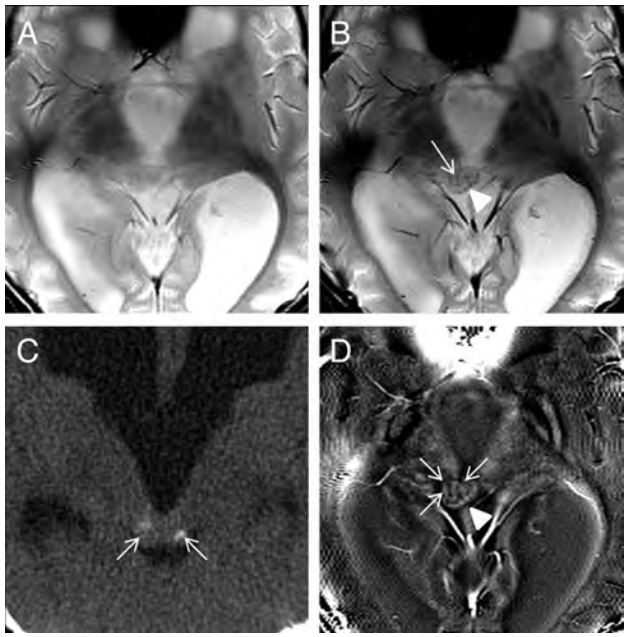

FIG 3. New T2* abnormality identified by 2D SWI. *A*, No T2* abnormality is seen on this baseline 2D GRE image in a 10-year-old boy with tectal glioma and associated ventriculomegaly. *B*, 2D SWI shows punctuate low-signal foci suggestive of T2* abnormality (*arrow, arrowhead*). *C*, This is shown as calcification/mineralization (*arrows*) by CT. *D*, 2D PU image shows a punctate low intensity (*arrows*) suggestive of calcification and foci of high intensity that may represent blood products (*arrowhead*) within the tumor.

Finally, for all cases, 2D SWI and 2D PU images were compared side by side to identify opposite intensities that would suggest the presence of calcification, and they were subsequently compared with CT.

Statistical Analysis

To statistically analyze the degree to which 2D SWI depicted T2* lesions seen on 2D GRE images with abnormal findings, the Wilcoxon signed rank test against a value of zero (no difference) was used. For the remaining binary measures, the percentage of positive outcomes was calculated. All statistical analyses were per-

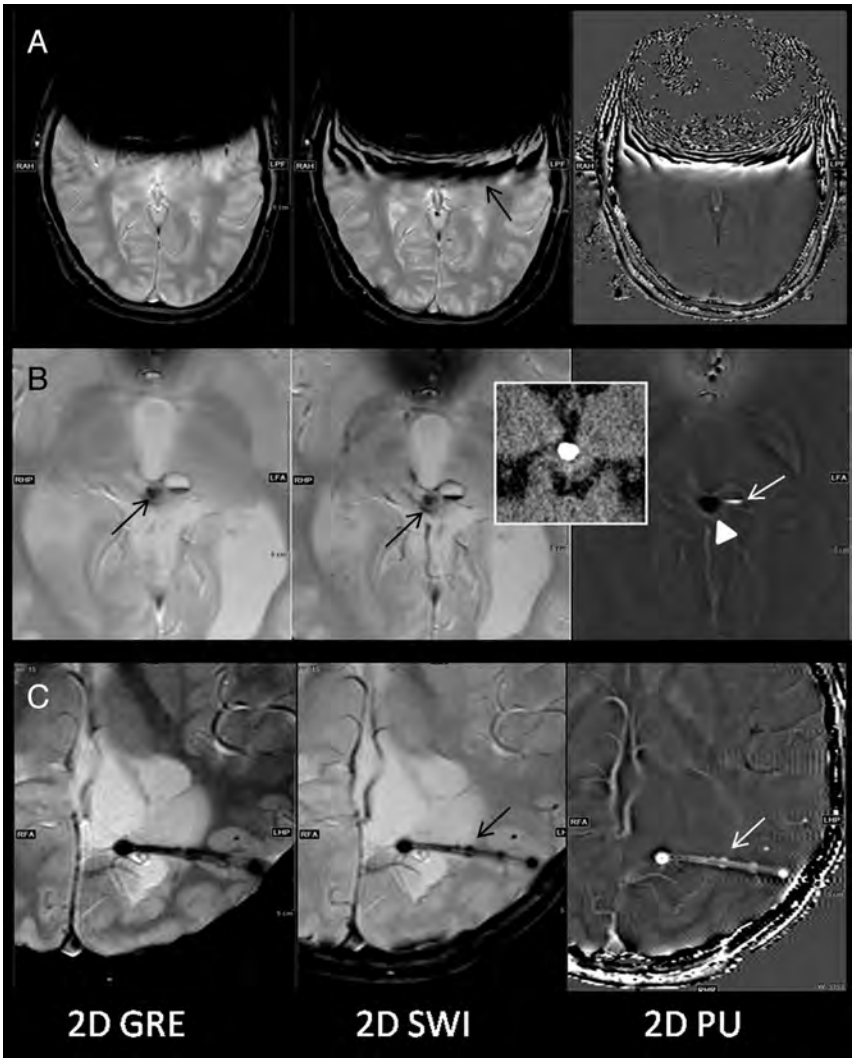

FIG 4. Other comparison features of 2D GRE and 2D SWI/PU. *A*, Dental braces artifacts. Note increased artifacts on 2D SWI (*arrow*) and 2D PU images resulting from dental braces in a 15-year-old boy. *B*, Calcification versus hemorrhage. A T2* lesion (*black arrows*) is detected on both 2D GRE and 2D SWI in a 12-year-old boy previously treated for pineal germinoma. Corresponding 2D PU image shows dark signal (*arrowhead*), opposite of the signal expected for hemorrhage. An adjacent fluid-level lesion demonstrates high intensity typical of hemorrhage (*white arrow*). The presence of calcification is confirmed by prior CT. *C*, Catheter detail. The side holes of the catheter are better delineated on 2D SWI/PU images (*arrows*), particularly on the 2D PU image in an 8-year-old girl with periventricular cyst or encystment. While patency or functionality cannot be assessed by this method, improved catheter detail could be helpful when the position of the side hole relative to the cyst or ventricular system is clinically queried.

formed by a biostatistician (J.R.) by using STATA, Release 9.2 (StataCorp, College Station, Texas).

RESULTS

Baseline 2D GRE

Of the 50 patients, 29 had abnormal findings on 2D GRE examinations that contained at least one T2* lesion; the patient demographics and types of T2* lesions are listed in the On-line Table. The remaining 21 patients had normal findings on 2D GRE examinations.

Comparison of 2D GRE and 2D SWI

Of the 29 patients with abnormal findings on 2D GRE examinations, the 2D SWI was scored as superior to the corresponding 2D GRE images with regard to conspicuity of T2* lesions by using the Wilcoxon signed rank test ($P < .0001$). In 21 of the 29 subjects (72%), T2* lesions were more conspicuous on 2D SWI than on 2D GRE images.

In 3 of the 29 patients (10%), new T2* foci were seen on 2D SWI, in addition to better conspicuity of other T2* lesions. In these instances, the lesions were presumed to represent additional foci of radiation-induced telangiectasias/cavernous malformations (Fig 1) and additional foci of hemorrhage for the other 2 cases.

In 3 patients (10%), no difference in T2* lesion conspicuity was noted between 2D GRE and 2D SWI.

In 2 patients, 2D GRE was considered better than 2D SWI with regard to T2* lesion conspicuity. These 2 cases consisted of cortical venous thrombosis and focal caudothalamic hemorrhage. Although T2* lesions themselves were more prominent on 2D SWI than on the respective 2D GRE images, increased prominence of deoxygenated and slow-flow veins (for both cases) and worsened calvarial artifacts adjacent to the T2* lesion (one of the cases) were considered distracting and thereby negatively impacted lesion conspicuity (Fig 2).

Of the 21 patients with normal baseline 2D GRE images, 2D SWI showed a new T2* lesion in 1 case, confirmed as a tumor calcification by corresponding CT (and potentially some blood products), that was not initially detected by the baseline 2D GRE image (Fig 3).

Other Imaging Features

T2* of Deep Gray Nuclei. Twenty-nine of 50 cases (58%; 95% confidence interval, 43%–72%) depicted new, additional, or more prominent deep gray (basal ganglia or dentate nuclei) mineralization on 2D SWI relative to the corresponding 2D GRE images.

Motion or Dental Artifacts. Motion degradation or dental hardware artifacts were identified on the 2D GRE images in 4 of 50 cases (8%), all of which were otherwise classified having normal findings. In all 4 cases, the artifacts were more pronounced on 2D SWI (Fig 4*A*).

Calcification versus Hemorrhage. Nine of 50 cases (18%; 95% confidence interval, 9%–31%) demonstrated signal intensity opposite what would be expected for iron or hemorrhage on the 2D PU images, suggesting the presence of calcifications, all of which were confirmed by CT (Fig 4*B*).

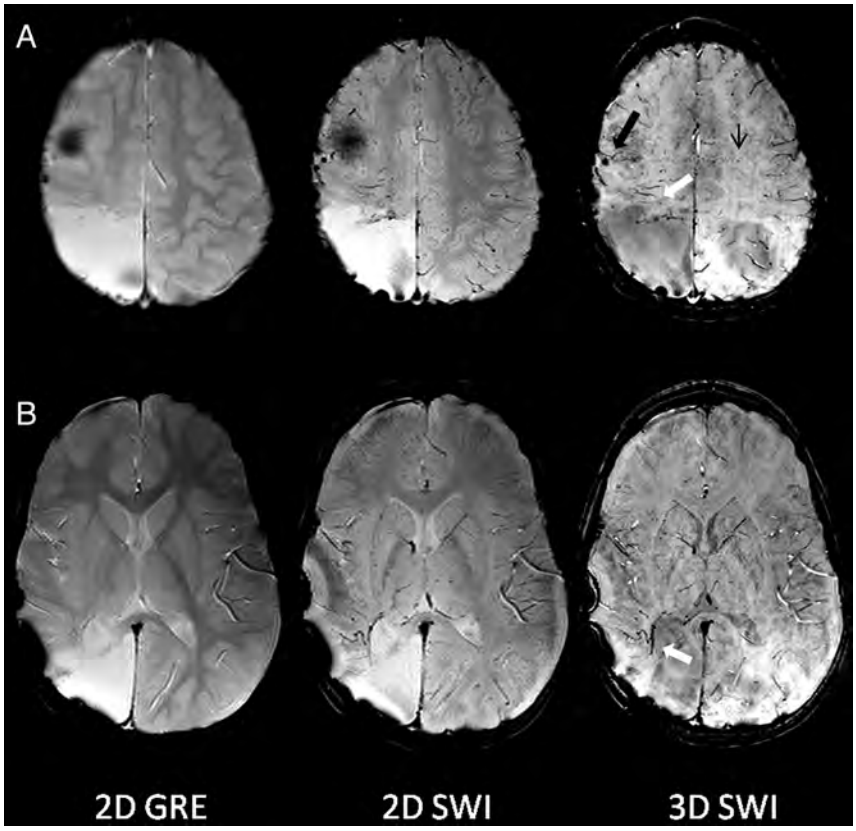

FIG 5. Sample case of 2D GRE, 2D SWI, and 3D SWI acquired in a 3-year-old boy with Sturge-Weber syndrome after surgical resection of the affected brain region. Axial images of the brain at the corona radiata (*A*) and basal ganglia (*B*) are shown. Note on 3D SWI, improved resolution and increased visualization of the venous structures, including prominent deep medullary venous drainage (*white arrows*) commonly seen in this condition. Note pulsation artifacts (*small black arrow*) associated with a large vessel (*large black arrow*) on 3D SWI. Longer scan time of 3D SWI (7 minutes, 40 seconds) compared with 2D SWI (1 minute, 50 seconds) has resulted in motion artifacts despite administration of general anesthesia in this child.

Normal Venous Structures (Including Developmental Venous Anomaly). In all 50 cases, normal venous structures previously identified by the baseline 2D GRE were considered more prominent, or better visualized. In 12 of 50 cases (24%; 95% confidence interval, 13%–38%), 2D SWI detected new linear low-signal intensities in a pattern representative of additional venous structures. Three cases of developmental venous anomaly detected by the baseline 2D GRE were considered more prominent on 2D SWI. No new developmental venous anomaly was identified by 2D SWI.

Surgical Hardware. In all 5 (5/50, 10%) cases in which a surgical catheter was present, the 2D SWI was preferred over the 2D GRE for catheter delineation, including better depiction of the side ports (Fig 4*C*).

DISCUSSION

Our results demonstrate that 2D SWI processed from standard 2D GRE imaging could improve the conspicuity of T2* lesions compared with the standard 2D GRE image and, in addition, identify new lesions. Furthermore, 2D SWI/PU images can help distinguish calcification from hemorrhage, similar to 3D SWI.[13,18] While prior work by Haacke et al and Sehgal et al.[3,18] suggested that 2D GRE acquisitions result in rapid dephasing across voxels that could inhibit the additional T2* visualization achieved with 3D GRE acquisitions of SWI, our results suggest that phase information derived from 2D GRE images has the capacity to produce 2D SWI/PU images that are superior to standard 2D GRE images.

A few pitfalls of 2D SWI were noted. Despite the increased prominence of the T2* lesions themselves, a case of focal caudothalamic hemorrhage was rendered less conspicuous due to distractions incurred by heightened visualization of adjacent veins, and a case of cortical venous thrombosis along brain convexity was deemed less conspicuous due to the combined effects of worsened calvarial bony artifacts and more numerous/better visualized adjacent deoxygenated veins. Additionally, motion degradation and dental artifacts were more pronounced on 2D SWI/PU images, which likely occurred due to incomplete phase unwrapping in regions with steep phase topography. These limitations of 2D SWI suggest that in certain instances, they may be best used in conjunction with standard 2D GRE images.

Gaining more information without an increase in scan time is particularly important in pediatric imaging, where long scan times render studies susceptible to motion degradation and could necessitate sedation. In addition to improved depiction of T2* lesions, other features, such as basal ganglia mineralization and venous structures (normal veins and developmental venous anomalies), were also better detected by 2D SWI. Routine use of 2D SWI may, in the future, reveal that basal ganglia mineralization may occur even earlier than previously proposed.[19] Also, improved delineation of catheter drainage holes, while not necessarily indicative of patency, may provide useful catheter information in relation to the ventricular system.

There were a few limitations to our study. In instances in which new T2* lesions were detected by 2D SWI, we presumed that they represented pathology on the basis of underlying patient history (eg, multiple telangiectasias/cavernous malformations, trauma, or hemorrhages elsewhere in the brain), but in the absence of a histologic correlate, the true nature of these T2* lesions cannot be confirmed. In addition, while CT was used to confirm 2D SWI/PU findings suspicious for calcification, we recognize that small foci may not be detectable by CT. While time constraints and the potential need for sedation did not permit simultaneous acquisition of 2D GRE and 3D GRE for SWI processing, direct comparison could have gauged 2D SWI performance against 3D SWI. An example that directly

compares 2D SWI and 3D SWI, by using the parameters described by Haacke et al,[3] is shown in Fig 5. With a higher resolution technique, 3D SWI better delineates small vessels. However, the longer scan time of 3D SWI (7 minutes, 40 seconds) compared with 2D SWI (1 minute, 50 seconds) has resulted in motion degradation. Future studies are needed to understand the performance of 2D SWI against 3D SWI.

At this time, given that vendor-supplied 2D GRE is an accepted part of standard MR imaging brain protocol in most institutions, our goal was to investigate what additional information could be garnered from SWI processing of a routine 2D GRE dataset. With automatic processing and return to PACS in <2 minutes, 2D SWI/PU can easily be incorporated into routine brain MR imaging. For example, the 2D GRE image could be used for surveillance of obvious T2* lesions and 2D SWI could be used in tandem to probe subtle hemorrhages or to further define abnormal vascularity in such cases as tumor or vascular malformations. Lesions manifest on T1WI or 2D GRE could also be compared with PU images, or PU images themselves could be used to help detect calcifications and potentially avoid CT when detection of calcification is desired in such cases as congenital infections or craniopharyngioma. Furthermore, with no additional scan time, 2D SWI may be an alternative when 3D SWI is not available or difficult to implement in motion-prone patients.

CONCLUSIONS

2D SWI/PU processed from standard 2D GRE can improve the conspicuity of T2* lesions, identify new lesions, and sometimes help distinguish calcification from hemorrhage and may therefore be a useful adjunct to routine 2D GRE imaging.

Disclosures: Samantha J. Holdsworth—*RELATED*: *Grant*: National Institutes of Health (NIH) (R01 EB 8706, R01 EB 11654, R01 EB 2711–08, R01 EB 6526).* Roland Bammer—*RELATED*: *Grant*: NIH (R01 EB 8706, R01 EB 11654, R01 EB 2711–08, R01 EB 6526),* *UNRELATED*: *Board Membership*: iSchemaView, *Comments*: I am a cofounder of iSchemaView, Inc and own stock, but I am not an employee of this company, nor do I receive a salary. This company was not involved in any form with this study. *Money paid to the institution.

REFERENCES

1. Castillo M. *The Core Curriculum: Neuroradiology*. Philadelphia: Lippincott Williams & Wilkins; 2002
2. Atlas S, Mark A, Grossman R, et al. **Intracranial hemorrhage: gradient-echo MR imaging at 1.5 T: comparison with spin-echo imaging and clinical applications.** *Radiology* 1988;168:803–07
3. Haacke EM, Xu Y, Cheng YC, et al. **Susceptibility weighted imaging (SWI).** *Magn Reson Med* 2004;52:612–18
4. Reichenbach JR, Venkatesan R, Schillinger DJ, et al. **Small vessels in the human brain: MR venography with deoxyhemoglobin as an intrinsic contrast agent.** *Radiology* 1997;204:272–77
5. Mittal S, Wu Z, Neelavalli J, et al. **Susceptibility-weighted imaging: technical aspects and clinical applications, part 2.** *AJNR Am J Neuroradiol* 2009;30:232–52
6. Tong KA, Ashwal S, Obenaus A, et al. **Susceptibility-weighted MR imaging: a review of clinical applications in children.** *AJNR Am J Neuroradiol* 2008;29:9–17
7. Zhu WZ, Qi JP, Zhan CJ, et al. **Magnetic resonance susceptibility weighted imaging in detecting intracranial calcification and hemorrhage.** *Chin Med J (Engl)* 2008;121:2021–25
8. Haacke EM, Mittal S, Wu Z, et al. **Susceptibility-weighted imaging: technical aspects and clinical applications, part 1.** *AJNR Am J Neuroradiol* 2009;30:19–30
9. Nair JR, Van Hecke W, De Belder F, et al. **High-resolution susceptibility-weighted imaging at 3 T with a 32-channel head coil: technique and clinical applications.** *AJR Am J Roentgenol* 2010;195:1007–14
10. Niwa T, Aida N, Takahara T, et al. **Imaging and clinical characteristics of children with multiple foci of microsusceptibility changes in the brain on susceptibility-weighted MRI.** *Pediatr Radiol* 2010;40:1657–62
11. Ong BC, Stuckey SL. **Susceptibility weighted imaging: a pictorial review.** *J Med Imaging Radiat Oncol* 2010;54:435–49
12. Robinson R, Bhuta S. **Susceptibility-weighted imaging: a major addition to the neuroimaging toolbox.** *J Neuroimaging* 2011;21:309
13. Robinson RJ, Bhuta S. **Susceptibility-weighted imaging of the brain: current utility and potential applications.** *J Neuroimaging* 2011;21:e189–204
14. Wycliffe ND, Choe J, Holshouser B, et al. **Reliability in detection of hemorrhage in acute stroke by a new three-dimensional gradient recalled echo susceptibility-weighted imaging technique compared to computed tomography: a retrospective study.** *J Magn Reson Imaging* 2004;20:372–77
15. Tong KA, Ashwal S, Holshouser BA, et al. **Hemorrhagic shearing lesions in children and adolescents with posttraumatic diffuse axonal injury: improved detection and initial results.** *Radiology* 2003;227:332–39
16. Yamada N, Imakita S, Sakuma T, et al. **Intracranial calcification on gradient-echo phase image: depiction of diamagnetic susceptibility.** *Radiology* 1996;198:171–78
17. Wu Z, Mittal S, Kish K, et al. **Identification of calcification with MRI using susceptibility-weighted imaging: a case study.** *J Magn Reson Imaging* 2009;29:177–82
18. Sehgal V, Delproposto Z, Haacke EM, et al. **Clinical applications of neuroimaging with susceptibility-weighted imaging.** *J Magn Reson Imaging* 2005;22:439–50
19. Cherubini A, Peran P, Caltagirone C, et al. **Aging of subcortical nuclei: microstructural, mineralization and atrophy modifications measured in vivo using MRI.** *Neuroimage* 2009;48:29–36

Regional Analysis of the Magnetization Transfer Ratio of the Brain in Mild Alzheimer Disease and Amnestic Mild Cognitive Impairment

M. Mascalchi, A. Ginestroni, V. Bessi, N. Toschi, S. Padiglioni, S. Ciulli, C. Tessa, M. Giannelli, L. Bracco, and S. Diciotti

ABSTRACT

BACKGROUND AND PURPOSE: Manually drawn VOI-based analysis shows a decrease in magnetization transfer ratio in the hippocampus of patients with Alzheimer disease. We investigated with whole-brain voxelwise analysis the regional changes of the magnetization transfer ratio in patients with mild Alzheimer disease and patients with amnestic mild cognitive impairment.

MATERIALS AND METHODS: Twenty patients with mild Alzheimer disease, 27 patients with amnestic mild cognitive impairment, and 30 healthy elderly control subjects were examined with high-resolution T1WI and 3-mm-thick magnetization transfer images. Whole-brain voxelwise analysis of magnetization transfer ratio maps was performed by use of Statistical Parametric Mapping 8 software and was supplemented by the analysis of the magnetization transfer ratio in FreeSurfer parcellation-derived VOIs.

RESULTS: Voxelwise analysis showed 2 clusters of significantly decreased magnetization transfer ratio in the left hippocampus and amygdala and in the left posterior mesial temporal cortex (fusiform gyrus) of patients with Alzheimer disease as compared with control subjects but no difference between patients with amnestic mild cognitive impairment and either patients with Alzheimer disease or control subjects. VOI analysis showed that the magnetization transfer ratio in the hippocampus and amygdala was significantly lower (bilaterally) in patients with Alzheimer disease when compared with control subjects (ANOVA with Bonferroni correction, at $P < .05$). Mean magnetization transfer ratio values in the hippocampus and amygdala in patients with amnestic mild cognitive impairment were between those of healthy control subjects and those of patients with mild Alzheimer disease. Support vector machine–based classification demonstrated improved classification performance after inclusion of magnetization transfer ratio–related features, especially between patients with Alzheimer disease versus healthy subjects.

CONCLUSIONS: Bilateral but asymmetric decrease of magnetization transfer ratio reflecting microstructural changes of the residual GM is present not only in the hippocampus but also in the amygdala in patients with mild Alzheimer disease.

ABBREVIATIONS: AD = Alzheimer disease; AUC = area under the receiver operating characteristic curve; DARTEL = Diffeomorphic Anatomical Registration through Exponentiated Lie Algebra; MCI = mild cognitive impairment; MT = magnetization transfer

Alzheimer disease (AD) is the most common cause of dementia and a major cause of morbidity worldwide.[1] In recent years, considerable efforts have been made to better understand the natural evolution of AD, with particular focus on the presymptomatic and early symptomatic phases of the disease, whose characterization could enable earlier and potentially more effective treatment. These efforts have led to identification of a heterogeneous condition called mild cognitive impairment (MCI), which is characterized by objective evidence of cognitive decline without deficit in daily living activities.[2] In particular, it is assumed that a particular form of MCI, termed amnestic MCI, can represent an intermediary predementia stage of AD.[3]

The search for biomarkers that may reflect specific in vivo features of pathophysiologic processes underlying AD is drawing increasing attention and financial resources.[1]

MRI allows in vivo investigation of the structural brain changes in AD.[4] T1WI shows global and local volume loss in

Received December 12, 2012; accepted after revision February 9, 2013.

From the Quantitative and Functional Neuroradiology Research Unit, Department of Experimental and Clinical Biomedical Sciences (M.M., A.G., S.C., S.D.), and Department of Neurological and Psychiatric Sciences (V.B., S.P., L.B.), University of Florence, Florence, Italy; Medical Physics Section (N.T.), Faculty of Medicine, University of Rome "Tor Vergata," Rome, Italy; Radiology Department (C.T.), Versilia Hospital, Lido di Camaiore (Lucca), Italy; and Unit of Medical Physics (M.G.), Pisa University Hospital, "Azienda Ospedaliero-Universitaria Pisana," Pisa, Italy.

Please address correspondence to Mario Mascalchi, MD, PhD, Quantitative and Functional Neuroradiology Research Unit, Department of Experimental and Clinical Biomedical Sciences, University of Florence, Viale Morgagni 85, Florence, Italy; e-mail: m.mascalchi@dfc.unifi.it

Indicates article with supplemental on-line figures

EBM 2 Evidence-Based Medicine Level 2.

http://dx.doi.org/10.3174/ajnr.A3568

structures typically affected by the disease such as the temporal lobe, including the hippocampus, amygdala, and enthorinal cortex.[5-8] DTI and magnetization transfer (MT) imaging allow assessment of the microstructure of the residual WM and GM in the same structures.[9-16] In particular, MT is a peculiar MR contrast that is based on the exchange of magnetization between free protons and protons bound to macromolecules and is influenced by the direct saturation of free protons by the radiofrequency pulse.[14,16] A more comprehensive analysis of the magnetization transfer phenomenon is possible with a quantitative approach, which, by use of different magnetization transfer models, enables determination of several parameters including the relative size of the restricted proton pool, the T2 relaxation time of the restricted pool and the relaxation times T1 and T2 of the free pool, and the forward exchange rate.[14-16]

In its simplest version, MT is obtained with acquisition of a pair of images without and with a specific radiofrequency off-resonance prepulse followed by image subtraction and computation of the MT ratio. MT ratio is decreased in the temporal lobe and hippocampus of patients with AD independent from atrophy[9-12,14,17,18]; is variably correlated with clinical severity, neuropsychological measurements, and disease duration[9-12]; and appears capable to track progression of regional GM microstructural changes in AD.[18] MT ratio was also reported to be decreased in the whole brain, whole temporal lobe, or temporal lobe GM and WM in patients with amnestic MCI as compared with age-matched healthy control subjects.[10,11,19,20] However, in 2 studies that compared the MT ratio with several parameters calculated with quantitative MT approach in the hippocampus, enthorinal cortex, insula, and temporal neocortex, the former delivered the worst performance in differentiating AD, MCI, or healthy control subjects.[14,16]

All the above MT imaging studies in AD and MCI used whole brain or temporal lobe segmentation, or involved analysis of manually drawn region of interest or VOI. Voxelwise analysis of MT ratio maps offers the advantage of an automatic whole-brain, voxel-based analysis without a priori assumptions about the specific region under investigation.[21] Thus far, this approach was applied in only 1 study that evaluated several sophisticated parameters calculated from quantitative MT imaging but not MT ratio and reported significantly reduced efficiency of the transfer of magnetization between the 2 pools in the hippocampus, temporal lobe, posterior cingulate, and posterior parietal cortex of patients with AD compared with healthy control subjects.[15]

In the present study, we evaluated the MT ratio with a voxelwise, whole-brain approach supplemented by automatic VOI analysis in a group of patients with mild AD, a group of patients with amnestic MCI, and a group of healthy elderly control subjects. The 2 aims of our study were 1) to map the regional distribution of MT ratio in mild AD and 2) to further explore the regional changes in MT ratio in amnestic MCI.

MATERIALS AND METHODS

Subjects

The study was based on 47 subjects referred to the memory clinic of the University of Florence who were consecutively observed over a period of 2 years and evaluated through an extensive standardized neuropsychological battery.[22]

Twenty (17 women and 3 men; mean age, 74.4 ± 7.0 years; range, 59–85 years) fulfilled the NINCDS-ADRDA criteria for probable AD,[23] and, on the basis of the results of the Mini-Mental State Examination (mean, 25 ± 2.5; range, 21.3–30), received a diagnosis of mild AD.

Twenty-seven (15 women and 12 men; mean age, 68.8 ± 7.8 years; range, 51–82 years) fulfilled the Winblad et al[2] criteria for amnestic MCI. In particular, they were judged as both not normal and not fulfilling diagnostic criteria for dementia (*Diagnostic and Statistical Manual of Mental Disorders IV*, ICD 10). Moreover, they had preserved basic activities of daily living or minimal impairment in complex instrumental functions in combination with evidence of memory decline, measured either by self-report and/or informant report in conjunction with deficits on objective cognitive tasks and/or evidence of memory decline over time on objective neuropsychological tests. Their mean Mini-Mental State Examination score was 27.9 ± 1.8 (range, 23–30).

Thirty healthy subjects (18 women and 12 men; mean age, 71.9 ± 6.1 years; range, 57–82) without familial or personal history of neurologic or psychiatric disorders served as control subjects. They underwent a neurologic examination that showed no abnormalities. Their mean Mini-Mental State Examination score was 28.8 ± 1.2 (range, 26.2–30).

The 3 groups of subjects were matched for sex (χ^2, $P = .12$). Patients with AD and healthy control subjects as well as patients with MCI and healthy control subjects did not differ significantly in terms of mean age, whereas the patients with MCI were younger than the patients with AD (ANOVA with Bonferroni correction, with $P < .05$).

MRI Protocol

Within 3 months of the clinical evaluation and recruitment, patients and control subjects underwent MRI examination on a 1.5T system (Intera; Philips, Best, the Netherlands) with 33 mT/m maximum gradient strength and a 6-channel head coil. After the scout image, a sagittal 3D T1-weighted turbo gradient-echo sequence (TR = 8.1 ms, TE = 3.7 ms, flip angle = 8°, TI = 764 ms, FOV = 256 × 256 mm, matrix size = 256 × 256, 160 contiguous sections, section thickness = 1 mm, NEX = 1, acceleration factor (SENSE) = 2) was acquired for quantitative volumetric assessment of GM and as a high-resolution anatomic reference of MT images. For MT imaging, axial images without (M0) and with (Ms) gaussian sinc-shaped off-resonance pulse (bandwidth = 342 Hz, offset frequency = 1100 Hz, duration = 17,500 μs) were acquired with a gradient recalled-echo sequence (TR = 37 ms, TE = 3.7 ms, flip angle = 8°, FOV = 256 × 256 mm, matrix size = 128 × 128, 100 contiguous sections, section thickness = 3 mm, NEX = 2, acceleration factor (SENSE) = 2). A coronal FLAIR sequence (TR = 11,000 ms, TE = 140 ms, TI = 2800 ms, FOV = 230 mm, matrix size = 320 × 216, contiguous sections, section thickness = 5 mm) was also performed for evaluation of nonspecific T2 hyperintensities of the cerebral WM observed in elderly subjects, termed leukoaraoisis.

The acquisition time for the entire MR protocol was approximately 17 minutes, with 8 minutes required for MT imaging.

T2 Hyperintensities of the Cerebral WM

One operator (M.M.) with 25 years of experience in clinical MRI who was blinded to the clinical data evaluated the FLAIR images of all subjects to rate the extension of cerebral leukoaraoisis by use of the 0–3 visual scale proposed by Fazekas et al.[24]

MT Ratio Map Computation

For each subject, after 6 *df* co-registration of M0–Ms images by use of FLIRT (FMRIB's Linear Image Registration Tool; http://www.fmrib.ox.ac.uk/fsl),[25] the MT ratio map was calculated, voxel by voxel, according to the following formula [(M0–Ms)/M0] × 100. A brain mask was also computed by use of the FSL Brain Extraction Tool on the Ms image. Values of MT ratio map >75, assumed to be caused by image noise or partial volume effects or outside the brain mask, were replaced by zeroes.[26]

Voxel-Based Morphometry

Preprocessing of the T1WI was performed by use of the Statistical Parametric Mapping 8 package (http://www.fil.ion.ucl.ac.uk/spm) and the Voxel Based Morphometry 8 toolbox (http://dbm.neuro.uni-jena.de).[27] All T1WI was corrected for bias-field inhomogeneities, then spatially normalized to the standard Diffeomorphic Anatomical Registration through Exponentiated Lie Algebra (DARTEL) T1 template in Montreal Neurological Institute space by means of linear and nonlinear transformations and segmented into GM, WM, and CSF within the same generative model.[28] The segmentation procedure was further extended by accounting for partial volume effects,[29] by applying adaptive maximum a posteriori estimations,[30] and by use of a hidden Markov random field model,[31] as described previously.[32] The resulting GM and WM images were modulated to account for volume changes resulting from the normalization process. We considered only nonlinear volume changes so that further analyses did not have to account for differences in head size. Finally, images were smoothed with a gaussian kernel of 8 mm (full width at half maximum).

Voxelwise GM and WM differences between patients with AD and patients with MCI and control subjects were examined by means of 1-way ANOVA with age and sex as nuisance variables. To avoid possible edge effects between different tissue types, we excluded all voxels with GM or WM tissue probability values of <.1 (absolute threshold masking). We applied a statistical threshold of $P < .05$ with family-wise error rate correction.

Voxelwise MT Ratio Analysis

For each subject, the Ms image was affinely co-registered with a 12 *df* transformation to the raw T1WI, and this transformation was applied to the MT ratio map. The MT ratio map was then normalized to the Montreal Neurological Institute space by means of the transformation previously computed when co-registering the raw T1WI to the standard DARTEL T1 template. Finally, voxelwise MT ratio differences between patients with AD and patients with MCI and control subjects were examined by means of 1-way ANOVA, with age and sex as nuisance variables. We applied a statistical threshold of $P < .05$ with family-wise error rate correction.

VOI-Based MT Ratio Analysis

Completely automated subcortical reconstruction and volumetric segmentation of each subject's structural T1-weighted MRI scan were performed with the FreeSurfer image analysis suite (http://surfer.nmr.mgh.harvard.edu/).[33] Briefly, this includes removal of nonbrain tissue by use of a hybrid watershed/surface deformation procedure, automated Talairach transformation, segmentation of the subcortical WM and deep GM volumetric structures, intensity normalization, tessellation of the GM/WM boundary, automated topology correction, and surface deformation after intensity gradients to optimally place the GM/WM and GM/CSF borders at the location where the greatest shift in intensity defines the transition to the other tissue class. Volumetric regions of interest delineating left and right hippocampus and amygdala in each subject's native T1 space were obtained by affine transformation. To reduce partial volume effects, each VOI was eroded with a 3D structural element with 1-mm radius. VOIs in the amygdala containing a small (<150 mm^3 of volume) number of voxels were excluded from further analyses. One operator (A.G.), blinded to the clinical data, visually judged the VOIs automatically placed in the hippocampus and amygdala as adequate or inadequate. In particular, he excluded the VOI with evident CSF contamination.

For each subject, the affine transformation from T1WI to the Ms image was computed as the inverse of the previously computed affine transformation from the Ms image to the T1WI. After erosion, the transformation from T1WI to the Ms image was applied to each VOI, and the mean MT ratio was determined in this transformed VOI.

The comparison of mean MT ratio within the hippocampus and amygdala VOIs in the healthy control subjects, patients with MCI, and patients with AD was performed by means of ANOVA test with post hoc Bonferroni correction, with $P < .05$.

Classification by Means of Support Vector Machines

With the goal of exploring the discriminative power of automatic VOI analysis of MT ratio in the hippocampus and amygdala, we trained a popular machine learning scheme, that is, a support vector machine (with linear kernel and complexity parameter $C = 1$), implemented through a sequential minimal optimization algorithm.[34] In this context, we considered only the subset of patients for which the complete set of hippocampus and amygdala VOI measurements was available. We took into account the imbalance in the number of subjects within the different classes by the cost matrix method.[34] We studied 2 different classification tasks: 1) patients with AD patients versus healthy subjects and 2) patients with AD versus with MCI. For each classification task, we initially fed the classifier with the VOI volumes only, and successively with both VOI volumes and VOI MT ratios. To fully explore the solution space in a rigorous manner, we performed an exhaustive search on the different feature vectors by use of a 10-fold cross-validation technique for training and testing the classifiers. Performances were evaluated through the area under receiver operating characteristic curve (AUC), in which highest values of AUC were considered better, and, in the case of equal ranking, the result obtained with a lower number of features was considered better. Sensitivity and specificity were also recorded.

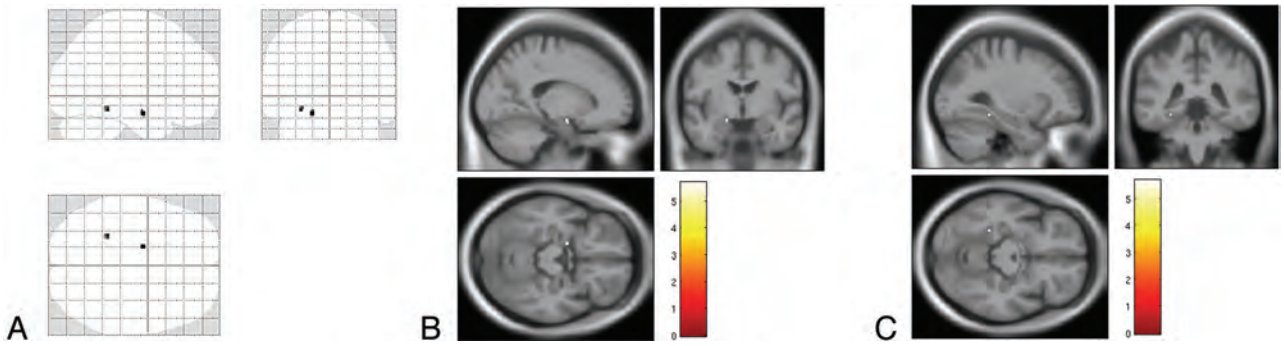

FIG 1. SPM8 "glass brain" representation *(A)* of voxelwise analysis between control subjects and patients with Alzheimer disease showing significant clusters of decreased magnetization transfer ratio in the left hippocampus and amygdala and in the posterior mesial temporal cortex (fusiform gyrus) ($P < .05$, with family-wise error rate correction). Superimposition onto T1 template of the cluster in the hippocampus and amygdala are demonstrated in *B* and of the cluster in the fusiform gyrus in *C*.

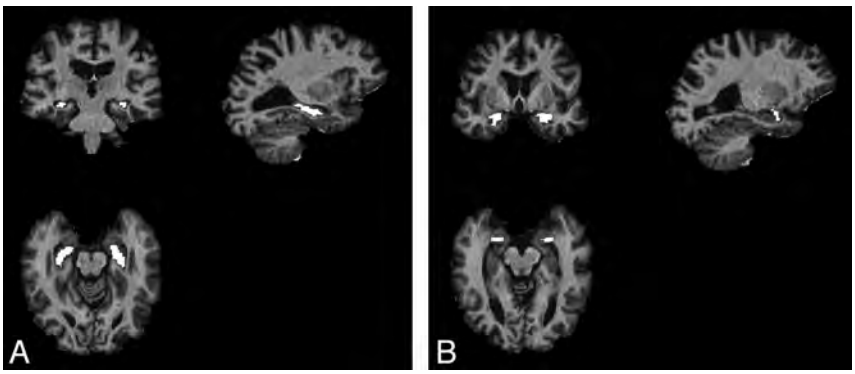

FIG 2. Example of the FreeSurfer automatic VOI segmentation of the hippocampus *(A)* and amygdala *(B)* eroded with a 3D structural element with 1-mm radius.

All classification tasks were performed with the use of WEKA software (http://www.cs.waikato.ac.nza/mL/weka, version 3.6.8).[34]

RESULTS

T2 Hyperintensities of the Cerebral WM

Extension of leukoaraoisis was similar in the 3 groups of subjects (mean in AD 1.00 ± 0.56; mean in amnestic MCI, 0.92 ± 0.61; mean in control subjects, 1.07 ± 0.58 [a nonsignificant difference at the Kruskal-Wallis test, $P = .66$]).

Regional Volume

Voxel-based morphometry ($P < .05$, ANOVA with family-wise error rate correction for multiple comparisons) showed 2 isolated clusters of cortical GM atrophy in the right ($x = 28$ mm, $y = -27$ mm, $z = -5$ mm) and left ($x = -28$ mm, $y = -30$ mm, $z = -8$ mm) hippocampus and parahippocampal gyrus, which appeared more extensive on the right side, in patients with AD as compared with healthy control subjects (On-line Fig 1) and 1 isolated cluster ($x = -15$ mm, $y = 56$ mm, $z = 15$ mm) in the left superior frontal gyrus in patients with amnestic MCI as compared with healthy control subjects (On-line Fig 2). No significant clusters were observed in patients with AD as compared with patients with amnestic MCI. No significant regional decrease of WM volume was observed in the 2 groups of patients with respect to each other and the control group.

Regional MT Ratio

Voxelwise analysis showed 2 circumscribed clusters of decreased MT ratio, 1 located in the left hippocampus and amygdala ($x = -16$ mm, $y = -6$ mm, $z = -17$ mm) and 1 in the posterior mesial temporal cortex (fusiform gyrus) ($x = -28$ mm, $y = -40$ mm, $z = -14$ mm) of patients with AD as compared with control subjects and no difference between patients with AD and patients with amnestic MCI or between patients with MCI and control subjects (Fig 1).

Automatic VOI Analysis

Fig 2 shows examples of the automatic VOIs obtained by use of FreeSurfer. Six (3 in patients with AD, 1 in a patient with MCI, and 2 in healthy subjects) of 144 VOIs were judged to partially fall outside the hippocampus, whereas 26 (9 in patients with AD, 5 in patients with MCI, and 12 in healthy subjects) of 144 VOIs in the amygdala were constituted by a number of voxels that was considered too small to afford a reliable evaluation of that structure.

The MT ratio in the bilateral hippocampus and amygdala was significantly lower in patients with AD when compared with control subjects (ANOVA with post hoc Bonferroni correction, with $P < .05$) (Fig 3).

The values of the mean MT ratio in hippocampus and amygdala in the patients with amnestic MCI were between those of healthy control subjects and those of patients with mild AD (Fig 3), and the differences were not significant with the exception of the MT ratio in the left amygdala, which was significantly lower in AD than in amnestic MCI.

Classification by Use of Support Vector Machines

The classification tasks were performed on the subset of subjects for which the complete set of hippocampus and amygdala VOI measurements were available (ie, 23 healthy subjects, 22 patients with MCI, and 12 patients with AD).

In the patients with AD versus control subjects classification task, the best feature vector was composed of the volumes of bilateral amygdala, right hippocampus, and of the MT ratio of left

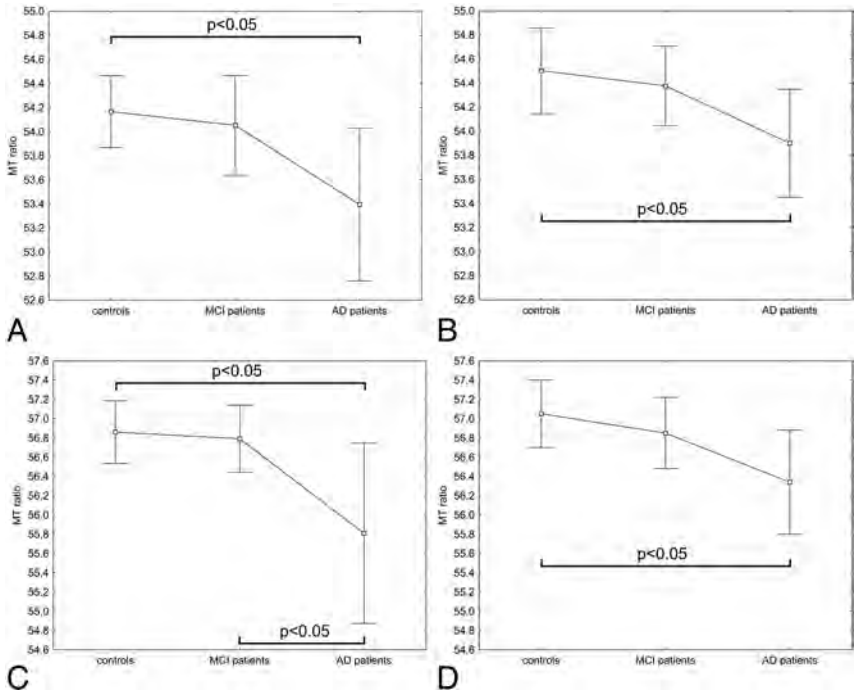

FIG 3. Magnetization transfer ratio of in the hippocampi [left *(A)* and right *(B)*] and amygdalae [left *(C)* and right *(D)*] in the 3 groups. Mean and 95% confidence intervals of mean MT ratio are reported. The MT ratio in the bilateral hippocampus and amygdala was significantly lower in patients with Alzheimer disease when compared with control subjects (ANOVA with post hoc Bonferroni correction, with $P < .05$). The values of the mean MT ratio in the hippocampus and amygdala in the patients with amnestic mild cognitive impairment were between those of healthy control subjects and those of patients with mild AD, and the differences were not significant with the exception of the MT ratio in the left amygdala, which was significantly lower in AD than in amnestic MCI.

hippocampus, reaching a 0.873 AUC, 83.3% sensitivity, and 95.7% specificity. This result was markedly higher than the best performance obtained with volumetric features only (0.788 AUC, 75.0% sensitivity, and 82.6% specificity, obtained by using bilateral amygdalae and right hippocampus volumes).

In the AD versus MCI classification task, the best feature vector was composed of the volumes of right hippocampus, left amygdala, and MT ratio of left hippocampus and right amygdala (0.761 AUC, 75.0% sensitivity, and 77.3% specificity). This result was slightly better than the best performance obtained with volumetric features only (0.746 AUC, 58.3% sensitivity, 90.9% specificity, and obtained by bilateral hippocampus).

DISCUSSION

Our investigation with the use of automatic whole-brain, voxelwise, and VOI analyses demonstrates that a decrease of MT ratio, presumably reflecting microstructural changes related to AD pathology, can be observed in patients with mild AD, not only in the hippocampus but also in the amygdala bilaterally (whereas more markedly on the left side). In patients with amnestic MCI, the MT ratio in the same structures tends to be decreased as compared with healthy control subjects but less conspicuously than in patients with mild AD.

The decreased MT ratio revealed by voxelwise analysis in the left hippocampus and amygdala and in the left posterior mesial temporal cortex in patients with mild AD as compared with healthy control subjects confirms previous data obtained by means of manually drawn regions of interest or VOIs in the hippocampus[9,12,14,18] and extends to the amygdala the capability of MT ratio to detect microstructural GM changes related to AD pathology.

The hippocampus and amygdala are among the earliest mesial temporal lobe structures affected by AD pathology along with transentorhinal regions, subiculum, and entorhinal cortex.[35] Moreover, volumetry MRI data in vivo indicate that both the hippocampus and amygdala show global or local atrophy in AD.[5-8]

The automatic VOI analysis in our study showed that the decrease of the MT ratio in the hippocampus and amygdala was prominent in the left side but was also significant in the right side.

Asymmetric distribution of pathologic changes[36] and atrophy[4,5] with an average predominance in the left temporal lobe side is a well-known feature of AD. However, cases with right-side predominance of AD pathologic changes were observed,[37] and the results of an MRI study specifically assessing lateral distribution of atrophy in vivo[38] justify the view that AD alterations are asymmetric but not lateralized. In all previous MT imaging studies in AD and MCI, no side evaluation of lobar or regional MT ratio was reported, and data related to the 2 sides were typically averaged.[9-12,14,18]

In our study, the voxelwise analysis did not show any region exhibiting significantly different MT ratio in the group of patients with amnestic MCI with respect to healthy control subjects, and automatic VOI analysis of the hippocampus and amygdala in the patients with amnestic MCI showed values for the MT ratio that were between the values computed for healthy control subjects and patients with AD. This result is in line with the results obtained with manual segmentation of the anterior hippocampus in a prior study,[14] whereas it represents a partial discrepancy with prior investigations in which the MT ratio of the whole brain or temporal lobe was found to be significantly decreased in patients with MCI as compared with healthy control subjects.[10,11,19,20]

Considering the fact that our study involved the highest number of subjects with amnestic MCI examined with MT imaging so far, we submit the following 2 (not mutually exclusive) explanations for this discrepancy.

First, global analyses of the whole temporal lobe or of the temporal GM or WM have an inherently higher statistical power when compared with regional analyses that are based on either voxelwise techniques or smaller VOIs, because the former techniques imply computation of the variable of interest (in our case,

MT ratio) in a far greater number of voxels. This aspect might also account for lack of significant changes of the MT ratio in other cortical GM regions and in the WM in patients with AD in the voxelwise analysis in our sample.

Second, MCI is a transitory heterogeneous condition, and progression of amnestic MCI to AD is observed only in a portion of subjects attending a memory clinic, namely, 9.6% per year, as indicated in a meta-analysis.[39] As a matter of fact, only approximately 60% of patients with amnestic MCI, termed converters, ultimately have development of probable AD after 5 years, whereas the remainder have other forms of dementia, remain stable, or even revert to normal.[40] We submit that in our cohort, the paucity of patients with MCI who had development of AD during the 2 years successive to their recruitment in the MRI study (5 of 27 individuals; namely, 18.5%) could justify the lack of significant changes of MT ratio in the patients with MCI considered as a group. Longitudinal clinical evaluation of our patients with MCI is underway to verify this hypothesis.

The latter explanation could also apply to the voxel-based morphometry results that we obtained. In fact, although the bilateral hippocampal atrophy observed in our patients with mild AD as compared with healthy control subjects is in line with all prior studies,[4] we identified only a small cluster of decreased GM in the left superior frontal gyrus in the amnestic MCI group as compared with healthy normal control subjects, with no significant changes in the temporal lobe. Indeed, thus far, MRI volumetry has provided contradictory results in groups of patients with MCI (including converters and nonconverters) when compared with healthy control subjects. Several studies, by use of manual VOI positioning or voxel-based morphometry techniques, have indicated that patients with MCI as a group showed atrophy of mesial temporal structures similar to those characteristic of AD.[5,41] However, no significant differences between patients with MCI and healthy elderly control subjects were reported in the mesial temporal lobe GM in voxel-based morphometry studies based on smaller cohorts that used restrictive statistical thresholds[42,43] or that considered age and Mini-Mental State Examination as nuisance variables.[44] Isolated decrease of GM volume in the left middle frontal gyrus was reported in a previous voxel-based morphometry study when comparing patients with amnestic MCI and healthy control subjects.[43]

It is important to note that in both classification tasks, the exhaustive search demonstrated that the best feature vector included the MT ratio value of 1 or 2 VOIs. In particular, we observed that including MT ratio–related features resulted in improved detection performance, both when discriminating patients with AD from healthy subjects (albeit to a lesser extent) and when discriminating patients with AD from patients with MCI. These results demonstrate that MT ratio–related features provide added value with improvement in classification performance, especially between patients with AD versus healthy subjects. This supports the inclusion of MT ratio in more articulate machine learning–based studies for discrimination of patients with AD.

We can only speculate about the pathologic substrate of the decreased MT ratio in the hippocampus and amygdala that we observed in patients with mild AD. It presumably reflects differences in macromolecular tissue composition associated with local accumulation of amyloid plaques, neurofibrillary tangles, or microglia cells, as observed in early AD.[35] In particular, a reduced capacity to exchange magnetization as the result of the presence of amyloid β plaques (a non–H-bonding group) through a surface-hydrophobicity effect was hypothesized as a possible mechanism underlying the decrease of MT ratio in AD.[14,15]

We recognize 2 main limitations of our study. First, we obtained source MT images with a relatively coarse spatial resolution as compared with T1WI. Three-dimensional sequences for MT imaging are now available and enable acquisition of images with increased spatial resolution,[45] especially in combination with higher magnetic field strength scanners. This improved spatial resolution of MT images could be valuable for VOI analysis of MT ratio in the cerebral gyri in which voxelwise analysis showed significantly decreased MT. Such an analysis could not be performed in the present investigation because of the small number of voxels that survived erosion in cortical GM.

Second, we investigated the crude MT ratio. More sophisticated quantitative analyses of MT effect in the whole or anterior hippocampus were successfully applied to the differentiation of patients with AD, patients with MCI, and healthy control subjects,[13,16] but they require longer acquisition times and complex data modeling.

CONCLUSIONS

Bilateral but asymmetric decrease of MT ratio reflecting microstructural changes of the residual GM is present not only in the hippocampus but also in the amygdala in patients with mild AD. Besides volume loss, regional decrease in MT ratio may contribute to MRI-based classification of single patients presenting with a memory complaint.

REFERENCES

1. Henry MS, Passmore AP, Todd S, et al. **The development of effective biomarkers for Alzheimer's disease: a review.** *Int J Geriatr Psychiatry* 2013;28:331–40.
2. Winblad B, Palmer K, Kivipelto M, et al. **Mild cognitive impairment—beyond controversies, towards a consensus: report of the International Working Group on Mild Cognitive Impairment.** *J Intern Med* 2004;256:240–46
3. Petersen RC, Trojanowski JQ. **Use of Alzheimer disease biomarkers: potentially yes for clinical trials but not yet for clinical practice.** *JAMA* 2009;302:436–37
4. Ramani A, Jensen JH, Helpern JA. **Quantitative MR imaging in Alzheimer's disease.** *Radiology* 2006;241:26–43
5. Risacher SI, Saykin AJ, West JD, et al. **Baseline MRI predictors of conversion from MCI to probable AD in the ADNI Cohort.** *Curr Alzheimer Res* 2009;6:347–61
6. Frisoni GB, Ganzola R, Canu E, et al. **Mapping local hippocampal changes in Alzheimer's disease and normal ageing with MRI at 3 Tesla.** *Brain* 2008;131:3266–76
7. Cavedo E, Boccardi M, Ganzola R, et al. **Local amygdala structural differences with 3T MRI in patients with Alzheimer disease.** *Neurology* 2011;76:726–33
8. Poulin SP, Dautoff R, Morris JC, et al. **Amygdala atrophy is prominent in early Alzheimer's disease and relates to symptom severity.** *Psychiatr Res Neuroimaging* 2011;194:7–13
9. Hanyu H, Asano H, Sakurai M, et al. **Magnetization transfer measurements of the hippocampus in the early diagnosis of Alzheimer's disease.** *J Neurol Sci* 2001;188:79–84

10. van der Flier WM, van den Heuvel DM, Weverling-Rijnsburger AW, et al. **Magnetization transfer imaging in normal aging, mild cognitive impairment, and Alzheimer's disease.** *Ann Neurol* 2002;52:62–67
11. Van Es ACGM, van der Flier WM, Admiraal Behloul F, et al. **Lobar distribution of changes in gray matter and white matter in memory clinic patients: detected using magnetization transfer imaging.** *AJNR Am J Neuroradiol* 2007;28:1938–42
12. Ridha BH, Symms MR, Tozer DJ, et al. **Magnetization transfer ratio in Alzheimer disease: comparison with volumetric measurements.** *AJNR Am J Neuroradiol* 2007;28:965–70
13. Ridha HB, Tozer DJ, Symms MR, et al. **Quantitative magnetization transfer imaging in Alzheimer disease.** *Radiology* 2007;244:832–37
14. Kiefer C, Brockhaus L, Cattapan-Ludewig K, et al. **Multi-parametric classification of Alzheimer's disease and mild cognitive impairment: the impact of quantitative magnetization transfer imaging.** *NeuroImage* 2009;48:657–67
15. Giulietti G, Bozzali M, Figura V, et al. **Quantitative magnetization transfer provides information complementary to grey matter atrophy in Alzheimer's disease brain.** *NeuroImage* 2012;59:1114–22
16. Wiest R, Burren Y, Hauf M, et al. **Classification of mild cognitive impairment and Alzheimer disease using model-based MR and magnetization transfer imaging.** *AJNR Am J Neuroradiol* 2013;34:740–46
17. Bozzali M, Franceschi M, Falini A, et al. **Quantification of tissue damage in AD using diffusion tensor and magnetization transfer MRI.** *Neurology* 2001;57:1135–37
18. Ropele S, Schmidt R, Enzinger C, et al. **Longitudinal magnetization transfer imaging in mild to severe Alzheimer disease.** *AJNR Am J Neuroradiol* 2012;33:570–75
19. Kabani NJ, Sled JG, Shuper A, et al. **Regional magnetization transfer ratio changes in mild cognitive impairment.** *Magn Reson Med* 2002;47:143–48
20. Kabani NJ, Sled JG, Chertkow H. **Magnetization transfer ratio in mild cognitive impairment and dementia of Alzheimer's type.** *NeuroImage* 2002;15:604–10
21. Draganski B, Ashburner J, Hutton C, et al. **Regional specificity of MRI contrast parameter changes in normal ageing revealed by voxel-based quantification (VBQ).** *NeuroImage* 2011;55:1423–34
22. Bracco L, Amaducci L, Pedone D, et al. **Italian Multicentre Study on Dementia (SMID): a neuropsychological test battery for assessing Alzheimer's disease.** *J Psychiatr Res* 1990;24:213–26
23. McKhann G, Drachman D, Folstein M, et al. **Clinical diagnosis of Alzheimer's disease: report of the NINCDS-ADRDA Work Group under the auspices of Department of Health and Human Services-Task Force on Alzheimer's disease.** *Neurology* 1984;34:939–44
24. Fazekas F, Chawluk JB, Alavi A, et al. **MR signal abnormalities at 1.5 T in Alzheimer's dementia and normal aging.** *AJNR Am J Neuroradiol* 1987;149:351–56
25. Jenkinson M, Bannister P, Brady JM, et al. **Improved optimisation for the robust and accurate linear registration and motion correction of brain images.** *NeuroImage* 2002;17:825–41
26. Jost G, Hähnel S, Heiland S, et al. **An automated method for volumetric quantification of magnetization transfer of the brain.** *Magn Reson Imaging* 2002;20:593–97
27. Franke K, Luders E, May A. **Brain maturation: predicting individual BrainAGE in children and adolescents using structural MRI.** *NeuroImage* 2012;63:1305–12
28. Ashburner J, Friston KJ. **Unified segmentation.** *NeuroImage* 2005;26:839–51
29. Tohka J, Zijdenbos A, Evans A. **Fast and robust parameter estimation for statistical partial volume models in brain MRI.** *NeuroImage* 2004;23:84–97
30. Rajapakse JC, Giedd JN, Rapoport JL. **Statistical approach to segmentation of single-channel cerebral MR images.** *IEEE Trans Med Imaging* 1997;16:176–86
31. Cuadra MB, Cammoun L, Butz T, et al. **Comparison and validation of tissue modelization and statistical classification methods in T1-weighted MR brain images.** *IEEE Trans Med Imaging* 2005;24:1548–65
32. Gaser C. **Partial volume segmentation with adaptive maximum a posteriori (MAP) approach.** *NeuroImage* 2009;47:S121
33. Fischl B. **FreeSurfer.** *NeuroImage* 2012 62:774–81
34. Witten IH, Frank E, Hall MA. *Data Mining: Practical Machine Learning Tools and Techniques, 3rd ed.* Burlington, Massachusetts: Margan Kaufmann; 2011
35. Castellani RJ, Rolston RK, Smith MA. **Alzheimer disease.** *Dis Mon* 2010;56:484–546
36. Janota I, Mountjoy CQ. **Asymmetry of pathology in Alzheimer's disease.** *J Neurol Neurosurg Psychiatry* 1988;51:1011–12
37. Stefanits H, Budka H, Kovacs GG. **Asymmetry of neurodegenerative disease-related pathologies: a cautionary note.** *Acta Neuropathol* 2012;123:449–52
38. Derflinger S, Sorg C, Gaser C, et al. **Grey-matter atrophy in Alzheimer's disease is asymmetric but not lateralized.** *J Alzheimers Dis* 2011;25:347–57
39. Mitchell AJ, Shiri-Feshki M. **Rate of progression of mild cognitive impairment to dementia–meta-analysis of 41 robust inception cohort studies.** *Acta Psychiatr Scand* 2009;119:252–65
40. Petersen RC, Smith GE, Waring SC, et al. **Mild cognitive impairment: clinical characterization and outcome.** *Arch Neurol* 1999;56:303–08
41. Pennanen C, Testa C, Laakso MP, et al. **A voxel based morphometry study on mild cognitive impairment.** *J Neurol Neurosurg Psychiatry* 2005;76:11–14
42. Kalus P, Slotboom J, Gallinat J, et al. **Examining the gateway to the limbic system with diffusion tensor imaging: the perforant pathway in dementia.** *NeuroImage* 2006;30:713–20
43. Han Y, Lui S Kuang W, et al. **Anatomical and functional deficits in patients with amnestic mild cognitive impairment.** *PLoS One* 2012;7:e28664
44. Chetelat GB. Landeau, F. Eustache, et al. **Using voxel-based morphometry to map the structural changes associated with rapid conversion in MCI: a longitudinal MRI study.** *NeuroImage* 2005;27:934–46
45. Cercignani M, Symms MR, Schmierer K, et al. **Three-dimensional quantitative magnetisation transfer imaging of the human brain.** *NeuroImage* 2005;27:436–41

Novel White Matter Tract Integrity Metrics Sensitive to Alzheimer Disease Progression

E. Fieremans, A. Benitez, J.H. Jensen, M.F. Falangola, A. Tabesh, R.L. Deardorff, M.V.S. Spampinato, J.S. Babb, D.S. Novikov, S.H. Ferris, and J.A. Helpern

ABSTRACT

BACKGROUND AND PURPOSE: Along with cortical abnormalities, white matter microstructural changes such as axonal loss and myelin breakdown are implicated in the pathogenesis of Alzheimer disease. Recently, a white matter model was introduced that relates non-Gaussian diffusional kurtosis imaging metrics to characteristics of white matter tract integrity, including the axonal water fraction, the intra-axonal diffusivity, and the extra-axonal axial and radial diffusivities.

MATERIALS AND METHODS: This study reports these white matter tract integrity metrics in subjects with amnestic mild cognitive impairment ($n = 12$), Alzheimer disease ($n = 14$), and age-matched healthy controls ($n = 15$) in an effort to investigate their sensitivity, diagnostic accuracy, and associations with white matter changes through the course of Alzheimer disease.

RESULTS: With tract-based spatial statistics and region-of-interest analyses, increased diffusivity in the extra-axonal space (extra-axonal axial and radial diffusivities) in several white matter tracts sensitively and accurately discriminated healthy controls from those with amnestic mild cognitive impairment (area under the receiver operating characteristic curve = 0.82–0.95), while widespread decreased axonal water fraction discriminated amnestic mild cognitive impairment from Alzheimer disease (area under the receiver operating characteristic curve = 0.84). Additionally, these white matter tract integrity metrics in the body of the corpus callosum were strongly correlated with processing speed in amnestic mild cognitive impairment ($r = |0.80–0.82|$, $P < .001$).

CONCLUSIONS: These findings have implications for the course and spatial progression of white matter degeneration in Alzheimer disease, suggest the mechanisms by which these changes occur, and demonstrate the viability of these white matter tract integrity metrics as potential neuroimaging biomarkers of the earliest stages of Alzheimer disease and disease progression.

ABBREVIATIONS: AD = Alzheimer disease; aMCI = amnestic mild cognitive impairment; AWF = axonal water fraction; CPS = composite processing speed; DKI = diffusional kurtosis imaging; FA = fractional anisotropy; NC = healthy controls; TBSS = tract-based spatial statistics; WMTI = white matter tract integrity

Alzheimer disease (AD) is a disorder with a pathologic cascade that long precedes its clinical manifestations,[1] motivating researchers to develop biomarkers of early pathologic changes on which therapies could more effectively focus.[2] Along with well-characterized cortical abnormalities,[3] postmortem studies have also provided evidence of pathologic changes in WM occurring early in the course of AD, including decreased myelin and axonal attenuation,[4-7] loss of oligodendrocytes,[8] and activation of glial cells.[7] Diffusion MRI allows the study of WM pathology in AD because it measures the μm-scale displacement of water molecules to index microstructural (ie, dendritic, axonal, and myelin) loss, which, in a recent meta-analysis, has been shown to better differentiate normal aging from mild cognitive impairment and AD than hippocampal atrophy.[9] Additionally, a comprehensive review of diffusion MRI studies of the largest cerebral WM tract, the corpus callosum, illustrated the distinct pathophysiologies underlying WM microstructural changes in AD[10]; the anterior

Received November 30, 2012; accepted after revision January 23.

From the Department of Radiology (E.F., J.S.B., D.S.N.), Center for Biomedical Imaging, and Department of Psychiatry (S.H.F.) and Alzheimer's Disease Center, New York University School of Medicine, New York, New York; and Department of Radiology and Radiological Science (A.B., J.H.J., M.F.F., A.T., R.L.D., M.V.S.S., J.A.H.), Center for Biomedical Imaging (A.B., J.H.J., M.F.F., A.T., R.L.D., M.V.S.S., J.A.H.), and Department of Neurosciences (M.F.F., J.A.H.), Medical University of South Carolina, Charleston, South Carolina.

E. Fieremans and A. Benitez contributed equally to the work.

This work was supported by the Alzheimer Drug Discovery Foundation, the Litwin Foundation, and the NIH (R01AG027852).

Preliminary analyses of some of these data previously presented at: 20th Annual Meeting of the International Society for Magnetic Resonance in Imaging, May 5–11, 2012; Melbourne, Australia; and the Alzheimer's Association International Conference, July 14–19, 2012; Vancouver, British Columbia.

Please address correspondence to Els Fieremans, PhD, Department of Radiology, New York University School of Medicine, 660 First Ave, 4th floor, New York, NY 10016; e-mail: Els.Fieremans@nyumc.org

Indicates open access to non-subscribers at www.ajnr.org
Indicates article with supplemental on-line appendix
http://dx.doi.org/10.3174/ajnr.A3553

Table 1: Demographic and medical history descriptive statistics for healthy controls, patients with amnestic MCI, and subjects with AD (*N* = 41)

	NC (*n* = 15) n (%)	aMCI (*n* = 12) n (%)	AD (*n* = 14) n (%)	χ^2/*F*-test	*P* Value
Demographics					
Age (mean) (yr)	77.54 ± 4.01	79.05 ± 7.23	78.30 ± 9.55	0.15	.87
Female	10 (66)	6 (50)	8 (57)	0.78	.68
Education (mean ± SD)	16.14 ± 2.51	15.08 ± 3.66	15.14 ± 2.83	0.54	.59
Right-handed	13 (87)	11 (92)	13 (93)	1.94	.75
White race	14 (93)	10 (83)	12 (86)	4.46	.62
Medical history					
Hypertension	8 (53)	8 (67)	4 (29)	3.95	.14
Hypercholesterolemia	12 (80)	9 (75)	6 (43)	3.09	.21
Diabetes	2 (13)	1 (8)	1 (7)	0.35	.84
Thyroid disease	3 (20)	2 (17)	1 (7)	1.01	.60
Cardiac arrest	2 (13)	3 (25)	1 (7)	2.01	.37
Cardiac bypass	1 (7)	1 (8)	0 (0)	1.13	.57
Stroke or TIA	1 (7)	1 (8)	1 (7)	0.03	.99
Depression within the past 2 years	4 (27)	1 (8)	4 (29)	1.85	.40

Note:—TIA indicates transient ischemic attack.

part of the corpus callosum (ie, the genu) appears to degenerate due to myelin breakdown,[11,12] while decline in the posterior part (ie, the splenium) is attributed to Wallerian degeneration[13] secondary to distal gray matter AD pathology in the temporoparietal areas to which the posterior callosum projects.[6]

To date, most diffusion MR imaging studies of WM pathology in AD and mild cognitive impairment have used DTI.[14] Here, we use diffusional kurtosis imaging (DKI), a clinically feasible extension of DTI that also examines the non-Gaussian diffusion effects of water known to occur in the brain.[15,16] While both DTI-derived and DKI-derived metrics may be altered in AD,[17] they lack microstructural and pathologic specificity. Indeed, empirical diffusion measures only provide indirect measurements of microstructure, making their physical meaning in terms of microscopic tissue parameters uncertain. To overcome this limitation, we used a WM model that was recently proposed to relate DKI-derived metrics directly to WM microstructure[18] by introducing WM tract integrity (WMTI) metrics, namely axonal water fraction (AWF), intra-axonal diffusivity (D_{axon}), and extra-axonal axial and radial diffusivities ($D_{e,\parallel}$ and $D_{e,\perp}$). These white matter tract integrity (WMTI) metrics are, by design, more specific to the underlying mechanisms of WM alterations than conventional diffusion measures.

In this study, we sought to demonstrate the utility of WMTI metrics in further clarifying the WM changes that occur as AD progresses. We also investigated the extent to which these metrics correlate with processing speed, a cognitive function known to decline due to aging, disease, and WM compromise. Our findings contribute to the growing literature on WM involvement in AD and offer novel candidate biomarkers of AD progression.

MATERIALS AND METHODS

Subjects and Procedures

Subjects were recruited from the NYU Alzheimer Disease Center. All subjects provided written informed consent before participating in this study, which was approved by the institutional review board of the NYU School of Medicine. Per study procedures, all subjects underwent full neurologic and psychiatric evaluations, a neuropsychological test battery, and an MR imaging brain scan. All diagnoses followed research criteria: healthy controls (NC) ($n = 15$) had no evidence of dementia or mild cognitive impairment and had a Global Deterioration Scale score[19] of 1–2; subjects with amnestic mild cognitive impairment (aMCI) ($n = 12$) were defined as having a self- and/or informant-reported memory loss, memory impairment based on performance that was at least 1 SD below the normative mean for age on Logical Memory-II of the Wechsler Memory Scale,[20] a Global Deterioration Scale score = 3, and no dementia. Subjects with AD ($n = 14$) were given a diagnosis based on the *Diagnostic and Statistical Manual of Mental Disorders-IV*[21] and the National Institute of Neurological Disorders and Stroke/Alzheimer's Disease and Related Disorders Association Criteria for probable AD[22] by a Global Deterioration Scale score = 4–5 and were not deemed to have any medical, neurologic, or psychiatric conditions that could otherwise account for the dementia. The groups significantly differed in their Mini-Mental State Examination[23] scores [$F(2, 38) = 18.60$, $P < .001$], in which NC (29.33 ± 0.72) and subjects with aMCI (27.75 ± 1.71) had significantly higher scores ($P < .001$) than subjects with AD (21.64 ± 5.80). Table 1 summarizes the subject demographic information and self-reported medical history.

Processing Speed

The 2 tests used in this study are classified under the cognitive domain of processing speed in the National Institute on Aging–Alzheimer's Disease Research Center designated Uniform Dataset neuropsychological battery.[24] In the Digit Symbol Substitution test, subjects are asked to rapidly copy symbols that correspond to a set of integers according to a provided key, in which a higher number of correctly copied symbols in 90 seconds indicates faster processing speed. In the Trail-Making Test-A, subjects are asked to rapidly connect 25 consecutively numbered circles. The test score is the time (in seconds) in which the participant completes the task; a lower completion time indicates faster processing speed. To facilitate the interpretation and analyses of these measures, we converted the raw score for each test to a *z* score by using the age, sex, and education normative data from the Uniform Dataset,[25] and both *z* scores were averaged to create a composite processing speed (CPS) *z* score. As expected, the 3 groups

differed on CPS [$F(2, 38) = 25.07$, $P < .001$], with the subjects with AD (-2.47 ± 1.62) scoring significantly lower ($P < .001$) than the NC (0.41 ± 0.55) and subjects with aMCI (0.15 ± 1.19).

MR Imaging Acquisition

MR imaging experiments were conducted on a 3T Trio MR imaging system (Siemens Medical Solutions, Erlangen, Germany) by using a 12-channel head coil. The MR imaging protocol, including DKI, is discussed in the On-line Appendix, Section 1.

WMTI Characterization with DKI

DKI provides both the diffusion and kurtosis tensors, from which standard diffusivity metrics (ie, mean diffusivity [MD], axial diffusivity [$D_{\parallel}$], radial diffusivity [$D_{\perp}$]), [D_{perp}]), fractional anisotropy (FA), and kurtosis metrics (ie, mean kurtosis [MK], axial kurtosis [$K_{\parallel}$], and radial kurtosis [$K_{\perp}$]) can be derived.[15,16] In addition, we recently introduced WM tract integrity metrics by defining a WM model that relates these DKI-derived metrics directly to WM microstructure.[18,26] In this model, we characterized WM microstructure that consists of aligned fiber bundles by assuming that the tissue comprises cylindrical axons, each surrounded by a myelin sheath. The relative volume of water within the collective intra-axonal space represents the axonal water fraction. The remainder of the WM is modeled as the extra-axonal space. Through the mathematic derivation described in Fieremans et al,[18] the WM model metrics (ie, AWF and the individual compartmental diffusion tensors for the intra-axonal space and extra-axonal space) can be calculated from the diffusion and kurtosis tensors. In this study, we focused on the following WMTI metrics and their proposed interpretation[27,28]:

- AWF (ie, axonal water fraction, a marker of axonal density)
- D_{axon} (ie, the intrinsic diffusivity inside the axons, a marker of axonal injury)
- $D_{e,\parallel}$ and $D_{e,\perp}$ (the axial and radial diffusivity in the EAS, markers of isotropic changes in extra-axonal diffusion [eg, due to gliosis, loss of oligodendrocytes, or extracellular inflammation]). In addition, $D_{e,\perp}$ is a marker for changes in extra-axonal diffusion transverse to the fibers (eg, due to myelin breakdown).

Image Processing and Analysis

Image processing and analysis are discussed in the On-line Appendix, Section 2. Both voxelwise analysis by using the standard procedure of tract-based spatial statistics (TBSS)[29,30] and region-of-interest analysis of the corpus callosum and the skeleton were performed by using the FMRIB Software Library (FSL, http://www.fmrib.ox.ac.uk/fsl).

Statistical Analyses

Statistical analyses are discussed in the On-line Appendix, Section 3. Because this is the first demonstration of the value of the recently proposed WMTI metrics in detecting in vivo alterations in WM architecture in the course of AD, we adopted an exploratory approach of performing both a voxelwise analysis by using the standard procedure of tract-based spatial statistics[29,30] and a ROI analysis of the corpus callosum to test differences between groups. Area under the receiver operating characteristic curve and linear discriminant analyses were conducted to assess the diagnostic utility of each regional metric in differentiating each group. Last, Spearman correlations of the age-residualized WMTI metrics of the ROIs and CPS score were conducted.

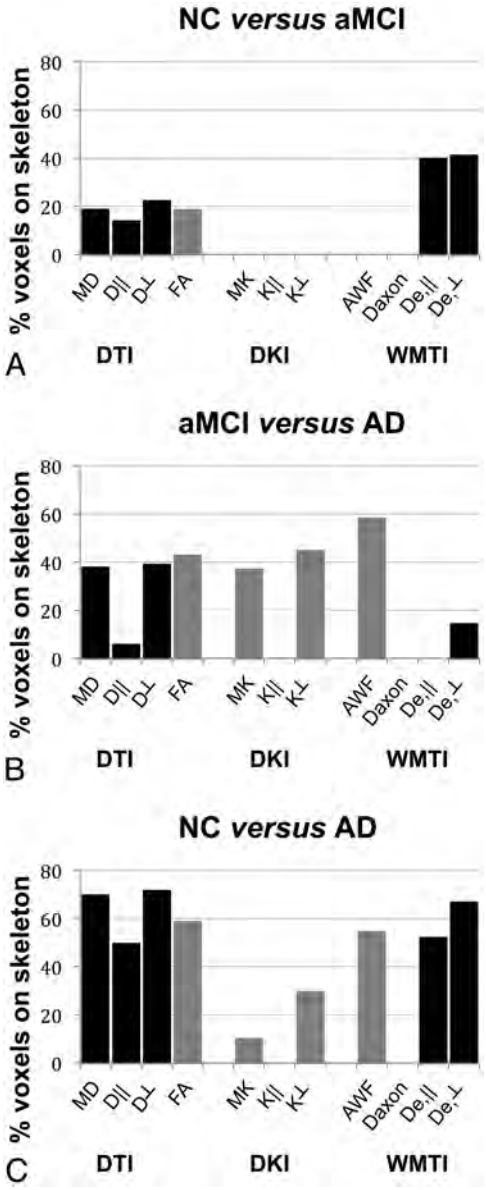

FIG 1. Bar graphs showing the percentage of significantly different voxels on the skeleton for each standard diffusivity, kurtosis, and WMTI metric and group comparison (*A*, NC versus aMCI; *B*, aMCI versus AD; *C*, NC versus AD) using TBSS. Black bars indicate increased; gray bars, decreased.

RESULTS

WMTI Metrics Sensitively Detect Group Differences

With TBSS, the percentage of significantly different voxels (one-sided $P < .05$, corrected for multiple comparisons) for each metric and group comparison is shown in Fig 1 to demonstrate the overall sensitivity of each diffusion measure to discriminate among the groups. Figure 1*A* shows the results for the NC versus aMCI groups: All standard diffusivity metrics were found to be significantly different between the NC and aMCI groups, with the diffusion coefficients (MD, $D_{\parallel}$, and $D_{\perp}$) being increased and the

FA decreased. Among all diffusion metrics examined, the metrics with the highest number of voxels that were significantly different between the NC and aMCI groups were the WMTI extra-axonal diffusivities, $D_{e\|}$ and $D_{e\perp}$, both significantly increased in 37% and 38% of the voxels on the skeleton, respectively. Figure 1*B* shows the results for the aMCI versus AD groups: All standard diffusivity metrics were found to be significantly different, with the diffusion coefficients being increased and FA decreased. The kurtosis metrics MK and $K_\perp$ were also found to be significantly decreased. The AWF had the highest number of voxels (ie, 55%) that were significantly decreased. $D_{e,\perp}$ was also significantly increased, but in fewer voxels. Figure 1*C* shows the results for the NC versus AD groups, where all metrics except $K_\|$ and D_{axon} were found to be significantly different, with the highest sensitivities for the metrics MD (67%), $D_\perp$ (69%), and $D_{e,\perp}$ (64%).

Figure 2 shows the spatial distribution of the TBSS analysis for the WMTI metrics that were found to be the most sensitive in differentiating NC from patients with aMCI, and patients with aMCI from those with AD (ie, $D_{e,\perp}$, $D_{e,\|}$, and AWF). When we compared the NC and aMCI groups, widespread differences in $D_{e,\perp}$ were evident, particularly in the corpus callosum (splenium, genu, and body), forceps major, and arcuate and uncinate fasciculi, while $D_{e,\|}$ was significantly different in periventricular regions, including the corpus callosum, anterior and posterior limbs of the internal capsule, and the uncinate and superior longitudinal fasciculi. In comparing aMCI and AD groups, differences in $D_{e,\perp}$ were observed in more circumscribed WM tracts (eg, the splenium of the corpus callosum and optic radiations). In contrast, AWF was significantly different between the aMCI and AD groups in widespread lateral clusters, particularly in the corticocortical fibers, splenium of the corpus callosum, forceps major, anterior limb of the internal capsule, corona radiata, and cingulum. Accordingly, widespread differences were found between NC and patients with AD in $D_{e,\perp}$, $D_{e,\|}$, and AWF.

Given that the WMTI metrics ($D_{e,\perp}$, $D_{e,\|}$, and AWF) were shown to be more sensitive (ie, detected more significantly different clusters) than the diffusivity/kurtosis metrics in distinguishing NC from patients with aMCI and subjects with aMCI from those with AD by using TBSS, ROI analyses of the corpus callosum were restricted to the 4 WMTI metrics. Table 2 lists the means and SDs of the 4 ROIs for each WMTI metric and the post hoc ANCOVA results. (On-line Table 1 provides these data for the standard diffusivity and kurtosis metrics.) The results in the ROI analyses for the WMTI metrics were consistent with the TBSS results that identified distinct WMTI metrics distinguishing NC from patients with aMCI and subjects with aMCI from those with AD. $D_{e,\|}$ was significantly increased in the aMCI group than in NC in all ROIs, while $D_{e,\perp}$ was also significantly increased in the aMCI group than in NC in the genu. On the other hand, the AWF in the skeleton was significantly decreased in those with AD than in those with aMCI, while $D_{e,\perp}$ was significantly increased in the AD group than in the aMCI group in the splenium. Also similar to the TBSS results, the NC group was significantly different from the AD group in all ROIs and metrics except for D_{axon}.

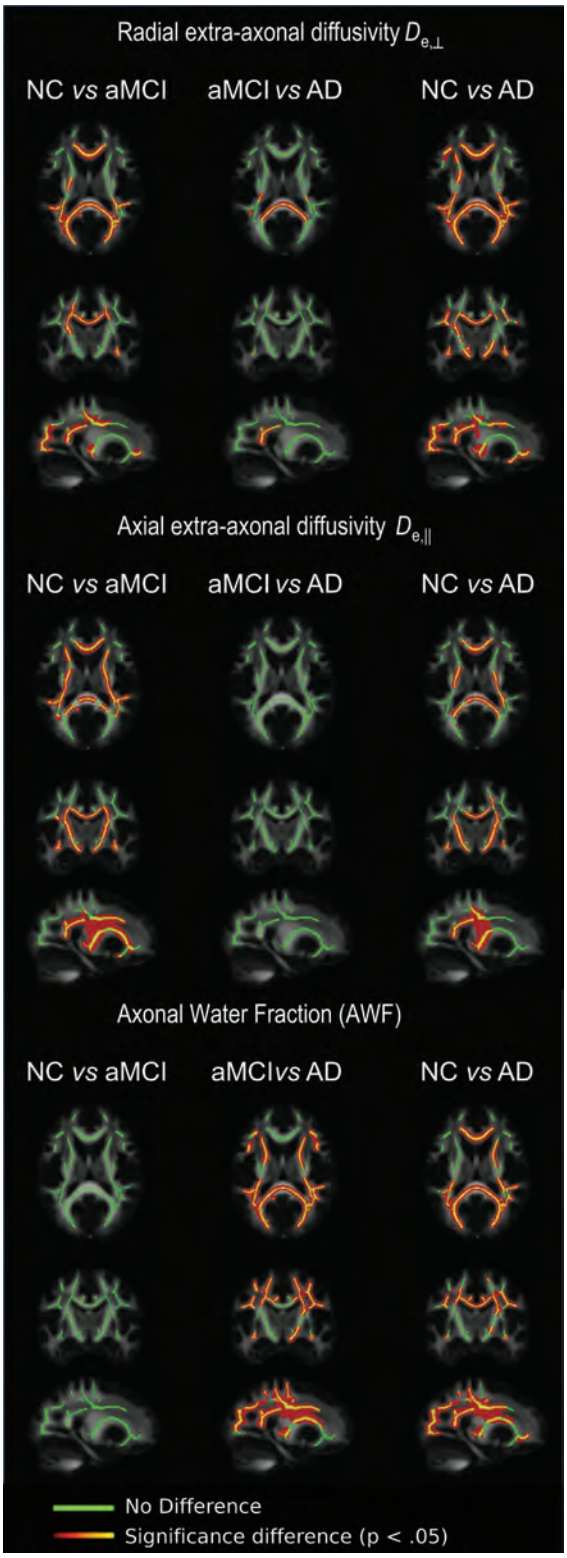

FIG 2. TBSS results showing all 3 group comparisons for WMTI metrics of radial extra-axonal diffusivity, axial extra-axonal diffusivity, and axonal water fraction: Clusters of significantly different voxels ($P < .05$) are shown in red-orange and overlaid on the FMRIB FA template, together with the mean skeleton (green). Clusters of increased radial extra-axonal diffusivity are found both for NC versus MCI groups and for MCI versus AD groups. Clusters of increased axial extra-axonal diffusivity are found for NC versus MCI groups, and clusters of decreased AWF are observed for MCI versus AD groups.

Table 2: ANCOVA pos hoc and AUC results of the WMTI metrics of each corpus callosum ROI and the FA skeleton

		NC (n = 15)	aMCI (n = 12)	AD (n = 14)	NC vs aMCI		aMCI vs AD		NC vs AD	
	ROI	Mean ± SD	Mean ± SD	Mean ± SD	*P* Value	AUC	*P* Value	AUC	*P* Value	AUC
AWF	Genu	0.35 ± 0.03	0.33 ± 0.03	0.32 ± 0.05	.25	0.75	.43	0.67	.01[a,b]	0.78
	Body	0.35 ± 0.03	0.33 ± 0.03	0.32 ± 0.04	.33	0.71	.35	0.65	.01[a,b]	0.76
	Splenium	0.41 ± 0.03	0.39 ± 0.03	0.35 ± 0.06	.36	0.69	.02[a]	0.79	<.01[c,b]	0.88
	Skeleton	0.39 ± 0.02	0.38 ± 0.02	0.36 ± 0.04	.93	0.64	.01[a,b]	0.84	<.01[d,b]	0.83
D_{axon}	Genu	1.09 ± 0.06	1.09 ± 0.05	1.10 ± 0.09	1.00	0.66	.88	0.53	.88	0.53
	Body	1.22 ± 0.10	1.18 ± 0.07	1.19 ± 0.10	.65	0.64	.98	0.54	.75	0.56
	Splenium	1.20 ± 0.09	1.17 ± 0.05	1.15 ± 0.12	.82	0.63	.62	0.71	.25	0.71
	Skeleton	0.96 ± 0.05	0.95 ± 0.04	0.93 ± 0.07	1.00	0.66	.57	0.77	.49	0.68
$D_{e,\parallel}$	Genu	2.90 ± 0.13	3.06 ± 0.07	3.10 ± 0.17	.01[a,b]	0.86	.57	0.60	<.01[c,b]	0.85
	Body	2.83 ± 0.11	3.01 ± 0.10	2.99 ± 0.15	<.01[d,b]	0.89	.93	0.54	<.01[d,b]	0.79
	Splenium	2.79 ± 0.11	2.93 ± 0.11	2.95 ± 0.11	.01[a,b]	0.82	.78	0.57	<.01[d,b]	0.88
	Skeleton	2.30 ± 0.07	2.39 ± 0.04	2.40 ± 0.07	<.01[c,b]	0.95	.88	0.53	<.01[c,b]	0.92
$D_{e,\perp}$	Genu	1.33 ± 0.11	1.52 ± 0.16	1.58 ± 0.27	.01[a,b]	0.91	.30	0.64	<.01[c,b]	0.91
	Body	1.43 ± 0.10	1.58 ± 0.12	1.62 ± 0.22	.03[a]	0.88	.49	0.63	<.01[c,b]	0.80
	Splenium	1.15 ± 0.10	1.29 ± 0.12	1.43 ± 0.25	.06	0.87	<.01[d,b]	0.77	<.01[c,b]	0.93
	Skeleton	1.06 ± 0.07	1.15 ± 0.07	1.20 ± 0.16	.04[a]	0.89	.06	0.77	<.0[c,b]	0.89

Note:—AUC indicates area under the receiver operating characteristic curve.
[a] $P < .05$.
[b] *P* values indicate that the difference remains significant after applying a Bonferroni correction for multiple ROI comparisons.
[c] $P < .001$.
[d] $P < .01$.

WMTI Metrics Predict aMCI and AD with High Diagnostic Accuracy

Given the corroborating TBSS and ROI results, area under the receiver operating characteristic curve analyses were conducted to demonstrate the diagnostic accuracy of the WMTI metrics (Table 2; see On-line Table 1 for these results for the standard diffusivity and kurtosis metrics). $D_{e,\perp}$ and $D_{e,\parallel}$ yielded the highest classification accuracies for discriminating NC from patients with aMCI (area under the receiver operating characteristic curve = 0.82–0.95), while aMCI was best discriminated from AD by the AWF (area under the receiver operating characteristic curve = 0.84). When we compared across the 4 ROIs, the FA skeleton consistently yielded the highest area under the receiver operating characteristic curve values.

Processing Speed Strongly Correlates with WMTI Metrics in aMCI

Consistent with prior reports of significant correlations between processing speed and MR imaging–based estimates of WM integrity,[31-33] the CPS score was strongly correlated with the WMTI metrics of diffusivity in the extra-axonal space: $D_{e,\parallel}$ ($r = -0.82$, $P < .001$), $D_{e,\perp}$ ($r = -0.80$, $P = .002$), and AWF ($r = 0.82$, $P < .001$), in the callosal body in aMCI—that is, lower CPS scores were associated with higher extra-axonal diffusivities in the callosal body in aMCI but not in any other group. CPS correlated with the AWF in the callosal body in aMCI, wherein higher CPS scores were associated with a higher AWF.

DISCUSSION

In this study, we demonstrated that WMTI metrics provide unique information regarding the specific underlying mechanisms of WM alterations that occur in the course of AD. By using TBSS, we confirmed prior research that showed increased mean, radial, and axial diffusivity, as well as decreased FA, in WM tracts in subjects with aMCI and AD compared with NC.[9,34] We also observed decreased mean and radial kurtosis values in AD compared with subjects with aMCI and NC. However, the specific novelty of this work is our application of the non-Gaussian diffusion information from DKI to a tissue-modeling technique that provides a more nuanced conceptualization of the microstructural changes occurring across stages of the disease. With high diagnostic accuracy, increased diffusivity in the extra-axonal space ($D_{e,\parallel}$, $D_{e,\perp}$) in several WM tracts sensitively distinguished NC from patients with aMCI, while widespread decreased AWF differentiated aMCI from AD groups. Additionally, these metrics of WM integrity in the body of the corpus callosum were strongly correlated with processing speed in aMCI. These findings have the following potential implications for the course and spatial progression of WM degeneration in AD, as well as the mechanisms by which these changes occur.

Alterations in Extra-Axonal Diffusion as Biomarkers of the Earliest Stages of AD

AD in its earliest stage is a new target phase for clinical trials because it is argued that addressing early pathologic changes may increase the likelihood of curtailing the disease.[2] The significant difference in extra-axonal diffusivity both in the radial ($D_{e,\perp}$) and axial ($D_{e,\parallel}$) directions between NC and aMCI groups suggests that pathologic changes in the extra-axonal space, including demyelination, loss of oligodendrocytes, astrocytosis, or extracellular inflammation may be especially salient in the earliest stages of disease. Our data provide strong evidence that increased $D_{e,\parallel}$ mainly occurs in periventricular regions in this stage, while $D_{e,\perp}$ is increased in widespread lateral regions from NC through aMCI and into AD. These observations suggest that $D_{e,\perp}$ and $D_{e,\parallel}$ may be sensitive to different underlying mechanisms, in which $D_{e,\perp}$ may be more sensitive to myelin breakdown than $D_{e,\parallel}$.[18,27] Indeed, $D_{e,\perp}$ was significantly increased in patients with aMCI in the late-myelinating genu than in NC, and it was significantly increased in those with AD in the early-myelinating splenium and optic tracts than in patients with aMCI. This observed

pattern appears consistent with the hypothesis of myelin breakdown being a significant pathogenic process in the course of AD,[11] first observed in late-myelinating tracts early in the disease.

Alterations in AWF as a Biomarker of AD Progression

Apart from potential myelin changes, our study also provides evidence for decreased AWF, which has been recently proposed as a specific marker of axonal density loss.[27] This finding corroborates known neurodegenerative processes in AD but further suggests that this occurs particularly in the transition from aMCI to AD. The significant decreases in AWF in the corticocortical fibers may suggest a reduction in axons due to Wallerian degeneration secondary to distal cortical atrophy as the primary pathologic event in these regions.[35] However, we also observed increased $D_{e,\perp}$ in the early-myelinating splenium of the corpus callosum from aMCI to AD, suggesting that myelin and axonal changes co-occur in advanced disease.

Definitive conclusions regarding the temporality of these changes are precluded by the cross-sectional design of this study, but these findings certainly support previous research indicating that both myelin breakdown and Wallerian degeneration are implicated in AD.[34] Interestingly, we did not find any significant results for D_{axon}, a marker of intra-axonal injury and axonal beading.[28] Although it is possible that the WM model is not sensitive to changes in the intra-axonal environment in AD, these negative findings encourage further speculation on potential disease-related factors that preferentially impact axonal density rather than the intra-axonal environment.

Correlation with Processing Speed

Processing speed peaks at around the third and fourth decade of life, slowly declines with age, and facilitates other higher-order cognitive processes such as verbal memory retrieval.[36,37] Although the neurobiologic mechanisms of processing speed have yet to be fully determined, histologic and ethologic studies of brain aging demonstrate that myelin integrity supports the rapid transmission necessary for the distributed neural networks that facilitate cognitive functions.[38-40] Human MR imaging studies provide further evidence for the association between estimates of myelin integrity in the anterior and posterior corpus callosum and processing speed in healthy older adults,[31-33] but these associations are less examined in the course of AD and have not been tested by using the WMTI metrics modeled to estimate specific WM microstructure. In this study, the WMTI metrics $D_{e,\perp}$, $D_{e,\parallel}$, and AWF yielded strong correlations with processing speed in aMCI. Our results are unique in that these correlations were exclusive to the body of the corpus callosum, rather than the genu or splenium, which were the regions reported in prior studies.[31-33] While these preliminary findings require replication before we can conjecture the functional relevance of the callosal body to cognition, they do provide unique insights into WM involvement in AD and to the links between diffusion MR imaging and behavioral metrics relevant to detecting disease onset and tracking its progression. For instance, it is possible that the strong correlations between the WMTI and processing speed metrics are due to the optimal level of variability in both metrics at the aMCI stage because of the presence of varying degrees of pathologic severity. This conceptualization suggests that changes in these metrics may signal a transition from normal aging to aMCI, though confirmation of this possibility is needed by using longitudinal data and other sensitive neurocognitive measures that have sufficient psychometric properties and are of clinical relevance to the progressive stages of disease.

Clinical Implications and Future Directions

This study demonstrates the sensitivity of WMTI metrics and their high diagnostic accuracy, which support the clinical potential of these metrics as biomarkers for the earliest stages of AD, disease progression, or treatment response. In particular, we report that axial and radial extra-axonal diffusivities most accurately distinguish patients with aMCI from NC, suggesting that these may be biomarkers for further exploration in the search for in vivo MR imaging markers of the earliest brain changes in the course of AD. On the other hand, our finding of decreased AWF from aMCI to AD could indicate that targeting axonal loss may be a possible strategy for slowing the trajectory of disease. Interestingly, while specific WMTI metrics most sensitively and accurately detect the differences between the NC and aMCI groups and between the aMCI and AD groups, we observed that the standard diffusivity metrics are the most sensitive in detecting differences between NC and patients with AD (Fig 1). This may, in part, be explained by the high specificity of the WMTI metrics to distinguish between groups, respectively. For example, $D_{e,\parallel}$ is only significantly different between NC and patients with aMCI, while AWF is only significantly different between the aMCI and AD groups. As a result, diffusivity metrics may be overall more sensitive in detecting differences between NC and patients with AD as they are a combination of several WMTI metrics. However, our finding of changes in the extra-axonal diffusivity from NC to aMCI may be of keen interest to the field of AD at large, which is currently focused on developing biomarkers for early detection. Moreover, in aMCI, these metrics yielded strong correlations with processing speed, further providing their functional relevance to this disease. Thus, albeit requiring further replication and validation, the WMTI metrics may provide promising methods of detection and description of WM changes that occur in the course of AD.

Subsequent investigations of WMTI metrics may be improved by using multiple image processing and analytic methods. In this study, which used both TBSS and the conventional ROI analyses, the WMTI metric values over the FA skeleton, as derived from TBSS, yielded the highest area under the receiver operating characteristic curve values. Although the results of both methods were similar, TBSS may be the preferred approach because this standardized procedure minimizes preprocessing, obviates subjective ROI outlining, and naturally selects WM voxels consisting of strongly aligned fibers in which the WMTI metrics are valid and partial volume effects are suppressed. Validation of the WMTI metrics is also of crucial importance, and it would be particularly useful to evaluate the sensitivity and specificity of both $D_{e,\perp}$ and $D_{e,\parallel}$ to the different pathologic processes in the extra-axonal space (eg, gliosis, demyelination, inflammation) by using both histologic validation and other imaging modalities (eg, PET).

Limitations

This study has some limitations that may be addressed in future research. First, this cross-sectional study only simulates the potential significance of the WMTI metrics in predicting conversion to aMCI or AD. Confirming these hypothesized changes by using a longitudinal design would be ideal. Second, WM lesion load may have influenced the diffusion metrics, though we did not find any significant differences in lesion load or vascular disease burden at the group level. While the extent of WM lesions associated with the metrics of WM integrity as defined via diffusion MR imaging remains under investigation,[41] improvement to this work can include both clinician-rated and automated methods of quantifying lesion burden or other vascular compromise. Third, because the underlying WM model is only applicable in regions consisting of aligned fiber bundles, we limited our analysis to voxels with high FA. Last, the sample size of this preliminary study limits the generalizability of these results and the applicability of the diagnostic accuracy of these metrics to community-based samples in which aMCI and AD are less prevalent.

CONCLUSIONS

This is the first study to demonstrate that WM tract integrity metrics significantly differentiate healthy controls and subjects with amnestic MCI and AD, yield diagnostically sensitive information regarding the underlying mechanisms of WM degeneration, and correlate with processing speed, a cognitive function most relevant to WM integrity. These novel WMTI metrics yield insights into underlying disease mechanisms in AD, which, with further investigation, can potentially yield promising biomarkers of the earliest brain changes in AD.

ACKNOWLEDGMENTS

We thank Vitria Adisetiyo, José Raya, and Henry Rusinek for technical assistance and helpful discussions while preparing this manuscript. We also thank Amanda Allen and Jane Kwon for their assistance with data analysis and research coordination.

Disclosures: Els Fieremans—RELATED: Grant: Alzheimer Drug Discovery Foundation, * Litwin Foundation,* Comments: This study was outlined as part of a research grant from the Alzheimer Drug Discovery Foundation (principal investigator [PI]: E. Fieremans), active between June 1, 2011 and May 31, 2012. UNRELATED: Siemens Medical owns a royalty-free nonexclusive license for diffusional kurtosis imaging with the pending patent held by New York University. I am one of the inventors. Jens H. Jensen—RELATED: Grant: NIH (R01AG027852),* Alzheimer Drug Discovery Foundation,* Litwin Foundation,* Comments: This article includes work that was funded in part by NIH grant R01AG027852 (PI: J.A. Helpern). Additional funding was provided by the Alzheimer Drug Discovery Foundation (PI: E. Fieremans) and the Litwin Foundation (PI: J.A. Helpern), UNRELATED: Siemens Medical owns a royalty-free nonexclusive license for diffusional kurtosis imaging with the pending patent held by New York University. I am one of the inventors. Maria F. Falangola—RELATED: Grant: NIH (R01AG027852),* Alzheimer Drug Discovery Foundation,*Litwin Foundation.* Ali Tabesh—UNRELATED: Siemens Medical owns a royalty-free nonexclusive license for diffusional kurtosis imaging with the pending patent held by New York University. I am one of the inventors. M. Vittoria Spampinato—RELATED: Grant: NIH (R01AG027852).* Dmitry S. Novikov—RELATED: Grant: Litwin Foundation.* Steven H. Ferris—RELATED: Grant: National Institute on Aging Alzheimer's Disease Core Center Grant, Comments: supported clinical/diagnostic evaluations for the clinical assessments of study participants prior to their initial enrollment in the current study. Joseph A. Helpern—RELATED: Grant: NIH (R01AG027852),* Litwin Foundation;* UNRELATED: Siemens Medical owns a royalty-free nonexclusive license for diffusional kurtosis imaging with the pending patent held by New York University. I am one of the inventors. * Money paid to the institution.

REFERENCES

1. Morris JC. **Mild cognitive impairment and preclinical Alzheimer's disease.** *Geriatrics* 2005;(suppl):9–14
2. Reiman EM, Langbaum JB, Tariot PN. **Alzheimer's prevention initiative: a proposal to evaluate presymptomatic treatments as quickly as possible.** *Biomark Med* 2010;4:3–14
3. Duyckaerts C, Delatour B, Potier MC. **Classification and basic pathology of Alzheimer disease.** *Acta Neuropathol* 2009;118:5–36
4. Sjöbeck M, Haglund M, Englund E. **Decreasing myelin density reflected increasing white matter pathology in Alzheimer's disease: a neuropathological study.** *Int J Geriatr Psychiatry* 2005;20:919–26
5. Brun A, Englund E. **A white matter disorder in dementia of the Alzheimer type: a pathoanatomical study.** *Ann Neurol* 1986;19: 253–62
6. Englund E. **Neuropathology of white matter changes in Alzheimer's disease and vascular dementia.** *Dement Geriatr Cogn Disord* 1998; 9(suppl 1):6–12
7. Gouw AA, Seewann A, Vrenken H, et al. **Heterogeneity of white matter hyperintensities in Alzheimer's disease: post-mortem quantitative MRI and neuropathology.** *Brain* 2008;131(pt 12): 3286–98
8. Sjöbeck M, Haglund M, Englund E. **White matter mapping in Alzheimer's disease: a neuropathological study.** *Neurobiol Aging* 2006;27:673–80
9. Clerx L, Visser PJ, Verhey F, et al. **New MRI markers for Alzheimer's disease: a meta-analysis of diffusion tensor imaging and a comparison with medial temporal lobe measurements.** *J Alzheimers Dis* 2012;29:405–29
10. Di Paola M, Spalletta G, Caltagirone C. **In vivo structural neuroanatomy of corpus callosum in Alzheimer's disease and mild cognitive impairment using different MRI techniques: a review.** *J Alzheimers Dis* 2010;20:67–95
11. Bartzokis G. **Alzheimer's disease as homeostatic responses to age-related myelin breakdown.** *Neurobiol Aging* 2011;32:1341–71
12. Englund E, Brun A. **White matter changes in dementia of Alzheimer's type: the difference in vulnerability between cell compartments.** *Histopathology* 1990;16:433–39
13. Coleman M. **Axon degeneration mechanisms: commonality amid diversity.** *Nat Rev Neurosci* 2005;6:889–98
14. Basser PJ, Pierpaoli C. **Microstructural and physiological features of tissues elucidated by quantitative-diffusion-tensor MRI.** *J Magn Reson B* 1996;111:209–19
15. Jensen JH, Helpern JA. **MRI quantification of non-Gaussian water diffusion by kurtosis analysis.** *NMR Biomed* 2010;23:698–710
16. Jensen JH, Helpern JA, Ramani A, et al. **Diffusional kurtosis imaging: the quantification of non-gaussian water diffusion by means of magnetic resonance imaging.** *Magn Reson Med* 2005;53: 1432–40
17. Helpern JA, Falangola MF, Tabesh A, et al. **Diffusional kurtosis imaging in mild cognitive impairment and Alzheimer's disease.** In: *Proceedings of the 19th Annual Meeting of the International Society for Magnetic Resonance in Medicine,* Montreal, Canada. May 6–13, 2011:4217
18. Fieremans E, Jensen JH, Helpern JA. **White matter characterization with diffusional kurtosis imaging.** *Neuroimage* 2011;58:177–88
19. Reisberg B, Ferris SH, De Leon MJ, et al. **The Global Deterioration Scale for assessment of primary degenerative dementia.** *Am J Psychiatry* 1982;139:1136–39
20. Wechsler D. *Manual for the Wechsler Memory Scale.* 3rd ed. San Antonio, Texas: Psychological Corporation; 1997
21. American Psychiatric Association. *Diagnostic and Statistical Manual of Mental Disorders.* 4th ed. Washington, DC: American Psychiatric Association
22. McKhann G, Drachman D, Folstein M, et al. **Clinical diagnosis of Alzheimer's disease: report of the NINCDS-ADRDA Work Group under the auspices of Department of Health and Human Services Task Force on Alzheimer's Disease.** *Neurology* 1984;34:939–44

23. Folstein MF, Folstein SE, McHugh PR. **"Mini-mental state": a practical method for grading the cognitive state of patients for the clinician.** *J Psychiatr Res* 1975;12:189–98
24. Weintraub S, Salmon D, Mercaldo N, et al. **The Alzheimer's Disease Centers' Uniform Data Set (UDS): the neuropsychologic test battery.** *Alzheimer Dis Assoc Disord* 2009;23:91–101
25. Shirk SD, Mitchell MB, Shaughnessy LW, et al. **A web-based normative calculator for the uniform data set (UDS) neuropsychological test battery.** *Alzheimers Res Ther* 2011;3:32
26. Fieremans E, Novikov DS, Jensen JH, et al. **Monte Carlo study of a two-compartment exchange model of diffusion.** *NMR Biomed* 2010;23:711–24
27. Fieremans E, Jensen JH, Helpern JA, et al. **Diffusion distinguishes between axonal loss and demyelination in brain white matter.** In: *Proceedings of the 20th Annual Meeting of the International Society for Magnetic Resonance Medicine,* Melbourne, Australia; May 5–11, 2012
28. Hui ES, Fieremans E, Jensen JH, et al. **Stroke assessment with diffusional kurtosis imaging.** *Stroke* 2012;43:2968–73
29. Smith SM, Jenkinson M, Johansen-Berg H, et al. **Tract-based spatial statistics: voxelwise analysis of multi-subject diffusion data.** *Neuroimage* 2006;31:1487–505
30. Smith SM, Johansen-Berg H, Jenkinson M, et al. **Acquisition and voxelwise analysis of multi-subject diffusion data with tract-based spatial statistics.** *Nat Protoc* 2007;2:499–503
31. Kochunov P, Coyle T, Lancaster J, et al. **Processing speed is correlated with cerebral health markers in the frontal lobes as quantified by neuroimaging.** *Neuroimage* 2010;49:1190–99
32. Kennedy KM, Raz N. **Aging white matter and cognition: differential effects of regional variations in diffusion properties on memory, executive functions, and speed.** *Neuropsychologia* 2009; 47:916–27
33. Lu PH, Lee GJ, Raven EP, et al. **Age-related slowing in cognitive processing speed is associated with myelin integrity in a very healthy elderly sample.** *J Clin Exp Neuropsychol* 2011;33: 1059–68
34. Sexton CE, Kalu UG, Filippini N, et al. **A meta-analysis of diffusion tensor imaging in mild cognitive impairment and Alzheimer's disease.** *Neurobiol Aging* 2011;32:2322.e5–18
35. Fellgiebel A, Schermuly I, Gerhard A, et al. **Functional relevant loss of long association fibre tracts integrity in early Alzheimer's disease.** *Neuropsychologia* 2008;46:1698–706
36. Hedden T, Lautenschlager G, Park DC. **Contributions of processing ability and knowledge to verbal memory tasks across the adult lifespan.** *Q J Exp Psychol A* 2005;58:169–90
37. Salthouse TA. **Aging and measures of processing speed.** *Biol Psychol* 2000;54:35–54
38. Meyer A. **Paul Flechsig's system of myelogenetic cortical localization in the light of recent research in neuroanatomy and neurophysiology: part I.** *Can J Neurol Sci* 1981;8:1–6
39. Peters A, Rosene DL, Moss MB, et al. **Neurobiological bases of age-related cognitive decline in the rhesus monkey.** *J Neuropathol Exp Neurol* 1996;55:861–74
40. Yakovlev P, Lecours A. *Regional Development of the Brain in Early Life.* Boston: Blackwell Scientific Publications; 1967
41. Maillard P, Carmichael O, Harvey D, et al. **FLAIR and diffusion MRI signals are independent predictors of white matter hyperintensities.** *AJNR Am J Neuroradiol* 2013;34:54–61

Evaluation of Parkinson Disease and Alzheimer Disease with the Use of Neuromelanin MR Imaging and ^{123}I-Metaiodobenzylguanidine Scintigraphy

F. Miyoshi, T. Ogawa, S.-i. Kitao, M. Kitayama, Y. Shinohara, M. Takasugi, S. Fujii, and T. Kaminou

ABSTRACT

BACKGROUND AND PURPOSE: Progressive changes in the substantia nigra pars compacta and locus ceruleus of patients with Parkinson disease and Alzheimer disease visualized by neuromelanin MRI and cardiac postganglionic sympathetic nerve function on ^{123}I-metaiodobenzylguanidine scintigraphy have not been fully evaluated. We compared the diagnostic value of these modalities among patients with early Parkinson disease, late Parkinson disease, and Alzheimer disease.

MATERIALS AND METHODS: We compared contrast ratios of signal intensity in medial and lateral regions of the substantia nigra pars compacta and locus ceruleus with those of the tegmentum of the midbrain and the pons, respectively, by use of neuromelanin MRI in patients with early Parkinson disease ($n = 13$), late Parkinson disease ($n = 31$), Alzheimer disease ($n = 6$), and age-matched healthy control subjects ($n = 20$). We calculated heart-to-mediastinum ratios on ^{123}I-metaiodobenzylguanidine scintigrams after setting regions of interest on the left cardiac ventricle and upper mediastinum.

RESULTS: The signal intensity of the lateral substantia nigra pars compacta on neuromelanin MRI was significantly reduced in early and late Parkinson disease, and that of the medial substantia nigra pars compacta was gradually and stage-dependently reduced in Parkinson disease. The signal intensity of the locus ceruleus was obviously reduced in late Parkinson disease. Signal reduction was not significant in the substantia nigra pars compacta and locus ceruleus of patients with Alzheimer disease. The heart-to-mediastinum ratio on ^{123}I-metaiodobenzylguanidine scintigrams was stage-dependently reduced in Parkinson disease and normal in Alzheimer disease. The signal intensity ratios in substantia nigra pars compacta and locus ceruleus on neuromelanin MRI positively correlated with the heart-to-mediastinum ratio on ^{123}I-metaiodobenzylguanidine scintigrams.

CONCLUSIONS: Both neuromelanin MRI and ^{123}I-metaiodobenzylguanidine scintigraphy can help to evaluate disease progression in Parkinson disease and are useful for differentiating Parkinson disease from Alzheimer disease.

ABREVIATIONS: LC = locus ceruleus; MIGB = ^{123}I-metaiodobenzylguanidine; NmMRI = neuromelanin MR imaging; PD = Parkinson disease; SNc = substantia nigra pars compacta

Early Parkinson disease (PD) can easily be mistaken for any number of disorders, including other forms of parkinsonism, such as multiple system atrophy, progressive supranuclear palsy, corticobasal degeneration, and dementia with Lewy bodies. Other degenerative diseases, such as Alzheimer disease and primary lateral sclerosis, can also be mistaken for PD.[1] Improving diagnostic accuracy is critical for the early differentiation of PD and other neurodegenerative types of parkinsonism because their prognoses are very different and the choice of treatment strategy is extremely important.

Neuromelanin is a dark pigment that locates within certain catecholamine neurons of the human brain, such as the dopaminergic neurons of the substantia nigra pars compacta (SNc) and the noradrenergic neurons of the locus ceruleus (LC).[2] It is thought to be formed as a by-product of the catecholamine metabolism cascade through enzymatic and/or oxidative polymerization.[2,3] PD is characterized by the progressive loss of dopaminergic neurons that contain neuromelanin in the SNc and of noradrenergic neurons in the LC. Several pathologic studies have shown the selective loss of ventral intermediate and lateral cell groups of the SNc in PD.[4-6] Noradrenergic neurons are also lost in the LC of patients with Alzheimer disease.[7]

It is reported that neuromelanin MRI (NmMRI) could visualize decreased signal intensity in regions that reflect the loss of

Received December 2, 2012; accepted after revision January 25, 2013.

From the Division of Radiology (F.M., T.O., S.-i.K., Y.S., M.T., S.F., T.K.), Department of Pathophysiological Therapeutic Science; and Division of Neurology (M.K.), Department of Brain and Neurosciences, Faculty of Medicine, Tottori University, Yonago, Japan.

Please address correspondence to Toshihide Ogawa, MD, Division of Radiology, Department of Pathophysiological Therapeutic Science, Faculty of Medicine, Tottori University, 36–1, Nishi-cho, Yonago 683–504, Japan; e-mail: ogawa@med.tottori-u.ac.jp

http://dx.doi.org/10.3174/ajnr.A3567

Table 1: Clinical characteristics of patient and control groups

	Early Parkinson Disease	Late Parkinson Disease	Alzheimer Disease	Control
Patients, *n*	13	31	6	20
Hoehn and Yahr stage	I:3, II:10	III:16, IV:12, V:3	/	/
Male/female	5/8	14/17	3/3	5/15
Age, y, mean ± SD	68.3 ± 5.88	71.8 ± 8.95	75.7 ± 9.52	74.8 ± 5.41
Duration, y, mean ± SD	4.30 ± 5.37	9.48 ± 6.86	2.5 ± 3	/
Hasegawa Dementia Scale-Revised, mean ± SD	/	/	12.8 ± 4.76	/

Note:—Age does not differ between patient and control groups ($P = .082$; 1-way analysis of variance).

neurons containing neuromelanin[8,9] and the signal intensity in the SNc and LC was greatly reduced on NmMRI from patients with PD. Several investigators subsequently reported that NmMRI could show a reduction in the contrast ratio and volume of the SNc.[10,11]

The physiologic analog of noradrenaline, ^{123}I-metaiodobenzylguanidine (MIBG), traces uptake and transport both in noradrenaline presynaptic sympathetic nerve terminals and in subsequent vesicular storage.[12] Postganglionic presynaptic cardiac sympathetic nerve endings can be noninvasively assessed by MIBG scintigraphy because a reduction of MIBG uptake indicates postganglionic sympathetic dysfunction. Cardiac MIBG uptake is reduced in patients with Lewy body diseases such as PD, as well as dementia with Lewy bodies, and MIBG scintigraphy can also help to differentiate PD from other types of parkinsonism.[13,14]

However, progressive changes in PD and Alzheimer disease have not been fully evaluated by NmMRI and MIBG scintigraphy. We determined the usefulness of these modalities for differentially diagnosing PD and Alzheimer disease by analyzing changes in signal intensity in the SNc and LC and MIBG uptake in the left cardiac ventricle and evaluated correlations between NmMRI and MIBG scintigraphy findings.

MATERIALS AND METHODS

Patients

We investigated patients who had been tentatively diagnosed with suspected PD and who were finally confirmed as having PD or Alzheimer disease between December 2008 and April 2012. Both MRI and MIBG scintigraphy acquired within 1 month were retrospectively evaluated. Probable PD and Alzheimer disease were diagnosed according to the criteria of the United Kingdom Brain Bank and National Institute of Neurologic and Communicative Disorders and Stroke and the Alzheimer Disease and Related Disorders Association, respectively. Patients with PD were assigned to groups with either early or late PD on the basis of Hoehn and Yahr staging.[15] Early PD comprised stages I and II, and late PD comprised stages III, IV, and V.

Patients with symptomatic cerebrovascular diseases and other central nervous system disorders were strictly excluded from the NmMRI evaluation, and those with cardiac diseases, diabetes mellitus, and/or medications that can interfere with MIBG uptake were excluded from the MIBG scintigraphy assessment.

We finally enrolled 13 (male, $n = 5$; female, $n = 8$), 31 (male, $n = 14$; female, $n = 17$), and 6 (male and female, $n = 3$ each) patients with early PD, late PD, and Alzheimer disease, respectively (Table 1) [ages (mean ± SD with range) 68.3 ± 5.88 (59–85), 71.8 ± 8.95 (59–83), and 75.7 ± 9.52 (58–84) years, respectively]. The mean (±SD with range) duration of early PD, late PD, and Alzheimer disease was 4.30 ± 5.37 (0–9), 9.48 ± 6.86 (2–27), and 2.5 ± 3.00 (1–3) years, respectively. We used the Hasegawa Dementia Scale-Revised[16] to determine cognitive impairment or dementia, which is similar to the Mini-Mental State Examination and has a total score of 30. Hasegawa Dementia Scale-Revised scores in patients with Alzheimer disease ranged from 6–17 (mean ± SD, 12.8 ± 4.76).

Twenty age-matched patients (male, $n = 5$; female, $n = 15$) [ages (mean ± SD with range) 74.8 ± 5.41 (64–87) years] without a history of motor or cognitive impairment and significant abnormalities on brain MRI during the same period served as a control group of NmMRI. However, we did not obtain MIBG scintigraphic data from the control group during this period.

Our institutional review board approved the study, and written informed consent was waived.

Image Acquisition

All MR images were acquired by means of a clinical 3T MR scanner (Signa Excite HD, GE Healthcare, Milwaukee, Wisconsin). Axial images were acquired parallel to the anterior/posterior commissure line. T1-weighted fast spin-echo sequences were applied to NmMRI with the following parameters: TR/TE, 600/13 ms; echo-train length, 2; section thickness, 2.5 mm with 1- mm intersection gaps; matrix size, 512 × 512; FOV, 220 mm; acquisition time, 12 minutes. The scan covered the area from the upper border of the midbrain to the inferior border of the pons. We excluded other coexisting central nervous system disorders by use of axial T1- and T2-weighted images, fluid-attenuated inversion recovery images, and diffusion-weighted images of the entire brain according to the following standard protocol for adult brain imaging at our hospital: T1-weighted spin-echo sequence, TR/TE, 600/15 ms; section thickness, 5 mm; FOV 220 mm; matrix 512 × 512; T2-weighted fast spin-echo sequence, TR/TE, 4000/90 ms; section thickness, 5 mm; FOV 220 mm; matrix 512 × 512; fluid attenuated inversion recovery sequence, TR/TE/IR, 4000/90/20; section thickness, 5 mm; FOV 220 mm; matrix 512 × 512; and diffusion-weighted imaging sequence, TR/TE, 4000/90 ms; section thickness, 5 mm; FOV 220 mm; matrix 512 × 512; maximum b factor, 1000 mm^2/s.

The patients received an intravenous injection of 111 MBq of ^{123}I-MIBG, and static planar images of the chest were acquired 30 minutes later for 4 minutes in a 256 × 256 matrix by use of a dual-head gamma camera with a large field of view and a low-energy, high-resolution collimator (e.cam; Siemens, Erlangen, Germany).[17]

Image Analysis

Signal intensity was measured for quantitative NmMRI by setting regions of interest. We equally divided the SNc into medial and lateral regions at the level of the inferior colliculus and defined

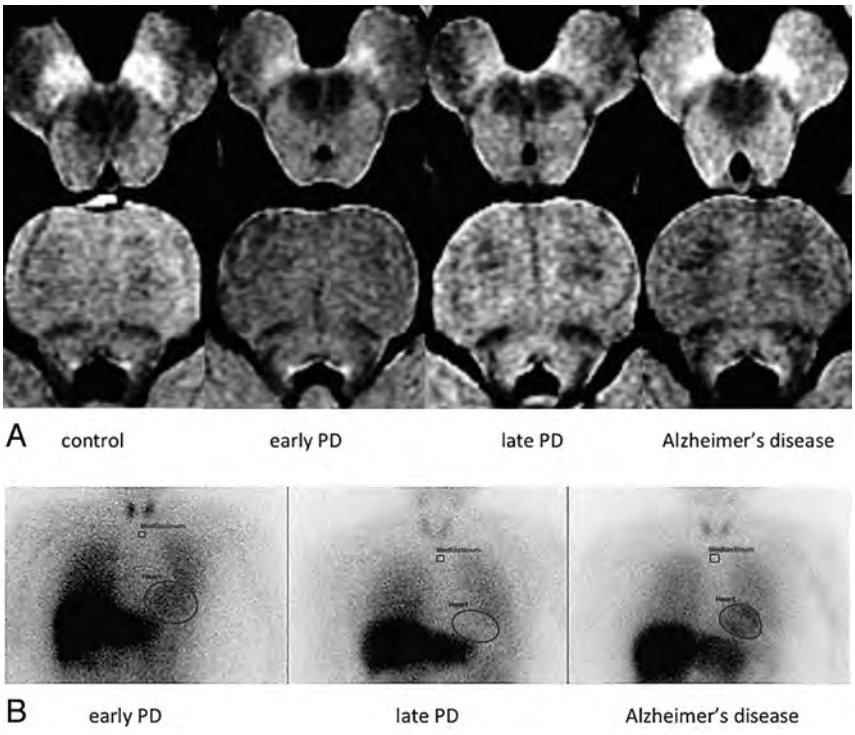

FIG 1. Findings of neuromelanin MRI and ^{123}I-metaiodobenzylguanidine scintigrams of patients and control subjects. *A*, NmMRI: Signals are reduced in NmMRI of substantia nigra pars compacta and locus ceruleus according to Parkinson disease stage. *B*, MIBG scintigraphy: MIBG scintigrams show PD stage-dependent cardiac MIBG reduction.

ROIs in these areas that included high signal intensity on NmMRI. We also defined ROIs symmetrically in the ventral tegmentum located in the anterolateral areas of aqueduct as controls. Concerning the LC, we defined the ROIs in the anterolateral areas around the fourth ventricle at the level of upper pons and also defined ROIs symmetrically in the tegmentum located just behind the medial lemniscus as controls. The sizes of the region of interest were 8, 2, and 10 mm^2 on the SNc, LC, and tegmentum of the midbrain and pons, respectively. We calculated the contrast ratios of the 3 bilateral portions by dividing their signal intensity by that of control areas such as the tegmentum of midbrain and pons.

An ROI was drawn manually over the whole heart on MIBG scintigrams to assess the global myocardial kinetics of MIBG. A second rectangular region of interest over the upper mediastinum served as a background reference region. The attenuation of the MIBG count in the heart and the mediastinum and heart-to-mediastinum count ratios were calculated for the images.

Statistical Analysis

Differences in contrast ratios between early PD, late PD, Alzheimer disease groups, and control subjects in the medial SNc, lateral SNc, and LC on NmMRI and between early PD, late PD, Alzheimer disease groups, and control subjects[17] on MIBG scintigraphy were then statistically analyzed. The medial SNc, lateral SNc, and MIBG scintigrams were analyzed by means of a 1-way analysis of variance and the Bonferroni post hoc test, and the LC was analyzed by means of the Kruskal-Wallis and Dunn post hoc tests. The level of statistical significance was defined as $P < .05$ for all tests. The contrast ratios of NmMRI and MIBG scintigram in early PD, late PD, and Alzheimer disease were analyzed by means of Spearman rank-order correlation coefficient test.

RESULTS

The signal intensity of the lateral SNc on NmMRI was reduced in early and late PD, and that of the medial SNc was gradually and stage-dependently reduced in PD. The signal intensity of LC was obviously reduced in late PD. Signal reduction was not significant in the SNc and LC of patients with Alzheimer disease (Fig 1*A*). The heart-to-mediastinum ratio on MIBG scintigrams was stage-dependently reduced in PD and normal in Alzheimer disease (Fig 1*B*).

Quantitative NmMRI revealed smaller contrast ratios in the lateral SNc of patients with early PD than in that of control patients, and in that of patients with late PD than in that of patients with Alzheimer disease and control subjects ($P <$ .05) (Fig 2*A*). The contrast ratios of the medial SNc were smaller in patients with early PD than in control subjects and in patients with late PD than in those with early PD, Alzheimer disease, and control subjects ($P < .05$) (Fig 2*B*). Contrast ratios in the LC of patients with late PD were smaller than in control patients ($P < .05$) (Fig 2*C*). Signals were not significantly reduced in the SNc and LC on NmMRI of patients with Alzheimer disease compared with control subjects.

The heart-to-mediastinum count ratio on the MIBG scintigram was stage-dependently reduced in patients with PD ($P <$ .05) and normal (mean ± SD, 2.15 ± 0.15[17]) in those with Alzheimer disease (mean ± SD, 2.19 ± 0.40) (Fig 2*D*).

Signal intensity ratios in the SNc on NmMRI positively correlated with heart-to-mediastinum count ratios on MIBG scintigrams (Fig 3). Spearman rank-order correlation coefficients in the medial and lateral SNc were 0.358 and 0.398, respectively, which reached statistical significance (Table 2).

DISCUSSION

Symmetrical spots of high signal intensity were visualized from around the anterolateral region to the floor of the fourth ventricle corresponding to the LC on axial NmMRI of the control group, and symmetrical bandlike high signal intensity was located around the posteromedial region of the cerebral peduncle corresponding to the SNc. Sasaki et al[8] reported that their distribution obviously correlated with those of neuromelanin in gross specimens of the SNc and the LC, suggesting that the high signal intensity areas corresponded to neurons containing neuromelanin. We proved that NmMRI can accurately reflect the amount of neurons containing neuromelanin in the SNc, on the basis of a direct comparison of histopathologic and NmMRI findings of autopsied brains (unpublished data).

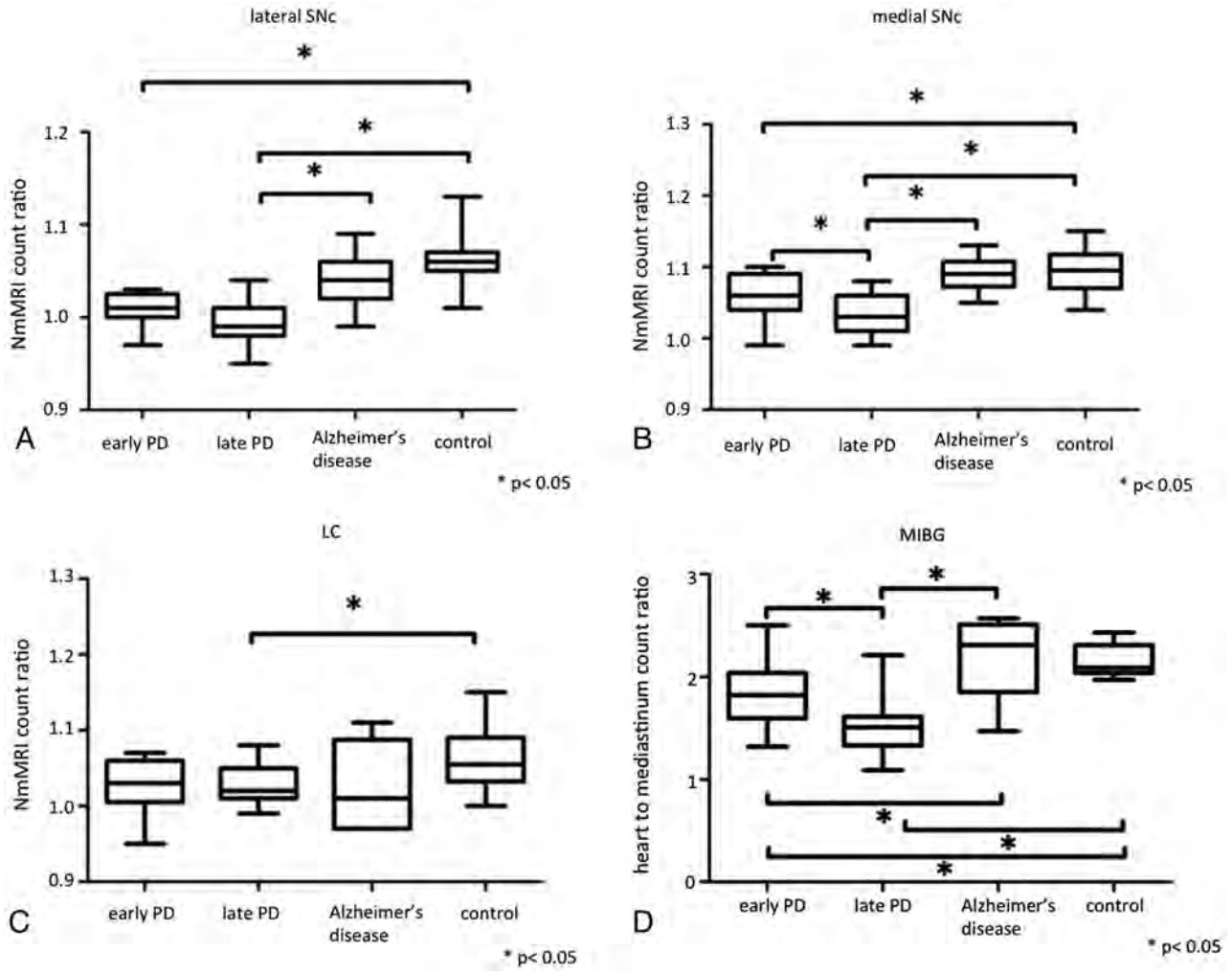

FIG 2. Box-and-whisker plots of signal intensity ratios on neuromelanin MRI and heart-to-mediastinum count ratios on ^{123}I-metaiodobenzylguanidine scintigrams in patients with Parkinson disease, patients with Alzheimer disease, and control subjects. Horizontal bars in boxes show median values. *A,* Lateral substantia nigra pars compacta; *B,* medial SNc; *C,* locus ceruleus; *D,* MIBG. *$P < .05$.

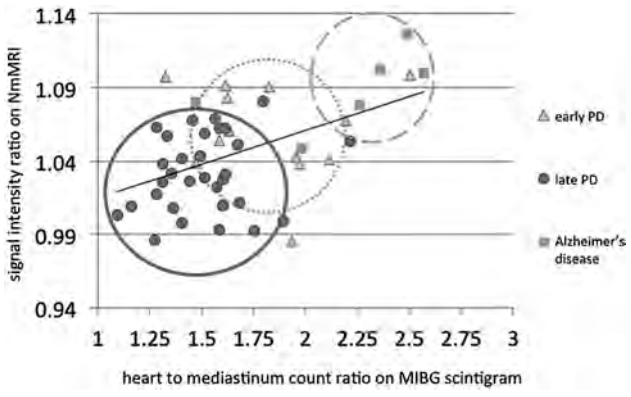

FIG 3. Correlation between signal intensity ratio in medial substantia nigra pars compacta on neuromelanin MRI image and heart-to-mediastinum count ratio on ^{123}I-metaiodobenzylguanidine scintigram. $\rho = 0.3984$.

We found that the contrast ratio of the lateral SNc was significantly decreased in early and late PD and that of the medial SNc gradually and stage-dependently decreased in PD, which corresponded to the pathologic lesions. These findings indicate that

Table 2: Correlation between signal intensity ratio in medial SNc on NmMRI and heart-to-mediastinum count ratio on MIBG scintigraphy

Spearman Coefficient Rate (ρ)	Lateral SNc	Medial SNc	LC
Heart-to-mediastinum count ratio	0.358	0.398	NS

SNc lesions extend from the lateral to the medial regions as PD progresses. Tanaka et al[18] reported that a reduction in neuromelanin contrast started ventrolaterally and advanced medially in the substantia nigra on the basis of a visual assessment of NmMRI. However, the present study is the first effort to quantify medial and lateral SNc by use of NmMRI, to the best of our knowledge.

Braak et al[19] proposed that α-synuclein–immunopositive Lewy neuritis and the accumulation of Lewy bodies that are characteristic pathologic features of PD emerge from the inferior brain stem and ascend to the nuclear gray and cortical areas. However, some studies have also indicated that Lewy bodies and neural cell loss are irrelevant in some regions of the brain in patients with PD. Noradrenergic neurons are relatively well preserved in the LC of patients with early PD, and they undergo different intracellular changes from the SNc.[20]

Reports indicate that the signal intensity of the LC on NmMRI

is significantly reduced in PD.[8] We identified significant signal reductions in the LC of patients with late PD, which suggests that lesions emerge in the LC during late PD. These findings are compatible with the findings of others indicating that the LC plays a compensatory role for the substantia nigra during early PD.[21,22]

Noradrenergic neurons containing neuromelanin in the LC are disrupted in Alzheimer disease, but the clinical or functional importance of such disruption remains unclear.[7] Some reports suggest that a reduction in the number of noradrenergic neurons affects the accumulation of β-amyloid, inflammation, or microcirculation in the LC.[23,24] Our NmMRI study could not identify a significant signal reduction in the LC of patients with Alzheimer disease. Busch et al[25] reported that the LC begins to lose cells only during the later stages of Alzheimer disease. Therefore, we consider that this result can be attributed to the relatively short duration (2.5 years) of the disease and the small number of patients with Alzheimer disease in this study. Signals were significantly more reduced in the medial and lateral SNc of patients with late PD compared with Alzheimer disease, which is useful for differentiating these diseases.

The neurologic diseases with significant reduction in MIBG scintigraphy uptake include PD, dementia with Lewy bodies, and pure autonomic failure, and they are recognized as characteristic findings of Lewy-body diseases. On the other hand, heart-to-mediastinum count ratios are higher in Parkinson syndromes such as multiple system atrophy, progressive supranuclear palsy, and corticobasal degeneration than in PD. Therefore, MIBG scintigraphy is an important supportive tool for discerning Parkinson syndromes.[26] Sympathetic nerves in patients with PD are generally disturbed, and Lewy bodies are found in sinoatrial nodal ganglia, the myocardium, and paravertebral ganglia.[27,28] A pathologic investigation has revealed that sympathetic nerve fibers are significantly reduced in patients with PD and well preserved in those with Alzheimer disease.[29] Although the heart-to-mediastinum count ratio is reduced on MIBG scintigrams of early PD, its relationship with progression remains controversial.[29,30] In our present study, we found that the heart-to-mediastinum count ratio was significantly lower in late PD than early PD, indicating that signal reduction is stage-dependent. On the other hand, we could not exclude the effect of a possible relationship between heart-to-mediastinum signal reduction and duration. The heart-to-mediastinum count ratio was well-preserved in patients with Alzheimer disease, which helped to differentiate it from late PD.

To the best of our knowledge, this is the first comparison of brain NmMRI and MIBG scintigraphy of PD and Alzheimer disease. We identified a weak correlation in the SNc, implying that the findings of both modalities can serve as indicators of progressive PD, which involves both the central and peripheral autonomic nervous systems. Our results revealed that the autonomic nervous system gradually becomes disturbed over time.

The limitations of the present study are as follows. Because the study comprised very few patients with Alzheimer disease, further studies of a large population are required to validate our findings. Second, iron concentrations in the SNc that increase with age can mask signal alterations on NmMRI.[3] Therefore, we could not exclude this effect when evaluating neuromelanin in elderly individuals. Third, the low spatial resolution of NmMRI did not allow 3D image acquisition. Therefore, measurement errors might have arisen due to partial volume effects particularly when assessing changes in the LC.

CONCLUSIONS

The SNc becomes disturbed from the lateral to the medial region on NmMRI of the SNc as PD progresses and the LC is also disturbed in late PD. The sympathetic nerves in the left cardiac ventricle are also disturbed in MIBG scintigrams of PD. Thus, NmMRI and MIBG scintigraphy can be helpful tools to evaluate PD progression and to differentiate PD from Alzheimer disease.

ACKNOWLEDGMENTS

We thank Eijirou Yamashita, PhD, of the Division of Clinical Radiology, Tottori University Hospital, for support with MR imaging.

REFERENCES

1. Pahwa R, Lyons KE. **Early diagnosis of Parkinson's disease: recommendations from diagnostic clinical guidelines.** *Am J Manag Care* 2010;16(Suppl):S94–99
2. Fedorow H, Tribl F, Halliday G, et al. **Neuromelanin in human dopamine neurons; comparison with peripheral melanins and relevance to Parkinson's disease.** *Prog Neurobiol* 2005;75:109–24
3. Zecca L, Tampellini D, Gerlach M, et al. **Substantia nigra neuromelanin: structure, synthesis, and molecular behavior.** *Mol Pathol* 2001;54:414–18
4. Damier P, Hirsch EC, Agid Y, et al. **The substantia nigra of the human brain, II: patterns of loss of dopamine-containing neurons in Parkinson's disease.** *Brain* 1999;122:1437–48
5. Fearnley JM, Lees AJ. **Aging and Parkinson's disease: substantia nigra regional selectivity.** *Brain* 1991;114:2283–301
6. Halliday GM, McRitchie DA, Cartwright HR, et al. **Midbrain neuropathology in idiopathic Parkinson's disease and diffuse Lewy body disease.** *J Clin Neurosci* 1996;3:52–60
7. Förstl H, Burns A, Luthert P, et al. **Clinical and neuropathological correlates of depression in Alzheimer's disease.** *Psychol Med* 1992;22:877–84
8. Sasaki M, Shibata E, Tohyama K, et al. **Neuromelanin magnetic resonance imaging of locus ceruleus and substantia nigra in Parkinson's disease.** *NeuroReport* 2006;17:1215–18
9. Mann DM, Yates PO. **Possible role of neuromelanin in the pathogenesis of Parkinson's disease.** *Mech Ageing Dev* 1983;21:193–203
10. Schwarz ST, Rittman T, Gontu V, et al. **T1-weighted MRI shows stage-dependent substantia nigra signal loss in Parkinson's disease.** *Mov Disord* 2011;26:1633–38
11. Kashihara K, Shinya T, Higaki F. **Neuromelanin magnetic resonance imaging of nigral volume loss in patients with Parkinson's disease.** *J Clin Neurosci* 2011;18:1093–96
12. Wieland DM, Brown LE, Rogers WL, et al. **Myocardial imaging with a radioiodinated norepinephrine storage analog.** *J Nucl Med* 1981;22:22–31
13. Druschky A, Hilz MJ, Platsch G, et al. **Differentiation of Parkinson's disease and multiple system atrophy in early disease stages by means of I-123-MIBG-SPECT.** *J Neurol Sci* 2000;175:3–12
14. Spiegel J, Hellwig D, Farmakis G, et al. **Myocardial sympathetic degeneration correlates with clinical phenotype of Parkinson's disease.** *Mov Disord* 2007;22:1004–08
15. Hoehn MM, Yahr MD. **Parkinsonism: onset, progression and mortality.** *Neurology* 1967;17:427–42
16. Imai Y, Hasegawa K. **The revised Hasegawa's dementia scale (HDS-R) - evaluation of its usefulness as a screening test for dementia.** *J Hong Kong Coll Psychiatr* 1994;4:20–24
17. Tanabe Y, Harada H, Sugihara S, et al. **123I-metaiodobenzylguani-**

dine myocardial scintigraphy in panic disorder. *J Nucl Med* 2004;45:1305–08
18. Tanaka M, Aihara Y, Ikeda S, et al. **Neuromelanin-related contrast in the substantia nigra semiquantitatively evaluated by magnetic resonance imaging at 3T: comparison between normal aging and Parkinson disease.** *Clin Neurol* 2011;51:14–20
19. Braak H, Del Tredici K, Rub U, et al. **Staging of brain pathology related to sporadic Parkinson's disease.** *Neurobiol Aging* 2003;24: 197–211
20. Halliday GM, Ophof A, Broe M, et al. **α-Synuclein redistributes to neuromelanin lipid in the substantia nigra early in Parkinson's disease.** *Brain* 2005;128:2654–64
21. Isaias IU, Marotta G, Pezzoli G, et al. **Enhanced catecholamine transporter binding in the locus coeruleus of patients with early Parkinson disease.** *BMC Neurol* 2011;11:88
22. Rommelfanger KS, Weinshenker D. **Norepinephrine: the redheaded stepchild of Parkinson's disease.** *Biochem Pharmacol* 2007;74: 177–90
23. Weinshenker D. **Functional consequences of locus coeruleus degeneration in Alzheimer's disease.** *Curr Alzheimer Res* 2008;5:342–45
24. Haneka MT, Nadrigny F, Regen T, et al. **Locus ceruleus controls Alzheimer's disease pathology by modulating microglial functions through norepinephrine.** *Proc Natl Acad Sci U S A* 2010;107: 6058–63
25. Busch C, Bohl J, Ohm TG. **Spatial, temporal and numeric analysis of Alzheimer changes in the nucleus ceruleus.** *Neurobiol Aging.* 1997;18:401–06
26. Nakajima K, Yoshita M, Matsuo S, et al. **Iodine-123-MIBG sympathetic imaging in Lewy-body diseases and related movement disorders.** *J Nucl Med Mol Imaging* 2008;52:378–87
27. Okada Y, Ito Y, Aida J, et al. **Lewy bodies in the sinoatrial nodal ganglion: clinicopathological studies.** *Pathol Int* 2004;54:682–87
28. Orimo S, Takahashi A, Uchihara T, et al. **Degeneration of cardiac sympathetic nerve begins in the early disease process of Parkinson's disease.** *Brain Pathol* 2007;17:24–30
29. Rascol O, Schelosky L. **^{123}I-metaiodobenzylguanidine scintigraphy in Parkinson's disease and related disorders.** *Mov Disord* 2009; 24(Suppl 2):S732–41
30. Watanabe M, Takeda T, Nakamagoe K, et al. **Sequential imaging analysis using MIBG scintigraphy revealed progressive degeneration of cardiac sympathetic nerve in Parkinson's disease.** *Eur J Neurol* 2011;18:1010–13

Normal-Appearing White Matter Permeability Distinguishes Poor Cognitive Performance in Processing Speed and Working Memory

A. Eilaghi, A. Kassner, I. Sitartchouk, P.L. Francis, R. Jakubovic, A. Feinstein, and R.I. Aviv

ABSTRACT

BACKGROUND AND PURPOSE: Secondary-progressive MS is characterized by reduced acute inflammation and contrast enhancement but with increased axonal degeneration and cognitive/clinical disability that worsens with advanced disease. Relative recirculation, extracted from DSC is a surrogate measure of BBB integrity. We hypothesized that normal-appearing white matter relative recirculation is reduced in cognitively impaired compared with nonimpaired secondary-progressive MS, reflecting more advanced disease.

MATERIALS AND METHODS: Cognitive performance was classified as impaired or nonimpaired by use of Minimal Assessment of Cognitive Function In MS test components. Demographic data, brain parenchymal fraction, WM lesion fraction, and weighted mean normal-appearing white matter relative recirculation were compared in cognitively dichotomized groups. Univariate and multivariate logistic regressions were used to study the association between cognitive test results and normal-appearing white matter relative recirculation.

RESULTS: The mean (SD) age of 36 patients with secondary-progressive MS studied was 55.9 ± 9.3 years; 13 of 36 (36%) patients were male. A highly significant difference between normal-appearing white matter relative recirculation and WM lesion relative recirculation was present for all patients ($P < .001$). Normal-appearing white matter relative recirculation in impaired patients was significantly lower than in nonimpaired subjects for the Symbol Digit Modalities Test ($P = .007$), Controlled Word Association Test ($P = .008$), and Paced Auditory Serial Addition Test ($P = .024$). The Expanded Disability Status Scale demonstrated an inverse correlation with normal-appearing white matter relative recirculation ($r = -0.319$, $P = .075$). After adjustment for confounders, significant normal-appearing white matter relative recirculation reduction persisted for the Symbol Digit Modalities Test ($P = .023$) and the Paced Auditory Serial Addition Test ($P = .047$) but not for the Controlled Word Association Test ($P = .13$) in impaired patients.

CONCLUSIONS: Significant normal-appearing white matter relative recirculation reduction exists in cognitively impaired patients with secondary-progressive MS, localizing to the domains of processing speed and working memory.

ABBREVIATIONS: rR = relative recirculation; NAWM = normal-appearing white matter; SPMS = secondary-progressive MS; RRMS = relapsing-remitting MS

MS is the most common inflammatory demyelinating disease of the central nervous system. Although the underlying etiology of the disease is still largely unknown, inflammation, demyelination, and neurodegeneration are pathologically implicated and eventually cause long-term impairment.[1] Cognitive impairment is reported in 40–70% of MS cases,[2] and the frequency and expression of impairment increases with disease duration.[3] Secondary-progressive MS is clinically distinct from relapsing-remitting MS. Patients with secondary-progressive MS do not manifest acute attacks[4] and demonstrate diminished response to immunosuppressives,[4] reduced lesional gadolinium enhancement,[5] and diffuse NAWM inflammation and axonal injury.[6]

Traditional structural markers including WM lesion load and cortical and WM atrophy demonstrate variable correlation with cognitive impairment.[7] Advanced MR imaging techniques are increasingly being investigated as surrogate markers of cognition. Techniques such as magnetization transfer imaging,[8] diffusion-

Received November 8, 2012; accepted after revision December 19.

From the Department of Medical Imaging (A.E., P.L.F., R.J., R.I.A.) and Department of Psychiatry (A.F.), Sunnybrook Health Sciences Centre, Toronto, Ontario, Canada; Department of Medical Biophysics (A.E.), University of Western Ontario, London, Ontario, Canada; Department of Medical Imaging (A.K., I.S., R.I.A.), University of Toronto, Toronto, Ontario, Canada; and Department of Physiology and Experimental Medicine (A.K.), Hospital for Sick Children, Toronto, Ontario, Canada.

Please address correspondence to Richard I. Aviv, MBChB, Sunnybrook Health Sciences Centre, 2075 Bayview Ave, Room AG 31, Toronto, Ontario M4N 3M5, Canada; e-mail: richard.aviv@sunnybrook.ca

Indicates article with supplemental on-line table

http://dx.doi.org/10.3174/ajnr.A3539

weighted imaging,[9] functional MR imaging,[10] MR spectroscopy,[11] and perfusion imaging[12] have previously been described. In RRMS, localized inflammation and BBB breakdown depicted with gadolinium-enhanced T1-weighted MR imaging are traditionally associated with disease activity.[13,14] Unlike RRMS, SPMS is characterized by reduced acute inflammation and few contrast-enhancing lesions.[5] A number of mechanisms are described for the reduced apparent inflammation, including "compartmentalization" of the inflammatory response behind an intact BBB,[6] balanced inflammation, activation of endogenous neuroprotection mechanisms,[15,16] and continued neurodegeneration independent of inflammation.[6,17] Despite a reduction of acute inflammatory changes, SPMS is associated with a higher prevalence of axonal degeneration, disability, and cognitive impairment, particularly in the domains of attention and processing speed. These functional domains may therefore serve as markers of more advanced axonal degeneration, distinguishing SPMS subgroups with more advanced disease.[18]

Relative recirculation (rR), a parameter extracted from DSC MR imaging, is shown to successfully identify regions of BBB breakdown in patients with brain tumors,[19,20] Moyamoya syndrome,[21] and acute ischemic stroke.[22] rR is a quantitative measure of contrast recirculation abnormalities after the first pass and is a practical surrogate for BBB permeability estimates that does not necessitate a separate dynamic contrast-enhanced MR imaging acquisition.[22] The role of rR as a surrogate measure of BBB integrity in MS has not been evaluated. The purpose of this study was to compare rR in SPMS subgroups with and without cognitive impairment. We hypothesized that NAWM rR would be lower in cognitively impaired compared with nonimpaired patients with SPMS, reflecting a more advanced disease state. We also hypothesized that rR would be higher in WM lesions compared with NAWM.

MATERIALS AND METHODS

Patient Cohort

The study was performed in accordance with our institution's guidelines for human research. Written informed consent was obtained for all imaging studies. Patients with clinically diagnosed SPMS were prospectively recruited from tertiary referral clinics. Two senior neurologists (20 years of experience) screened potential subjects to ensure they fulfilled the revised McDonald criteria. Exclusion criteria included patients with a history of drug/alcohol abuse, disease modifying drug or steroid use within the last 6 months, premorbid psychiatric history, head injury with loss of consciousness, concurrent medical diseases (eg, cerebrovascular disease), and MR imaging or contrast agent contraindications. Thirty-six patients with secondary-progressive MS fulfilled the screening criteria and were included in the study. Demographic data obtained included age, sex, years of education, and disease duration. Expanded Disability Status Scale assessment and cognitive testing was completed by a senior neurologist. No Expanded Disability Status Scale threshold was applied to patient eligibility. Neurologic examination, Expanded Disability Status Scale, and neurocognitive assessments were completed in order, on the same day within 6 hours of each other.

Imaging Protocol

Imaging parameters included volumetric T1 turbo field-echo (TR/TE/flip angle: 9.5 ms/2.3 ms/12°; number of averages: 1; FOV: 24 cm; matrix size: 256 × 164; section thickness: 1.4 mm); proton attenuation/T2 (TR/TE/flip angle: 2900 ms/10.7 ms/90°; FOV: 23 cm; matrix: 256 × 261; section thickness: 3 mm); field-echo echo-planar imaging DSC (for rR calculation) (TR/TE/flip angle: 1610 ms/30 ms/60°; FOV: 22 cm; section thickness: 4 mm; matrix: 128 × 128; in-plane voxel size: 1.7 × 1.7 mm; no gap; signal bandwidth: 1260 Hz/pixel). Ten milliliters of gadobutrol (Gadovist; Bayer, Toronto, Canada) (1 mmol/mL) was administered by a power injector at a rate of 5 mL/s followed by a 25-mL bolus of saline at 5 mL/s. Sixty volumes were acquired at 1.6-second intervals with the injection occurring at the 10th volume. DSC acquisition covered 10 cm (25 sections at 4 mm per section) and extended from the cerebral convexity to the midbrain level. Acquisition placement was supervised by an experienced neuroradiologist (8 years of experience) to ensure consistent coverage across patients.

Image Analysis

Gray matter, WM, and CSF were segmented from T1-weighted scans by use of a previously validated tissue segmentation method.[23] Segmented regions were imported into Analyze 8.0 (Analyze AVW, Rochester, Minnesota),[24] and WM lesion regions of interest were manually drawn. Brain parenchymal and WM lesion fractions were calculated as previously described.[25] NAWM regions of interest were selected from within the WM tissue by use of four 16-voxel blocks located in anterior and posterior regions of both hemispheres. All WM lesion and NAWM regions of interest were subsequently co-registered to the equivalent DSC-MR imaging datasets by means of the rigid body algorithm of Statistical Parametric Mapping version 8 (SPM8; Wellcome Department of Imaging Neuroscience, London, United Kingdom). Contrast enhancement was systematically evaluated by use of a cross-reference tool by comparing FLAIR and proton attenuation/T2 lesions with precontrast and postcontrast imaging.

rR was calculated within each region of interest by use of in-house software (MR Analyst version 4.0) developed in Matlab (MathWorks, Natick, Massachusetts).[22] In brief, selected DSC perfusion datasets were preprocessed by inspecting signal intensity versus time curves for outlier data points. Spurious points were identified by visual inspection and replaced with interpolated values. The first 2 dynamic phases were automatically omitted because magnetization cannot be assumed to have reached steady-state this early in the series. For each region of interest and each DSC image, the T2* relaxation rate was determined by evaluating the change in signal intensity from baseline and assuming[26]:

$$1) \qquad \Delta R_2{}^*{}_{\text{measured}} = -\ln(\Delta SI)/TE$$

$\Delta R2^*$measured data were subsequently fitted to a γ-variate function to produce a theoretic first-pass ΔR2*theoretic curve, that is, one that was free of recirculation effects. The rR was calculated as described by Kassner et al[27] as:

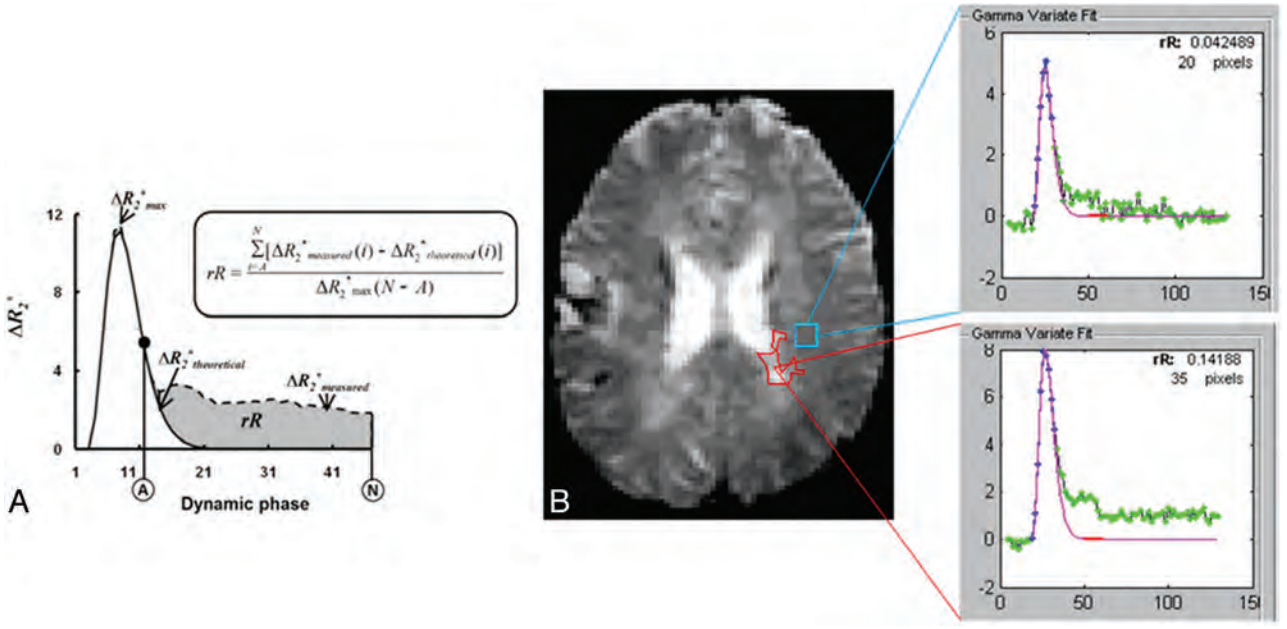

FIG 1. *A*, Estimation of *rR* by use of the ΔR_2^* versus time curve measured from the DSC regions of interest ($\Delta R_2^*_{measured}$) as well as its γ-variate fit ($\Delta R_2^*_{fit}$). $\Delta R_2^*_{max}$ is the maximum of $\Delta R_2^*_{theoretical}$. *A* is the dynamic phase corresponding to the onset of the recirculation phase measured at half-height of the descending aspect of the ΔR_2^* curve, and *N* is the final DSC phase. *B*, Example of rR measurement: case 733, section 11, perfusion scan. MS lesion (red region of interest) and NAWM (blue region of interest) and rR calculation results. rR for WM lesion is 0.142; rR for NAWM region is 0.042.

$$2) \qquad rR = \frac{\sum_{i=A}^{N} [\Delta R_2^* measured(i) - \Delta R_2^*_{theoretical}(i)]}{\Delta R_2^*_{max}(N - A)}$$

where $\Delta R_2^*_{max}$ is the maximum of $\Delta R_2^*_{theoretical}$, *A* is the dynamic phase corresponding to the onset of the recirculation phase measured at half-height of the descending aspect of the ΔR_2^* curve, and *N* is the final dynamic phase (Fig 1). Mean WM lesion rR and NAWM rR were determined for each patient by calculating the weighted average over WM lesion and NAWM regions of interest, respectively.

Cognitive Assessment

Cognitive assessments were performed by a neuropsychiatrist (20 years of experience) by use of an MS-specific neurocognitive tool, which is a 90-minute neurocognitive test proposed by an expert panel for clinical monitoring and research.[28] The Minimal Assessment of Cognitive Function in Multiple Sclerosis is a comprehensive and efficient assessment tool consisting of 7 neuropsychological tests: Paced Auditory Serial Addition Test [working memory/processing speed], Symbol Digit Modalities Test [processing speed], California Verbal Learning Test, 2nd edition [verbal memory], Brief Visuospatial Memory Test, revised [visuospatial memory], Delis-Kaplan Executive Function System [executive function], Controlled Word Association Test [verbal fluency], and judgment of line orientation [visuospatial perception].Impairment on an individual test was defined as scoring >1.5 standard deviations below normative data from healthy controls. Beck Depression Inventory and the Expanded Disability Status Scale were also obtained.

Statistical Analysis

Univariate comparisons of demographic data for impaired and nonimpaired groups were performed by use of the Mann-Whitney rank sum test. Demographic data were expressed as mean (SD) for continuous variables such as age, education, and disease duration; median with interquartile range for categorical variables such as the Beck Depression Inventory and the Expanded Disability Status Scale; and proportions for binary data such as sex. Segmented regional data for brain parenchymal fraction, gray matter fraction, WM fraction, and WM lesion fraction were similarly compared. The 10th and 90th percentile values for rR distribution of each group were calculated, and values beyond these limits were excluded. For each cognitive test, potentially confounding factors of age, sex, years of education, disease duration, Beck Depression Inventory score, Expanded Disability Status Scale, brain parenchymal fraction, WM fraction, WM lesion fraction, and gray matter fraction were compared. Potential confounders with *P* values <0.3 (On-line Table) were included in further multivariate logistic regression. All statistical analyses were performed in SigmaStat3.5 (Systat Software, San Jose, California).

RESULTS

There were 36 patients, with a mean (SD) age of 55.9 ± 9.3 years; 13 of 36 (36%) were male. Mean (SD) years of education and disease duration were 15.3 (2.6) and 20.4 (10.0). Median (IQR) for the Beck Depression Inventory and the Expanded Disability Status Scale were 8 (5–11) and 6.5 (6.0–7.0). Mean (SD) brain parenchymal fraction, WM fraction, WM lesion fraction, and gray matter fraction were 80.6 (4.1), 36.7 (3.0), 1.4 (1.2), and 41.5 (2.4), respectively. A highly significant difference between

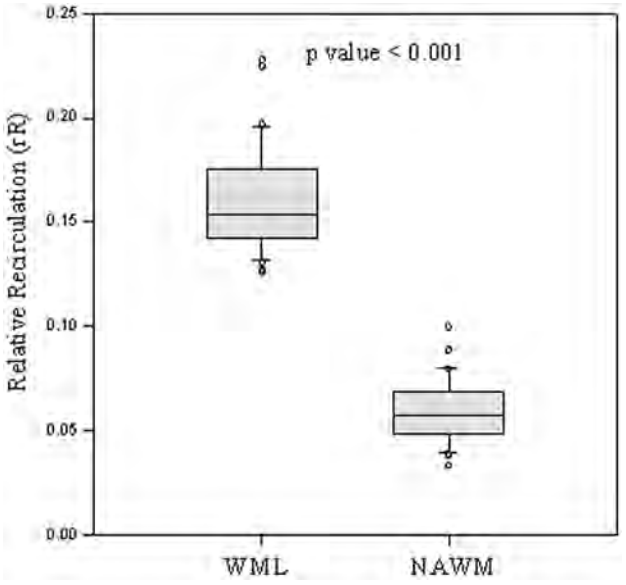

FIG 2. rR values of NAWM and WM lesion.

Outcomes of multivariate logistic regression analyses for NAWM rR after controlling for potential confounders

Cognitive Test	Odds Ratio (5–95% CI)	*P* Value
SDMT	0.177 (0.040–0.785)	.023
COWAT	0.662 (0.002–2.226)	.130
PASAT 1.6	0.053 (0.003–0.961)	.047

Note:—SDMT indicates Symbol Digit Modalities Test; COWAT, Controlled Word Association Test; PASAT, Paced Auditory Serial Addition Test.
Confounders for Symbol Digit Modalities Test: brain parenchymal fraction, WM fraction, WM lesion fraction; Controlled Word Association Test: WM fraction, WM lesion fraction, gray matter fraction; and Paced Auditory Serial Addition Test: brain parenchymal fraction, WM fraction, WM lesion fraction.
NAWM rR continues to be significantly lower in the impaired group for both the Symbol Digit Modalities Test and the Paced Auditory Serial Addition Test.

NAWM rR and WM lesion rR was present for all patients ($P <$ .001; Fig 2). No enhancing WM lesions were present in either SPMS subgroup.

No significant differences between NAWM rR in impaired and nonimpaired patients were observed for the Brief Visuospatial Memory Test ($P = .161$), judgment of line orientation ($P = .493$), California Verbal Learning Test ($P = .669$), or Delis-Kaplan Executive Function System ($P = .680$) impairment. NAWM rR was significantly lower in impaired patients than in nonimpaired subjects for the Symbol Digit Modalities Test ($P = .007$), Controlled Word Association Test ($P = .008$), and Paced Auditory Serial Addition Test ($P = .024$) (On-line Table). The mean WM lesion fraction was higher in impaired patients (0.02) than in nonimpaired (0.01) for all tests (Symbol Digit Modalities Test: $P = .020$; Controlled Word Association Test: $P = .014$; and Paced Auditory Serial Addition Test: $P = .033$). No significant correlation was found between NAWM rR with brain parenchymal fraction ($\rho = 0.010$; $P = .955$), WM fraction ($\rho = 0.187$; $P = .272$), WM lesion fraction ($\rho = -0.260$; $P = .124$), or GM fraction ($\rho = -0.295$; $P = .080$).

After adjusting for confounders (Table 1), significant NAWM rR reduction persisted in impaired patients for the Symbol Digit Modalities Test ($P = .023$) and Paced Auditory Serial Addition Test ($P = .047$) (Table) but not for the Controlled Word Association Test impairment ($P = .13$). Figure 3 illustrates the distribution of rR values of NAWM for impaired and nonimpaired Symbol Digit Modalities Test and Paced Auditory Serial Addition Test groups. The Paced Auditory Serial Addition Test and Symbol Digit Modalities Test in impaired patients demonstrated a 3.2- and 4.6-year longer disease duration than in their nonimpaired counterparts. The difference did not however reach clinical significance ($P = .3$ and $P = .6$, respectively).

The Expanded Disability Status Scale demonstrated an inverse correlation with NAWM rR (correlation coefficient = −0.319, $P = .075$).

DISCUSSION

NAWM rR reduction was present in patients with secondary-progressive MS with poor performance on the Paced Auditory Serial Addition Test and Symbol Digit Modalities Test representing deficits in processing speed and working memory. NAWM rR values were significantly lower in impaired patients persisting after correction for potential confounding factors. Secondarily, WM lesion rR was higher than NAWM for all patients irrespective of cognitive impairment and in the absence of overt contrast enhancement.

Acute inflammation and BBB permeability in RRMS, manifesting as enhancing lesions, are linked with clinical and cognitive disability. The progressive phase of MS, however has a distinct disease pathogenesis compared with the acute or relapsing-remitting phases.[29,30] SPMS is characterized by progressive axonal degeneration with clinical and cognitive disability but little lesion enhancement. A number of explanations for these findings are offered. Concepts of balanced inflammation, activation of endogenous neuroprotection mechanisms,[15,16] entrapped inflammation behind intact or repaired BBB,[6] and continued neurodegeneration independent of inflammation[17] were previously proposed. Zeis et al[15] demonstrated that genes known to be involved in anti-inflammatory and protective mechanisms are upregulated more regularly than pro-inflammatory mechanisms in NAWM in progressive MS. Correlation between brain atrophy and cognitive impairment increases with longer disease duration and SPMS subtype, in which impairment is reported in 50% of patients.[2,3,18] In the present study, therefore, the association between cognitive impairment as a marker of disease severity and rR reduction as a surrogate marker of reduced measurable inflammation is expected. Supporting the association between disease duration, increased disability, and inflammation is the observed negative correlation between NAWM rR and disease severity (measured by the Expanded Disability Status Scale) in the present study.[31] Additionally, cognitively impaired patients demonstrated longer disease duration than did cognitively nonimpaired patients, though this did not reach statistical significance.

Information processing speed and working memory are the most affected cognitive domains in patients with MS.[3,32] The Symbol Digit Modalities Test and Paced Auditory Serial Addition Test have been shown in large series to be sensitive indicators of impairments in these domains.[33] Both the Symbol Digit Modalities Test and Paced Auditory Serial Addition Test correlate with several brain imaging findings such as lesion volume and central cerebral atrophy.[34-36] The correlation expectedly increases with disease duration and SPMS subtype reflecting greater disease burden and axonal degeneration.[18] Previous studies also show that

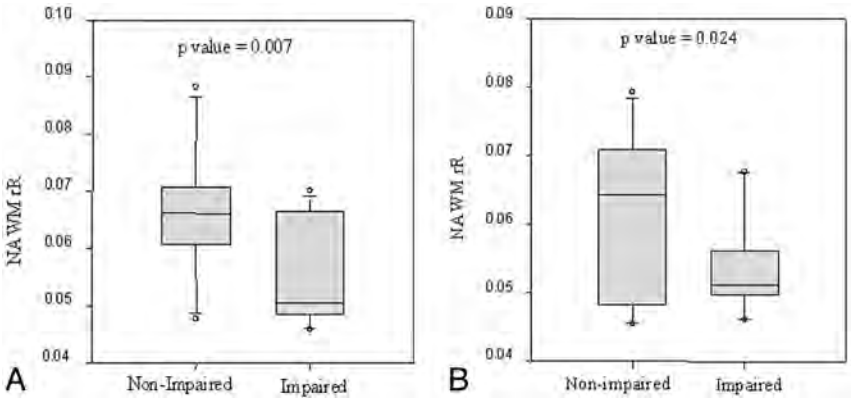

FIG 3. rR values of NAWM are significantly lower in impaired than in nonimpaired groups by use of *A*, the Symbol Digit Modalities Test ($P = .007$), and *B*, the Paced Auditory Serial Addition Test ($P = .024$).

NAWM abnormalities, even independent of lesion location, may correlate with cognition response.[37] NAWM abnormalities measured by diffusion-weighted MR imaging also predict the speed of information deficits in MS.[3,14] Our study, like others,[3] highlights the need for longitudinal study of associations between NAWM abnormalities and cognitive impairment.

In RRMS, contrast enhancement indicates increased risk of relapses and may also be associated with long-term dysfunction.[38] However, contrast enhancement is weakly correlated with clinical attacks[39] and is age-dependent.[40] For enhancement to be present, a critical but unknown degree of BBB permeability must be present. Prior quantitative analysis of enhancement demonstrates the dose and time dependency of enhancement and the relative insensitivity of qualitative designation of enhancement.[41] rR as a surrogate marker of permeability was first studied in brain tumors[19,20] and Moyamoya syndrome.[21] More recently, rR was shown to strongly correlate ($r = 0.67$) with an established measure of BBB permeability (KPS) in acute ischemic stroke.[22] Relative recirculation has the advantage of being extracted from standard DSC-MR imaging acquisitions without the need for a further contrast injection required for KPS determination. This is particularly important given the relationship between increasing contrast use and nephrogenic systemic fibrosis.[42] Additionally, unlike KPS, the technique is model-free, with no need to obtain an input function avoiding a potential source of noise,[43] as recently described.[44] Last, rR provides a surrogate measure of BBB permeability as a continuum as compared with the current "binary" view of contrast enhancement as present or absent.

The study is limited by a relatively small sample size. As an exploratory study, we analyzed a strictly homogeneous selection of patients with secondary-progressive MS, controlling for multiple potentially confounding structural parameters. Pragmatically, because of high lesion load, NAWM was selected from the bilateral centrum semiovale, representing the largest WM region available for interrogation. Cognition represents a complex interplay of multiple domains that cannot be captured by a single region of interest at any location. However, injury to the centrum is strongly associated with neurocognitive dysfunction in leukoaraiosis,[45] carbon monoxide poisoning,[46] and trauma,[47] potentially mediated by "disconnection" of important projection and association fibers.[45] However, despite these limitations, significant results were obtained for the Paced Auditory Serial Addition Test and the Symbol Digit Modalities Test, both sensitive indicators of information processing speed and working memory. Although perfusion and permeability techniques offer potential useful adjuncts to conventional imaging for monitoring disease activity, they are affected by recent bouts of acute inflammation, disease-modifying drugs, and steroid use. These limitations may limit their applicability in relapsing-remitting MS subgroups as the result of the heterogeneous nature of treatment and inflammation present but are less of a concern within the secondary-progressive MS subgroup. We limited our focus to patients with secondary-progressive MS because of the higher rate of cognitive impairment and relative stability of the disease. Future studies would benefit from control comparison and well-controlled relapsing-remitting MS cohorts. Nevertheless, the results appear clinically meaningful, warranting further exploration of the association between rR, cognition, disease progression, and treatment response. If an association is found, rR could be a useful target for future pharmacologic and rehabilitative treatment strategies.

CONCLUSIONS

Significant NAWM rR reduction exists in cognitively impaired patients with SPMS, localizing to the domains of processing speed and working memory.

Disclosures: Andrea Kassner—*RELATED: Grant:* Canada Research Chair, Comments: Salary award and research allowance. Anthony Feinstein—*UNRELATED: Grants/Grants Pending:* MS Society of Canada;* *Payment for Lectures (including service on speakers bureaus):* Speakers honoraria paid to me from Merck Serono, Biogen, Teva, and Novartis; *Royalties:* Cambridge University Press. Richard Aviv—*RELATED: Grant:* MS Society,* PSI,* (**money paid to institution*).

REFERENCES

1. Barnett MH, Sutton I. **The pathology of multiple sclerosis: a paradigm shift.** *Curr Opin Neurol* 2006;19:242–47
2. Chiaravalloti ND, DeLuca J. **Cognitive impairment in multiple sclerosis.** *Lancet Neurol* 2008;7:1139–51
3. Filippi M, Rocca MA, Benedict RH, et al. **The contribution of MRI in assessing cognitive impairment in multiple sclerosis.** *Neurology* 2010;75:2121–28
4. Compston A, Coles A. **Multiple sclerosis.** *Lancet* 2008;372:1502–17
5. Soon D, Tozer DJ, Altmann DR, et al. **Quantification of subtle blood-brain barrier disruption in non-enhancing lesions in multiple sclerosis: a study of disease and lesion subtypes.** *Mult Scler* 2007;13:884–94
6. Kutzelnigg A, Lucchinetti CF, Stadelmann C, et al. **Cortical demyelination and diffuse white matter injury in multiple sclerosis.** *Brain* 2005;128(Part 11):2705–12
7. Sperling RA, Guttmann CR, Hohol MJ, et al. **Regional magnetic resonance imaging lesion burden and cognitive function in multiple sclerosis: a longitudinal study.** *Arch Neurol* 2001;58:115–21
8. van Buchem MA, Grossman RI, Armstrong C, et al. **Correlation of**

volumetric magnetization transfer imaging with clinical data in MS. *Neurology* 1998;50:1609–17
9. Benedict RH, Bruce J, Dwyer MG, et al. **Diffusion-weighted imaging predicts cognitive impairment in multiple sclerosis.** *Mult Scler* 2007;13:722–30
10. Mainero C, Caramia F, Pozzilli C, et al. **fMRI evidence of brain reorganization during attention and memory tasks in multiple sclerosis.** *Neuroimage* 2004;21:858–67
11. Penny S, Khaleeli Z, Cipolotti L, et al. **Early imaging predicts later cognitive impairment in primary progressive multiple sclerosis.** *Neurology* 2010;74:545–52
12. Inglese M, Adhya S, Johnson G, et al. **Perfusion magnetic resonance imaging correlates of neuropsychological impairment in multiple sclerosis.** *J Cereb Blood Flow Metab* 2008;28:164–71
13. Zivadinov R, Sepcic J. **[Use of magnetic resonance imaging in the diagnosis and prognosis of multiple sclerosis].** *Lijec Vjesn* 2006;128:295–308
14. Filippi M, Agosta F. **Imaging biomarkers in multiple sclerosis.** *J Magn Reson Imaging* 2010;31:770–88
15. Zeis T, Graumann U, Reynolds R, et al. **Normal-appearing white matter in multiple sclerosis is in a subtle balance between inflammation and neuroprotection.** *Brain* 2008;131(Part 1):288–303
16. Graumann U, Reynolds R, Steck AJ, et al. **Molecular changes in normal appearing white matter in multiple sclerosis are characteristic of neuroprotective mechanisms against hypoxic insult.** *Brain Pathol* 2003;13:554–73
17. Lassmann H. **Multiple sclerosis: is there neurodegeneration independent from inflammation?** *J Neurol Sci* 2007;259:3–6
18. Lanz M, Hahn HK, Hildebrandt H. **Brain atrophy and cognitive impairment in multiple sclerosis: a review**. *J Neurol* 2007;254(Suppl 2):II43–48
19. Jackson A, Kassner A, Zhu XP, et al. **Reproducibility of T2* blood volume and vascular tortuosity maps in cerebral gliomas.** *J Magn Reson Imaging* 2001;14:510–16
20. Jackson A, Kassner A, Annesley-Williams D, et al. **Abnormalities in the recirculation phase of contrast agent bolus passage in cerebral gliomas: comparison with relative blood volume and tumor grade.** *AJNR Am J Neuroradiol* 2002;23:7–14
21. Kassner A, Zhu XP, Li KL, et al. **Neoangiogenesis in association with Moyamoya syndrome shown by estimation of relative recirculation based on dynamic contrast-enhanced MR images.** *AJNR Am J Neuroradiol* 2003;24:810–18
22. Wu S, Thornhill RE, Chen S, et al. **Relative recirculation: a fast, model-free surrogate for the measurement of blood-brain barrier permeability and the prediction of hemorrhagic transformation in acute ischemic stroke.** *Invest Radiol* 2009;44:662–68
23. Dade LA, Gao FQ, Kovacevic N, et al. **Semiautomatic brain region extraction: a method of parcellating brain regions from structural magnetic resonance images.** *Neuroimage* 2004;22:1492–502
24. Robb RA, Hanson DP, Karwoski RA, et al. **Analyze: a comprehensive, operator-interactive software package for multidimensional medical image display and analysis.** *Comput Med Imaging Graph* 1989;13:433–54
25. Aviv RI, Francis PL, Tenenbein R, et al. **Decreased frontal lobe gray matter perfusion in cognitively impaired patients with secondary-progressive multiple sclerosis detected by the bookend technique.** *AJNR Am J Neuroradiol* 2012;33:1779–85
26. Rosen BR, Belliveau JW, Vevea JM, et al. **Perfusion imaging with NMR contrast agents.** *Magn Reson Med* 1990;14:249–65
27. Kassner A, Annesley DJ, Zhu XP, et al. **Abnormalities of the contrast re-circulation phase in cerebral tumors demonstrated using dynamic susceptibility contrast-enhanced imaging: a possible marker of vascular tortuosity.** *J Magn Reson Imaging* 2000;11:103–13
28. Benedict RH, Fischer JS, Archibald CJ, et al. **Minimal neuropsychological assessment of MS patients: a consensus approach.** *Clin Neuropsychol* 2002;16:381–97
29. Thompson AJ, Polman CH, Miller DH, et al. **Primary progressive multiple sclerosis.** *Brain* 1997;120(Part 6):1085–96
30. Heaton RK, Nelson LM, Thompson DS, et al. **Neuropsychological findings in relapsing-remitting and chronic-progressive multiple sclerosis.** *J Consult Clin Psychol* 1985;53:103–10
31. Frischer JM, Bramow S, Dal-Bianco A, et al. **The relation between inflammation and neurodegeneration in multiple sclerosis brains.** *Brain* 2009;132(Part 5):1175–89
32. Benedict RH, Cookfair D, Gavett R, et al. **Validity of the minimal assessment of cognitive function in multiple sclerosis (MACFIMS).** *J Int Neuropsychol Soc* 2006;12:549–58
33. Drake AS, Weinstock-Guttman B, Morrow SA, et al. **Psychometrics and normative data for the Multiple Sclerosis Functional Composite: replacing the PASAT with the Symbol Digit Modalities Test.** *Mult Scler* 2010;16:228–37
34. Benedict RH, Weinstock-Guttman B, Fishman I, et al. **Prediction of neuropsychological impairment in multiple sclerosis: comparison of conventional magnetic resonance imaging measures of atrophy and lesion burden.** *Arch Neurol* 2004;61:226–30
35. Christodoulou C, Krupp LB, Liang Z, et al. **Cognitive performance and MR markers of cerebral injury in cognitively impaired MS patients.** *Neurology* 2003;60:1793–98
36. Lockwood AH, Linn RT, Szymanski H, et al. **Mapping the neural systems that mediate the Paced Auditory Serial Addition Task (PASAT).** *J Int Neuropsychol Soc* 2004;10:26–34
37. Dineen RA, Vilisaar J, Hlinka J, et al. **Disconnection as a mechanism for cognitive dysfunction in multiple sclerosis.** *Brain* 2009;132(Part 1):239–49
38. Zivadinov R, Bakshi R. **Role of MRI in multiple sclerosis I: inflammation and lesions.** *Front Biosci* 2004;9:665–83
39. Zivadinov R, Leist TP. **Clinical-magnetic resonance imaging correlations in multiple sclerosis**. *J Neuroimaging* 2005;15(4 Suppl):10S–21S.
40. Filippi M, Wolinsky JS, Sormani MP, et al. **Enhancement frequency decreases with increasing age in relapsing-remitting multiple sclerosis.** *Neurology* 2001;56:422–23
41. Silver NC, Tofts PS, Symms MR, et al. **Quantitative contrast-enhanced magnetic resonance imaging to evaluate blood-brain barrier integrity in multiple sclerosis: a preliminary study.** *Mult Scler* 2001;7:75–82
42. Rydahl C, Thomsen HS, Marckmann P. **High prevalence of nephrogenic systemic fibrosis in chronic renal failure patients exposed to gadodiamide, a gadolinium-containing magnetic resonance contrast agent.** *Invest Radiol* 2008;43:141–44
43. Cheng HL. **Investigation and optimization of parameter accuracy in dynamic contrast-enhanced MRI.** *J Magn Reson Imaging* 2008;28:736–43
44. Ingrisch M, Sourbron S, Morhard D, et al. **Quantification of perfusion and permeability in multiple sclerosis: dynamic contrast-enhanced MRI in 3D at 3T.** *Invest Radiol* 2012;47:252–58
45. O'Sullivan M, Morris RG, Huckstep B, et al. **Diffusion tensor MRI correlates with executive dysfunction in patients with ischaemic leukoaraiosis.** *J Neurol Neurosurg Psychiatry* 2004;75:441–47
46. Parkinson RB, Hopkins RO, Cleavinger HB, et al. **White matter hyperintensities and neuropsychological outcome following carbon monoxide poisoning.** *Neurology* 2002;58:1525–32
47. Kennedy MR, Wozniak JR, Muetzel RL, et al. **White matter and neurocognitive changes in adults with chronic traumatic brain injury.** *J Int Neuropsychol Soc* 2009;15:130–36

Perfusion Deficits Detected by Arterial Spin-Labeling in Patients with TIA with Negative Diffusion and Vascular Imaging

X.J. Qiao, N. Salamon, D.J.J. Wang, R. He, M. Linetsky, B.M. Ellingson, and W.B. Pope

ABSTRACT

BACKGROUND AND PURPOSE: A substantial portion of clinically diagnosed TIA cases is imaging-negative. The purpose of the current study is to determine if arterial spin-labeling is helpful in detecting perfusion abnormalities in patients presenting clinically with TIA.

MATERIALS AND METHODS: Pseudocontinuous arterial spin-labeling with 3D background-suppressed gradient and spin-echo was acquired on 49 patients suspected of TIA within 24 hours of symptom onset. All patients were free of stroke history and had no lesion-specific findings on general MR, DWI, and MRA sequences. The calculated arterial spin-labeling CBF maps were scored from 1–3 on the basis of presence and severity of perfusion disturbance by 3 independent observers blinded to patient history. An age-matched cohort of 36 patients diagnosed with no cerebrovascular events was evaluated as a control. Interobserver agreement was assessed by use of the Kendall concordance test.

RESULTS: Scoring of perfusion abnormalities on arterial spin-labeling scans of the TIA cohort was highly concordant among the 3 observers ($W = 0.812$). The sensitivity and specificity of arterial spin-labeling in the diagnosis of perfusion abnormalities in TIA was 55.8% and 90.7%, respectively. In 93.3% (70/75) of the arterial spin-labeling CBF map readings with positive scores (≥ 2), the brain regions where perfusion abnormalities were identified by 3 observers matched with the neurologic deficits at TIA onset.

CONCLUSIONS: In this preliminary study, arterial spin-labeling showed promise in the detection of perfusion abnormalities that correlated with clinically diagnosed TIA in patients with otherwise normal neuroimaging results.

ABBREVIATIONS: ASL = arterial spin-labeling; ATT = arterial transit time; PCT = contrast-enhanced perfusion CT; PLD = postlabel delay

TIA is traditionally defined as the sudden onset of a neurologic deficit(s) as a result of transient ischemia of the eloquent brain, which resolves completely within 24 hours. TIA is presumed to have a vascular cause and is considered to be an important risk factor for stroke.[1,2] In practice, the unequivocal diagnosis of TIA has been limited by the high percentage of patients who had suspected neurologic deficits, but lacked confirmatory imaging. This contributes to lack of agreement in the diagnosis of TIA among practicing physicians[3] and has led to proposals advocating the incorporation of imaging data, in addition to clinical findings, in the diagnosis of TIA. For instance, this new paradigm has been adopted by American Stroke Association.[4] In addition to diagnosis, detection of malperfused tissue is considered to be important in understanding the extent of the initial perfusion deficit and may be helpful in guiding therapeutic decisions.

SPECT and contrast-enhanced perfusion CT (PCT) have been previously used to investigate perfusion disturbances in clinical TIA cases.[5-7] However, these CT-based imaging techniques have several disadvantages including invasiveness, reliance on radioactive materials, adverse reactions to contrast material, as well as technical difficulties in covering large brain volumes.[5,8,9] More recently, the introduction of advanced MR imaging technology has enabled better visualization of ischemic cerebral regions corresponding both anatomically and temporally to symptoms of TIA. For example, DWI results were positive for acute ischemic lesions in 24%–40% of patients referred for evaluation of TIA.[10-14] In addition, contrast-based PWI has shown promise in the identification of abnormalities in approximately one-third of patients with TIA, some of whom had negative DWI results.[15,16] Nonetheless, a substantial portion of patients diagnosed with TIA clinically lack confirmatory imaging findings.

The arterial spin-labeling (ASL) technique provides CBF measurements without the use of a contrast agent. ASL has shown

Received September 7, 2012; accepted after revision January 31, 2013.

From the Departments of Radiological Sciences (X.J.Q., N.S, M.L., B.M.E., W.B.P.), and Neurology (D.J.J.W.), David Geffen School of Medicine; and Department of Biostatistics (R.H.), School of Public Health, UCLA, Los Angeles, California.

Please address correspondence to Whitney B. Pope, MD, PhD, Department of Radiological Sciences, David Geffen School of Medicine, UCLA Medical Center, 10833 Le Conte Ave, BL-428/CHS Los Angeles, CA 90095-1721; e-mail: wpope@mednet.ucla.edu

Indicates open access to non-subscribers at www.ajnr.org

indicates article with supplemental on-line table

http://dx.doi.org/10.3174/ajnr.A3551

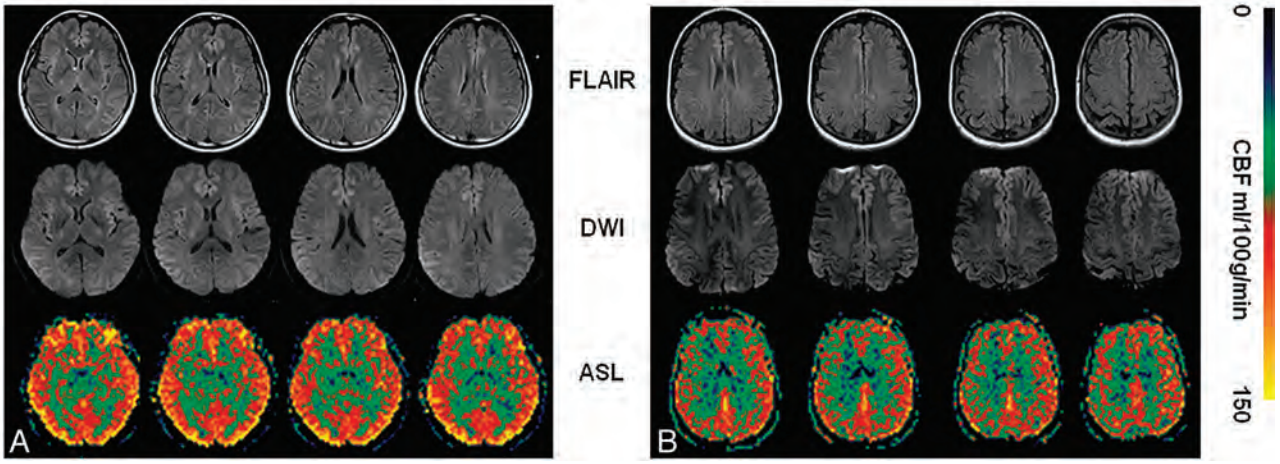

FIG 1. Representative cases from the control cohort. *A*, A 50-year-old woman was evaluated for dizziness after an automobile crash. No specific findings are reported on the standard MR, DWI, and MRA tests. ASL reading scores are rated 1, 1, 1 by 3 raters. *B*, A 49-year old woman was evaluated for a chronic headache of unknown cause. No specific findings are reported on the standard MR, DWI, and MRA tests. ASL reading scores are rated 2, 2, 2 by 3 raters.

promise in clinical studies of ischemic pathologic conditions, such as acute stroke[17-19] and large-artery occlusion.[20,21] In a limited number of published studies, ASL has demonstrated a high sensitivity for detection of minor perfusion alterations in patients with TIA.[12,22] With the goal of establishing a vascular cause of TIA symptoms, the current study investigated the value of ASL in the detection of hypoperfusion abnormalities in a TIA cohort free of stroke history and without confirmatory findings on standard MR, DWI, and MRA examinations.

MATERIALS AND METHODS

Patients

From an ongoing prospective registry of consecutive patients evaluated for suspected TIA from July 2010 to July 2011 at our medical center, imaging data were selected from all patients who had 1) transient neurologic symptoms judged by clinical neurologists at the end of the evaluation to have a possible vascular cause; 2) no stroke history; 3) MR images performed within 24 hours of symptom onset; and 4) nonspecific findings on general MR, DWI, and MRA examinations. ASL imaging was used only in this retrospective analysis but not in the clinical evaluation of the patients. The selected patients were then followed up in clinic for complaints of any new neurologic symptoms until December 31, 2011, when the study was terminated. A control cohort of age-matched patients (>40 years old), who had received a brain MR imaging scan because of neurologic symptoms thought to be irrelevant to vascular events, was selected from another ongoing prospective registry of consecutive patients during the same period (Fig 1). For all selected patients in the TIA cohort (Fig 2), $ABCD^2$ scores were generated based on the presence of pre-existing conditions.[10,11] This study was approved by our institutional review board and was Health Insurance Portability and Accountability Act compliant.

MR Imaging Protocols

MR imaging scans were performed on a 1.5T Avanto or 3T Tim Trio system (Siemens, Erlangen, Germany) by use of a 12-channel head coil. The stroke imaging protocol included DWI, FLAIR, and gradient recalled-echo. ASL scans were performed by use of pseudocontinuous pulse sequence with background-suppressed 3D gradient and spin-echo readout (labeling pulse duration, 1.5 seconds; postlabel delay [PLD], 2 seconds; no flow-crushing gradient; FOV, 22 cm; matrix size, 64 × 64; number of 5-mm sections, 26; generalized autocalibrating partially parallel acquisition, 2; TE, 22 ms; TR, 4000 ms; with 30 pairs of tag and control volumes acquired within a total of 4 minutes).[23,24]

ASL Postprocessing and Evaluation

ASL images were corrected for motion; pair-wise subtracted between labeled and unlabeled images; and averaged to generate mean difference images, or ASL CBF maps. ASL CBF maps of patients with TIA ($n = 49$) and control patients ($n = 36$) were scored by 3 independent observers (2 board-certified neuroradiologists and 1 nonradiologist physician experienced in MR imaging processing) blinded to patient history. The reading scores, ranging from a scale of 1–3, reflected the presence and severity of the perfusion disturbance (usually hypoperfusion in this study): "1" for normal (no readable altered perfusion), "≥2" being defined as "positive" readings indicating recognizable ischemic lesions ("2" for subtle abnormalities only identified by careful study of ASL CBF maps, and "3" for prominent perfusion deficits easily identified on ASL CBF maps). The laterality of the perfusion disturbance was recorded in patients with hemispheric TIA for comparison with neurologic symptoms at onset. ASL reading scores were compared between patients grouped by field strength (1.5T vs 3T) of the scanner on which ASL images were obtained.

Statistical Analysis

The agreement in reading scores from 3 observers ($n = 49 \times 3$ for the TIA cohort; $n = 36 \times 3$ for the control cohort) was assessed by use of a Kendall concordance test. Kendall W, also known as the Kendall coefficient of concordance, was calculated to evaluate the degree of consensus. Pooled observations from all 3 observers ($n = 49 \times 3$ for the TIA cohort; $n = 36 \times 3$ for the control cohort) were recorded in a 2 × 2 contingency table reflecting the frequency of true-positive, true-negative, false-positive, and false-

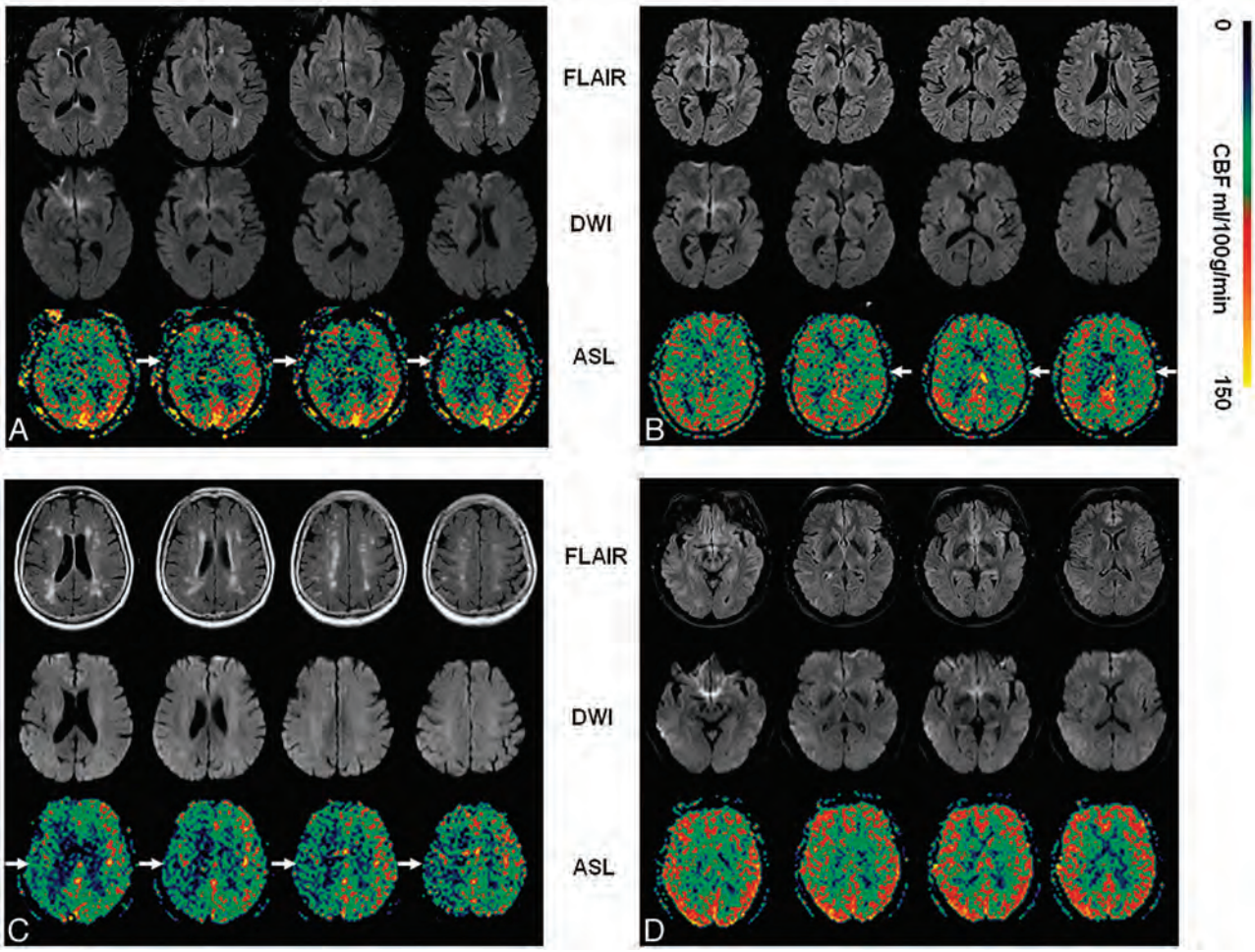

FIG 2. Representative cases from the TIA cohort. *A*, A 75-year-old woman with a history of hypertension and diabetes had an acute onset of transient blurry vision, slurred speech, dysarthria, and word-finding difficulties that lasted for 20–30 minutes. $ABCD^2$ score is 5. The standard MR imaging results demonstrate a few nonspecific T2/FLAIR hyperintensities in the cerebral white matter bilaterally. DWI and MRA study results are normal. ASL CBF map shows perfusion deficits in the right MCA region (*arrow*). ASL reading scores are rated 2, 2, 2 by 3 raters. *B*, A 57-year old woman with a history of hypertension had right facial droop and right arm numbness for 6 hours. $ABCD^2$ score is 3. Nonspecific T2/FLAIR hyperintensities are seen in the cerebral white matter. DWI and MRA study results are normal. ASL CBF map shows perfusion deficits in the regions of the left MCA and left posterior cerebral artery (*arrow*). ASL scores are rated 2, 2, 2 by 3 raters. *C*, A 80-year old woman with a history of hyperlipidemia had transient global amnesia, left-sided sensory deficit, and a positive Babinski sign on the left side for 6 hours. $ABCD^2$ score is 3. Scattered T2/FLAIR hyperintensities are seen in the periventricular and subcortical white matter on standard MR imaging. DWI and MRA study results are normal. ASL CBF map shows perfusion deficits in the right MCA region (*arrow*). ASL scores are rated 3, 3, 3 by 3 raters. *D*, A 57-year-old woman with a history of hypertension had right facial droop and slurred speech for more than 1 hour. $ABCD^2$ score was 4. The standard MR, DWI, and MRA study results are normal. ASL reading scores are rated 1, 1, 1 by 3 raters.

negative observations as rated by ASL CBF maps compared with the clinical diagnosis of TIA (reference standard). A true-positive result was obtained from a patient clinically diagnosed with TIA with an ASL CBF map reading score ≥2. Conversely, a true-negative result was obtained from a control patient with an ASL CBF map reading score of 1. Sensitivity and specificity were calculated. A *t* test was used to compare ASL reading scores between imaging performed on scanners with different magnetic field strengths (1.5T vs 3T). The significance level was defined as $P < .05$ (2-sided).

RESULTS

Patient Characteristics

From July 2010 to July 2011 at our medical center, we recorded 165 patients who were suspected of having a TIA, among whom 67 (40.6%) had a history of ischemic stroke. In patients who tested negative for a stroke history (98/165), 23 patients (23.4%) had positive DWI findings, and 30 patients (30.6%) had vascular lesions identified by MRA. In this particular subgroup, 4 patients (4.1%) showed positive findings on both DWI and MRA. Finally, 49 patients (50.0%) were "imaging negative" and were selected for our current analysis. Until December 31, 2011, the selected imaging-negative patients with TIA were followed up in clinic for 164–538 days (median, 370 days) for complaints of new neurologic symptoms. Patients did not receive follow-up MR imaging.

Another cohort of 36 age-matched patients (>40 years old), who had received a brain MR imaging scan because of neurologic symptoms thought to be irrelevant to vascular events, was selected from another ongoing prospective registry of consecutive patients during the same period as a control (On-Line Table).

Table 1 shows baseline characteristics of "imaging-negative" patients with TIA ($n = 49$) at symptom onset and control patients

Table 1. Basic characteristics of patient cohorts

Characteristics	Cohort	
	TIA[a] (n = 49)	Control (n = 36)
Age (mean ± SD y)[b]	65.6 ± 14.6	60.2 ± 12.2
Sex (F/M)	27/22	24/12
MR imaging delay median (h)[c]	6.5	N/A
ABCD^2 score median	4	N/A
Prior TIA, n (%)[d]	9 (18.4)	0 (0)
Coronary artery disease, n (%)[d]	10 (20.4)	3 (8.3)
Atrial fibrillation, n (%)[b]	1 (2.0)	1 (2.8)
Hyperlipidemia, n (%)[d]	24 (49.0)	5 (13.9)
Hypertension, n (%)[d]	31 (63.3)	7 (19.4)
Diabetes, n (%)[d]	9 (18.4)	2 (5.6)

[a] Diagnosis of TIA was made clinically without ASL imaging.
[b] No significant difference exists between the groups.
[c] Based on 40 patients, data were not available for 9 patients.
[d] Significant differences exist between the groups, $P < .001$.

Table 2. Sensitivity and specificity of ASL CBF map reading[a]

	Cohort		
	TIA[b]	Control	
ASL positive[c]	82	10	92
ASL negative[d]	65	98	163
	147	108	
	Sensitivity, 55.78%	Specificity, 90.73%	

[a] Based on pooled data from 3 independent observers, $n = 49$ for TIA cohort and $n = 36$ for control cohort, with scores of ≥2 being defined as "positive" readings indicating recognizable ischemic lesions (82/147 = 49 × 3 for the TIA cohort, and 10/108 = 36 × 3 for the control cohort).
[b] Diagnosis of TIA was made clinically without ASL imaging.
[c] Defined as a reading score of 2 or 3.
[d] Defined as a reading score of 1.

($n = 36$) on MR imaging dates. Patients with a clinical diagnosis of TIA ($n = 49$) but no prior stroke and positive MR imaging findings, had a sudden onset of neurologic deficits that lasted anywhere from seconds to hours. In all cases, symptoms resolved by the time of MR scanning, which was performed within 1–11 hours after the initial onset of symptoms. The TIA and control cohorts showed no significant difference in mean age but were significantly different for pre-existing conditions associated with stroke risk, including the incidence of TIA, coronary heart disease, hyperlipidemia, hypertension, and diabetes mellitus. The TIA cohort has a median ABCD^2 score of 4. All patients in the TIA cohort were followed up for an average period of 1 year (range, 164–538 days), and none of the patients was found to have a post-TIA stroke on the basis of absence of complaints of any new neurologic symptoms.

Evaluation of ASL CBF Maps

Results suggested relatively high concordance scores (Kendall concordance test), indicating good agreement in evaluating ASL CBF maps of both TIA ($W = 0.812$) and control cohorts ($W = 0.642$) among 3 observers. With scores of ≥2 being defined as "positive" readings indicating recognizable ischemic lesions (82/147 = 49 × 3 for the TIA cohort, and 10/108 = 36 × 3 for the control cohort), the sensitivity and specificity of the ASL CBF map in the diagnosis of TIA were 55.8% (95% CI, 0.49–0.63) and 90.7% (95% CI, 0.87–0.95), respectively (Table 2). The magnetic field strength (23 patients on 1.5T, 26 patients on 3T in the TIA cohort; 17 patients on 1.5T, 19 patients on 3T in the control cohort) was not associated with a significant difference in mean reading scores of ASL CBF maps (t test). In the TIA cohort, 44 (89.8%) of 49 patients presented with hemispheric symptoms, such as focal weakness and aphasia. In this subgroup of patients with hemispheric TIA and positive ASL CBF map readings (score ≥2), 93.3% (70/75 positive readings) of the cases showed brain regions where the hypoperfusion identified matched the laterality of the neurologic symptoms at TIA onset. In the rest of the observations (5/75), hyperperfusion was characterized in brain regions corresponding to transient neural deficits during the TIA attacks.

DISCUSSION

The widespread adoption of newer advanced MR imaging, such as DWI, has significantly improved the characterization of ischemic lesions in patients with TIA. However, the diagnosis of TIA in a substantial proportion of cases remains purely clinically based, as no corroborating imaging findings exist by standard MR imaging. Therefore, it would be of potential value to identify imaging technologies with a high sensitivity for the detection of minor cerebral perfusion abnormalities, to more confidently establish the diagnosis of TIA in clinical practice. ASL has emerged as such an imaging technique with a purported high sensitivity for the detection of perfusion abnormalities in both TIA and acute stroke.[17-19,22] In our current study, we explored the value of ASL in the detection of perfusion deficits in a cohort of clinically diagnosed patients with TIA with unremarkable standard MR imaging results. To avoid confounding factors that are known to produce positive findings on ASL images, we excluded patients with a history of stroke and those with any brain lesions that can be identified on DWI and MRA sequences. As a preliminary investigation of the value of ASL in TIA, our current analysis was limited by small study size and discrepancy in the sex ratio between TIA and control cohorts (Table 1). The power of the study was further affected by the gap in the median age of the TIA and control cohorts (70.7 years and 61.4 years, respectively), though there was no significant difference in the mean age of the patient cohorts (65.6 years and 60.2 years, respectively; $P > .05$, t test).

We found that ASL provided imaging evidence of disturbed perfusion (this study focused on hypoperfusion) in 55.8% of imaging-negative TIA cases, as judged by the standard imaging protocols including DWI and MRA. ASL CBF map reading also showed a high specificity (90.7%) for abnormal perfusion in our patient cohort. Positive ASL CBF map readings showed that the location of the hypoperfusion was consistent with the neurologic symptoms at TIA onset in 93.3% (70/75) of the total observations. These findings support the hypothesis that ASL is a feasible and practical method for detection of perfusion abnormalities, with good sensitivity in patients with a clinical diagnosis of TIA. The evaluation of ASL CBF maps demonstrated good agreement in reading scores from 3 observers ($W = 0.812$ for TIA and $W = 0.642$ for control), suggesting that ischemic lesions in ASL CBF maps could be consistently recognized by different readers, and thus supporting the conclusion that ASL has good reliability as well. In practice, ASL has the advantages of being contrast-free and requiring a relatively short scan time (<4 minutes in our protocol), which may allow this technique to be widely used in the clinical management of TIA and other clinical emergencies that mimic it.

Prospective studies have shown a high risk for stroke within the immediate hours and days after TIA.[2] In our current study, we followed up on the TIA cohort for an average period of 1 year (range, 164–538 days), and none of the patients experienced a post-TIA stroke. The reported factors correlating with the risk for post-TIA stroke include ABCD/ABCD^2 scores[10,11,25] and positive MR imaging findings on DWI[25-29] and MRA.[28-30] As a clinical score based on the presence of pre-existing conditions to determine the risk for stroke after a TIA, the value of ABCD/ABCD^2 scores in the prediction of post-TIA stroke risk have been controversial and vary greatly by patient cohort and clinical protocol.[10,11,25,30] Our TIA cohort had a high median ABCD^2 score of 4; however, none of the patients appeared to have a stroke during the average 1-year follow-up period, though silent infarcts could have gone undetected (as patients had routine clinical follow-up but no additional MR imaging).

The lack of clinically evident strokes in our TIA cohort may be surprising, but it may suggest that the negative standard imaging being used as a criterion for study inclusion could be associated with reduced stroke risk. Although the power of the current analysis was limited by a relatively small cohort size, we found that patients with TIA with positive findings on DWI and MRA are more likely to display readable abnormalities on ASL than imaging-negative cases used in the current study (data not shown), raising the question of whether ASL data should be included in criteria for the evaluation of stroke risk after TIA onset. Better characterization of such a patient cohort may help to clarify the value of ABCD/ABCD^2 scores in the prediction of post-TIA stroke. Specifically, future studies of much larger sizes will be necessary to determine stroke risks in these patient groups: those with TIA with MR imaging abnormalities (including DWI and MRA), those with TIA with ASL abnormalities only, and those with TIA with no MR imaging or ASL abnormalities.

Low SNR and low spatial resolution are major limitations of ASL. The SNR is directly proportional to voxel size and the PLD time, which is defined as the duration between labeling of the spins and acquisition of the images, and is typically between 1.5 and 2.0 seconds. Longer PLDs (>2 seconds) could help to improve CBF quantification, however, at the cost of a further decrease in SNR.[31] In the current analysis, a single PLD of 2.0 seconds was used, resulting in the detection of focal hypoperfusion in 55.8% of imaging-negative patients with TIA. Considering the universal existence of multiple conditions in patients with TIA that related to vascular pathogenesis, arterial transit time (ATT) could vary greatly among individual patients. Therefore, 1 calculated CBF map on the basis of a single PLD might not be the best approach to accurately reflect the perfusion status in these patients. In this case, an option would be to obtain images at multiple PLDs, which offers the potential to quantify ATT[32] and effectively map the inflow of label into the tissue.[20,33] In future studies, we plan to perform ASL scans by using multiple PLDs and calculate ATT-adjusted CBF maps, aiming to improve the sensitivity in the detection of minor perfusion changes in patients with TIA.

CONCLUSIONS

Our results suggest the potential value of ASL perfusion data in the detection of abnormalities in patients with TIA, which may help improve the diagnostic certainty in otherwise imaging-negative patients with TIA.

Disclosures: Danny JJ Wang—*RELATED: Grant:* NIMH.* Whitney Pope—*UNRELATED: Consultancy:* Genentech. **Money paid to institution.*

REFERENCES

1. Rothwell PM, Giles MF, Flossmann E, et al. **A simple score (ABCD) to identify individuals at high early risk of stroke after transient ischaemic attack.** *Lancet* 2005;366:29–36
2. Giles M, Rothwell P. **Risk of stroke early after transient ischaemic attack: A systematic review and meta-analysis.** *Lancet Neurol* 2007;6:1063–72
3. Castle J, Mlynash M, Lee K, et al. **Agreement regarding diagnosis of transient ischemic attack fairly low among stroke-trained neurologists.** *Stroke* 2010;41:1367–70
4. Easton JD, Saver JL, Albers GW, et al. **Definition and evaluation of transient ischemic attack: a scientific statement for healthcare professionals from the American Heart Association/American Stroke Association Stroke Council; Council on Cardiovascular Surgery and Anesthesia; Council on Cardiovascular Radiology and Intervention; Council on Cardiovascular Nursing; and the Interdisciplinary Council on Peripheral Vascular Disease.** *Stroke* 2009;40:2276–93
5. Laloux P, Jamart J, Meurisse H, et al. **Persisting perfusion defect in transient ischemic attacks: a new clinically useful subgroup?** *Stroke* 1996;27:425–30
6. Lu J, Li KC, Hua Y. **Primary study on imaging in transient ischemic attack.** *Chin Med J* 2005;118:1812–16
7. Prabhakaran S, Patel SK, Samuels J, et al. **Perfusion computed tomography in transient ischemic attack.** *Arch Neurol* 2011;68:85–89
8. Eastwood JD, Lev MH, Wintermark M, et al. **Correlation of early dynamic CT perfusion imaging with whole-brain MR diffusion and perfusion imaging in acute hemispheric stroke.** *AJNR Am J Neuroradiol* 2003;24:1869–75
9. Koenig M, Klotz E, Luka B, et al. **Perfusion CT of the brain: diagnostic approach for early detection of ischemic stroke.** *Radiology* 1998;209:85–93
10. Merwick A, Albers GW, Amarenco P, et al. **Addition of brain and carotid imaging to the ABCD^2 score to identify patients at early risk of stroke after transient ischaemic attack: a multicentre observational study.** *Lancet Neurol* 2010;9:1060–69
11. Giles MF, Albers GW, Amarenco P, et al. **Early stroke risk and ABCD2 score performance in tissue- vs time-defined TIA: a multicenter study.** *Neurology* 2011;77:1222–28
12. Zaharchuk G, Olivot JM, Fischbein NJ, et al. **Arterial spin labeling imaging findings in transient ischemic attack patients: comparison with diffusion- and bolus perfusion-weighted imaging.** *Cerebrovasc Dis* 2012;34:221–28
13. Ay H, Arsava EM, Johnston SC, et al. **Clinical- and imaging-based prediction of stroke risk after transient ischemic attack: the CIP model.** *Stroke* 2009;40:181–86
14. Sylaja PN, Coutts SB, Krol A, et al. **When to expect negative diffusion-weighted images in stroke and transient ischemic attack.** *Stroke* 2008;39:1898–900
15. Krol AL, Coutts SB, Simon JE, et al. **Perfusion MRI abnormalities in speech or motor transient ischemic attack patients.** *Stroke* 2005;36:2487–89
16. Mlynash M, Olivot JM, Tong DC, et al. **Yield of combined perfusion and diffusion MR imaging in hemispheric TIA.** *Neurology* 2009;72:1127–33
17. Chalela JA, Alsop DC, Gonzalez-Atavales JB, et al. **Magnetic resonance perfusion imaging in acute ischemic stroke using continuous arterial spin labeling.** *Stroke* 2000;31:680–87
18. Wang DJ, Alger JR, Qiao JX, et al. **The value of arterial spin-labeled perfusion imaging in acute ischemic stroke: comparison**

with dynamic susceptibility contrast-enhanced MRI. *Stroke* 2012;43:1018–24
19. Zaharchuk G. **Arterial spin label imaging in acute ischemic stroke and transient ischemic attack.** *Neuroimaging Clin N Am* 2011;21: 285–301, x
20. Hendrikse J, van Osch MJ, Rutgers DR, et al. **Internal carotid artery occlusion assessed at pulsed arterial spin-labeling perfusion MR imaging at multiple delay times.** *Radiology* 2004;233:899–904
21. van Laar PJ, Hendrikse J, Klijn CJ, et al. **Symptomatic carotid artery occlusion: flow territories of major brain-feeding arteries.** *Radiology* 2007;242:526–34
22. MacIntosh BJ, Lindsay AC, Kylintireas I, et al. **Multiple inflow pulsed arterial spin-labeling reveals delays in the arterial arrival time in minor stroke and transient ischemic attack.** *AJNR Am J Neuroradiol* 2010;31:1892–94
23. Fernández-Seara MA, Edlow BL, Hoang A, et al. **Minimizing acquisition time of arterial spin labeling at 3T.** *Magn Reson Med* 2008;59:1467–71
24. Wu WC, Fernandez-Seara M, Detre JA, et al. **A theoretical and experimental investigation of the tagging efficiency of pseudo-continuous arterial spin labeling.** *Magn Reson Med* 2007;58:1020–27
25. Ghia D, Thomas P, Cordato D, et al. **Low positive predictive value of the ABCD2 score in emergency department transient ischaemic attack diagnoses: the South Western Sydney tRansient Ischaemic Attack study.** *Intern Med J* 2012;42:913–18
26. Crisostomo RA, Garcia MM, Tong DC. **Detection of diffusion-weighted MRI abnormalities in patients with transient ischemic attack: correlation with clinical characteristics.** *Stroke* 2003; 34:932–37
27. Ay H, Oliveira-Filho J, Buonanno FS, et al. **'Footprints' of transient ischemic attacks: a diffusion-weighted MRI study.** *Cerebrovasu Dis* 2002;14:177–86
28. Calvet D, Touzé E, Oppenheim C, et al. **DWI lesions and TIA etiology improve the prediction of stroke after TIA.** *Stroke* 2009; 40:187–92
29. Ssi-Yan-Kai G, Nasr N, Faury A, et al. **Intracranial artery stenosis or occlusion predicts ischemic recurrence after transient ischemic attack.** *AJNR Am J Neuroradiol* 2013;34:185–90
30. Hotter BA, Lechner JM, Nolte CH, et al. **ABCD (2) as a screening tool for cerebral infarction on stroke MRI?** *Eur Neurol* 2012;67:315–20
31. Alsop DC, Detre JA. **Reduced transit time sensitivity in noninvasive magnetic resonance imaging of human cerebral blood flow.** *J Cereb Blood Flow Metab* 1996;16:1236–49
32. Buxton RB, Frank LR, Wong EC, et al. **A general kinetic model for quantitative perfusion imaging with arterial spin labeling.** *Magn Reson Med* 1998;40:383–96
33. Petersen ET, Lim T, Golay X. **Model-free arterial spin labeling quantification approach for perfusion MRI.** *Magn Reson Med* 2006;55: 219–32

C-Arm CT Measurement of Cerebral Blood Volume and Cerebral Blood Flow Using a Novel High-Speed Acquisition and a Single Intravenous Contrast Injection

K. Royalty, M. Manhart, K. Pulfer, Y. Deuerling-Zheng, C. Strother, A. Fieselmann, and D. Consigny

ABSTRACT

BACKGROUND AND PURPOSE: Assessment of perfusion parameters is important in the selection of patients who are most likely to benefit from revascularization after an acute ischemic stroke. The aim of this study was to evaluate the feasibility of measuring cerebral perfusion parameters with the use of a novel high-speed C-arm CT acquisition in conjunction with a single intravenous injection of contrast.

MATERIALS AND METHODS: Seven canines had experimentally induced focal ischemic regions confirmed by CT perfusion imaging. Four hours after ischemic injury creation, each subject underwent cerebral perfusion measurements with the use of standard perfusion CT, immediately followed by the use of C-arm CT. Cerebral blood flow and cerebral blood volume maps measured by C-arm CT were quantitatively and qualitatively compared with those measured by perfusion CT for 6 of the 7 canine subjects.

RESULTS: Results from independent observer evaluations of perfusion CT and C-arm perfusion maps show strong agreement between observers for identification of ischemic lesion location. Significant percentage agreement between observers for lesion detection and identification of perfusion mismatch between CBV and CBF maps indicate that the maps for both perfusion CT and C-arm are easy to interpret. Quantitative region of interest–based evaluation showed a strong correlation between the perfusion CT and C-arm CBV and CBF maps (R^2 = 0.68 and 0.85). C-arm measurements for both CBV and CBF were consistently overestimated when compared with perfusion CT.

CONCLUSIONS: Qualitative and quantitative measurements of CBF and CBV with the use of a C-arm CT acquisition and a single intravenous injection of contrast agent are feasible. Future improvements in flat detector technology and software algorithms probably will enable more accurate quantitative perfusion measurements with the use of C-arm CT.

ABBREVIATIONS: AIF = arterial input functions; PCT = perfusion CT; TAC = time-attenuation curves

Assessment of the impact of an ischemic insult on brain viability is best performed with the use of physiologic rather than morphologic criteria. This is especially so during the acute phase of an ischemic stroke, when anatomic changes are minimal and the options for revascularization are greater and most effective.[1] Because of limitations in the temporal resolution of angiographic C-arm rotational acquisitions, measurement of cerebral perfusion parameters has required either CT or MR imaging. Recent studies, however, have now demonstrated the feasibility of measuring CBV (in animals and humans) and CBF (in animals) with the use of flat detector C-arm angiographic systems.[2-6]

"Time is brain," but time is not an optimal indicator for selecting patients who are most likely to benefit from revascularization. There is also wide variation in the size and rate of infarct development, depending on many variables, for example, collateral supply, thrombus location and type, and age. In our opinion, these factors combined with the ability to distinguish infarcted brain from ischemic but still viable tissue provide strong motivation to identify techniques that will provide physicians with not only anatomic information but also the physiologic information that is necessary for optimization of patient selection for revascularization within a timeframe in which treatment may be most effective. The angiographic suite provides unparalleled anatomic information; in addition, the ability to obtain measurements of

Received October 18, 2012; accepted after revision January 9, 2013.

From the Department of Biomedical Engineering (K.R.), and School of Medicine and Public Health (K.P., C.S., D.C.), University of Wisconsin, Madison, Wisconsin; Siemens Medical Solutions USA (K.R.), Hoffman Estates, Illinois; Pattern Recognition Lab (M.M.), Friedrich-Alexander University, Erlangen, Germany; and Siemens AG, Healthcare Sector (Y.D.-Z., A.F.), Forchheim, Germany.

Please address correspondence to Kevin L. Royalty, MS, MBA, University of Wisconsin, Department of Biomedical Engineering, 1550 Engineering Dr, Madison, WI 53706; e-mail: kevin.royalty@siemens.com

Indicates open access to non-subscribers at www.ajnr.org

http://dx.doi.org/10.3174/ajnr.A3536

perfusion parameters would seem to create an ideal venue for the diagnosis and treatment of patients with an acute ischemic stroke.

To date, dynamic perfusion imaging with the C-arm angiographic systems has been limited by the slow gantry rotation times, typically on the order of 5–20 seconds. Previous work in both CT perfusion imaging and C-arm CT perfusion imaging demonstrates that temporal resolution in this range is not sufficient to yield accurate results for the measurement of dynamic cerebral perfusion measurements.[7,8] Previous work has demonstrated qualitative and quantitative accuracy of CBV measurements made with the use of C-arm CT in conjunction with a contrast injection protocol aimed at delivering a steady-state of contrast in the parenchyma.[2-5,9-11] Although this method provides information that is helpful in better understanding the viability of ischemic tissue (ie, identifying tissue when autoregulation appears to be intact), it does not provide the ability to distinguish ischemic core from penumbra. Ganguly et al[8] and others[12,13] have recently demonstrated, in a swine model, the feasibility of the use of C-arm CT for dynamic perfusion measurement. Our aim was to further evaluate, in a canine stroke model, the feasibility of performing dynamic cerebral perfusion measurements with the use of a novel high-speed C-arm CT data acquisition in conjunction with a single intravenous (IV) injection of contrast medium.

MATERIALS AND METHODS

Creation of Canine Ischemia and Core Lesion

Under an institutionally approved Animal Care and Use Committee protocol, 7 canines were studied. General anesthesia was introduced with propofol 10 mL/kg IV injection and maintained with the use of 1–5% isoflurane and 100% oxygen. Heart rate, respiration rate, blood oxygen saturation level, end-tidal CO_2 level, and body temperature were monitored and recorded for each subject throughout the duration of the procedure. Initial 2D angiography was performed to verify that cerebral vessels were patent and exhibited normal flow. An ischemic injury was successfully induced in 1 of the cerebral hemispheres in all subjects. Ischemia was created by the use of a 4F catheter (Tempo 4; Cordis, Miami Lakes, Florida) that was placed into either the common carotid artery or the vertebral artery. A microcatheter (FasTracker 18; Target Therapeutics, Fremont, California) was then advanced to the origin of the middle cerebral artery or the internal carotid artery, and embolic material mixed with contrast medium (Avitene; Bio-Medicine, Houston, Texas) was then slowly injected until there was angiographic evidence of stasis of contrast in the arteries of the ipsilateral middle cerebral artery distribution. The Avitene mixture was concentrated to provide a proximal occlusion to avoid only being distributed to the small distal branches of the middle cerebral artery territory.

CT Perfusion Acquisition

Perfusion CT (PCT) imaging was performed 3.5 hours after induction of ischemia by means of a 64-section volume scanner (Discovery CT750 HD; GE Health Care, Waukesha, Wisconsin). An IV injection of iopamidol, 370 mgI/mL (Isovue 370; Bracco, Princeton, New Jersey) was performed with the use of a dual-syringe power injector (Mark V ProVis; Medrad, Indianola, Pennsylvania) with a monophasic injection of 16 mL of contrast at a rate of 2.0 mL/s immediately followed with a 10-mL saline chase with a rate of 2 mL/s. After the injection and after a 5-second prep delay, continuous scanning was initiated with the use of the following parameters: 80 kVp, 200 mA, 1 second per rotation for 50 seconds.

C-Arm CT Perfusion Acquisition

Immediately after the PCT examination, the canine was brought to the angiography suite (Artis Zeego; Siemens, Erlangen, Germany) for C-arm CT perfusion imaging. Identical contrast medium was used for the C-arm CT as was used for the PCT scan. Contrast was injected directly into a peripheral vein with the use of a dual-syringe angiographic power injector (Medtron, Saarbrücken, Germany) at a rate of 3.5 mL/s, with a total volume of 28 mL, immediately followed by a saline chase at a rate of 3.5 mL/s, with a total volume of 10 mL. Before the start of the injection, a series of 2 bi-direction high-speed baseline scans were performed to obtain a baseline set of nonenhanced (mask) images. For the first animal subject, 8 seconds after the start of the peripheral contrast injection, a bi-directional series of 7 sequential high-speed C-arm CT rotational acquisitions was initiated. Data from these rotations were then used to calculate time-attenuation curves (TAC). On review of the results from the initial animal subject, it was determined that the 8-second x-ray delay was too long because there was already significant enhancement of the basilar artery at the time of the initial acquisition. An x-ray delay of 5 seconds was used for the remaining 6 studies. Physiologic parameters monitored during the study did not significantly change between the CT perfusion and C-arm perfusion acquisitions. Canine subjects were euthanized immediately after the C-arm CT acquisitions according to the approved protocol.

The mechanical properties of the robotic C-arm system allow for the design of custom high-speed rotations for CT imaging. For this experiment, a custom high-speed bi-directional acquisition protocol was developed as follows: seven 200° rotations over 2.8 seconds with a 1.5-second pause between rotations (4 forward rotations and 3 reverse rotations). During each rotation, the C-arm system acquires 133 projections at approximately 60 projections per second. Each projection was acquired at 70 kVp and 1.2 μGy/frame dose level, with the automatic exposure control enabled for the duration of the acquisition with a bit-depth of 14 bits. This acquisition protocol resulted in a sampling rate of approximately 4.3 seconds, with a total acquisition duration of 28.6 seconds (excluding the initial 5-second delay).

C-Arm CT Reconstruction of Temporal 3D Datasets

The basic reconstruction process follows a modified version of the algorithm reported by Ganguly et al[8] and Fieselmann et al.[12] Each C-arm CT rotation is first individually reconstructed (by use of a standard filtered back-projection algorithm) resulting in 2 baseline (nonenhanced) volumes and 7 contrast-enhanced volumes, each of which individually represents a composite of the contrast dynamics occurring within each of the seven 2.8 second rotations. An in-plane gaussian kernel (SD = 1 mm) and an axial moving average filter (5 mm) were used to improve the signal-to-noise ratio of the parenchyma. To correct for motion, each recon-

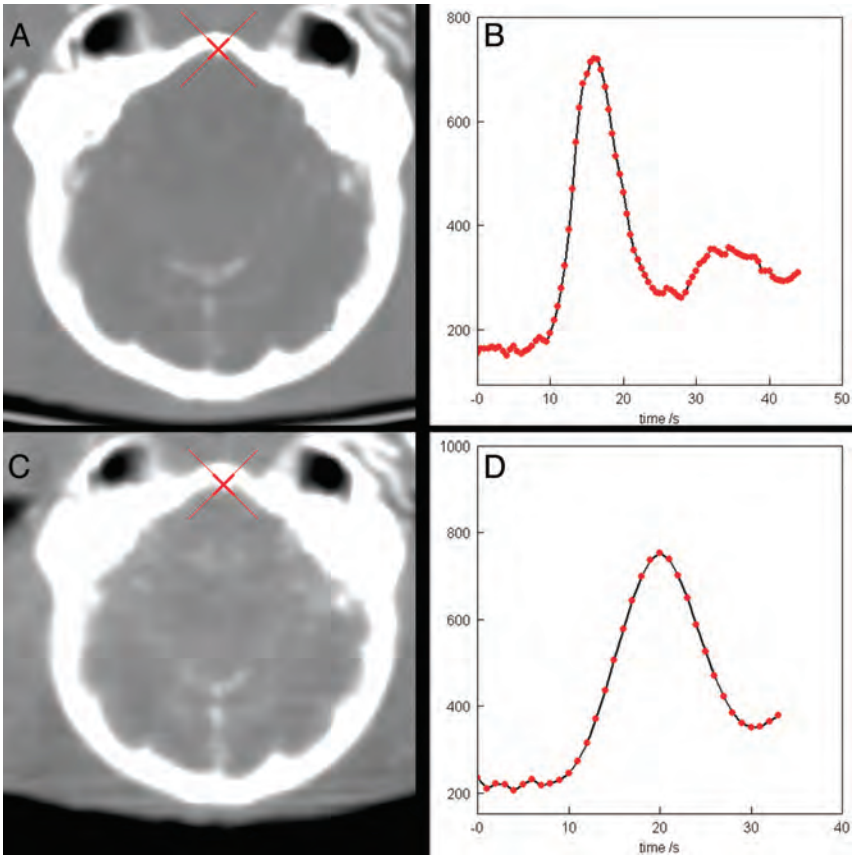

FIG 1. The canine basilar artery was selected as the arterial input function (AIF) reference for all subjects and modalities. *A*, CT section and location of AIF; *B*, TAC for CT AIF location; *C*, C-arm CT section and location of AIF; and *D*, TAC for C-arm CT AIF location.

structed volume was registered with the appropriate baseline volume, that is, forward or reverse. After the motion correction, each voxel was then interpolated to a temporal resolution of 1 volume per second by use of a cubic spline interpolation method and then archived in a standard DICOM CT perfusion format.

Perfusion Data Processing

In an effort to minimize the effect on the measurements as a result of processing the data by use of perfusion software algorithms from 2 vendors,[14] prototype perfusion software (Siemens) was used to calculate the perfusion parameters for both the PCT and C-arm CT datasets. The prototype software consisted of a modified version of the software used by Ganguly et al[8] and Fieselmann et al,[12] which uses a widely accepted deconvolution approach to calculate the dynamic perfusion parameters. To optimize comparison of perfusion maps done on the 2 modalities, C-arm CT and PCT datasets were co-registered.

After co-registration, arterial input functions (AIF) were manually selected in the canine basilar artery (Fig 1). It was chosen as the site of the AIF for 3 reasons. First, the inability to acquire acquisitions with the C-arm in >29 seconds dictated that we use an intracranial vessel rather than an early-filling extracranial vessel to maximize the temporal coverage of the canine's brain enhancement (particularly in the ischemic territory). Second, the multi-section CT orientation made it difficult to obtain section orientations for other intracranial vessels (such as the anterior communicating or middle cerebral arteries) that were not orthogonal to the vessel orientation.[15] Third, the basilar artery has been shown to provide a significant amount of blood flow to the canine cerebral parenchyma.[16] The basilar artery for the canine is approximately 1 mm or less in diameter, which makes it difficult to define the region of interest for the input function in such a way where there is no partial volume effect. To keep the partial volume effects similar between C-arm CT and PCT, the spatial resolution of the reconstructions was kept as similar as possible between the 2 modalities (0.5 mm and 0.6 mm for C-arm and PCT, respectively). A section thickness of 5 mm was used for both modalities.

Qualitative Reader Evaluation

For qualitative analysis of the perfusion maps, 3 experts (2 neuroradiologists and 1 endovascularly trained neurosurgeon with more than 10 years of experience treating cerebrovascular disease) were asked to evaluate 2 series of perfusion maps. The first series of maps was intended to evaluate the independent observer agreement for the identification of an ischemic lesion location within a given perfusion map. The series of maps consisted of both CBV and CBF maps from each of the modalities selected at 2 different nonadjacent section levels (chosen from PCT sections) for each subject (n = 48 total maps from both modalities). For each map, the observers were asked to provide a score of "N" for no lesion, "L" for left hemisphere lesion, "R" for right hemisphere lesion, or "B" for bilateral hemisphere lesion.

The second series of perfusion maps were intended to evaluate the ability for the observers to detect a perfusion mismatch. The observers were presented with a random pair of CBV and CBF maps. Each pair of CBV and CBF maps was from the same technique, the same canine subject, and matched at the same section level. For each pair of maps, the observers were asked to decide if a lesion was present on one or both maps and if there was a mismatch in the size of the lesion, that is, a perfusion mismatch. A mismatch was defined as a difference in the size (area) of the ischemic lesion between the presented CBV and CBF maps. Twenty-four pairs of maps (combined PCT and C-arm CT) were presented to each observer.

The results were then evaluated for interobserver agreement by use of the κ coefficient statistical method.[17]

Quantitative Evaluation

For each technique, CBV and CBF maps (Fig 2) were generated by the prototype and exported in standard DICOM format. Region-of-interest evaluation was performed on a standard syngo X Workplace (Siemens). For each perfusion map, a 0.6-

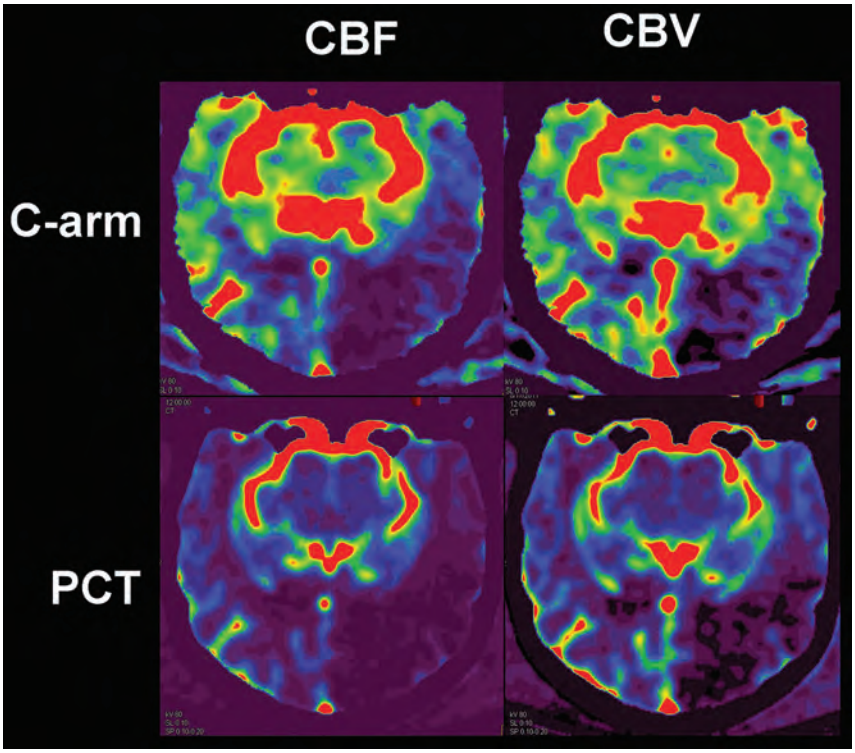

FIG 2. Example of CBV and CBF maps from each technique as presented to the observers. A commercial color map (Syngo PBV Neuro IR; Siemens) was used. All CBF maps used a range of 0–100 mL/100 g/s. All CBV maps used a range of 0–10 mL/100 g.

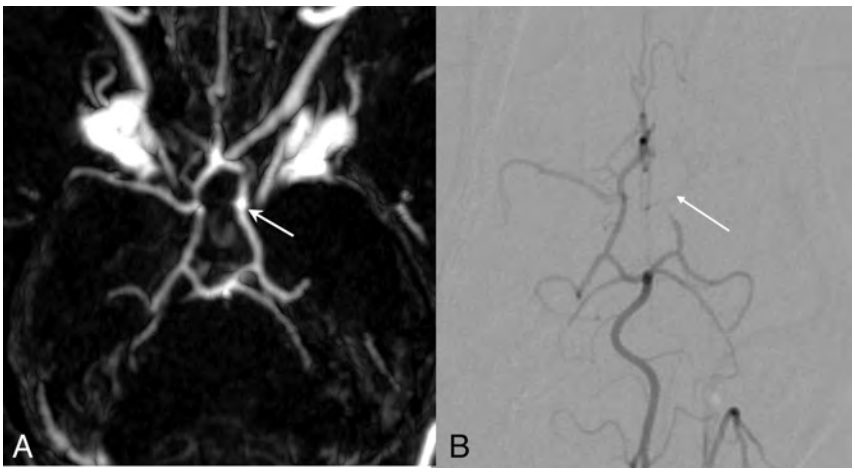

FIG 3. *A,* C-arm CT arterial phase 3D reconstruction show a proximal middle cerebral artery occlusion *(white arrow). B,* Comparison with 2D DSA selective angiogram performed 4 hours earlier also shows a proximal MCA occlusion.

cm^2 region of interest was placed in the center of the ischemic lesion, and a second region of interest was then placed in a symmetric point in the contralateral hemisphere. Care was taken not to include any significant blood vessels within the region circumscribed by the region of interest. This process was performed at 2 different section levels for each subject and for each technique. These perfusion maps were then presented to readers for interpretation and analysis. In addition to the perfusion maps, CTA-like reconstructions were performed with the use of the same datasets (Fig 3).

RESULTS

After review of the results from the first canine, it was determined that an x-ray delay of 8 seconds was too long to capture the rise in arterial enhancement in the basilar artery and thus resulted in a TAC that did not accurately represent the contrast bolus. This resulted in data that were not representative of the other 6 subjects, and, for the purposes of statistical and qualitative analysis, this subject was excluded.

Qualitative Evaluation Results

The combined results of all observers for the lesion detection study are presented in Table 1. Each observer scored a total of 24 randomly presented perfusion maps for each technique. Table 2 presents the statistical results of the κ interobserver agreement evaluation for the lesion detection study.

Table 3 presents the combined observer results from the mismatch detection study. Each observer scored a total of 12 randomly presented section-matched pairs (CBV and CBF) of maps for each technique. Table 4 presents the statistical results of the κ interobserver agreement evaluation for the mismatch detection study.

Quantitative Evaluation Results

For each subject, a region of interest was placed, as closely as possible, in the center of the ischemic lesion; a second region of interest was then placed in a symmetric location in the contralateral hemisphere. This process was performed at 2 different nonadjacent section levels for each subject. Table 5 summarizes the mean values and standard deviations for CBF measurements for each technique. A similar comparison of CBV results is shown in Table 6.

A regression analysis of the C-arm and PCT CBF and CBV region-of-interest measurements indicates an R^2 value of 0.85 for CBF measurements and 0.68 for CBV, indicating a relatively strong correlation for both values. Concordance correlation coefficients were also calculated as 0.56 and 0.39, respectively, for CBF and CBV measurements.

A Bland-Altman analysis was also performed for both the CBV and CBF measurements between the 2 modalities. The results in Fig 4 show that there is a systematic overestimation of both CBF and CBV for the C-arm CT measurements relative to the PCT measurements. The degree of overestimation by C-arm CT is shown to in-

Table 1: Combined observer results for lesion identification and location by modality

	Left	Right	Bilateral	None
C-arm ($n = 72$)	60	12	0	0
PCT ($n = 72$)	49	16	3	4

Note:—n = total number of CBV and CBF perfusion maps presented to all observers per modality.

Table 2: Kappa statistical evaluation for interobserver performance of ischemic lesion detection for 3 independent observers

	κ Coefficient	Percentage Agreement	Statistical Significance
C-arm ($n = 24$)	1.00	100.0%	$P < .01$
PCT ($n = 24$)	0.74	87.5%	$P < .01$

Note:—n = total number of perfusion maps presented to a single observer.

Table 3: Combined observer results for mismatch identification by modality

	CBV/CBF Mismatch (Yes)	CBV/CBF Mismatch (No)
C-arm ($n = 36$)	21	15
PCT ($n = 36$)	31	5

Note:—n = total number of CBV and CBF perfusion map pairs presented to all observers per modality.

Table 4: Kappa statistical evaluation for interobserver performance of ischemic lesion mismatch (CBF/CBV lesion size) detection for 3 independent observers

	κ Coefficient	Percentage Agreement	Statistical Significance
C-arm ($n = 12$)	0.31	66.6%	$P = .03$
PCT ($n = 12$)	0.07	77.7%	$P = .34$

Note:—n = total number of perfusion maps presented to a single observer.

Table 5: Summary of CBF measurements

	Ischemic Hemisphere	Normal Hemisphere
Mean C-arm CBF measurements	13.2 ± 7.4	40.3 ± 13.6
Mean PCT CBF measurements	3.9 ± 2.0	18.6 ± 7.7

Note:—All values are listed in units of mL/100 g/s.

Table 6: Summary of CBV measurements

	Ischemic Hemisphere	Normal Hemisphere
Mean C-arm CBV measurements	1.6 ± 0.9	4.9 ± 1.6
Mean PCT CBV measurements	0.8 ± 0.5	2.0 ± 0.6

Note:—All values are listed in units of mL/100 g.

crease with higher measured CBF and CBV values. The line fit of the data are plotted on each Bland-Altman plot to illustrate this trend of the C-arm CT perfusion region-of-interest measurements.

C-arm CT and PCT exhibited an agreement in 10 of 12 regions of interest (83%) of a CBF reduction in the ischemic hemisphere (relative to the normal hemisphere) of at least 50%. An agreement was found in 7 of 12 regions of interest (58%) for the CBV measurement.

DISCUSSION

The goal of this study was to evaluate the feasibility of performing measurements of CBV and CBF with the use of a novel high-speed 3D acquisition on a flat detector C-arm angiographic system (with PCT used as a criterion standard), in a canine stroke model. Statistical analysis of the region-of-interest data indicates a good correlation between C-arm CT and PCT measured perfusion values, with the C-arm CT tending to overestimate the measured perfusion value (both CBV and CBF) relative to PCT (Fig 4). Our qualitative analysis also demonstrates similar interobserver agreement between the C-arm CT and PCT modalities for both lesion detection and identification of perfusion mismatch.

The statistical results from the observer-based lesion detection study (Table 2) indicate that there is substantial to almost perfect agreement among the observers for detection and location of the ischemic lesions for both the PCT and C-arm CT perfusion maps. An interobserver agreement of 100% was found for the lesion identification on C-arm CT maps, indicating that C-arm CT maps are relatively easy to read and interpret.

The statistical results from the observer-based mismatch detection study (Table 4) indicate that the interobserver agreement for mismatch identification (as measured by the κ coefficient) is significantly less than for the lesion detection. Despite the relatively low κ coefficients, the readers show a similar percentage agreement between PCT and C-arm modalities for the mismatch study, indicating that the observers had similar interpretations of the maps for both C-arm and PCT modalities. One well-known drawback of the κ statistic is the loss of significance when measuring agreement between observers in cases with a rare number of findings.[18] It is important to note that observers identified a small number of cases with no mismatch (Table 3) for both the C-arm maps ($n = 15$) and the PCT maps ($n = 5$). It is likely that the κ statistic is unfairly penalized as a result of this issue.

Three factors help to explain limitations of the C-arm CT acquisition and the lack of agreement seen in the measurements of CBV and CBF obtained with C-arm CT and PCT. First, it is well documented that because of limitations in low contrast resolution, the current commercially available flat detector C-arm CT systems are not capable of tissue contrast at the level of accuracy and sensitivity that is possible with the use of standard diagnostic CT; the limit of C-arm CT contrast resolution is approximately 10 HU for the highest-quality scan protocols.[19-21] Many standard CT perfusion protocols are performed with the use of injections of 40–60 mL of contrast agent at a rate of 4–5 mL/s. This results in time enhancement curves for arteries and veins that often peak on the order of several hundreds of HU (or more) relative to the baseline. The contrast resolution of C-arm CT is sufficiently sensitive to measure intensity values of this magnitude for arterial and venous anatomic structures. However, with the use of such an injection protocol, the time enhancement curves in normal parenchyma (white/gray matter) often peak at <20 HU (relative to baseline) and even less in the ischemic tissue.[22] These levels are just at the limit of the contrast resolution of currently available C-arm CT detectors. The experimental high-speed C-arm CT protocol used in our study captured only 133 projection images during each of the 7 rotations, and this undersampled acquisition further limits the contrast resolution as compared with the highest-quality C-arm CT scans, which acquire almost 500 projections over a period of 20 seconds. Second, the lower temporal resolution (in addition to the applied smoothing kernels) of the C-arm CT results in an interpolated time attenuation curve that is broader and peaks significantly lower when compared with conventional CT, an effect more pronounced for arterial voxels (Fig

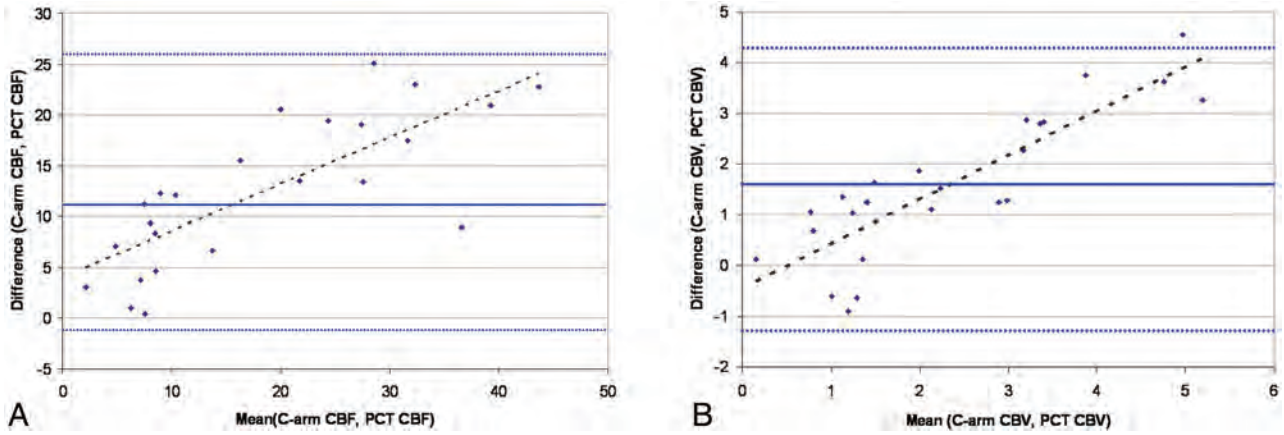

FIG 4. *A,* Bland-Altman analysis of CBF measurements; *B,* Bland-Altman analysis of CBV measurements.

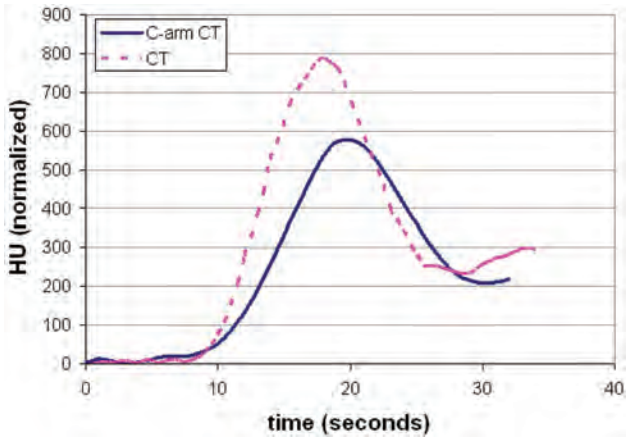

FIG 5. CBF overestimation by C-arm CT primarily caused by differences in AIF measurements between PCT and C-arm CT.

5). As a result, the underestimated arterial AIF curve enhancement level inversely impacts the global scaling of the perfusion parameters and thus introduces our overestimation of these values. Third, at the time of the study, the C-arm system was limited to a maximum of 7 bidirectional rotations, which resulted in a window of data acquisition that was limited to 33.6 seconds from the start of the injection. Because of the canine's relatively fast circulation times, this constraint presented truncation of TAC data for only the ischemic regions of the brain and probably was a factor in the lower number of identified perfusion mismatches for the C-arm perfusion maps compared with PCT (Table 3). This limited temporal window probably would present issues for TAC measurement in humans for both normal and ischemic tissue because of the relatively slower circulation times relative to that of the canine.

To compensate somewhat for the lack of contrast resolution, contrast was injected at a higher rate for the C-arm CT studies than what was used for the standard PCT (3.5 mL/s versus 2 mL/s). This provided a higher level of peak enhancement in the parenchyma and simultaneously allowed us to minimize the differences in the total duration (length) of the contrast bolus as compared with that used for PCT. In further efforts to maximize contrast resolution SNR was improved in the images by use of a smooth kernel for reconstruction (noise reduction) and by performing additional smoothing along the sections (z-direction). Whereas these smoothing algorithms do provide increased SNR for the parenchyma, the smoothing operation removes high spatial frequency content such that the true HU measurements are no longer maintained. This (combined with the low temporal sampling of C-arm CT) causes the issue of underestimation of the Hounsfield level measurements of the arterial curves (Fig 5) and can result in the overestimation of parenchymal enhancement in the vicinity of highly enhancing arteries and veins.

The fastest commercial C-arm CT acquisition protocols are typically ≥6 seconds for a temporal series of 3D acquisitions. Our prototype high-speed rotational protocol increased the speed of the gantry rotation so that it allowed a temporal sampling rate of 4.3 seconds. Wintermark et al[7] performed a systematic in vivo evaluation of the impact of varying temporal sampling rates for PCT measurements and found that there was a significant increase in measured values for CBV and CBF as the temporal resolution decreased beyond 1 sample every 3 seconds (based on a total volume of 40 mL injected at 4 mL/s). These findings are in line with our C-arm CT measurements (acquired at 1 sample every 4.3 seconds) of CBF and CBV because our measurements consistently overestimated these values relative to PCT (acquired at 1 sample per second) and led us to conclude that the overestimation for C-arm CT CBV and CBF parameters is primarily caused by low sampling frequency.[7]

Wintermark et al[7] also showed that injecting contrast for a longer duration, while by using the same injection rate, can effectively widen the contrast bolus. This can also help to compensate for a lack of temporal resolution. They were able to achieve quantitatively accurate measurements with a temporal sample rate of 1 sample every 4 seconds simply by increasing the total volume of the contrast from 40 mL to 60 mL. This would indicate that a similar strategy could potentially be applied to perfusion measurements performed with a C-arm CT protocol as one method to compensate for the limitations in temporal resolution. This was not performed in our study because the C-arm CT system was limited to a maximum of 7 bi-directional rotations (total scan time of 28.6 seconds). This limitation thus prevented us from further increasing the injection duration because severe truncation of the enhancement curves would occur.

Ongoing improvements to both system hardware (detector

and C-arm gantry) and processing algorithms are likely to further improve the contrast resolution limitations with the current high-speed C-arm CT acquisitions. The next generation of flat detectors will exhibit increased readout rates (allowing for more projections and faster acquisition times), increased contrast sensitivity, and increased bit depth, which will all lead to reconstructions with superior SNR to currently available systems. Software algorithms such as edge-preserving bi-lateral filters,[23] iterative reconstruction techniques,[24] compressed sensing algorithms,[25] and many other state-of-the-art image processing and image reconstruction algorithms must be evaluated to further optimize the image quality and quantitative accuracy of this technique.

Future engineering improvements in the C-arm gantry as well as the control and data acquisitions systems are necessary to improve temporal resolution limitations by shortening the delay time between rotations and further increasing speed of the C-arm rotation. Additional engineering efforts are also necessary to allow for series of bidirectional acquisitions that can extend up to 50 seconds from the start of the injection to prevent truncation of the TAC curves in the ischemic regions of the brain.

At the time of the study, the prototype and visualization software had not yet been optimized to generate and process high-quality MTT and TTP maps. Future work will also include the generation and evaluation of the full suite of cerebral perfusion parameters with C-arm CT perfusion imaging protocols. A comparison of radiation dose was also not considered for this study, and further studies must be performed to optimize and characterize the radiation dose to the patient with the C-arm CT perfusion imaging technique. Flat detector C-arm CT also provides the possible advantage of whole-brain perfusion imaging because the field of view is adequate to image the entire human brain with each rotational acquisition and should be considered for evaluation in future studies.

This study has shown the feasibility of acquiring dynamic cerebral perfusion measurements with the use of C-arm CT on a commercially available angiography system. This technology has the potential to provide physicians with the ability to evaluate both the physiologic state and vascular anatomic details of a patient in the angiography suite before, during, and after an intervention. Furthermore, this technology takes us 1 step closer to providing the necessary tools that will allow suitable patients with acute ischemic stroke to be taken directly from the emergency department to the interventional suite for diagnosis, triage, and treatment, potentially saving significant amounts of time otherwise spent in transport to and from diagnostic imaging modalities.

CONCLUSIONS

Qualitative and semi-quantitative measurements of CBF and CBV with the use of a C-arm CT system and a single intravenous injection of contrast agent are feasible. Further imminent improvements in C-arm system design, detector sensitivity and readout rates, and software algorithms seem likely to improve the ability to accurately measure (quantify) perfusion parameters by using flat detector angiographic systems. Availability of these tools has the potential to allow for a decrease in time to revascularization and further assessment of physiologic changes in patients with stroke during treatment in the angiographic suite.

ACKNOWLEDGMENTS

We thank our colleagues, Dr Beverly Aagaard-Kienitz and Dr David Niemann, who reviewed and scored the CBF and CBV maps.

Disclosures: Kevin Royalty—*RELATED: Grant:* Siemens Medical Solutions USA,* Comments: Funding for project was provided by Siemens; *UNRELATED: Employment:* Siemens Medical Solutions USA; OTHER RELATIONSHIPS: Full-time PhD student at University of Wisconsin Department of Biomedical Engineering. Michael Manhart—*RELATED: Grant:* Siemens AG, Angiography & Interventional X-Ray Systems, Forchheim, Germany.* Yu Deuerling-Zheng—*UNRELATED: Employment:* Siemens Healthcare. Charles Strother—*RELATED: Grant:* Siemens Healthcare,* Comments: Master Research agreement with UW; *Support for Travel to Meetings for the Study or Other Purposes:* Siemens Healthcare (under the Master Research agreement with UW), Comments: For scientific peer-reviewed meeting presentations; *UNRELATED: Other:* Payment for IP licensed by Siemens Healthcare. Andreas Fieselmann—*UNRELATED: Employment:* Siemens AG (**money paid to institution*).

REFERENCES

1. Lees KR, Hankey GJ, Hacke W. **Design of future acute-stroke treatment trials.** *Lancet Neurol* 2003;2:54–61
2. Struffert T, Deuerling-Zheng Y, Kloska S, et al. **Cerebral blood volume imaging by flat detector computed tomography in comparison to conventional multislice perfusion CT.** *Eur Radiol* 2010;21:882–89
3. Struffert T, Deuerling-Zheng Y, Kloska S, et al. **Flat detector CT in the evaluation of brain parenchyma, intracranial vasculature, and cerebral blood volume: a pilot study in patients with acute symptoms of cerebral ischemia.** *AJNR Am J Neuroradiol* 2010;31:1462–69
4. Ahmed AS, Zellerhoff M, Strother CM, et al. **C-arm CT measurement of cerebral blood volume: an experimental study in canines.** *AJNR Am J Neuroradiol* 2009;30:917–22
5. Bley T, Strother CM, Pulfer K, et al. **C-arm CT measurement of cerebral blood volume in ischemic stroke: an experimental study in canines.** *AJNR Am J Neuroradiol* 2010;31:536–40
6. Yasuda R, Royalty K, Pulfer K, et al. **C-arm CT measurement of cerebral blood volume using intra-arterial injection of contrast medium: an experimental study in canines.** *AJNR Am J Neuroradiol* 2012;33:1696–1701
7. Wintermark M, Smith WS, Ko NU, et al. **Dynamic perfusion CT: optimizing the temporal resolution and contrast volume for calculation of perfusion CT parameters in stroke patients.** *AJNR Am J Neuroradiol* 2004;25:720–29
8. Ganguly A, Fieselmann A, Marks M, et al. **Cerebral CT perfusion using an interventional C-arm imaging system: cerebral blood flow measurements.** *AJNR Am J Neuroradiol* 2011;32:1525–31
9. Mordasini P, El-Koussy M, Brekenfeld C, et al. **Applicability of table-side flat panel detector CT parenchymal cerebral blood volume measurement in neurovascular interventions: preliminary clinical experience.** *AJNR Am J Neuroradiol* 2011;33:154–58
10. Zellerhoff M, Deuerling-Zheng Y, Strother CM, et al. **Measurement of cerebral blood volume using angiographic C-arm systems.** *Proc. SPIE* 7262, Medical Imaging 2009: Biomedical Applications in Molecular, Structural, and Functional Imaging, 72620H (February 27, 2009)
11. Van der Bom IMJ, Mehra M, Walvick RP, et al. **Quantitative evaluation of C-Arm CT cerebral blood volume in a canine model of ischemic stroke.** *AJNR Am J Neuroradiol* 2012;33:353-58
12. Fieselmann A, Ganguly A, Deuerling-Zheng Y, et al. **A dynamic reconstruction approach for cerebral blood flow quantification with an interventional C-arm CT.** *2010 IEEE International Symposium on Biomedical Imaging: From Nano to Macro* 2010:53–56
13. Fieselmann A, Ganguly A, Deuerling-Zheng Y, et al. **Interventional 4-D C-arm CT perfusion imaging using interleaved scanning and partial reconstruction interpolation.** *IEEE Trans Med Imaging* 2012;31:892–906

14. Kudo K, Sasaki M, Yamada K, et al. **Differences in CT perfusion maps generated by different commercial software: quantitative analysis by using identical source data of acute stroke patients.** *Radiology* 2010;254:200–09
15. Konstas AA, Goldmakher GV, Lee TY, et al. **Theoretic basis and technical implementations of CT perfusion in acute ischemic stroke, part 2: technical implementations.** *AJNR Am J Neuroradiol* 2009;30:885–92
16. Wellens D, Wouters L, De Reese R, et al. **The cerebral blood distribution in dogs and cats: an anatomical and functional study.** *Brain Res* 1975;86:429–38
17. Vierra AJ, Garrett JM. **Understanding interobserver agreement: the kappa statistic.** *Fam Med* 2005;37:360–61
18. Feinstein AR, Cicchetti DV. **High agreement but low kappa: I. The problems of two paradoxes.** *J Clin Epidemiol* 1990;43:543–49
19. Struffert T, Richter G, Engelhorn T, et al. **Visualisation of intracerebral haemorrhage with flat-detector CT compared to multislice CT: results in 44 cases.** *Eur Radiol* 2009;19:619–25
20. Kalender WA. **Der Einsatz von Flachbilddetektoren für die CT-Bildgebung.** *Der Radiologe* 2003;43:379–87
21. Loose R, Wucherer M, Brunner T. **Visualization of 3D low contrast objects by CT cone-beam reconstruction of a rotational angiography with a dynamic solid body detector.** *RoFo* 2005;S1:PO 160
22. Silvennoinen HM, Hamberg LM, Valanne L, et al. **Increasing contrast agent concentration improves enhancement in first-pass CT perfusion.** *AJNR Am J Neuroradiol* 2007;28:1299–303
23. Manduca A, Yu L, Trzasko JD, et al. **Projection space denoising with bilateral filtering and CT noise modeling for dose reduction in CT.** *Med Phys* 2009;36:4911–19
24. Supanich, M, Tao Y, Nett B, et al. **Radiation dose reduction in time-resolved CT angiography using highly constrained back projection reconstruction.** *Phys Med Biol* 2009;54:4575–93
25. Nett BE, Brauweiler R, Kalender W, et al. **Perfusion measurements by micro-CT using prior image constrained compressed sensing (PICCS): initial phantom results.** *Phys Med Biol* 2010;55:2333–50

Arterial Spin-Labeled Perfusion Imaging Reflects Vascular Density in Nonfunctioning Pituitary Macroadenomas

N. Sakai, S. Koizumi, S. Yamashita, Y. Takehara, H. Sakahara, S. Baba, Y. Oki, H. Hiramatsu, and H. Namba

ABSTRACT

BACKGROUND AND PURPOSE: Angiogenesis is very important in clinical features of pituitary adenomas. We investigated the relationship between the blood flow of nonfunctioning pituitary macroadenomas measured by arterial spin-labeled perfusion imaging and the microvessel attenuation of the tissue.

MATERIALS AND METHODS: Conventional MR imaging with contrast-enhanced T1WI and arterial spin-labeled perfusion imaging were performed before surgery in 11 consecutive patients with nonfunctioning pituitary macroadenomas. ROIs were drawn on the tumors, and the degrees of enhancement were calculated by dividing the signal intensity on the contrast-enhanced T1WI by that on the nonenhanced T1WI. As an index of tumor perfusion, a quantitative analysis was performed by using normalized tumor blood flow values calculated by dividing the mean value of the tumor region of interest by the mean region of interest values in the 2 cerebellar hemispheres. The relative microvessel attenuation was determined as the total microvessel wall area divided by the entire tissue area on CD-31-stained specimens. The degree of enhancement and the normalized tumor blood flow values were compared with relative microvessel attenuation. Additionally, intra- and postoperative tumor hemorrhages were visually graded.

RESULTS: The degree of enhancement was not correlated with relative microvessel attenuation. Statistically significant correlations were observed between normalized tumor blood flow values and relative microvessel attenuation ($P < .05$). At surgery, 3 cases were visually determined to be hypervascular tumors, and 1 of these cases had symptomatic postoperative hemorrhage. A statistically significant difference in normalized tumor blood flow values was observed visually between the intraoperative hypovascular and hypervascular groups ($P < .05$).

CONCLUSIONS: Arterial spin-labeled perfusion imaging reflects the vascular density of nonfunctioning pituitary macroadenomas, which may be useful in the preoperative prediction of intra- and postoperative tumor hemorrhage.

ABBREVIATIONS: ASL-PI = arterial spin-labeled perfusion imaging; nTBF = normalized tumor blood flow; TBF = tumor blood flow; %Vessel = relative microvessel attenuation

Pituitary adenomas are common intracranial neoplasms, with up to 16.7% of the population harboring an incidental tumor.[1] Although most pituitary adenomas grow slowly, some may begin to grow rapidly and become invasive.[2] Solid tumors are dependent on the process of angiogenesis for growth.[3] The measurement of microvessel attenuation has been shown to be a useful quantitative method for assessing angiogenesis.[2] The assessment of the differences in vascular density in pituitary adenomas may be helpful for predicting subsequent tumor aggressiveness[4-6] and vascular complications associated with transsphenoidal surgery.[7,8]

Arterial spin-labeled perfusion imaging is a noninvasive MR perfusion technique that measures CBF by using arterial water as a freely diffusing tracer without the requirement of exogenous contrast material.[9] In clinical applications, ASL-PI has been proved reliable and reproducible for the assessment of CBF in various pathologic states,[1] including cerebrovascular diseases,[10,11] neurodegenerative diseases,[12] and brain tumors.[13,14] ASL-PI may predict histopathologic vascular density[15] and may reflect angiogenesis in tumors. The purpose of our study was to determine the relationship between the blood flow of nonfunctioning pituitary macroadenomas measured by using ASL-PI and histopathologic findings of microvessel attenuation. Furthermore, we examined the utility of ASL-PI in predicting intra- and postoperative tumor hemorrhage.

Received November 1, 2012; accepted after revision January 26, 2013.

From the Departments of Neurosurgery (N.S., S.K., H.H., H.N.), Radiology (S.Y., Y.T., H.S.), Diagnostic Pathology (S.B.), and Endocrinology and Metabolism (Y.O.), Hamamatsu University School of Medicine, Hamamatsu, Japan.

Please address correspondence to Naoto Sakai, MD, PhD, Department of Neurosurgery, Hamamatsu University School of Medicine, 1-20-1, Handayama, Higashi-ku, Hamamatsu, Japan 431-3192; e-mail: nsakaineurosurg@gmail.com

http://dx.doi.org/10.3174/ajnr.A3564

Summary of patient characteristics, histopathologic findings, tumor volume and enhancement, microvessel density, and intra- and postoperative hemorrhages in 11 patients with nonfunctioning pituitary macroadenomas

Case/Age (yr)/Sex	Initial/ Recurrence	Histopathology	Tumor Volume (cm)	Degree of Enhancement of Tumor	ASL-PI nTBF	ASL-PI TBF (mL/min/100 g)	CD-31 %Vessel	Intraoperative Vascularity Findings	Postoperative Hemorrhage
1/72/M	Initial	SGA	11.4	1.48	1.94	94.4	24.0	(+)	(+)[a]
2/52/M	Recurrence	NCA	8.7	1.50	0.47	29.5	1.3	(−)	(−)
3/63/M	Initial	SGA	4.7	1.36	0.96	22.7	0.7	(−)	(−)
4/48/F	Recurrence	SGA	2.2	1.44	0.75	51.0	1.7	(−)	(−)
5/54/M	Initial	SGA	6.0	1.71	1.88	74.2	17.0	(+)	(+)
6/69/M	Recurrence	NCA	7.7	1.81	0.72	26.6	2.6	(−)	(−)
7/60/F	Initial	NCA	2.8	1.27	0.51	38.0	1.1	(−)	(−)
8/34/F	Initial	SGA	4.9	1.88	0.73	59.5	1.2	(−)	(−)
9/68/M	Recurrence	NCA	3.4	1.82	0.76	26.6	2.6	(−)	(−)
10/60/F	Initial	NCA	9.9	1.68	2.45	102.6	19.0	(+)	(+)
11/67/M	Recurrence	SGA	4.7	1.96	1.03	46.2	6.4	(−)	(−)

Note:—SGA indicates gonadotroph adenoma; NCA, null cell adenoma; ASL-PI nTBF, tumor blood flow normalized to the cerebellum measured with ASL-PI; ASL-PI TBF, absolute tumor blood flow (milliliters per minute per 100 g) measured with ASL-PI; (−), hypovascular; +, hypervascular.
[a] Symptomatic hemorrhage.

MATERIALS AND METHODS

Patients

Between June 2011 and March 2012, eleven consecutive patients (7 men and 4 women) with pituitary macroadenomas were admitted to the University Hospital of Hamamatsu University School of Medicine for surgery. All patients were evaluated by 1 endocrinologist (Y.O.) and were diagnosed as having clinically nonfunctioning pituitary adenomas. They underwent ASL-PI with conventional MR imaging and MR angiography. Written informed consent was obtained from all patients. The mean age of the patients was 58 years (range, 34–72 years). Six cases were of initial macroadenomas, and 5 showed recurrences. The chief concerns were visual disturbance in 9 cases and headache and amenorrhea in 1 case each. All patients underwent transsphenoidal surgery performed by a single neurosurgeon (N.S.). All surgical procedures were recorded by using a digital video recorder (DATA Gen Pro; Seventh Dimension Design, Hyogo, Japan) and were reviewed for this study. Intraoperative tumor hemorrhage was rated as hypovascular or hypervascular at surgery by 2 neurosurgeons (N.S. and S.K.) in consensus. "Hypovascular tumors" were defined as tumors with a normal amount of arterial bleeding that rapidly decreased during the process of resection. "Hypervascular tumors" were defined as tumors with a higher-than-normal amount of arterial bleeding that continued throughout the operation. Postoperative hemorrhage from the residual tumor or pituitary gland was estimated by using MR imaging studies performed within 2 days after the operation. The hematoma volume was visually assessed by 2 experienced radiologists (S.Y. and Y.T.) in consensus on sagittal T1WI with fat suppression.

Conventional MR Imaging, MRA, ASL-PI, and ASL Data Processing

Conventional MR imaging studies for pituitary adenomas and MRA were performed on a 1.5T scanner (Signa HDx TwinSpeed; GE Healthcare, Milwaukee, Wisconsin) with an 8-channel brain phased array coil or a 3T scanner (Discovery 750; GE Healthcare) with a 32-channel head-neck-spine array coil.

The sequences of conventional MR imaging included coronal and sagittal fat-suppressed T1WI, fat-suppressed T2WI, and contrast-enhanced fat-suppressed T1WI. The imaging parameters for the 1.5T scanner were as follows: TR/ TE/NEX, 600 ms/9.4 ms/2; receiver bandwidth, 22.7 kHz; section thickness, 3 mm; spacing, 0.3 mm; number of sections, 9; FOV, 15 cm; matrix, 192 × 160 for the fat-suppressed T1WI; and TR/TE/NEX, 3000 ms/101.3 ms/2; receiver bandwidth, 15.6 kHz; section thickness, 3 mm; spacing, 0.3 mm; number of sections, 9; FOV, 15 cm; and matrix, 192 × 160 for the fat-suppressed T2WI. The imaging parameters of the 3T scanner were as follows: TR/TE/NEX, 600 ms/9.2 ms/3; receiver bandwidth, 41.7 kHz; section thickness, 3 mm; spacing, 0.3 mm; number of sections, 9; FOV, 16 cm; and matrix, 320 × 192 for the fat-suppressed T1WI; and TR/TE/NEX, 2000 ms/82.7 ms/2; receiver bandwidth, 41.7 kHz; section thickness, 3 mm; spacing, 0.3 mm; number of sections, 9; FOV, 16 cm; matrix, 320 × 224 for the fat-suppressed T2WI. Fat-suppressed contrast-enhanced T1WI was performed after intravenous administration of gadopentetate dimeglumine (Magnevist; Bayer Schering Pharma, Berlin, Germany) or gadodiamide hydrate (Omniscan;

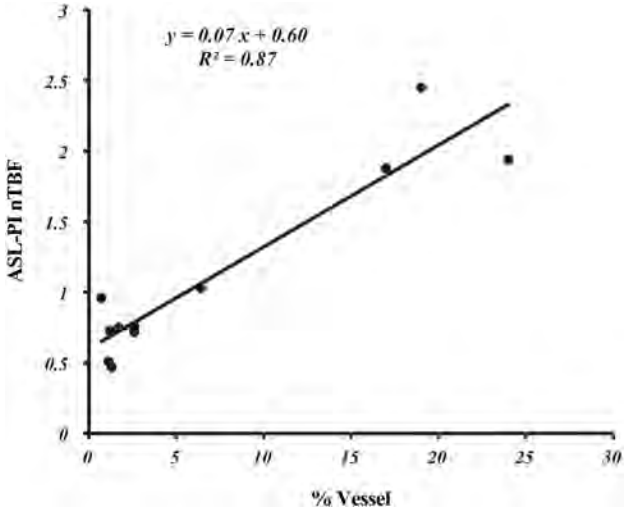

FIG 1. Scatterplot of nTBF determined by arterial spin-labeled perfusion imaging and %Vessel determined by histopathologic examination with regression lines in 11 patients with nonfunctioning pituitary macroadenomas. The correlation between normalized tumor blood flow and %Vessel is statistically significant ($P < .05$) (Spearman rank-order correlation).

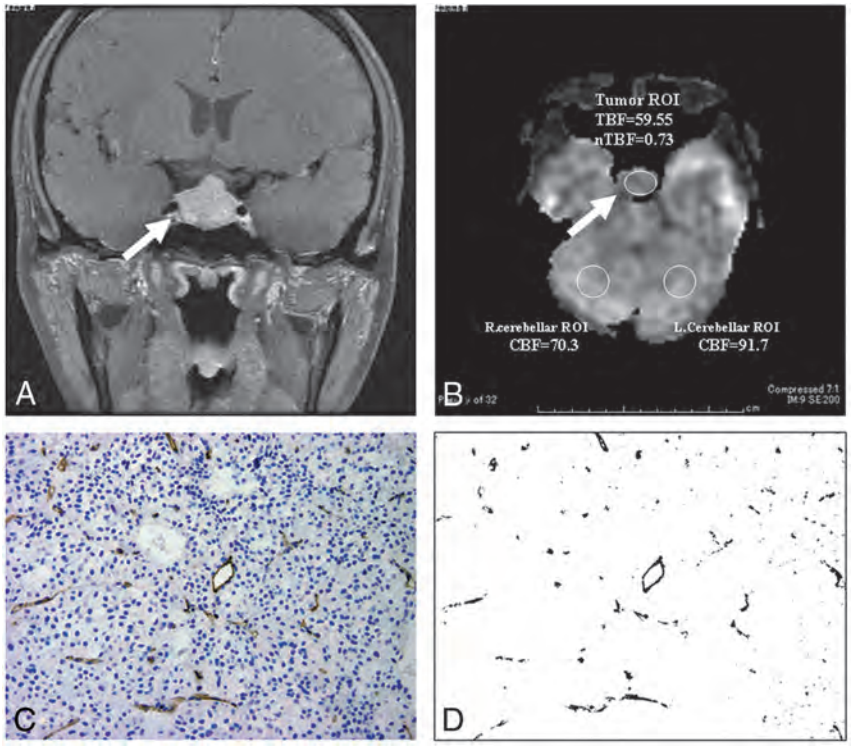

FIG 2. Nonfunctioning pituitary macroadenoma with hypovascularity in a 34-year-old woman (case 8). *A*, Coronal postcontrast fat-suppressed T1WI (TR/TE/NEX = 600 ms/9.4 ms/2) by using a 1.5T scanner shows a strongly enhanced pituitary tumor (*arrow*) (degree of enhancement = 1.88). *B*, Arterial spin-labeled perfusion imaging (TR/TE/NEX = 4594 ms/10.6 ms/3; postlabel delay = 1525 ms; section thickness = 3.8 mm) by using a 3T scanner shows a relatively low signal intensity at the pituitary tumor (*arrow*) (TBF = 59.5 mL/min/100 g, nTBF = 0.73). nTBF = TBF/(Right Cerebellar CBF + Left Cerebellar CBF)/2. The CD-31-immunostained histopathologic specimen (*C*) and the black on the vessel wall area (*D*) indicate low microvascular density (%Vessel = 1.2%).

Daiichi-Sankyo Pharma, Tokyo, Japan) at 0.1 mmol/kg body weight. For contrast-enhanced images, the degree of enhancement was calculated by dividing the mean signal intensity of the region of interest drawn on the tumor on contrast-enhanced fat-suppressed T1WI by the signal intensity in the region of interest drawn on the macroadenoma on the nonenhanced fat-suppressed T1WI. Tumor volumes (cubic centimeters) were calculated by multiplying the vertical and anteroposterior and right-to-left maximum dimensions on postcontrast T1WI and subsequently dividing this value by 2.

We performed 3D time-of-flight MRA on all patients before surgery to confirm that obstructive lesions were not present at the cervical common and internal carotid arteries and intracranial arteries. We used the following parameters: TR/TE/NEX, 30 ms/2.7 ms/0.75; flip angle, 20; receiver bandwidth, 31.2 kHz; section thickness, 1.2 mm; overlap, 0.6 mm; number of sections, 176; FOV, 20 cm; and matrix, 288 × 192 on the 1.5T scanner; and TR/TE/NEX, 18 ms/2.6 ms/1; flip angle, 18; receiver bandwidth, 41.7 kHz; section thickness, 1 mm; overlap, 0.5 mm; number of sections, 208; FOV, 20 cm; and matrix, 320 × 192 on the 3T scanner.

All ASL-PI examinations were performed on the 3T scanner. The imaging parameters were as follows: TR/TE/NEX, 4594 ms/10.6 ms/3; receiver bandwidth, 62.5 kHz; postlabel delay, 1525 ms; section thickness, 3.8 mm; number of sections, 32; FOV, 24 cm; and matrix, 512. These parameters have been fixed in the routine clinical setting at our university hospital for stroke and brain tumors. We performed a pilot study to compare CBF measured by ASL-PI and brain perfusion SPECT in 7 cases of internal carotid artery stenosis. In these cases, a significant linear correlation was obtained between the CBF measured by ASL-PI and the CBF measured by SPECT (coefficient of correlation = 0.5; H.H., unpublished data, December 2012). Therefore, we used the same parameters for ASL-PI in this study. The region of interest was located at the maximal axial cross-section of the pituitary adenomas by referring to the findings on contrast-enhanced fat-suppressed T1WI. To evaluate normalized tumor blood flow, we calculated tumor-to-healthy tissue perfusion ratios by dividing the mean value of the tumor region of interest by the mean value of the ROIs in the bilateral cerebellar hemispheres (approximately 2.5 cm^2 each) by following the method of Järnum et al (Figs 2*B* and 3*B*).[14]

Histopathologic Evaluations

Hematoxylin-eosin-stained sections and immunohistochemical stains against adrenocorticotrophic hormone, prolactin, growth hormone, luteinizing hormone, follicle-stimulating hormone, and thyroid-stimulating hormone were examined by 1 pathologist (S.B.). The samples were classified as null cell adenoma or silent gonadotroph adenoma. We immunostained the tissue sections with CD-31, the most sensitive and specific marker for endothelial cells, to evaluate the vascularity of the nonfunctioning pituitary adenomas. Sections for CD-31 staining were pretreated with Tris-EDTA buffer, pH 9.0, at 95°C for 40 minutes for antigen activation. The monoclonal mouse antihuman CD-31 antibody, clone JC70A (M0823; Dako, Glostrup, Denmark), was applied at a dilution of 1:20 for 30 minutes at room temperature, and the ChemMate EnVision Detection Kit Peroxidase/DAB, Rabbit/Mouse Autostainer (Dako) was used for staining. The CD-31-positive endothelial cell layers indicated the vessel walls. The relative microvessel attenuation (%Vessel) was calculated as the total area of the vessel walls divided by the entire tissue area by following the method of Noguchi et al.[15] A microscopic field of the most intense vascularization in each specimen under a ×20 objective field (area = 0.33 mm^2) was photographed as a JPEG file (1600 × 1200 pixels, 16.7 million colors, 8 bit) by using a microscopic digital color camera. The JPEG files were converted to TIFF files by using Photoshop (Adobe Systems, San Jose, California). The images were analyzed by using ImageJ 1.45s (National Institutes of Health, Bethesda, Maryland) to measure %Vessel by counting the pixel number of the total vessel walls and that of the entire tissue sample.

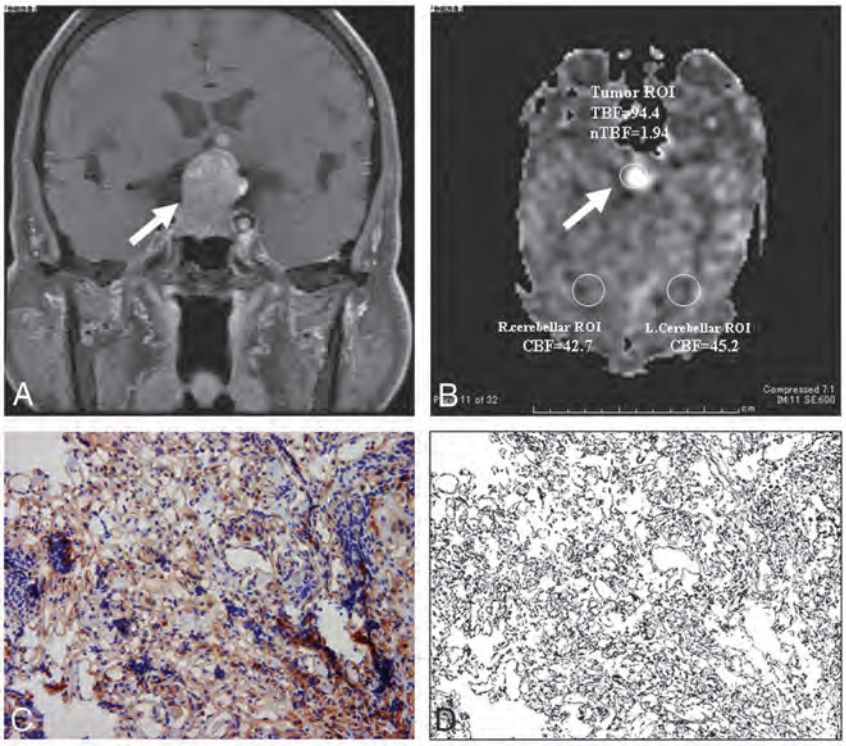

FIG 3. Nonfunctioning pituitary macroadenoma with hypervascularity in a 72-year-old man (case 1) in whom a postoperative symptomatic hemorrhage with visual deterioration required an emergent reoperation to resolve the visual disturbance. *A*, Coronal postcontrast fat-suppressed T1WI (TR/TE/NEX = 600 ms/9.4 ms/2) by using a 1.5T scanner shows a strongly enhanced pituitary tumor (*arrow*) (degree of enhancement = 1.48). *B,* Arterial spin-labeled perfusion imaging (TR/TE/NEX = 4594 ms/10.6 ms/3; postlabel delay = 1525 ms; section thickness = 3.8 mm) by using a 3T scanner shows a relatively high signal intensity at the pituitary tumor (*arrow*) (TBF = 94.4 mL/min/100 g, nTBF = 1.94). nTBF = TBF/(Right Cerebellar CBF + Left Cerebellar CBF)/2. The CD-31-immunostained histopathologic specimen (*C*) and the black on the vessel wall area (*D*) indicate high microvascular density (%Vessel = 24%).

Statistical Analysis

An Excel Statistical Program File ystat2008.xls (programmed by Shinya Yamazaki, DDS, PhD; Igaku-Tosho-Shuppan, Tokyo, Japan) was used for analysis.

The correlation between nTBF and tumor volume was evaluated by using the Spearman rank-order correlation. The differences in nTBF between intraoperative hypovascular and hypervascular tumors were compared by using the Mann-Whitney *U* test. The correlations between the degree of enhancement and %Vessel and between nTBF and %Vessel were evaluated by using the Spearman rank-order correlation. Probability values $< .05$ were considered significant.

RESULTS

Patient characteristics, histopathologic findings, tumor volumes, the degree of enhancement of tumors, ASL-PI nTBF, ASL-PI TBF (milliliter per minute per 100 g), %Vessel of CD-31, and findings of intraoperative tumor vascularity and postoperative hemorrhage are summarized in the Table. The tumor volumes ranged from 2.2 to 11.4 cm^3 (mean, 6.0 ± 3.0 cm^3). The degree of enhancement of the tumors ranged from 1.27 to 1.96 (mean, 1.63 ± 0.23). The ASL-PI nTBF ranged from 0.47 to 2.45 (mean, 1.11 ± 0.66), and the ASL-PI TBF ranged from 22.7 to 102.6 (mean, 51.9 ± 27.9) mL/min/100 g. The %Vessel of CD-31 ranged from 0.7% to 24% (mean, 7.1 ± 8.6%). Five cases were classified as null cell adenomas; and 6, as silent gonadotroph adenomas. A statistically significant correlation was not observed between ASL-PI nTBF and tumor volume. The degree of enhancement was statistically correlated with neither ASL-PI nor %Vessel.

Statistically significant differences in ASL-PI nTBF were observed between hypovascular tumors and hypervascular tumors ($P < .05$). At surgery, 8 cases were determined to be hypovascular tumors, and 3 cases were determined to be hypervascular. The postoperative MR imaging did not reveal any hemorrhages in the hypovascular tumors. On the other hand, all of the hypervascular tumors exhibited postoperative hemorrhage that filled the space after tumor removal. An emergent reoperation the day after the surgery was required for one of these patients because of visual acuity deterioration due to compression by the hematoma. The patient's visual acuity fully recovered after the surgery.

The correlation between ASL-PI nTBF and %Vessel in the 11 cases is shown in Fig 1. Statistically significant positive correlations were found between ASL-PI nTBF and %Vessel (x, %Vessel; y, ASL-PI nTBF; $y = 0.07x + 0.60$, $R^2 = 0.87$, $P \leq .05$).

A representative case of a hypovascular tumor (case 8) and a hypervascular tumor (case 1) are shown in Figs 2 and 3, respectively. A distinctly high signal was observed in the hypervascular pituitary tumor with high microvessel attenuation on ASL-PI (Fig 3; TBF = 94.4 mL/min/100 g, nTBF = 1.94, and CD-31%Vessel = 24.0%). However, a nonspecific signal equivalent to the background cerebellar hemispheres was observed in the hypovascular pituitary tumor with low microvessel attenuation (Fig 2; TBF = 59.5 mL/min/100 g, nTBF = 0.73, and CD-31%Vessel = 1.2%). The degree of enhancement was 1.48 in the hypervascular tumor (case 1) and 1.88 in the hypovascular tumor (case 8).

DISCUSSION

The ASL-PI technique has been developed since its inception in the early 1990s and is now used routinely in daily clinical practice for patients with stroke.[9] This technique is noninvasive, does not require injection of an exogenous contrast agent, and was recently shown to evaluate the perfusion in brain tumors.[13-15] Although the absolute blood flow values could be theoretically determined by ASL-PI,[9] the quantitative CBF determined by ASL-PI can be affected by unstable factors in individual cases such as the arterial transit time of the labeled blood from the labeling plane to the brain tissue within the imaging plane.[15] Lower perfusion with a longer transit time in elderly subjects results in underestimation of the CBF because the distal end of the labeled bolus does not reach the capillary bed.[13] Therefore, the TBF has been normalized

to healthy tissue such as the contralateral gray matter,[13,15] white matter,[13] or the cerebellum[14] in ASL-PI studies. In this study, we chose the cerebellum as the internal reference because cerebellar perfusion usually is unaffected by pathology in the pituitary gland and is easier to measure in the same imaging plane with pituitary adenomas.[14]

In our study, 3 of 11 cases were categorized as hypervascular tumors on the basis of intraoperative findings, and the nTBF of the hypervascular tumors was significantly higher than that of the hypovascular tumors ($P < .05$). Furthermore, all of the hypervascular tumors with a high nTBF showed postoperative hemorrhage. These findings suggest that ASL-PI is useful for predicting intra- and postoperative tumor hemorrhage. Preoperative evaluation of ASL-PI provides useful information for avoiding or preparing for the vascular complications of transsphenoidal surgery, which can lead to mortality and serious morbidity.[7,8]

We found a strong positive correlation between nTBF and %Vessel in the 11 patients with nonfunctioning pituitary macroadenomas, suggesting that ASL-PI reflects the vascular density of nonfunctioning pituitary macroadenomas. To date, the source of the blood supply to pituitary tumors has not been fully elucidated.[2] A portion of the blood supply to tumors is presumably derived from the branches of the internal carotid artery, most commonly the capsular and inferior hypophyseal arteries.[16] The sequential enhancement pattern of pituitary adenomas detected during a dynamic contrast- enhanced study suggests that pituitary adenomas have a direct arterial blood supply.[17] We speculate that ASL-PI measures the arterial blood flow of the pituitary adenoma that is derived mainly from the branches of the internal carotid artery and, to some extent, from the external carotid artery. However, further studies are necessary to characterize the blood supply of pituitary tumors fully.

Although we observed a trend toward a positive correlation between nTBF and tumor volumes in this study, this correlation did not reach statistical significance. Further studies with a larger sample size are necessary to reveal the chronologic changes of the arterial blood supply to the tumor reflected by nTBF in the process of tumor enlargement.

All of the 11 cases in this study showed strong contrast enhancement. If the contrast agent was confined to the intravascular space and caused a signal enhancement proportional to its concentration, the degree of enhancement could have reflected the vascular density of the tumors. However, nonspecific gadolinium chelates rapidly equilibrate between the intravascular and extracellular matrix of tumors.[18] This phenomenon may primarily explain why the degree of enhancement did not linearly correlate with the vascular density in this study.

The lack of a quantitative analysis of intraoperative tumor hemorrhage was a limitation of our study. The decision regarding tumor vascularization depended on the surgeon's subjective measurement. Intraoperative angiography by using indocyanine green fluorescence with a quantitative analysis may be helpful for evaluating tumor vascularization. The low spatial resolutions and limited section coverage of the present ASL-PI were major technical limitations. The measurement of CBF in the normal pituitary gland and microadenomas is difficult by the present methods. The difference in the feeding arteries between the internal carotid artery and the external carotid artery may have affected the timing of the bolus arrival, possibly resulting in bias. ASL-PI with selective labeling of the external carotid artery[19] may resolve this bias. Finally, possible disagreements existed between the measurement region of nTBF and %Vessel in the histopathologic specimen.

CONCLUSIONS

Our study results revealed a positive correlation between nTBF and %Vessel in nonfunctioning pituitary macroadenomas, suggesting that ASL-PI reflects the vascular density of nonfunctioning pituitary macroadenomas. ASL-PI may be useful in the preoperative prediction of intra- or postoperative tumor hemorrhage.

REFERENCES

1. Ezzat S, Asa SL, Couldwell WT, et al. **The prevalence of pituitary adenomas.** *Cancer* 2004;101:613–19
2. Turner HE, Harris AL, Melmed S, et al. **Angiogenesis in endocrine tumors.** *Endocr Rev* 2003;24:600–32
3. Folkman J. **Seminars in medicine of the Beth Israel Hospital, Boston: clinical applications of research on angiogenesis.** *N Engl J Med* 1971;285:1182–86
4. Jugenburg M, Kovacs K, Stefaneanu L, et al. **Vasculature in nontumorous hypophyses, pituitary adenomas, and carcinomas: a quantitative morphologic study.** *Endocr Pathol* 1995;6:115–24
5. Turner HE, Nagy ZN, Gatter KC, et al. **Angiogenesis in pituitary adenomas and the normal pituitary gland.** *J Clin Endocrinol Metab* 2000;85:1159–62
6. de la Torre NG, Turner HE, Wass JA. **Angiogenesis in prolactinoma: regulation and relationship with tumor behaviour.** *Pituitary* 2005;8:17–23
7. Laws ER Jr. **Vascular complications of transsphenoidal surgery.** *Pituitary* 1999;2:163–70
8. Berker M, Aghayev K, Saatci I, et al. **Overview of vascular complications of pituitary surgery with special emphasis on unexpected abnormality.** *Pituitary* 2010;13:160–67
9. Deibler AR, Pollock JM, Kraft RA, et al. **Arterial spin-labeling in routine clinical practice. Part 1. Technique and artifacts.** *AJNR Am J Neuroradiology* 2008;29:1228–34
10. Wang DJ, Aloger JR, Quiao JX, et al. **The value of arterial spin-labeled perfusion imaging in acute ischemic stroke: comparison with dynamic susceptibility contrast-enhanced MRI.** *Stroke* 2012;43:1018–24
11. Bokkers ROH, Hermandez DA, Merino HJ, et al. **Whole-brain arterial spin labeling perfusion in patients with acute stroke.** *Stroke* 2012;43:1290–94
12. Alsop DC, Detre JA, Grossman M. **Assessment of cerebral blood flow in Alzheimer's disease by spin-labeled magnetic resonance imaging.** *Ann Neurol* 2000;47:93–100
13. Warmuth C, Günther M, Zimmer C. **Quantification of blood flow in brain tumors: comparison of arterial spin labeling and dynamic susceptibility-weighted contrast-enhanced MR imaging.** *Radiology* 2003;228:523–32
14. Järnum H, Steffensen EG, Knutsson L, et al. **Perfusion MRI of brain tumours: a comparative study of pseudo-continuous arterial spin labeling and dynamic susceptibility contrast imaging.** *Neuroradiology* 2010;52:307–17
15. Noguchi T, Yoshiura T, Hiwarashi A, et al. **Perfusion imaging of brain tumors using arterial spin-labeling: correlation with histopathologic vascular density.** *AJNR Am J Neuroradiol* 2008;29:688–93
16. Powell DF, Baker HL, Laws ER. **The primary angiographic findings in pituitary adenomas.** *Radiology* 1974;110:589–95
17. Yuh WT, Fisher DJ, Nguyen HD, et al. **Sequential MR enhancement pattern in normal pituitary gland and in pituitary adenoma.** *AJNR Am J Neuroradiol* 1994;15:101–08
18. Roberts TPL, Roberts HC. **Macromolecular contrast agents.** In: Dawson P, Cosgrove DO, Grainger RG, eds. *Textbook of Contrast Media.* San Francisco: Isis Medical Media Ltd; 1999:355–71
19. Sasao A, Hirai T, Nishimura S, et al. **Assessment of vascular supply of hypervascular extra-axial brain tumors with 3T MR regional perfusion imaging.** *AJNR Am J Neuroradiol* 2010;31:554–58

Effect of Age on MRI Phase Behavior in the Subcortical Deep Gray Matter of Healthy Individuals

J. Hagemeier, M.G. Dwyer, N. Bergsland, F. Schweser, C.R. Magnano, M. Heininen-Brown, D.P. Ramasamy, E. Carl, C. Kennedy, R. Melia, P. Polak, A. Deistung, J.J.G. Geurts, J.R. Reichenbach, and R. Zivadinov

ABSTRACT

BACKGROUND AND PURPOSE: It has been demonstrated that increased levels of iron in the brain occur with aging. In this study we investigated the nature of the association between age and SWI-filtered phase values, indicative of iron content, in the subcortical deep gray matter of healthy individuals.

MATERIALS AND METHODS: A total of 210 healthy individuals (men: $n = 89$, women: $n = 121$), mean age, 39.8 years (standard deviation = 15.5; range = 6–76 years), were imaged on a 3T scanner. Mean MRI phase, mean phase of low-phase voxels, and normalized volumes were determined for total subcortical deep gray matter, caudate, putamen, globus pallidus, thalamus, pulvinar nucleus, hippocampus, amygdala, nucleus accumbens, red nucleus, and substantia nigra. Linear and nonlinear regression models were used to explore the relationship between phase and volume measures, and aging.

RESULTS: Mean phase values of subcortical deep gray matter structures showed a quadratic relationship, with individuals in late middle age (40–59 years) having the lowest mean phase values, followed by a reversal of this trend in the elderly. In contrast, mean phase of low-phase voxel measurements showed strong negative linear relationships with aging. Significantly lower phase values were detected in women compared with men ($P < .001$), whereas no sex differences were observed for mean phase of low-phase voxels. Normalized volume measurements were also linearly related to aging, and women showed smaller normalized volumes of subcortical deep gray matter structures than men ($P < .001$). Lower mean phase of low-phase voxels was related to decreased volume measures.

CONCLUSIONS: A strong association between phase (quadratic effect; phase decreases are followed by increases), mean phase of low-phase voxels (linear effect), volume (linear effect), and age was observed. Low phase was related to brain atrophy.

ABBREVIATIONS: SDGM = subcortical deep gray matter; MP-LPV = mean phase of low-phase voxels; NC = neocortex

For decades, changes in brain iron levels have been known to occur as a function of age.[1] Brain iron has been investigated in healthy individuals in both postmortem[1,2] and, more recently, in vivo studies with the use of different MR-based techniques.[3-11] Increased iron levels predominantly occur in brain subcortical deep gray matter (SDGM) structures such as the caudate, putamen, thalamus, red nucleus, and substantia nigra. Furthermore, it has been found that brain iron accumulation is influenced by sex.[3,12-14] Extensive increases in brain iron content occur in neurodegenerative disorders such as Alzheimer disease,[15] Parkinson disease,[16] Huntington disease,[17] and Friedreich ataxia.[18] Most of these disorders have a disease onset at or after middle age (40–59 years). Brain iron accumulation is currently discussed as a contributing, modulating, and even initiating factor in the development of neurodegenerative and neuroinflammatory disorders such as multiple sclerosis,[19] because of its neurotoxic effects caused by free radical generation.[20]

Several MRI techniques allow for the in vivo imaging of paramagnetic substances such as iron in the brain. In this study, we used SWI-filtered phase imaging.[21] This technique takes advantage of magnetic field changes caused by substances such as iron or ferritin through their influences on the phase of the proton spin.[21,22] Although it does have nonlocal dipole field effects that can potentially be alleviated by susceptibility mapping, it involves fewer

Received December 26, 2012; accepted after revision February 12, 2013.

From the Buffalo Neuroimaging Analysis Center (J.H., M.G.D., N.B., C.R.M., M.H.-B., D.P.R., E.C., C.K., R.M., P.P., R.Z.), Department of Neurology, University at Buffalo, Buffalo, New York; Medical Physics Group (F.S., A.D., J.R.R.), Institute of Diagnostic and Interventional Radiology I, Jena University Hospital–Friedrich Schiller University, Jena, Germany; and Department of Anatomy and Neurosciences (J.J.G.G.), Section of Clinical Neuroscience, VU University Medical Center, Amsterdam, The Netherlands.

Please address correspondence to Robert Zivadinov, MD, PhD, FAAN, Department of Neurology, School of Medicine and Biomedical Sciences, Buffalo Neuroimaging Analysis Center, 100 High St, Buffalo, NY 14203; e-mail: zivadinov@hotmail.com

Indicates open access to non-subscribers at www.ajnr.org

Indicates article with supplemental on-line figures.

http://dx.doi.org/10.3174/ajnr.A3569

Table 1: Demographic characteristics and global volumetric MRI measures of study participants

	Total	Male	Female	*P*
n (%)	210	89 (42.4)	121 (57.6)	
Age (SD) median	39.8 (15.5) 41	38 (16.1) 38	41.1 (14.9) 44	.202
Race, *n* (%) of available cases				
White	139 (87.4)	58 (87.9)	81 (87.1)	.617
African American	13 (8.2)	5 (7.6)	8 (8.6)	
Other	7 (4.4)	3 (4.5)	4 (4.3)	
Education, *n* (%) of available cases				
No high school	15 (9.7)	7 (11.3)	8 (8.7)	.893
High school	24 (15.6)	11 (17.7)	13 (14.1)	
Some college	32 (20.8)	14 (22.6)	18 (19.6)	
Associate/technical	22 (14.3)	7 (11.3)	15 (16.3)	
Bachelor level	36 (23.4)	12 (19.4)	24 (26.1)	
Graduate level	23 (14.9)	10 (16.1)	13 (14.1)	
Postgraduate	2 (1.3)	1 (1.6)	1 (1.1)	
MRI volumes in cm^3, mean (SD)				
WM hyperintensities	1.26 (4.47)	1.74 (6.50)	0.87 (1.29)	.160
GM	791.93 (65.56)	787.64 (69.36)	795.02 (62.81)	.525
Cortical GM	644.30 (56.33)	637.10 (62.11)	649.56 (51.36)	.181
WM	761.95 (41.39)	771.66 (39.57)	754.97 (41.41)	.008
Lateral ventricles	31.66 (12.70)	33.46 (13.36)	30.35 (12.07)	.136

Note:—Differences between men and women were assessed by means of the χ^2 test (race and education) and Student *t* test (age and normalized volumes).

assumptions caused by the ill-posed problem of dipole de-convolution, is still widely used by researchers, and is more generally applicable because it is directly available on some scanners. Furthermore, both post-mortem[23-26] and in vivo [27] studies confirmed associations between the local SWI-filtered phase shift and the underlying magnetic susceptibility, which is affected by the tissue iron content. In the present study, both mean phase (indicative of overall iron content) and mean phase of low-phase voxels (MP-LPV) (indicative of high iron content) measures were used. Recent work has shown strong correlations between SDGM MP-LPV measurements and brain volume reductions in patients with multiple sclerosis.[19]

In the present study, we sought to investigate age- and sex-dependent changes in SWI-filtered phase in healthy individuals by assessing mean phase, MP-LPV, and volumetric measures. Age-associated patterns of these MR imaging measures were investigated on a structure-by-structure basis. Furthermore, the relationship between SWI-filtered phase and structural volumes was explored.

MATERIALS AND METHODS

Subjects

A total of 210 volunteers without known CNS pathology (men: $n = 89$, women: $n = 121$) were recruited from community and hospital staff. Inclusion criteria for this study were fulfilling health screen questionnaire requirements containing information about medical history (illnesses, surgeries, medications, etc) or physical examination and being capable of undergoing a diagnostic examination with MR imaging. Exclusion criteria were pre-existing medical conditions known to be associated with CNS pathology. Age of the participants ranged between 6–76 years (mean = 39.8 years, standard deviation [SD] = 15.5 years, median = 41, interquartile range = 24.3). Demographic characteristics of the subjects are shown in Table 1.

The study protocol was approved by the local institutional review board, and all participants provided their written informed consent before examination.

Image Acquisition

All scans were carried out on a 3T Signa Excite HD 12.0 scanner (GE Healthcare, Milwaukee, Wisconsin), with the use of a multi-channel head and neck coil. SWI was acquired by use of a 3D flow-compensated gradient-echo sequence with 64 sections, 2-mm section thickness, FOV = 25.6 cm × 19.2 cm, and in-plane resolution of 0.5 mm × 1 mm (flip angle = 12°; TE/TR = 22/40 ms; acquisition time = 8:46 min:s; bandwidth = 13.89 kHz).[19]

Additional 2D sequences were acquired by use of a 256 × 192 matrix (frequency × phase), 25.6 cm × 19.2 cm FOV, resulting in an in-plane resolution of 1 mm × 1 mm, with 48 gapless 3-mm sections for whole-brain coverage. Sequence-specific parameters were dual FSE proton attenuation and T2WI (TE1/TE2/TR = 9 /98/5300 ms; echo-train length = 14); FLAIR (TE/TI/TR = 120/2100/8500 ms; flip angle = 90°; echo-train length = 24); and spin-echo T1WI (TE/TR = 16/600 ms). Moreover, a 3D high-resolution T1WI fast spoiled gradient-echo sequence with a magnetization-prepared inversion recovery pulse was acquired (TE/TI/TR = 2.8/900/5.9 ms, flip angle = 10°) by use of 184 locations 1 mm thick, resulting in isotropic resolution.

All scans were prescribed parallel to the subcallosal line in an axial-oblique orientation, and no averaging was performed.

Image Analyses

Mean and Low Mean Phase Identification. Segmentation of SDGM structures for volumetric and SWI analysis was performed by use of the FMRIB Software Library's integrated registration and segmentation tool (FIRST; http://www.fmrib.ox.ac.uk/fsldownloads/) on the 3D T1WI.[28] Additional structures not identifiable this way (red nucleus, pulvinar nucleus, and substantia nigra) were manually delineated on the most representative section by a single operator (M.H.-B.) with the use of JIM5 (Xinapse Systems Ltd, Northamptonshire, United Kingdom), as reported previously.[29]

An overview of the SWI processing, analysis method, and reproducibility results used in the present study is discussed elsewhere.[19] In this study, the MP-LPV of each structure was determined by thresholding the phase images to retain only those voxels with phase values lower than 2 SD below the reference group means, as explained elsewhere.[19,30] However, for the present study, normal reference phase values (both means and SDs) for each structure were determined on a group of 330 healthy control subjects distributed in age groups ranging from 8–87 years who obtained their SWI scans on the same scanner. The volumes of thresholded voxels were subsequently used to compute the proportion of low-phase voxels versus normalized volume, on a structure-by-structure basis. As a measure of the degree

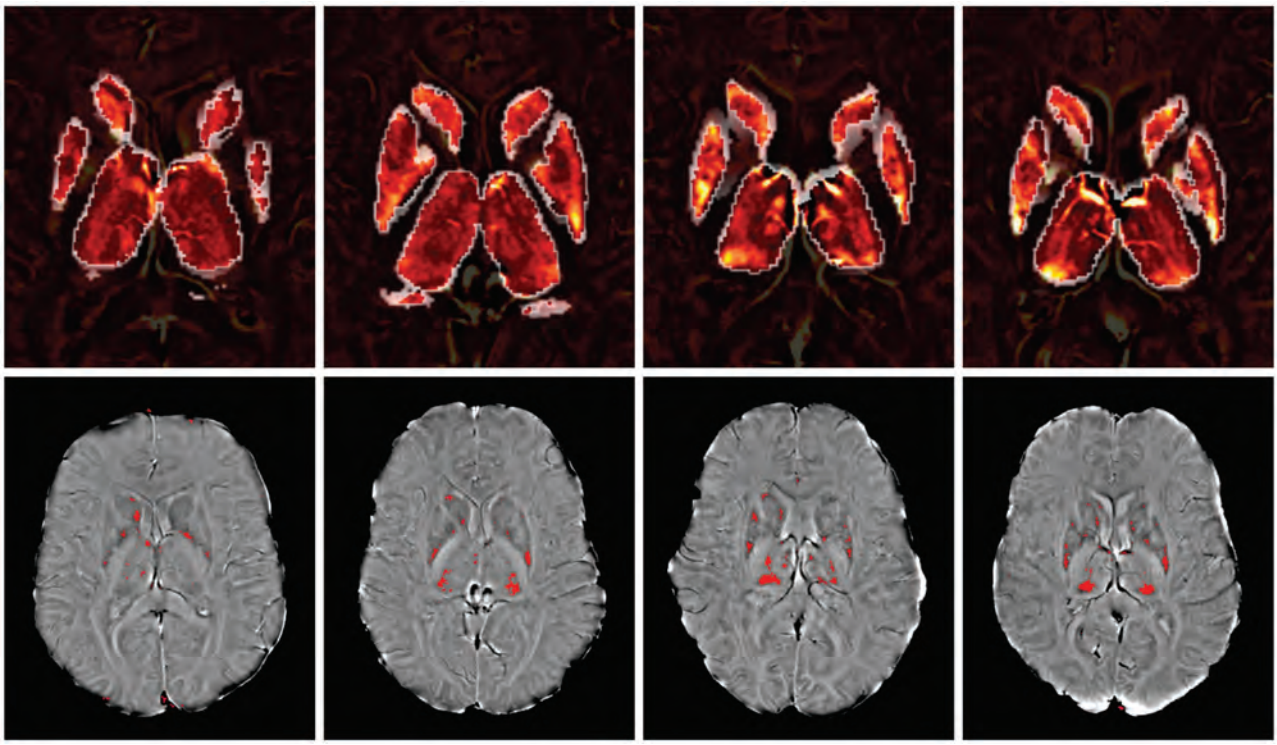

FIG 1. Phase maps (*upper row*) and thresholded low-phase voxels used in mean phase of low-phase voxel (MP-LPV) calculation (*bottom row*) of subcortical deep gray matter structures. MP-LPV was determined by thresholding the phase images to retain only those voxels with phase values lower than 2 standard deviations below reference group. Upper and lower rows show the same subjects, and each column contains a representative subject from each age group (left to right, <25 years, 25–39 years, 40–55 years, >55 years).

of phase abnormality, the mean phase values of the resulting thresholded voxels were calculated, yielding MP-LPV (Fig 1). Structure-specific maps of voxels with phase and low phase are presented in radians, with lower phase and MP-LPV values suggesting increased iron content.

Global Volumetric and WM Hyperintensity Analyses. SIENAX version 2.6 in FSL (http://www.fmrib.ox.ac.uk/fsl/feeds/doc/index.html) was used for brain extraction and tissue segmentation on 3D T1WI.[19] Normalized volume measures of the whole brain, GM, neocortex (NC), WM, and lateral ventricles were acquired.[31] WM hyperintensity volumes were calculated by means of a semi-automated edge-detection contouring-thresholding technique, as previously described.[19]

Statistical Analysis

All analyses were carried out by use of IBM SPSS Statistics 20 (IBM Corp, Armonk, New York). Demographic and sex differences of mean phase, MP-LPV, and normalized volumes were assessed by means of independent-samples *t* test and the Mann-Whitney *U* test, as well as the χ^2 test, where appropriate.

Linear regression models were fitted on the data, adjusting for the effects of sex. Models of mean phase and MP-LPV were also adjusted for normalized structural volume to reduce the confounding effects atrophy may have on phase shift. After this, it was determined whether a quadratic regression function yielded a more reasonable fit than a linear slope by assessing the change in R^2 between the models and determining statistical significance by means of an *F* test. This allowed us to determine the relationship between structural mean phase, MP-LPV, and normalized volumes with aging in both linear, and, when applicable, nonlinear models. Interaction terms between sex and age were added to the models to assess sex differences, as a function of age. Additional general linear models were computed to assess whether the relative volume of structural low phase tissue versus total structural volume differs among age groups.

To evaluate the association between mean phase and MP-LPV measurements with volumes, we used Spearman rank correlations. The Benjamini-Hochberg correction at the $P < .05$ level was used to minimize the false discovery rate.[32]

RESULTS

No significant differences were observed between men and women regarding demographic or global volumetric MRI characteristics (Table 1).

Sex Differences

Table 2 lists mean phase, MP-LPV, and normalized volumes for SDGM structures, according to sex. Normalized WM volume was smaller among women ($P = .008$, Table 1). Significantly lower phase values were detected in women compared with men in the caudate ($P < .001$). Phase values in the total SDGM and putamen were also lower among women. No sex differences were observed in MP-LPV, whereas normalized volumes of most SDGM structures were significantly smaller among women than men (Table 2).

Age-Dependent Effects

Because sex differences were observed (Table 2), initial linear regression models included sex as a covariate (Table 3). A decrease

Table 2: Sex differences of mean phase, mean phase of low-phase voxels, and normalized volume values of subcortical deep gray matter structures

	Mean Phase			MP-LPV			Normalized Volume		
	Male (n = 89)	Female (n = 121)	P	Male (n = 89)	Female (n = 121)	P	Male (n = 89)	Female (n = 121)	P
Total SDGM	−.012 (.014)	−.016 (.014)	.036	−.144 (.022)	−.149 (.027)	.573	49.209 (5.474)	44.442 (3.551)	<.001
Caudate	−.054 (.017)	−.064 (.018)	.001	−.170 (.016)	−.167 (.014)	.525	7.398 (1.079)	6.832 (.890)	<.001
Putamen	−.018 (.028)	−.027 (.029)	.028	−.175 (.039)	−.183 (.047)	.487	10.471 (1.386)	9.426 (.914)	<.001
Globus pallidus	−.016 (.025)	−.015 (.024)	.643	−.184 (.033)	−.183 (.042)	.348	3.809 (.442)	3.431 (.399)	<.001
Thalamus	.005 (.008)	.003 (.009)	.210	−.095 (.015)	−.091 (.013)	.157	16.474 (1.923)	14.661 (1.188)	<.001
Pulvinar	−.042 (.030)	−.042 (.028)	.657	−.139 (.017)	−.140 (.018)	.689	.456 (.092)	.419 (.090)	.010
Hippocampus	.024 (.032)	.031 (.039)	.073	−.161 (.044)	−.165 (.049)	.822	7.559 (.956)	6.981 (.817)	<.001
Amygdala	.011 (.039)	−.007 (.066)	.086	−.214 (.051)	−.210 (.075)	.086	2.634 (.424)	2.326 (.307)	<.001
Accumbens	−.179 (.140)	−.230 (.163)	.035	−.744 (.203)	−.80 (.252)	.298	.865 (.199)	.784 (.189)	.006
Red nucleus	−.050 (.057)	−.059 (.051)	.331	−.238 (.027)	−.232 (.026)	.225	.179 (.023)	.162 (.022)	<.001
Substantia nigra	−.097 (.056)	−.096 (.057)	.765	−.305 (.039)	−.308 (.041)	.574	.305 (.048)	.282 (.053)	.005

Note:—Results are shown as mean (standard deviation); volume measurements are expressed in cubic centimeters. Mean phase and mean phase of low-phase tissue (MP-LPV) measurements are expressed in radians. Statistical analyses were carried out by use of independent-samples t test and Mann-Whitney U test.

Table 3: Linear regression analyses assessing the association between age and mean phase, mean phase of low-phase tissue, and normalized volumes, adjusted for sex

	Mean phase[a]		MP-LPV[a]		Normalized Volume	
	β	P	β	P	β	P
Total SDGM	−.102	.057	−.255	<.001	−.245	<.001
Caudate	−.102	.068	−.350	<.001	−.247	<.001
Putamen	−.208	<.001	−.193	<.001	−.239	<.001
lobus pallidus	.210	<.001	−.273	<.001	.049	.352
Thalamus	−.178	<.001	−.521	<.001	−.299	<.001
Pulvinar nucleus	−.384	<.001	−.340	<.001	−.105	.059
Hippocampus	−.027	.645	.033	.589	−.075	.163
Amygdala	.039	.525	−.029	.631	.069	.197
Accumbens	−.051	.376	.112	.043	−.271	<.001
Red nucleus	−.301	<.001	−.252	<.001	−.195	<.001
Substantia nigra	−.207	.006	−.256	<.001	.023	.687

[a] Adjusted for the effects of normalized volume.

in mean phase values in the red nucleus, pulvinar nucleus, putamen, and thalamus, as well as an increase in mean phase values in the globus pallidus, were strongly related with increasing age ($P <$ .001). The strongest associations with age were observed in MP-LPV measurements of the caudate, pulvinar nucleus, total SDGM, substantia nigra, globus pallidus, red nucleus, and putamen ($P <$ .001). The association of age and thalamus MP-LPV was particularly strong ($\beta = -.521$, $P < .001$). Thalamus, nucleus accumbens, caudate, total SDGM, putamen, and red nucleus normalized volumes were inversely related to aging ($P < .001$). There was also an interaction effect of sex for both putamen mean phase and MP-LPV ($P = .010$) and substantia nigra MP-LPV ($P = .003$) (Fig 2).

Fitting of curved regression lines was conducted to determine whether the association between MR imaging measurements and age were better represented by nonlinear slopes. The linear and quadratic effects, as determined by R^2 fit parameters, of the association between age and representative SDGM structure mean phase, MP-LPV, and normalized volume are represented in Online Figs 1 and 2. Regression line fits for each structure were similar for both sexes. The relationship between age and mean phase of the total SDGM ($R^2 = 0.055$, $F = 11.96$), caudate ($R^2 = 0.087$, $F = 19.25$), thalamus ($R^2 = 0.126$, $F = 29.26$), pulvinar nucleus ($R^2 = 0.161$, $F = 38.85$), and red nucleus ($R^2 = 0.240$, $F = 63.90$) were significantly quadratically related to aging ($P < .001$), with individuals in late middle age having the lowest mean phase values followed by a reversal of this trend in the elderly. Associations between age and the mean phase of the putamen, globus pallidus, hippocampus, amygdala, nucleus accumbens, and substantia nigra were best explained by linear slopes. MP-LPV measurements showed strong linear relationships with age, with only the red nucleus having a quadratic effect ($R^2 = 0.123$, $F = 24.63$, $P <$ .001). Normalized volume measurements were not quadratically related to aging.

The relative size of structural low-phase tissue volume versus normalized structural volume was also investigated (Table 4) to assess whether a greater proportion of a given SDGM structure can be considered to consist of low-phase voxels after thresholding. Older patients had a significantly higher proportion of MP-LPV volume in the total SDGM, caudate, putamen, thalamus, pulvinar nucleus, red nucleus (all $P < .001$), and substantia nigra ($P = .002$). In contrast, the proportion of MP-LPV volume decreased in the globus pallidus as a function of age ($P < .001$). There was no effect of sex on the proportion of MP-LPV volume.

Relationship Between Iron and Volumetric MRI Outcomes

We used Spearman rank correlations to assess the relationship between mean phase and MP-LPV measurements and brain volumetric measures. Associations were observed between normalized GM and NC volume with mean phase values of the total SDGM, caudate, putamen, thalamus, hippocampus, and red nucleus ($r = .139$–$.272$, $P < .01$) and inversely with the globus pallidus ($r = -.226$ to $-.232$, $P < .001$). The strongest associations of mean phase measurements were observed in the pulvinar nucleus with normalized GM ($r = 0.387$, $P < .001$), lateral ventricle ($r = -.234$, $P < .001$), and NC ($r = 0.399$, $P <$ .001) volumes.

Associations ($P < .001$) were also observed between the MP-LPV measurements of the total SDGM, caudate, putamen, globus pallidus, and thalamus with GM, lateral ventricle, and NC volumes, with the strongest correlations occurring between thalamic MP-LPV and normalized GM ($r = .487$, $P < .001$), lateral ventricle ($r = -.376$, $P < .001$), and NC volumes ($r = .472$, $P < .001$). Correlations of MP-LPV measurements with WM volume were less robust ($r = .105$–$.171$, $P < .05$).

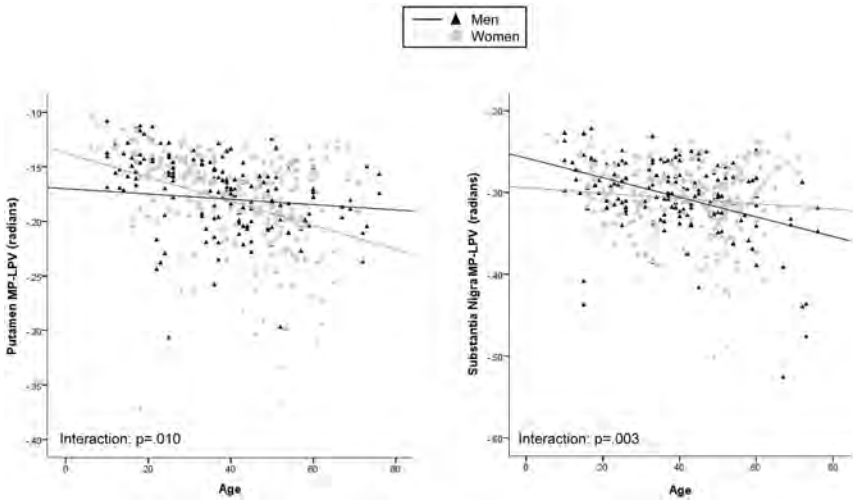

FIG 2. Scatterplots showing significant interaction effects between sex and the mean phase of low-phase voxels (MP-LPV) of the putamen and substantia nigra.

Table 4: Proportion of structural low-phase voxels versus structural normalized volume within age groups, adjusted for sex

	Age (years)				
	<25 *n* = 43	25–39 *n* = 56	40–55 *n* = 72	≥55 *n* = 39	*P*
Total SDGM	.29 (.04)	.32 (.03)	.34 (.04)	.35 (.04)	<.001
Caudate	.27 (.09)	.33 (.08)	.36 (.07)	.35 (.08)	<.001
Putamen	.17 (.08)	.26 (.06)	.33 (.07)	.32 (.09)	<.001
Globus pallidus	.42 (.07)	.40 (.06)	.38 (.06)	.35 (.06)	<.001
Thalamus	.40 (.03)	.43 (.03)	.44 (.04)	.43 (.04)	<.001
Pulvinar nucleus	.11 (.08)	.24 (.16)	.28 (.15)	.29 (.14)	<.001
Hippocampus	.15 (.08)	.19 (.09)	.18 (.07)	.18 (.07)	.319
Amygdala	.17 (.14)	.18 (.10)	.17 (.10)	.16 (.08)	.738
Accumbens	.15 (.14)	.14 (.14)	.12 (.13)	.13 (.16)	.703
Red nucleus	.05 (.05)	.13 (.12)	.21 (.13)	.17 (.11)	<.001
Substantia nigra	.17 (.11)	.23 (.11)	.27 (.11)	.24 (.14)	.002

General linear modeling comparing the proportion of structural low-phase voxels versus structural normalized volume between age groups. Results are presented as mean (standard deviation).

DISCUSSION

In the present study, we aimed to investigate the relationship between aging and SWI-filtered phase measures in the SDGM of healthy individuals. The aging behavior of total mean phase and the mean phase of low-phase voxels, which are indicative of brain iron levels, were assessed in a large cohort of healthy individuals. After adjusting for confounders, strong associations were observed between SDGM structure mean phase, MP-LPV, and normalized volumes with age, corroborating previous findings that brain iron content increases when a person ages.[1,3,6,10,33] Interestingly, strong correlations were observed especially between the MP-LPV and brain volume.

In this study, we used the SWI-filtered phase imaging method, which has been proposed as a method to indirectly measure iron content. MP-LPV was used as a measure of the level of high iron content and its volume, because only the mean phase values of the most severely affected voxels are measured, as previously determined by assessing only voxels with phase values more than 2 SD from the mean.[19,30] On the basis of the examined structures, the proportion of these voxels ranged from 5% in the red nucleus in age group <25 years to 44% in the thalamus in age group 40–55 years.

Sex Phase Differences

As indicated by interaction effects, women had a slightly higher rate of decrease in mean phase and MP-LPV over time in the putamen, whereas men showed a more steady decrease of substantia nigra MP-LPV as a function of age. This suggests that among women, MP-LPV increases at a more rapid pace in the putamen, whereas in men the substantia nigra has an accelerated rate. Previous MR imaging findings reported decreased brain iron levels among women in the caudate, thalamus, and several WM regions.[12] However, Xu et al[3] did not observe any significant sex differences by use of SWI. We suspect that sex differences are present on a minor level, and these became detectable because of our sizeable sample.[34-37] Future studies should further elucidate the relationship between sex-specific factors possibly influencing MR imaging phase (menses, child birth, hysterectomy, etc).

Aging Phase Behavior

Regression analyses showed strong associations between SWI-filtered phase measurements of the putamen, thalamus, red nucleus, and pulvinar nucleus with age, confirming previous findings.[1,6,9,33] However, mean phase measures of the total SDGM, caudate, hippocampus, amygdala, and nucleus accumbens were not significantly associated with aging. In addition, we did not observe an association between hippocampus mean phase and age, which is in contrast to a recent study in which a linear dependence was observed between hippocampal T2* and age.[8] Interestingly, the globus pallidus showed an inverse relationship of age with mean phase, suggesting that in this structure, the overall phase increases over time. This finding is in contrast to previous histologic publications[1] and may be due to the effect of the relatively high myelin content of the structure on MR imaging phase[38] or the presence of diamagnetic substances (eg, calcium) in elderly subjects.[39] However, a recent phase-imaging study also found slightly increased phase in older subjects.[3] Overall, the strongest associations were observed in MP-LPV measures, in which thalamic MP-LPV showed a particularly strong association with age. Although these and several previous[1,40] results implicate the thalamus, a recent study only found caudate and putamen but not thalamus relaxation rates to be increased with age.[41] This may be explained by the overall lower iron content of this structure,[1] making it more difficult to detect small age-related changes with the use of less sensitive MR imaging techniques.

In addition to finding significant linear relationships, when examining individual structure scatterplots, distinct age-dependent patterns were observed. Mean phase measures increased with age until early middle age and then tended to level off, some-

thing which was observed histopathologically in 1958.[1] Most studies have also shown either early-life MR imaging changes suggestive of increased iron, followed by flattening of the curve at later ages, or have reported linearly increasing effects.[3,7,10,11,33,41] In several structures, such as the caudate, putamen, thalamus, pulvinar nucleus, red nucleus, and substantia nigra, we observed slight reversions of the phase values after approximately 50 years of age. In fact, in several of the largest SDGM structures, a quadratic line fit was better than a linear one, including the caudate, thalamus, and pulvinar nucleus. This is a departure from conventional thinking that iron levels increase or level off with age. It appears that a decrease in iron content in older age is not confined to the thalamus, a phenomenon that was observed by Hallgren and Sourander,[1] but that also basal ganglia and red nucleus mean phase levels slightly increase again in the elderly after observing marked decreases before middle age. In contrast to these nonlinear findings of mean phase measures versus age, MP-LPV measures increased linearly with age in most investigated structures, with the exception of the hippocampus, amygdala, and nucleus accumbens, which did not show any notable upward or downward trend over time, and the red nucleus, which showed a curved relationship. A strong, strictly linear increase over time in MP-LPV indicates that high iron content accumulates continuously among the elderly, in contrast to mean phase measurements. In a recent study,[40] through the use of manually segmented SDGM structures, it was shown that not only did measures of high iron-content brain structures increase continuously with time, it appeared to accelerate with age. In the present study, we used automatically segmented SDGM structures, and the decrease in MP-LPV corresponded strikingly with decreases in normalized volumes in the corresponding structures. This suggests that there is an association between the mean phase of severely affected tissues and structural atrophy, though it is unknown at this time which of these observations, if any, is causative. Furthermore, with the exception of the globus pallidus, the volume of low-phase voxels (with <2 SD mean phase levels) encompasses a greater proportion of the corresponding SDGM structure volume in older subjects. This suggests that a larger percentage of SDGM structures is considered to consist of low-phase voxels. In neurodegenerative disorders in which increased iron content is observed, the age of onset is at or after middle age. Considering that mean phase measures tend to reverse in the elderly but that the MP-LPV continuously decreases with age would suggest that it is the severely affected tissues that are potentially related to neurodegenerative disease pathology.

Different aging behavior between mean phase and MP-LPV may have important implications for conducting longitudinal clinical trials in which measurement of iron content is one of the primary outcomes of the study. Linear increase of the MP-LPV with aging, as evidenced in the present study, may make this measure more suitable for use in longitudinal trials of patients affected by neurodegenerative disorders than mean phase, which showed quadratic behavior.

Phase and Atrophy

Modest to strong relationships were found between SDGM mean phase and MP-LPV measurements and reductions of the global brain volumes, such as reductions in the volume of the GM and NC, or increases in ventricular size. The SDGM structure showing the most prominent association with GM loss was the thalamus. The strong correlation of the thalamic MP-LPV with GM volume loss is an intriguing finding, suggesting that these 2 separate observations may be intricately related. The thalamus has a plethora of cortical and subcortical connections throughout the brain,[42,43] and it is therefore reasonable that local pathology has widespread consequences. However, whether increased iron content is causally related to such volume loss, an effect of it, or both remains to be determined.

Even though mean phase values increased in the globus pallidus, MP-LPV values decreased, the normalized volume remained constant over time, and there was a reduction in the relative amount of low-phase voxels. This suggests that unlike other brain structures in which MP-LPV and volume loss were strongly related, in this particular structure, focal phase shifts were not associated with an increased loss of corresponding tissue. Also, in the pulvinar nucleus and substantia nigra, decreases in MP-LPV values were observed without corresponding structural atrophy. This indicates that these particular phase effects are likely to be caused exclusively by increased iron content, because atrophy effects could not have strongly influenced the phase measurements. Perhaps even more interesting, there were strong correlations of several brain structure mean phase (hippocampus and pulvinar) and MP-LPV (globus pallidus) findings with lateral ventricles, GM, and NC atrophy, even though there was no structural volume loss in the corresponding SDGM structures as determined by regression analyses. This, together with the strong findings in the thalamus, may suggest that independent of any age effects, pathology observed in SWI-filtered phase is related to widespread damage even in the absence of structure-specific damage.

Limitations and Implications

Paramagnetic substances, mostly in the form of ferritin and iron, influence the phase of proton spin. It is unlikely, yet it remains possible, that other paramagnetic substances influence MR imaging phase measures, considering that these substances are not present in high enough concentrations.[44] Even though mean phase measures are probably caused by iron, phase shifts could potentially also be caused by other factors,[23,24,27,45] for example, by the diamagnetic properties of myelin.[27] In the present study, only GM structures were investigated, minimizing the confounding effects of myelin, which would be of greater concern if studying WM.[38] However, it must noted that some SDGM structures, most notably the thalamus, have relatively high myelin content, which could potentially have influenced phase measurements. Mean phase changes could also be influenced by atrophy or high-pass filtering effects.[27] However, this potential effect was limited by adding normalized volume to the regression models as a confounding factor to adjust for such structural atrophy effects influencing phase measures. In addition, findings from the present study largely replicate previous postmortem histopathologic findings.[1,2] SWI-filtered phase imaging is an in vivo method; therefore, all values are merely indirect measurements of iron levels. Furthermore, this was a cross-sectional study with all its inherent limitations, and longitudinal confirmation is needed. Because

most neurodegenerative disorders are linked to both age and brain iron deposition, and increased brain iron levels have detrimental effects through the generation of free radicals,[46] it is crucial to fully understand the relationship between increased brain iron levels in healthy individuals and their potential relationship with brain disorders through the use of different MR imaging techniques sensitive to paramagnetic substances.

CONCLUSIONS

The present study shows both linear (MP-LPV) and quadratic (mean phase) effects in healthy individuals by use of SWI-filtered phase imaging. In addition, decreased MP-LPV in the SDGM was shown to be strongly related to global brain atrophy.

ACKNOWLEDGMENTS

The authors thank Eve Salczynski for technical assistance in the preparation of the manuscript.

Disclosures: Robert Zivadinov—*UNRELATED: Consultancy* and *Payment for Lectures (including service on speakers bureaus):* Biogen Idec, EMD Serono, Teva Pharmaceuticals, Genzyme-Sanofi, Novartis; *Grants/Grants Pending:* Biogen Idec, EMD Serono, Teva Pharmaceuticals, Genzyme-Sanofi. Jeroen Geurts—*UNRELATED: Consultancy:* Merck Serono, Biogen Idec, Teva Pharmaceuticals.

REFERENCES

1. Hallgren B, Sourander P. **The effect of age on the non-haemin iron in the human brain.** *J Neurochem* 1958;3:41–51
2. Connor JR, Snyder BS, Beard JL, et al. **Regional distribution of iron and iron-regulatory proteins in the brain in aging and Alzheimer's disease.** *J Neurosci Res* 1992;31:327–35
3. Xu X, Wang Q, Zhang M. **Age, gender, and hemispheric differences in iron deposition in the human brain: an in vivo MRI study.** *Neuroimage* 2008;40:35–42
4. Thomas LO, Boyko OB, Anthony DC, et al. **MR detection of brain iron.** *AJNR Am J Neuroradiol* 1993;14:1043–48
5. Pfefferbaum A, Adalsteinsson E, Rohlfing T, et al. **MRI estimates of brain iron concentration in normal aging: comparison of field-dependent (FDRI) and phase (SWI) methods.** *Neuroimage* 2009;47:493–500
6. Bartzokis G, Beckson M, Hance DB, et al. **MR evaluation of age-related increase of brain iron in young adult and older normal males.** *Magn Reson Imaging* 1997;15:29–35
7. Adisetiyo V, Jensen JH, Ramani A, et al. **In vivo assessment of age-related brain iron differences by magnetic field correlation imaging.** *J Magn Reson Imaging* 2012;36:322–31
8. Rodrigue KM, Haacke EM, Raz N. **Differential effects of age and history of hypertension on regional brain volumes and iron.** *Neuroimage* 2011;54:750–59
9. Bilgic B, Pfefferbaum A, Rohlfing T, et al. **MRI estimates of brain iron concentration in normal aging using quantitative susceptibility mapping.** *Neuroimage* 2012;59:2625–35
10. Schenker C, Meier D, Wichmann W, et al. **Age distribution and iron dependency of the T2 relaxation time in the globus pallidus and putamen.** *Neuroradiology* 1993;35:119–24
11. Hardy PA, Gash D, Yokel R, et al. **Correlation of R2 with total iron concentration in the brains of rhesus monkeys.** *J Magn Reson Imaging* 2005;21:118–27
12. Bartzokis G, Tishler TA, Lu PH, et al. **Brain ferritin iron may influence age- and gender-related risks of neurodegeneration.** *Neurobiol Aging* 2007;28:414–23
13. Tishler TA, Raven EP, Lu PH, et al. **Premenopausal hysterectomy is associated with increased brain ferritin iron.** *Neurobiol Aging* 2012;33:1950–58
14. Bartzokis G, Tishler TA, Shin IS, et al. **Brain ferritin iron as a risk factor for age at onset in neurodegenerative diseases.** *Ann N Y Acad Sci* 2004;1012:224–36
15. Bartzokis G, Sultzer D, Mintz J, et al. **In vivo evaluation of brain iron in Alzheimer's disease and normal subjects using MRI.** *Biol Psychiatry* 1994;35:480–87
16. Sian-Hulsmann J, Mandel S, Youdim MB, et al. **The relevance of iron in the pathogenesis of Parkinson's disease.** *J Neurochem* 2011;118:939–57
17. Bartzokis G, Tishler TA. **MRI evaluation of basal ganglia ferritin iron and neurotoxicity in Alzheimer's and Huntington's disease.** *Cell Mol Biol* 2000;46:821–33
18. Waldvogel D, van Gelderen P, Hallett M. **Increased iron in the dentate nucleus of patients with Friedrich's ataxia.** *Ann Neurol* 1999;46:123–25
19. Zivadinov R, Heininen-Brown M, Schirda CV, et al. **Abnormal subcortical deep-gray matter susceptibility-weighted imaging filtered phase measurements in patients with multiple sclerosis: a case-control study.** *Neuroimage* 2012;59:331–39
20. Jomova K, Valko M. **Advances in metal-induced oxidative stress and human disease.** *Toxicology* 2011;283:65–87
21. Haacke EM, Xu Y, Cheng YC, et al. **Susceptibility weighted imaging (SWI).** *Magn Reson Med* 2004;52:612–18
22. Haacke EM, Cheng NY, House MJ, et al. **Imaging iron stores in the brain using magnetic resonance imaging.** *Magn Reson Imaging* 2005;23:1–25
23. Bagnato F, Hametner S, Yao B, et al. **Tracking iron in multiple sclerosis: a combined imaging and histopathological study at 7 Tesla.** *Brain* 2011;134(Pt 12):3602–15
24. Yao B, Bagnato F, Matsuura E, et al. **Chronic multiple sclerosis lesions: characterization with high-field-strength MR imaging.** *Radiology* 2012;262:206–15
25. Walsh AJ, Wilman AH. **Susceptibility phase imaging with comparison to R2 mapping of iron-rich deep grey matter.** *Neuroimage* 2011;57:452–61
26. Liem MK, Lesnik Oberstein SA, Versluis MJ, et al. **7 T MRI reveals diffuse iron deposition in putamen and caudate nucleus in CADASIL.** *J Neurol Neurosurg Psychiatry* 2012;83:1180–85
27. Schweser F, Deistung A, Lehr BW, et al. **Quantitative imaging of intrinsic magnetic tissue properties using MRI signal phase: an approach to in vivo brain iron metabolism?** *Neuroimage* 2011;54:2789–807
28. Patenaude B, Smith S, Kennedy D, et al. **A Bayesian model of shape and appearance for subcortical brain segmentation.** *Neuroimage* 2011;56:907–22
29. Batista S, Zivadinov R, Hoogs M, et al. **Basal ganglia, thalamus and neocortical atrophy predicting slowed cognitive processing in multiple sclerosis.** *J Neurol* 2012;259:139–46
30. Habib CA, Liu M, Bawany N, et al. **Assessing abnormal iron content in the deep gray matter of patients with multiple sclerosis versus healthy controls.** *AJNR Am J Neuroradiol* 2012;33:252–58
31. Zivadinov R, Weinstock-Guttman B, Benedict R, et al. **Preservation of gray matter volume in multiple sclerosis patients with the Met allele of the rs6265 (Val66Met) SNP of brain-derived neurotrophic factor.** *Hum Mol Genet* 2007;16:2659–68
32. Benjamini Y, Hochberg Y. **Controlling the false discovery rate: a practical and powerful approach to multiple testing.** *J R Stat Soc Series B-Methodological* 1995;57:289–300
33. Martin WR, Ye FQ, Allen PS. **Increasing striatal iron content associated with normal aging.** *Mov Disord* 1998;13:281–86
34. Zacharski LR, Ornstein DL, Woloshin S, et al. **Association of age, sex, and race with body iron stores in adults: analysis of NHANES III data.** *Am Heart J Jul* 2000;140:98–104
35. Milman N. **Serum ferritin in Danes: studies of iron status from infancy to old age, during blood donation and pregnancy.** *Int J Hematol* 1996;63:103–35
36. Youdim MB, Ben-Shachar D, Yehuda S. **Putative biological mechanisms of the effect of iron deficiency on brain biochemistry and behavior.** *Am J Clin Nutr* 1989;50(3 Suppl):607–15
37. Rouault TA, Zhang DL, Jeong SY. **Brain iron homeostasis, the choroid plexus, and localization of iron transport proteins.** *Metab Brain Dis* 2009;24:673–84

38. Langkammer C, Krebs N, Goessler W, et al. **Susceptibility induced gray-white matter MRI contrast in the human brain.** *Neuroimage* 2012;59:1413–19
39. Wu Z, Mittal S, Kish K, et al. **Identification of calcification with MRI using susceptibility-weighted imaging: a case study.** *J Magn Reson Imaging* 2009;29:177–82
40. Haacke EM, Miao Y, Liu M, et al. **Correlation of putative iron content as represented by changes in R2* and phase with age in deep gray matter of healthy adults.** *J Magn Reson Imaging* 2010;32:561–76
41. Cherubini A, Peran P, Caltagirone C, et al. **Aging of subcortical nuclei: microstructural, mineralization and atrophy modifications measured in vivo using MRI.** *Neuroimage* 2009;48:29–36
42. Stein T, Moritz C, Quigley M, et al. **Functional connectivity in the thalamus and hippocampus studied with functional MR imaging.** *AJNR Am J Neuroradiol* 2000;21:1397–401
43. Herrero MT, Barcia C, Navarro JM. **Functional anatomy of thalamus and basal ganglia.** *Childs Nerv Syst* 2002;18:386–404
44. Schenck JF, Zimmerman EA. **High-field magnetic resonance imaging of brain iron: birth of a biomarker?** *NMR Biomed* 2004; 17:433–45
45. Langkammer C, Krebs N, Goessler W, et al. **Quantitative MR imaging of brain iron: a postmortem validation study.** *Radiology* 2010;257:455–62
46. Zecca L, Youdim MB, Riederer P, et al. **Iron, brain ageing and neurodegenerative disorders.** *Nat Rev Neurosci* 2004;5:863–73

Structural Abnormalities in Patients with Insular/Peri-insular Epilepsy: Spectrum, Frequency, and Pharmacoresistance

M.-C. Chevrier, C. Bard, F. Guilbert, and D.K. Nguyen

ABSTRACT

SUMMARY: Between 2002 and 2010, a total of 48 patients were seen at our epilepsy clinic with insular/peri-insular cortex epilepsy. Review of their MR imaging scans revealed a neoplastic lesion in 27% of patients, a malformation of cortical development in 21%, a vascular malformation in 19%, and atrophy/gliosis from an acquired insult in 17%. MR imaging results were normal in 4 patients. Other miscellaneous findings included a case of Rasmussen encephalitis, a nonspecific insular millimetric T2 signal abnormality, a neuroepithelial cyst, and hippocampal sclerosis without MR imaging evidence of dual insular pathologic features (despite depth electrode–proven insular seizures). Refractoriness to antiepileptic drug treatment was present in 56% of patients: 100% for patients with malformations of cortical development (1.0; 95% CI, 0.72–1.0), 50.0% (0.5; 95% CI, 0.21–0.78) in the presence of atrophy/gliosis from acquired insults, 39% (0.39; 95% CI, 0.14–0.68) for neoplastic lesions, and 22.2% (0.22; 95% CI, 0.06–0.55) for vascular malformations.

ABBREVIATIONS: IPICE = insular/peri-insular cortex epilepsy; MCD = malformation of cortical development

Structural abnormalities underlying temporal and frontal lobe epilepsies have been well described.[1,2] Little is known about the type and frequency of structural brain abnormalities that give rise to insular/peri-insular cortex epilepsy (IPICE).[3] The insula is a highly developed structure, totally encased within the brain in the depths of the Sylvian fissure and covered by the frontal, parietal, and temporal opercula.[4] Insular seizures are typically associated with a sensation of laryngeal constriction and paresthesias affecting perioral or large cutaneous territories with preserved consciousness, followed by dysarthric speech and/or elementary auditory hallucinations or motor signs.[5] Later observations have also showed that insular seizures could feature hypermotor symptoms resembling frontal lobe seizures,[6] early visceral signs or dysphasia with subsequently altered consciousness suggesting temporal lobe seizures, and early somatosensory symptoms in the absence of laryngeal constriction mimicking parietal lobe seizures.[7] The purpose of our study was to ascertain 1) the overall type and distribution of structural abnormalities, identified by MR imaging, in association with IPICE; and 2) their refractoriness to antiepileptic drug therapy.

CASE SERIES

Materials and Methods

Charts from all patients seen at the epilepsy clinic by one of the authors (D.K.N.) from August 2002–May 2010 were reviewed retrospectively to find patients with IPICE. Patients were classified as having 1) definite IPICE when insular seizures were confirmed by intracerebral recordings; 2) probable IPICE in partial epilepsy with early ictal somatosensory symptoms and/or a sensation of laryngeal constriction associated with insular/peri-insular lesions; and 3) possible IPICE in partial epilepsy with early viscerosensory symptoms, speech arrest, dysphasia, or hypermotor ictal manifestations coupled with insular/peri-insular lesions on MR imaging or clear insular activation on ictal SPECT. Pharmacoresistance was defined as failure of the epilepsy to be controlled with 3 appropriate antiepileptic drug trials.

Imaging protocols varied because this study was retrospective, and some imaging was performed at referring centers. Most were standard MR imaging protocols, tumor protocols, or epilepsy protocols. MR imaging scans of all patients with IPICE were reviewed retrospectively by a neuroradiologist with 15 years of experience and a senior resident in radiology. The following features were noted: type of structural abnormality, anatomic location, and extent.

Received August 8, 2012; accepted after revision February 5, 2013.

From the Radiology Department (M.-C.C., C.B., F.G.) and Neurology Service (D.K.N.), Centre hospitalier de l'Université de Montréal (CHUM) – Hôpital Notre-Dame and Université de Montréal, Montreal, Quebec, Canada.

Paper previously presented as a scientific poster at: Annual Meeting of the Radiological Society of North America, November 28–December 3, 2010; Chicago, Illinois.

Please address correspondence to Dang K. Nguyen, MD, FRCPC, Service de neurologie, CHUM – Hôpital Notre-Dame, 1560 rue Sherbrooke est, Montréal, Québec H2L 4M1, Canada; e-mail: d.nguyen@umontreal.ca

Indicates article with supplemental on-line table.

http://dx.doi.org/10.3174/ajnr.A3636

For statistical analysis, patients were partitioned within 6 radiopathologic categories: 1 (neoplastic), 2 (malformations of cortical development [MCDs], 3 (vascular malformations), 4 (atrophy/gliosis from acquired insults), 5 (other), and 6 (normal). A 2×6 contingency table was constructed partitioning patients between pharmacoresistant and responsive to medication. A Fisher exact test was performed on this 2×6 contingency table assuming that categories are mutually exclusive, followed by a Fisher exact test for each category when appropriate. A Bonferroni correction was used to control for multiplicity ($\alpha = 0.05/6$ or $\alpha = 0.008$). For each category presenting a significant association with pharmacoresistance, the risk was reported with a 95% CI. Calculations were produced on StatsDirect statistical software (version 2.7.9, http://www.statsdirect.com).

RESULTS

A total of 59 (6.4%) of 920 patients with epilepsy had IPICE. Eleven patients were excluded because MR imaging scans of 5 patients were destroyed, no MR imaging scans were taken of 2 patients because of contraindications (eg, pacemaker), and MR imaging was not available before surgical treatment in 4 patients. Hence, we retrospectively reviewed the MR imaging results of 48 patients with IPICE. Of these patients, 7 had definite IPICE, 24 had probable IPICE, and 17 had possible IPICE. The group included 21 men and 27 women with a median age of 39 years (age range, 2–73 years).

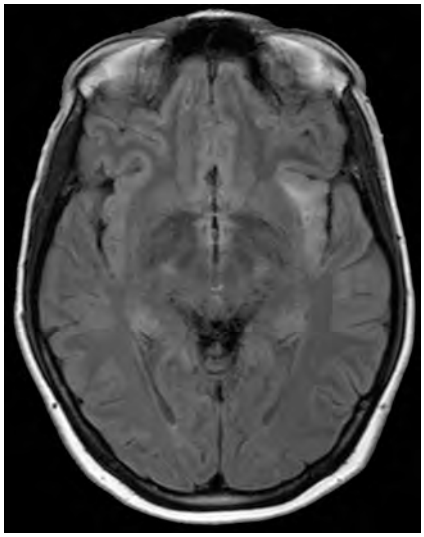

FIG 1. Axial FLAIR MR imaging scan of a 24-year-old woman with low-grade glioma in whom left IPICE (probable) developed. A hyperintense FLAIR lesion can be seen infiltrating the left insula.

The On-line Table lists the pathologic patterns detected on MR imaging in the 48 patients and refractoriness to antiepileptic drug treatment. It disclosed neoplastic lesions in 13 patients (27%). Eight patients presented pathologic features compatible with low-grade glioma and 5 patients, with high-grade glioma. Eight patients had astrocytomas (Fig 1), 4 of which were low-grade, and 4 were high-grade. Three patients had low-grade oligoastrocytoma. MR imaging results in these patients demonstrated infiltrative masses centered over the insula with extension to the frontal and temporal lobes. One patient, who had a previously resected, low-grade oligodendroglioma, went on to have IPICE many years later in the context of insular tumor recurrence. Another patient had glioblastoma multiforme involving the insula and the temporal operculum.

MCDs were detected in 10 patients (20%). Five patients had cortical dysplasia involving the insula; 4 had polymicrogyria implicating the insula with perisylvian extension (Fig 2), including 1 patient with bilateral perisylvian polymicrogyria; and another patient had tuberous sclerosis presenting multiple cortical tubers, 1 being located in the operculoinsular region (Fig 3). Vascular malformations were found in 9 patients (19%). Four patients had an arteriovenous malformation (Fig 4) with a nidus in the insula or inducing a FLAIR signal abnormality in the insula. Three patients had a Sylvian bifurcation aneurysm with mass effect on the insular cortex, and 2 others had a cavernoma centered on the insula (Fig 5).

Atrophy/gliosis from acquired insults was observed in 8 patients (17%). Two patients had encephalomalacia and atrophy after trauma (Fig 6): one involving the temporal operculum and insula after surgical evacuation of a hematoma, and the other involving the insula and frontal and temporal opercula. One patient had signs of an old ischemic infarct exclusively in the insular cortex. Another patient had cystic encephalomalacia after herpes encephalitis affecting the insula and temporal lobes. Yet another patient had encephalomalacia and atrophy after a congenital insult, 2 patients had encephalomalacia and atrophy of indeterminate cause involving the insula and the frontal or temporal opercula, and 1 other patient had pial enhancement over the insula and frontal operculum of unknown cause.

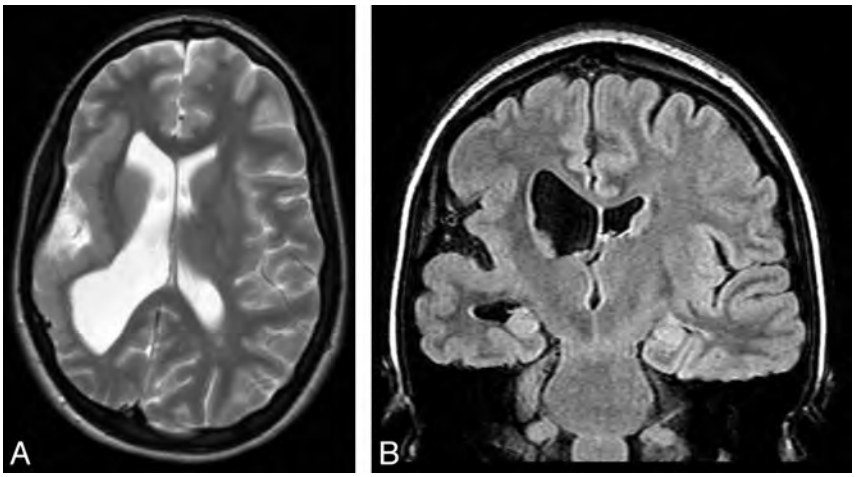

FIG 2. Coronal FLAIR and axial T2 MR imaging scans of a 19-year-old woman with epilepsy with polymicrogyria in the right insula and postcentral gyrus.

Serial MR imaging in a patient with Rasmussen encephalitis revealed an initial insular FLAIR signal abnormality followed by unilateral fronto-temporo-insular atrophy and gliosis. A millimetric, innocuous-looking T2 signal abnormality over the posterior insula was

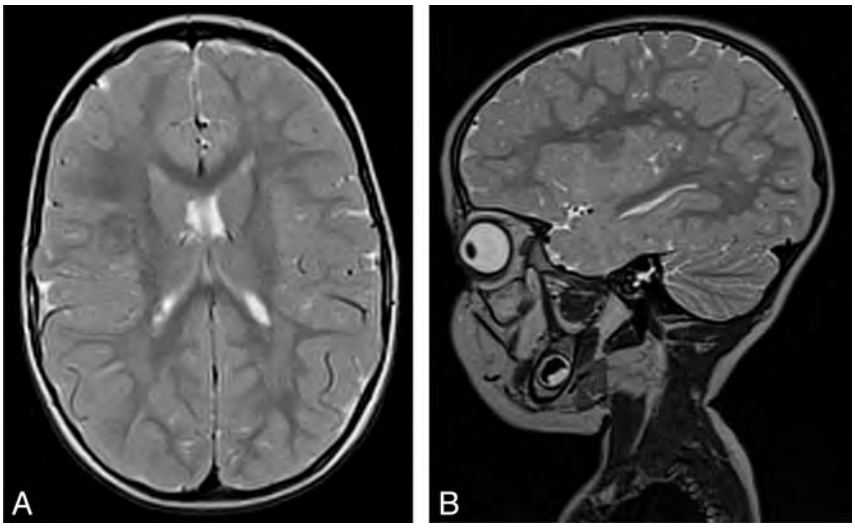

FIG 3. Axial and sagittal T2 MR imaging scan of a 2-year-old girl with tuberous sclerosis in whom right insular epilepsy (definite) developed. Cortical tuber involving the short posterior and long anterior gyri of the insula. Note the white matter abnormalities of tuberous sclerosis.

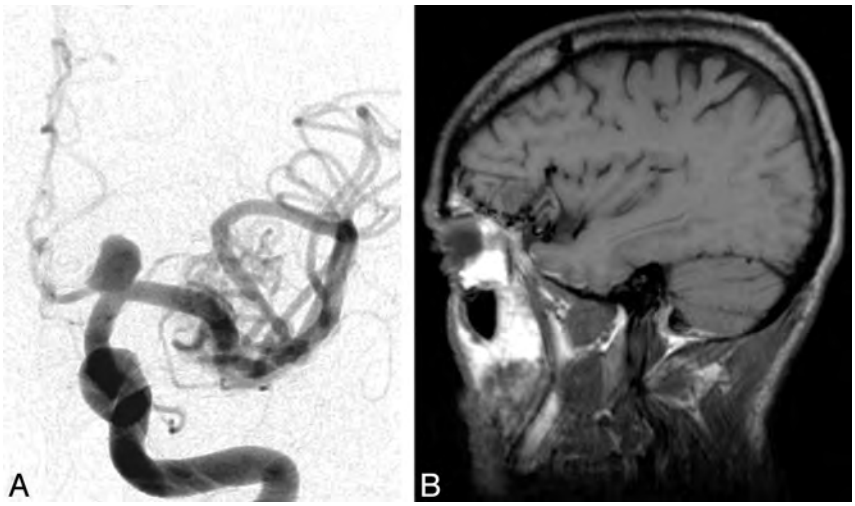

FIG 4. Angiography of the left carotid artery with sagittal T1 MR imaging scan of a 54-year-old man with left fronto-insular epilepsy (probable). Angiography shows an arteriovenous malformation fed by the left middle cerebral artery and a left supraclinoid internal carotid artery aneurysm. MR imaging scan reveals the arteriovenous malformation centered on the left frontal operculum with mass effect on the anterior short gyrus of the insula.

found in 1 patient. A neuroepithelial cyst vs a signal abnormality in the insula was seen in another patient. One patient had no insular lesions (despite depth electrode–proven insular seizures) but rather hippocampal sclerosis (and concomitant hippocampal seizures). MR imaging results were normal in 4 patients: 2 of whom had definite IPICE, and 2 of whom had possible IPICE.

Among the 43 patients with lesions in the insula, damage was confined to the insular cortex with or without involvement of the adjacent operculum in 20 patients. More than 1 operculum was affected in the remaining 23 patients.

Refractoriness to antiepileptic drug treatment was 100% for the 10 patients with MCD (1.0; 95% CI, 0.72–1.0), 50.0% (0.5; 95% CI, 0.21–0.78) in the presence of atrophy/gliosis from acquired insults, 39% (0.39; 95% CI, 0.14–0.68) for neoplastic lesions, and 22.2% (0.22; 95% CI, 0.06–0.55) for vascular malformations. An estimated 75% of patients with normal MR imaging results (0.75; 95% CI, 0.19–0.99) had refractory epilepsy (Table). The patient with Rasmussen encephalitis had refractory epilepsia partialis continua with occasionally complex partial seizures.

DISCUSSION

Some epileptogenic lesions are more commonly found in certain regions of the brain. For example, typical epileptogenic lesions diagnosed in patients with temporal lobe epilepsy are hippocampal atrophy/sclerosis, dysembryoplastic neuroepithelial tumors, gangliogliomas, postherpetic encephalitic gliosis, and posttraumatic encephalomalacia.[2,8,9] Until now, little was known about the epileptogenic lesions associated with IPICE. In our study, 13 patients (27%) with IPICE manifested tumors, 8 of whom had low-grade gliomas. Duffau et al[10] had previously reported that the insular cortex itself may induce chronic seizures when injured by tumors. In 2010, Lee et al[11] observed that 34% of patients with high-grade tumors and 62% of those with low-grade tumors had epilepsy. Among patients with low-grade gliomas, those with tumors located in the temporal lobe as well as in the insular region were more likely to present with seizures. MCDs constitute 4%–25% of all epileptogenic lesions in adults and 10%–50% in pediatric populations.[12-14] Our study determined that 10 patients (20.8%) with IPICE had MCDs, 4 (8.3%) of whom had perisylvian polymicrogyria. This preferential localization in the perisylvian area for polymicrogyria has been well demonstrated by Leventer et al,[15] who found this pattern in 200 (61%) of 328 patients. Cortical tubers, which histologically resemble cortical dysplasias, can also induce seizures in this zone.[16]

Nine patients (18.8%) with IPICE had vascular lesions. By its very location, the insula is susceptible to vascular lesions.[17] It is closely related to the Sylvian artery, from which it receives its blood supply via numerous perforating arteries from the M2 and M3 segments. As reported by Malak et al,[18] unruptured Sylvian bifurcation aneurysms can present with a combination of viscerosensitive, motor, language, autonomic, and somatosensory symptoms related to the proximity of the insula. Arteriovenous malformations and cavernomas can also cause IPICE by direct compression or hemorrhage. Any previous intracranial insult can result in epilepsy. In our series, 8 patients (17%) with IPICE had

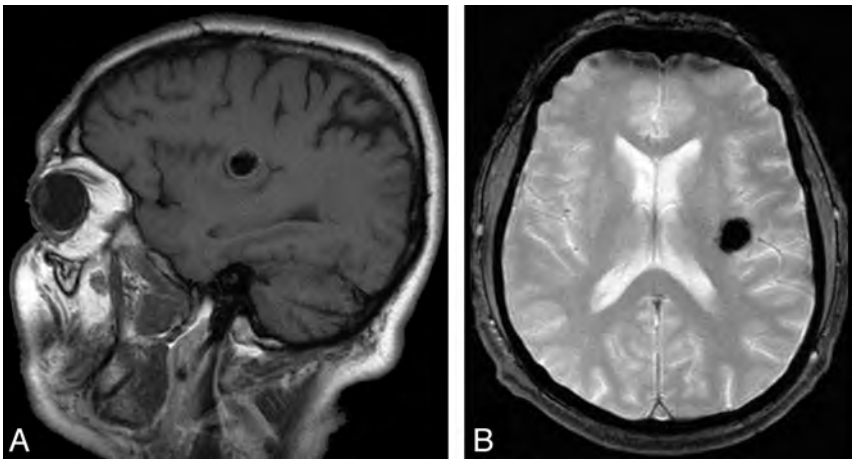

FIG 5. Sagittal T1 and gradient-echo MR imaging of a 64-year-old man with a left insular cavernoma in whom left insular epilepsy (definite) developed. Round, hypointense T1, T2, and T2* lesion involves the anterior and posterior long gyri of the insula.

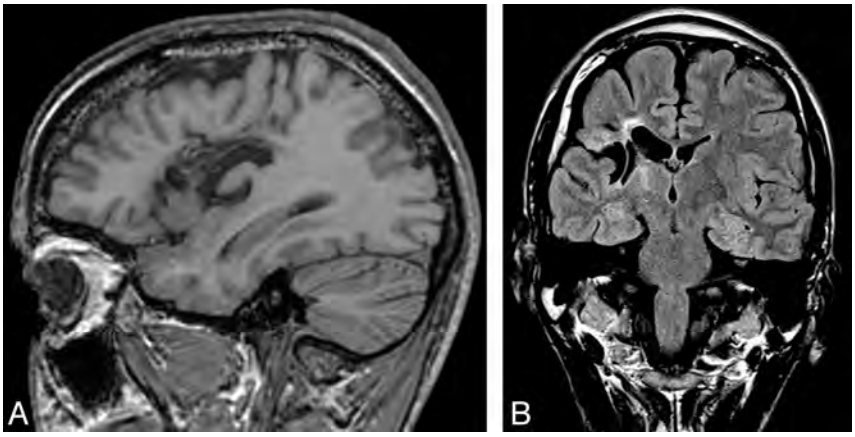

FIG 6. Sagittal T1 and coronal FLAIR MR imaging of a 53-year-old man with a history of trauma in whom right fronto-temporo-insular epilepsy (definite) developed. Encephalomalacia and atrophy involve the insula, frontal operculum, and superior temporal gyrus.

Distribution of patients according to radiopathologic categories and refractoriness to medication

Pathologic Features	Medication		*P* Value
	Response (*n*)	Refractoriness (*n*)	
Neoplastic lesion	8	5	.19
Malformations of cortical development	0	10	.001[a]
Vascular lesions	7	2	.03
Atrophy/gliosis from acquired insults	4	4	.71
Other	1	3	.49
Normal	1	3	.62
Total	21	27	.004[b]

[a] Statistical significance threshold after Bonferroni method, $P = .008$.

[b] *P* value obtained by Fisher exact test on the overall 2×6 contingency table (statistical significance threshold $P = .05$).

atrophy or encephalomalacia from acquired insults. Trauma and herpes encephalitis classically injure the temporal lobes, but damage may extend to the insula. Although strokes are the most common source of epilepsy in elderly people, they were not found here to be a cause of IPICE, likely because of the rare occurrence of pure insular ischemic strokes.[19] One patient with IPICE had Rasmussen encephalitis, a chronic inflammatory disease of unknown origin affecting 1 hemisphere.[20] Some imaging studies have previously suggested that the progressive hemiatrophy associated with Rasmussen encephalitis starts preferentially in the insula and in the perisylvian area.[21-23]

Refractoriness to antiepileptic drug treatment was 100% for MCDs in the insular/peri-insular region, which is not necessarily surprising, as such entities located in other areas are generally linked with drug-resistant epilepsies as well.[3] The refractoriness rate was 38.5% (5/13) for patients with tumors in our series, most of which were low-grade gliomas (4/5; 80%). These findings are consistent with the observations of Duffau et al,[10] who recorded a refractoriness rate of 58% with insular low-grade gliomas and suggested that the latter are more prone to eliciting drug-resistant epilepsy than tumors invading other brain structures.[10,24] Although half (2/4) of patients with IPICE related to atrophy/gliosis had drug-resistant seizures, their low number did not allow further interpretation. Although some studies have reported a high rate of drug-resistant seizures in posttraumatic[25,26] or postencephalitic epilepsies,[27] epilepsies after strokes usually respond to medical treatment.[28] Of interest, 1 patient with a millimetric T2 signal abnormality in the posterior insula (initially dismissed as nonspecific), 1 patient with hippocampal sclerosis but no insular lesion, and 3 of 4 patients with normal MR imaging results had refractory insular seizures confirmed by invasive recordings. This finding raises the possibility that a certain proportion of patients with persisting seizures, despite temporal, frontal, or parietal lobe epilepsy surgeries, might have unrecognized IPICE.[29,30]

The limitations of our study are inherent to any retrospective design. Because MR imaging scans were not standardized (magnet strength, acquisition protocols), anatomic delineation of insular involvement was constrained in some cases. Coronal and sagittal T2-weighted sequences with thin sections on the insula would certainly have increased the precision. Although the lesions were centered on the insular/peri-insular area, some extended slightly beyond, and we cannot exclude that seizures originated from adjacent lobes with rapid propagation to the insular/peri-insular area. Finally, selecting patients from a specialized epilepsy clinic in a tertiary academic center may have biased the study into finding a higher rate of lesions associated with intractable epilepsy.

CONCLUSIONS

A spectrum of structural abnormalities may evoke IPICE. In order of frequency, we noted tumors, MCDs, vascular lesions, and atrophy/gliosis from acquired insults. IPICE related to MCDs, atrophy/gliosis from acquired insults, and tumors is frequently refractory to antiepileptic drugs.

REFERENCES

1. Chugani HT. *Neuroimaging in Epilepsy*. New York: Oxford University Press; 2011:3–37
2. Cakirer S, Başak M, Mutlu A, et al. **MR imaging in epilepsy that is refractory to medical therapy.** *Eur Radiol* 2002;12:549–58
3. Surbeck W, Bouthillier A, Nguyen DK. **Refractory insular cortex epilepsy: clinical features, investigation and treatment.** *Future Neurol* 2010;5:491–99
4. Naidich TP, Kang E, Fatterpekar GM, et al. **The insula: anatomic study and MR imaging display at 1.5T.** *AJNR Am J Neuroradiol* 2004;25:222–32
5. Isnard J, Guenot M, Sindou M, et al. **Clinical manifestations of insular lobe seizures: a stereo-electroencephalographic study.** *Epilepsia* 2004;45:1079–90
6. Ryvlin P, Minotti L, Demarquay G, et al. **Nocturnal hypermotor seizures, suggesting frontal lobe epilepsy, can originate in the insula.** *Epilepsia* 2006;47:755–65
7. Nguyen DK, Nguyen DB, Malak R, et al. **Revisiting the role of the insula in refractory partial epilepsy.** *Epilepsia* 2009;50:510–20
8. Lefkopoulos A, Haritanti A, Papadopoulou E, et al. **Magnetic resonance imaging in 120 patients with intractable partial seizures: a preoperative assessment.** *Neuroradiology* 2005;47:352–61
9. Zentner J, Hufnagel A, Wolf HK, et al. **Surgical treatment of temporal lobe epilepsy: clinical, radiological, and histopathological findings in 178 patients.** *J Neurol Neurosurg Psychiatry* 1995;58:666–73
10. Duffau H, Capelle L, Lopes M, et al. **Medically intractable epilepsy from insular low-grade gliomas: improvement after an extended lesionectomy.** *Acta Neurochir (Wien)* 2002;144:563–72; discussion 572–73
11. Lee JW, Wen PY, Hurwitz S, et al. **Morphological characteristics of brain tumors causing seizures.** *Arch Neurol* 2010;67:336–42
12. Brodtkorb E, Nilsen G, Smevik O, et al. **Epilepsy and anomalies of neuronal migration: MRI and clinical aspects.** *Acta Neurol Scand* 1992;86:24–32
13. Kuzniecky RI. **MRI in cerebral developmental malformations and epilepsy.** *Magn Reson Imaging* 1995;13:1137–45
14. Raymond AA, Fish DR, Sisodiya SM, et al. **Abnormalities of gyration, heterotopias, tuberous sclerosis, focal cortical dysplasia, microdysgenesis, dysembryoplastic neuroepithelial tumour and dysgenesis of the archicortex in epilepsy. Clinical, EEG and neuroimaging features in 100 adult patients.** *Brain* 1995;118:629–60
15. Leventer RJ, Jansen A, Pilz DT, et al. **Clinical and imaging heterogeneity of polymicrogyria: a study of 328 patients.** *Brain* 2010;133:1415–27
16. Vinters HV, Kerfoot C, Catania M, et al. **Tuberous sclerosis-related gene expression in normal and dysplastic brain.** *Epilepsy Res* 1998;32:12–23
17. Stehbens WE. **Etiology of intracranial berry aneurysms.** *J Neurosurg* 1989;70:823–31
18. Malak R, Nguyen DK, Bojanowski MW. **Non ruptured MCA aneurysms presenting with insular related symptoms.** *Can J Neurol Sci* 2010;37:219–22
19. Cereda C, Ghika J, Maeder P, et al. **Strokes restricted to the insular cortex.** *Neurology* 2002;59:1950–55
20. Bien CG, Widman G, Urbach H, et al. **The natural history of Rasmussen's encephalitis.** *Brain* 2002;125:1751–59
21. Granata T, Gobbi G, Spreafico R, et al. **Rasmussen's encephalitis: early characteristics allow diagnosis.** *Neurology* 2003;60:422–25
22. Chiapparini L, Granata T, Farina I, et al. **Diagnostic imaging in 13 cases of Rasmussen's encephalitis: can early MRI suggest the diagnosis?** *Neuroradiology* 2003;45:171–83
23. Wagner J, Schoene-Bake JC, Bien CG, et al. **Automated 3D MRI volumetry reveals regional atrophy differences in Rasmussen encephalitis.** *Epilepsia* 2012;53:613–21
24. Taillandier L, Duffau H. **Epilepsy and insular grade II gliomas: an interdisciplinary point of view from a retrospective monocentric series of 46 cases.** *Neurosurg Focus* 2009;27:E8
25. Caveness WF. **Epilepsy, a product of trauma in our time.** *Epilepsia* 1976;17:207–15
26. Annegers JF, Hauser WA, Coan SP, et al. **A population-based study of seizures after traumatic brain injuries.** *N Engl J Med* 1998;338:20–24
27. Pomeroy SL, Holmes SJ, Dodge PR, et al. **Seizures and other neurologic sequelae of bacterial meningitis in children.** *N Engl J Med* 1990;323:1651–57
28. Gupta S, Naheedy M, Elias D, et al. **Post infarction seizures: a clinical study.** *Stroke* 1988;19:1477–81
29. Aghakhani Y, Rosati A, Dubeau F, et al. **Patients with temporoparietal ictal symptoms and inferomesial EEG do not benefit from anterior temporal resection.** *Epilepsia* 2004;45:230–36
30. Harroud A, Bouthillier A, Weil A, et al. **Temporal lobe epilepsy surgery failures: a review.** *Epilepsy Res Treat* 2012;201651

Stent-Assisted Coiling in Endovascular Treatment of 500 Consecutive Cerebral Aneurysms with Long-Term Follow-Up

S. Geyik, K. Yavuz, N. Yurttutan, I. Saatci, and H.S. Cekirge

ABSTRACT

BACKGROUND AND PURPOSE: Stent-assisted coil embolization has become one of the most preferred techniques in the treatment of wide-neck intracranial aneurysms; however, long-term patency and safety of the self-expanding neurostents and their role in durability of the endovascular treatment has remained ambiguous. We sought to retrospectively examine the long-term results of self-expanding stent usage in conjunction with coil embolization in treatment of wide-neck cerebral aneurysms.

MATERIALS AND METHODS: We coiled 500 wide-neck cerebral aneurysms with different types of self-expanding neurostent assistance in 468 patients. Patient and aneurysm characteristics, pharmacologic therapy protocol, complications, and initial occlusion grades were analyzed. Patients underwent angiographic follow-up at 6 months to 7 years after treatment. DSA or MRA images of all patients were analyzed to assess the occlusion rate of aneurysms and patency of the parent artery.

RESULTS: Enterprise ($n = 340$), Solitaire ($n = 98$), Wingspan ($n = 41$), LEO ($n = 16$), and Neuroform ($n = 5$) stent systems were used in this series. Stent-related thromboembolic events occurred in 21 patients and intraoperative rupture occurred in 4 patients. Initially, complete occlusion was achieved in 42.2% of the aneurysms, and, according to the last follow-up data, the rate had progressed to 90.8%. Recanalization rate at 6 months was 8%, whereas the late recanalization rate was 2%.

CONCLUSIONS: The use of stents in endovascular treatment provides high rates of complete occlusion and low rates of recurrence at a long-term follow-up study.

The use of self-expanding neurostents has ensured a significant advance in the endovascular treatment of wide-neck or fusiform aneurysms. However, one of the most important concerns about their use has been the lack of long-term follow-up data to show the long-term safety and durability.

To date, clinical experiences with midterm follow-up results of different self-expandable stents have been reported[1-5]; however, few reports exist in the literature publishing long-term data in regard to durability and long-term safety of these devices with or without comparison to other endovascular treatment techniques without the use of adjunctive stent placement.[6-13] In all these previous reports, the authors concur that stents have been associated with a significant decrease in angiographic recurrences. However, procedural and late complications caused by stent use remain controversial.

This study reports on our 500 consecutive aneurysms treated with a single stent–assisted coiling technique by use of a variety of stents including Enterprise (Codman & Shurtleff, Raynham, Massachusetts), Solo/Solitaire (ev3, Irvine, California), Wingspan (Boston Scientific, Natick, Massachusetts), LEO (Balt, Montmorency, France), and Neuroform (Stryker Neurovascular, Fremont, California) with emphasis on the long-term results.

MATERIALS AND METHODS

Patient and Aneurysm Characteristics

All patients whose intracranial aneurysms were treated in Hacettepe University and in private practice by the senior author (H.S.C.) by use of a single self-expanding stent (regardless of the stent type) and detachable platinum coils between May 2004 (the initiation of our data base records) and December 2010 have been reviewed based on the data base, medical records and image archive. All procedures were performed with the provision of written informed consent.

Aneurysm sizes were classified as small (<1 cm), large (≥1 cm and ≤2.5 cm), and giant (>2.5 cm). The aneurysms are referred

Received November 26, 2012; accepted after revision February 6, 2013.

From the Department of Radiology, Hacettepe University Hospitals, Ankara, Turkey.

Please address correspondence to Kivilcim Yavuz, MD, Hacettepe University Hospitals, Department of Radiology, 06100 Sihhiye, Ankara Turkey; e-mail: kivilcimyvz@yahoo.com

http://dx.doi.org/10.3174/ajnr.A3574

to as wide-neck when the dome/neck ratio is <2.0 and/or neck length was ≥4 mm.

Pharmacologic Therapy Protocol and Endovascular Procedures

Patients with unruptured aneurysms were premedicated with 300 mg of aspirin and a loading dose of 300–600 mg of clopidogrel 1 week before the procedure, followed by 75 mg daily. On the other hand, patients with ruptured aneurysms, which were to be treated at least 14 days after SAH, premedicated with the same loading dose, started 2–3 days before the procedure. This was considered sufficient to test for clopidogrel responsiveness. Thrombocyte inhibition levels were confirmed by use of whole-blood impedance platelet aggregation (Multiplate; Dynabyte Medical, Munich, Germany) and, since February 2006, the rapid platelet function assay VerifyNow P2Y12 (Accumetrics, San Diego, California). Patients with inhibition value >30% were treated, low responders (<30%) without resistance to clopidogrel were loaded again, and patients with clopidogrel resistance were medicated with ticlopidine 2 × 250 mg. All patients received heparin to maintain an activated clotting time level elevated to 2–3 times of the baseline value during the procedure.

For the stents used without premedication, 500 mg ticlopidine or 600 mg clopidogrel and 300 mg aspirin was administered by naso/orogastric tube combined with low-molecular-weight heparin. These patients also received 1–2 mg of IV tirofiban (a glycoprotein IIb/IIIa inhibitor) during the procedure, as soon as the stent was deployed. Tirofiban infusion (IV and/or intra-arterial) was performed in the case of thrombus formation during the procedure, as well.

After the control angiogram was obtained at 6 months, clopidogrel was discontinued and aspirin was to be taken life-long.

Endosaccular coiling was performed immediately after the stent deployment through the microcatheter, which was either advanced through the stent struts after stent deployment or had been placed inside the aneurysm sac before the stent deployment and jailed between the stent and the vessel wall.

Follow-Up

Angiographic results were classified as complete, near complete (>95% occlusion but minimal residual filling with coils at the neck), and incomplete occlusion (<95% occlusion). Any further filling of the aneurysm neck or sac over time was referred to as "recanalization," whereas a decrease in filling was referred to as "further occlusion."

Thromboembolic complications were classified as minor if transient or if the mRS was <2 and major if the mRS was ≥2.

Patients underwent angiographic follow-up at 6 months after treatment (midterm) with DSA or gadolinium-enhanced MRA. When there was no in-stent stenosis or recanalization, the subsequent angiographic evaluation was performed 18 months after treatment (long-term). In the case of recanalization, we either scheduled a retreatment or an earlier angiographic follow-up after cessation of clopidogrel/ticlopidine with continuation of aspirin alone. A last DSA follow-up of longer term was planned ≥5 years after the initial treatment.

Table 1: Patient profile

Total No. of patients treated	468
Age, y	
Range	10–96
Mean	50.1
Sex	
Female	302 (64.5%)
Male	166 (35.5%)
Presenting symptom	
SAH	70 (15%)
Headache	274 (58.5%)
Incidental	104 (22.2%)
Cranial nerve palsy	9 (1.9%)
Ischemic events	6 (1.3%)
Epilepsy	4 (0.9%)
Mass effect	1 (0.2%)

Table 2: Aneurysm characteristics

Total No. of aneurysms treated	500
Size	
Small	304 (60.8%)
Large	176 (35.2%)
Giant	20 (4%)
Location	
Anterior circulation	445 (89%)
ICA	240 (48%)
Extradural	14 (2.8%)
Intradural	226 (45.2%)
ACA (A1)	5 (1%)
AcomA	93 (18.6%)
Distal ACA	9 (1.8%)
MCA (M1)	11 (2.2%)
MCA bifurcation	82 (16.4%)
Distal MCA	5 (1%)
Posterior circulation	55 (11%)
VA intradural	7 (1.4%)
PICA	7 (1.4%)
Vertebrobasilar junction	3 (0.6%)
Basilar artery	22 (4.4%)
SCA	3 (0.6%)
PCA (P1)	12 (2.4%)
Distal PCA	1 (0.2%)
Previous treatment	
Balloon-assisted coiling	27
Primary coiling	7
Onyx embolization	2
Onyx + coil embolization	1

Note:—ACA indicates anterior cerebral artery; AComA, anterior communicating artery; VA, vertebral artery; SCA, superior cerebellar artery; PCA, posterior cerebral artery.

RESULTS

The patient characteristics and the aneurysm features are given in Tables 1 and 2. This series included 468 patients (302 female and 166 male), with a mean age of 50.1 years (range, 10–96), harboring 500 aneurysms treated with single stent–assisted coil embolization.

Of the 500 aneurysms, 445 were located in the anterior circulation and 55 were located in the posterior; 304 aneurysms were small (60.8%), 176 were large (35.2%), and 20 (4%) aneurysms were giant.

The presenting symptoms of the aneurysms and the previous treatments of the retreatment cases are given in Tables 1 and 2, respectively. Forty of 70 aneurysms that were ruptured were treated at the acute phase of subarachnoid hemorrhage within 14

Table 3: Medication and stents

Antiplatelet regimen	
Clopidogrel	406 (86.7%)
Ticlopidine	62 (13.3%)
Stents used for treatment[a,b]	
Enterprise	340 (68%)
Solitaire (Solo)	98 (19.6%)
Wingspan	41 (8.2%)
LEO	16 (3.2%)
Neuroform	5 (1%)

[a] Percentages are obtained over the total number of aneurysms treated ($n = 500$), whereas others are over the number of patients ($n = 468$).
[b] Stents with technical failure are not included in this table.

Table 4: Complications

Complication	Total	Ruptured	Unruptured
Procedure-related			
Thromboembolic[a]	28 (5.6%)	7 (1.4%)	21 (4.2%)
Related to stent	21 (4.2%)	4 (0.8%)	17 (3.4%)
Minor	14 (2.8%)	2 (0.4%)	12 (2.4%)
Major	7 (1.4%)	2 (0.4%)	5 (1%)
Unrelated to stent	7 (1.4%)	3 (0.6%)	4 (0.8%)
Minor	7 (1.4%)	3 (0.6%)	4 (0.8%)
Major	- (0%)	-	-
Hemorrhagic[a]	4 (0.8%)	1 (0.2%)	3 (0.6%)
Aneurysm rupture	2 (0.8%)	1 (0.2%)	1 (0.2%)
Parent artery perforation	2 (0.8%)	-	2 (0.4%)
Other			
Dissection[b]	5 (1%)	4 (0.8%)	1 (0.2%)
Groin complications	23 (5%)	3 (0.7%)	20 (4.3%)
Disease-related (SAH)			
Vasospasm	4	4	NA
Hydrocephalus	1	1	NA
Late complications	4 (0.8%)	1 (0.2%)	3 (0.6%)
In-stent stenosis	4 (0.8%)	1 (0.2%)	3 (0.6%)

[a] Percentages are obtained over the total number of aneurysms treated ($n = 500$), whereas others are over the number of patients ($n = 468$).
[b] Dissections are unrelated to stent placement.

days. Among the 37 aneurysms that received stent-assisted coiling as a retreatment, 14 had history of treatment in the acute stage of SAH.

Clopidogrel was used as the antiplatelet agent in most of the patients ($n = 406$) (86.8%), with the remaining patients receiving ticlopidine ($n = 62$) (13.2%). All patients received 300 mg aspirin (Table 3).

Stents Used in Treatment and Technical Difficulties

Coil embolization was performed with the assistance of the Enterprise stent in 340 aneurysms (68%), the Solitaire (or Solo) stent in 98 aneurysms (19.6%), the Wingspan stent in 41 aneurysms (8.2%), the LEO stent in 16 aneurysms (3.2%), and the Neuroform stent in 5 aneurysms (1%) (Table 3).

Technical difficulties were encountered during stent deployment in 4 patients, resulting in a technical success rate of 99.2%. The stent prolapsed into the aneurysm sac in 2 cases, distally migrated with proximal end prolapse into the sac in 1, and was misplaced in another. Coil embolization was performed without difficulty in these patients, with an additional stent placement in 2 cases.

Complications

All complications are shown in Table 4.

Procedure-Related Complications

Thromboembolic complications were seen in 28 patients (minor in 21 patients, major in 7 patients). Of the 7 major thromboembolic events, 5 occurred before we started to use the VerifyNow P2Y12 test. In 7 of the 21 patients with minor thromboembolic events, the primary treatment strategy was not stent-assisted coiling. Instead, a stent was used, without premedication, for the treatment of a thromboembolic event caused by coil protrusion into the parent artery during primary or balloon-assisted coiling. These thromboembolic events were considered to be unrelated to stent placement. Therefore, minor thromboembolic events related to stent-assisted coiling occurred in 14 patients. Overall stent-related thromboembolic complication rate was 4.2% (major = 1.4%, minor = 2.8%) (Table 4).

In this series, stents were used to stabilize the protruded or migrated coils during primary or balloon-assisted coiling procedures in 23 patients. In 7 of these 23 patients, associated thrombus formation was present on angiography, as described above. These patients also received 1–2 mg IV and/or intra-arterial tirofiban infusion during the procedure. All these patients were discharged with normal neurologic status.

Dissection in a parent artery during endovascular procedure occurred in 5 patients during catheterization, none related to stent placement. Four occurred in the proximal parent arteries and 1 in the ICA intracranial portion. All except 1 was treated with stent placement without clinical consequence.

Intraoperative rupture occurred in 4 patients. In 2 of these patients, rupture was from the aneurysm. In the other 2, extravasation from a parent artery occurred as the result of wire perforation. Two of these 4 patients died. One patient had permanent disabling neurologic deficit (mRS >2). Minimal extravasation was observed in angiography, and hemostasis was achieved rapidly in the last patient. This patient was awakened from anesthesia without neurologic deficit.

Hemorrhagic groin puncture site complications occurred in 23 patients. In 11 of these patients, blood transfusion was needed. In only 2 of these 23 patients, additional interventional treatments were needed for iatrogenic arteriovenous fistulas, and stent-grafts were used for treatment.

Disease-Related Complications

In 4 patients treated at the acute stage of SAH, severe vasospasm occurred within 10 days after treatment. Two of these patients were discharged without neurologic deficits after intra-arterial treatments. Two patients did not respond to any treatment and died.

Hydrocephalus developed in 1 patient treated after SAH, and ventriculostomy was needed. This patient had no neurologic deficit at discharge.

Mortality

Nine patients died in this series. Three of these patients died unrelated to the disease and procedure, as the result of cardiac and renal disease 6 months after treatment. Of the other 6 patients, 4 died of causes related to the procedure and 2 died of causes related to disease. Procedure-related mortality was due to intraoperative rupture in 2 patients; acute stent occlusion in 1 patient; and mass

Table 5: Mortality and morbidity

		Ruptured	Unruptured
Overall mortality	9 (1.9%)	3 (0.6%)	6 (1.3%)
Procedure-related	4 (0.8%)	1	3
Hemorrhagic	2 (0.4%)	–	2
Thromboembolic	1 (0.2%)	1	–
Mass effect	1 (0.2%)	–	1
Disease-related (SAH)	2	2	NA
Vasospasm	2	2	NA
Other	3 (0.6%)	1	2
Overall morbidity (mRS ≥2)	4 (0.8%)	2 (0.4%)	2 (0.4%)
Hemorrhagic	1 (0.2%)	–	1
Thromboembolic	3 (0.6%)	2	1

Percentages are obtained over the total number of patients ($n = 468$).

effect on brain stem aggravated after treatment in 1 patient. Disease-related mortality was caused by severe vasospasm in 2 patients. The overall mortality rate was 1.9% (9/468), including procedure-related mortality rate of 0.8% (4/468) and disease-related mortality of 0.4% (2/468) (Table 5).

Immediate and Long-Term Angiographic Results

Angiographic follow-up was available in 440 patients with 467 aneurysms, with a follow-up rate of 94% of patients and 93.4% of aneurysms. Follow-up data were collected for the aneurysms until April 2012, with a range of 6 months to 7 years (mean, 19.2 months). Thirty-three aneurysms of 28 patients did not have a follow-up because of death ($n = 9$), loss of communication, or patient refusal. Of the 467 aneurysms, 6-month angiographic follow-up was performed with DSA for 459 aneurysms (98%), and with MRA (2%) for 8 aneurysms. For 409 aneurysms, at least 1 year, and for 190 aneurysms, at least 2 years of follow-up results were obtained.

On the basis of postembolization angiography studies, complete occlusion was achieved in 211 of 500 aneurysms (42.2%). In the remaining 289 aneurysms, there was near complete occlusion in 257 (51.4%) and incomplete occlusion in 32 (6.4%). For the 467 aneurysms that had follow-up examinations, the initial angiographic results were as follows: complete occlusion in 194 aneurysms (41.6%), near complete occlusion in 242 aneurysms (51.8%), and incomplete occlusion in 31 aneurysms (6.6%) (Table 6).

Six-month follow-up angiograms of 467 aneurysms showed complete occlusion in 380 (81.3%), near complete occlusion in 51 (11%), and incomplete occlusion in 36 (7.7%). At 6-months, stable occlusion was observed in 223 aneurysms (48%), further occlusion in 206 aneurysms (44%), and recanalization in 38 aneurysms (8%)(Table 6). Of the recanalized aneurysms, 5 were giant, 28 were large, and 5 were small.

Of the 38 aneurysms that were recanalized at 6 months, 23 that also showed evident coil compaction were retreated: once in 19 aneurysms, twice in 3 aneurysms, and 3 times in 1 aneurysm.

In the remaining 15 patients with recanalized aneurysms showing no apparent coil compaction (with incomplete occlusion in 11 patients and near complete in 4 patients) at 6 months, clopidogrel was discontinued and 1-year control DSA was scheduled. Further occlusion did not occur in these aneurysms; therefore 11 aneurysms with an occlusion grade of class 3 were retreated. At 2-year control angiography, all these retreated aneurysms showed complete occlusion. Overall, the total number of retreated aneurysms after stent-assisted coiling was 34, and 5 aneurysms had retreatments of >1.

Table 6: Immediate and long-term angiographic results of aneurysms with follow-up

No. of aneurysms with follow-up	467
Follow-up duration	
Range	6–84 months
Mean	19.2 months
Immediate occlusion grades in the entire group	500
Complete	211 (42.2%)
Near complete	257 (51.4%)
Incomplete	32 (6.4%)
Six-month follow-up results	467
Complete	380 (81.3%)
Near complete	51 (11%)
Incomplete	36 (7.7%)
Stable occlusion	223 (48%)
Further occlusion	206 (44%)
Recanalization	38 (8%)
Last follow-up results	
Complete	424 (90.8%)
Near complete	35 (7.5%)
Incomplete	8 (1.7%)
Recanalization	
At 6 months	38 (8%) (38/467)
Late (1–5 years)	8 (2%) (8/409)
Retreatment	34 (7%) (34/467)

Late recanalization (>6 months) was observed in 8 aneurysms (8/409) (2%) (1–5 years; mean, 2 years). Six-month follow-up of all these aneurysms showed stable occlusion. Of these 8 belatedly recanalized aneurysms, 5 were recanalized in the first year, 2 in the third year, and the remaining 1 in the fifth year. Five of these aneurysms were retreated, and 3 are being followed. Overall, recanalization was observed in 46 aneurysms (9.9%), and mean recanalization time was 9.1 months.

According to the last follow-up data, overall occlusion rates were complete in 424 aneurysms (90.8%), near complete in 35 aneurysms (7.5%), and incomplete in 8 aneurysms (1.7%).

All but 7 stents were shown to be patent during follow-up. Asymptomatic parent artery occlusion was observed in 6 patients (6/467, 1.2%). All 6 of these patients were taking clopidogrel and aspirin as the antiplatelet therapy; 1 patient discontinued his drugs by himself and in 1 patient, another physician discontinued clopidogrel and continued with aspirin alone. One of these patients had significant in-stent stenosis resulting parent artery occlusion with no clinical consequence discovered in the follow-up, despite continued dual antiplatelet therapy. In the remaining patient, parent artery occlusion was due to the procedural thromboembolic complication. Asymptomatic intimal hyperplasia or in-stent stenosis was observed in 4 stents (4/467, 0.8%). Clopidogrel and aspirin were continued in these patients. Two remained stable, 1 improved and 1 occluded during follow-up.

DISCUSSION

Having been reported to be safe and effective in the preliminary experiences and midterm follow-up results,[1-5] stent-assisted coil embolization has become one of the most preferred techniques. Technological advancements resolved the previously reported

limitations[2,14] of the first-generation stents; however, long-term patency and safety of neurostents and their durability remains ambiguous.

Recanalization has been one of the leading issues regarding endovascular treatment of intracranial aneurysms.[15,16] Several studies on comparison of coiling without stent use versus stent-assisted coiling have demonstrated significant superiority of stent-assisted groups in terms of avoiding recanalization and even providing further occlusion.[9,13,17,18] On the contrary, in their series, including 216 consecutive aneurysms with long-term follow-up (mean, 14 months), Piotin et al[9] claimed that stent use is associated with higher mortality and morbidity rates because of increased procedure-related complications. However, their results are controversial because of inclusion of balloon-expandable stents in the study group, which are more traumatic for the arterial wall during navigation and delivery.

In our series, we included only the self-expanding stents. These self-expanding stents can be easily delivered and deployed wherever a microcatheter can be navigated.

Deployment is not a traumatic process. This may explain our lower overall mortality rate of 1.9% (compared with 6% mortality rate in the Piotin et al study[9]), with a rate of procedure-related mortality of 0.8% (versus their rate of 4.6%). Our results are comparable with the series with long-term follow-up in which self-expanding stents were used.[7,8,11,12,18] Because of the ease of delivery and deployment, the Wingspan stent was used in endovascular treatment of aneurysms instead of Neuroform 3 and when the Solo and Enterprise stent systems were not available in our department.

In our series, the overall stent-related thromboembolic complication rate was 4.2% (major = 1.4%, minor = 2.8%), comparable with 2 large series with long-term follow-up,[11,12] and favorably lower than those in the large series of Piotin et al[9] and Fiorella et al.[8] Piotin et al reported that thromboembolic complications were also more frequent in the stented patients in their comparative study of coiling versus stent-assisted coiling.[9] However, they found that these complications were higher in the patients treated before antiplatelet activity assessment and diminished when the patients who did not respond to antiplatelet drugs were identified. We think that stent use does not increase the thromboembolic event rate if the dual antiplatelet regimen is used and the response in thrombocyte aggregation level is evaluated rigorously. On the contrary, stents may act as a "lifesaver " in the case of thromboembolic events caused by coil protrusion into the parent artery during endovascular treatment of wide-neck aneurysms. In this series, we used stents in 7 patients to restore the normal patency of the parent artery after a thromboembolic event occurred during a coiling procedure without a stent. All these patients were discharged without neurologic deficits. We did not have a control group of coiling without stent assistance in this study; however, previous comparative studies have shown no increase in the frequency of thromboembolic events with the adjunctive use of these devices.[13,18,19]

Recently, long-term safety and durability of stent-assisted coiling with Neuroform and Enterprise stents have been investigated.[6-13] We previously reported our preliminary experience with Solo and Wingspan stents, including the immediate and midterm follow-ups.[1,5] In this present series, we aimed at extension of the follow-up durations with the addition of newly enrolled patients treated with a variety of stents and evaluation of the overall long-term angiographic outcomes of endovascular treatment by use of the stent-assisted coiling technique; therefore, we included all self-expanding stent types that we have been using (but not a specific brand) because all these stents are neuro-dedicated and have had their particular series in the literature.

In our study, 440 patients with 467 aneurysms had follow-up imaging with a follow-up rate of 94%. In our study, initial complete occlusion rate was 42.2% (211/500) overall, and that in the aneurysms with follow-up ($n = 467$) was 41.6%, which is comparable with previously reported studies of Piotin et al[9] (46.3%) and Santillan et al[12] (42.3%).

In 6-month angiographic follow-up, complete occlusion rate increased to 81.3%; stable and further occlusion rates were 48% and 44%, respectively. The recanalization rate was 8%, which occurred mainly in large and giant aneurysms (87%, 33/38) when compared with small ones (13%, 5/38). All recanalized aneurysms with an incomplete occlusion were retreated immediately or after a second 6-month follow-up. We observed recanalization in the latter controls in only a few aneurysms (1.9%, 8/409).

Overall complete occlusion rate according to the latest follow-up reached the rate of 90.8%, comparable to the Santillan et al[12] series and even favorable to other previous series that give the complete occlusion rates at the latest follow-up.[7,11] Eventually, incomplete occlusion remained only in 1.7% of all aneurysms. No early or late rebleeds occurred.

On the basis of these findings, we may argue that 1) stent use provides better scaffolding for coils at the aneurysm neck so that better packing may be performed without concern of protrusion into the parent artery; 2) with the help of hemodynamic and biologic mechanisms,[20,21] stents ensure further aneurysmal thrombosis, resulting in improved occlusion rates; 3) complete and nearly complete initial aneurysm occlusion is associated with high final stable and complete occlusion rates; and 4) most recanalizations occur within 6 months after treatment; therefore, 6-month follow-up is essential to probe the early recanalizations.

The survey of stent patency is another important focus of this study. Asymptomatic parent artery occlusion was observed in 6 patients (1.2%). In 2 of these patients, cessation of dual antiplatelet therapy probably resulted in parent artery occlusion. On the other hand, in-stent stenosis was recorded in 4 (0.8%), a rate comparable to that of Santillan et al[12] (1.3%) but lower than those of Fargen et al[11] and Fiorella et al,[8] with rates of 3.4% and 5.6%, respectively. These patients continued taking clopidogrel and aspirin and they remained asymptomatic.[12] Whereas 2 of 4 patients remained stable, angiographic study revealed spontaneous partial resolution in 1 and total occlusion in the other. Spontaneous resolution of delayed in-stent stenosis was first described by Fiorella et al[22] with the use of Neuroform stents and was postulated to be an event unique to the deployment of a low radial force stent within the cerebrovasculature. However, our patient with spontaneous partial resolution was treated by use of a Wingspan stent, designed to exert active, controlled, outward radial force in atherosclerotic lesions; therefore, this cannot be explained solely by low radial force. Nevertheless, being aware of this phenomenon is

important to follow the patients clinically and angiographically with prolonged dual antiplatelet use and to prevent unnecessary interventions.[5,22]

CONCLUSIONS

Stent-assisted coiling is a safe, effective, and durable treatment of wide-neck intracranial aneurysms. The use of stents in endovascular treatment provides high rates of complete occlusion and low rates of recurrence at long-term follow-up. Proper dual antiplatelet regimen and antiplatelet activity assessment are the key points in preventing procedure-related thromboembolic complications. Six-month follow-up appears to be crucial in detecting recurrence and in-stent stenosis.

Disclosures: Isil Saatci—*UNRELATED: Consultancy:* Covidien/ev3. Saruhan Cekirge—*UNRELATED: Consultancy:* MicroVention; *Other:* Proctoring agreement with Covidien/ev3.

REFERENCES

1. Benitez RP, Silva MT, Klem J, et al. **Endovascular occlusion of wide-necked aneurysms with a new intracranial microstent (Neuroform) and detachable coils.** *Neurosurgery* 2004;54:1359–68
2. Fiorella D, Albuquerque FC, Han P, et al. **Preliminary experience using the Neuroform stent for the treatment of cerebral aneurysms.** *Neurosurgery* 2004;54:6–17
3. Mocco J, Snyder KV, Albuquerque FC, et al. **Treatment of intracranial aneurysms with the Enterprise stent: a multicenter registry.** *J Neurosurg* 2009;110:35–39
4. Yavuz K, Geyik S, Pamuk AG, et al. **Immediate and midterm follow-up results of using an electrodetachable, fully retrievable SOLO stent system in the endovascular coil occlusion of wide-necked cerebral aneurysms.** *J Neurosurg* 2007;107:49–55
5. Yavuz K, Geyik S, Saatci I, et al. **Wingspan stent system in the endovascular treatment of intracranial aneurysms: clinical experience with midterm follow-up results.** *J Neurosurg* 2008;109:445–53
6. Ishii A, Murayama Y, Nien YL, et al. **Immediate and midterm outcomes of patients with cerebral aneurysms treated with Matrix1 and Matrix2 coils: a comparative analysis based on a single-center experience in 250 consecutive cases.** *Neurosurgery* 2008;63:1071–79
7. Sedat J, Chau Y, Mondot L, et al. **Endovascular occlusion of intracranial wide-necked aneurysms with stenting (Neuroform) and coiling: mid-term and long-term results.** *Neuroradiol* 2009;51:401–09
8. Fiorella D, Albuquerque FC, Woo H, et al. **Neuroform stent assisted aneurysm treatment: evolving treatment strategies, complications and results of long term follow-up.** *J NeuroIntervent Surg* 2010;2:16–22
9. Piotin M, Blanc R, Spelle L, et al. **Stent-assisted coiling of intracranial aneurysms: clinical and angiographic results in 216 consecutive aneurysms.** *Stroke* 2010;41:110–15
10. Raslan AM, Oztaskin M, Thompson EM, et al. **Neuroform stent-assisted embolization of incidental anterior communicating artery aneurysms: long-term clinical and angiographic follow-up.** *Neurosurgery* 2011;69:27–37
11. Fargen KM, Hoh BL, Welch BG, et al. **Long-term results of Enterprise stent-assisted coiling of cerebral aneurysms.** *Neurosurgery* 2012;71:239–44
12. Santillan A, Greenberg E, Patsalides A, et al. **Long-term clinical and angiographic results of Neuroform stent-assisted coil embolization in wide-necked intracranial aneurysms.** *Neurosurgery* 2012;70:1232–37
13. Colby GP, Paul AR, Radvany MG, et al. **A single center comparison of coiling versus stent assisted coiling in 90 consecutive paraophthalmic region aneurysms.** *J NeuroIntervent Surg* 2012;4:116–20
14. Broadbent LP, Moran CJ, Cross DT III, et al. **Management of neuroform stent dislodgement and misplacement.** *AJNR Am J Neuroradiol* 2003;24:1819–22
15. Raymond J, Guilbert F, Weill A, et al. **Long-term angiographic recurrences after selective endovascular treatment of aneurysms with detachable coils.** *Stroke* 2003;34:1398–403
16. Raja PV, Huang J, Germanwala AV, et al. **Microsurgical clipping and endovascular coiling of intracranial aneurysms: a critical review of the literature.** *Neurosurgery* 2008;62:1187–202
17. Lawson MF, Newman WC, Chi YY, et al. **Stent-associated flow remodeling causes further occlusion of incompletely coiled aneurysms.** *Neurosurgery* 2011;69:598–604
18. Izar B, Rai A, Raghuram K, et al. **Comparison of devices used for stent-assisted coiling of intracranial aneurysms.** *PLoS ONE* 2011;6:e24875
19. Brooks NP, Turk AS, Niemann DB, et al. **Frequency of thromboembolic events associated with endovascular aneurysm treatment: retrospective case series.** *J Neurosurg* 2008;108:1095–100
20. Canton G, Levy DI, Lasheras JC, et al. **Flow changes caused by the sequential placement of stents across the neck of sidewall cerebral aneurysms.** *J Neurosurg* 2005;103:891–902
21. Lopes D, Sani S. **Histological postmortem study of an internal carotid artery aneurysm treated with the Neuroform stent.** *Neurosurgery* 2005;56:E416
22. Fiorella D, Albuquerque FC, Woo H, et al. **Neuroform in-stent stenosis: incidence, natural history, and treatment strategies.** *Neurosurgery* 2006;59:34–42

Reduction of Coil Mass Artifacts in High-Resolution Flat Detector Conebeam CT of Cerebral Stent-Assisted Coiling

I.M.J. van der Bom, S.Y. Hou, A.S. Puri, G. Spilberg, D. Ruijters, P. van de Haar, B. Carelsen, S. Vedantham, M.J. Gounis, and A.K. Wakhloo

ABSTRACT

BACKGROUND AND PURPOSE: Developments in flat panel angiographic C-arm systems have enabled visualization of both the neurovascular stents and host arteries in great detail, providing complementary spatial information in addition to conventional DSA. However, the visibility of these structures may be impeded by artifacts generated by adjacent radio-attenuating objects. We report on the use of a metal artifact reduction algorithm for high-resolution contrast-enhanced conebeam CT for follow-up imaging of stent-assisted coil embolization.

MATERIALS AND METHODS: Contrast-enhanced conebeam CT data were acquired in 25 patients who underwent stent-assisted coiling. Reconstructions were generated with and without metal artifact reduction and were reviewed by 3 experienced neuroradiologists by use of a 3-point scale.

RESULTS: With metal artifact reduction, the observers agreed that the visibility had improved by at least 1 point on the scoring scale in >40% of the cases ($\kappa = 0.6$) and that the streak artifact was not obscuring surrounding structures in 64% of all cases ($\kappa = 0.6$). Metal artifact reduction improved the image quality, which allowed for visibility sufficient for evaluation in 65% of the cases, and was preferred over no metal artifact reduction in 92% ($\kappa = 0.9$). Significantly higher scores were given with metal artifact reduction ($P < .0001$).

CONCLUSIONS: Although metal artifact reduction is not capable of fully removing artifacts caused by implants with high x-ray absorption, we have shown that the image quality of contrast-enhanced conebeam CT data are improved drastically. The impact of the artifacts on the visibility varied between cases, and yet the overall visibility of the contrast-enhanced conebeam CT with metal artifact reduction improved in most the cases.

ABBREVIATIONS: MAR = metal artifact reduction; CBCT = conebeam CT; VasoCT = high-resolution contrast-enhanced CBCT

Ever since its introduction, the stent-assisted coil embolization technique has broadened the field for endovascular treatment of intracranial aneurysms to wide-neck aneurysms.[1-8] The use of neurovascular stents that serve as a scaffold allows for higher coil packing densities with a relatively low chance of coils herniating into parent arteries.[9] Currently, its application is not limited only to giant and fusiform aneurysms but it is also being used for smaller berrylike aneurysms.[10]

Because of the potential risk of aneurysm regrowth and of in-stent stenosis with the use of neurovascular stents, careful patient monitoring after endovascular treatment is essential. Patient follow-up is conventionally performed by catheter-based DSA because it provides a high spatial and temporal resolution. However, a disadvantage of this technique is that it only provides 2D information of the vascular anatomy, and the relationship of the vascular anatomy to the stent and coil mass may not be fully appreciated.

The latest generation of angiographic C-arm systems equipped with flat panel technology not only provide conventional 2D fluoroscopy but enable in situ 3D conebeam CT (CBCT) that can be can used for peri-interventional evaluation.[11] Recently, the development and application of high-resolution contrast-enhanced conebeam CT (VasoCT; Philips, Best, the Netherlands) with the use of an angiographic flat-panel C-arm system has been reported.[12,13] This technique enables detailed 3D visualization of neurovascular stents and host arteries that allows

Received October 11, 2012; accepted after revision January 28, 2013.

From the Department of Radiology (I.M.J.v.d.B., S.V.H., A.P., G.S., S.V., M.J.G., A.K.W.), New England Center for Stroke Research, University of Massachusetts Medical School, Worcester, Massachusetts; and Interventional X-Ray (D.R., P.v.d.H., B.C.), Philips Healthcare, Best, The Netherlands.

This article received funding from (RO1 CA128906).

Please address correspondence to I.M.J. van der Bom, PhD, University of Massachusetts, Department of Radiology, New England Center for Stroke Research, 55 Lake Ave North, SA-107F, Worcester, MA 01655; e-mail: martijn.vanderbom@umassmed.edu

http://dx.doi.org/10.3174/ajnr.A3561

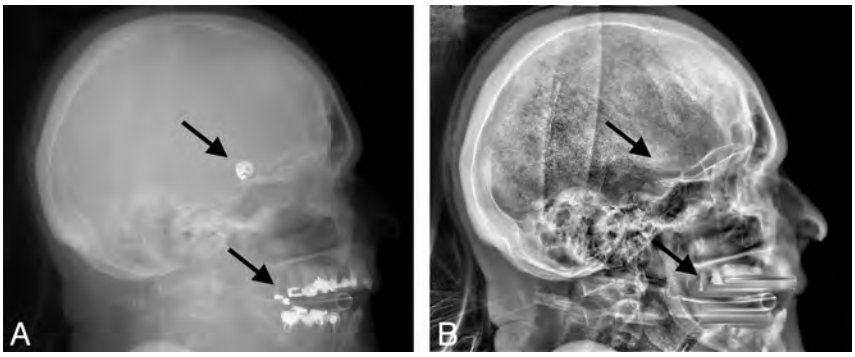

FIG 1. Example x-ray image acquired by the flat panel angiographic C-arm system before *(left)* and after *(right)* removal and replacement of the high-absorption areas caused by coils and dental fillings *(arrows)*.

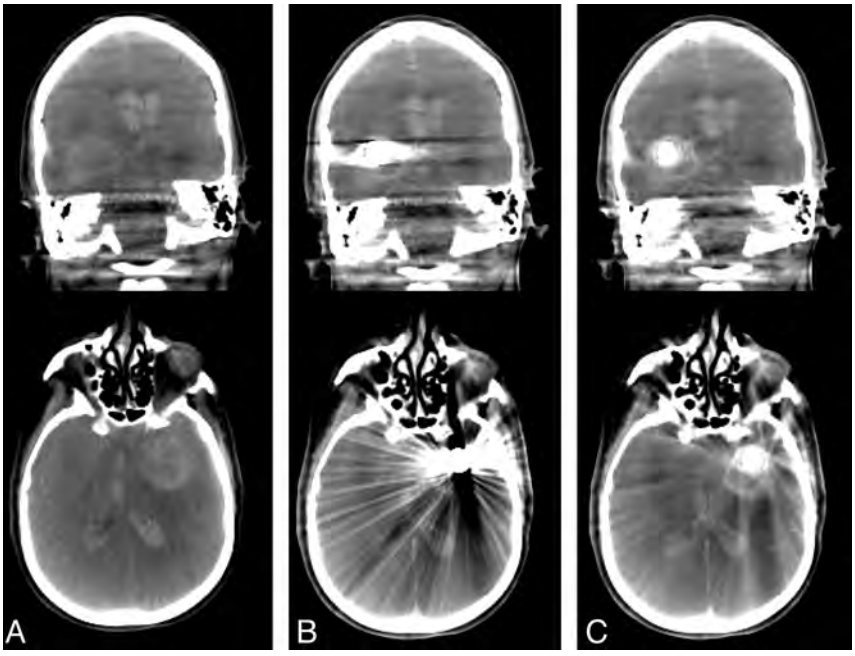

FIG 2. Coronal *(top row)* and axial sections *(bottom row)* of conebeam CT data of a patient acquired before coil embolization *(column A)*, after coil embolization without MAR *(column B)*, and after coil embolization with MAR *(column C)*.

for a more complete determination of stent-wall apposition and in-stent stenosis. However, in cases of stent-assisted coiling, the high x-ray absorption of the coil mass generates streak artifacts that obscure surrounding structures and therefore severely limit the diagnostic quality of the acquisition.

In the 1980s, Glover and Pelc[14] and Kalender et al[15] suggested manipulating raw data before reconstruction to reduce the effect of metallic implants in CT. Since these first reports, a diversity of similar algorithms have been proposed that address the occurrence of metal artifacts in multidetector CT data. Various methods that aim to replace sinogram data have been investigated, of which most explore different methods of segmentation and interpolation.[15-21] Veldkamp et al[18] have shown, however, that replacement of missing sinogram data with more advanced routines than linear interpolation has a minor impact on the image quality. Other suggested methods to reduce metal artifacts include dual energy,[22] iterative reconstruction,[23-25] manipulation of reconstructed CT data,[26,27] and combinations of methods.[28] Thus far, these methods have not found their way into clinical routine, which is mainly caused by their computational complexity. Prell et al[29,30] have elaborated on the method proposed by Kalender et al[15] for CBCT, which replaces underexposed pixels in the raw projection images rather than sinograms. Their results showed an overall improvement of visibility of neurovascular implants and surrounding brain tissue.

Our research objective was to determine whether application of a multipass reconstruction algorithm that reduces the artifacts caused by implants with high x-ray absorption improves the visibility of VasoCT data. The effects of this technique on the diagnostic image quality of VasoCT data acquired after stent-assisted coil embolization were evaluated by an observer study. In the following section, a brief description of the multipass reconstruction algorithm used for metal artifact reduction (MAR) is given.

MATERIALS AND METHODS

The MAR algorithm used in our study is based on the algorithm proposed by Prell et al.[29,30] With this method, a reconstruction is generated during the first pass by use of a regular filtered back-projection algorithm.[31] Regions within the primary reconstruction that display relatively high x-ray absorption are automatically isolated from the volumetric data by use of a predefined threshold value of 4000 HU. Subsequently, the volumetric regions of high absorption are mapped onto the original x-ray images by forward projection,[32] which is achieved by accurate geometric calibration of the C-arm system.[33] The high-absorption regions within the original x-ray images are replaced by gray-values linearly interpolated from the surrounding scan lines (Fig 1). Finally, a new reconstruction is formed by filtered back-projection in the second pass, with the use of the adjusted x-ray images (Fig 2). Reconstruction of a CBCT volume with matrix 256^3 (voxel size, 0.2^3 mm^3) with and without MAR takes approximately 72 and 138 seconds, respectively, on a Dual Core Xeon processor (Intel, Santa Clara, California).

Thirty patients (66.7% women; mean age, 57.2 years; age range, 36–81 years) who underwent stent-assisted coil embolization were retrospectively included in this study. Mean ± standard deviation aneurysm size and packing density were 5.5 ± 4.6 mm (range, 1.8–27 mm) and 46.3 ± 39.4%, respectively. In 90% of the cases, the aneurysm was located in the anterior circulation. High-

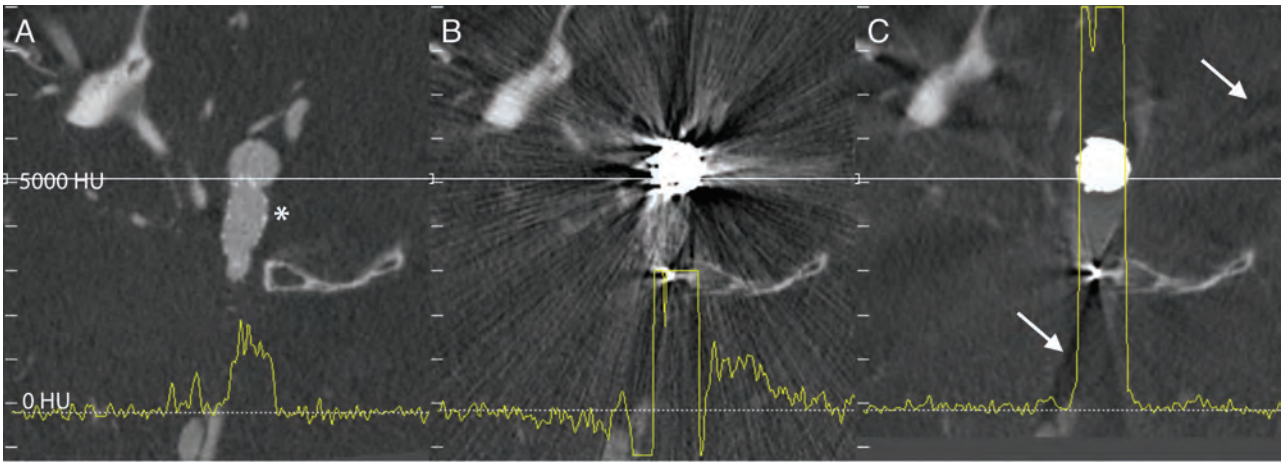

FIG 3. Corresponding axial sections of VasoCT data acquired after stent placement (*A*, stent indicated by asterisk) and after coil embolization (*B* and *C*). Streak artifacts generated by the coil mass visible in VasoCT data without MAR (*B*) are severely reduced with MAR (*C*). Because of the replacement of absent data in the raw projections, subtle new artifacts appear in VasoCT with MAR (*C, arrows*). Intensity profiles (*yellow lines*) were generated for all 3 images by use of the same physical coordinates (*white lines*). The intensity scale of the profile analysis is given on the left-hand side of the figure. Profile plots show that severe fluctuations outside the coil mass are reduced by MAR and the resulting profile in *C* is similar to the profile in *A*.

resolution contrast-enhanced CBCT data were obtained immediately after stent-assisted coil embolization or at 6-month follow-up, as is regularly performed at our institution. Image data were acquired with a flat panel angiographic C-arm system (Allura Xper FD20, Philips) by use of a reduced detector size of 22 cm to obtain high-resolution nonbinned images. Iodinated contrast (Iopamidol 51%, 510 mg/mL, Isovue; Bracco Diagnostics, Princeton, New Jersey) diluted to 20% was injected from the internal carotid artery with 3 mL/s, or from the vertebral artery with 2 mL/s for a total of 23 seconds by use of a 5F or 6F catheter and an imaging delay of 2 seconds. VasoCT volumes were generated from 621 x-ray images (80 kv, 260 mA) with a matrix size of 1016^2 (pixel size: 0.15^2 mm^2) obtained during the rotational sweep of the x-ray source of approximately 200° in 20 seconds and by use of a filtered back-projection reconstruction algorithm. For all included patients, VasoCT data were generated both with and without usage of the metal artifact reduction algorithm and were reviewed in a blinded fashion by 3 experienced neuroradiologists on a dedicated workstation and a medical grade monitor. The diagnostic quality of both reconstructions were rated by means of a 3-point scale (1 = insufficient for evaluation, 2 = sufficient for evaluation, 3 = excellent) questionnaire addressing the: 1) visibility of the stent directly adjacent to the coil mass, 2) the visibility of the host artery directly adjacent to the coil mass, and 3) the visibility of the relationship between the aneurysm, host artery, stent, and coil mass. In addition, the observers were asked whether streak artifacts were obscuring the vessel beyond the actual coil mass (yes/no) and which of the 2 reconstructions offered overall better visibility. During review, observers were allowed to adjust window-level settings and section thickness of the image data as well as zoom, pan, and rotate to optimize viewing. A general consensus regarding the 3-point scale was established with the use of 5 cases that were excluded from the actual observer study. The overall agreements were calculated by means of raw statistics, and the reliability of agreement was analyzed by the Fleiss κ method.[34] Significance of the results was evaluated by means of Fisher exact test for the categoric and yes/no questions. A 2-tailed significance level of $P < .05$ was considered significant. Intraobserver and interobserver analyses were performed by means of a Wilcoxon matched-pairs signed-rank test. Statistical analyses were performed by means of Prism Five (GraphPad, San Diego, California).

RESULTS

The effect of MAR on VasoCT data of a patient who underwent stent-assisted coil embolization is demonstrated in example data given in Fig 3. Corresponding axial sections of VasoCT data acquired immediately after stent placement (Fig 3*A*, stented segment is indicated by the asterisk), after coil embolization without MAR (Fig 3*B*), and after coil embolization with MAR (Fig 3*C*) are shown. Comparison of Figs 3*B* and 3*C* reveals the evident reduction of streak artifacts caused by the coil mass. Although the streak artifacts caused by the coil mass were mostly eliminated, new, more subtle streak artifacts appear in VasoCT data with MAR (indicated by the arrows in Fig 3*C*), which is caused by interpolation of missing data in the raw projection images. The effect of subtle streak artifacts caused by the MAR algorithm is demonstrated more clearly in Fig 4. Profile plots in Fig 3 (yellow line) are generated of the same physical coordinates (white line) of VasoCT data. The intensity scales are indicated on the left of each image and range from −1200 to 9000 HU. It should be noted that for reconstructions without MAR and with MAR, intensities are automatically truncated at 3000 HU and 9000 HU, respectively. Low-frequency fluctuations adjacent to the coil mass present in the profile plot in Fig 3*B* are removed by MAR. As a result, the profiles in Figs 3*A* and 3*C* have a similar noise pattern outside the coil mass.

The results of the observer study are summarized in the Table. The average overall agreement of the observer study was 78%. In more than half of the cases without MAR, all observers agreed that the visibility of the stent, the host artery, and relationship between aneurysm, host artery, stent, and coil mass was insufficient for

evaluation (score of 1, $\kappa = 0.7$). In addition, the observers agreed in 56% of all cases that the artifact was obscuring the host artery beyond the actual coil mass when MAR was not used.

With MAR, the number of cases in which the observers agreed on giving a score of 1 (insufficient for evaluation) was reduced by >50% for the visibility of the stent and host artery. The visibility of the relationship between the stent, host artery, the aneurysm, and the coil mass was improved by at least 1 point on the scoring system in 40% of the cases ($\kappa = 0.6$), and in 36% of the cases, the observers agreed that the visibility was sufficient for evaluation (score ≥2). In 64% of the cases, the observers agreed that the streak artifact was not obscuring the host artery and on average the overall visibility of the VasoCT data were sufficient for evaluation (score ≥2) in 65% of the cases with MAR. The observers concluded with high overall agreement (92%, $\kappa = 0.9$) that the overall visibility was improved when MAR was used. VasoCT data with MAR were rated with significantly higher scores ($P < .05$) than without MAR for all categories. A Wilcoxon matched-pairs signed-rank test showed that for all categories, the pooled and unpooled scores given by the observers to VasoCT data without MAR were significantly improved when the MAR algorithm was used ($P < .0001$). Intraobserver analysis performed by a single observer revealed no significant difference in scoring ($P > .5$).

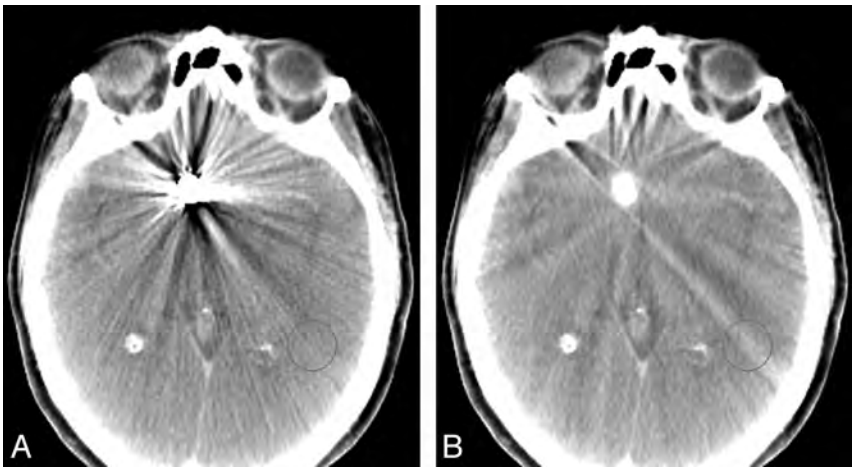

FIG 4. Conebeam CT data without *(A)* and with *(B)* MAR demonstrating the reduction of coil mass artifacts and the appearance of subtle streak caused by the algorithm, which is specifically well visualized in the indicated circular region of interest.

Illustrative Cases

Case 1. A 51-year-old woman had a history of subarachnoid hemorrhage secondary to a ruptured right middle cerebral artery aneurysm that was treated by surgical clipping. On the diagnostic cerebral angiogram obtained for evaluation of the surgical clipping procedure, an incidental unruptured wide-neck left posterior communicating artery aneurysm was observed. This posterior communicating artery aneurysm was endovascularly treated by stent-assisted coil

Results of the observer study rating the visibility without and with MAR

	Without MAR				With MAR			
	Overall Agreement, %	Score 1 Agreement, %	Score ≥2 Agreement, %	κ	Overall Agreement, %	Score 1 Agreement, %	Score ≥2 Agreement, %	κ
Stent visibility $P < .05$ OR = 7.8 CI = 1.6–38.8	77	56	12	0.66	76	24	40	0.64
Vessel visibility $P < .05$ OR = 8.7 CI = 1.7–45.2	76	52	12	0.64	72	20	40	0.58
Relationship $P < .05$ OR = 9.0 CI = 1.7–47.0	81	60	12	0.72	70	20	36	0.56

	Overall Agreement, %	Yes Agreement, %	No Agreement, %	κ	Overall Agreement, %	Yes Agreement, %	No Agreement, %	κ
Obscuring beyond coil mass? ($P < .0001$ OR = 224.0 CI = 12.8–3926.0)	73	56	4	0.47	78	4	64	0.57

	Overall Agreement, %	Without MAR Agreement, %	With MAR Agreement, %	κ
Overall best visibility	94	0	92	0.89

Note:—The rows "stent visibility," "vessel visibility," and "relationship" show the summarized results to the 3-point scale questions. Given are the percent overall agreement (ie, the number of cases that all reviewers agreed in total, calculated using the Fleiss method), the percent agreement for a score 1 (ie, the number of cases all reviewers agreed on giving a score of 1), and the percent agreement for a score ≥2 (ie, the number of cases all reviewers agreed on giving a score of 2 or 3). Similarly, agreements for the binary questions are indicated. For each observer question, the κ values, *P* value, odds ratio (OR), and 95% confidence intervals (CI) are given when applicable. OR represents the improvement of classification of 1 to ≥2 with MAR.

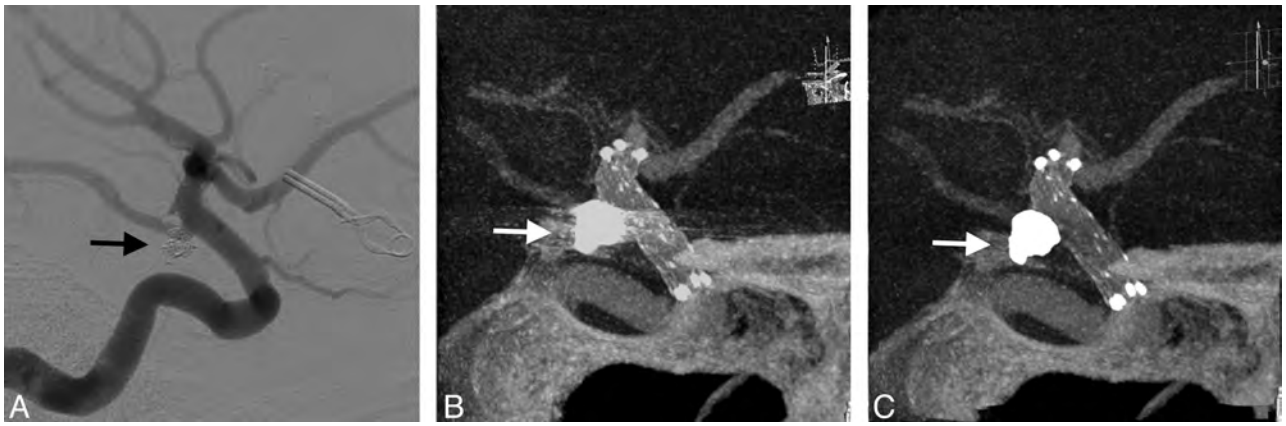

FIG 5. Illustrative case 1. DSA at 6-month follow-up shows no recanalization of the embolized posterior communicating artery aneurysm *(A)*. Streak artifacts caused by the coil mass *(arrows)* in maximum intensity projection of VasoCT data without MAR *(B)* partially obscures visualization of stent and host artery. After MAR *(C)*, streak artifacts in VasoCT data were removed, revealing the stent and host artery.

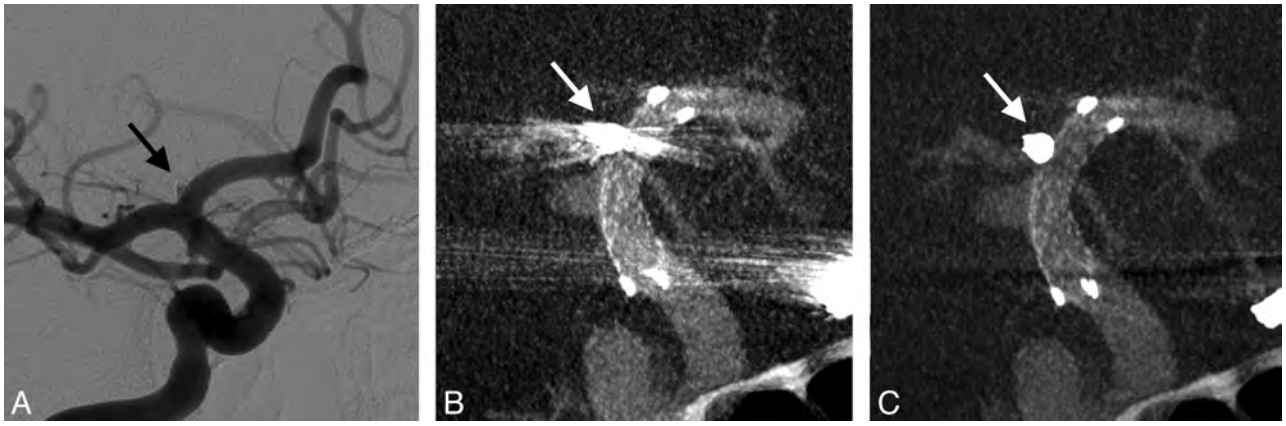

FIG 6. Illustrative case 2. Immediate DSA *(A)* maximum intensity projection of VasoCT data without MAR *(B)* and with MAR *(C)* of stent-assisted coil embolized aneurysm at the right A1 segment. Visibility is significantly affected by streak artifacts caused by the coil mass *(arrows)* and contralateral clip in VasoCT without MAR. With MAR, stent apposition to the vascular wall is fully appreciated.

embolization technique. The illustrated case (Fig 5) shown was the 6-month follow-up VasoCT examination of her left posterior communicating artery aneurysm. This case received the following median scores without MAR versus with MAR, respectively: stent visibility: 2 versus 2; vessel visibility: 2 versus 3; and relationship: 2 versus 3.

Case 2. A 40-year-old man with a ruptured left ophthalmic artery aneurysm underwent surgical clip ligation. The diagnostic cerebral angiogram examination for postsurgical evaluation revealed an incidental unruptured posteriorly projecting small aneurysm at the A1 segment of the right anterior communicating artery. This second aneurysm was endovascularly treated by stent-assisted coil embolization. Fig 6 shows the immediate posttreatment DSA and VasoCT examinations. This case received the following median scores without MAR versus with MAR, respectively: stent visibility: 2 versus 3; vessel visibility: 2 versus 3; and relationship: 2 versus 3.

Case 3. A 61-year-old woman with a family history of brain aneurysms was brought in to our hospital for a diagnostic work-up. MRA examination of the head showed a left internal carotid artery terminus aneurysm that was treated by stent-assisted coiling. The illustrated case (Fig 7) shown was the immediate posttreatment DSA and VasoCT examination. This case received the following median scores without MAR versus with MAR, respectively: stent visibility: 2 versus 2; vessel visibility: 2 versus 3; and relationship: 2 versus 3.

Case 4. A 64-year-old woman with a family history of ruptured intracranial aneurysms underwent a diagnostic work-up for her chronic dizziness. MRA revealed bilateral unruptured (middle cerebral artery) brain aneurysms. Both aneurysms were treated by coil embolization; however, the right middle cerebral artery bifurcation aneurysm was treated by stent-assisted technique. In Fig 8, DSA and VasoCT acquired immediately after embolization are shown. This case received the following median scores without MAR versus with MAR, respectively: stent visibility: 1 versus 2; vessel visibility: 2 versus 2; and relationship: 2 versus 2.

DISCUSSION

Stent-assisted coil embolization is very effective for treating fusiform and wide-neck aneurysms. This technique enables improved packing density with a relative low risk of coils herniating into the parent artery, which may also be beneficial for small to medium aneurysms.[35] In addition, a fully deployed stent may function as a scaffold for endothelial growth.[7]

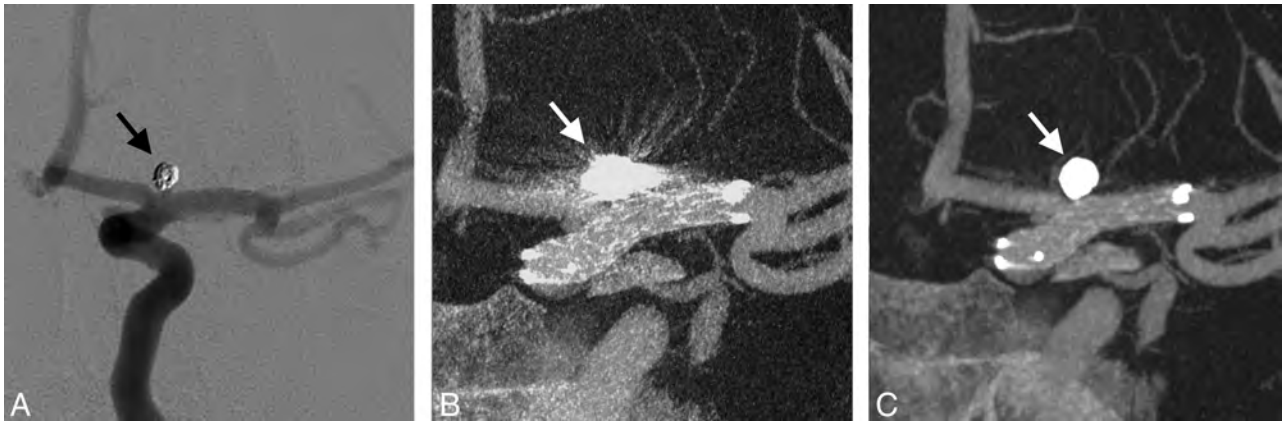

FIG 7. Illustrative case 3. DSA *(A),* maximum intensity projections of VasoCT without *(B),* and with MAR *(C)* acquired immediately after stent-assisted coil *(arrows)* embolization procedure. Streak artifacts partially obscuring the host artery and side branches are removed by the MAR method.

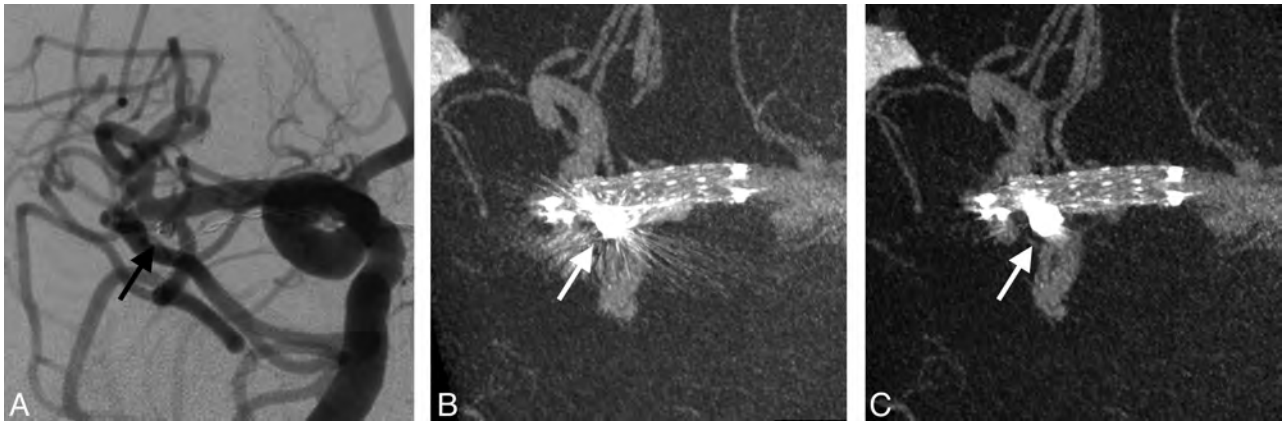

FIG 8. Illustrative case 4. Immediate DSA *(A),* VasoCT without MAR *(B),* and VasoCT with MAR *(C)* after stent-assisted coiling of an unruptured middle cerebral artery aneurysm. Although streak artifacts caused by the coil mass *(arrows)* are significantly reduced, a small amount of streak remains after application of MAR.

The standard technique for follow-up imaging after (stent-assisted) coil embolization of intracranial aneurysms is DSA, which only provides a 2D projection of the vascular anatomy and implants. Diagnostic interpretation is therefore determined by the projection angle of the x-ray source and may not fully disclose adjacent vascular anatomy and potential clot formation, stent-wall apposition, stent herniation, recanalization, intimal tissue growth, or hyperplasia. In situ–acquired high-resolution contrast-enhanced CBCT (VasoCT) allows visualization of vascular implants and host arteries with 3D spatial information. However, the presence of streak artifacts caused by the coil mass may severely reduce the diagnostic quality of CBCT data, making this technique less valuable for imaging of patients with implants with high x-ray absorption.

We have shown that usage of MAR significantly improves image visibility by reducing the presence of metal streak artifacts caused by coil masses in VasoCT data acquired from patients after stent-assisted coil embolization. As a result, the overall visibility of surrounding vascular anatomy and neurovascular stents was improved with respect to data without MAR in >90% of the cases. Streak artifacts that were extending beyond the actual coil mass in 56% without MAR were reduced to 4% with MAR. The observers agreed in 64% of the cases with MAR that the artifacts were not obscuring the host artery beyond the coil mass, which is lower than would be expected considering the drop from 56–4%. This is potentially caused by the different interpretation of the subtle streak artifacts caused by the MAR algorithm as is shown in Figs 3*C* and 4*B*. Prell et al[30] have shown that 3D linear interpolation is less prone to introduce new artifacts than a technique that uses fewer dimensions. Factors that influence the outcome of the algorithm include the location and orientation of the coiled aneurysm with respect to the host artery and the size of the coil mass, which varied between cases. Overall, the visibility of VasoCT data was improved by MAR.

In principle, the MAR algorithm used in this study was based on a method previously proposed.[30] In their work, Prell et al[30] implemented an adaptive segmentation method to detect metallic objects in the primary reconstruction and correct for possible misalignment in the geometry calibration of the system. We found that the CBCT image quality of the primary reconstruction allowed segmentation by a fixed threshold value without causing oversegmentation or undersegmentation of the implants. In addition, the accuracy of the geometry calibration of the system used in our study was sufficient to perform forward projection without additional geometry corrections and image morphology. To limit the total processing time, a 1D linear interpolation routine was

used to replace underexposed data in the raw projections. Although the results show that this simple interpolation method provides significant improvement in the overall visibility, the benefit of the use of advanced interpolation techniques should be assessed in further research. Furthermore, postprocessing methods such as attenuation-normalization and edge-enhancement as performed in a second correction step were not used here.[29] The total reconstruction time with MAR was approximately 138 seconds per dataset. Preliminary data show that prototype software with the use of the graphics processing unit reduced the total reconstruction time with MAR to approximately 50 seconds.

There are limitations to the use of MAR. Although successful removal of streak artifacts from CBCT results in a more appealing image in almost all cases, the diagnostic information may not always be improved compared with data without MAR. CBCT data generated during the second pass may contain some blurred regions and new subtle artifacts that are caused by the replacement of image content of the original x-ray data. However, these generally do not obscure the image content as severely as the artifacts caused by the coil mass. Furthermore, it should be noted that MAR is not capable of fully correcting all metal artifacts because data that are absent in the x-ray images as the result of photon starvation cannot be recovered. As a result of these limitations, diagnosis of recanalization at the aneurysm neck directly adjacent to the coil mass remains challenging. The development of more advanced methods is required to completely remove all artifacts caused by implants with high x-ray absorption, which may include alternative imaging protocols rather than postprocessing techniques.

CONCLUSIONS

We conclude that with the use of MAR on VasoCT data acquired for evaluation of patients who underwent stent-assisted coil embolization, overall reduced streak artifacts caused by coil masses, enhance the visibility of neurovascular stents and host arteries and therefore improve diagnostic quality.

ACKNOWLEDGMENTS

We gratefully acknowledge Philips Healthcare and NIH R01 CA128906 (PI: SV). The contents are solely the responsibility of the authors and do not represent the official views of the NIH or Philips Healthcare.

Disclosures: Daniel Ruijters—*UNRELATED: Employment:* Philips HealthCare. Peter van de Haar—*UNRELATED: Employment:* Philips Electronics, Netherlands, Comments: I am a full-time employee of Philips. Bart Carelsen—*UNRELATED: Employment:* Philips HealthCare, Comments: Clinical Scientist with the Business Innovation Unit Interventional X-ray. Srinivasan Vedantham—*RELATED: Grant* and *Support for Travel to Meetings for the Study or Other Purposes:* National Institutes of Health,* Comments: R01 CA128906; *UNRELATED: Grants/Grants Pending:* 1) National Institutes of Health,* 2) Toshiba Medical Research Comments: 1) Multi-institution collaborative research involving Hologic, Inc; 2) Co-investigator in grant to Stephen J. Glick (Principal Investigator), University of Massachusetts Medical School. Matthew Gounis—*UNRELATED: Consultancy:* Stryker Neurovascular, Codman Neurovascular, Soteira, Surpass Medical, Comments: Fee-per-hour consultancy; *Grants/Grants Pending:* NIH,* Codman Neurovascular,* Stryker Neurovascular,* eV3 Neurovascular,* Thrombolysis Science Inc,* Sanofi-Avantis,* Neuravi,* Neurointerventional Technologies Inc,* Surpass Medical.* Ajay Wakhloo—*RELATED: Grant:* Philips Medical HealthCare,* Comments: Research funding; *UNRELATED: Board Membership:* Surpass Medical; *Consultancy:* Surpass Medical, Boston Biomedical Associates, Stryker Neurovascular, Codman Neurovascular; *Payment for Lectures (including service on speakers bureaus):* Harvard Postgraduate Program, Miami Baptist Stroke Meeting; *Stock/Stock Options:* Surpass Medical (*Money paid to institution).

REFERENCES

1. Benitez RP, Silva MT, Klem J, et al. **Endovascular occlusion of wide-necked aneurysms with a new intracranial microstent (Neuroform) and detachable coils.** *Neurosurgery* 2004;54:1359–67
2. Fiorella D, Albuquerque FC, Deshmukh VR, et al. **Usefulness of the Neuroform stent for the treatment of cerebral aneurysms: results at initial (3–6-mo) follow-up.** *Neurosurgery* 2005;56:1191–202
3. Higashida RT, Smith W, Gress D, et al. **Intravascular stent and endovascular coil placement for a ruptured fusiform aneurysm of the basilar artery: case report and review of the literature.** *J Neurosurg* 1997;87:944–49
4. Lanzino G, Wakhloo AK, Fessler RD, et al. **Efficacy and current limitations of intravascular stents for intracranial internal carotid, vertebral, and basilar artery aneurysms.** *J Neurosurg* 1999;91:538–46
5. Massoud TF, Turjman F, Ji C, et al. **Endovascular treatment of fusiform aneurysms with stents and coils: technical feasibility in a swine model.** *AJNR Am J Neuroradiol* 1995;16:1953–63
6. Wakhloo AK, Mandell J, Gounis MJ, et al. **Stent-assisted reconstructive endovascular repair of cranial fusiform atherosclerotic and dissecting aneurysms: long-term clinical and angiographic follow-up.** *Stroke* 2008;39:3288–96
7. Wakhloo AK, Schellhammer F, De Vries J, et al. **Self-expanding and balloon-expandable stents in the treatment of carotid aneurysms: an experimental study in a canine model.** *AJNR Am J Neuroradiol* 1994;15:493–502
8. Wakhloo AK, Linfante I, Silva CF, et al. **Closed-cell stent for coil embolization of intracranial aneurysms: clinical and angiographic results.** *AJNR Am J Neuroradiol* 2012;33:1651–56
9. Bendok BR, Parkinson RJ, Hage ZA, et al. **The effect of vascular reconstruction device-assisted coiling on packing density, effective neck coverage, and angiographic outcome: an in vitro study.** *Neurosurgery* 2007;61:835–40
10. Piotin M, Blanc R, Spelle L, et al. **Stent-assisted coiling of intracranial aneurysms: clinical and angiographic results in 216 consecutive aneurysms.** *Stroke* 2010;41:110–15
11. Söderman M, Babic D, Holmin S, et al. **Brain imaging with a flat detector c-arm.** *Neuroradiology* 2008;50:863–68
12. Patel NV, Gounis MJ, Wakhloo AK, et al. **Contrast-enhanced angiographic cone-beam CT of cerebrovascular stents: experimental optimization and clinical application.** *AJNR Am J Neuroradiol* 2010;32:137–44
13. Snoeren RM, Söderman M, Kroon JN, et al. **High-resolution 3D x-ray imaging of intracranial nitinol stents.** *Neuroradiology* 2012;54:155–62
14. Glover GH, Pelc NJ. **An algorithm for the reduction of metal clip artifacts in CT reconstructions.** *Med Phys* 1981;8:799
15. Kalender WA, Hebel R, Ebersberger J. **Reduction of CT artifacts caused by metallic implants.** *Radiology* 1987;164:576–77
16. Abdoli M, De Jong JR, Pruim J, et al. **Reduction of artefacts caused by hip implants in CT-based attenuation-corrected PET images using 2-D interpolation of a virtual sinogram on an irregular grid.** *Eur J Nucl Med Mol* 2011;38:2257–68
17. Abdoli M, Ay MR, Ahmadian A, et al. **Reduction of dental filling metallic artifacts in CT-based attenuation correction of PET data using weighted virtual sinograms optimized by a genetic algorithm.** *Med Phys* 2010:6166–77
18. Veldkamp WJH, Joemai RMS, van der Molen AJ, et al. **Development and validation of segmentation and interpolation techniques in sinograms for metal artifact suppression in CT.** *Med Phys* 2010;37:620–28
19. Zhao S, Robeltson D, Wang G, et al. **X-ray CT metal artifact reduction using wavelets: an application for imaging total hip prostheses.** *IEEE Trans Med Imaging* 2000;19:1238–47
20. Lell MM, Meyer E, Kuefner MA, et al. **Normalized metal artifact**

reduction in head and neck computed tomography. *Invest Radiol* 2012;47:415–21
21. Kachelrieß M, Watzke O, Kalender WA. **Generalized multi-dimensional adaptive filtering for conventional and spiral single-slice, multi-slice, and cone-beam CT.** *Med Phys* 2001;28:475–90
22. Bamberg F, Dierks A, Nikolaou K, et al. **Metal artifact reduction by dual energy computed tomography using monoenergetic extrapolation.** *Eur Radiol* 2011;21:1424–29
23. Wang G, Snyder DL, O'Sullivan JA, et al. **Iterative deblurring for CT metal artifact reduction.** *IEEE Trans Med Imaging* 1996;15:657–64
24. Robertson DD, Yuan J, Wang G, et al. **Total hip prosthesis metal-artifact suppression using iterative deblurring reconstruction.** *J Comput Assist Tomogr* 1997;21:293–98
25. De Man B, Nuyts J, Dupont P, et al. **An iterative maximum-likelihood polychromatic algorithm for CT.** *IEEE Trans Med Imaging* 2001;20:999–1008
26. Hamill JJ, Brunken RC, Bybel B, et al. **A knowledge-based method for reducing attenuation artefacts caused by cardiac appliances in myocardial PET/CT.** *Phys Med Biol* 2006;51:2901–18
27. Kennedy JA, Israel O, Frenkel A, et al. **The reduction of artifacts due to metal hip implants in CT-attenuation corrected PET images from hybrid PET/CT scanners.** *Med Biol Eng Comput* 2007;45:553–62
28. Lemmens C, Faul D, Nuyts J. **Suppression of metal artifacts in CT using a reconstruction procedure that combines map and projection completion.** *IEEE Trans Med Imaging* 2009;28:250–60
29. Prell D, Kyriakou Y, Struffert T, et al. **Metal artifact reduction for clipping and coiling in interventional C-arm CT.** *AJNR Am J Neuroradiol* 2010;31:634–39
30. Prell D, Kalender W, Kyriakou Y. **Development, implementation and evaluation of a dedicated metal artefact reduction method for interventional flat-detector CT.** *Br J Radiol* 2010;83:1052–62
31. Feldkamp LA, Davis LC, Kress JW. **Practical cone-beam algorithm.** *J Opt Soc Am* 1984;1:612–19
32. Ruijters D, ter Haar Romeny BM, Suetens P. **GPU-accelerated digitally reconstructed radiographs.** BioMED'08: Proceedings of the Sixth IASTED International Conference on Biomedical Engineering. Anaheim, California: ACTA Press. 2008, pp. 431–435
33. Ruijters D, Homan R, Mielekamp P, et al. **Validation of 3D multimodality roadmapping in interventional neuroradiology.** *Phys Med Biol* 2011;56:5335–54
34. Fleiss JL, Cohen J. **The equivalence of weighted kappa and the intraclass correlation coefficient as measures of reliability.** *Educ Psychol Meas* 1973;33:613–19
35. Parkinson RJ, Eddleman CS, Batjer HH, et al. **Giant intracranial aneurysms: endovascular challenges.** *Neurosurgery* 2006;59: S103–12

Stent-Assisted Coil Embolization of Posterior Communicating Artery Aneurysms

Y.D. Cho, W.J. Lee, K.M. Kim, H.-S. Kang, J.E. Kim, and M.H. Han

ABSTRACT

BACKGROUND AND PURPOSE: Use of protective stents may not be effective in coil embolization of wide-neck aneurysms involving the posterior communicating artery. Successful implementation depends on the caliber of the vessel, its angle of origin, and the manner in which its orifice is incorporated into the aneurysm. Presented here are the results (clinical and radiographic) of coil embolization in aneurysms of the ICA-posterior communicating artery junction, variably aided by stents. The primary focus is angiographic configurations that impact stent placement.

MATERIALS AND METHODS: From a prospective data repository, we retrieved records of 32 consecutive patients with 33 posterior communicating artery aneurysms, all of which were treated by stent-assisted coil embolization between June 2008 and August 2012. Outcomes were analyzed in terms of aneurysm configuration and clinical status.

RESULTS: Stents were positioned entirely in the ICA ($n = 26$), from the ICA to the posterior communicating artery ($n = 2$), in the posterior communicating artery only ($n = 3$), and retrograde from the posterior communicating artery to the ICA terminus ($n = 2$). Procedure-related complications occurred in 3 patients (9.1%), but only 1 (3.0%) had mild neurologic sequelae (Glasgow Outcome Score 4). Using coil embolization, we achieved successful occlusion in 24 aneurysms (72.7%), and in 9 others, subtotal occlusion was conferred. During a mean follow-up of 15.7 ± 10.7 months, imaging of 27 aneurysms documented stable occlusion in 19 (70.4%), whereas angiography of 15 aneurysms (39.5%) disclosed 2 instances of in-stent stenosis (13.3%) and a solitary occurrence of stent migration (6.7%).

CONCLUSIONS: In posterior communicating artery aneurysms, stent protection during coil embolization is feasible by adjusting the procedural strategy to accommodate differing configurations of the aneurysm and its vascular source.

ABBREVIATIONS: GOS = Glasgow Outcome Score; PcomA = posterior communicating artery

ICA-PcomA junctional aneurysms constitute about 50% of ICA aneurysms and 25% of all intracranial aneurysms.[1] Due to anatomic variations in parent arteries and the array of configurations displayed by the aneurysms themselves, these lesions may be among the easiest or the most difficult to treat by any means, surgical or endovascular.[2] Technologic advancements and improved coiling techniques have made it possible to treat a large percentage of oddly configured aneurysms, otherwise inconducive to endovascular coil embolization. The utility of augmenting coil embolization through stent usage has also been recognized in recent years and is now established as a useful and effective mode of treatment.[3-9] However, the protective effect of a stent is sometimes limited in wide-neck PcomA aneurysms. Such aneurysms tend to incorporate the origin of the PcomA, and the affected branch often arises from the ICA or the aneurysm neck at an acute angle. Herein we present the clinical and radiographic outcomes of stent-assisted coil embolization in ICA-PcomA aneurysms, focusing on case-specific dictates of stent placement (vessel anatomy and configuration of the aneurysm) and immediate or delayed stent-related complications.

Received November 20, 2012; accepted after revision January 21, 2013.

From the Departments of Radiology (Y.D.C., W.J.L., K.M.K., M.H.H.) and Neurosurgery (H.-S.K., J.E.K., M.H.H.), Seoul National University Hospital, Seoul National University College of Medicine, Seoul, Korea.

This study was supported by a grant of the Korea Health Care Technology R&D Project, Ministry for Health, Welfare and Family Affairs, Republic of Korea (A111101).

Please address correspondence to Moon Hee Han, MD, PhD, Departments of Radiology and Neurosurgery, Seoul National University College of Medicine, 28 Yongon-dong, Jongno-gu, Seoul, Korea, 110-744; e-mail: hanmh@snuh.org

http://dx.doi.org/10.3174/ajnr.A3541

MATERIALS AND METHODS

Population

Between June 2008 and August 2012, we performed endovascular treatment of 1745 intracranial aneurysms for 1373 patients, including 227 PcomA aneurysms. Of these, 32 consecutive patients with 33 PcomA aneurysms were reviewed via prospectively ac-

crued data. Stent assistance had been used in each instance. Patients with nonjunctional PcomA aneurysms (so-called "true" PcomA aneurysms) were excluded from the study, as were those with dissecting, fusiform, blood blister–like, or false aneurysms. Informed consent was obtained from each patient on the basis of the perceived risks, benefits, and treatment alternatives (ie, aneurysm clipping) after thorough evaluations. Therapeutic decision-making entailed a multidisciplinary deliberation of both surgical and nonsurgical neurointerventions.

DSA and Endovascular Procedures

The configuration of each aneurysm and the architecture of its arterial supply were delineated by using an Integris V (Philips Healthcare, Best, the Netherlands) biplane system, which included high-resolution 3D rotational angiography. The size of the aneurysm was defined as its broadest diameter in 3D configuration. Neck size and depth-to-neck ratio were measured on a working projection of the DSA. The following PcomA types were designated on the basis of the PcomA-to-P1 ratio of arterial diameters (PcomA/P1): fetal (no P1), dominant (>1.5), iso-type (0.5–1.5), hypoplastic (<0.5), and perforator (when the PcomA is a thalamoperforator, with no connection to P1). In addition, aneurysms were stratified by the degree of neck incorporation as PcomA incorporation, equivocal, or ICA incorporation type. The latter was based on the degree of PcomA involvement in the aneurysm neck (relative to its diameter). The angle of the PcomA was estimated at its origin from the distal ICA.

In all cases, the procedures were performed with the patient under general anesthesia, and all patients with unruptured aneurysms were given antiplatelet medication before the procedure. According to the protocol of our institution, dual antiplatelet agents (clopidogrel and aspirin) were administered when stent protection was anticipated during the procedure. In patients showing poor response to clopidogrel based on the VerifyNow P2Y12 assay (Accumetrics, San Diego, California),[10] cilostazol was added. A bolus of 3000 IU of heparin was administered after femoral artery sheath placement, and intermittent boluses of 1000 IU per hour were then administered. Activated clotting time was monitored every hour. On completing the endovascular procedure, tirofiban or heparin infusion was maintained for up to 12 hours in cases involving procedural thromboembolism. Maintenance of dual antiplatelet medication was recommended for at least 3 months after the procedure, and a single agent, for at least 1 year.

In patients with ruptured aneurysms, antiplatelet premedication was not performed. In these cases, systemic heparinization was initiated after adequate protection of the aneurysms. After the procedure, a loading dose of clopidogrel and aspirin was administered and maintenance of the medication was the same as that in unruptured aneurysms.

Clinical and Radiologic Follow-Up

In patients with unruptured aneurysms, MRA with 3D reconstruction or plain radiography or both were recommended 6, 12, 24, and 36 months after coil embolization. Additional plain radiography was recommended 1 and 3 months postembolization in patients presenting with hemorrhage. Conventional angiography was recommended at the time of 12-month follow-up when assessing the status of the treated aneurysms with MRA was not feasible or when aneurysmal recanalization was suspected by noninvasive evaluation, such as MRA or plain radiography, to decide whether further treatment was necessary.

Immediate and Final Outcome

The degree of aneurysmal occlusion was assessed by completion angiography with a 3-point scale: total occlusion (no residual filling of contrast medium in the aneurysm), near-total occlusion (a small amount of residual contrast filling at the base of the aneurysm), and subtotal occlusion (any contrast filling in the aneurysmal sac).

Clinical outcomes were assessed with the Glasgow Outcome Score, and anatomic follow-up results were categorized as follows: stable occlusion (no interval change since the procedure or progressive thrombosis within the aneurysm), minor recanalization (progressive filling limited at the neck of the aneurysm), and major recanalization (aneurysmal sac filling).

This study was conducted with the approval of the institutional review board of the Seoul National University Hospital.

RESULTS

Population Distribution

Study subjects included 4 men and 28 women, with a mean age of 60.0 ± 10.1 years. Five aneurysms (15.2%) presented with subarachnoid hemorrhage, and a stent was used to treat 12 (36.4%) recanalized aneurysms. Aneurysm size (excluding recanalized lesions) ranged from 3.0 to 17.2 mm (mean, 7.1 ± 4.0 mm). All 33 aneurysms were wide-neck, with dome-to-neck ratios <1.5.

The distribution of PcomA types was as follows: fetal, 6; dominant, 5; iso, 9; hypoplastic, 8; and perforator, 2. In 3 instances, a determination could not be made by angiography. The angles of PcomA origin ranged from −19° to 102° (mean, 26.9 ± 30.0°). The necks of the aneurysms primarily incorporated the ICA in 21, whereas 8 were considered equivocal and only 4 distinctly involved the PcomA.

An algorithm of stent positioning in coil embolization of PcomA aneurysms, as generated by this study, is shown in Fig 1. The strategies are differentiated by the degree of PcomA integration into the aneurysm neck, PcomA type, and angle of PcomA origin.

Procedural Results

Stent Deployment. In our series, stents were deployed as follows: 1) the distal ICA to the ICA bifurcation ($n = 26$); 2) the distal ICA to the PcomA ($n = 2$); 3) the PcomA only, aligning the proximal portion of the stent to the aneurysm neck ($n = 3$); and 4) the PcomA to the ICA bifurcation, retrograde ($n = 2$) (Fig 2). Open-cell stents (Neuroform; Stryker Neurointerventional, Fremont, California) were used in 5 aneurysms, with closed-cell stent placement (Enterprise; Codman & Shurtleff, Raynham, Massachusetts) in the remaining 28. The stents were used to prevent coil protrusion into the parent artery in 25 aneurysms, to stabilize protruded coils in 6, and to anticipate the flow-diversion effect of the stent in 2 aneurysms in which successful occlusion failed. Stents were deployed before coil insertion in 15 aneurysms, during the coiling procedure in 12, and after completion of coiling in 6.

In patients stented entirely in the ICA, coil embolization of the

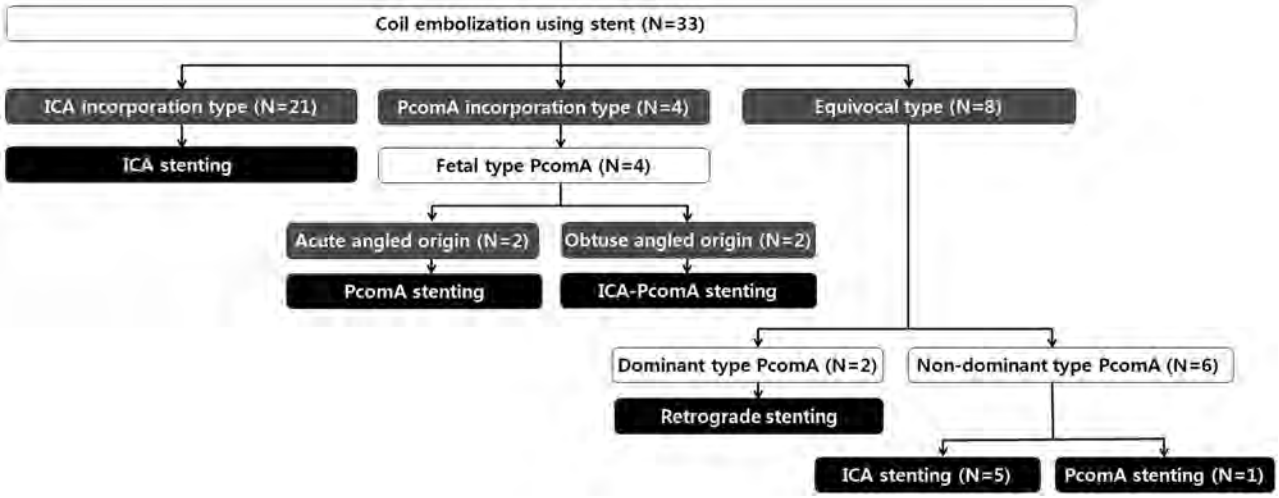

FIG 1. Algorithm for positioning of the stent in coil embolization of PcomA aneurysms, adjusting for PcomA integration into the aneurysm neck, PcomA type, and angle of PcomA origin.

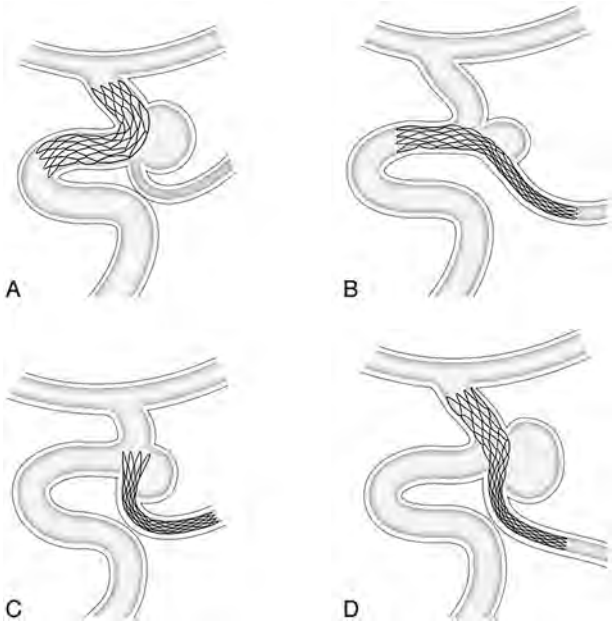

FIG 2. *A*, If the aneurysm neck mostly incorporates the distal ICA or the coil protrudes into the distal ICA, stent positioning from the distal ICA to the terminal ICA preserves ICA patency. *B*, If the aneurysm neck mostly incorporates the PcomA or the coil protrudes into the PcomA, stent positioning from the distal ICA to the PcomA preserves PcomA patency. *C*, If the PcomA warrants protection and originates from the ICA or the aneurysm neck at an acute angle, stent positioning is through the PcomA only, aligning the proximal portion of the stent with the aneurysm neck. *D*, If the aneurysm neck broadly incorporates both the ICA and the PcomA and the ipsilateral P1 is of sufficient caliber to pass a 0.021 microcatheter for stent delivery, stent positioning is retrograde from the PcomA to the terminal ICA.

aneurysm necessitated sacrifice of the PcomA orifice in 3 patients with a hypoplastic-type PcomA. None of the patients had any neurologic complications.

Initial Occlusion Results and Procedural Complications. Successful occlusion after coil embolization was achieved in 24 aneurysms (72.7%), including total occlusion in 4 and near-total in 20; in the other 9 (27.3%), occlusion was subtotal.

Procedure-related complications were few, including 1 instance each of asymptomatic thromboembolism, symptomatic thromboembolic infarction, and stent malpositioning. Of these, only 1 patient experienced minor neurologic sequelae (GOS 4).

Clinical and Radiographic Follow-Up Results. Among the 33 saccular aneurysms, follow-up imaging of 27 aneurysms was performed >6 months after coil embolization. This follow-up rate, excluding 6 patients recently retreated (<6 months), constituted 100%. The mean follow-up period for the 27 aneurysms was 15.7 ± 10.7 months, during which imaging showed stable occlusion in 19 aneurysms (70.4%), minor recanalization in 4 instances (14.8%), and major recanalization in another 4 (14.8%).

Conventional angiography was performed as a follow-up in 15 aneurysms (39.5%) >6 months after coil embolization. Two instances (13.3%) of in-stent stenosis were documented, both mild (<50%) and asymptomatic. Delayed distal stent migration was observed in 1 patient.

None of the patients experienced delayed infarction during follow-up monitoring.

DISCUSSION

PcomA aneurysms have unique features in terms of coil embolization. Although classified with the posterior circulation (relative to the risk of rupture) in 1 randomized study (the International Study of Unruptured Intracranial Aneurysms),[11] Clarke et al[12] suggested that the rate of rupture for PcomA aneurysms is similar to that of the anterior circulation. These aneurysms may qualify as either bifurcation or sidewall variants, depending on the ratio of PcomA-to-P1 calibers. A study assessing major recurrence of aneurysms treated during the International Subarachnoid Aneurysm Trial indicates that PcomA aneurysms carry a considerably higher risk of major recanalization.[13] However, the risk of rebleeding is relatively low, with a range of 0.6%–2.6%.[2,13,14]

The protection afforded by stent placement is occasionally limited in wide-neck PcomA aneurysms, particularly when the PcomA originates from the ICA or from the aneurysm neck at an acute angle. In our experience, stents are used less for PcomA aneurysms compared with aneurysms at other intracranial sites or

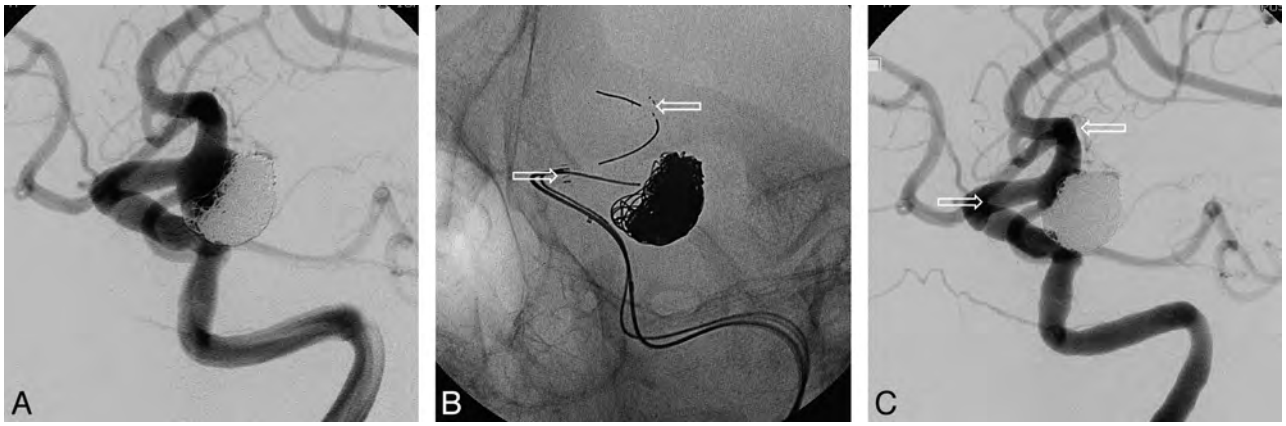

FIG 3. *A*, Conventional angiography of the recanalized PcomA aneurysm, mostly incorporating the distal ICA. *B*, Coil embolization under stent protection (stent placement through the ICA). *C*, Completion angiography shows satisfactory occlusion of aneurysm. Arrows indicate both ends of the stent.

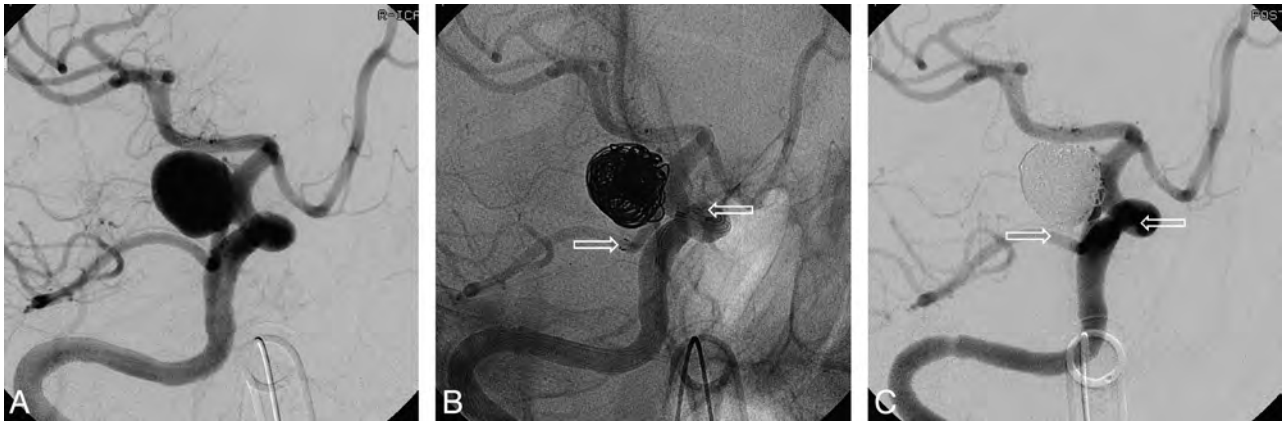

FIG 4. *A*, Conventional angiography of a wide-neck PcomA aneurysm, incorporating the orifice of the PcomA (fetal type). *B*, An Enterprise stent (4.5 × 22 mm) is deployed (distal ICA to the PcomA), and a coil is inserted under stent protection. *C*, Completion angiography shows occlusion of the aneurysm with a residual neck. Arrows indicate both ends of the stent.

intracranial aneurysms in general. Given that the preservation of both the ICA and PcomA is at stake in this setting, we found that maintenance of patency differed individually, depending on the precise configuration of the aneurysm and the nature of coil embolization achieved. In instances in which the aneurysm neck essentially incorporates the distal ICA or the coil protrudes into the distal ICA, the stent should be placed from the distal ICA to the ICA terminus, covering the distal neck of the aneurysm (Fig 3).

Open-cell stents could be of benefit when protection of the PcomA by a stent inserted through the ICA is required or when the ICA is of a large caliber. If the PcomA is predominantly incorporated into the aneurysm, a stent would serve better by covering the orifice of the PcomA, provided that the caliber of the PcomA is sufficient for stent placement (dominant or fetal type). The angle at which the PcomA originates is also a determinant of stent deployment. Stent placement from the ICA to the PcomA is a viable option if the PcomA originates from the distal ICA at an obtuse angle (Fig 4); whereas stent placement through the PcomA only (aligning the proximal portion of the stent to the aneurysm neck) may be preferable if the PcomA arises from the distal ICA at an acute angle (Fig 5).[15] Placement from the ICA to the PcomA at an acute-angled origin may induce kinking or narrowing ("ovalization") of the stent, but malposition or delayed stent migration is risked if deployment is via the PcomA only. In the event that the aneurysm neck incorporates the ICA and the PcomA in equal measure and the PcomA originates from the ICA at an acute angle, retrograde stent insertion (via the vertebral artery) may be considered, provided that the ipsilateral P1 vessel is of adequate size to pass a microcatheter for stent delivery (Fig 6).

We have devised 4 methods of stent positioning to support coil embolization of PcomA aneurysms, based on aneurysm configuration and specifics of the arterial vasculature. It is our view that stent protection is feasible and efficacious in wide-neck PcomA aneurysms if the stent is positioned in accordance with these variables.

Similar to that in aneurysms in other location, stent protection in wide-neck PcomA aneurysms is not always recommended as a first-line therapeutic strategy because of stent-induced complications such as procedural or delayed thromboembolic infarction and in-stent stenosis. The balloon-remodeling method could have good protection effect, mainly in an ICA-incorporation type. In our series, the balloon-remodeling technique was applied in 35 PcomA aneurysms (35/229, 15.3%). Flow diverters can also be an alternative option in PcomA aneurysms with wide necks, though they have the possible risk of PcomA occlusion by a compact strut.

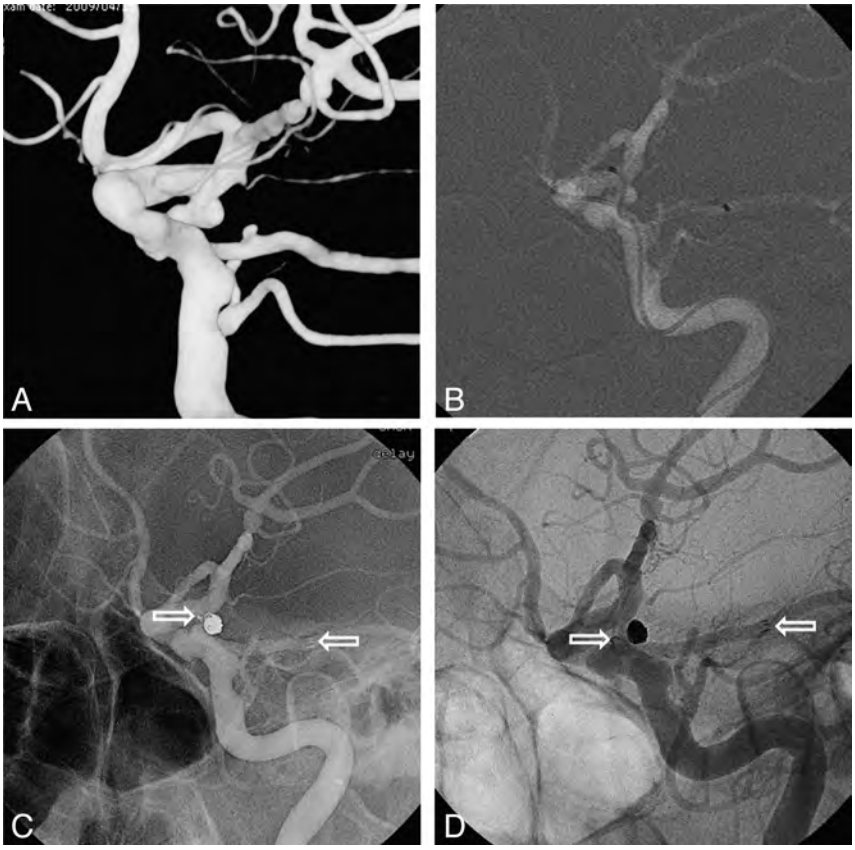

FIG 5. *A*, 3D image of a wide-neck PcomA aneurysm, mostly incorporating the orifice of the PcomA (PcomA origin at the ICA forms an acute angle). *B*, Microcatheter for stent delivery is introduced into the PcomA, while a second microcatheter for coil delivery is advanced into the sac of the aneurysm. *C*, An Enterprise stent (4.5 × 22 mm) is deployed via the PcomA (aligning the proximal portion of the stent with the neck of the aneurysm) and a coil is inserted successfully under stent protection. *D*, Conventional angiography 12 months later shows an occluded aneurysm and distal stent migration. Arrows indicate both ends of the stent.

Many important vessels branch from the PcomA to supply the optic chiasm, oculomotor nerve, ventral thalamus, mammillary body, tuber cinereum, hypothalamus, and internal capsule.[1] However, ischemic complications following coil embolization of PcomA aneurysms are not fully understood, especially when the PcomA is sacrificed.[16] Although the Allcock test is considered useful for evaluating collateral blood flow, to predict postoperative ischemic complications of PcomA sacrifice, the ramifications of sacrificing the PcomA orifice in patients with PcomA aneurysms are still unknown. Endo et al[16] reported 7 cases of tuberothalamic artery territory infarction following coil embolization of 14 ruptured PcomA aneurysms. PcomA sacrifice was regarded as unsafe, even with a preoperative Allcock test confirming retrograde filling of the PcomA by the posterior cerebral artery. Under these circumstances, stent placement in a PcomA aneurysm may preserve PcomA flow, thus avoiding ischemic complications from lack of collateral supply. Coil embolization required PcomA sacrifice in 3 of our patients. All had hypoplastic-type PcomAs, and retrograde filling of the PcomA with contrast medium was observed by vertebral angiography without carotid compression. None of them had detectable neurologic sequelae.

Because PcomA caliber is a potential issue, an Enterprise stent was used routinely for PcomA stent placement in our patients, on the basis of its ease of navigation and delivery and the microcatheter that is mandatory for deployment. A parent vessel diameter of at least 2.5 mm is recommended for this device, but we have used it for stent placement in vessels of a 1.7- to 2.1-mm range (mean, 1.9 ± 0.1 mm). Several other sources have reported safely deploying stents in parent arteries <2.0 mm in diameter.[17-19]

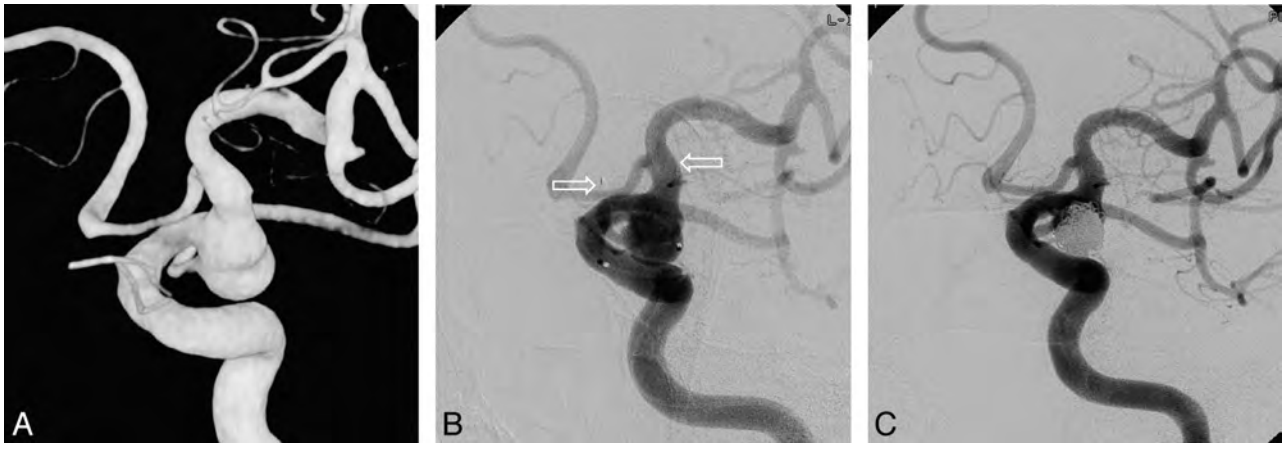

FIG 6. *A*, 3D image of a wide-neck aneurysm at the PcomA orifice, evenly incorporating the ICA and the orifice of the PcomA (PcomA origin at the neck of the aneurysm forms an acute angle). *B*, Microcatheter for stent delivery is introduced through the ipsilateral P1 and is navigated retrograde into the left distal ICA via the PcomA; then, the Enterprise stent (4.5 × 22 mm) is deployed (PcomA to terminal ICA). *C*, Completion angiography shows occlusion of the aneurysm with a residual neck after coil insertion under stent protection. Arrows indicate both ends of the stent.

None of our patients developed arterial occlusion or thromboembolism subsequent to stent placement in the PcomA.

CONCLUSIONS

Despite some limitations, stent-assisted coil embolization of PcomA aneurysms is feasible and efficacious, by using strategies that accommodate the anatomic variations of cerebral vasculature and the array of configurations displayed by these aneurysms.

ACKNOWLEDGMENTS

We thank Yoon-Kyung Choi for preparation of the illustrations.

Disclosures: Moon Hee Han—*RELATED*: *Consulting Fee or Honorarium*: MicroVention,* *UNRELATED*: *Grants/Grants Pending*: MicroVention,* *Travel/Accommodations/Meeting Expenses Unrelated to Activities Listed*: MicroVention. *Money paid to the institution.

REFERENCES

1. He W, Gandhi CD, Quinn J, et al. **True aneurysms of the posterior communicating artery: a systematic review and meta-analysis of individual patient data.** *World Neurosurg* 2011;75:64–72
2. Golshani K, Ferrell A, Zomorodi A, et al. **A review of the management of posterior communicating artery aneurysms in the modern era.** *Surg Neurol Int* 2010;1:88
3. Peluso JP, van Rooij WJ, Sluzewski M, et al. **A new self-expandable nitinol stent for the treatment of wide-neck aneurysms: initial clinical experience.** *AJNR Am J Neuroradiol* 2008;29:1405–08
4. Weber W, Bendszus M, Kis B, et al. **A new self-expanding nitinol stent (Enterprise) for the treatment of wide-necked intracranial aneurysms: initial clinical and angiographic results in 31 aneurysms.** *Neuroradiology* 2007;49:555–61
5. Biondi A, Janardhan V, Katz JM, et al. **Neuroform stent-assisted coil embolization of wide-neck intracranial aneurysms: strategies in stent deployment and midterm follow-up.** *Neurosurgery* 2007;61:460–68
6. Piotin M, Blanc R, Spelle L, et al. **Stent-assisted coiling of intracranial aneurysms: clinical and angiographic results in 216 consecutive aneurysms.** *Stroke* 2010;41:110–15
7. Higashida RT, Halbach VV, Dowd CF, et al. **Initial clinical experience with a new self-expanding nitinol stent for the treatment of intracranial cerebral aneurysms: the Cordis Enterprise stent.** *AJNR Am J Neuroradiol* 2005;26:1751–56
8. Benitez RP, Silva MT, Klem J, et al. **Endovascular occlusion of wide-necked aneurysms with a new intracranial microstent (Neuroform) and detachable coils.** *Neurosurgery* 2004;54:1359–67
9. Lozen A, Manjila S, Rhiew R, et al. **Y-stent-assisted coil embolization for the management of unruptured cerebral aneurysms: report of six cases.** *Acta Neurochir (Wien)* 2009;151:1663–72
10. Kang HS, Kwon BJ, Kim JE, et al. **Preinterventional clopidogrel response variability for coil embolization of intracranial aneurysms: clinical implications.** *AJNR Am J Neuroradiol* 2010;31:1206–10
11. Wiebers DO, Whisnant JP, Huston J 3rd, et al, for the International Study of Unruptured Intracranial Aneurysms Investigators. **Unruptured intracranial aneurysms: natural history, clinical outcome, and risks of surgical and endovascular treatment.** *Lancet* 2003;362:103–10
12. Clarke G, Mendelow AD, Mitchell P. **Predicting the risk of rupture of intracranial aneurysms based on anatomical location.** *Acta Neurochir (Wien)* 2005;147:259–63, discussion 263
13. Campi A, Ramzi N, Molyneux AJ, et al. **Retreatment of ruptured cerebral aneurysms in patients randomized by coiling or clipping in the International Subarachnoid Aneurysm Trial (ISAT).** *Stroke* 2007;38:1538–44
14. Raymond J, Guilbert F, Weill A, et al. **Long-term angiographic recurrences after selective endovascular treatment of aneurysms with detachable coils.** *Stroke* 2003;34:1398–403
15. Lee SJ, Cho YD, Kang HS, et al. **Coil embolization using the self-expandable closed-cell stent for intracranial saccular aneurysm: a single-center experience of 289 consecutive aneurysms.** *Clin Radiol* 2013;68:256–63
16. Endo H, Sato K, Kondo R, et al. **Tuberothalamicartery infarctions following coil embolization of ruptured posterior communicating artery aneurysms with posterior communicating artery sacrifice.** *AJNR Am J Neuroradiol* 2012;33:500–06
17. Roh HG, Chun YI, Choi JW, et al. **Retrograde stent placement for coil embolization of a wide-necked posterior inferior cerebellar artery aneurysm.** *Korean J Radiol* 2012;13:510–14
18. Kim MJ, Chung J, Kim SL, et al. **Stenting from the vertebral artery to the posterior inferior cerebellar artery.** *AJNR Am J Neuroradiol* 2012;33:348–52
19. Chung J, Kim BS, Lee D, et al. **Vertebral artery occlusion with vertebral artery-to-posterior inferior cerebellar artery stenting for preservation of the PICA in treating ruptured vertebral artery dissection.** *Acta Neurochir (Wien)* 2010;152:1489–92

In Vitro and In Vivo Imaging Characteristics Assessment of Polymeric Coils Compared with Standard Platinum Coils for the Treatment of Intracranial Aneurysms

P. Mordasini, A.K. Kraehenbuehl, J.V. Byrne, S. Vandenberghe, M. Reinert, H. Hoppe, and J. Gralla

ABSTRACT

BACKGROUND AND PURPOSE: Conventional platinum coils cause imaging artifacts that reduce imaging quality and therefore impair imaging interpretation on intraprocedural or noninvasive follow-up imaging. The purpose of this study was to evaluate imaging characteristics and artifact production of polymeric coils compared with standard platinum coils in vitro and in vivo.

MATERIALS AND METHODS: Polymeric coils and standard platinum coils were evaluated in vitro with the use of 2 identical silicon aneurysm models coiled with a packing attenuation of 20% each. DSA, flat panel CT, CT, and MR imaging were performed. In vivo evaluation of imaging characteristics of polymeric coils was performed in experimentally created rabbit carotid bifurcation aneurysms. DSA, CT/CTA, and MR imaging were performed after endovascular treatment of the aneurysms. Images were evaluated regarding visibility of individual coils, coil mass, artifact production, and visibility of residual flow within the aneurysm.

RESULTS: Overall, in vitro and in vivo imaging showed relevantly reduced artifact production of polymeric coils in all imaging modalities compared with standard platinum coils. Image quality of CT and MR imaging was improved with the use of polymeric coils, which permitted enhanced depiction of individual coil loops and residual aneurysm lumen as well as the peri-aneurysmal area. Remarkably, CT images demonstrated considerably improved image quality with only minor artifacts compared with standard coils. On DSA, polymeric coils showed transparency and allowed visualization of superimposed vessel structures.

CONCLUSIONS: This initial experimental study showed improved imaging quality with the use of polymeric coils compared with standard platinum coils in all imaging modalities. This might be advantageous for improved intraprocedural imaging for the detection of complications and posttreatment noninvasive follow-up imaging.

ABBREVIATION: FP-CT = flat panel CT

After the International Subarachnoid Aneurysm Trial (ISAT) study,[1] endovascular treatment of cerebral aneurysms with the use of platinum coils has become the main treatment technique for cerebral aneurysms in most of the centers worldwide. However, approximately 20% of coiled aneurysms demonstrate signs of recanalization in their further course,[2-5] which is more likely to occur in large or giant and wide-neck aneurysms.[6,7] As a result, routine posttreatment imaging follow-up for coiled aneurysms is mandatory to detect re-growth and to determine the need for re-treatment.

However, current coil systems are made of platinum alloy, which is prone to artifact production during imaging. Imaging artifacts induced by platinum coils may significantly reduce imaging quality and influence interpretation of noninvasive follow-up imaging with the use of MRI/MRA preventing adequate diagnosis of residual intra-aneurysmal flow and areas close to the treated aneurysm. Furthermore, extensive metal-induced beam-hardening and streak artifacts deteriorate imaging quality and significantly impair the diagnostic accuracy of postprocedural CT scans, important for the recognition and management of complications, such as re-bleedings and aneurysm rupture during endovascular treatment. Moreover, even during endovascular treatment procedures, coil artifacts may impair the ability to optimally

Received November 14, 2012; accepted after revision February 23, 2013.

From the Institute of Diagnostic and Interventional Neuroradiology (P.M., J.G.) and Institute of Diagnostic, Pediatric, and Interventional Radiology (H.H.), Inselspital; Department of Neurosurgery (A.K.K., M.R.); and ARTORG Center for Biomedical Engineering Research (S.V.), University of Bern, Bern, Switzerland; and Neurovascular and Neuroradiology Research Unit (J.V.B.), Nuffield Department of Surgery, The John Radcliffe Hospital, University of Oxford, Oxford, United Kingdom.

P.M. was supported by a scientific grant from the Swiss Foundation for Grants in Biology and Medicine (SFGBM).

Please address correspondence to Pasquale Mordasini, MD, MSc, Department of Diagnostic and Interventional Neuroradiology, Inselspital, University of Bern, Freiburgstr 4, CH-3010 Bern, Switzerland; e-mail: pasquale.mordasini@insel.ch

Indicates open access to non-subscribers at www.ajnr.org

Indicates article with supplemental on-line table

http://dx.doi.org/10.3174/ajnr.A3589

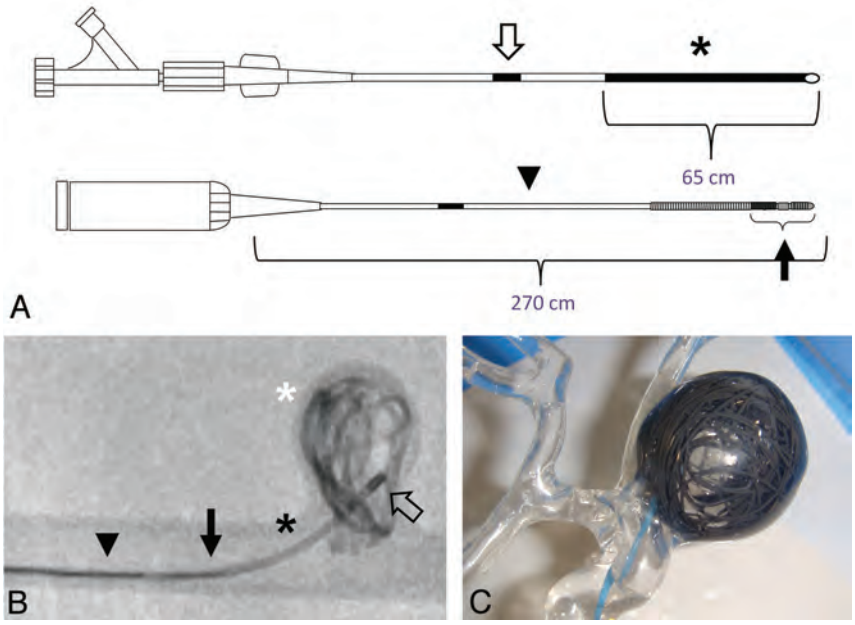

FIG 1. *A,* Schematic illustration of the polymeric coil system (above) and the delivery/detacher device (below). The coil system consists of a proximal shaft (*open arrow,* ink marker) attached to a hemostatic valve and a distal 65-cm-long radiopaque polymeric strand with an outer diameter of 0.018 inch (*asterisk*). The delivery/detacher device (total length, 270 cm) is introduced through the hemostatic valve into the inner lumen of the coil system. The delivery/detacher device consists of the microwire (*arrowhead*) and the heater coil attached to its distal tip (*arrow*). *B,* Fluoroscopy of an in vitro silicon aneurysm model showing the radiopaque polymeric strand (*black asterisk*) within the microcatheter placed in the aneurysm (microcatheter tip, *open arrow*) and its unfolded distal part within the aneurysm sac (*white asterisk*). Note the radiopaque section of the heater coil (*arrow*) at the distal tip of the delivery/detacher device (*arrowhead*) running within the coil strand. The polymeric strand can be detached at any point by advancing the radiopaque section of the heater coil at the level of the microcatheter tip and activating the thermal detachment. *C,* Photographic depiction of the silicon aneurysm model after introduction of the polymeric coil.

visualize the vessel anatomy on DSA by superimposing vessel structures of interest, such as branches arising from or close to the aneurysmal neck, especially in larger aneurysms and aneurysms with a complex anatomy.[8-16]

Therefore, from an imaging point of view, the optimal coil material should be the least prone to imaging artifacts as possible to permit optimal visualization of the vessel anatomy and adjacent brain tissue for endovascular treatment as well as for follow-up imaging. Metal-free, polymeric material potentially offers the ability for reduced artifact production compared with platinum. To date, only limited data about polymeric-based embolization material for endovascular treatment of cerebral aneurysms are available in the literature.[17-19]

The purpose of this study was to evaluate the imaging characteristics and artifact production of a polymeric coil system for the treatment of intracranial aneurysms compared with standard platinum coils.

MATERIALS AND METHODS

We compared the imaging characteristics of standard platinum coils and polymeric coils in vitro with the use of a silicon model, with DSA, flat panel CT (FP-CT), CT, and MR imaging. Furthermore, imaging characteristics of polymeric coils were assessed in vivo with the use of an experimental rabbit carotid bifurcation aneurysm model, with DSA, CT, CTA, and MR imaging.

Embolic Devices: Polymeric Coil System and Standard GDC-18 Coils

The detachable polymeric coil system (cPAX; NeuroVasx, Maple Grove, Minnesota) was approved in 2011 by the US Food and Drug Administration for the treatment of large intracranial aneurysms. The coil system consists of a proximal shaft and a distal section of detachable polymeric strand (65 cm long, 0.018-inch outer diameter) with an inner lumen to introduce the delivery/detacher device. The polymeric strand has tantalum incorporated within to gain radio-opacity to assist during navigation and placement under fluoroscopy. The shaft has an ink mark to indicate when fluoroscopic guidance is required. A manifold with a rotating hemostatic valve is attached at the proximal end for flushing the coil system before use and to introduce the delivery/detacher device. The delivery/detacher device is a 0.011-inch microwire device consisting of a core with an electric lead wire attached to a heater coil at its distal end. It is intended for the delivery of the polymer strand into the aneurysm and subsequent thermal detachment. The distal end of the device is radiopaque to assist in guidance and placement of the device under fluoroscopy. The delivery/detacher device is packaged within the lumen of the coil system and can be moved within the inner lumen to assist navigation of the strand for deployment within the aneurysm. The proximal end of the delivery/detacher device consists of an electrical connector, which is connected via a jumper cable to a power supply box for detachment. The polymeric strand and the delivery/detacher device within it are delivered into a cerebral aneurysm through a standard 0.021F microcatheter by use of the same delivery technique as the currently used platinum coil technology. The strand is fully retrievable before detachment. Thermal detachment can be accomplished at any point along the polymer strand by placing the heater coil under fluoroscopic control at the tip of the microcatheter. The strand design of the device and the thermal detachment by use of the heater coil within the strand allow continuous filling of the aneurysms and detachment at any point versus the fixed detachment zone of a standard platinum coil (Fig 1).

To compare imaging characteristics with standard platinum coils in vitro with a comparable diameter, GDC-18 coils (0.018-inch outer diameter; Boston Scientific/Stryker Neurovascular, Natick, Massachusetts) were used for embolization of an identical silicon model in standard coiling technique.

In Vitro Experimental Setup

Two identical commercially available silicon models of a large wide-neck right internal carotid artery aneurysm (diameter, 23 mm; neck, 5.7 × 8.2 mm; Elastrat, Geneva, Switzerland) were

used for coiling with polymeric coils and standard platinum coils. Both aneurysms were coiled up to a calculated packing attenuation of 20% each. Calculation of packing attenuation was performed with the use of an on-line cerebral aneurysm calculator software (www.angiocalc.com) with a 2D spherical function with a diameter of 23 mm for aneurysm volume calculation. The silicon aneurysm models were connected for imaging to a pulsating circulatory pump (Medos VAD; Medos Medizintechnik AG, Stolberg, Germany) with a frequency of pulsation of 80 beats per minute, a flow volume of 300 mL/min, and a systolic speed of 80–100 cm/s.

Imaging Protocol

DSA was performed in a clinical angiography suite (Axiom Artis z; Siemens, Erlangen, Germany) with the use of 10-mL hand injections of iodinated contrast material (Iopamiro 300; Bracco, Milano, Italy).

On the table, noncontrast FP-CT (DynaCT, Siemens) was performed for the in vitro experiments with the use of the following parameters: 20-second acquisition, 0.4° increment, 512 × 512 matrix, 220° total angle, 20°/s, and 15 frames per second.

MRI was performed with the use of a 3T clinical MR scanner (Magnetom Trio, Siemens) with a 32-channel head coil (Siemens). Imaging was performed with a routine scanning protocol by use of a 3D TOF sequence (TR, 22; TE, 3.9; flip angle, 18; matrix, 384 × 224; FOV, 166 × 200; voxel size, 0.5 × 0.5 × 0.6 mm), T2 (TR, 5470 ms; TE, 81 ms; matrix, 512 × 314; FOV, 180 × 180 mm), T1 (TR, 250 ms; TE, 3 ms; matrix, 224 × 512; FOV, 180 × 180 mm), and, in addition, B0 (TR, 488 ms; TE, 5.2 ms; matrix, 64 × 64; FOV, 192 × 192 mm) and true fast imaging with steady state precession (TR, 4.4; TE, 2.2 ms; matrix, 256 × 256; FOV, 200 × 200) sequences in the in vitro experiments.

CT and CTA were performed by use of an 8-row multidetector clinical CT scanner (LightSpeed Ultra, GE Healthcare, Milwaukee, Wisconsin). CT was performed with the use of the following parameters: 140 kV; 70 mAs; section thickness, 1.25 mm; table increment, 2.01 mm; FOV, 250 × 250. CTA in the in vivo experiment was carried out by use of hand injection of 10 mL of iodinated contrast (Iopamiro 300) through the groin sheath left in place for imaging after the coiling procedure. CTA was triggered visually on a transverse section of the descending aorta at the level of the heart when contrast media opacification became visible.

Postprocessing was performed on a workstation for viewing and creation of multiplanar reformatted images (Syngo Workplace, Siemens).

Experimental Aneurysm Creation: Animal Model

All procedures were performed according to local regulations and were approved by the responsible local authorities. Experimental bifurcation aneurysms were surgically created in 4 female adult New Zealand White rabbits (3–4.5 kg). All animals were anesthetized with an intramuscular injection of ketamine (65 mg/kg) and xylazine (5 mg/kg) 30 minutes before surgery, which was repeated if necessary during the procedure. Carotid bifurcation aneurysms were surgically created as previously described,[20] by means of a modification of the venous pouch aneurysm model to create aneurysms >10 mm in diameter. In brief, a venous pouch was created from a 1- to 1.5-cm-long section of the jugular vein. The right common carotid artery was temporarily clipped, and an oval arteriotomy was performed. The left common carotid artery was temporarily clipped proximally and permanently ligated distally. The left common carotid artery was then cut proximally to the ligature. The proximal part of the left common carotid artery was mobilized to the right side to create an end-to-side anastomosis of the left-to-right common carotid artery to the proximal part of the arteriotomy by use of single-knot 10–0 nylon sutures. The venous pouch was finally sutured into the resulting arteriotomy defect in this artificial vessel bifurcation (Fig 6 *A*, *-B*). Four weeks after surgery, the aneurysms were embolized through a 5F sheath in the right femoral artery as completely as possible with poly-

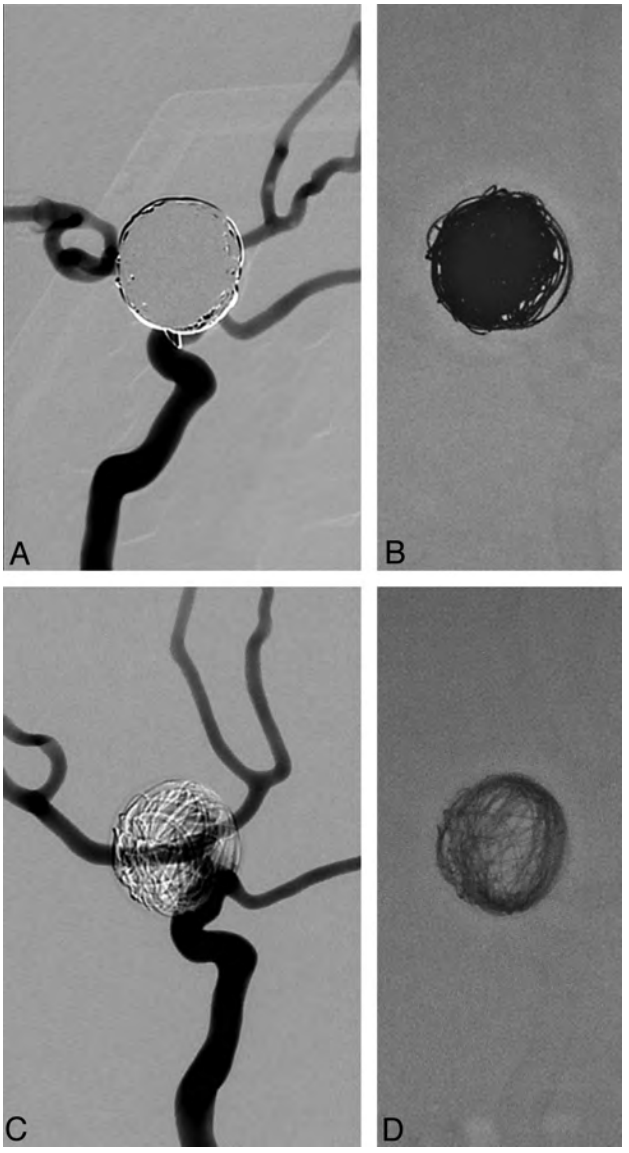

FIG 2. DSA of the in vitro silicon aneurysm model coiled with a calculated packing attenuation of 20%. Note the transparency of the polymeric coils *(C)* with persistent visualization of the superimposed vessel anatomy, which is completely obscured by standard platinum coils *(A)*. Fluoroscopic images show the difference in radio-opacity of polymeric *(D)* and standard platinum coils *(B)*.

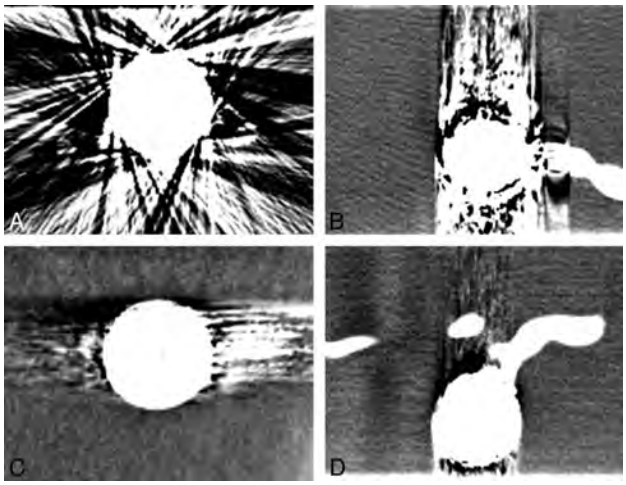

FIG 3. Flat panel CT images of standard platinum coils *(A* and *B)* and polymeric coils *(C* and *D)*. Note significant artifact reduction of polymeric coils compared with standard platinum coils; however, visualization of the peri-aneurysmal area is still significantly impaired.

meric coils. DSA, CT, CTA, and MR imaging were performed immediately after endovascular treatment. The animals were euthanized immediately after the experiment by a lethal injection of sodium pentobarbital (400 mg/kg intra-peritoneally).

Evaluation Criteria

The images from the in vitro DSA were qualitatively evaluated for transparency and visibility of superimposed vessels (visible, not visible). The FP-CT, CT/CTA, and MR images were evaluated for artifact production (none, minor, major), visibility of individual coils, coil mass, residual aneurysm, and peri-aneurysmal area for diagnostic value (not acceptable, acceptable, excellent). All scores were assessed in consensus by the authors (P.M. and J.G.).

RESULTS

Qualitative assessment scores for the in vitro and in vivo experiments are summarized in the On-line Table. Overall, in vitro and in vivo imaging demonstrated reduced artifact production and higher scoring assessments for polymeric coils in all imaging modalities compared with standard platinum coils.

On DSA, polymeric coils demonstrated transparency that permitted visualization of superimposed vessel structures in vitro and in vivo, whereas platinum coils were not transparent and completely masked superimposed vessel structures because of their high radio-attenuation (Figs 2 and 6). Polymeric coils showed satisfying radio-opacity and visibility under fluoroscopy for safe and controlled endovascular coil delivery. FP-CT in vitro demonstrated improved image quality as the result of reduced artifact production by use of polymeric coils compared with standard platinum coils. However, the image quality was still not of full diagnostic value for both coil materials because of massive beam-hardening and streak artifacts (Fig 3). Image quality of CT and MR imaging was improved by use of polymeric coils, which permitted enhanced depiction of individual coil loops and residual aneurysm lumen as well as the peri-aneurysmal area (Figs 4 and 5). Susceptibility artifacts in vitro on B0 images were not visible with the use of polymeric coils. TOF imaging demonstrated residual flow in the aneurysm sac and neck area in both coil groups; however, this was improved and rated excellent for polymeric coils (Fig 5). In vivo MRI in aneurysms embolized with polymeric coils was able to depict the aneurysm wall and the surrounding soft tissue without obscuring susceptibility artifacts by use of T1WI and even more accurately delineated on T2WI (Fig 6). Remarkably, CT images demonstrated considerably improved image quality with only minor artifact production compared with standard platinum coils. Depiction of the embolic mass, individual coils, and the peri-aneurysmal area on CT and residual intra-aneurysmal flow on CTA was considered acceptable for diagnostic purposes by use of polymeric coils. On the other hand, CT image quality with the use of standard platinum coils was not acceptable because of extensive beam-hardening and streak artifacts that obscured the area of interest (Figs 4, 6, and 7).

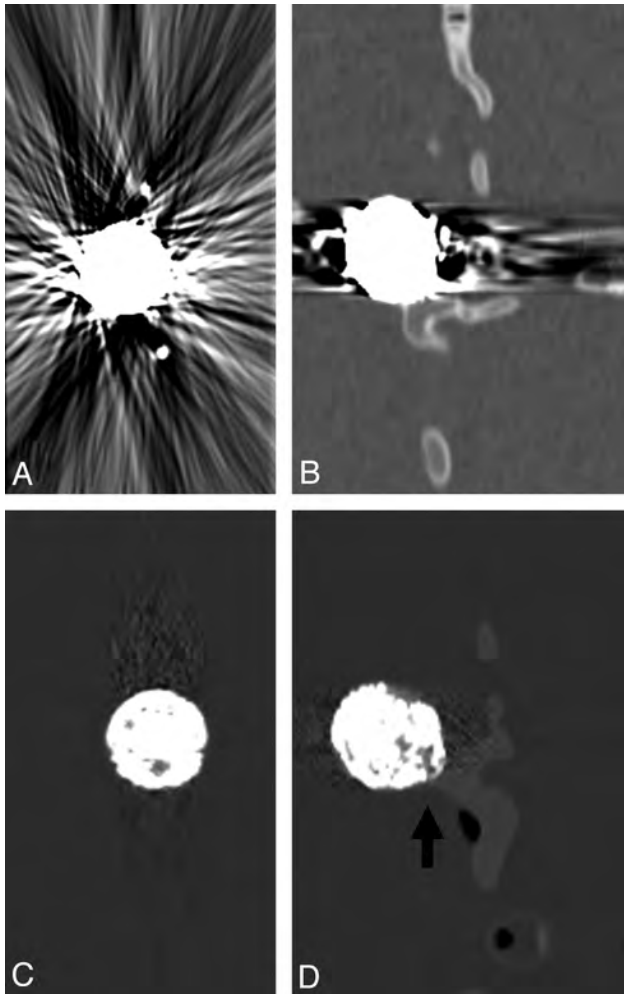

FIG 4. CT scan of standard platinum coils *(A* and *B)* and polymeric coils *(C* and *D)*. Note significant reduction of beam-hardening artifacts compared with standard platinum coils. In the aneurysm embolized with polymeric coils, individual coils as well as residual aneurysm lumen and neck (*arrow*) can be distinguished.

DISCUSSION

Endovascular coiling has become a well-established and increasingly performed treatment technique for ruptured and unruptured intracranial aneurysms.[1] However, because of the risk of aneurysm re-growth and neck recurrence after coil treatment,

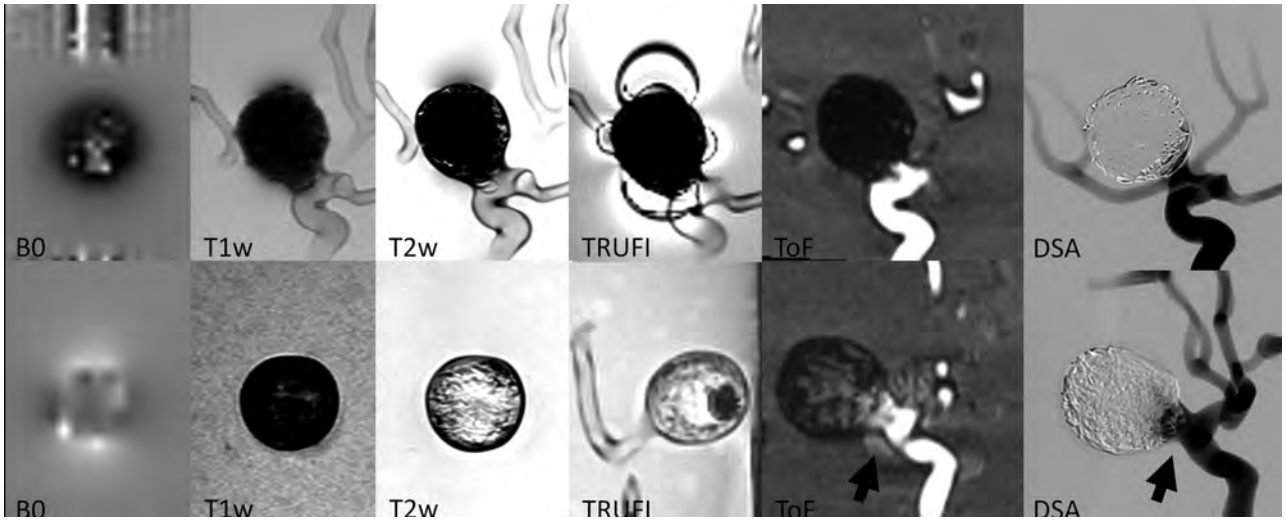

FIG 5. MR images and corresponding DSA of standard platinum coils (upper row) and polymeric coils (lower row) in vitro. Less magnetic field distortion and artifact production are seen with polymeric coils with the use of MRI. Individual coils can be distinguished in T2WI, TRUFI (true fast imaging with steady state precession), and TOF images as compared with standard coils. Note the visualization of residual flow within the aneurysm sac and the neck area in the aneurysm treated with polymeric coils in the TOF and DSA (*arrows*) compared with standard platinum coils at the same packing attenuation.

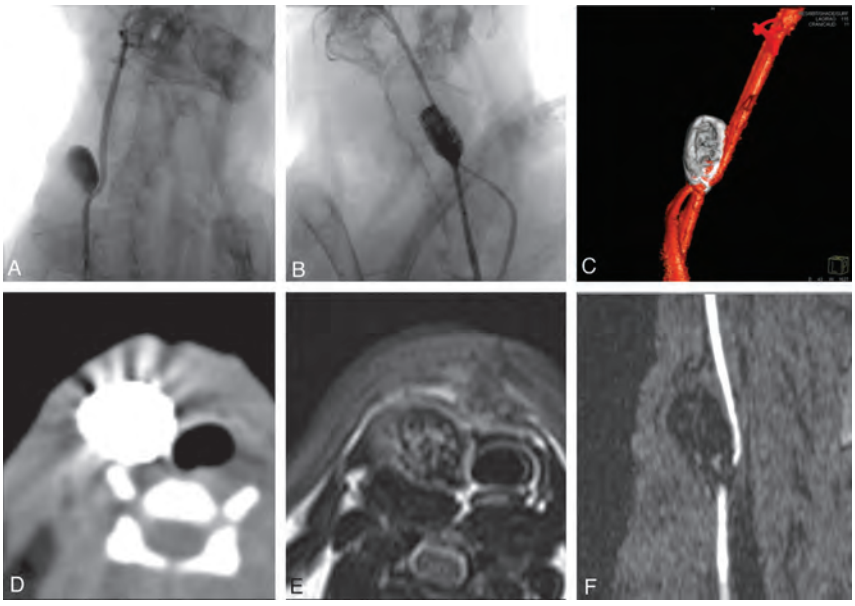

FIG 6. DSA demonstrates the anatomy of the venous patch carotid artery bifurcation model with the anastomosis of the left carotid artery proximal to the aneurysm *(A* and *B)*. Posttreatment DSA *(B)* and 3D rotational angiography *(C)* show complete obliteration of the aneurysm *(B)*. Note the persistent visibility of the right carotid artery despite superimposition by the coil mass. Note the minor effect of beam-hardening artifacts on the surrounding soft tissue on CT imaging *(D)*. MR images demonstrate visibility of individual coil loops in the T2WI *(E)* and the lack of intra-aneurysmal flow in the TOF image *(F)*.

follow-up imaging is mandatory. DSA has been used as the criterion standard for follow-up assessment of coiled aneurysms. However, diagnostic DSA is an invasive, comparatively expensive, and time-consuming procedure with the potential risk of clinical complications.[21,22] To overcome the disadvantages of DSA noninvasive imaging, follow-up is performed as an alternative. Imaging artifacts caused by the metallic nature of coils are an important factor influencing the quality of posttreatment imaging. MRI/MRA has been increasingly used as the imaging technique of choice for posttreatment follow-up of coiled aneurysms.[9,11,15,16,23-25] However, despite encouraging imaging quality and improving artifact reduction of MRI/MRA, disadvantages of this technique include comparatively long examination time, limited availability, and contraindication for patients with pacemakers and biostimulators. Metallic implants cause massive beam-hardening and streak artifacts on CT images, which deteriorate image quality and furthermore superimpose other brain structures of interest. The metallic nature of standard platinum coils precludes the use of CT or CTA as imaging techniques after coil treatment.[26,27] Therefore, from an imaging point of view, an optimal coil material would permit artifact-free imaging or cause the least possible imaging artifacts and would allow reliable and accurate imaging diagnosis. Polymeric-based coil material has the potential to offer these features. However, to date, only limited data about metal-free polymeric-based embolic material for the treatment of intracranial aneurysms are available. Hydrogel filaments opacified with barium sulfate or iodine have been used in experimental studies to evaluate occlusion of aneurysms on CT and CTA. These studies have shown promising results in detecting aneurysmal remnants after treatment with hydrogel filaments and demonstrate the potential of CTA to provide images suitable to determine whether re-treatment is necessary.[17-19]

The present study, through the use of different imaging modalities, has demonstrated that polymeric coils cause less imaging artifacts compared with standard platinum coils on all imaging modalities. Overall, they provided better imaging and visualiza-

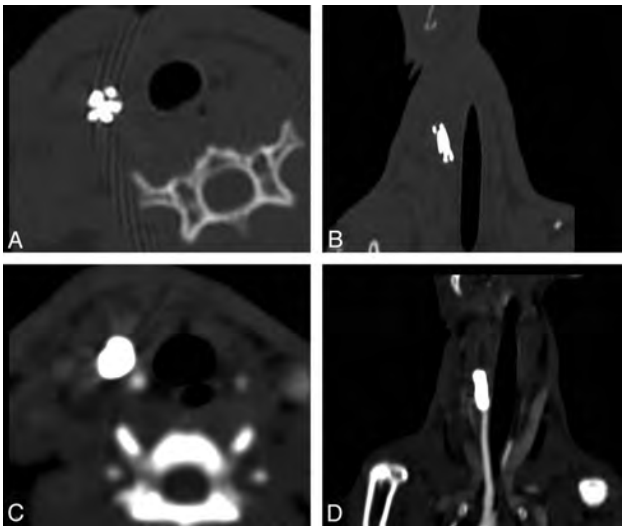

FIG 7. CT images of a coiled carotid bifurcation aneurysm. Note the reduced artifact production and visibility of individual coils on the unenhanced CT scan *(A* and *B)*. CTA shows complete occlusion of the aneurysm and minimal artifact production *(C* and *D)*.

tion of the coil mass, coil details, and the soft tissue area adjacent to the embolized aneurysm. Therefore, polymeric coils might be able to improve posttreatment surveillance as well as detection and avoidance of peri-procedural complications.

MRI examinations in vitro as well as in vivo have demonstrated excellent visualization of details of the coil mass and individual coils. With the use of TOF sequences, the presence of residual flow within an embolized aneurysm was visible, a feature of greatest significance for follow-up imaging of coiled aneurysms. The lack of susceptibility artifacts demonstrated on B0 images permits artifact-free imaging of soft tissue structures immediately adjacent to the embolized aneurysm on T1WI and T2WI. Furthermore, detailed depiction of the aneurysm wall could be achieved in the experimentally created in vivo aneurysms.

On conventional CT, the aneurysms embolized with polymeric coils demonstrated only minimal beam-hardening and streak artifacts. The beam-hardening artifacts of the polymeric coils were significantly reduced compared with platinum coils, with only minimal residual artifacts. The improved image quality allowed depiction of single-coil loops and residual aneurysm lumen. In our opinion, the residual artifacts are caused by the tantalum added to the polymer to gain some radio-opacity for visualization of the coil strand on fluoroscopy during the procedure. This artifact reduction may significantly improve diagnostic accuracy of posttreatment CT examinations. CT has an important role in the emergency and acute settings of subarachnoid hemorrhage to recognize potential hemorrhagic complications and rebleedings, which can be masked by metallic coil artifacts. Furthermore, position of single coils and coil loops could be visualized, a feature that is of accurate.

The endovascular treatment of large and giant aneurysms may still necessitate the introduction of considerably large coil masses. Superimposition of a radio-attenuated coil mass may impair visualization of vessel structures of interest, especially in the treatment of complex aneurysms and in aneurysms with vessels arising near or at the aneurysm neck. In some clinical settings, incomplete treatment caused by insufficient visualization of crucial anatomic information must be accepted to avoid inadvertent vessel occlusion. Furthermore, DSA has been shown to be less accurate in detecting aneurysm body remnants extending or invaginating into the coil mass. Coils surrounding the aneurysmal remnant form a radio-attenuated, helmet-like mass around the remnant, causing difficulties in delineating the remnant, a phenomenon previously referred to as the helmet effect.[16] The DSA examinations in the current study have demonstrated excellent visibility of superimposed vessel structures through the coil mass during and after coiling. This feature may improve procedural safety and efficacy of the treatment or re-treatment of complex and large to giant cerebral aneurysms.

On the other hand, reduced radio-opacity of the polymeric coil system might also cause potential disadvantages in the clinical setting. Visual assessment and determination of adequacy of coil packing and residual filling of a treated aneurysm might be more difficult to judge as compared with platinum coils because of the better appreciation of these findings. Furthermore, the polymeric coils are less fluoroscopically visible than platinum coils, and overlapping bone and soft tissue structures might further impede intraprocedural visibility. Last, because the system consists of a polymer strand without preformed loops, it must bend at the aneurysm wall to adapt to the aneurysm geometry, which makes the system more rigid to place within an aneurysm compared with similar-sized platinum coils.

Although the present experimental study has shown promising imaging characteristics of polymeric coils and potential implications for clinical management, it has its inherent limitations. First, only a small sample of in vitro and in vivo imaging was performed and qualitatively analyzed. The study was conducted with the aim to preliminarily evaluate the imaging characteristics and artifact production of a polymeric-based coil system through the use of different imaging modalities compared with standard platinum coils. Second, these preliminary imaging findings must be further investigated in experimental and clinical studies, which are lacking at the moment. Clinically significant properties such as potential thrombogenicity and biologic behavior of the coil mass as well as the durability of the treatment compared with standard coils have not been addressed in this study. Last, the clinical value of reduced imaging artifacts and especially the potential role of CT/CTA examinations in the acute setting and during follow-up of endovascular aneurysm treatment must be further established.

CONCLUSIONS

This initial experimental study demonstrated improved imaging quality with the use of polymeric coils compared with standard platinum coils in all examined imaging modalities. Artifact reduction permits better visualization of coils and coil loops as well as the surrounding soft tissue. This might be advantageous for improved intraprocedural imaging for the detection of complications and posttreatment noninvasive follow-up imaging. Further investigation and evaluation of the clinical value and imaging characteristics of polymeric embolization material is needed.

Disclosures: Pasquale Mordasini—*RELATED: Grant:* P.M. was supported by a scientific grant of the Swiss Foundation for Grants in Biology and Medicine (SFGBM). James Byrne—*UNRELATED: Board Membership:* Codman Neurovascular, Comments: SAB member; *Grants/Grants Pending:* Balt International,* Siemens AG*; *Royalties:* Springer-Verlag, Comments: Portion of book sales. Michael Reinert—*UNRELATED: Consultancy:* Oxygen Biotherapeutics.* Jan Gralla—*UNRELATED: Consultancy:* Covidien–Ischemic Stroke Intervention*; *Grants/Grants Pending:* Swiss National Foundation* (**money paid to institution*).

REFERENCES

1. Molyneux AJ, Kerr RS, Yu LM, et al. **International Subarachnoid Aneurysm Trial (ISAT) of neurosurgical clipping versus endovascular coiling in 2143 patients with ruptured intracranial aneurysms: a randomised comparison of effects on survival, dependency, seizures, rebleeding, subgroups, and aneurysm occlusion.** *Lancet* 2005;366:809–17
2. Byrne JV, Sohn MJ, Molyneux AJ, et al. **Five-year experience in using coil embolization for ruptured intracranial aneurysms: outcomes and incidence of late rebleeding.** *J Neurosurg* 1999;90:656–63
3. Raymond J, Guilbert F, Weill A, et al. **Long-term angiographic recurrences after selective endovascular treatment of aneurysms with detachable coils.** *Stroke* 2003;34:1398–403
4. Kang HS, Han MH, Kwon BJ, et al. **Repeat endovascular treatment in post-embolization recurrent intracranial aneurysms.** *Neurosurgery* 2006;58:60–70
5. Campi A, Ramzi N, Molyneux AJ, et al. **Retreatment of ruptured cerebral aneurysms in patients randomized by coiling or clipping in the International Subarachnoid Aneurysm Trial (ISAT).** *Stroke* 2007;38:1538–44
6. Fernandez ZA, Guglielmi G, Vinuela F, et al. **Endovascular occlusion of intracranial aneurysms with electrically detachable coils: correlation of aneurysm neck size and treatment results.** *AJNR Am J Neuroradiol* 1994;15:815–20
7. Ries T, Siemonsen S, Thomalla G, et al. **Long-term follow-up of cerebral aneurysms after endovascular therapy prediction and outcome of retreatment.** *AJNR Am J Neuroradiol* 2007;28:1755–61
8. Bakker NA, Westerlaan HE, Metzemaekers JD, et al. **Feasibility of magnetic resonance angiography (MRA) follow-up as the primary imaging modality after coiling of intracranial aneurysms.** *Acta Radiol* 2010;51:226–32
9. Ferre JC, Carsin-Nicol B, Morandi X, et al. **Time-of-flight MR angiography at 3T versus digital subtraction angiography in the imaging follow-up of 51 intracranial aneurysms treated with coils.** *Eur J Radiol* 2009;72:365–69
10. Wallace RC, Karis JP, Partovi S, et al. **Noninvasive imaging of treated cerebral aneurysms, part I: MR angiographic follow-up of coiled aneurysms.** *AJNR Am J Neuroradiol* 2007;28:1001–08
11. Urbach H, Dorenbeck U, von Falkenhausen M, et al. **Three-dimensional time-of-flight MR angiography at 3 T compared to digital subtraction angiography in the follow-up of ruptured and coiled intracranial aneurysms: a prospective study.** *Neuroradiology* 2008;50:383–89
12. Gonner F, Heid O, Remonda L, et al. **MR angiography with ultrashort echo time in cerebral aneurysms treated with Guglielmi detachable coils.** *AJNR Am J Neuroradiol* 1998;19:1324–28
13. Walker MT, Tsai J, Parish T, et al. **MR angiographic evaluation of platinum coil packs at 1.5T and 3T: an in vitro assessment of artifact production: technical note.** *AJNR Am J Neuroradiol* 2005;26:848–53
14. Hennemeyer CT, Wicklow K, Feinberg DA, et al. **In vitro evaluation of platinum Guglielmi detachable coils at 3 T with a porcine model: safety issues and artifacts.** *Radiology* 2001;219:732–37
15. Gauvrit JY, Leclerc X, Caron S, et al. **Intracranial aneurysms treated with Guglielmi detachable coils: imaging follow-up with contrast-enhanced MR angiography.** *Stroke* 2006;37:1033–37
16. Agid R, Willinsky RA, Lee SK, et al. **Characterization of aneurysm remnants after endovascular treatment: contrast-enhanced MR angiography versus catheter digital subtraction angiography.** *AJNR Am J Neuroradiol* 2008;29:1570–74
17. Constant MJ, Keeley EM, Cruise GM. **Preparation, characterization, and evaluation of radiopaque hydrogel filaments for endovascular embolization.** *J Biomed Mater Res B Appl Biomater* 2009;89:306–13
18. McCoy MR, Cruise GM, Killer M. **Angiographic and artefact-free computed tomography imaging of experimental aneurysms embolised with hydrogel filaments.** *Eur Radiol* 2010;20:870–76
19. Killer M, McCoy MR, Vestal MC, et al. **Use of CT angiography in comparison with other imaging techniques for the determination of embolus and remnant size in experimental aneurysms embolized with hydrogel filaments.** *AJNR Am J Neuroradiol* 2011;32:923–28
20. Forrest MD, O'Reilly GV. **Production of experimental aneurysms at a surgically created arterial bifurcation.** *AJNR Am J Neuroradiol* 1989;10:400–02
21. Willinsky RA, Taylor SM, TerBrugge K, et al. **Neurologic complications of cerebral angiography: prospective analysis of 2,899 procedures and review of the literature.** *Radiology* 2003;227:522–28
22. Kaufmann TJ, Huston J III, Mandrekar JN, et al. **Complications of diagnostic cerebral angiography: evaluation of 19,826 consecutive patients.** *Radiology* 2007;243:812–19
23. Anzalone N, Scomazzoni F, Cirillo M, et al. **Follow-up of coiled cerebral aneurysms: comparison of three-dimensional time-of-flight magnetic resonance angiography at 3 Tesla with three-dimensional time-of-flight magnetic resonance angiography and contrast-enhanced magnetic resonance angiography at 1.5 Tesla.** *Invest Radiol* 2008;43:559–67
24. Sprengers ME, Schaafsma JD, van Rooij WJ, et al. **Evaluation of the occlusion status of coiled intracranial aneurysms with MR angiography at 3T: is contrast enhancement necessary?** *AJNR Am J Neuroradiol* 2009;30:1665–71
25. Pierot L, Portefaix C, Boulin A, et al. **Follow-up of coiled intracranial aneurysms: comparison of 3D time-of-flight and contrast-enhanced magnetic resonance angiography at 3T in a large, prospective series.** *Eur Radiol* 2012;22:2255–63
26. Richter G, Engelhorn T, Struffert T, et al. **Flat panel detector angiographic CT for stent-assisted coil embolization of broad-based cerebral aneurysms.** *AJNR Am J Neuroradiol* 2007;28:1902–08
27. Masaryk AM, Frayne R, Unal O, et al. **Utility of CT angiography and MR angiography for the follow-up of experimental aneurysms treated with stents or Guglielmi detachable coils.** *AJNR Am J Neuroradiol* 2000;21:1523–31

Thrombus Attenuation Does Not Predict Angiographic Results of Mechanical Thrombectomy with Stent Retrievers

U. Yilmaz, C. Roth, W. Reith, and P. Papanagiotou

ABSTRACT

BACKGROUND AND PURPOSE: Mechanical thrombectomy with stent retrievers in acute stroke has emerged as a promising new technique, with the highest recanalization rate of the therapeutic procedures available thus far. However, in up to 20% of the cases, mechanical thrombectomy with stent retrievers results in poor angiographic outcomes, with Thrombolysis in Cerebral Infarction scores ≤2a. The purpose of this study was to investigate whether thrombus attenuation on the initial CT scan can predict the angiographic outcome of the recanalization procedure in MCA occlusions.

MATERIALS AND METHODS: The data of 70 patients with acute MCA occlusions who underwent endovascular treatment with stent retrievers in our department were included. We analyzed thrombus attenuations, angiographic outcome, and periprocedural thrombus fragmentation.

RESULTS: The mean thrombus attenuation was 49.8 ± 7.8 HU and the mean difference from the attenuation of the contralateral MCA was 9.9 ± 8.0 HU. There were no significant differences in the thrombus attenuations of occlusions that were successfully recanalized (modified Thrombolysis in Cerebral Infarction ≥2b) and those that were not. Neither were there significant correlations of thrombus attenuations and periprocedural thrombus fragmentations that occurred in 64.3%. We found a nonsignificantly higher rate of recanalizations with modified Thrombolysis in Cerebral Infarction ≥2b when the difference from the attenuation of the contralateral MCA was between 1–20 HU.

CONCLUSIONS: In contrast to results of other revascularization procedures as published in a recent study, the angiographic result of mechanical thrombectomy with stent retrievers is not predicted by thrombus attenuation.

ABBREVIATIONS: mTICI = modified Thrombolysis in Cerebral Infarction; CAS = carotid artery stenting; ΔTM = difference between thrombus attenuation and attenuation of the contralateral MCA

In the last 2 years, endovascular treatment of acute intracerebral artery occlusions received impetus through a new technique that uses fully retrievable self-expanding stents. With the use of these stent retrievers, several studies have reported recanalization rates with TICI ≥2b from 79–90%.[1-5] However, in up to 20% of cases, mechanical thrombectomy with stent retrievers results in poor angiographic outcomes, with TICI scores ≤2a.

It has been shown in a recent study that preinterventional thrombus attenuations on initial CT scans and recanalization results correlate for treatments with IV rtPA and intra-arterial rtPA and mechanical treatments with the Merci (Concentric Medical, Mountain View, California) and Penumbra (Penumbra, Alameda, California) devices.[6]

To explore whether thrombus attenuation on the initial CT scan can predict the angiographic outcome of mechanical thrombectomy with stent retrievers, we performed a retrospective analysis of patients with acute MCA occlusions who have been treated with stent retrievers in our department.

MATERIALS AND METHODS

Between October 2009 and October 2012, 89 patients with acute occlusions of the M1 segment of an MCA underwent mechanical recanalization with stent retrievers in our department. The data of 19 of these patients were excluded from analysis because the initial CT scans were not performed in our department but at the external referring hospitals ($n = 17$), because of a high contrast artifact at the occluded MCA ($n = 1$), and because of an initial MRI scan instead of a CT scan ($n = 1$).

Received November 11, 2012; accepted after revision February 14, 2013.

From the Department of Neuroradiology, Saarland University Hospital, Homburg, Germany.

Please address correspondence to Umut Yilmaz, MD, Saarland University Hospital, Kirrberger Str D-66424 Homburg, Germany; e-mail: umut.yilmaz@uks.eu

http://dx.doi.org/10.3174/ajnr.A3565

Table 1: Influence of extracranial ICA occlusion on thrombus attenuation

	ICA Occlusion	No ICA Occlusion	*P* Value
Thrombus attenuation (HU ± SD)	56.5 ± 4.7	48.3 ± 7.7	<.001
ΔTM (HU ± SD)	17.0 ± 6.4	8.3 ± 7.5	<.001

Table 2: Angiographic results and thrombus attenuation

	mTICI ≥2b (*n* = 57)	mTICI ≤2a (*n* = 13)	*P* Value
Thrombus attenuation (HU ± SD)	50.1 ± 7.8	48.7 ± 8.2	.567
ΔTM (HU ± SD)	9.9 ± 7.6	10.2 ± 9.7	.887

Table 3: Thrombus fragmentation and thrombus attenuation

	Fragmentation (*n* = 45)	No Fragmentation (*n* = 25)	*P* Value
Thrombus attenuation (HU ± SD)	50.3 ± 7.7	49.0 ± 8.1	.494
ΔTM (HU ± SD)	10.4 ± 8.5	9.1 ± 7.0	.504

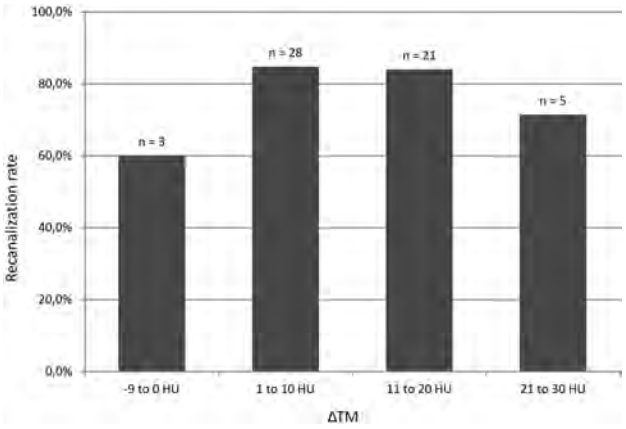

FIG 1. Recanalization rates for groups of different ΔTM values.

The data of 70 patients were included (37 male, 33 female; mean age, 72 ± 12 years). The imaging protocol for patients with suspected stroke in our department consists of a NCCT, followed by CT angiography and CT perfusion scans. NCCT scans were performed on an Aquilion 32-section CT scanner (Toshiba Medical Systems, Tokyo, Japan) in helical mode (0.5-mm thickness, 120 kV) and reconstructed in the axial, sagittal, and coronal planes (5-mm thickness). Patients meeting the following criteria were selected for endovascular therapy: 1) neurologic examination demonstrated a significant neurologic deficit (paresis of arm or leg, aphasia, dysarthria), 2) intracranial hemorrhage and established infarction were excluded by NCCT, 3) CT angiography confirmed major vessel occlusion. Procedures were performed on a biplane angiography machine (Axiom Artis; Siemens, Erlangen, Germany) as described before.[1] Stent retrievers used were Solitaire FR (Covidien, Irvine, California), pREset (Phenox, Bochum, Germany), Trevo (Stryker, Kalamazoo, Michigan), and Aperio (Acandis, Pforzheim, Germany). Balloon guide catheters for the recanalization procedures were not used. Thirty-six patients were administered IV thrombolysis before endovascular therapy. Thirty-four patients were treated only endovascularly because of contraindications against IV thrombolysis.

Angiograms and CT scans were analyzed retrospectively by 2 raters in consensus, and angiographic results were scored according to the modified TICI (mTICI) score.[7] A thrombus was considered fragmented when its shape and/or length changed in the angiogram after a recanalization maneuver. Thrombus attenuations and attenuations of the contralateral MCA were measured in manually placed regions of interest perpendicular to the vessel on sagittal reconstructions of the CT scans. To take individual baseline blood attenuation into account for statistical analysis, the difference of the thrombus attenuations and the attenuations of the contralateral MCA were calculated (referred to as ΔTM).

Statistical analysis was performed with the use of PASW 17.0 (IBM, Armonk, NY). The χ^2 test was applied to determine differences in frequencies. Differences in means were tested by means of Student *t* test.

RESULTS

Recanalization with mTICI ≥2b was achieved in 57 cases (81.4%). For the group of patients who were treated by combined IV rtPA and mechanical thrombectomy, this rate was 80.6%; for the group treated only by mechanical thrombectomy, the rate was 82.4% ($P = .847$). The mean thrombus attenuation was 49.8 ± 7.8 HU, and the mean attenuation of contralateral MCA was 39.9 ± 5.0 HU, with a mean difference (ΔTM) of 9.9 ± 8.0 HU ($P < .001$; 95% CI, 8.0–11.8). In 5 cases (7.1%), the attenuations of the contralateral MCAs were higher than those of the clots (resulting in a negative ΔTM). Thrombus attenuations and ΔTMs were significantly higher in patients who had additional proximal occlusions of the extracranial ICA that were treated by stent placement first to obtain access to the MCA occlusion (Table 1).

As shown in Table 2, there were no significant differences in the thrombus attenuations of occlusions that were successfully recanalized (mTICI ≥2b) and those that were not. Neither was there a significant difference when ΔTMs were compared instead of thrombus attenuations alone.

Periprocedural thrombus fragmentation occurred in 45 (64.3%) cases. Again, there was no significant correlation with thrombus attenuations (Table 3).

To test for a nonlinear relation, we subdivided attenuations and values of ΔTM into steps of 10 HU and compared recanalization rates (Fig 1). Although there were no differences between the groups when comparing absolute attenuations of the clots (data not shown), we found a nonsignificantly higher rate of recanalization mTICI ≥2b when values of ΔTM were 1–20 HU (84.5% versus 66.7%, $P = .149$). This tendency increased in the group of patients who were treated by combined IV rtPA and mechanical thrombectomy (86.2% versus 57.1%, $P = .081$) and disappeared in the group of patients who were treated by mechanical thrombectomy only (82.8% versus 80.0%, $P = .881$).

DISCUSSION

In this study, we investigated whether differences in thrombus composition, as far as detectable by different attenuations on CT

scans, influence angiographic results of mechanical thrombectomy with stent retrievers. Mechanical thrombectomy with stent retrievers has been shown to result in the highest recanalization rates in acute intracerebral vessel occlusions reported thus far.[1-5] However, up to 20% of the cases result in poor angiographic outcome (TICI ≤2a).

Very recently, Moftakhar et al[6] reported significant correlations of preinterventional thrombus attenuations and recanalization results for IV rtPA, intra-arterial rtPA, and mechanical treatments with the Merci and Penumbra devices. In their study, cases with lower HU values of the clots on initial CT scans had poorer angiographic outcomes.

In our study, we did not find significant differences in the thrombus attenuations of occlusions that were successfully recanalized (mTICI ≥2b) and those that were not successfully recanalized. Neither were there significant correlations of thrombus attenuations and periprocedural thrombus fragmentations.

Recently, the randomized Stroke Warning Information and Faster Treatment (SWIFT) trial has reported a significantly higher recanalization rate of mechanical thrombectomy with the Solitaire stent retriever compared with the Merci device.[8] Our results indicate that this higher performance of stent retrievers might in part be due to an insensibility of stent retrievers to different clot compositions.

However, in 5 cases, ΔTM was negative because the attenuations of the contralateral MCAs were higher than those of the clots, and we found a nonsignificant yet interesting higher recanalization rate in cases treated with combined IV rtPA and mechanical thrombectomy when ΔTM was between 1–20 HU. This observation might be explained by a lower performance of stent retrievers on clots of a very lipid-rich composition, but it must be readdressed in studies with larger case numbers.

Furthermore, we found that the mean thrombus attenuation is significantly higher in cases with additional proximal extracranial ICA occlusions. This information may be of value in centers in which CT angiography is not implemented in the stroke-imaging protocol.

Our study has some limitations. First, for all differences that were found between patients who were administered IV rtPA and those who were not administered IV rtPA, it has to be taken into account that these 2 groups of patients are substantially different. Patients who were not administered IV rtPA were either out of the time window for IV thrombolysis or had other serious contraindications against IV thrombolysis that might have affected the parameters that we investigated as well. In addition, the number of cases is relatively small when considering that the group of cases with values of ΔTM outside the range from 1–20 HU who showed differences in the rate of recanalization consisted of only 12 patients. The significance of this difference must be re-evaluated in larger studies.

CONCLUSIONS

In contrast to results of other revascularization procedures as published in a recent study,[6] the angiographic result of mechanical thrombectomy with stent retrievers is not predicted by thrombus attenuation. This might indicate that higher performance of stent retrievers is in part due to an insensibility of stent retrievers to different clot compositions. Yet, when IV rtPA and mechanical thrombectomy are combined, there is a nonsignificant difference in the rate of successful recanalization, which must be re-evaluated in larger studies.

REFERENCES

1. Roth C, Papanagiotou P, Behnke S, et al. **Stent-assisted mechanical recanalization for treatment of acute intracerebral artery occlusions.** *Stroke* 2010;41:2559–67
2. Castaño C, Dorado L, Guerrero C, et al. **Mechanical thrombectomy with the Solitaire AB device in large artery occlusions of the anterior circulation: a pilot study.** *Stroke* 2010;41:1836–40
3. Stampfl S, Hartmann M, Ringleb PA, et al. **Stent placement for flow restoration in acute ischemic stroke: a single-center experience with the Solitaire stent system.** *AJNR Am J Neuroradiol* 2011;32:1245–48
4. Dorn F, Stehle S, Lockau H, et al. **Endovascular treatment of acute intracerebral artery occlusions with the Solitaire stent: single-centre experience with 108 recanalization procedures.** *Cerebrovasc Dis* 2012;34:70–77
5. Dávalos A, Pereira VM, Chapot R, et al. **Retrospective multicenter study of Solitaire FR for revascularization in the treatment of acute ischemic stroke.** *Stroke* 2012;43:2699–705
6. Moftakhar P, English JD, Cooke DL, et al. **Density of thrombus on admission CT predicts revascularization efficacy in large vessel occlusion acute ischemic stroke.** *Stroke* 2013;44:243–45
7. Tomsick T, Broderick J, Carrozella J, et al. **Revascularization results in the Interventional Management of Stroke II trial.** *AJNR Am J Neuroradiol* 2008;29:582–87
8. Saver JL, Jahan R, Levy EI, et al. **Solitaire flow restoration device versus the Merci retriever in patients with acute ischaemic stroke (SWIFT): a randomised, parallel-group, non-inferiority trial.** *Lancet* 2012;380:1241–49

Analysis of Morphologic and Hemodynamic Parameters for Unruptured Posterior Communicating Artery Aneurysms with Oculomotor Nerve Palsy

Y. Yu, J. Xu, Y. Fang, X. Wu, P. Yang, C. Jiang, Y. Qian, J. Liu, and Q. Huang

ABSTRACT

BACKGROUND AND PURPOSE: Posterior communicating artery aneurysms with oculomotor nerve palsy may imply sudden enlargement of the aneurysm sac and have a high risk of rupture. Our aim was to identify the morphologic and hemodynamic parameters in this special period of aneurysm progression and to assess related rupture risk indices.

MATERIALS AND METHODS: We analyzed the morphologic and hemodynamic parameters of 9 unruptured posterior communicating artery aneurysms with oculomotor nerve palsy and 9 ruptured ones. The morphologic parameters were measured and calculated from patient-specific 3D rotational angiographic images, and pulsatile computational fluid dynamic simulation was then performed for hemodynamic parameters.

RESULTS: There was no significant statistical difference between the 2 groups in size, aspect ratio, size ratio, aneurysm angle, or vessel angle; analysis only demonstrated a significantly lower wall shear stress of the aneurysm wall in the symptomatic unruptured group in hemodynamics ($P = .024$), whereas there were no differences in wall shear stress of the parent artery, low wall shear stress area, and oscillatory shear index.

CONCLUSIONS: From morphologic and hemodynamic perspectives, we demonstrated that posterior communicating artery aneurysms with oculomotor nerve palsy had characteristics similar to those of ruptured ones, except for lower wall shear stress on the aneurysm wall, which might indicate an important role in aneurysm rupture.

ABBREVIATIONS: IA = intracranial aneurysm; PcomA = posterior communicating artery; CFD = computational fluid dynamics; AR = aspect ratio; SR = size ratio; WSS = wall shear stress; LSA = low wall shear stress area; OSI = oscillatory shear index

Rupture risk evaluation for an unruptured intracranial aneurysm (IA) is the critical factor for clinical decision-making. Many studies using image-based computational fluid dynamics (CFD) to evaluate rupture risk for unruptured IAs by hemodynamic and morphologic characteristics have been reported, however, most compared findings with ruptured IAs.[1,2] The CFD study of ready-to-rupture IAs, which is very difficult in clinical data acquisition, should be more reasonable and revealing but is less practical. Oculomotor nerve palsy occurring in unruptured posterior communicating artery (PcomA) aneurysms is considered a result of the pulsatile compression of sudden enlargement of the aneurysm sac.[3,4] Neurosurgeons and neurointerventionalists agree that a PcomA aneurysm with oculomotor nerve palsy is at high rupture risk, and it is an indication for urgent treatment. The hemodynamic and morphologic characteristics of this special type of IA with sudden enlargement should be similar to ready-to-rupture aneurysms, and the differences from ruptured PcomA aneurysms would more accurately indicate the hemodynamic and morphologic characteristics facilitating IA rupture. Thus, our aim was to identify the morphologic and hemodynamic parameters in this special period of aneurysm progression and to assess related rupture risk indices.

MATERIALS AND METHODS

Patient Population

The medical records and 3D angiography data of patients with IAs that were diagnosed and treated in our department for the period

Received December 2, 2012; accepted after revision February 15, 2013.

From the Department of Neurosurgery (Y.Y., J.X., Y.F., X.W., P.Y., C.J., J.L., Q.H.), Changhai Hospital, Second Military Medical University, Shanghai, China; and Australian School of Advanced Medicine (Y.Q.), Macquarie University, Sydney, Australia.

Y. Yu and J. Xu are co-first authors.

This study was supported by National Natural Science Foundation of China (Grant No.81171092, J. Liu; Grant No.81171093, Q. Huang; Grant No. 81000494, P. Yang); Rising-star Plan and Key Project of Shanghai Science and Technology Committee, China (Grant No. 11QA1408400, Q. Huang; Grant No. 11JC1415800, J. Liu); the Dawn Project of Shanghai, China (Grant No. 11CG043, P. Yang); Australian Research Council (Grant Nos. DP110102985 and LP0990263, Y. Qian).

Please address correspondence to Qinghai Huang, MD, Department of Neurosurgery, Changhai Hospital, 168 Changhai Rd, Shanghai, 200433, China; e-mail: ocinhqh@163.com

Indicates open access to non-subscribers at www.ajnr.org

http://dx.doi.org/10.3174/ajnr.A3575

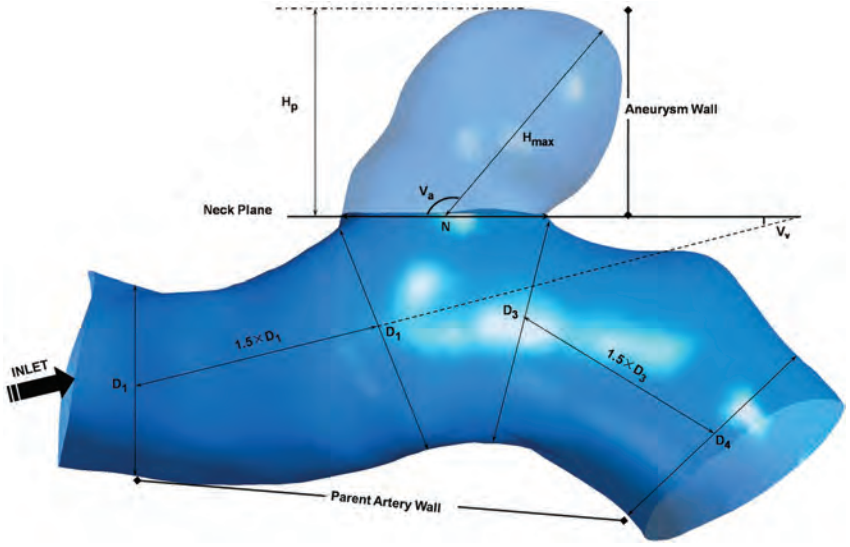

FIG 1. Measurement of morphologic parameters and division of the vessel wall. Size = H_p; AR = H_p/N; SR = H_{max}/D_m, where $D_m = (D_1+D_2)/2$.

2006–2012 were reviewed. Only patients with unruptured PcomA aneurysms who had sudden homolateral oculomotor nerve palsy and whose 3D data were of sufficient quality for further CFD study were included. Nine aneurysms from 9 patients were used in this study. The mean age in this case series was 65.7 years, with a range of 37–82 years. The time interval between the onset of first symptom and admission was 14.3 days on average. The control group consisted of 9 patients with angiographically confirmed ruptured PcomA aneurysms that were chosen randomly from the case library. The institutional review board in our hospital approved this study.

DSA Image Acquisition and Hemodynamic Modeling

Patient-specific 3D rotational angiographic images were obtained by standard transfemoral catheterization of the cerebral vessels with the use of Allura Xper FD20 (Philips, Best, the Netherlands). Stereolithography format files were imported into the software ICEM CFD (ANSYS, Canonsburg, Pennsylvania) to generate volumetric finite-element grids after 3D reconstruction on a 3D workstation (Philips). The number of total elements of each vessel luminal model was approximately 550,000–800,000. We defined the vessel wall as divided into 3 parts: aneurysm wall, parent artery wall, and other vessel wall (Fig 1).

CFX 11.0 (ANSYS) was used for CFD simulation. We simulated 3 continuous 0.8-second pulsatile cardiac cycles.[5] There are 800 time-steps in each cycle. Blood was considered an incompressible Newtonian fluid with attenuation $\rho = 1.0$ g/cm^3 and viscosity $\mu = 0.035$ poise and modeled on the basis of the unsteady Navier-Stokes equations. A traction-free boundary condition was imposed to the outlets. The vessel wall was assumed to be rigid with no-slip boundary conditions.

After simulation, the time-averaged wall shear stress (WSS) of the aneurysm wall and parent artery wall over the second cardiac cycle were calculated. Low wall shear stress area (LSA) was defined as the area of the aneurysm wall where the WSS is <10% of the mean parent arterial WSS[5-7] and then normalized by dome area[7]. Oscillatory shear index (OSI) was calculated by the formula described by He et al[8] and then was also averaged over the dome area.

Morphologic Parameter Calculations

Morphologic metrics were calculated from 3D angiographic data obtained and reconstructed as described previously by 2 individuals (Y.Y. and J.X.), and their average values were obtained. All the morphological parameters such as aneurysm size, aspect ratio (AR), size ratio (SR), aneurysm angle (V_a), and vessel angle (V_v) were defined and calculated as described in the study performed by Dhar et al[9] (Fig 1). Specifically, because most vessels in patients bend in all 3 dimensions, the values of these morphologic parameters depend on the direction from which the geometry is viewed. The correct viewing plane must be determined as follows before measuring: Aneurysm neck plane is kept parallel with the viewing plane, and the geometry is rotated about the axis that passes through the neck centroid and is perpendicular to the neck plane until the value of apparent vessel angle is minimum.[9] We considered all the aneurysms to be side wall aneurysms and ignored the effects of posterior communicating artery that are <0.5 mm in diameter on morphologic metrics.

Statistical Analysis

First, normality and homogeneity of variance tests were performed by application of Shapiro-Wilk and Levene statistics to all the data, respectively. Considering the small sample size, for data that conformed to both the normality and homogeneity of variance, a 2-tailed Student *t* test was performed to check the statistical significance of the mean difference between the unruptured and ruptured groups, and a nonparametric Mann-Whitney *U* test was used for the assessment of other parameters. Both methods are adequate for small sample size. We hope that proper statistical methods reduce the probability of type 2 error caused by small sample size and the conclusions are reasonable. The *P* value was calculated for each test, and significance was assumed as $P < .05$.

RESULTS

All results are detailed in the Table. Figs 2 and 3 depict the contour of time-averaged WSS and OSI. Because most parameters did not conform to both the normality and homogeneity of variance tests, we then performed a statistical analysis of all the parameters by use of the Mann-Whitney *U* test. All results are recorded as median (25% percentile, 75% percentile) or median ± interquartile range. The symptomatic unruptured PcomA aneurysms were very similar to ruptured ones in morphology and hemodynamics. There was no significant statistical difference between the 2 groups in any morphologic parameters, such as V_a, V_v, size, AR, and SR. AR in the symptomatic unruptured group was slightly higher than that in the ruptured group (1.35 ± 1.12 versus 0.97 ± 0.49, $P = .050$). We

demonstrated a lower WSS in the symptomatic unruptured group (5.27 ± 3.20 versus 8.11 ± 4.93, $P = .024$). For other hemodynamic parameters, including WSS of the parent artery wall, LSA, and OSI, there were no significant differences between the 2 groups.

DISCUSSION

With the development of CFD techniques, more neurointerventionalists are realizing their clinical utility and are trying to use these powerful tools to guide neurointerventional practice in treating IAs. The morphologic and hemodynamic differences between ruptured and unruptured aneurysms were compared among different individuals to evaluate the rupture risk of IAs.[9-13] However, most of time, we only obtain the postrupture details of an aneurysm and its parent artery. Once an aneurysm ruptures, sudden expansion of a pseudosac or ruptured points may cause great change in intra-aneurysmal hemodynamic environment and mitigate the blood flow to stabilize the ruptured aneurysm. Accordingly, the best way to evaluate the rupture risk of IA is to study the aneurysm in the ready-to-rupture state. A few cases of gross blood-flow characteristics of IA just before rupture have been reported,[14,15] but without comparison with ruptured aneurysms. The exact morphology and hemodynamics just before aneurysm rupture are not clear yet, but both studies of aneurysms before their rupture demonstrated low WSS on the aneurysm sacs. Some studies revealed lower WSS on ruptured aneurysms than on asymptomatic unruptured ones.[5,7,16] A CFD study of hemodynamic differences between unruptured and ruptured IAs during observation has been reported recently. Thirteen aneurysms that ruptured during the course of follow-up observation were included in this study, and averaged WSS in the unruptured group was lower than in the rup-

Statistical analysis of morphologic and hemodynamic parameters

	Symptomatic Unruptured (n = 9)	Ruptured (n = 9)	P Value
V_a	111.61 (85.30, 125.60)	101.20 (65.42, 125.15)	.796
V_v	11.50 (9.77, 17.05)	11.50 (6.65, 30.65)	.730
Size	5.73 (4.11, 8.97)	5.35 (4.63, 6.03)	.546
AR	1.35 (0.99, 2.14)	0.97 (0.84, 1.33)	.050
SR	1.94 (1.51, 3.30)	1.74 (1.57, 2.53)	.489
WSS of aneurysm wall	5.27 (3.11, 6.31)	8.11 (5.57, 10.50)	.024
WSS of parent artery wall	11.58 (9.13, 12.57)	13.06 (11.48, 17.02)	.077
LSA	0.100 (0.001, 0.278)	0.006 (0.002, 0.667)	.258
OSI	0.035 (0.008, 0.054)	0.015 (0.009, 0.042)	.666

Note:—All results are recorded as median (25% percentile, 75% percentile); unit of V_a and V_v is degree; unit of size is cm; unit of WSS is Pa.
V_a indicates aneurysm angle; V_v, vessel angle; AS, aneurysm size.

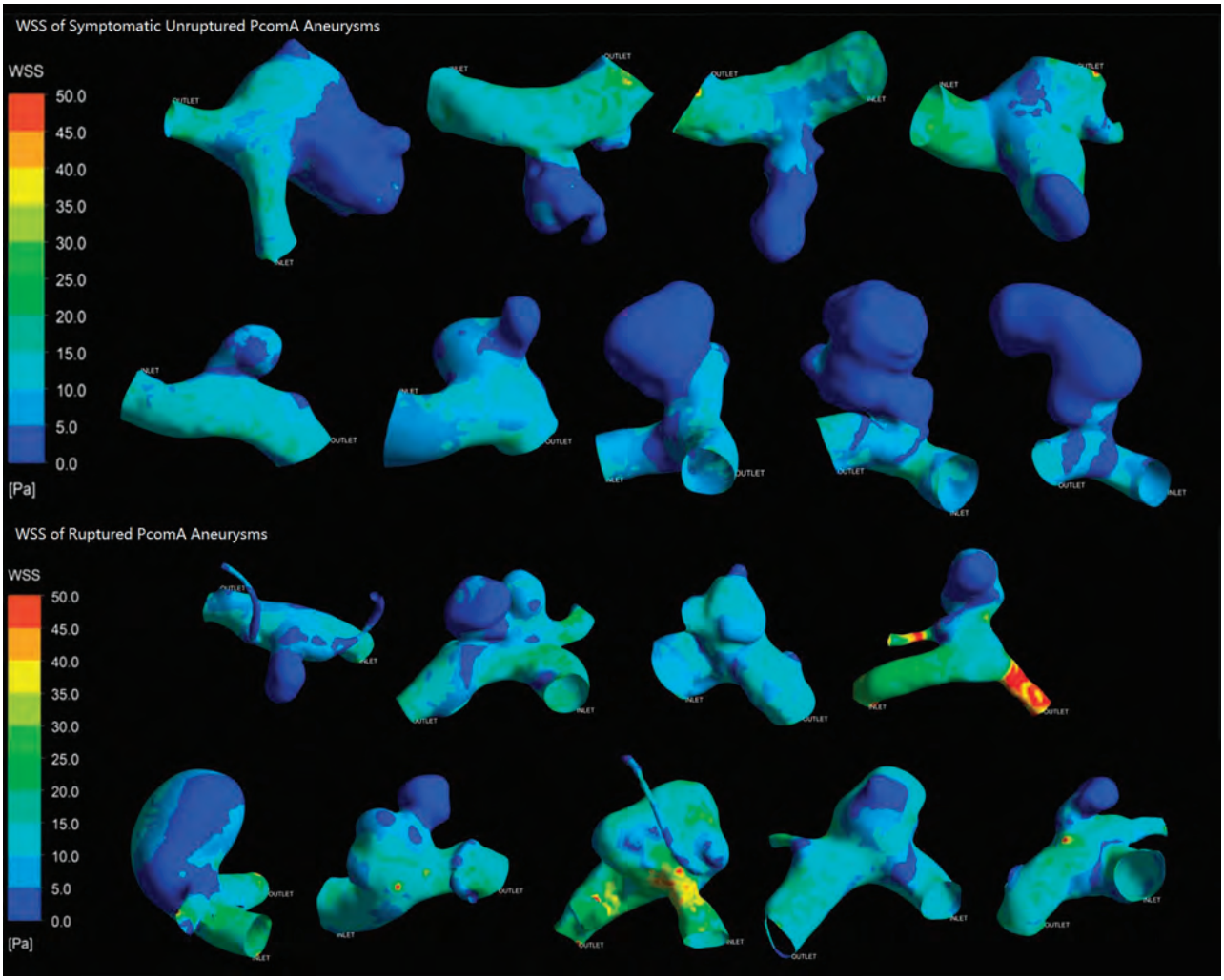

FIG 2. Wall shear stress of symptomatic unruptured and ruptured posterior communicating artery aneurysms.

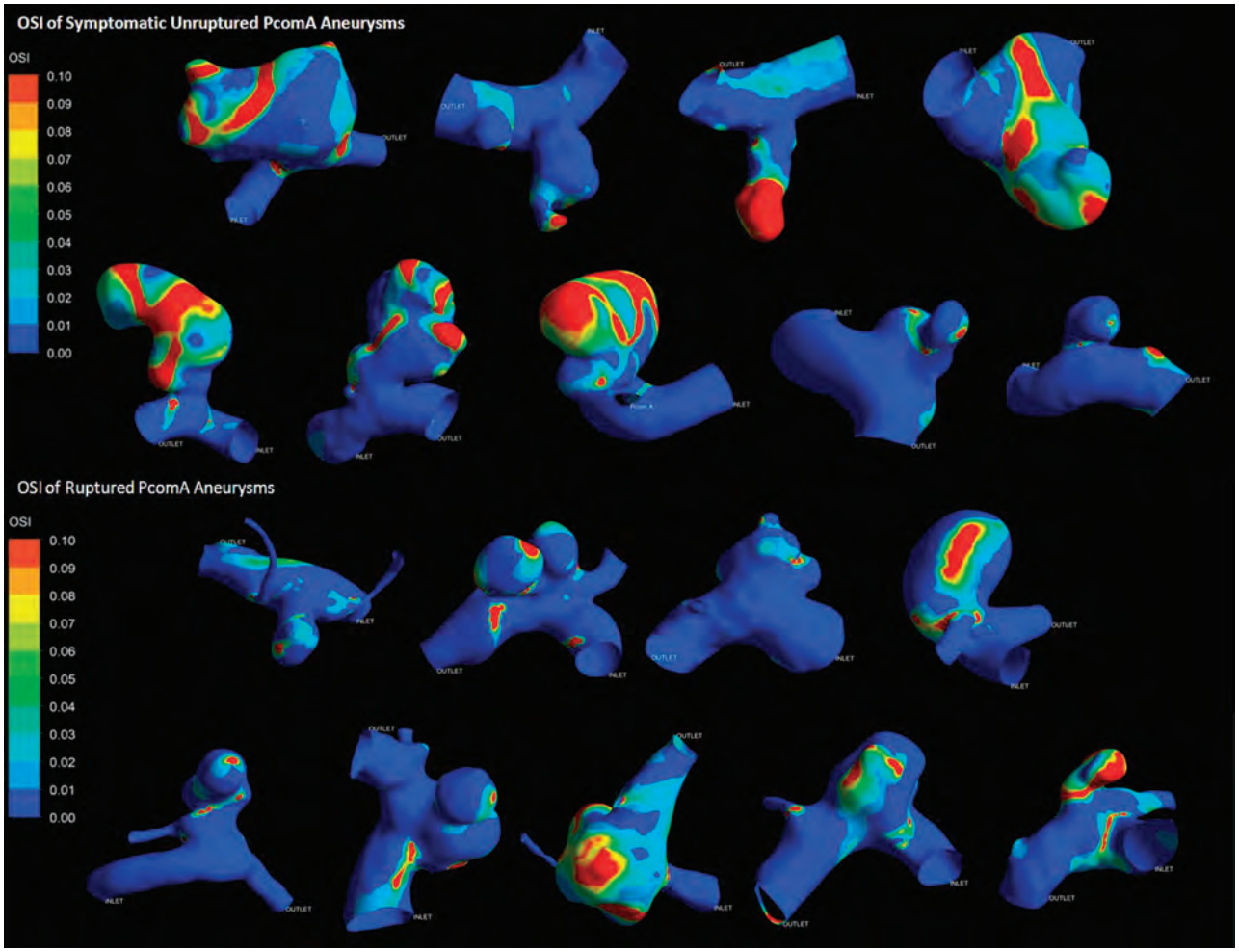

FIG 3. Oscillatory shear index of symptomatic unruptured and ruptured posterior communicating artery aneurysms.

tured group in the MCA. In our study, we also noticed a lower WSS in the unruptured PcomA aneurysms with oculomotor nerve palsy than in the ruptured ones (5.27 ± 3.20 versus 8.11 ± 4.93, $P = .024$), which is similar to the qualitative trend in the Takao et al study.[17] Also, the AR was larger in the symptomatic unruptured group, and the P value of AR was very close to statistical significance (1.35 ± 1.12 versus 0.97 ± 0.49, $P = .050$). This means that compared with ruptured PcomA aneurysms, symptomatic unruptured ones have a more irregular shape. Destructive remodeling may take place, which facilitates IA rupture caused by pathobiologic responses induced by low WSS, such as matrix metalloproteinase production by macrophages,[18,19] increased inflammatory cell infiltration,[20] and increased reactive oxygen species.[21] A recent study performed on an animal model also proved that high AR appears more deleterious to the aneurysm wall with pathologically low WSS.[22] Above all, in this case series, it inferred that low WSS might play an important role in aneurysm rupture.

In another study we performed, we analyzed morphologic and hemodynamic parameters of mirror PcomA aneurysms.[23] We found that lower WSS, higher LSA, and higher OSI contribute to aneurysm rupture. However, our results in this study only demonstrated that WSS of the aneurysm wall was significantly different between the 2 groups, instead of LSA or OSI hemodynamically. This discrepancy may be caused by small sample size, and it may reveal the particularity of these special symptomatic aneurysms in some ways. We should note that all unruptured aneurysms in the previous study were asymptomatic ones. This indicates that PcomA aneurysms with oculomotor nerve palsy, such as symptomatic IAs, might be different from asymptomatic unruptured or ruptured ones, which deserve separate study. Oculomotor nerve palsy is an indication for urgent treatment. This consensus is mainly based on vast clinical observations and physician clinical experience. Statistical analysis of morphologic and hemodynamic parameters revealed that unruptured PcomA aneurysms with oculomotor nerve palsy had almost the same morphologic and hemodynamic characteristics as that of ruptured ones. From this point of view, urgent treatment should be reasonable to prevent severe consequences after aneurysm rupture.

The small sample size is due to the fact that a PcomA aneurysm that has sudden unilateral oculomotor nerve palsy before it ruptures is relatively rare. That was the main limitation of this study. Larger case series are needed for further study and to generalize the result. As a retrospective study, we could not use the patient-specific boundary conditions to perform the CFD simulation. The same and specified initialization settings and inlet boundary conditions made hemodynamic results depend on the geometry of the luminal models. Also, traction-free outlet boundary conditions were another limitation to this study, but proper assump-

tions of outlet boundary conditions must be further investigated.[7,24] In some cases, it was arbitrary to ignore the influence of the poorly developed posterior communicating artery, the diameter of which was <0.5 mm.

CONCLUSIONS

From morphologic and hemodynamic perspectives, we demonstrated that PcomA aneurysms with oculomotor nerve palsy had characteristics similar to those of ruptured ones, except for lower WSS on the aneurysm wall, which might indicate an important role in aneurysm rupture.

ACKNOWLEDGMENTS

We gratefully acknowledge Shanghai Supercomputer Center for their helpful provision of the calculation software. We are also grateful for the generous support of Jianping Xiang from Toshiba Stroke Research Center, State University of New York at Buffalo, Buffalo New York; Shengzhang Wang, from the Department of Mechanics and Engineering Science, Fudan University, Shanghai, China, and Pengfei Luo, from the Department of Burns, Changhai Hospital, Second Military Medical University, Shanghai, China.

REFERENCES

1. Jeong W, Rhee K. **Hemodynamics of cerebral aneurysms: computational analyses of aneurysm progress and treatment.** *Comput Mathematic Methods Med* 2012;2012:782801
2. Sforza DM, Putman CM, Cebral JR. **Hemodynamics of cerebral aneurysms.** *Annu Rev Fluid Mech* 2009;41:91–107
3. Scholtes F, Martin D. **Strategical implications of aneurysmal cranial nerve compression.** *Neuro-Chirurgie* 2012;58:146–55
4. Langner S, Schroeder HW, Hosten N, et al. **[Diagnosing neurovascular compression syndromes].** *RoFo* 2012;184:220–28
5. Shojima M, Oshima M, Takagi K, et al. **Magnitude and role of wall shear stress on cerebral aneurysm: computational fluid dynamic study of 20 middle cerebral artery aneurysms.** *Stroke* 2004;35:2500–05
6. Tremmel M, Dhar S, Levy EI, et al. **Influence of intracranial aneurysm-to-parent vessel size ratio on hemodynamics and implication for rupture: results from a virtual experimental study.** *Neurosurgery* 2009;64:622–30
7. Jou LD, Lee DH, Morsi H, et al. **Wall shear stress on ruptured and unruptured intracranial aneurysms at the internal carotid artery.** *AJNR Am J Neuroradiol* 2008;29:1761–67
8. He X, Ku DN. **Pulsatile flow in the human left coronary artery bifurcation: average conditions.** *J Biomech Eng* 1996;118:74–82
9. Dhar S, Tremmel M, Mocco J, et al. **Morphology parameters for intracranial aneurysm rupture risk assessment.** *Neurosurgery* 2008;63:185–96
10. Cebral JR, Mut F, Weir J, et al. **Quantitative characterization of the hemodynamic environment in ruptured and unruptured brain aneurysms.** *AJNR Am J Neuroradiol* 2011;32:145–51
11. Beck J, Rohde S, Berkefeld J, et al. **Size and location of ruptured and unruptured intracranial aneurysms measured by 3-dimensional rotational angiography.** *Surg Neurol* 2006;65:18–25
12. Saitua F, Acuna R, Herrera P. **Percutaneous endoscopic gastrostomy: the technique of choice?** *J Pediatr Surg* 2003;38:1512–15
13. Xiang J, Natarajan SK, Tremmel M, et al. **Hemodynamic-morphologic discriminants for intracranial aneurysm rupture.** *Stroke* 2011;42:144–52
14. Sforza DM, Putman CM, Scrivano E, et al. **Blood-flow characteristics in a terminal basilar tip aneurysm prior to its fatal rupture.** *AJNR Am J Neuroradiol* 2010;31:1127–31
15. Cebral JR, Hendrickson S, Putman CM. **Hemodynamics in a lethal basilar artery aneurysm just before its rupture.** *AJNR Am J Neuroradiol* 2009;30:95–98
16. Goubergrits L, Schaller J, Kertzscher U, et al. **Statistical wall shear stress maps of ruptured and unruptured middle cerebral artery aneurysms.** *J R Soc Interface* 2012;9:677–88
17. Takao H, Murayama Y, Otsuka S, et al. **Hemodynamic differences between unruptured and ruptured intracranial aneurysms during observation.** *Stroke* 2012;43:1436–39
18. Newby AC. **Metalloproteinase expression in monocytes and macrophages and its relationship to atherosclerotic plaque instability.** *Arterioscler Thromb Vasc Biol* 2008;28:2108–14
19. Galis ZS, Sukhova GK, Lark MW, et al. **Increased expression of matrix metalloproteinases and matrix degrading activity in vulnerable regions of human atherosclerotic plaques.** *J Clin Invest* 1994;94:2493–503
20. Gui T, Shimokado A, Sun Y, et al. **Diverse roles of macrophages in atherosclerosis: from inflammatory biology to biomarker discovery.** *Mediat Inflamm* 2012;2012:693083
21. Chiu JJ, Chien S. **Effects of disturbed flow on vascular endothelium: pathophysiological basis and clinical perspectives.** *Physiol Rev* 2011;91:327–87
22. Zeng Z, Durka MJ, Kallmes DF, et al. **Can aspect ratio be used to categorize intra-aneurysmal hemodynamics? A study of elastase induced aneurysms in rabbit.** *J Biomech* 2011;44:2809–16
23. Xu J, Yu Y, Wu X, et al. **Morphological and hemodynamic analysis of mirror posterior communicating artery aneurysms.** *PloS One.* 2013;8:e55413
24. Castro M, Putman C, Radaelli A, et al. **Hemodynamics and rupture of terminal cerebral aneurysms.** *Acad Radiol* 2009;16:1201–07

Histopathologic Evaluation of Arterial Wall Response to 5 Neurovascular Mechanical Thrombectomy Devices in a Swine Model

B. Gory, D. Bresson, I. Kessler, M.L. Perrin, A. Guillaudeau, K. Durand, S. Ponsonnard, C. Couquet, C. Yardin, and C. Mounayer

ABSTRACT

BACKGROUND AND PURPOSE: Five commercial devices are available for mechanical thrombectomy in acute ischemic stroke. This study evaluated and compared the resultant arterial damage from these devices.

MATERIALS AND METHODS: Wall damage after 4 wall-contact devices (the Merci retriever, Catch thromboembolectomy system, and Solitaire FR revascularization devices of 4 and 6 mm) and 1 aspiration device (the Penumbra System) was evaluated in the superficial femoral arteries of 20 male swine. Each device was tested with and without intraluminal clot. Twenty control vessels were not subjected to any intervention. Acute histopathologic changes were evaluated.

RESULTS: In the device samples, endothelial denudation (72.8 ± 29.4% versus 0.9 ± 1.9%, $P < .0001$), medial layer edema (52 ± 35.9% versus 18.1 ± 27.8%, $P = .004$), and mural thrombus (5.3 ± 14.2% versus 0%, $P = .05$) were found to a greater extent compared with the control samples. The aspiration device provoked more intimal layer (100 ± 79.1% versus 58.8 ± 48.9%, $P = .27$) and medial layer (75 ± 35.4% versus 46.3 ± 34.8%, $P = .13$) edema than the wall-contact devices.

CONCLUSIONS: All devices caused vascular injuries extending into the medial layer. The aspiration device was associated with more intimal and medial layer edema, compared with the wall-contact devices except for the Catch thromboembolectomy system.

ABBREVIATIONS: EEL = external elastic lamina; IEL = internal elastic lamina; MET = mechanical endovascular thrombectomy; SFA = superficial femoral artery

Recanalization is a powerful predictor of stroke outcome in patients with arterial occlusion treated with either IV rtPA or an endovascular approach.[1,2] IV thrombolysis has been limited by its low recanalization rate in the setting of large-artery occlusions,[3] whereas mechanical endovascular thrombectomy devices can result in higher rates of recanalization in patients with stroke with similar proximal arterial occlusions.[4-6] The recanalization rate with MET is approximately 80%, and approximately 40% of patients have a favorable clinical outcome.[7]

A number of new thrombectomy devices have recently been introduced, with varying theoretic mechanisms of action. They can be classified into 2 major groups, according to their mechanism of retrieving the clot. Aspiration devices apply force to the proximal base of the thrombus[6,8]; this group includes various aspiration catheters and systems. Wall-contact devices can be divided into distal devices (brushlike, basketlike, or coil-like devices)[9] and stentlike devices (including various self-expandable stent retrievers).[10] With both types, the force is applied to the distal base of the clot. So far, to our knowledge, no systematic study has been performed comparing various MET devices under standardized conditions in vivo, in terms of arterial wall response (MEDLINE data base research by using the terms "endovascular," "mechanical thrombectomy," "clot removal," "arterial wall," and "animal model").

The purpose of this study was to evaluate and compare arterial wall responses to 5 neurovascular mechanical thrombectomy devices: 4 wall-contact devices (the Merci retriever; Concentric Medical, Mountain View, California; the Catch thromboembolectomy system; Balt, Montmorency, France; and the Solitaire FR revascularization devices, 4 and 6 mm; Covidien, Irvine, California) and 1 aspiration device (Penumbra System; Penumbra, Alameda, California).

MATERIALS AND METHODS

Animal Care

All procedures were conducted according to international guidelines and were approved by the responsible local authorities.

Received September 9, 2012; accepted after revision January 3, 2013.

From the Departments of Interventional Neuroradiology (B.G., D.B., C.M.), Anatomopathology (M.L.P., A.G., K.D.), Cytology (C.Y.), and Anesthesiology (S.P.), Le Centre Hospitalier et Universitaire (CHU) de Dupuytren, Limoges, France; Department of Interventional Neuroradiology (I.K.), University of Brasilia Faculty of Medicine, Campus Universitário Darcy Ribeiro, Brasilia, Brazil; and Haute-Vienne Research and Analysis Department (C.C.), Limoges, France.

This work was supported by MicroVention Inc.

Please address correspondence to Charbel Mounayer, MD, PhD, Department of Interventional Neuroradiology, CHU Dupuytren, 2 Ave Martin Luther King, Limoges, France; e-mail: cmounayer@hotmail.com

http://dx.doi.org/10.3174/ajnr.A3531

Table 1: Neurovascular thrombectomy devices

Description	Solitaire FR 4 mm	Solitaire FR 6 mm	Catch	Merci Retriever V 2.5 Firm	Penumbra 0.32
Recommended guide catheter (F)	6	6	6	9	6
Microcatheter (F)	2.4	2.8	2.4	2.4	3.4
Element design	Stent retriever	Stent retriever	Basket-like	5 Helical loops	Aspiration
Outer diameter (mm)	4	6	4	2.5	Not described
Length (mm)	20	20	18	6	30
Recommended vessel diameter (mm)	2.0–4.0	3.0–5.5	≤4	2.0–3.5	2.0–3.0

Note:—F indicates French.

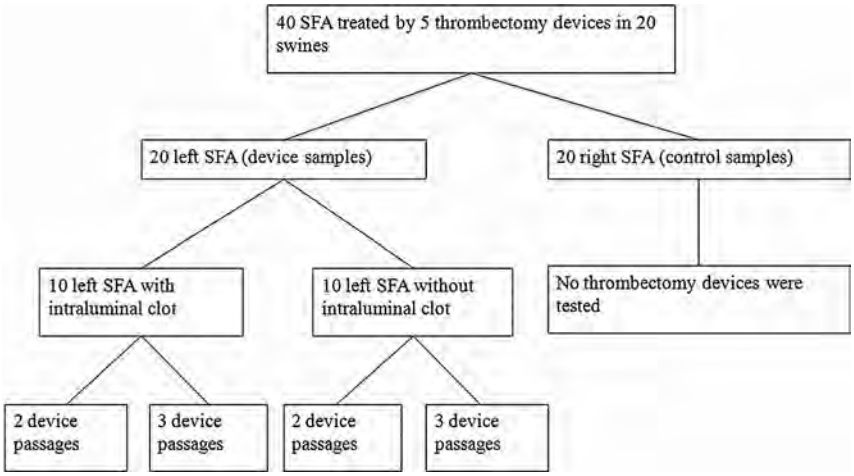

FIG 1. Study protocol.

Twenty male swine ranging from 20 to 25 kg (Haute-Vienne Research and Analysis Department, Haute-Vienne, France) were used in this study. The procedures were conducted with the swine under general anesthesia. No further heparin bolus or other thrombolytic drugs were administered. Further details are described in previous studies.[9] Vital parameters, such as arterial blood pressure, heart rate, and carbon dioxide levels, were continuously recorded. Expired carbon dioxide levels were maintained at 30–35 mm Hg. One hour after the end of the last retrieval, the animals were euthanized.

Description of the Neurovascular Thrombectomy Devices

We tested 5 devices: 4 wall-contact devices and 1 aspiration device. Their properties are summarized in Table 1. The wall-contact devices were the following:

- Two Solitaire FR revascularization devices: diameters of 4 and 6 mm (Solitaire FR 4 mm and Solitaire FR 6 mm). These are self-expanding, closed-cell nitinol stent devices that can be fully deployed and fully resheathed, and their design allows immediate blood-flow restoration and clot retrieval.
- The Catch thromboembolectomy system consists of a self-expanding, basketlike device that has a maximum diameter of 4 mm and is fixed to a pusher wire. After the microcatheter, equipped with a microwire (SilverSpeed 14; ev3, Irvine, California), was placed in the common femoral artery, the microcatheter was navigated into the occluded vessel, past the thrombus. The basket was deployed distal to the thrombus. Then both the basket and the microcatheter were pulled back, simultaneously, into the guiding catheter.
- The Merci retrieval system is a tapered wire with 5 helical loops of decreasing diameter at its distal end. In this study, the Merci retriever V 2.5 Firm was used, with a maximal loop diameter of 2.5 mm. The microcatheter was advanced beyond the thrombus. Both the microcatheter and the Merci retriever were pulled back to contact the thrombus, and the remaining loops were deployed within the thrombus. During retrieval, aspiration was applied through the guide catheter, by using a 50-mL syringe.

The aspiration device was the Penumbra System 0.32 (Penumbra). This is a platform that includes a reperfusion microcatheter connected to an aspiration pump via aspiration tubing, generating a suction force of 0.9 bar (700 mm Hg). When the microcatheter tip was placed in contact with the thrombus, the aspiration was applied during the clot fragmentation by using a separator.

Clot Preparation

Radiopaque clots were prepared in vitro, as recently described by Kan et al.[11] In brief, 20 mL of whole blood was mixed with 2 g of barium sulfate powder to obtain radiopacity, and the mixture in the syringe was incubated at room temperature for 120 minutes. The solid component was separated from the serum component, and a piece of clot was resected. Each prepared thrombus, which measured 25 mm in length, was inserted into a Cole-Parmer silicone tube (Vernon Hills, Illinois) with saline and was prepared for injection.

Study Protocol

The protocol is detailed in Fig 1. Twenty swine had their superficial femoral arteries dissected bilaterally. The 20 right SFA samples were not subjected to any kind of intervention (control samples). The 20 left SFA samples were randomly submitted to thrombectomy with 1 of the 5 devices (device samples) (Fig 2*A*). Ten of the samples had an intraluminal clot, and 10 were normally patent. Each device was retrieved 2 times (2 passages) or 3 times (3 passages), resulting in 4 target arteries per device.

Concerning the aspiration system, the clot retrieval was conducted according to 2 scenarios: 100 and 200 passages of the fragmentation separator under aspiration of 0.9 bar (similar to the clinical use).

Angiography and Clot Placement

A short 6F catheter sheath (Terumo, Tokyo, Japan) was inserted into the right common femoral artery and continuously flushed with

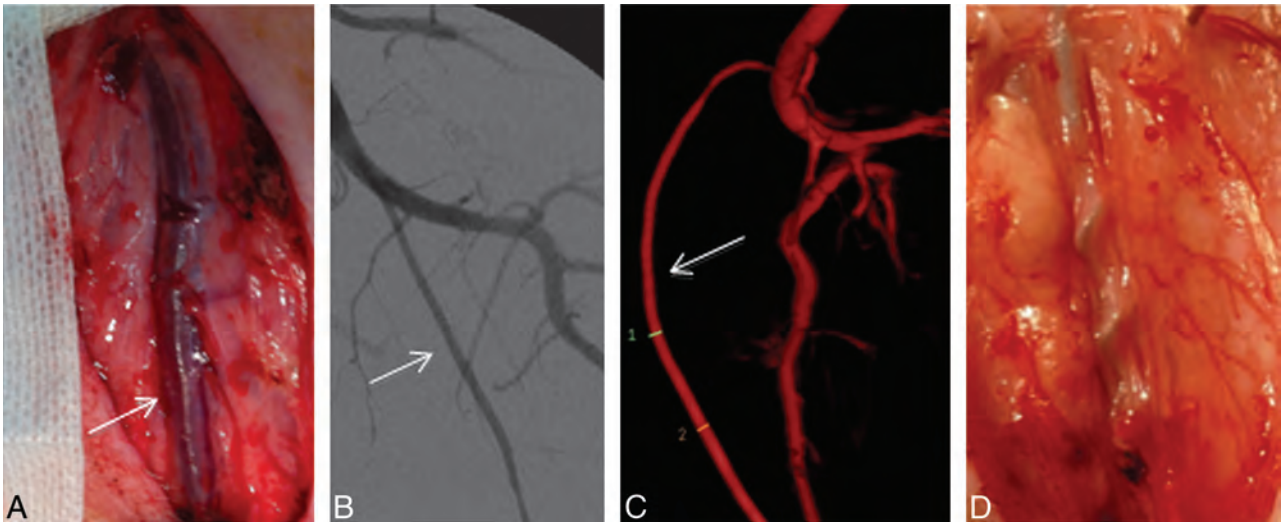

FIG 2. Mechanical endovascular thrombectomy in the left SFA by using the Merci retrieval system. *A*, Photograph shows the superficial position of the left SFA (*arrow*), allowing easy resection. *B*, Anteroposterior angiogram of the left SFA (*arrow*). *C*, 3D reconstruction of the SFA (*arrow*). Note the size (inner diameter, 2.7–2.9 mm) of this artery, which reproduces the characteristics of proximal intracranial arteries, such as the MCA or basilar artery. *D*, Photograph shows the extension of the Merci retrieval system inserted into the vessel lumen.

physiologic saline. A 6F guiding catheter (Neuropath guiding catheter; DePuy, Raynham, Massachusetts) was introduced and continuously flushed with physiologic saline. Angiography of the left SFA was performed on a biplane system (Integris; Philips, Best, the Netherlands) (Fig 2*B*). Rotational angiography, followed by 3D reconstruction of the native projections (Fig 2*C*), was performed just before the thrombectomy procedure was begun. The diameters of the vessels were measured in 3D reconstruction images.

For selective thromboembolization, the preformed thrombus was injected into a 5F guide catheter (Chaperon; MicroVention, Aliso Viejo, California) positioned in the left SFA. After connecting the silicone tube containing a prepared clot into the guiding catheter, we injected 2 mL of saline into the tube to propel the clot into the catheter. The clot migrated to the SFA to achieve the occlusion. After an angiogram had been obtained to document occlusion, the guiding catheter was retrieved. The occlusion was maintained for 1 hour (± 30 minutes) before mechanical retrieval was attempted (Fig 2*D*).

All procedures were performed with the swine under general anesthesia through a 6F guiding catheter placed in the left SFA. The retrieval attempts were conducted according to the requirements of the manufacturers. During retrieval, only the microwire, microcatheter, and device entered the target vessel. For repeated attempts, the devices were cleaned, inspected, and, if still intact, reinserted.

Study End Point

The protocol was strictly designed to assess the degree of vascular damage. The recanalization rate, time to achieve recanalization, vasospasm, arterial perforation, and distal embolism were not evaluated.

Histopathologic Evaluation

Both of the SFAs were dissected away from the surrounding tissue, and each was cut transversely into 6 individual pieces, numbered proximally to distally, with regard to arterial blood flow. The most proximal and distal 2 cm of the SFAs were excluded to avoid ligature sites occurring during surgery. The vessel sections from each artery were processed and embedded in paraffin, according to standard laboratory operating procedures. They were subsequently sectioned at 5–7 μm and stained with hematoxylin-eosin and orcein (elastic fibers). The sections were examined with an optical microscope by using magnification ranging from 40 to 400 times by 2 independent board-certified pathologists who were blinded to the device used (A.G. and C.Y., who had 5 and 21 years of experience, respectively).

A grading system to evaluate the acute mural response to the MET devices was developed (Fig 3). We assessed the following: 1) amount of endothelial denudation (percentage of surface area), 2) presence of mural thrombus (vascular occlusion percentage), 3) intimal layer edema (inner intima circumference percentage), 4) medial layer edema (inner media circumference percentage), and 5) internal elastic lamina fracture (percentage).

Statistical Analysis

The data from the histologic grading were independently analyzed by using SAS, Version 9.1.3 (SAS Institute, Cary, North Carolina). The statistical differences in arterial damage grades among the 5 devices were analyzed by the Mann-Whitney test. A P value $< .05$ was considered significant.

RESULTS

Forty SFAs with diameters of 2.0–3.5 mm from 20 swine were studied. The model of arterial occlusion was effective in all target vessels. The five devices were applied to 20 vessels (4 vessels each)—2 with clots and 2 without—and they were successfully retrieved in every case.

Histopathologic Results

All of the MET devices caused lesions, which extended from the intimal layer to the medial layer. In the device samples versus the control samples, these were characterized by significant endothelial denudation and medial layer edema (Table 2). Intimal layer edema and fracture of the IEL were also found in all of the device samples but with insignificant differences for all device samples combined compared with the control samples. No other lesions were found deeper in the external elastic lamina or adventitia, nor were there perforations or dissections in any samples.

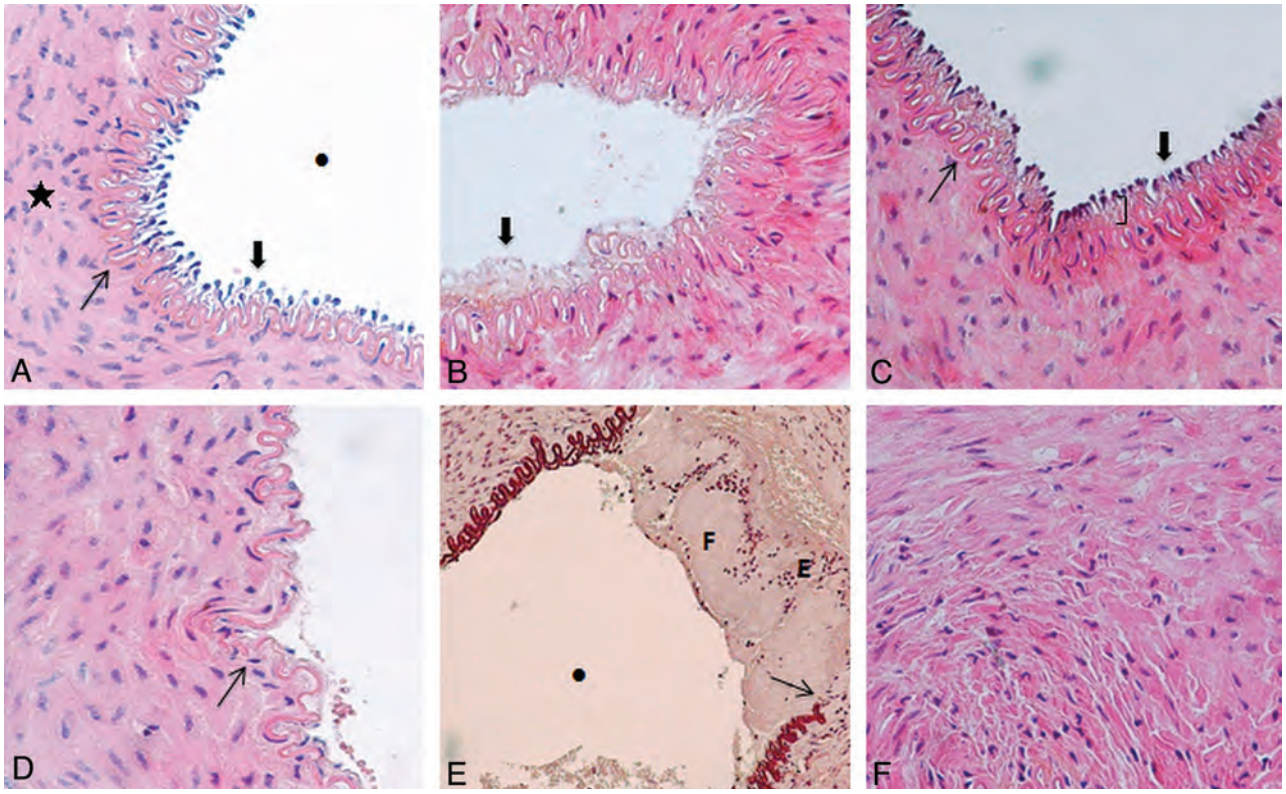

FIG 3. Histopathologic grading systems. *A*, Microscopic view of a right SFA (control sample) (hematoxylin-eosin [HE] staining, original magnification × 400) demonstrates well-maintained tissue integrity throughout the internal layers of the vessel. Endothelial cells (*thick arrow*) protruded toward the vascular lumen (*dot*), and the IEL (*thin arrow*) is intact. The medial layer (*star*) has homogeneous layers of smooth muscle cells. *B*, Microscopic view of a left SFA (device sample) (HE staining, original magnification × 400) shows total denudation of the endothelium (*thick arrow*) (100% of the surface area). *C*, Microscopic view of a left SFA (device sample) (HE staining, original magnification × 400) shows focal intimal thickening (parentheses) due to edema. Endothelial cells (*thick arrow*) and the IEL (*thin arrow*) are intact. *D*, Microscopic view of a left SFA (device sample) (HE staining, original magnification × 400) shows a focal fracture (*thin arrow*) of the IEL and denudation of the endothelium. *E*, Microscopic view of a left SFA (device sample) (orcein staining, original magnification × 200) demonstrates a fracture of the IEL (*thin arrow*) and mural thrombus with a layered pattern including both fibrin-rich (*F*) and erythrocyte-rich (*E*) layers. The mural thrombus does not compromise the lumen of the vessel (*dot*). *F*, Microscopic view of a left SFA (device sample) (HE staining, original magnification × 400) demonstrates edema within the media layer visualized as interstitial infiltration among smooth-muscle cells.

Table 2: Comparison of arterial damage in the device and control samples[a]

	Solitaire 4 Samples (*n* = 4)	Solitaire 6 Samples (*n* = 4)	Catch Samples (*n* = 4)	Merci Retriever Samples (*n* = 4)	Penumbra Samples (*n* = 4)	All Device Samples (*n* = 20)	Control Samples (*n* = 20)	*P* Value[b]
Mural thrombus (%)	14.1 ± 28.1	0	9.4 ± 15.6	3.1 ± 6.2	0	5.3 ± 14.2	0	.05
Endothelial denudation (%)	85.8 ± 22.9	76.2 ± 12.8	76.1 ± 21.2	85.9 ± 12.1	40.1 ± 47.6	72.8 ± 29.4	0.9 ± 1.9	.0001
Intimal layer edema (%)	43.8 ± 51.5	81.3 ± 65.7	43.8 ± 37.5	66.5 ± 47.1	100 ± 89.1	67 ± 56.2	44.6 ± 43.6	.25
IEL fractured (%)	12.5 ± 14.4	25 ± 35.4	18.8 ± 23.9	50 ± 100	12.5 ± 14.4	23.7 ± 46.2	20.6 ± 33.3	.78
Medial layer edema (%)	25 ± 0	37.5 ± 43.3	81.3 ± 23.9	41.5 ± 35.2	75 ± 35.4	52 ± 35.9	18.1 ± 27.8	.004
EEL fractured (%)	0	0	0	0	0	0	0	Not applicable
Adventitia edema (%)	0	0	0	0	0	0	0	Not applicable

[a] Data are means +/− standard deviations.

[b] Mann-Whitney test comparing all device samples combined with control samples.

There were no statistically significant differences in the arterial damage among the 5 device groups. However, the aspiration device (Fig 4) created less endothelial denudation and mural thrombus than the wall-contact device samples (Fig 5), but more intimal and medial layer edema, though none of these differences were significant (Table 3).

Mural Thrombus

Overall, the MET devices caused more mural thrombus in the arterial lumen of the device samples compared with control samples (Table 2). Three MET devices (the Solitaire FR 4 mm, Merci retrieval system, and Catch thromboembolectomy system) caused mural thrombus after their use, but the Penumbra system and Solitaire FR 6 mm did not.

Intraluminal Clot

There was a predominance of intimal layer edema in arteries without intraluminal clots, compared with the clotted ones, but there were no other significant histopathologic differences (Table 4).

Number of Attempts

For each device, 2 and 3 retrieval attempts were performed in samples both with and without a clot (resulting in 4 procedures per device). The

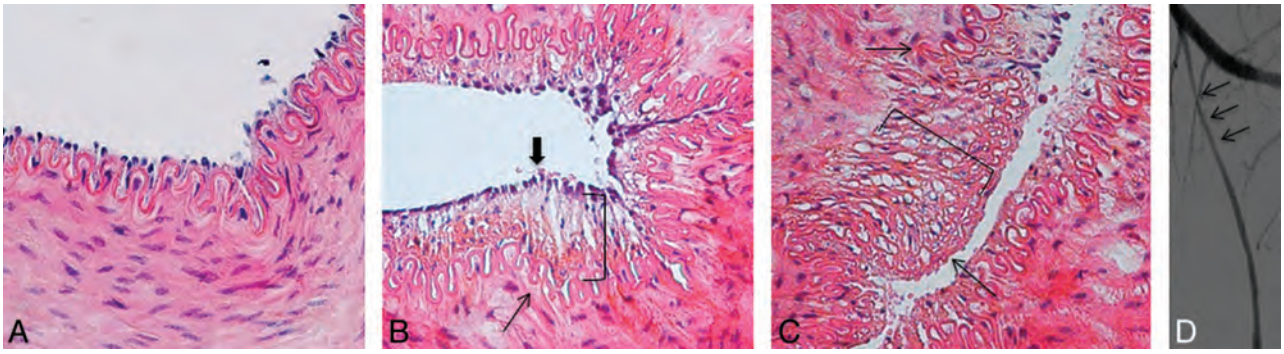

FIG 4. Histopathologic findings after mechanical thrombectomy by using the Penumbra system. *A*, Microscopic view of a right SFA (control sample) shows all layers preserved (hematoxylin-eosin [HE] staining, original magnification × 400). *B* and *C*, Microscopic view of a left SFA demonstrates the intact internal elastic lamina (*thin arrow*) and a single layer of endothelial cells (*thick arrow*). The parentheses show edema of the subendothelial layer in *B* and the medial layer in *C*. There is no thrombus (HE staining, original magnification × 400). *D*, Anteroposterior angiogram of the left SFA immediately after thrombectomy shows moderate diffuse vasospasm (*thin arrows*).

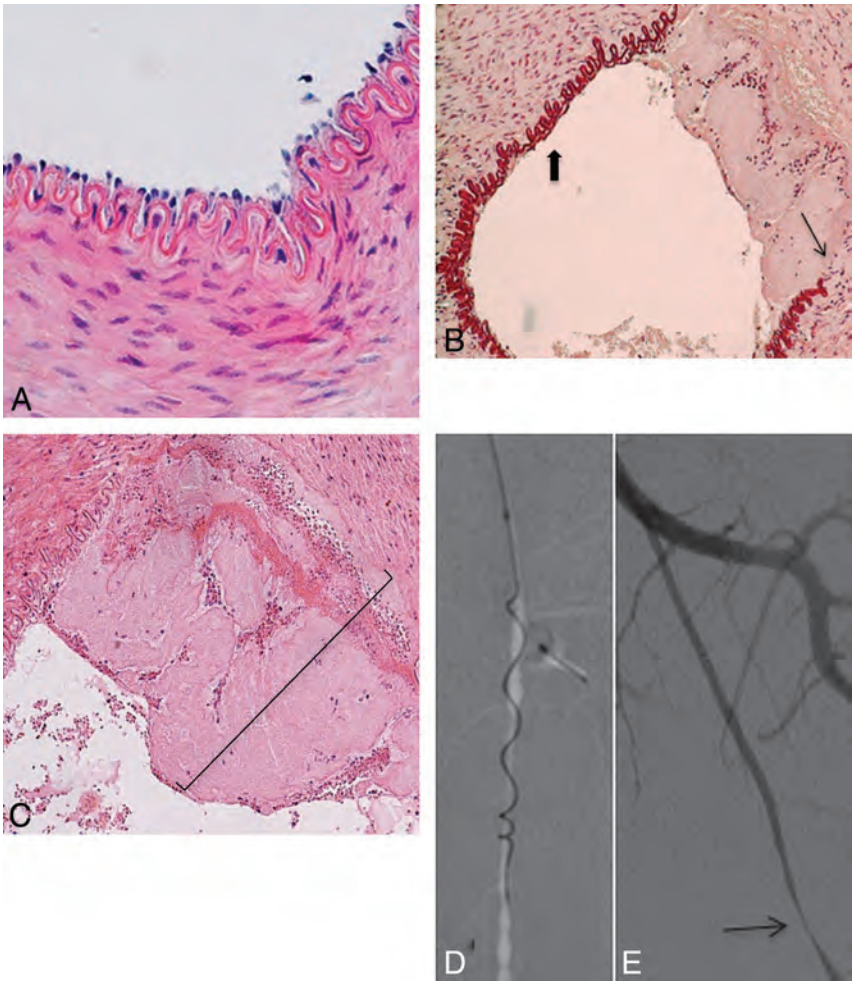

FIG 5. Histopathologic findings after mechanical thrombectomy by using the Catch thromboembolectomy system. *A*, Microscopic view of a right SFA (control sample) shows all layers preserved (hematoxylin-eosin [HE] staining, original magnification × 400). *B*, Microscopic view of a left SFA demonstrates the denudation of endothelial cells (*thick arrow*) and the broken IEL (*thin arrow*) (orcein staining, original magnification × 200). *C*, Microscopic view of a left SFA shows a mural clot (parentheses) and the IEL fractured. (HE staining, original magnification × 200). *D*, Anteroposterior angiogram of the left SFA shows the Merci clot device during the retrieval. *E*, Anteroposterior angiogram of the left SFA immediately after thrombectomy demonstrates focal stenosis (*thin arrow*).

mean arterial damage for each retrieval attempt with and without clot is summarized in Table 4. The number of attempts with each device in both groups of arteries (with and without clot) did not influence the histopathologic results; there was no statistical difference shown, but variability was large and sample sizes were small.

DISCUSSION

The approved medical therapy in acute ischemic stroke is IV rtPA within 4.5 hours.[12] Recently, mechanical thrombectomy has been demonstrated to successfully restore large-vessel patency and therefore provide an alternative and synergistic method for flow restoration.[4-6,10,13,14] Thrombectomy devices offer many potential advantages over pharmacologic thrombolysis, including more rapid achievement of recanalization, enhanced efficacy in treating large-vessel occlusions, and a potentially lower risk for hemorrhagic events.[15] However, mechanical manipulation of a thrombus in intracranial arteries might cause complications such as vasospasm, dissection, or perforation and may worsen clinical outcome at discharge.[16,17]

Nonetheless, arterial wall changes after endovascular treatment with mechanical devices in acute stroke are poorly reported and compared. There are no standards to evaluate such devices. The first in vivo model dedicated to MET in ischemic stroke was reported by Gralla et al.[18] It permits an angiographic evaluation and comparison of neurovascular mechanical thrombectomy devices.[9,19-21] However, no study has evaluated the histopathologic responses induced by devices, to our knowledge. Recently, a model has been specifically developed in swine, by using the superficial cervical artery to evaluate arterial structural changes.[22] Compared with this model, surgical access to swine SFA is not technically difficult, due to its superficial

Table 3: Comparison of arterial damage by the wall-contact devices and the aspiration device[a]

	Wall-Contact Devices (n = 16)	Aspiration System (n = 4)	P Value[b]
Mural thrombus (%)	6.6 ± 15.7	0 ± 0	.28
Endothelial denudation (%)	81.0 ± 16.8	40.1 ± 47.5	.15
Intimal layer edema (%)	58.8 ± 48.9	100 ± 79.1	.27
IEL fractured (%)	26.6 ± 51.2	12.5 ± 14.4	.92
Medial layer edema (%)	46.3 ± 34.8	75 ± 35.4	.13

[a] Data are means +/− standard deviations.
[b] Mann-Whitney test comparing wall-contact device samples combined with aspiration system (Penumbra) samples.

position. The normal histologic characteristics of the porcine femoral artery are well known[23] and raise the possibility of evaluating pathologic lesions. In a postmortem study of 5 patients who died acutely after MET procedures, vascular pathologic abnormalities affecting the proximal arteries were variable, but 1 patient (20%) showed a subintimal dissection with resultant occlusion of the middle cerebral artery.[24] In the current study, 5 mechanical devices (4 wall-contact devices and 1 aspiration device) were evaluated and the grading scale analyzing the acute extent of the injury caused by the device (from the inner layer to the adventitia layer) and the presence of swelling or an intraluminal thrombus were reported.

It was observed that the devices caused significant endothelial and medial damage to the vessel walls. Intimal and subintimal damage seemed higher, but no intimal dissection was found histologically. Little is known about the response of the arterial wall after mechanical thrombectomy, partly due to limited angiographic/histologic data from the treated arteries. Recently, an angiographic follow-up study in 261 patients with 265 embolic vessel occlusions revealed 26.0% vasospasm and 0.4% dissection in the acute phase.[25] On follow-up, 0.9% target-vessel occlusion and 3.4% of de novo stenosis were reported. These data may suggest that arterial wall injuries are probably reversible in the long term.

The aspiration device was responsible for more intimal and medial layer edema. However, these differences were not statistically significant, though this result could be due to the small animal sample. These results are probably related to the fact that the designs and mechanisms of these 2 types of devices are completely different. The aspiration device applies aspiration force to the proximal base of the thrombus.[6,8,9] As opposed to this suction device, wall-contact devices capture the clot by exerting continuous radial force against the vessel wall, which may injure the endothelium in the process.[9,10] These devices can lead to diverse effects on the vascular wall, as described in this article. These findings are in accordance with the animal study by Gralla et al,[9] in which histologic findings were not reported. The authors compared the in vivo effectiveness and thrombus/device interaction of a proximal approach (such as the Penumbra system) and a distal approach (such as the Catch thromboembolectomy system). The authors found that the former appeared to reduce irritation in the vessel wall, thus lowering the risk and severity of vasospasm, because it does not require repositioning and passing procedures.[9]

An important finding was the presence of less arterial wall damage in vessels with clots. The clot samples had significantly less intimal layer edema than those without clots (35 ± 33.4% versus 99.11 ± 57%, P = .009). Regarding these results, we deduced that the length of the device should be close to the length of the clot, to reduce the lesions on the wall. Also, wall damage was not significantly increased when the devices were passed 3 times rather than twice.

Another point was the presence of a mural thrombus in the vessel walls submitted to 3 of the wall-contact devices, specifically the Merci retrieval system, the Catch thromboembolectomy system, and the Solitaire FR 4 mm. However, the lesion was limited to the intimal layer attached to the endothelium, and it was not associated with significant reduction of the arterial lumen. The Solitaire FR 6 mm device caused less endothelial damage and no mural thrombus compared with the Solitaire FR 4 mm device. The Solitaire FR 6 mm exerts a greater radial force at all diameters compared with the Solitaire FR 4 mm. The increased intimal tearing could be attributed to the greater length of the Solitaire FR 4 mm (31.8 versus 26.2 mm),[21] having more surface area in contact with the vessel wall. Thus radial force could be considered a less important contributor to arterial wall injury.

Because this study was restricted to the acute phase, performing further studies at later stages—subacute and chronic—would be of great value to identify the progression of these lesions. Previous research has shown that the extent and depth of the vascular lesion may be contributing factors in promoting early atherosclerotic and accelerated hyperplastic intimal and medial changes.[26] Large areas of endothelial denudation without substantial medial trauma caused only mild intimal thickening, whereas focal endothelial denudation with substantial medial trauma produces marked delayed intimal thickening.[27] These results are substantiated by those of other studies that have shown that smooth muscle cells are normally quiescent with respect to proliferation but that deep injuries result in the expression of a phenotype of vascular smooth-muscle cells that exhibits a high proliferative response to other mitogens.[28]

Given these results, the aspiration device resulted in a less traumatic acute injury in the vascular wall. However, this study did not analyze the vascular recanalization rate; therefore, deducing

Table 4: Comparison of arterial damage by the device samples according to the presence or absence of a clot and the number of retrievals[a]

	With Clot (10 Samples)	Without Clot (10 Samples)	P Value[b]	Two Retrievals (10 Samples)	Three Retrievals (10 Samples)	P Value[c]
Mural thrombus (%)	0.5 ± 1.6	10.1 ± 19.3	.21	3.2 ± 10.3	7.3 ± 17.6	.31
Endothelial denudation (%)	81.8 ± 18.9	63.8 ± 35.8	.25	68.9 ± 28.8	76.6 ± 30.0	.41
Intimal layer edema (%)	35 ± 33.4	99.1 ± 57	.009	84.1 ± 62.8	50 ± 45.6	.24
IEL fractured (%)	10 ± 17.5	37.5 ± 61.5	.18	40 ± 61.5	7.5 ± 12.1	.27
Medial layer edema (%)	45 ± 43.8	59.1 ± 26.5	.44	56.6 ± 37	47.5 ± 36.2	.58

[a] Data are means +/− standard deviations.
[b] Mann-Whitney test for samples with versus without clots.
[c] Mann-Whitney test for 2 versus 3 retrievals.

that the aspiration device would have better functional results is not appropriate. These findings warrant further study of these devices in a model with a longer follow-up.

We acknowledge several limitations of the current study and proposed animal model, as with any in vivo experimental model. First, the swine SFAs are less tortuous without atherosclerosis compared with intracranial arteries in humans. Second, the present study compared arterial wall responses in 5 mechanical thrombectomy devices uncorrelated with their angiographic efficacy. We can imagine that 1 passage may suffice with stent retrievers, while many more passages may be necessary with aspiration devices. It is probably total injuries for effective recanalization that count. Another limitation is that endothelial denudation is difficult to quantify with routine pathologic stains. Further methodologic limitations of the study are the small number of experiments per device and the lack of follow-up angiographic and pathologic data to assess whether damage leads to stenosis. In addition, because of the differences in the arterial wall (lack of adventitia in intracranial arteries), the histologic results of this model may not be applicable to cerebral arteries in clinical practice. Our new model does not represent a counterpart to the entire phenomenon seen in patients with stroke. However, we believe that it may expand the analysis of the safety profile and offer the possibility of an experimental model for the preclinical development and evaluation of mechanical devices.

CONCLUSIONS

We have demonstrated in this swine model that both the aspiration device and the wall-contact devices caused vascular injuries extending into the medial layer. However, it would appear that the aspiration device was associated with more intimal and medial-layer edema, compared with the wall-contact devices except for the Catch thromboembolectomy system.

ACKNOWLEDGMENTS

We thank Heath Bowman, MSc, for assistance in the concept and design of the study and the provision of thrombectomy devices, and Karine Durand, PhD, for her statistical assistance.

Disclosures: Sebastien Ponsonnard—*UNRELATED: Payment for Manuscript Preparation*: web-anesthesie.fr (Wolters-Kluwer), *Comments*: about a lung sonography article. Charbel Mounayer—*UNRELATED: Consultancy*: MicroVention,* *Expert Testimony*: MicroVention. *Money paid to the institution.

REFERENCES

1. Mazighi M, Serfaty JM, Labreuche J, et al. **Comparison of intravenous alteplase with a combined intravenous-endovascular approach in patients with stroke and confirmed arterial occlusion (RECANALISE study): a prospective cohort study.** *Lancet Neurol* 2009;8:802–09
2. Rha JH, Saver JL. **The impact of recanalization on ischemic stroke outcome: a meta-analysis.** *Stroke* 2007;38:967–73
3. del Zoppo GJ, Poeck K, Pessin MS, et al. **Recombinant tissue plasminogen activator in acute thrombotic and embolic stroke.** *Ann Neurol* 1992;32:78–86
4. Smith WS, Sung G, Starkman S, et al. **Safety and efficacy of mechanical embolectomy in acute ischemic stroke: results of the MERCI trial.** *Stroke* 2005;36:1432–38
5. Smith WS, Sung G, Saver J, et al. **Mechanical thrombectomy for acute ischemic stroke: final results of the Multi MERCI trial.** *Stroke* 2008;39:1205–12
6. Penumbra Pivotal Stroke Trial Investigators. **The Penumbra pivotal stroke trial: safety and effectiveness of a new generation of mechanical devices for clot removal in intracranial large vessel occlusive disease.** *Stroke* 2009;40:2761–68
7. Rouchaud A, Mazighi M, Labreuche J, et al. **Outcomes of mechanical endovascular therapy for acute ischemic stroke: a clinical registry study and systematic review.** *Stroke* 2011;42:1289–94
8. Bose A, Henkes H, Alfke K, et al. **The Penumbra system: a mechanical device for the treatment of acute stroke due to thromboembolism.** *AJNR Am J Neuroradiol* 2008;29:1409–13
9. Gralla J, Schroth G, Remonda L, et al. **Mechanical thrombectomy for acute ischemic stroke: thrombus-device interaction, efficiency, and complications in vivo.** *Stroke* 2006;37:3019–24
10. Roth C, Papanagiotou P, Behnke S, et al. **Stent-assisted mechanical recanalization for treatment of acute intracerebral artery occlusions.** *Stroke* 2010;41:2559–67
11. Kan I, Yuki I, Murayama Y, et al. **A novel method of thrombus preparation for use in a swine model for evaluation of thrombectomy devices.** *AJNR Am J Neuroradiol* 2010;31:1741–43
12. Bluhmki E, Chamorro A, Dávalos A, et al. **Stroke treatment with alteplase given 3.0–4.5 h after onset of acute ischaemic stroke (ECASS III): additional outcomes and subgroup analysis of a randomised controlled trial.** *Lancet Neurol* 2009;8:1095–102
13. Castaño C, Dorado L, Guerrero C, et al. **Mechanical thrombectomy with the Solitaire AB device in large artery occlusions of the anterior circulation: a pilot study.** *Stroke* 2010;41:1836–40
14. Costalat V, Machi P, Lobotesis K, et al. **Rescue, combined, and standalone thrombectomy in the management of large vessel occlusion stroke using the Solitaire device: a prospective 50-patient single-center study: timing, safety, and efficacy.** *Stroke* 2011;42:1929–35
15. Leary MC, Saver JL, Gobin YP, et al. **Beyond tissue plasminogen activator: mechanical intervention in acute stroke.** *Ann Emerg Med* 2003;41:838–46
16. Gupta R. **Arterial vasospasm during mechanical thrombectomy for acute stroke.** *J Neuroimaging* 2009;19:61–64
17. Shi ZS, Liebeskind DS, Loh Y, et al. **Predictors of subarachnoid hemorrhage in acute ischemic stroke with endovascular therapy.** *Stroke* 2010;41:2775–81
18. Gralla J, Schroth G, Remonda L, et al. **A dedicated animal model for mechanical thrombectomy in acute stroke.** *AJNR Am J Neuroradiol* 2006;27:1357–61
19. Brekenfeld C, Schroth G, El-Koussy M, et al. **Mechanical thromboembolectomy for acute ischemic stroke: comparison of the Catch thrombectomy device and the Merci retriever in vivo.** *Stroke* 2008;39:1213–19
20. Mordasini P, Hiller M, Brekenfeld C, et al. **In vivo evaluation of the Phenox CRC mechanical thrombectomy device in a swine model of acute vessel occlusion.** *AJNR Am J Neuroradiol* 2010;31:972–78
21. Mordasini P, Frabetti N, Gralla J, et al. **In vivo evaluation of the first dedicated combined flow-restoration and mechanical thrombectomy device in a swine model of acute vessel occlusion.** *AJNR Am J Neuroradiol* 2011;32:294–300
22. Yuki A, Kan I, Golshan A, et al. **A swine model to analyze arterial structural changes induced by mechanical thrombectomy.** *AJNR Am J Neuroradiol* 2013;34:E87–90
23. Solanes N, Rigol M, Ramirez J, et al. **Histological basis of the porcine femoral artery for vascular research.** *Anat Histol Embryol* 2005;34:105–11
24. Yin NS, Benavides S, Starkman S, et al. **Autopsy findings after intracranial thrombectomy for acute ischemic stroke: a clinicopathologic study of 5 patients.** *Stroke* 2010;41:938–47
25. Chidi CC, DePalma RG. **Atherogenic potential of the embolectomy catheter.** *Surgery* 1978;83:549–57
26. Kurre W, Pérez MA, Horvath D, et al. **Does mechanical thrombectomy in acute embolic stroke have long-term side effects on intracranial vessels? An angiographic follow-up study.** *Cardiovasc Intervent Radiol* 2012 Oct 20. [Epub ahead of print]
27. Walker LN, Ramsay MM, Bowyer DE. **Endothelial healing following defined injury to rabbit aorta: depth of injury and mode of repair.** *Atherosclerosis* 1983;47:123–30
28. Grünwald J, Haudenschild CC. **Intimal injury in vivo activates vascular smooth muscle cell migration and explant outgrowth in vitro.** *Arteriosclerosis* 1984;4:183–88

Are Routine Intensive Care Admissions Needed after Endovascular Treatment of Unruptured Aneurysms?

A.M. Burrows, A.A. Rabinstein, H.J. Cloft, D.F. Kallmes, and G. Lanzino

ABSTRACT

SUMMARY: Routine intensive care unit monitoring is common after elective embolization of unruptured intracranial aneurysms. In this series of 200 consecutive endovascular procedures for unruptured intracranial aneurysms, 65% of patients were triaged to routine (non-intensive care unit) floor care based on intraoperative findings, aneurysm morphology, and absence of major co-morbidities. Only 1 patient (0.5%) required subsequent transfer to the intensive care unit for management of a perioperative complication. The authors conclude that patients without major co-morbidities, intraoperative complications, or complex aneurysm morphology can be safely observed in a regular ward rather than being admitted to the intensive care unit.

ABBREVIATION: ICU = intensive care unit

The number of unruptured intracranial aneurysms treated in the past 2 decades has increased with advances in endovascular techniques and imaging.[1] This has resulted in increased hospital resource utilization and increasing costs.[2] There are no guidelines as to the postoperative disposition of patients after endovascular coil embolization of unruptured intracranial aneurysms, yet intensive care unit (ICU) admissions are common after these procedures. We report the results of a policy of selective ICU admission after elective aneurysm treatment.

MATERIALS AND METHODS

Institutional review board approval was obtained for data collection. A prospective, consecutive series of patients treated for unruptured intracranial aneurysms by the senior author was created. Information collected included patient demographics, presentation, aneurysm size, location, treatment, admission (floor or ICU), change of care level, 24-hour complications, and 30-day follow-up. Institutional protocols regarding postsurgical care are listed in the On-line Appendix. The senior author determined the disposition of each patient on the basis of criteria outlined in Table 1. Patient records were dichotomized to floor and ICU groups and compared. Continuous independent variables, including age, aneurysm size, and length of stay, were compared with unpaired Student *t* tests. Independent categoric values, including anterior circulation and presentation (incidental, unrelated SAH, or symptomatic), were compared by means of χ^2 analysis.

RESULTS

Two hundred consecutive endovascular embolization procedures for unruptured aneurysms were performed in 178 patients. After 131 (65.2% of 200) procedures, patients were admitted to a neurosurgical floor (Fig 1). After 69 (34.8%) of 200 procedures, patients were admitted to the ICU for the following reasons: intraoperative complications (n = 16, 23%), investigational device (n = 14, 20%), aneurysmal morphology (n = 26, 38%), and medical co-morbidities (n = 13, 19%). Among all the patients, 79% were women, 18% had aneurysms discovered after SAH from another aneurysm more than 30 days previously, 27% had symptomatic aneurysms, and 55% had incidental aneurysms (On-line Appendix). The most common locations were internal carotid (47%) and basilar (13%) arteries. Sixty-eight percent of the aneurysms were small, 25% large, and 7% giant. Treatments included coil embolization (62%) and Pipeline Embolization Device (Covidien, Irvine, California) (25.5%). Further information regarding aneurysm location and treatments are listed in the On-line Appendix.

Patients admitted to the ICU had larger aneurysms than those who went to the floor (12.6 ± 9.2 mm versus 7.7 ± 4.7 mm, $P < .001$). Patients admitted to the ICU were also more likely to have had symptomatic aneurysms than patients admitted to the floor (37.7% versus 21.3%, $\chi^2 = 4.43$, $P = .0353$) (Table 2).

Received November 27, 2012; accepted after revision February 15, 2013.

From the Departments of Neurologic Surgery (A.M.B., G.L.), Neurology (A.A.R.), and Radiology (H.J.C., D.F.K., G.L.), Mayo Clinic, Rochester Minnesota.

Please address correspondence to Giuseppe Lanzino, MD, Department of Neurologic Surgery, Mayo Clinic, 200 1st St SW, Rochester, MN 55905; e-mail: lanzino.giuseppe@mayo.edu

Indicates article with supplemental on-line appendix and tables

http://dx.doi.org/10.3174/ajnr.A3566

Table 1: Criteria for ICU Admission

Criterion	Example	*n* (% of 69)
Intraoperative complications	Hemorrhage, thrombosis, access site complication	16 (23)
Investigational device	Pipeline Embolization Device	14 (20)
Aneurysmal complexity	Multilobulated, wide neck	26 (38)
Medical co-morbidities	Coronary artery disease, pulmonary disease, thrombophilia	13 (19)

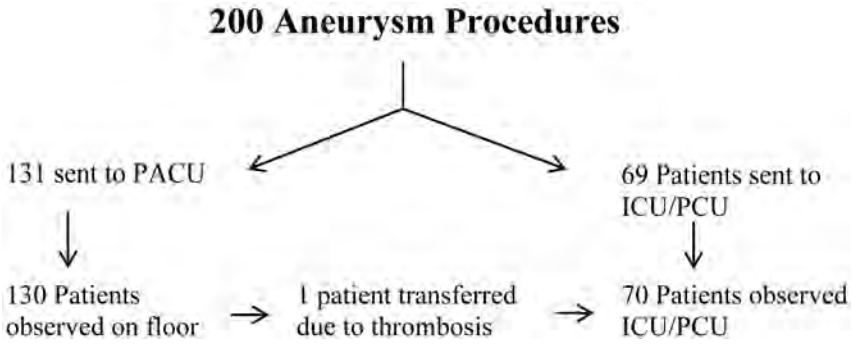

FIG 1. Disposition after endovascular treatment of unruptured aneurysms. PCU indicates Progressive Care Unit; PACU, Postoperative Recovery Unit.

Table 2: Floor versus Intensive Care Comparison

	Floor	ICU	*P*
Age, y	56	55	.52
Female sex, %	77	83	.74
Anterior circulation, %	78.2	84.1	.74
Aneurysm size, mm (SD)	7.7 ± 4.7 mm	12.6 ± 9.2 mm	<.001
Prior unrelated SAH	16.8%	20.3%	.48
Asymptomatic presentation	61.8%	42.0%	.07
Symptomatic presentation	21.3%	37.7%	.035
Length of stay, d	1.1 ± 1.2	1.5 ± 0.9	.026
24-Hour complications	1 (0.8%)	1 (1.9%)	.563
30-Day morbidity	1 (0.8%)	1 (1.9%)	.563

Admission to the ICU also led to significantly longer lengths of stay (1.1 versus 1.5 days, $P = .026$).

A change of admission status occurred after 1 (0.8%) of 131 procedures. This patient had undergone coiling of an anterior choroidal aneurysm, recovered to her baseline postoperatively, and developed an acute hemiparesis in the recovery unit. The angiogram revealed thrombosis of the anterior choroidal artery, which was reversed with abiciximab. Another complication within 24 hours was seen in a patient originally admitted to the ICU and discharged the following day who had noncardiac chest pain that was evaluated in the emergency department. Neither of these patients had permanent morbidity at 30-day follow-up.

Two patients of 200 (1%) had morbidity persistent at 30 days. One was admitted to the ICU after intraoperative aneurysm rupture. Another patient was admitted to the floor and discharged the next day but had a thromboembolic stroke on postoperative day 4. There were no significant differences in early (24-hour) complications resulting in permanent morbidity between the floor and ICU groups (0.8% versus 1.9%, $P = .56$).

Overall, 88% of complications were apparent in the angiography suite, either during the procedure or on awakening from anesthesia, and 12% of complications developed during the first 24 hours. Further information regarding intraoperative and 24-hour complications is listed in the On-line Appendix.

DISCUSSION

We have prospectively evaluated a policy of selective ICU admission in a consecutive, unselected population of patients undergoing endovascular treatment of unruptured intracranial aneurysms. Since adoption of this policy, >60% of patients were admitted to the floor, which has resulted in reduced utilization of specialized hospital resources. Only 1 patient required a change of admission status because of a deficit noted on admission to the neurosurgical ward. This event was promptly recognized, and the patient was treated without any untoward neurologic sequelae. Our study suggests that a large number of patients who undergo elective endovascular treatment of unruptured intracranial aneurysms do not need the specialized and intensive monitoring provided in an ICU environment. There were no complications seen among patients in the ICU admitted for aneurysmal morphology or investigational device reasons, perhaps indicating a more aggressive policy of admission to the floor is possible.

As shown by other authors, both thromboembolic and hemorrhagic complications are not infrequent during endovascular procedures for intracranial aneurysms but can be promptly recognized and treated in the angiographic suite, thus resulting in a low rate of permanent co-morbidity and mortality.[3,4] In our series, most complications were evident during the procedure or on awakening from anesthesia.

There is limited information about the need and indications for ICU admission in patients undergoing elective endovascular procedures. Studies on neurosurgical patients after craniotomy have suggested that ICU care after craniotomy may not be necessary.[5,6] Zimmerman et al[7] conducted a multicenter analysis of 3000 patients admitted to ICU care for neurosurgical diseases and found that among patients who were only observed in the ICU, <10% were likely to need any ICU treatments. Their analysis highlighted the need for comprehensive admission guidelines to the ICU. Beauregard and Friedmann[6] reported that 2 of 132 patients required ICU admission from the floor after craniotomy. Similarly, Bui et al[5] reported 10 response calls among 343 elective craniotomy patients, none of which resulted in ICU transfer. Clearly, patients with some neurologic interventions can be safely observed in a general ward, and the safety of this practice among patients undergoing elective aneurysm treatment is shown for the first time in this study.

Our study has limitations. It is a single-center study, we did not include a cost-saving analysis, and the triaging criteria that we used have not been validated and were only carried out by the senior author. Admission of the selected patients to the ICU may have avoided a complication, and this is not accounted for in our analysis. However, none of the complications that could have been prevented by ICU admission (such as prompt recognition of new ischemic symptoms, hemodynamic instability in a patient with large access hematoma, or cardio-respiratory issues) occurred in our cohort of patients admitted to the ICU who were stable in the angiography suite and did not have intraprocedural events. It can also be argued that the rate of transfer to the ICU after floor admission would have been higher had all of the patients been admitted directly to a regular ward. However, as previously mentioned, there were no complications observed in the patients admitted to the ICU who were stable after awakening from anesthesia and who had had a "straightforward" procedure. Moreover, the paradigm presented may not be applicable in every center because patients are admitted to a regular floor or to the ICU, depending on the level of comfort with floor care, which is variable from center to center.

CONCLUSIONS

Serious complications after endovascular elective aneurysm treatment are most often evident during the procedure or immediately on awakening. The presence of intraoperative complications, complex aneurysm morphology, or severe medical comorbidities may predispose to ICU admission. In the absence of these complications or predisposing factors, patients may safely be observed on the floor.

Disclosures: Giuseppe Lanzino—*UNRELATED: Consultancy:* ev3/Covidien.* Alejandro Rabinstein—*UNRELATED: Consultancy:* Boehringer Ingelheim, Comments: Participation in a single advisory meeting; *Royalties:* Elsevier, Comments: Authored books. Harry Cloft—*UNRELATED: Grants/Grants Pending:* Cordis Endovascular.* David Kallmes—*UNRELATED: Consultancy:* ev3,* Medtronic,* Cordis*; *Grants/Grants Pending:* ev3,* MicroVention,* Codman,* Benvenue*; *Payment for Lectures (including service on speakers bureaus):* MicroVention*; *Royalties:* UVA Patent Foundation; *Travel/Accommodations/Meeting Expenses Unrelated to Activities Listed:* MicroVention,* ev3.* (**money paid to institution*).

REFERENCES

1. Andaluz N, Zuccarello M. **Recent trends in the treatment of cerebral aneurysms: analysis of a nationwide inpatient database.** *J Neurosurg* 2008;108:1163–69
2. Brinjikji W, Kallmes DF, Lanzino G, et al. **Hospitalization costs for endovascular and surgical treatment of ruptured aneurysms in the United States are substantially higher than Medicare payments.** *AJNR Am J Neuroradiol* 2012;33:1037–40
3. Ries T, Siemonsen S, Grzyska U, et al. **Abciximab is a safe rescue therapy in thromboembolic events complicating cerebral aneurysm coil embolization: single center experience in 42 cases and review of the literature.** *Stroke* 2009;40:1750–57
4. Naggara ON, White PM, Guilbert F, et al. **Endovascular treatment of intracranial unruptured aneurysms: systematic review and meta-analysis of the literature on safety and efficacy.** *Radiology* 2010;256:887–97
5. Bui JQ, Mendis RL, van Gelder JM, et al. **Is postoperative intensive care unit admission a prerequisite for elective craniotomy?** *J Neurosurg* 2011;115:1236–41
6. Beauregard CL, Friedmann WA. **Routine use of postoperative ICU care for elective craniotomy: a cost-benefit analysis.** *Surg Neurol* 2003;60:483–89
7. Zimmerman JE, Junker CD, Becker RB, et al. **Neurological intensive care admissions: identifying candidates for intermediate care and the services they receive.** *Neurosurgery* 1998;42:91–101

Routine and Dynamic MR Imaging Study of Lobular Capillary Hemangioma of the Nasal Cavity with Comparison to Inverting Papilloma

B.T. Yang, S.P. Li, Y.Z. Wang, J.Y. Dong, and Z.C. Wang

ABSTRACT

BACKGROUND AND PURPOSE: Lobular capillary hemangioma is an uncommon lesion, and its MR imaging appearance has not been fully characterized. The purpose of this study was to determine the MR imaging features of nasal lobular capillary hemangioma and contrast its imaging characteristics to inverting papilloma.

MATERIALS AND METHODS: The MR imaging signals of 32 patients with histopathologically proven nasal lobular capillary hemangiomas and 53 patients with nasal inverted papillomas were retrospectively studied. The findings of dynamic contrast-enhanced MR imaging in 24 lobular capillary hemangiomas and in 53 inverted papillomas were also analyzed. The Monte Carlo exact test was used for comparison of the time-intensity curve patterns of lobular capillary hemangioma and inverted papilloma.

RESULTS: All lobular capillary hemangiomas appeared to be homogeneously isointense to gray matter on T1-weighted images. On T2-weighted images, all lesions showed heterogeneous hyperintensity, and a thin peripheral isointense or hypointense ring was seen in 28 patients. All lesions showed marked enhancement on enhanced images, with the exception of enhancement of the T2 isointense or hypointense ring. Forty-three (81.1%) inverted papillomas had moderate heterogeneous T2 signal intensity, and a characteristic "cerebriform" appearance was detected in 45 (84.91%) of 53 inverted papillomas. The time-intensity curves showed a washout pattern in 18 and a plateau pattern in 6 patients, whereas inverted papillomas showed a washout pattern in 12, a plateau pattern in 35, and a persistent pattern in 6 patients. There was a statistically significant difference as to time-intensity curve pattern between the 2 groups ($P < .05$).

CONCLUSIONS: Hyperintensity on T2-weighted images, marked enhancement of tumor with a nonenhancing thin peripheral ring, and a washout time-intensity curve pattern are characteristic MR imaging features of nasal lobular capillary hemangiomas.

ABBREVIATIONS: LCH = lobular capillary hemangioma; DCE = dynamic contrast-enhanced; IP = inverted papilloma; ESS = endoscopic sinus surgery; TIC = time-intensity curve

Lobular capillary hemangioma is a benign, rapidly growing lesion characterized by a lobular proliferation of capillaries and previously described by multiple names, including pyogenic granuloma, eruptive hemangioma, granulation tissue-type hemangioma, granuloma gravidarum, pregnancy tumor, granulopyogenicum, and benign hemangioendothelioma.[1-13] LCH is now accepted as the preferred nomenclature because it best represents the true nature of the lesion, which consists of capillaries arranged in lobules and separated by an edematous fibroblastic stroma infiltrated by inflammatory cells.[1,4,12]

LCH usually originates from the vascular tissue of the skin, mucosa, muscle, gland, and bone. Most LCHs of the head and neck occur in the oral cavity; nasal LCH is uncommon and typically arises from the mucosa of the nasal cavity. It occurs most frequently in the anterior nasal septum, followed by the inferior turbinate and the nasal vestibule.[4,5] The differential diagnosis primarily includes inverting papilloma, angiomatous polyp, juvenile angiofibroma, and hemangiopericytoma. MR imaging studies can be helpful by suggesting the preoperative diagnosis and guiding treatment planning, though the MR-related literature is sparse. Most papers focus on the CT features,[14-17] but the preoperative definitive diagnosis for this entity is often challenging on CT alone. Because MR imaging has become the optimal technique for delineation and characterization of nasal masses, we reviewed all the histopathologically proven cases

Received October 22, 2012; accepted after revision January 6, 2013.

From the Department of Radiology (B.T.Y., Y.Z. Wang, J.Y.D., Z.C. Wang), Beijing Tongren Hospital, Capital Medical University, Beijing, China; and Department of Radiology (S.P.L.), Zaozhuang Municipal Hospital, Shandong Province, China.

B.T. Yang and S.P. Li are co-first authors.

This work was supported by grants from the Special Fund of Sanitation Elite Reconstruction of Beijing (2011"C3"C048).

Please address correspondence to Ben Tao Yang, Department of Radiology, Beijing Tongren Hospital, Capital Medical University, No. 1, Dongjiaominxiang, Dongcheng District, Beijing 100730, China; e-mail: cjr.yangbentao@vip.163.com

http://dx.doi.org/10.3174/ajnr.A3523

of nasal LCH in our hospital over the past 9 years to describe the conventional MR imaging features of nasal LCHs, to determine the diagnostic value of the time-intensity curve for nasal LCHs, and to compare routine and MR perfusion findings with a commonly diagnosed nasal cavity mass, the IP.

MATERIALS AND METHODS

Patients

This study was approved by our institutional review board. Thirty-two patients with histopathologically confirmed nasal LCHs over a 9-year period (May 2003 to April 2012) were retrospectively reviewed. The ratio of male to female was 9:7. The average age was 45 years (range, 6–73 years). All 32 patients underwent surgical removal of LCHs by endoscopic sinus surgery. Their clinical presentations, physical and nasal endoscopy examinations, and treatment plans were extracted from the medical records.

To help assess the role of TIC pattern for predicting nasal LCH, we selected IP, the most common benign tumor of the nasal cavity, for comparison. We randomly selected 53 patients (32 men, 21 women; age range, 26–78 years; mean age, 52 years) with histopathologically confirmed nasal cavity IP who underwent dynamic contrast-enhanced MR imaging during the same period.

MR Imaging Technique

Before ESS, 32 patients with LCH and 53 patients with IP underwent paranasal sinus MR imaging. The MR imaging examinations were performed on a 1.5T unit (Signa TwinSpeed Excite; GE Healthcare, Milwaukee, Wisconsin) or 3T unit (Signa HDx, GE Healthcare) with an 8-channel head coil. Fast spin-echo pulse sequences were used in these patients. They underwent pre-enhanced axial and coronal T1WI and axial T2WI and postenhanced axial, coronal, and sagittal T1WI. Frequency-selective fat saturation was added in the postcontrast axial or coronal plane. The imaging parameters were as follows: T1WI: TR, 500–600 ms; TE, 10–15 ms; T2WI: TR, 3500–4000 ms; TE, 120–130 ms; NEX, 2–4; echo-train length, 11–27; matrix, 256 × 256; FOV, 18 × 18 cm; section thickness, 4–5 mm; intersection gap, 0.5 mm.

Gadopentetate dimeglumine (Magnevist; Bayer Schering, Berlin, Germany) was administered intravenously at a flow rate of 2 mL/s (total dose, 0.1 mmol per kilogram of body weight) by use of a power injector (Medrad, Indianola, Pennsylvania) followed by a 10-mL flush of normal saline solution. DCE-MR imaging was performed by use of 3D fast-spoiled gradient recalled imaging before conventional postcontrast T1WI in 24 patients. The following scan parameters were used: TR, 8.4 ms; TE, 4.0 ms; NEX, 1; matrix, 256 × 160; FOV, 18 × 18 cm; section thickness, 3.2 mm; intersection gap, 0 mm. Twelve sets of dynamic images were acquired. Each set included 6 images and required 13 seconds; the interset time gap was 12 seconds. The acquisition time of the entire dynamic series was 5 minutes.

Image Analysis

The MR images were interpreted in consensus by 2 authors (B.T.Y. and Y.Z.W.) with 14 and 8 years of experience in head and neck MR imaging, respectively. DCE-MR imaging source images were transferred to a workstation (Advantage 4.4, GE Healthcare) for further analysis.

One author (J.Y.D.), with 6 years of experience in head and neck MR imaging, manually placed the region of interest on the dynamic images for assessment of the enhancement kinetics of nasal lesions. The area of the region of interest was approximately 3–4 mm in diameter, and the area that showed the greatest degree of early enhancement was chosen for region of interest placement. A similar-size region of interest was placed on the masseter muscle for reference purposes. The TICs were generated for both regions of interest in each patient. The spread pattern of contrast enhancement (starting from a small point or portion, or from a wide area) was first analyzed. Then the contrast index was calculated from the signal intensity, as follows:

$$\text{contrast index} = (\text{contrast-enhanced signal intensity} - \text{unenhanced signal intensity})/\text{unenhanced signal intensity}.$$

The washout ratio, expressed as a percentage, was defined as follows:

$$\text{washout ratio} = [(\text{maximum enhanced signal intensity} - \text{end contrast-enhanced signal intensity})/(\text{maximum enhanced signal intensity} - \text{unenhanced signal intensity})] \times 100\%,$$

where end signal intensity is the signal intensity at 5 minutes after the administration of contrast material. With the use of the classification scheme of DCE-MR imaging proposed by Yabuuchi et al[18] and Hisatomi et al,[19] with slight modifications based on our previous studies,[20,21] the TICs were qualitatively segregated into 3 types in the current study:

Type I (persistent pattern) appears as a straight or curved line, and enhancement continues over the entire dynamic study (TTP >60 seconds).

Type II (plateau pattern) appears as growing enhancement in the early stage and then displays a sharp bend to form a plateau in the middle and later stages (TTP ≤60 seconds; washout ratio, 10–20%).

Type III (washout pattern) appears as rapid enhancement during the early stage and then rapidly decreases in the middle and later stages (TTP ≤60 seconds; washout ratio >20%).

Statistical Analysis

The statistical analysis was conducted with the Statistical Package for the Social Sciences, Version 11.0 software (SPSS, Chicago, Illinois). We used the Monte Carlo exact test for comparison of the TIC pattern and independent-samples *t* test for comparison of the studied parameters of DCE-MR imaging between LCH and IP. A *P* value of <.05 was considered statistically significant.

RESULTS

The common clinical manifestations of LCH were progressive nasal obstruction (30 patients, 93.75%), intermittent epistaxis (26 patients, 81.25%), rhinorrhea (25 patients, 78.12%), headache (5

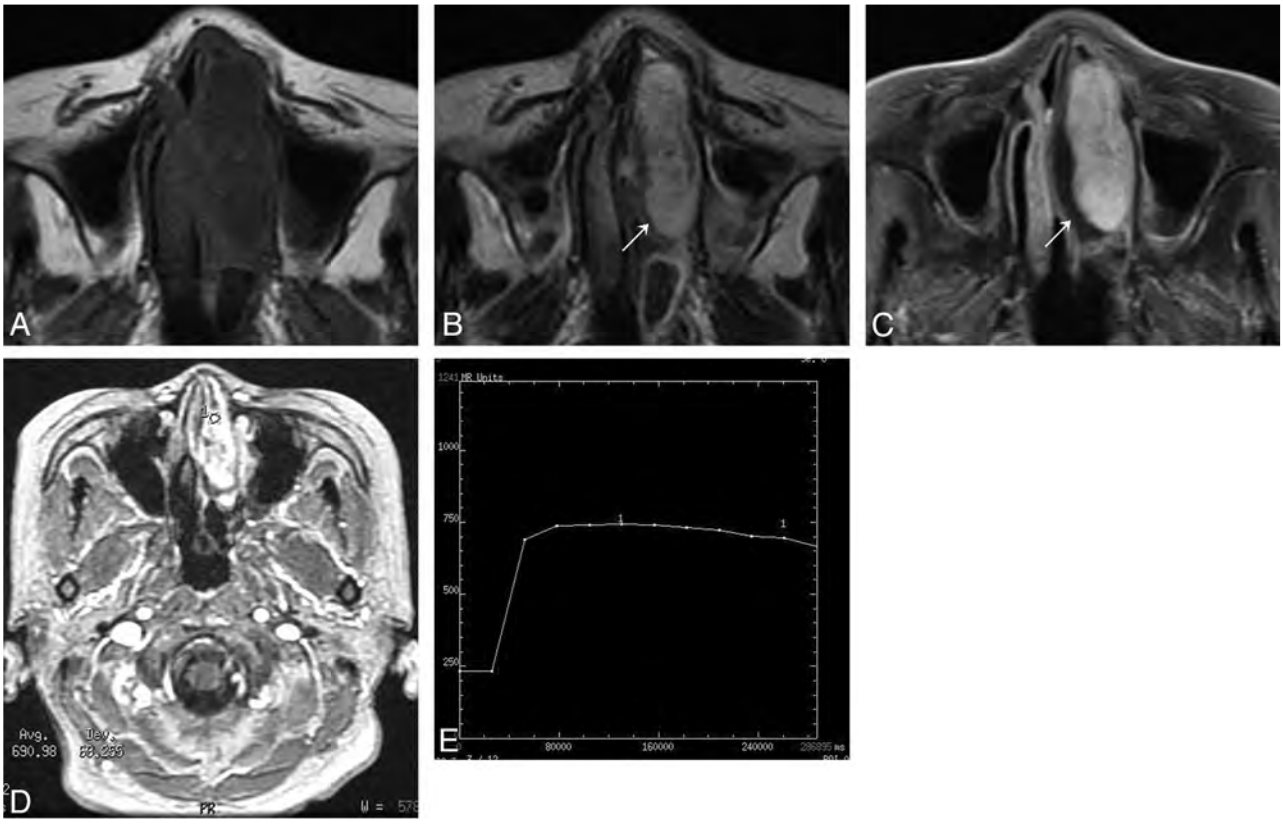

FIG 1. Woman, 74 years old. *A,* Axial T1-weighted MR imaging shows a homogeneous isointense signal mass in the left nasal cavity. *B,* Axial T2-weighted MR imaging shows a heterogeneous high signal mass with a thin peripheral isointense signal ring (↗). *C,* Axial enhanced MR imaging shows marked tumor enhancement with a nonenhanced thin peripheral ring (↗). *D,* The round cursor marks the region of interest of the lesion selected for signal intensity measurement at dynamic MR imaging. *E,* Corresponding axial DCE MR imaging depicts a plateau pattern (type II) TIC.

patients, 15.63%), and anosmia (2 patients, 6.25%).The average duration of the 32 patients' symptoms before diagnosis was 5 years (range, 0.5–10 years). On nasal endoscopy, LCHs appeared as a red to purple polypoid mass.

On histopathologic examination, the lesions exhibited multiple capillaries arranged in lobules with an ulcerated area composed of neutrophilic infiltrates and irregular dilation of blood vessels. Immunohistochemistry revealed positivity for CD34 and a-smooth muscle actin.

Seventeen LCHs occurred in the right nasal cavity and 15 in the left nasal cavity. Twenty-eight LCHs were located in the anterior nasal cavity and 4 around the posterior nasal cavity. The lesions were found to arise from the nasal septum in 4 patients, the nasal vestibule in 5, the middle turbinate in 9, and the inferior turbinate in 14. These lesions appeared lobular in configuration and had a well-defined margin. The mean maximum diameter was 28 mm (range, 10–51 mm).

On T1-weighted images, nasal LCHs appeared homogeneously isointense compared with cerebral gray matter in 32 patients (Fig 1*A*). On T2-weighted images, all lesions were heterogeneously hyperintense (Fig 1*B* and Fig 2*A*), with a thin peripheral isointense or hypointense ring seen in 28 patients (Figs 1*B* and 2*A*). The lesions typically demonstrated marked enhancement of most of the tumor on the enhanced MR images, with lack of enhancement of the T2 isointense or hypointense ring in 28 patients (Figs 1*C* and 2*B*). The sites of origin of these 28 LCHs were located in the opposite direction of the incomplete peripheral ring. Multiple flow voids were demonstrated in 5 patients. Five patients had intratumoral patchy hemorrhage, which showed high signal on both the T1-weighted and T2-weighted images. Both hemorrhage and flow-void signals were identified in 2 patients (Figs 3*A*, -*B*).

On T1-weighted images, 48 (48/53, 90.6%) IPs of the nasal cavity were isointense relative to cerebral gray matter, and 5 (5/53, 9.4%) were hypointense. On T2-weighted images, 43 (43/53, 81.1%) IPs were heterogeneously isointense (Fig 4*A*) and 10 (10/53, 18.9%) were heterogeneously hyperintense. The lesions demonstrated moderate enhancement on enhanced T1-weighted images. Forty-five (45/53, 84.91%) IPs had a convoluted "cerebriform" pattern on both T2-weighted and enhanced T1-weighted MR images (Fig 4*B*).

The findings of DCE-MR imaging for both LCHs and IPs were as follows: 1) The spread pattern of contrast enhancement started from a wide area; 2) the contrast index, TTP, and washout ratio values of LCHs and IPs were 2.31 ± 0.62 versus 0.89 ± 0.25, 43.85 ± 14.29 seconds versus 62.12 ± 12.25 seconds, and 29.66 ± 10.85% versus 13.78 ± 7.67%, respectively. There were statistically significant differences for the 3 parameters between the 2 groups ($P < .05$); and 3) the TIC patterns (Figs 1*D*, 1*E*, 2*C*, and 2*D*) are summarized in the Table. There was a statistically significant difference in the prevalence of TIC pattern between LCH and IP of the nasal cavity ($P < .05$).

All 32 patients were followed up for 0.5–10 years (average, 3.9 years) after ESS and showed no evidence of recurrence.

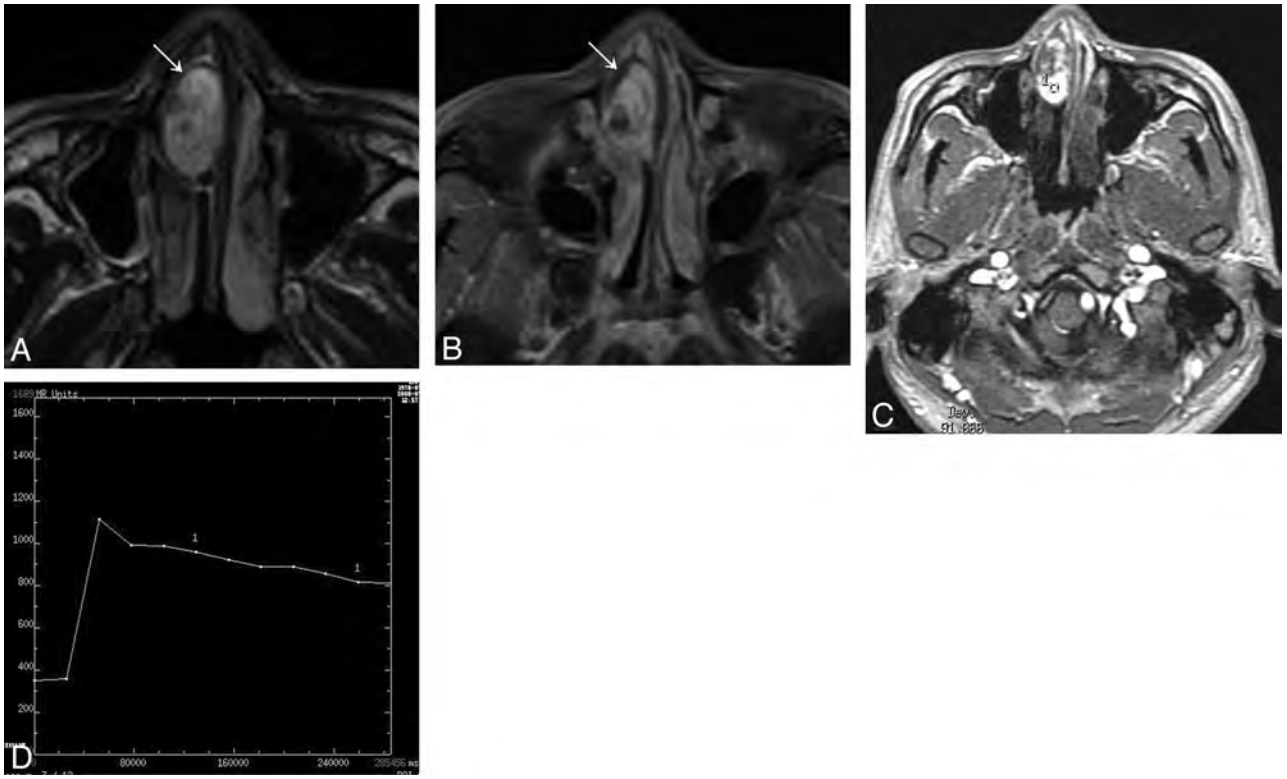

FIG 2. Man, 30 years old. *A,* Axial T2-weighted MR imaging shows a heterogeneously hyperintense signal mass in the right nasal cavity with a thin peripheral low signal ring (↘). *B,* Axial enhanced MR imaging shows marked tumor enhancement with a nonenhanced thin peripheral ring (↘). *C,* The round cursor marks the region of interest of the lesion selected for signal intensity measurement at dynamic MR imaging. *D,* Corresponding axial DCE-MR imaging depicts a washout pattern (type III) TIC.

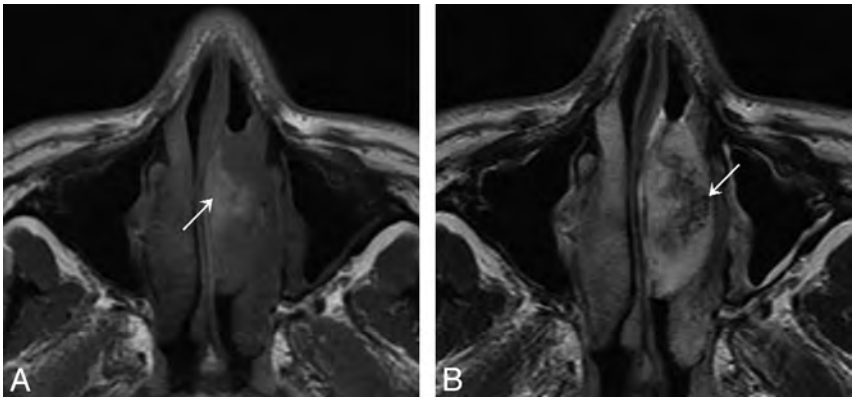

FIG 3. Man, 44 years old. *A,* Axial T1-weighted MR imaging shows a heterogeneously isointense signal mass in the left nasal cavity with patchy high signal area (↗), corresponding to hemorrhage. *B,* Lesion shows heterogeneously hyperintense on axial T2-weighted MR imaging with multiple flow voids (↙).

DISCUSSION

The mechanism of development of nasal LCH is still unclear, but proposed etiologic factors have included trauma, hormonal imbalance, viral oncogenes, microscopic arteriovenous malformations, angiogenic growth factors, and cytogenetic abnormalities.[4,11] On histopathologic examination, LCH generally consists of circumscribed anastomosing networks of capillaries arranged in 1 or more lobules in edematous and fibromyxoid stroma. According to the histopathologic study performed by Toida et al,[22] most LCHs can be divided into a lobular area and a superficial ulcerative area. The lobular area has a characteristic lobular architecture with capillary proliferation. The ulcerative area is composed of neutrophilic infiltrates and irregular dilation of blood vessels, which may undergo secondary nonspecific changes, including stromal edema, inflammation, and a granulation tissue reaction.[4,5]

Nasal LCH may develop at any age but is more frequent in the third and fourth decades and in females,[3,4,7,8,11] though our study showed a slight male predominance. LCH usually manifests as recurrent unilateral epistaxis, nasal obstruction, and purulent nasal discharge. Facial pain, hyposmia, and headache may occasionally occur as well. At nasal endoscopy, the lesion usually appears as a red to purple polypoid mass that easily bleeds.[3,4]

In the literature, nasal LCHs occur more frequently in the septum, followed by the lateral wall and the vestibule,[4,5] whereas the lateral wall (71.9%), followed by the vestibule (15.6%) and the septum (12.5%) were the most common sites of origin in our study. According to the literature[14,15] and the present study, nasal LCHs characteristically appear as a lobular and well-defined soft tissue mass. On nonenhanced CT, these lesions tend to be isoattenuated relative to gray matter, and they usually have marked enhancement after the administration of contrast material. Bony remodeling and local erosion may be noted in large nasal LCHs.

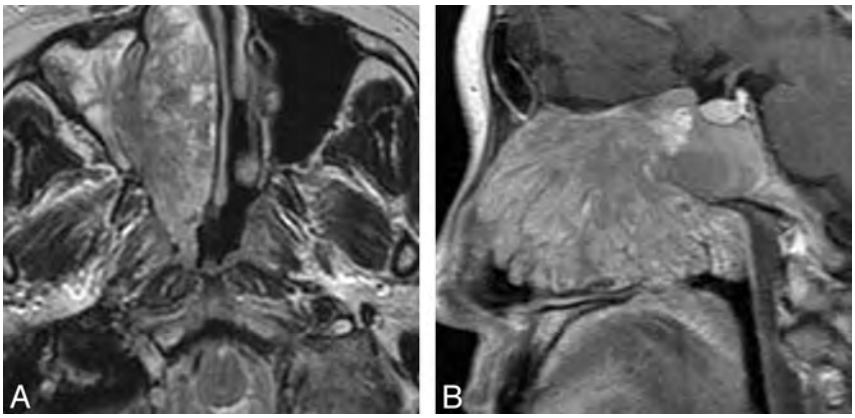

FIG 4. Woman, 56 years old. *A,* Axial T2-weighted MR imaging shows a heterogeneously isointense signal mass in the right nasal cavity with associated obstructive maxillary sinusitis. *B,* Lesion shows a characteristic "cerebriform" appearance on sagittal enhanced T1-weighted MR imaging with associated obstructive sphenoid sinusitis.

Comparison of TIC patterns between 24 LCHs and 53 IPs of the nasal cavity

TIC Pattern	LCH	IP
I	0	6
II	6	35
III	18	12
Total	24	53

Note:— All IPs without malignant transformation.

Compared with CT, MR imaging demonstrates more characteristic features. These lesions usually are homogeneously isointense to gray matter on T1-weighted images. On T2-weighted images, most LCHs appear heterogeneously hyperintense with a thin peripheral isointense or hypointense ring. Marked enhancement of nasal LCHs is generally noted because of their high vascularity, which is a key MR imaging feature. In our series, nasal LCHs generally show marked post-gadolinium enhancement in most of the lesion, with only a thin peripheral ring that is not enhancing, and this characteristic finding gives rise to a diagnostic clue. The central markedly enhancing areas may be correlated histopathologically with the lobular area in these patients, whereas the nonenhancing peripheral ring may correspond to either a superficial ulcerative area or inflammatory secretions. Additionally, the site of origin of LCH is generally located at the opposite side of the incomplete peripheral ring, which was confirmed during surgery in our cases. Seven cases showed multiple flow voids within the tumors, which may represent fast-flow vessels.

DCE-MR imaging can provide information related to tumor perfusion, microvascular permeability, and volume of the extracellular space, which may aid in the specific diagnosis of head and neck lesions and predict their biologic behavior.[17-19] The TICs of 18 (18/24, 75%) LCHs in the present study show a washout pattern (type III) and 6 (6/24, 25%) show a plateau pattern (type II). Our study showed a statistically significant difference in the TIC pattern between LCH and IP in the nasal cavity, with the plateau pattern TIC (type II) (35/53, 66%) being the most common in the latter. This demonstrates that type III TIC is relatively characteristic for nasal LCHs; hence, this technique may give an important clue to diagnosis of a suspected LCH in the nasal cavity.

IP is the most common benign nasal tumor and represents 70–80% of all benign tumors of this region.[20,23] IP has a tendency for a high rate of recurrence, local aggressiveness, and association with carcinoma; hence, it needs more aggressive surgical resection compared with LCH. Thus, preoperative differentiation of IP from LCH can be helpful for surgical planning. On the basis of our study and the literature,[23] IPs typically show heterogeneously isointense T2 signal and a convoluted "cerebriform" pattern on both T2-weighted and enhanced T1-weighted MR images.[23] Other considerations in the differential diagnosis of nasal LCH include angiomatous polyps, juvenile angiofibroma, and hemangiopericytoma. Angiomatous polyps often arise from the choanal region. The lesions usually show hyperintense signal on T2-weighted images and marked enhancement on enhanced T1-weighted images.[24] Juvenile angiofibromas occur almost exclusively in male adolescent patients and usually arise from or near the sphenopalatine foramen with extension into the posterior nasal cavity and the nasopharynx. The typical imaging characteristic is marked post-gadolinium enhancement with associated multiple flow voids. Hemangiopericytoma is a rare tumor of the nasal cavity and often arises from the posterior nasal cavity. The typical imaging manifestations include isointense signal on T2-weighted images, marked post-gadolinium enhancement, and a plateau TIC pattern (type II) on DCE-MR imaging.[25]

This study has some limitations. First, the regions of interest that were used for generating TICs could not be precisely correlated to histopathologic findings. Second, region of interest placement was performed by a single author, which could have introduced a bias. Despite these limitations, our study suggests that MR imaging and generation of TICs could be useful in assessing nasal LCHs.

CONCLUSIONS

Although the definitive diagnosis of nasal LCHs is dependent on histopathologic findings and characteristic immunohistochemical staining, MR imaging may suggest the diagnosis before surgery. The typical MR imaging characteristics of nasal LCHs include hyperintense signal on T2-weighted images, marked enhancement of most tumor with a nonenhancing thin peripheral ring on enhanced T1-weighted images, and a washout TIC pattern.

Disclosures: Ben Tao Yang, S.P. Li, Y.Z. Wang, J.Y. Dong, Z.C. Wang; *RELATED: Grant:* This work was supported by grants from the Special Fund of Sanitation Elite Reconstruction of Beijing (2011″C3″C048)* (**Money paid to institution*).

REFERENCES

1. Mills SE, Cooper PH, Fechner RE. **Lobular capillary hemangioma: the underlying lesion of pyogenic granuloma: a study of 73 cases from the oral and nasal mucous membranes.** *Am J Surg Pathol* 1980;4:470–79

2. Karagama YG, Howarth K, Steel PR, et al. **Lobular capillary haemangioma of the nasal vestibule: a rare entity.** *Int J Pediatr Otorhinolaryngol* 2002;66:71–75
3. Wood JW, Casiano RR. **Inverted papillomas and benign nonneoplastic lesions of the nasal cavity.** *Am J Rhinol Allergy* 2012;26:157–63
4. Puxeddu R, Berlucchi M, Ledda GP, et al. **Lobular capillary hemangioma of the nasal cavity: a retrospective study on 40 patients.** *Am J Rhinol* 2006;20:480–84
5. Delbrouck C, Chamiec M, Hassid S, et al. **Lobular capillary haemangioma of the nasal cavity during pregnancy.** *J Laryngol Otol* 2011;125:973–77
6. Miller FR, D'Agostino MA, Schlack K. **Lobular capillary hemangioma of the nasal cavity.** *Otolaryngol Head Neck Surg* 1999;120:783–84
7. Lee HM, Lee SH, Hwang SJ. **A giant pyogenic granuloma in the nasal cavity caused by nasal packing.** *Eur Arch Otorhinolaryngol* 2002;259:231–33
8. Ozcan C, Apa DD, Gorur K. **Pediatric lobular capillary hemangioma of the nasal cavity.** *Eur Arch Otorhinolaryngol* 2004;261:449–51
9. Katori H, Tsukuda M. **Lobular capillary hemangioma of the nasal cavity in child.** *Auris Nasus Larynx* 2005;32:185–88
10. Kurtaran H, Uraldi C, Ark N, et al. **Lobular capillary haemangioma of the middle turbinate.** *Acta Otolaryngol* 2006;126:442–44
11. Karakus MF, Ozcan KM, Bilal N, et al. **Pediatric lobular capillary hemangioma accompanied with a foreign body in the nasal cavity.** *Int J Pediatr Otorhinolaryngol Extra* 2007;2:231–34
12. Gernon TJ, McHugh JB, Thorne MC. **Pathology quiz case 2: diagnosis: nasal lobular capillary hemangioma (pyogenic granuloma).** *Arch Otolaryngol Head Neck Surg* 2010;136:930, 932–33
13. Benoit MM, Fink DS, Brigger MT, et al. **Lobular capillary hemangioma of the nasal cavity in a five-year-old boy.** *Otolaryngol Head Neck Surg* 2010;142:290–91
14. Lance E, Schatz C, Nach R, et al. **Pyogenic granuloma gravidarum of the nasal fossa: CT features.** *J Comput Assist Tomogr* 1992;16:663–64
15. Lee DG, Lee SK, Chang HW, et al. **CT features of lobular capillary hemangioma of the nasal cavity.** *AJNR Am J Neuroradiol* 2010;31:749–54
16. Dillon WP, Som PM, Rosenau W. **Hemangioma of the nasal vault: MR and CT features.** *Radiology* 1991;180:761–65
17. Sasaki M, Sumi M, Eida S, et al. **Multiparametric MR imaging of sinonasal diseases: time-signal intensity curve- and apparent diffusion coefficient-based differentiation between benign and malignant lesions.** *AJNR Am J Neuroradiol* 2011;32:2154–59
18. Yabuuchi H, Fukuya T, Tajima T, et al. **Salivary gland tumors: diagnostic value of gadolinium-enhanced dynamic MR imaging with histopathologic correlation.** *Radiology* 2003;226:345–54
19. Hisatomi M, Asaumi J, Yanagi Y, et al. **Diagnostic value of dynamic contrast-enhanced MR imaging in the salivary gland tumors.** *Oral Oncol* 2007;43:940–47
20. Yang BT, Wang ZC, Liu S, et al. **MRI diagnosis of inverted papilloma in the sinonasal cavity.** *Chin J Radiol* 2008;42:572–76
21. Yang BT, Wang YZ, Dong JY, et al. **MR imaging study of solitary fibrous tumor in the orbit.** *AJR Am J Roentgenol* 2012;199:W506–11
22. Toida M, Hasegawa T, Watanabe F, et al. **Lobular capillary hemangioma of the oral mucosa: clinicopathological study of 43 cases with a special reference to immunohistochemical characterization of the vascular elements.** *Pathol Int* 2003;53:1–7
23. Jeon TY, Kim HJ, Chung SK, et al. **Sinonasal inverted papilloma: value of convoluted cerebriform pattern on MR imaging.** *AJNR Am J Neuroradiol* 2008;29:1556–60
24. De Vuysere S, Hermans R, Marchal G. **Sinochoanal polyp and its variant, the angiomatous polyp: MR imaging findings.** *Eur Radiol* 2001;11:55–58
25. Palacios E, Restrepo S, Mastrogiovanni L, et al. **Sinonasal hemangiopericytomas: clinicoapathologic and imaging findings.** *Ear Nose Throat J* 2005;84:99–102

New MR Imaging Assessment Tool to Define Brain Abnormalities in Very Preterm Infants at Term

H. Kidokoro, J.J. Neil, and T.E. Inder

ABSTRACT

BACKGROUND AND PURPOSE: WM injury is the dominant form of injury in preterm infants. However, other cerebral structures, including the deep gray matter and the cerebellum, can also be affected by injury and/or impaired growth. Current MR imaging injury assessment scales are subjective and are challenging to apply. Thus, we developed a new assessment tool and applied it to MR imaging studies obtained from very preterm infants at term age.

MATERIALS AND METHODS: MR imaging scans from 97 very preterm infants (< 30 weeks' gestation) and 22 healthy term-born infants were evaluated retrospectively. The severity of brain injury (defined by signal abnormalities) and impaired brain growth (defined with biometrics) was scored in the WM, cortical gray matter, deep gray matter, and cerebellum. Perinatal variables for clinical risks were collected.

RESULTS: In very preterm infants, brain injury was observed in the WM (n=23), deep GM (n=5), and cerebellum (n=23). Combining measures of injury and impaired growth showed moderate to severe abnormalities most commonly in the WM (n=38) and cerebellum (n=32) but still notable in the cortical gray matter (n=16) and deep gray matter (n=11). WM signal abnormalities were associated with a reduced deep gray matter area but not with cerebellar abnormality. Intraventricular and/or parenchymal hemorrhage was associated with cerebellar signal abnormality and volume reduction. Multiple clinical risk factors, including prolonged intubation, prolonged parenteral nutrition, postnatal corticosteroid use, and postnatal sepsis, were associated with increased global abnormality on MR imaging.

CONCLUSIONS: Very preterm infants demonstrate a high prevalence of injury and growth impairment in both the WM and gray matter. This MR imaging scoring system provides a more comprehensive and objective classification of the nature and extent of abnormalities than existing measures.

ABBREVIATIONS: GM = gray matter; VPT = very preterm

With advances in obstetric and neonatal care of the preterm infant, the incidence of cerebral palsy has been decreasing,[1,2] yet preterm-born children remain at high risk for cognitive, behavioral, academic, and social challenges later in life.[3,4] The neuropathologic conditions leading to adverse neurodevelopmental sequelae in later life in former preterm infants are areas of active research and clinical focus.

MR imaging plays a crucial role in the identification of structural brain abnormalities, and the cerebral WM is the most commonly identified site for brain injury in the preterm infant.[5] However, recent studies have also highlighted the significant involvement of the cortical GM, deep GM, and cerebellum.[6-8] In addition to brain injury identified by signal abnormalities on conventional (T1- and T2-weighted) MR imaging, 3D volumetric approaches with MR imaging have defined global and regional alterations in brain structure in former preterm children.[9-11] Thus, to fully capture the effect of preterm birth on the immature brain, a systematic assessment of both brain injury and altered brain growth is required.

Several MR imaging evaluation scales have been developed to define the severity of brain abnormality at term-equivalent postmenstrual age and to predict neurodevelopmental outcome in preterm infants.[12-14] However, these scoring systems often address only cerebral WM and cortical GM and may thereby underestimate the full extent of brain abnormalities. In addition, the

Received August 17, 2012; accepted after revision January 8, 2013.

From the Departments of Pediatrics (H.K., J.J.N., T.E.I.), Neurology (J.J.N., T.E.I.), and Radiology (J.J.N., T.E.I.); Washington University in St. Louis, St. Louis, Missouri.

Funding/Support: National Institute of Child Health and Development (R01HD057098; 1P0HD062171) and the Doris Duke Charitable Foundation.

Contributions: H.K. wrote the first draft, and all authors reviewed the final version of the manuscript. T.I. and J.N. have been principal investigators in the grants that collected the data presented in this study.

Please address correspondence to Terrie E. Inder, MBChB, MD, Departments of Pediatrics, Neurology, and Radiology; Washington University in St. Louis, 660 South Euclid Ave, St. Louis, MO 63110; e-mail: inder_t@kids.wustl.edu

http://dx.doi.org/10.3174/ajnr.A3521

scorings in this scale are somewhat subjective, with variable relationships to neurodevelopmental outcome.

The aim of our study was to develop a new scoring system for conventional MR imaging that more comprehensively and objectively defines both brain injury and impaired brain growth. This scoring system was applied to MR imaging studies obtained from VPT infants at term-equivalent postmenstrual age to characterize brain injury in this population. Perinatal risk factors for these abnormalities were also explored.

MATERIALS AND METHODS

Participants

VPT infants (< 30 weeks' gestation) were recruited between April 2007 and June 2010 at St. Louis Children's Hospital. Of 121 infants recruited, 97 survivors (80%) fulfilled the criteria of having undergone MR imaging at ≥36 to ≤42 weeks' gestation. During the same study period, term-born control infants were also enrolled. They were required to have mothers > 18 years old who received regular prenatal care without medications or drug/alcohol use. In addition, the control infants did not receive any resuscitative procedures or neonatal medical care after birth. All infants were enrolled in the study after their parents had signed informed consent. The study protocols were approved by the local human research and ethics bodies.

MR Imaging Acquisition

MR imaging was undertaken by using a 3T Tim Trio system (Siemens, Erlangen, Germany) without sedation and included anatomic images obtained with an axial magnetization-prepared rapid acquistion of gradient echo T1-weighted sequence (TR, 1500 ms; TE, 3 ms; voxel size, $1 \times 0.7 \times 1$ mm^3), and a turbo spin-echo T2-weighted sequence (TR, 8600 ms; TE, 160 ms; voxel size, $1 \times 1 \times 1$ mm^3; echo-train length, 17).

MR Imaging Assessment

A standardized scoring system was used to evaluate cerebral WM and cortical GM abnormalities in a similar fashion to our previous study,[12] augmented with quantitative biometrics. In addition, scales for the deep GM and cerebellum were developed and were included. All of the qualitative and quantitative assessments of MR images were performed by a single neonatal neurologist (H.K.) with sufficient experience to assess clinical MR images. Interobserver reliabilities (intraclass correlation coefficients) from 20 scans scored by 2 observers (H.K., T.I.) and intraobserver reliabilities (H.K.) from 20 scans scored 1 month apart by a single observer were > 0.90 in the qualitative assessment. No infant had changed category of scoring between raters.

Cerebral WM Abnormality

Cerebral WM abnormality was graded on a scale between zero and 4 for 6 variables: 1) cystic degeneration, 2) focal signal abnormalities, 3) delayed myelination, 4) thinning of the corpus callosum, 5) dilated lateral ventricles, and 6) reduction of WM volume (Fig 1 and Table 1). Thinning of the corpus callosum was assessed with measurements of callosal thickness at 3 positions (genu, midportion of the body, and splenium) on a midsagittal section. Lateral ventricular dilation was assessed by measurement of the lateral ventricular diameter on a coronal section at the level of the ventricular atrium. Reduction of WM volume was determined by measurement of biparietal width on a coronal section by use of a DICOM viewer (Onis 2.3; DigitalCore, Tokyo, Japan) according to the definition in a previous report (Fig 2).[15] Because biparietal width increases with postmenstrual age on MR imaging, we corrected the measured value with linear regression analysis according to the following equation: corrected biparietal width = measured biparietal width + the slope × (40 – postmenstrual age on MR imaging).

Cortical GM Abnormality

Cortical GM abnormality was graded on a scale between zero and 4 for 3 variables: 1) signal abnormality; 2) delayed gyration; and 3) dilated extracerebral CSF space, as previously reported.[12] In this study, the degree of extracerebral CSF space was determined with a measurement of interhemispheric distance between the crowns of the superior frontal gyri at the same section for measurement of biparietal width (Fig 2).

Deep GM and Cerebellar Abnormality

New criteria for deep GM and cerebellar abnormalities were defined. These scores are a composite of signal abnormality (Fig 1) and volume reduction (Fig 2). Deep GM volume was assessed with a measurement of deep GM area on a single axial section on which the caudate heads, lentiform nuclei, and thalami were maximally visible. Cerebellar volume was categorized with a measurement of transcerebellar diameter according to the definition in a previous report.[15] Because the deep GM area and transcerebellar diameter correlate positively with postmenstrual age on MR imaging, they were corrected by use of equations analogous to that above.

The total cerebral WM score was categorized into 4 grades: no (total score, 0–2), mild (total score, 3–4), moderate (total score, 5–6), or severe (total score, ≥7) WM abnormality. Total cortical GM, deep GM, or cerebellar scores were also categorized into 4 grades: no (total score, 0), mild (total score, 1), moderate (total score, 2), and severe (total score ≥3). Finally, a global brain abnormality score was calculated as the sum of these regional total scores and was classified as normal (total score, 0–3), mild (total score, 4–7), moderate (total score, 8–11), and severe (total score ≥12).

Besides the scoring items, we also noted the presence or absence of subependymal hemorrhage and intraventricular hemorrhage, grading them on the basis of the Papile classification (grade I–III).[16] Cystic WM lesions were categorized as cystic periventricular leukomalacia, periventricular hemorrhagic infarction, or other conditions.[17]

Clinical Data

All clinical variables were collected from maternal and infant hospital records. Chorioamnionitis was identified by use of clinical criteria consisting of maternal fever and/or elevated inflammatory markers on laboratory testing. Confirmed postnatal sepsis was defined as culture-positive sepsis. Necrotizing enterocolitis was defined according to the Bell criteria.[18] Treated patent ductus arteriosus included pharmacologic and/or surgical treatment. Inotropic agents were used according to clinical needs for maintenance of systemic blood pressure. Postnatal steroids include hydrocortisone and dexamethasone.

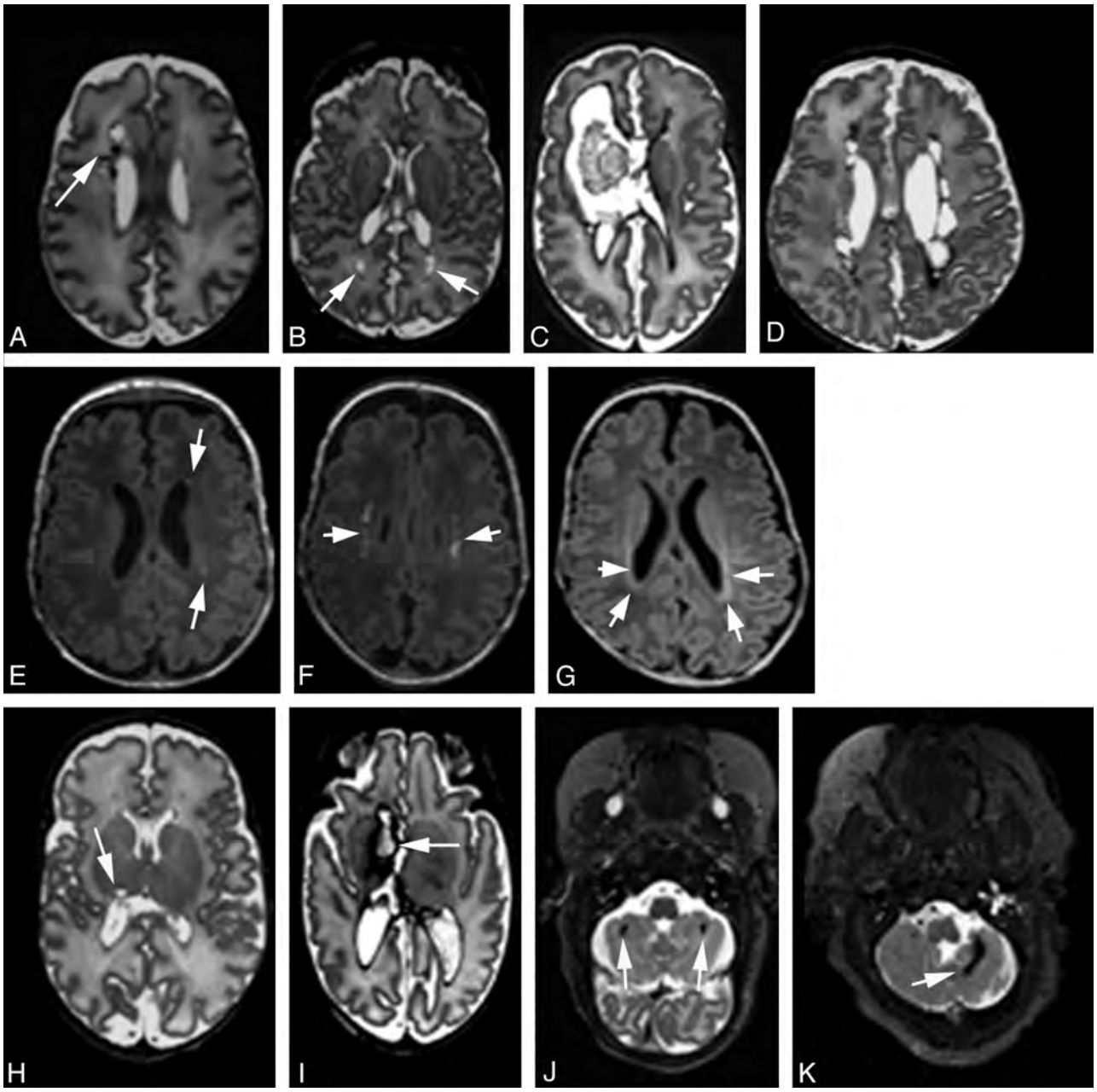

FIG 1. Representative MR images of regional injury. Axial T1- or T2-weighted MR images demonstrating classification of cystic WM lesions (*A–D*), focal WM signal abnormalities (*E–G*), deep GM lesions (*H* and *I*), and cerebellar lesions (*J* and *K*). Cystic WM lesions are defined by their extent: focal unilateral (*arrow, A*), focal bilateral (*arrows, B*), extensive unilateral (*C*), and extensive bilateral (*D*). Focal WM signal abnormalities are classified as focal punctate (*arrows, E*), extensive punctate (*arrows, F*), or linear lesions corresponding to gliosis (*arrows, G*). Deep GM and cerebellar injuries are classified into 4 grades by their extent. Representative images of focal unilateral (*arrow, H*) or extensive unilateral (*arrow, I*) deep GM lesions, and images of focal bilateral (*arrows, J*) or focal extensive (*arrow, K*) cerebellar lesions are shown.

Statistical Analyses

Data were analyzed with SPSS version 20.0 software (SPSS, Chicago, Illinois). Student *t* test or analysis of variance was used when continuous parametric variables were compared between 2 or 3 groups. Mann-Whitney *U* tests or Kruskal-Wallis tests were used to compare continuous nonparametric variables. χ^2 tests were used with categoric variables. Simple linear regression analysis was used to obtain the slopes of the association between different measurements and postmenstrual age on MR imaging. Two-sided *P* values $< .05$ were used to indicate statistical significance.

RESULTS

Participants

For the 97 VPT infants, the mean (SD) gestational age at birth was 26.7 (1.8) weeks, and mean birth weight was 949 (250) g. The VPT group included 6 small-for-gestational-age infants (birth weight of $<$ -2 SD for gestational age), 43 male infants (44%), and 64 singletons (66%). In the 22 term-born infants, mean gestational age at birth was 39.1 (1.0) weeks, and mean birth weight was 3285 (508) g. The term group included 9 male infants (41%), and all of the infants were singleton with age-appropriate birth weight. The mean postmen-

Table 1: Prevalence of infants with each item in cerebral WM score (VPT infants/term infants)

Variables	WM Score				
	Score 0	Score 1	Score 2	Score 3	Score 4
Cerebral WM					
Cystic lesions	None (90/22)	Focal unilateral (3/0)	Focal bilateral (1/0)	Extensive unilateral (2/0)	Extensive bilateral (1/0)
Focal signal abnormality	None (77/20)	Focal punctate (13/2)	Extensive punctate (5/0)	Linear (2/0)	
Myelination delay	PLIC & corona radiata (65/22)	Only PLIC (26/0)	Minimal—no PLIC (6/0)		
Thinning of the corpus callosum	None (40/18)	Partial (genu/body $<$ 1.3 mm or splenium $<$ 2.0 mm) (53/4)	Global (genu/body $<$ 1.3 mm and splenium $<$ 2.0 mm) (4/0)		
Dilated lateral ventricles	Both sides VD $<$ 7.5 mm (26/17)	One side 7.5 mm $\leq$ VD $<$ 10 mm (19/4)	Both sides 7.5 mm $\leq$ VD $<$ 10 mm or one side VD $\geq$ 10 mm (42/1)	Both sides VD $\geq$ 10 mm (10/0)	
Volume reduction	cBPW $\geq$77 mm (21/19)	77 mm $>$ cBPW $\geq$72 mm (30/2)	72 mm $>$ cBPW $\geq$67 mm (40/1)	67 mm $>$ cBPW (6/0)	

Note:—cBPW indicates corrected biparietal width; PLIC, posterior limb of internal capsule; VD, ventricular diameter.

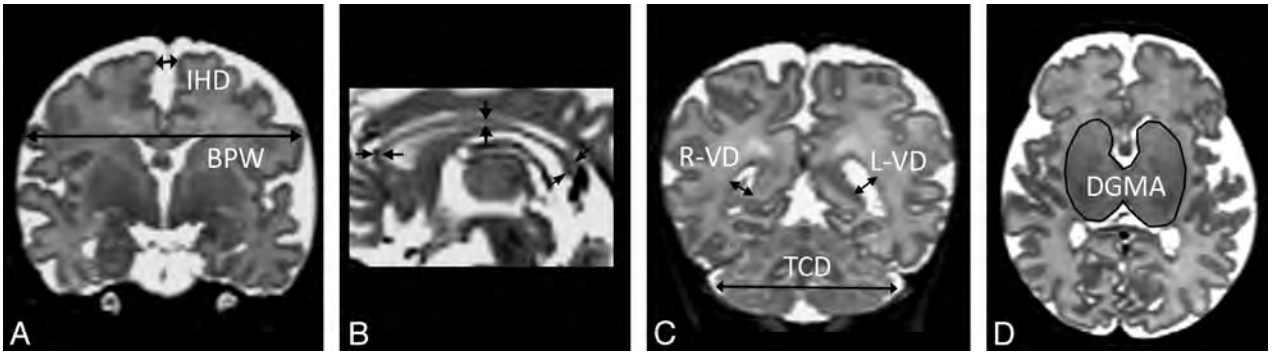

FIG 2. Regional measurements. *A*, Biparietal width (BPW) and interhemispheric distance (IHD) are measured on a single coronal section by use of the cochlea and basilar truncus as landmarks. *B*, Callosal thickness is measured on a midsagittal view at 3 different regions: the genu, the midportion, and the splenium. *C*, Ventricular diameters (VDs) and transcerebellar diameter (TCD) are measured on a coronal view at the level of the ventricular atrium. *D*, The deep GM area (DGMA) is measured on a single axial section at the level at which the caudate heads, the lentiform nuclei, and the thalami are maximally visible.

strual age on MR imaging in VPT infants was younger than that in term-born infants (38.0 [1.5] weeks vs 39.4 [1.1] weeks; $P = .001$).

Brain Measurements in VPT and Term Infants

In the VPT group, a linear association was found between postmenstrual age at scan and biparietal width ($R = 0.41$; $P < .001$; slope, 1.4 mm/week), deep GM area ($R = 0.36$; $P < .001$; slope, 0.26 cm^2/week), and transcerebellar diameter ($R = 0.35$; $P < .001$; slope, 0.83 mm/week), whereas no significant association was identified with interhemispheric distance, ventricular diameter, or callosal thickness. In contrast to the VPT group, no significant associations between postmenstrual age at scan and any brain measurements were observed in the term group.

Mean corrected biparietal width and corrected transcerebellar diameter were 72.4 (4.5) mm and 49.2 (3.3) mm in the VPT group, whereas biparietal width and transcerebellar diameter in the term group were 81.7 (4.7) mm and 52.6 (2.2) mm, respectively (both $P < .001$). Mean corrected deep GM area was 9.7 (1.0) cm^2 in the VPT group, whereas deep GM area was 10.5 (0.8) cm^2 in the term group ($P < .001$). Interhemispheric distance, ventricular diameters, and callosal thickness were also different between the VPT group and the term group (3.6 [1.7] mm vs 2.6 [1.1] mm in interhemispheric distance, $P = .001$; 7.6 [1.8] mm vs 6.2 [1.4] mm in right ventricular diameter, $P = .001$; 7.9 [2.2] mm vs 6.3 [0.8] mm in left ventricular diameter, $P < .001$; 1.8 [0.4] mm vs 2.3 [0.6] mm in the genu, $P = .002$; 1.4 [0.3] mm vs 1.6 [0.2] mm in the body, $P = .004$; and 2.3 [0.6] mm vs 2.7 [0.5] mm in the splenium of the corpus callosum, $P = .011$).

Prevalence of Each Finding in the Cerebral WM in VPT and Term Infants

Table 1 shows the prevalence of abnormalities in the cerebral WM. For VPT infants, 7 infants (7%) had cystic lesions, whereas 20 infants (21%) had noncystic signal abnormalities in the WM. Myelination delay, thinning of the corpus callosum, dilated lateral ventricles, and volume reduction were also common in the VPT group. For the total WM score, 38 infants (39%) were categorized as having moderate to severe abnormalities.

Table 2 shows the prevalence of each MR imaging finding in the cortical GM, deep GM, and cerebellum. Signal abnormality was rare in the cortical GM ($n = 0$) and deep GM ($n = 5$ [5%]), but it was common in the cerebellum ($n = 23$ [24%]) in VPT infants. Except for 1 cystic lesion in the pulvinar of the right thal-

Table 2: Prevalence of infants with each item in GM or cerebellum score (VPT infants/term infants)

Variables	GM or Cerebellum Score				
	Score 0	Score 1	Score 2	Score 3	Score 4
Cortical GM					
Signal abnormality	None (97/22)	Focal unilateral (0/0)	Focal bilateral (0/0)	Extensive unilateral (0/0)	Extensive bilateral (0/0)
Gyral maturation	Delay < 2 weeks (96/22)	2 ≤ delay < 4 weeks (1/0)	Delay ≥4 weeks (0/0)		
Increased extracerebral space	IHD < 4 mm (61/20)	4 mm ≤ IHD < 5 mm (20/2)	5 mm ≤ IHD < 6 mm (8/0)	IHD ≥6 mm (8/0)	
Deep GM					
Signal abnormality	None (92/22)	Focal unilateral (2/0)	Focal bilateral (2/0)	Extensive unilateral (0/0)	Extensive bilateral (1/0)
Volume reduction	cDGMA ≥9.5 (53/20)	9.5 > cDGMA ≥8.5 (35/2)	8.5 > cDGMA ≥7.5 (8/0)	7.5 > cDGMA (1/0)	
Cerebellum					
Signal abnormality	None (74/22)	Punctate unilateral (10/0)	Punctate bilateral (5/0)	Extensive unilateral (4/0)	Extensive bilateral (4/0)
Volume reduction	cTCD ≥50 mm (43/20)	50 mm > cTCD ≥47 mm (31/2)	47 mm > cTCD ≥44 mm (18/0)	cTCD < 44 mm (5/0)	

Note:—cDGMA indicates corrected deep GM area (cm^2); cTCD, corrected transcerebellar diameter; IHD, interhemispheric distance.

Table 3: Effect of WM injury or intraventricular hemorrhage on deep GM or cerebellum in VPT infants

		Deep GM		Cerebellum	
		Signal Abnormality *n* (%)	Corrected Deep GM Area Mean (SD)	Signal Abnormality *n* (%)	Corrected Transcerebellar Diameter Mean (SD)
WM injury[c]	Yes ($n = 23$)	4 (17)[a]	9.4 (1.2)[b]	7 (30)	49.0 (2.8)
	No ($n = 74$)	1 (1.4)	9.9 (0.9)	16 (22)	49.3 (3.4)
Intraventricular hemorrhage	Yes ($n = 31$)	3 (9.7)	9.4 (0.9)[b]	12 (39)[b]	48.2 (3.5)[b]
	No ($n = 66$)	2 (3)	9.9 (1.0)	11 (17)	49.7 (3.0)

[a] < .01 vs without WM injury or intraventricular hemorrhage.

[b] < .05.

[c] WM injury defined by the presence of cystic or focal signal abnormality.

Table 4: Perinatal variables and grade of global brain abnormality in VPT infants

Variables	Global Brain Abnormality				*P* Value
	Normal (Score 0–3) *n* = 18	Mild (Score 4–7) *n* = 45	Moderate (Score 8–11) *n* = 21	Severe (Score ≥12) *n* = 13	
Gestation at birth (weeks)	27.4 (1.5)	26.9 (1.6)	25.9 (1.7)	26.2 (2.5)	.03
Birth weight (g)	1067 (222)	992 (235)	789 (185)	897 (305)	.002
Birth weight < −2 SD	1 (6%)	3 (7%)	1 (5%)	1 (8%)	.99
Male sex	9 (50%)	22 (49%)	6 (29%)	6 (46%)	.43
Singleton	9 (50%)	13 (29%)	6 (29%)	5 (39%)	.40
Critical Risk Index for Babies score	1 [1–4]	2 [1–5.5]	4 [1.5–7.5]	4 [1–9]	.06
Days of intubation	1 [0.75–2.25]	2 [1–8.5]	4 [1–28]	21 [3.5–52.5]	.004
Oxygen at 36 weeks	5 (28%)	23 (51%)	12 (57%)	9 (69%)	.12
Postnatal steroid use	0	9 (20%)	10 (48%)	7 (54%)	.001
Inotrope use	1 (6%)	12 (27%)	11 (52%)	9 (69%)	<.001
Patent ductus arteriosus	5 (28%)	14 (31%)	11 (52%)	9 (69%)	.04
Total parenteral nutrition	10.5 [9–16.5]	16 [12.5–26.5]	29 [14.5–47]	25 [10–36]	.004
Chorioamnionitis	5 (28%)	19 (42%)	9 (45%)	4 (31%)	.61
Confirmed sepsis	2 (11%)	10 (22%)	9 (43%)	8 (62%)	.007
Necrotizing enterocolitis	0	2 (4%)	3 (14%)	2 (15%)	.19

Note:—Data are mean (SD), number (%), or median [lower-upper quartile].

amus (Fig 1*H*), all of the other findings with signal abnormalities in the deep GM and the cerebellum corresponded to hemorrhagic lesions (ie, associated with shortened T1 and T2 relaxation time constants). Moderate to severe abnormalities in the cortical GM, deep GM, or cerebellum were observed in 16 infants (16%), 11 infants (12%), or 32 infants (33%), respectively.

In contrast, none of the 22 term-born infants were classified as being in the moderate-to-severe category in any brain region. One term infant was classified as being in the mild category in the total WM score; 2 each were categorized as being in the mild category in the cortical GM score, deep GM score, and cerebellar score.

Structural Correlation between WM Injury and Deep GM or Cerebellar Abnormality

Of the 7 infants with cystic WM lesions, 3 were diagnosed with cystic periventricular leukomalacia and 4 with periventricular

hemorrhagic infarction. All 7 infants were categorized as having moderate or severe WM abnormalities, whereas 20 infants with noncystic focal WM signal abnormalities varied in the total WM score according to differences in items related to volume. These cystic or focal WM signal abnormalities were associated with a reduced deep GM area but not with cerebellar abnormalities. On the other hand, intraventricular hemorrhage and/or periventricular hemorrhagic infarction were observed in 31 VPT infants (grade I [$n = 8$], grade II [$n=18$], grade III [$n=1$], periventricular hemorrhagic infarction [$n=4$]) and were associated with cerebellar signal abnormalities and volume reduction (Table 3).

Risk Factors for Grades of Global Brain Abnormality Score

For the global brain score in VPT infants, 18 infants (19%) were categorized as normal, 45 (46%) as mild, 21 (22%) as moderate, and 13 (13%) as severe. All term-born infants were categorized as normal. Gestational age at birth and birth weight correlated with the grade of global brain abnormality, but postmenstrual age at scan did not ($P = .99$). Multiple clinical risk factors were associated with worsening severity of global brain abnormalities, including days of intubation, postnatal corticosteroid use, demand for inotrope, treated patent ductus arteriosus, days of parenteral nutrition, and confirmed sepsis (Table 4).

DISCUSSION

Our study applies a new scoring system for conventional (T1- and T2-weighted) MR imaging to define the nature and extent of regional and global brain abnormalities in the VPT infant at term-equivalent postmenstrual age. It extends the analysis of cerebral structures and incorporates objective measures of brain growth. Although primary injury, best defined by signal abnormalities on MR imaging, is important, impaired brain growth at term-equivalent postmenstrual age is also an important sequela of preterm birth. Impaired brain growth can result from secondary degeneration after injury and/or impairments in typical development that may result from poor nutrition[19] or other adverse exposures, including postnatal corticosteroids[20] and stress.[21,22]

Although the cerebral WM is a commonly injured area in the preterm infant because of its maturation-specific vulnerability, there is increasing recognition of brain injury beyond the cerebral WM. Recent investigations suggest that the deep GM and the cerebellum are also vulnerable to stresses encountered during the second to third trimesters. Histopathologic studies reveal that neuronal loss and gliosis occur within the thalamus of 40%–60% of VPT infants and in the cerebellum of 30%.[6] Our present study confirms that VPT infants have a high prevalence of primary brain injury in multiple regions including, but not limited to, the WM (24%). A similar prevalence of injury was found in the cerebellum (24%). Of note, no correlation was observed between the occurrence of WM and cerebellar injuries, indicating potentially independent pathologic pathways. Although the pathologic mechanism(s) of cerebellar hemorrhage remain uncertain, germinal matrix bleeding within the subpial external granular cell layer has been considered.[23] Indeed, the etiologic factors reported for cerebellar hemorrhage are similar to those in intraventricular hemorrhage, including extreme prematurity, fetal distress, increased venous pressure, and impaired autoregulation of cerebral flow.[24] In contrast, the pathogenesis for WM injury includes arterial hypoperfusion, systemic infection/inflammation, and the intrinsic vulnerability of preoligodendrocytes.[5] Thus, considering its relatively high prevalence and likely etiologic differences from WM injury, a systematic assessment of cerebellar injury should be included in evaluations of the effect of preterm birth.

Using objective measurements, our study further demonstrates that each brain structure is reduced in size in the VPT infant assessed at term-equivalent postmenstrual age. Studies with 3D volumetric MR imaging methods demonstrate that preterm children have reduced volume in the cerebral WM,[25,26] cortical GM,[26,27] deep GM,[28] and cerebellum,[29,30] and such volume reductions correlate with neurodevelopmental disabilities.[26,27,30] During the second to third trimesters, all brain structures are rapidly expanding. Such volume expansion is driven by the maturational processes of axon extension, dendrite elaboration, synaptogenesis, glial proliferation, and glial maturation. Widespread injury may have a particular effect on the thalamus. Thalamocortical neurons project to all parts of the cortical GM, and in turn, corticothalamic axons reach targeted thalamic neurons by term-equivalent postmenstrual age. Appropriate growth of the thalamus could be impaired by a primary insult, such as ischemia or hemorrhage, or by the secondary effects of degeneration or deafferentation caused by WM and/or cortical GM injury.[31] Thus, deep GM volume may, in effect, integrate the consequences of injury to the WM and cortical GM, thereby more fully defining the effect of overall abnormalities[32,33] and reflecting the global nature of disturbances in brain development.

The scoring system that we have developed in our study helps to comprehensively define the complicated nature of brain abnormalities and to stratify the severity of brain abnormalities in the VPT infant. The grade of global brain abnormality defined with this scoring system was associated with clinical risk factors, including low systemic blood pressure, prolonged hypoxia, infection/inflammation, nutritional challenges, and drug therapies. Each of these causal factors is known to have a tight relationship to injury and/or disturbances of brain growth.[34-36] This cohort of VPT infants has not yet completed neurodevelopmental assessment at age 2 years, but an evaluation of the relationship between these scores and short-term outcomes would provide further validation.

Qualitative assessment of brain volumes is challenging, and the reference standard for quantitative measurement of volumes is 3D volumetry. Although the MR imaging data used for our study are of sufficiently high spatial resolution ($1 \times 1 \times 1\ mm^3$) to use a volumetric approach, we chose instead to use simple 1D or 2D brain metrics to indicate volumes. This was because 3D volumetric data are not readily available in clinical practice because of computational requirements and the relatively lower spatial resolution of typical clinical images. The use of simpler brain metrics will make this scoring system more widely available. Furthermore, the brain metrics that we used show reasonable correlations with 3D volumetric measurements,[15] and several of the regional metrics used in our study have been shown to predict subsequent motor or cognitive outcomes in the preterm population.[37,38]

CONCLUSIONS

We have developed a scoring system for conventional MR images that provides a comprehensive and objective characterization of

regional and global brain injury and brain growth. This system may assist in clarifying the effect of preterm birth and the relationship between MR imaging–defined structural alterations of the brain at term-equivalent postmenstrual age and subsequent neurodevelopmental outcome in VPT survivors.

ACKNOWLEDGMENTS

We thank Drs. C. Vavasseur and T. Tjoeng; research staff K. Lukas, A. Barton, D. Alexopoulos, and J. Ackerman; and the families for their participation in this study.

Disclosures: The authors declare no conflicts of interest. We have not been paid to write this manuscript by pharmaceutical companies, medical equipment manufacturers, biomedical device manufacturers, or any companies with significant involvement in health care. Jeffrey Neil—*RELATED: Grant:* NIH.* Terrie Inder—*RELATED: Grant:* National Institutes of Health (NICHD RO1HD057098); *UNRELATED: Expert Testimony:* Occasional medical expert opinion in term infant brain injury cases. **Money paid to institution.*

REFERENCES

1. Platt MJ, Cans C, Johnson A, et al. **Trends in cerebral palsy among infants of very low birthweight (<1500 g) or born prematurely (<32 weeks) in 16 European centres: a database study.** *Lancet* 2007;369:43–50
2. Robertson CM, Watt MJ, Yasui Y. **Changes in the prevalence of cerebral palsy for children born very prematurely within a population-based program over 30 years.** *JAMA* 2007;297:2733–40
3. Anderson P, Doyle LW. **Neurobehavioral outcomes of school-age children born extremely low birth weight or very preterm in the 1990s.** *JAMA* 2003;289:3264–72
4. Hack M, Flannery DJ, Schluchter M, et al. **Outcomes in young adulthood for very-low-birth-weight infants.** *N Engl J Med* 2002;346:149–57
5. Volpe JJ, Kinney HC, Jensen FE, et al. **Reprint of "The developing oligodendrocyte: key cellular target in brain injury in the premature infant".** *Int J Dev Neurosci* 2011;29:565–82
6. Pierson CR, Folkerth RD, Billiards SS, et al. **Gray matter injury associated with periventricular leukomalacia in the premature infant.** *Acta Neuropathol* 2007;114:619–31
7. Merrill JD, Piecuch RE, Fell SC, et al. **A new pattern of cerebellar hemorrhages in preterm infants.** *Pediatrics* 1998;102:E62
8. Messerschmidt A, Brugger PC, Boltshauser E, et al. **Disruption of cerebellar development: potential complication of extreme prematurity.** *AJNR Am J Neuroradiol* 2005;26:1659–67
9. Peterson BS, Vohr B, Staib LH, et al. **Regional brain volume abnormalities and long-term cognitive outcome in preterm infants.** *JAMA* 2000;284:1939–47
10. Nosarti C, Al-Asady MHS, Frangou S, et al. **Adolescents who were born very preterm have decreased brain volumes.** *Brain* 2002;125:1616–23
11. Peterson BS, Anderson AW, Ehrenkranz R, et al. **Regional brain volumes and their later neurodevelopmental correlates in term and preterm infants.** *Pediatrics* 2003;111:939–48
12. Inder TE, Wells SJ, Mogridge NB, et al. **Defining the nature of the cerebral abnormalities in the premature infant: a qualitative magnetic resonance imaging study.** *J Pediatr* 2003;143:171–79
13. Sie LT, Hart AA, van Hof J, et al. **Predictive value of neonatal MRI with respect to late MRI findings and clinical outcome. A study in infants with periventricular densities on neonatal ultrasound.** *Neuropediatrics* 2005;36:78–89
14. Miller SP, Ferriero DM, Leonard C, et al. **Early brain injury in premature newborns detected with magnetic resonance imaging is associated with adverse early neurodevelopmental outcome.** *J Pediatr* 2005;147:609–16
15. Nguyen The Tich S, Anderson PJ, Shimony JS, et al. **A novel quantitative simple brain metric using MR imaging for preterm infants.** *AJNR Am J Neuroradiol* 2009;30:125–31
16. Papile LA, Burstein J, Burstein R, et al. **Incidence and evolution of subependymal and intraventricular hemorrhage: a study of infants with birth weights less than 1,500 gm.** *J Pediatr* 1978;92:529–34
17. Barkovich AJ. **Brain and spine injuries in infancy and childhood** In: Barkovich AJ, ed. *Pediatric Neuroimaging* 4th ed. Philadelphia: Lippincott Williams & Wilkins; 2005:207–26
18. Bell MJ, Ternberg JL, Feigin RD, et al. **Neonatal necrotizing enterocolitis. Therapeutic decisions based upon clinical staging.** *Ann Surg* 1978;187:1–7
19. Tan M, Abernethy L, Cooke R. **Improved head growth in preterm infants–a randomised controlled trial II: MRI and developmental outcomes in the first year.** *Arch Dis Child Fetal Neonatal Ed* 2008;93:F342–46
20. Murphy BP, Inder TE, Huppi PS, et al. **Impaired cerebral cortical gray matter growth after treatment with dexamethasone for neonatal chronic lung disease.** *Pediatrics* 2001;107:217–21
21. Smith GC, Gutovich J, Smyser C, et al. **Neonatal intensive care unit stress is associated with brain development in preterm infants.** *Ann Neurol* 2011;70:541–49
22. Brummelte S, Grunau RE, Chau V, et al. **Procedural pain and brain development in premature newborns.** *Ann Neurol* 2012;71:385–96
23. Volpe JJ. **Cerebellum of the premature infant: rapidly developing, vulnerable, clinically important.** *J Child Neurol* 2009;24:1085–104
24. Limperopoulos C, Benson CB, Bassan H, et al. **Cerebellar hemorrhage in the preterm infant: ultrasonographic findings and risk factors.** *Pediatrics* 2005;116:717–24
25. Northam GB, Liégeois F, Chong WK, et al. **Total brain white matter is a major determinant of IQ in adolescents born preterm.** *Ann Neurol* 2011;69:702–11
26. Nagy Z, Ashburner J, Andersson J, et al. **Structural correlates of preterm birth in the adolescent brain.** *Pediatrics* 2009;124:e964–72
27. Inder TE, Warfield SK, Wang H, et al. **Abnormal cerebral structure is present at term in premature infants.** *Pediatrics* 2005;115:286–94
28. Srinivasan L, Dutta R, Counsell SJ, et al. **Quantification of deep grey matter in preterm infants at term-equivalent age using manual volumetry of 3-Tesla magnetic resonance images.** *Pediatrics* 2007;119:759–65
29. Van Kooij BJ, Benders MJ, Anbeek P, et al. **Cerebellar volume and proton magnetic resonance spectroscopy at term, and neurodevelopment at 2 years of age in preterm infants.** *Dev Med Child Neurol* 2012;54:260–66
30. Parker J, Mitchell A, Kalpakidou A, et al. **Cerebellar growth and behavioral & neuropsychological outcome in preterm adolescents.** *Brain* 2008;131:1344–51
31. Boardman JP, Counsell SJ, Reuckert D, et al. **Abnormal deep gray matter development following preterm birth detected using deformation-based morphometry.** *Neuroimage* 2006;32:70–78
32. Lin Y, Okumura A, Hayakawa F, et al. **Quantitative evaluation of thalami and basal ganglia in infants with periventricular leukomalacia.** *Dev Med Child Neurol* 2001;43:481–85
33. Zubiaurre-Elorza L, Soria-Pastor S, Junqué C, et al. **Thalamic changes in a preterm sample with periventricular leukomalacia: correlation with white-matter integrity and cognitive outcome at school age.** *Pediatr Res* 2012;71:354–60
34. Stoll BJ, Hansen NI, Adams-Chapman I, et al. **Neurodevelopmental and growth impairment among extremely low-birth-weight infants with neonatal infection.** *JAMA* 2004;292:2357–65
35. Short EJ, Klein NK, Lewis BA, et al. **Cognitive and academic consequences of bronchopulmonary dysplasia and very low birth weight: 8-year-old outcomes.** *Pediatrics* 2003;112:e359
36. Lucas A, Morley R, Cole TJ. **Randomised trial of early diet in preterm babies and later intelligence quotient.** *BMJ* 1998;317:1481–87
37. Spittle AJ, Doyle LW, Anderson PJ, et al. **Reduced cerebellar diameter in very preterm infants with abnormal general movements.** *Early Hum Dev* 2010;86:1–5
38. Tich SN, Anderson PJ, Hunt RW, et al. **Neurodevelopmental and perinatal correlates of simple brain metrics in very preterm infants.** *Arch Pediatr Adolesc Med* 2011;165:216–22

Optimized T1-MPRAGE Sequence for Better Visualization of Spinal Cord Multiple Sclerosis Lesions at 3T

G. Nair, M. Absinta, and D.S. Reich

ABSTRACT

BACKGROUND AND PURPOSE: Spinal cord lesions are highly prevalent in MS, and their visualization can help both in diagnosis and patient follow-up. However, the sensitivity of MR imaging to spinal cord lesions remains poor, primarily because of suboptimal contrast between lesions and a normal-appearing cord. Here, we propose an optimized 3D MPRAGE sequence for improved detection of MS lesions in the spinal cord at 3T.

MATERIALS AND METHODS: Images were acquired by use of T2 FSE, STIR, T1-gradient recalled-echo (for T1 mapping), and T1-MPRAGE in the sagittal plane, and T2*-weighted scans in the axial plane, on 40 patients with MS and 7 healthy volunteers. Two observers qualitatively evaluated the images for lesion conspicuity. Lesions seen between the C1 and C4 segments in 10 randomly selected patients with MS were further evaluated quantitatively for contrast-to-noise ratio between the lesion and normal-appearing cord, and for lesion burden.

RESULTS: Spinal cord lesions were more conspicuous on the optimized T1-MPRAGE sequence than on any other sequence tested. Detailed analysis revealed that lesions were almost 3 times more conspicuous ($P < .01$), and the total lesion volume was 2 times greater ($P < .05$, $n = 10$), in the T1-MPRAGE sequence compared with the standard STIR sequence. Correlation of clinical disability (Expanded Disability Status Score) with lesion load from each sequence also demonstrated the importance of the improved lesion conspicuity with T1-MPRAGE.

CONCLUSIONS: The optimized T1-MPRAGE sequence described here improves the reliability of lesion visualization and estimation of lesion burden, especially when used in conjunction with other well-established clinical sequences.

ABBREVIATIONS: CNR = contrast-to-noise ratio; EDSS = Expanded Disability Status Score; GRAPPA = generalized autocalibrating partially parallel acquisition; MERGE = multi-echo recombined gradient-echo; NAC = normal-appearing cord; PSIR = phase-sensitive inversion recovery; GRE = gradient recalled-echo

MS is a disease of the central nervous system, and spinal cord lesions are widely prevalent in patients with MS. It is thought that, in the proper context, the presence of cord lesions is highly specific for the diagnosis of MS,[1-3] and several studies have shown spinal cord abnormalities in 75%–90% of patients clinically diagnosed with MS.[4-7] Visualization of spinal cord lesions allows approximately 18% more patients to meet the McDonald dissemination in space criteria for the diagnosis of MS.[8] Cord lesions are also believed to occur in isolation, further highlighting the importance of visualizing lesions in the spinal cord for the diagnosis of MS.[8-10]

MR imaging of the spinal cord is challenging not only because of the small size of structures but also because of artifacts from respiration, cardiac, and CSF pulsation, and cord movement during the cardiac cycle. Although advances in MR imaging hardware and pulse sequences have mitigated some of these challenges, sensitivity to visualization of cord lesion remains poor.[11,12] Several studies have proposed specialized and optimized sequences for improving lesion visualization in the spinal cord, especially the cervical cord, including double-echo spin-echo,[13] STIR,[14-16] phase-sensitive inversion recovery (PSIR),[17] and multi-echo recombined gradient-echo (MERGE on GE scanners, also called Multi-Echo Data Image Combination or MEDIC on Siemens

Received December 28, 2012; accepted after revision February 18, 2013.

From the National Institute of Neurological Disorders and Stroke (G.N., M.A., D.S.R.), National Institutes of Health, Bethesda, Maryland; Neuroimaging Research Unit (M.A.) and Department of Neurology, Institute of Experimental Neurology, Division of Neuroscience, San Raffaele Scientific Institute, Vita-Salute San Raffaele University, Milan, Italy; and Department of Radiology and Neurology (D.S.R.), Johns Hopkins University, Baltimore, Maryland.

Support: Intramural Research Program of NINDS.

Paper previously presented at: Annual Meeting of the Americas Committee for Treatment and Research in Multiple Sclerosis (ACTRIMS), May 30–June 2, 2012; San Diego, California.

Please address correspondence to Govind Nair, Translational Neuroradiology Unit, National Institute of Neurological Disorders and Stroke, National Institutes of Health; Bldg 10, Rm 5C103; 10 Center Dr, MSC 1400; Bethesda, MD 20892; e-mail: reichds@ninds.nih.gov

http://dx.doi.org/10.3174/ajnr.A3637

scanners and multi-echo Fast Field Gradient Echo or mFFE on Philips scanners).[18-20] Of these, the proton density and T2 (double-echo) spin-echo or FSE[21] and STIR[14] sequences have been accepted as a clinical standard for spinal cord imaging in MS,[13] primarily because of the ease of implementation on a wide range of scanners. However, lesions are demonstrably more conspicuous in sequences such as PSIR[17] and MERGE.[18] Furthermore, despite sequence improvements, the correlation between lesion volume and clinical Expanded Disability Status Score (EDSS) remains low.[22,23] One contributing factor could be that MR imaging sequences are insensitive to many lesions in the cord, and that radiologic calculation of lesion burden is inaccurate.[15]

An optimized sequence for detection of cord lesions may improve diagnostic efficiency and accuracy of CNS lesion load estimation. The MPRAGE sequence offers a unique opportunity, through optimization of T1-contrast and SNR. Here, we qualitatively evaluate a T1-weighted MPRAGE sequence for efficiency of visualizing lesions in the cervical and thoracic spinal cord and quantitatively compare its performance with other sequences including STIR, T2-weighted, T2*-weighted, and noninversion-prepared T1-weighted gradient-echo sequences in the upper cervical spinal cord.

MATERIALS AND METHODS

Patients

MR imaging of the cervical and thoracic spinal cord was performed on 40 patients and 7 healthy control participants. MR images from 10 patients with MS were randomly selected for a more detailed quantitative analysis of lesions in the upper cervical cord. Written, informed consent was obtained from all participants, and the Institutional Review Board at the National Institutes of Health approved all protocols.

MR Imaging

MR imaging was performed on a 3T Skyra system (Siemens, Erlangen, Germany) equipped with a 20-channel head-neck coil and a 16-channel spine-array coil. Standard clinical sequences and sequences optimized elsewhere that have been traditionally used to visualize spinal cord lesions such as T2-weighted FSE, STIR, T1-weighted gradient recalled-echo (GRE), and T2*-weighted GRE sequences were compared with the optimized T1-MPRAGE sequence in the cervical and thoracic regions separately.

In the cervical spine, T2-weighted images were acquired in the sagittal plane by use of a 2D FSE sequence (T2-FSE) with TR, 3500 ms; TE, 102 ms; 0.7-mm nominal in-plane resolution; and 1-mm section thickness (no intersection gap), with a scan time of 3 minutes 40 seconds. STIR images were acquired in the sagittal plane with a 2D inversion-prepared FSE sequence with TR, 4000 ms; TE, 68 ms; TI, 210 ms; parallel imaging with generalized autocalibrating partially parallel acquisition (GRAPPA 2); 0.8-mm nominal in-plane resolution; 2-mm section thickness; a 10% gap between sections; and a scan time of 4 minutes 30 seconds. A 3D-MPRAGE sequence (T1-MPRAGE) was acquired in the sagittal plane with TR, 3000 ms; TE, 4.5 ms; TI, 750 ms; flip angle, 8°; parallel imaging (GRAPPA 2); 1-mm isotropic resolution; and a scan time of 7 minutes 30 seconds. T1 mapping was done by use of two 3D-gradient-echo sequences with TR, 7.8 ms; TE, 3 ms; 1-mm isotropic resolution; and flip angles of 3° and 16° (T1-GRE), for a scan time of approximately 3 minutes per flip angle. Finally, T2*-weighted images were acquired in the axial plane with the 2D MEDIC sequence (T2*-GRE) with TR, 775 ms; TE, 11 ms; flip angle, 20°; parallel imaging (GRAPPA 2); nominal in-plane resolution, 0.58 mm; section thickness, 5 mm (no intersection gap); and a scan time of 3 minutes 30 seconds. The protocols were very similar for imaging of the thoracic spine, except that the sequence was GRE, and field-of-view and acquisition matrix were modified to cover the entire thoracic spinal cord. The T1-GRE sequence was repeated postgadolinium (gadobutrol, 0.1 mmol/kg) only if clinically indicated.

Data Analysis

By consensus, a neurologist (M.A., with 7 years of experience) and a neuroradiologist (D.S.R., with 10 years of experience) rated each lesion from the MS and healthy control groups in a blinded fashion. Images obtained from all of the sequences were assessed simultaneously, and lesions that were conspicuous in any of the pulse sequences were counted, and their vertebral levels noted for each patient. For detailed quantitative analysis, scans from 10 patients were randomly selected from the MS group. 3D scans were reformatted only in orthogonal (axial, coronal, and sagittal) planes in OsiriX (http://www.osirix-viewer.com/)[24] for qualitative evaluation, and a lesion was labeled confirmed if it was present in more than 1 sequence or if it had a characteristic appearance on reformation. None of the quantitative analysis used curved or oblique reformatting. The conspicuity of each lesion in the various pulse sequences was scored as being absent or of poor, good, or excellent conspicuity (scores from 0–3). Lesion detection efficiency for each sequence was calculated as an average percent of lesions detected with good or excellent conspicuity to the total number of lesions seen in each patient. T1 maps were calculated on a pixel-by-pixel basis in Matlab (MathWorks, Natick, Massachusetts) by use of the variable flip-angle GRE scans, described elsewhere.[25] ROIs were drawn on visible lesions (L) and normal-appearing brain stem or cord (NAC) at the C1 level in each sequence, and the contrast-to-noise ratios (CNRs) were calculated with the formula $(S_L - S_{NAC})/(S_L + S_{NAC})$, where S is a signal in an ROI. Lesion volumes in the C1–C4 region were determined from each patient on the basis of conspicuity (only lesions of good or excellent conspicuity) in each imaging sequence, and the total lesion volume was normalized and compared with that derived from a STIR sequence (paired t test). The lesion volumes from each sequence were also correlated with EDSS.

RESULTS

Of the 40 patients studied, 1 patient was diagnosed with neuromyelitis optica, and the data from this patient were not analyzed. Detailed demographic information is shown in the accompanying Table. In the blinded analysis, a total of 324 lesions were identified in the spinal cords of 39 patients with MS; no lesions were identified in the healthy volunteer group. Typical lesions in the cervical cord from 2 different participants (top and bottom row) are shown in Fig 1. Focal and diffuse lesions in the cervical spinal cord could be clearly and consistently visualized in the T1-MPRAGE

Demographic data for participant groups

Group	No. of Patients (Sex)	Age (y)	Diagnosis (MS Subtype)	Disease Duration (y)	EDSS (Range)
Healthy volunteers	7 (5 F)	44 ± 7	–	–	–
All patients with MS	39 (21 F)[a]	49 ± 12	Relapsing-remitting ($n = 14$) Secondary-progressive ($n = 10$) Primary-progressive ($n = 15$)	13 ± 11	1.0–7.0
MS subgroup for quantitative analysis	10 (9 F)	47 ± 12	Relapsing-remitting ($n = 4$) Secondary-progressive ($n = 5$) Primary-progressive ($n = 1$)	17 ± 14	1.0–6.5

[a] One of 40 patients recruited was dropped from the analysis when clinically diagnosed with neuromyelitis optica.

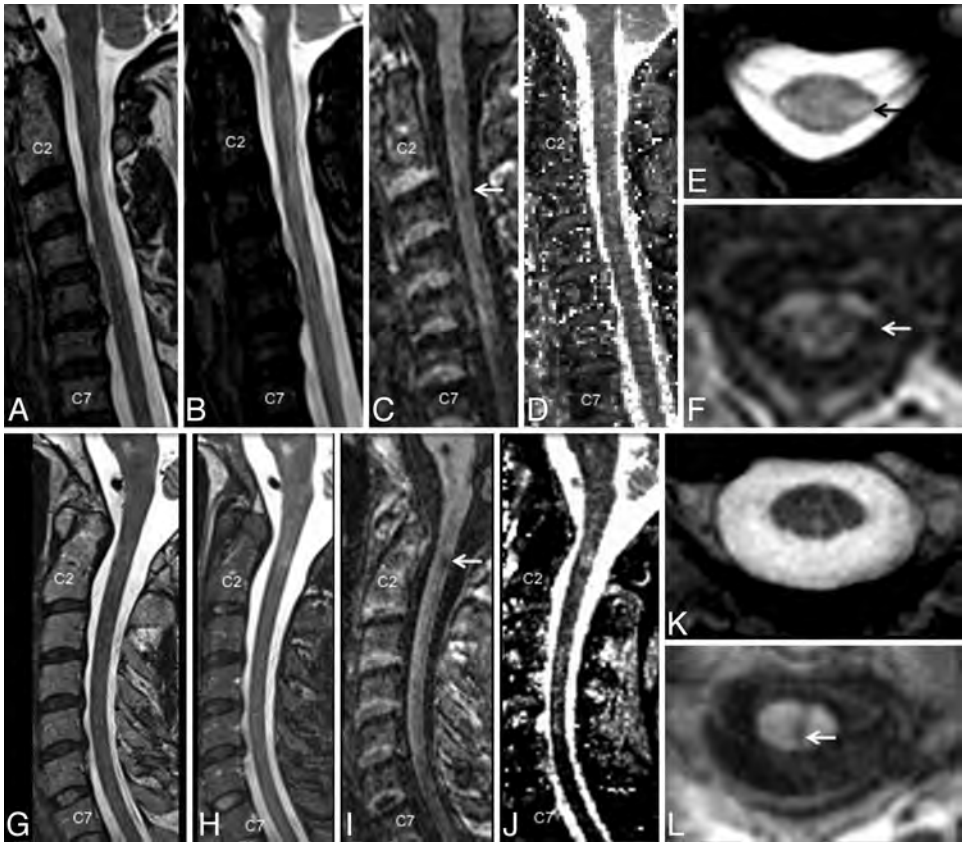

FIG 1. A comparison of imaging techniques for visualization of cervical cord lesions in a 45-year-old woman (*A–F*) and a 43-year-old man (*G–L*), both with relapsing-remitting MS. T1-weighted MPRAGE (*C* and *I*) performed better than routine clinical T2-weighted FSE (*A* and *G*), STIR (*B* and *H*), and quantitative T1 maps of the cervical cord (*D* and *J*), generated by use of a multiple flip angle gradient-echo sequence. The lesions were also visible on axially reformatted T1-MPRAGE images (*F* and *L*) and in these cases were also well visualized on axial T2*-GRE (*E* and *K*).

sequence (Fig 1*C, -F, -I, -L*). T2*-GRE images were consistently good at visualizing lesions with some portion extending into the cord (Fig 1*E*) but performed more poorly for lesions on the surface of the cord (Fig 1*K*). Lesions were consistently less conspicuous on the STIR and T2-FSE images (Fig 1*A, -B, -G*).

Similar results were observed from the thoracic spine, with most lesions being conspicuous on the T1-MPRAGE images followed by T2*-GRE, STIR, and T2-FSE (Fig 2). T1-MPRAGE was able to detect acute lesions as well (Fig 3*A–C*). Neither the T1-MPRAGE nor the other scans from the healthy control participants showed any focal hypointense lesions (Fig 3*D*) such as those seen in the patients with MS. Coronal and curved reformatted (used only for visualization in this figure and not for quantitative analysis) T1-MPRAGE of the cervical cord in patients with MS (Fig 4*A, -B*) depicts the lesions mainly on the surface of the cord. A plot of average incidence of lesions that were conspicuous in any of the pulse sequences, as a function of vertebral body level, is shown in Fig 4*C*. Forty percent of all lesions occurred in the C1–C4 segments; therefore, these levels were chosen for detailed quantitative analysis.

Quantitative analysis from 10 patients with MS showed that the CNR between the lesion and NAC was 0.5 ± 0.12 for T1-MPRAGE, 0.15 ± 0.07 for STIR, 0.13 ± 0.07 for T2-FSE, and 0.08 ± 0.03 for T2*-GRE (Fig 5*A*, $^{**}P < .01$, unpaired *t* test). The T1 maps calculated from the 2-flip angle method yielded a T1 of 1749 ± 260 ms (mean ± SD) in the lesions compared with 1027 ± 193 ms in the NAC, yielding a CNR of 0.25 ± 0.08, which was significantly lower than that of the T1-MPRAGE sequence.

In the C1–C4 segments, the T1-MPRAGE sequence detected 59 of the 60 observed lesions that were judged to have good or excellent conspicuity by the 2 expert observers, resulting in a lesion detection efficiency of 98% per patient (Fig 5*B*; $n=10$ pa-

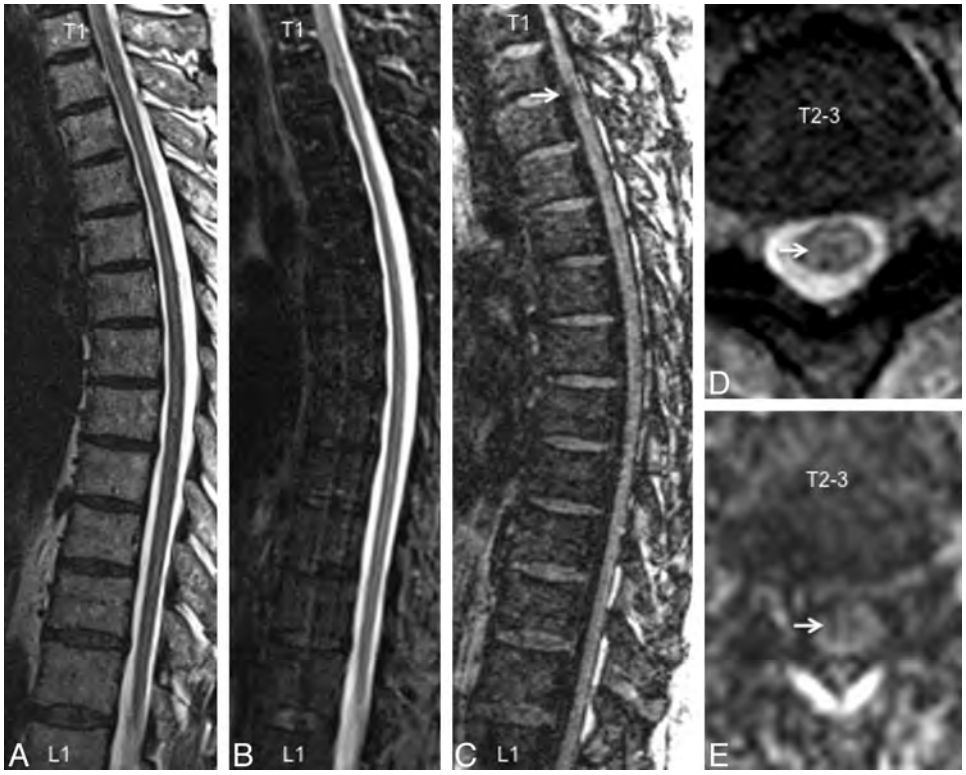

FIG 2. A comparison of imaging techniques for visualization of thoracic cord lesions in a 45-year-old woman with relapsing-remitting MS. Just as in the cervical cord, T1-weighted MPRAGE (*C*) performed better than routine clinical T2-weighted FSE (*A*), STIR (*B*), and T2*-GRE (*D*) for visualization of lesions. The lesion denoted by an arrow has a typical appearance and could be confirmed on axially reformatted T1-MPRAGE images (*E*).

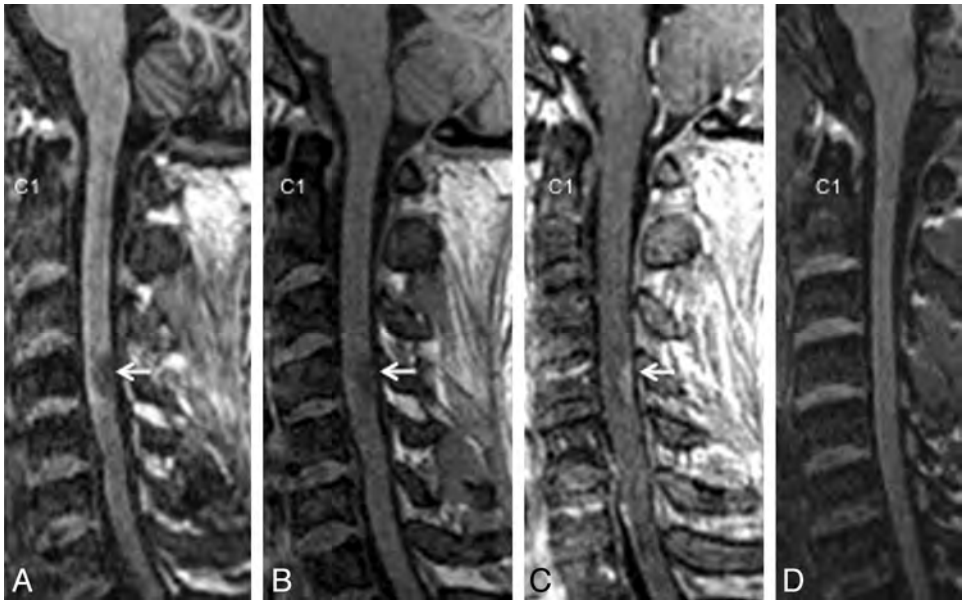

FIG 3. An acute spinal cord lesion in the C4 region (*arrow*, 31-year-old man) as seen in T1-MPRAGE (*A*), precontrast (*B*), and postcontrast (*C*) T1-weighted gradient-echo (*C*) images. (*D*) T1-MPRAGE from a healthy control participant (38-year-old man) for comparison.

tients). Forty-five of the 60 lesions were conspicuous in the axial T2* sequences (75% of the lesions; lesions detected in 82% of the patients with cord lesions). The average length of lesions judged to have excellent conspicuity was 7.2 ± 0.6 mm in the inferior-superior direction, compared with 5.2 ± 0.6 mm for lesions judged to be less conspicuous ($P = .02$; lengths calculated on the T1-MPRAGE sequence). Only 26 of the 60 lesions were conspicuous on the STIR (43% of the lesions; lesions detected in 51% of the patients with cord lesions), and only 15 were conspicuous on the T2-FSE sequences (25% of the lesions; lesions detected in 32% of the patients with cord lesions).

Average lesion volume from the T1-MPRAGE sequence was more than twice that calculated from the clinical standard STIR sequence and was significantly higher than that determined from

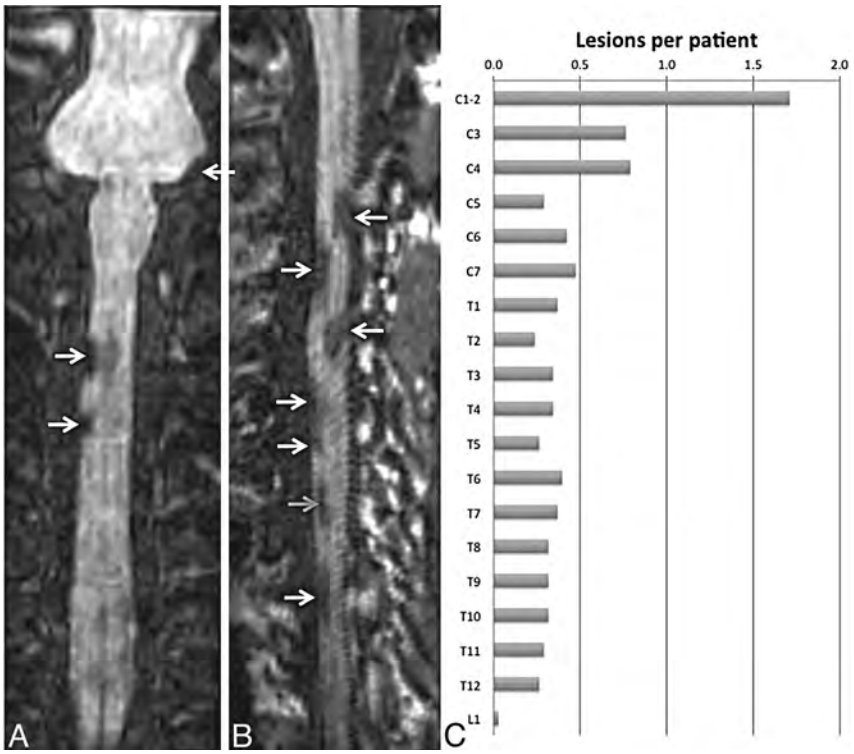

FIG 4. Coronal (*A*) and curved-reformatted (*B*) images from the T1-weighted MPRAGE sequence in the cervical cord of 2 patients, showing lesions mainly on the surface of the cord (*white arrows*) and a lesion that appears to be completely within the cord (*gray arrow*). *C*, Incidence of lesions per vertebral body segment derived from all scans acquired in the MS population studied herein (Table, 39 patients with MS).

all other sequences ($P < .05$; $n=10$ patients). Lesion volume, calculated relative to the STIR sequence, was 1.95 for T1-MPRAGE, 1.67 for T2*-GRE, and 0.6 for T2-FSE ($P < .05$ by paired *t* test; Fig 5*C*). The smallest conspicuous lesion was 11.8 mm^3 in the T1-MPRAGE sequence, 16.6 mm^3 in the T2*-GRE, 21.3 mm^3 in the T2-FSE, and 24.8 mm^3 in the STIR. Pearson correlation coefficient, determined between EDSS and lesion volume, approached significant levels only in the T1-MPRAGE (Pearson $r = 0.52$; 1-tailed $P = .06$; Fig 5*D*), and the correlation coefficients were larger in sequences that had better lesion conspicuity (T1-MPRAGE and T2*-GRE).

DISCUSSION

The optimized T1-MPRAGE sequence was better at lesion visualization in both the cervical and thoracic spinal cord than the STIR, T2-FSE, T1-GRE, and T2*-GRE sequences tested herein. The optimized T1-MPRAGE sequence was able to reliably and distinctly detect both acute and chronic lesions in the cord. The high CNR of the optimized T1-MPRAGE played an important role in lesion detection. Reformatting the images in the axial and coronal planes proved to be useful in identification of the lesions, which was made easier because of the high isotropic resolution of the T1-MPRAGE.

It should also be noted that the central canal of the spinal cord was hypointense compared with the NAC in the T1-MPRAGE, and there was subtle hypointensity in the areas surrounding the central canal. Such signal changes are commonly seen in other high-resolution sequences, as well as in the healthy control participants (Fig 3*D*). However, the signal in the confirmed lesions was distinctly more hypointense and focal than these other signal changes and could easily be characterized as such (Figs 1 and 2). Only 1 of 60 confirmed lesions was of poor conspicuity on the T1-MPRAGE sequence.

Comparison of Sequences

Most lesions (45/60, or 75%) were also conspicuous on the T2*-GRE images. The lesions that were conspicuous on the T2*-GRE had a significantly larger extent in the superior-inferior direction than those that were inconspicuous on the T2*-GRE, emphasizing the role of partial volume averaging and image resolution in the detection of lesions. However, it must be noted that 7 of the 15 lesions that were inconspicuous on the T2*-GRE were larger than 5 mm in the superior-inferior direction, indicating that other factors, such as proximity to CSF (eg, Fig 1*K*) and motion or pulsation artifacts, can be detrimental to lesion visualization on T2*-GRE. Several improvements have been suggested to the T2*-GRE sequence, including higher resolution, 3D acquisition, and magnetization transfer preparation, all of which could improve the conspicuity of MS lesions; these were not explored herein.[20] Indeed, not every lesion was better seen on the T1-MPRAGE, and a few were even better depicted in the T2*-GRE-sequences, as can be seen in Fig 1 (top row). Nevertheless, more lesions with typical MS configuration were appreciated on the T1-MPRAGE overall. The T1-MPRAGE sequence may therefore be used in conjunction with other well-established clinical sequences, such as T2*-GRE, to improve diagnostic confidence.

The T2-FSE sequence was optimized for T2 contrast and resolution but proved to be inadequate for visualization of lesions. As many as 45 (75%) of the 60 lesions were invisible or were of poor conspicuity on the T2-FSE sequence. It is conceivable that the TE used herein is suboptimal for lesion detection in the spinal cord, and that lesions may be more conspicuous in proton attenuation–weighted conventional spin-echo images such as those described elsewhere for diffuse lesions.[14,16] However, such sequences were not explored herein because of potential motion artifacts, low resolution, and total scan time considerations. The STIR sequence has long been known to be useful for lesion detection,[15,16,26,27] and a standard clinical fast-STIR sequence with an inversion time of 200 ms was used here. The STIR sequence did indeed perform better than T2-FSE in both CNR and lesion visualization, as expected, despite the larger section thickness and a gap between sections.

Others have calculated the lesion-to-cord CNR from various sequences as a normalized difference in signal intensity from the lesion to cord. Hittmair et al[14] demonstrated a 187% increase in lesion-to-cord CNR with the STIR sequence compared with routine T2-FSE, by using a 1.5T scanner with lower

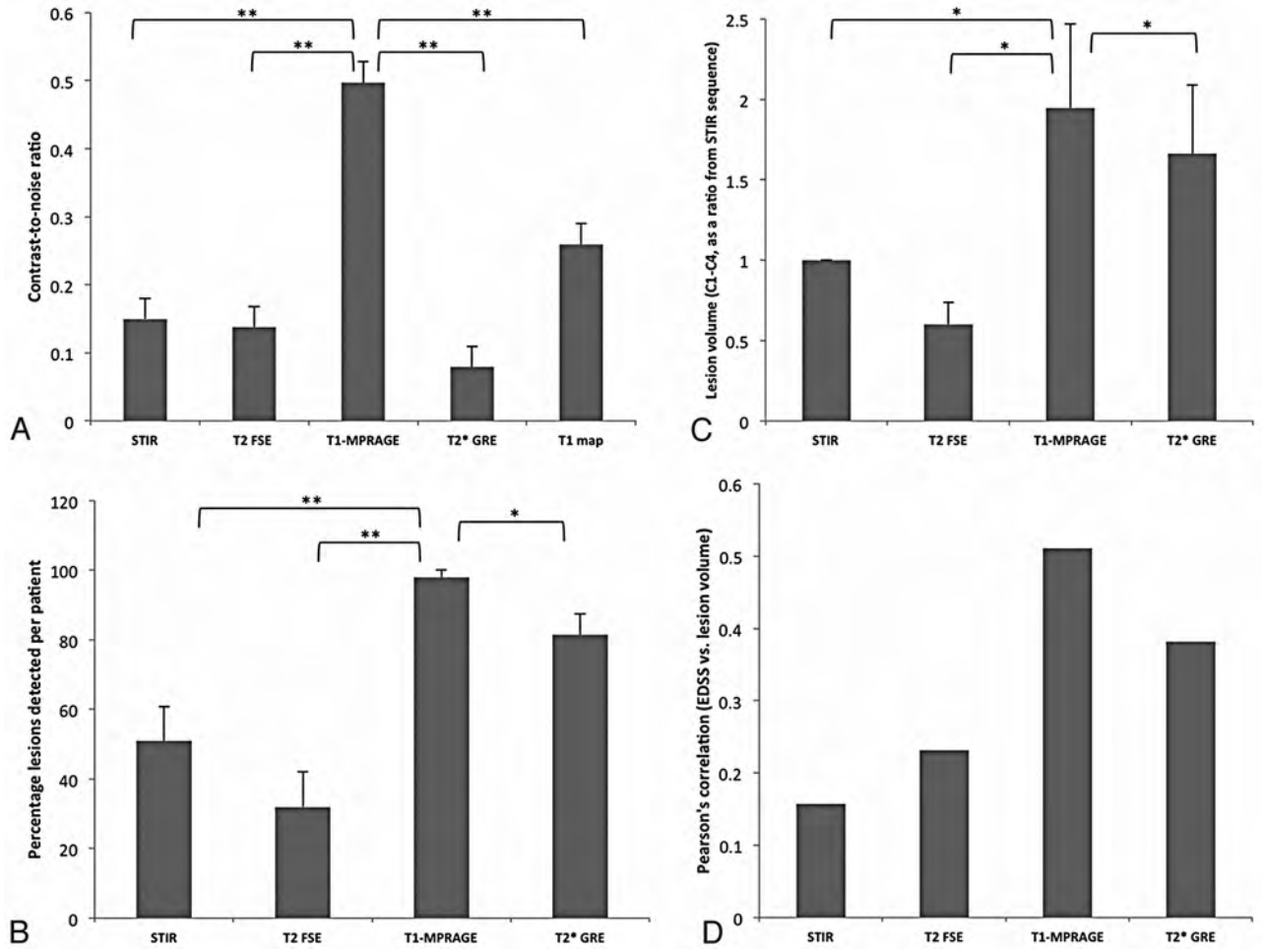

FIG 5. CNR (*A*), percentage of lesions detected per patient (*B*), lesion volume (in mm^3) between the C1 and C4 vertebral body segments (*C*), and Pearson correlation coefficient between lesion load and EDSS from 10 participants obtained by use of various pulse sequences for imaging cord lesions. The CNR and lesion volume calculated from the T1-MPRAGE sequence were significantly higher than other sequences tested (*$P < .05$, **$P < .01$, paired *t* test).

spatial resolution. The CNR from the T2*-MERGE sequence was reported to be approximately 200% higher than the T2-FSE sequence in the study by White et al,[18] and Poonawalla et al[17] demonstrated an approximately 200% increase in the CNR in STIR compared with T2-FSE at 3T. This result is similar to the observation herein of increased lesion conspicuity in the T2*-GRE and STIR images compared with the T2-FSE images. The formula for the CNR used herein normalized its value between 0 and 1, with 1 being the best contrast. Repeating the calculation by using formulas similar to the prior reports, on the data presented herein, shows a 190% increase in the CNR in STIR compared with T2-FSE, and a further 180% increase in CNR in T1-MPRAGE compared with STIR. However, the difference in CNR between T2*-GRE and T2-FSE was far lower than reported elsewhere,[18] probably because of differences in the pulse sequence parameters such as image resolution and the axial vs sagittal section plane. Furthermore, the T2*-GRE sequence herein used a section thickness of 5 mm for adequate whole-spine coverage in a reasonably short scan time, as opposed to 3 mm in prior reports. This larger section thickness, which engenders more partial volume averaging, may contribute to the reduced CNR seen here; reducing the section thickness could potentially increase the lesion detection rate at the cost of reduced SNR and increased scan time. As noted previously, the thick sections used in the T2*-GRE sequence made it difficult to pick up small lesions, especially on the surface of the cord (because of proximity to bright CSF). Despite these shortcomings, the availability of both the axially acquired T2*-GRE scans, with high in-plane resolution, as well as the isotropic T1-MPRAGE scans that can be reformatted in any plane, acts to substantially improve confidence in lesion detection and discrimination.

In a technique known as PSIR, reconstruction of real images (rather than magnitude images) in an inversion-prepared 2D gradient-echo sequence has been shown to be useful in the detection of cord lesions.[17] We did not observe any immediate advantage of reconstructing the real component with the optimized T1-MPRAGE sequence, mainly because the signal from the lesion was close to null. This modification is very easily implemented on most MR imaging scanners if needed.

Technical Considerations

The T1-MPRAGE pulse sequence has been well described and is now commonly used in clinical imaging of the brain.[28] As

demonstrated here, this sequence offers a unique opportunity to visualize lesions in the cord, as it offers ways to optimize the imaging contrast by using inversion pulses. However, the 3D acquisition technique is more susceptible to motion artifacts. Use of a spine array coil and parallel imaging enabled improved SNR while reducing artifacts, particularly in the cervical region. Sagittal acquisition, rather than coronal or axial sections, allowed coverage of the spinal cord in the least amount of time without having to change the acquisition matrix in a subject-size–dependent manner. SNR of the T1-MPRAGE was boosted by increasing the TR as well as the flip angle, while at the same time maintaining the contrast between lesions and the normal-appearing spinal cord.

3D acquisition allowed for high isotropic resolution and more accurate calculation of lesion load. Isotropic high-resolution images can also be reformatted in different planes for better visualization of lesions, especially those on the surface of the cord.[6] However, 3D acquisition also makes the images more susceptible to movement artifacts, which is especially relevant for the spinal cord. Spinal cord MR imaging is plagued with artifacts from respiration, swallowing, and cardiac movement, as well as from movement of the cord during a cardiac cycle. Placing a saturation pulse anterior to the vertebral bodies can be considered to eliminate most of the movement artifacts from outside the cord. Movement of the cord itself was not found to be a major source of artifacts, however. Finally, a large acquisition matrix and small bandwidth helped mitigate truncation artifacts in the spinal cord.

Study Limitations

The major limitation of this study was the lack of a reference standard for lesion presence, because such data would require postmortem pathologic examination. In the absence of a pathologic reference standard, we used consensus between experienced observers as a radiologic reference standard, and we compared our results from T1-MPRAGE with STIR, which is the accepted standard for sagittal imaging. An additional limitation was that we only performed detailed, quantitative, volumetric analysis in a fraction of the cases; however, the qualitative analysis in the larger cohort suggests that the results from those cases would have generalized. A further limitation was that the quantitative analysis focused only on the upper cervical cord, rather than the whole cord; this region was chosen because prior studies[6,7] have demonstrated that roughly 60% of spinal cord lesions occur in the cervical cord. Indeed, in the patient population studied herein, the C1–C4 segments accounted for 40% of all lesions seen in the spinal cord. Moreover, lesions in the WM of the upper cervical cord can affect both the upper and lower limbs, potentially improving correlations with disability scores, which were moderate in the analysis reported here. Further analysis could entail correlation of lesion burden along specific tracts from the entire cord with individual functional systems scores, including sensory, motor, and bowel/bladder.[5] Such studies would require a larger patient cohort. Finally, the protocol parameters used for the T1-MPRAGE could not differentiate between the GM and WM in the cord, thereby necessitating the use of additional sequences for complete characterization of lesion location.

CONCLUSIONS

The optimized T1-MPRAGE sequence was more efficient in the visualization of spinal cord lesions compared with other standard clinical sequences. EDSS correlated better with cord lesion volumes calculated from the T1-MPRAGE sequence than from the other sequences, suggesting that a substantial proportion of the lesion burden in the spinal cord has been missed in prior studies. Therefore, T1-MPRAGE can help in a more accurate estimation of the lesion load and, when used in conjunction with other sequences such as T2*-GRE and STIR, can increase diagnostic confidence through better visualization of these lesions.

ACKNOWLEDGMENTS

This study was supported by the Intramural Research Program of the National Institute of Neurologic Disorders and Stroke (NINDS), National Institutes of Health. We also thank the National Institute of Mental Health (NIMH)/NINDS Functional Magnetic Resonance Facility, John Ostuni (NINDS), Souheil Inati (NIMH), and the Neuroimmunology Branch clinical group for their help.

REFERENCES

1. Bot JC, Barkhof F, Lycklama a Nijeholt G, et al. **Differentiation of multiple sclerosis from other inflammatory disorders and cerebrovascular disease: value of spinal MR imaging.** *Radiology* 2002;223:46–56
2. Lycklama à Nijeholt GJ, Barkhof F, Scheltens P, et al. **MR of the spinal cord in multiple sclerosis: relation to clinical subtype and disability.** *AJNR Am J Neuroradiol* 1997;18:1041–48
3. Simon JH. **The contribution of spinal cord MRI to the diagnosis and differential diagnosis of multiple sclerosis.** *J Neurol Sci* 2000;172 Suppl 1:S32–35
4. Ikuta F, Zimmerman HM. **Distribution of plaques in seventy autopsy cases of multiple sclerosis in the United States.** *Neurology* 1976;26:26–28
5. Nijeholt GJ, van Walderveen MA, Castelijns JA, et al. **Brain and spinal cord abnormalities in multiple sclerosis. Correlation between MRI parameters, clinical subtypes and symptoms.** *Brain* 1998; 121(Pt 4):687–97
6. Weier K, Mazraeh J, Naegelin Y, et al. **Biplanar MRI for the assessment of the spinal cord in multiple sclerosis.** *Mult Scler* 2012; 18:1560–69
7. Qiu W, Raven S, James I, et al. **Spinal cord involvement in multiple sclerosis: a correlative MRI and high-resolution HLA-DRB1 genotyping study.** *J Neurol Sci* 2011;300:114–19
8. Bot JC, Barkhof F, Polman CH, et al. **Spinal cord abnormalities in recently diagnosed MS patients: added value of spinal MRI examination.** *Neurology* 2004;62:226–33
9. Thorpe JW, Kidd D, Moseley IF, et al. **Spinal MRI in patients with suspected multiple sclerosis and negative brain MRI.** *Brain* 1996; 119(Pt 3):709–14
10. Brex PA, O'Riordan JI, Miszkiel KA, et al. **Multisequence MRI in clinically isolated syndromes and the early development of MS.** *Neurology* 1999;53:1184–90
11. Vaithianathar L, Tench CR, Morgan PS, et al. **Magnetic resonance imaging of the cervical spinal cord in multiple sclerosis–a quantitative T1 relaxation time mapping approach.** *J Neurol* 2003; 250:307–15
12. Barkhof F. **The clinico-radiological paradox in multiple sclerosis revisited.** *Curr Opin Neurol* 2002;15:239–45
13. Simon JH, Li D, Traboulsee A, et al. **Standardized MR imaging protocol for multiple sclerosis: Consortium of MS Centers consensus guidelines.** *AJNR Am J Neuroradiol* 2006;27:455–61

14. Hittmair K, Mallek R, Prayer D, et al. **Spinal cord lesions in patients with multiple sclerosis: comparison of MR pulse sequences.** *AJNR Am J Neuroradiol* 1996;17:1555–65
15. Philpott C, Brotchie P. **Comparison of MRI sequences for evaluation of multiple sclerosis of the cervical spinal cord at 3 T.** *Eur J Radiol* 2011;80:780–85
16. Thorpe JW, MacManus DG, Kendall BE, et al. **Short tau inversion recovery fast spin-echo (fast STIR) imaging of the spinal cord in multiple sclerosis.** *Magn Reson Imaging* 1994;12:983–89
17. Poonawalla AH, Hou P, Nelson FA, et al. **Cervical spinal cord lesions in multiple sclerosis: T1-weighted inversion-recovery MR imaging with phase-sensitive reconstruction.** *Radiology* 2008;246:258–64
18. White ML, Zhang Y, Healey K. **Cervical spinal cord multiple sclerosis: evaluation with 2D multi-echo recombined gradient echo MR imaging.** *J Spinal Cord Med* 2011;34:93–98
19. Martin N, Malfair D, Zhao Y, et al. **Comparison of MERGE and axial T2-weighted fast spin-echo sequences for detection of multiple sclerosis lesions in the cervical spinal cord.** *AJR Am J Roentgenol* 2012;199:157–62
20. Ozturk A, Aygun N, Smith SA, et al. **Comparison of axial MR sequences for the detection of multiple sclerosis lesions in the cervical spinal cord at 3 T.** In: *Proceedings of the Annual Meeting of the American Society of Neuroradiology*, New Orleans, Louisiana, June 2–5, 2008:316
21. Bot JC, Barkhof F, Lycklama a Nijeholt GJ, et al. **Comparison of a conventional cardiac-triggered dual spin-echo and a fast STIR sequence in detection of spinal cord lesions in multiple sclerosis.** *Eur Radiol* 2000;10:753–58
22. Stankiewicz JM, Neema M, Alsop DC, et al. **Spinal cord lesions and clinical status in multiple sclerosis: A 1.5 T and 3 T MRI study.** *J Neurol Sci* 2009;279:99–105
23. Filippi M, Paty DW, Kappos L, et al. **Correlations between changes in disability and T2-weighted brain MRI activity in multiple sclerosis: a follow-up study.** *Neurology* 1995;45:255–60
24. Rosset A, Spadola L, Ratib O. **OsiriX: an open-source software for navigating in multidimensional DICOM images.** *J Digit Imaging* 2004;17:205–16
25. Deoni SC, Rutt BK, Peters TM. **Rapid combined T1 and T2 mapping using gradient recalled acquisition in the steady state.** *Magn Reson Med* 2003;49:515–26
26. Mascalchi M, Dal Pozzo G, Bartolozzi C. **Effectiveness of the short TI inversion recovery (STIR) sequence in MR imaging of intramedullary spinal lesions.** *Magn Reson Imaging* 1993;11:17–25
27. Campi A, Pontesilli S, Gerevini S, et al. **Comparison of MRI pulse sequences for investigation of lesions of the cervical spinal cord.** *Neuroradiology* 2000;42:669–75
28. Deichmann R, Good CD, Josephs O, et al. **Optimization of 3-D MP-RAGE sequences for structural brain imaging.** *Neuroimage* 2000;12:112–27

AJNR CLASSIFIEDS

President's Distinguished University Chair in Translational Stroke Research University of Texas Health Science Center at San Antonio (UTHSCSA)

We are searching for an outstanding candidate (PhD and/or MD) to fill the **USAA Foundation President's Distinguished University Chair,** to lead and develop world-class research programs in **Translational Stroke Research.** Applicants must have high quality peer-reviewed publications, experience building research teams, existing peer-reviewed funding and have attained the rank of Associate Professor or Professor. Emphasis on recovery from stroke or on the use of novel imaging technologies in the study of stroke is particularly desirable. UTHSCSA is an Equal Employment Opportunity/ Affirmative Action employer and is committed to excellence through diversity among its faculty, staff and students. Visit **http://som.uthscsa.edu/FacultyPositions/** for more information.

Interested candidates should email a curriculum vitae, names of three references and a statement of interest addressed to: Dr. Timothy Duong PhD, Committee Chair, c/o: **ainswortha@uthscsa.edu**

All faculty appointments are designated as security sensitive positions.

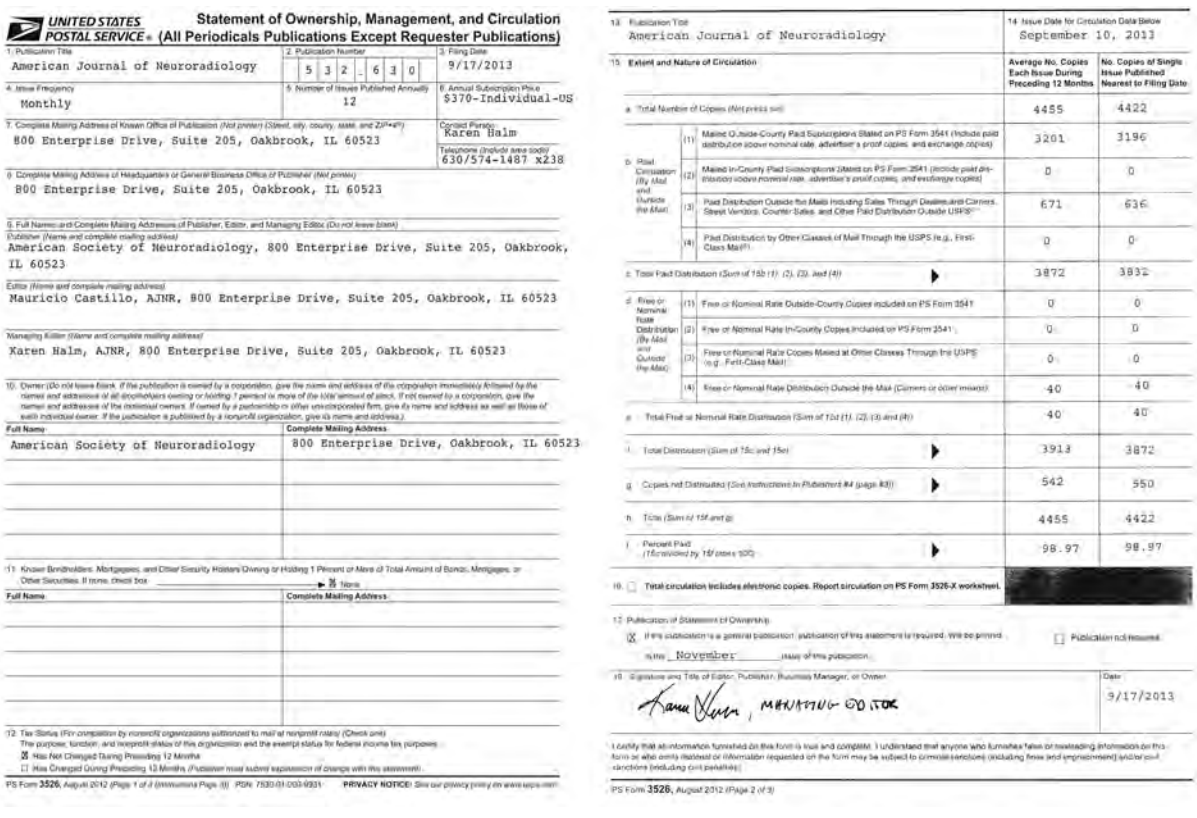

UNITED STATES POSTAL SERVICE® **Statement of Ownership, Management, and Circulation (All Periodicals Publications Except Requester Publications)**

1. Publication Title	2. Publication Number	3. Filing Date
American Journal of Neuroradiology	5 3 2 - 6 3 0	9/17/2013
4. Issue Frequency: Monthly	5. Number of Issues Published Annually: 12	6. Annual Subscription Price: $370-Individual-US

7. Complete Mailing Address of Known Office of Publication (Not printer) (Street, city, county, state, and ZIP+4®): 800 Enterprise Drive, Suite 205, Oakbrook, IL 60523 — Contact Person: Karen Halm; Telephone (Include area code): 630/574-1487 x238

8. Complete Mailing Address of Headquarters or General Business Office of Publisher (Not printer): 800 Enterprise Drive, Suite 205, Oakbrook, IL 60523

9. Full Names and Complete Mailing Addresses of Publisher, Editor, and Managing Editor (Do not leave blank)

Publisher (Name and complete mailing address): American Society of Neuroradiology, 800 Enterprise Drive, Suite 205, Oakbrook, IL 60523

Editor (Name and complete mailing address): Mauricio Castillo, AJNR, 800 Enterprise Drive, Suite 205, Oakbrook, IL 60523

Managing Editor (Name and complete mailing address): Karen Halm, AJNR, 800 Enterprise Drive, Suite 205, Oakbrook, IL 60523

10. Owner (Do not leave blank. If the publication is owned by a corporation, give the name and address of the corporation immediately followed by the names and addresses of all stockholders owning or holding 1 percent or more of the total amount of stock. If not owned by a corporation, give the names and addresses of the individual owners. If owned by a partnership or other unincorporated firm, give its name and address as well as those of each individual owner. If the publication is published by a nonprofit organization, give its name and address.)

Full Name	Complete Mailing Address
American Society of Neuroradiology	800 Enterprise Drive, Oakbrook, IL 60523

11. Known Bondholders, Mortgagees, and Other Security Holders Owning or Holding 1 Percent or More of Total Amount of Bonds, Mortgages, or Other Securities. If none, check box → ☒ None

Full Name	Complete Mailing Address

12. Tax Status (For completion by nonprofit organizations authorized to mail at nonprofit rates) (Check one)
The purpose, function, and nonprofit status of this organization and the exempt status for federal income tax purposes:
☒ Has Not Changed During Preceding 12 Months
☐ Has Changed During Preceding 12 Months (Publisher must submit explanation of change with this statement)

PS Form 3526, August 2012 (Page 1 of 3 (Instructions Page 3)) PSN: 7530-01-000-9931 PRIVACY NOTICE: See our privacy policy on www.usps.com

13. Publication Title: American Journal of Neuroradiology	14. Issue Date for Circulation Data Below: September 10, 2013	
15. Extent and Nature of Circulation	Average No. Copies Each Issue During Preceding 12 Months	No. Copies of Single Issue Published Nearest to Filing Date
a. Total Number of Copies (Net press run)	4455	4422
b. Paid Circulation (By Mail and Outside the Mail) (1) Mailed Outside-County Paid Subscriptions Stated on PS Form 3541 (Include paid distribution above nominal rate, advertiser's proof copies, and exchange copies)	3201	3196
(2) Mailed In-County Paid Subscriptions Stated on PS Form 3541 (Include paid distribution above nominal rate, advertiser's proof copies, and exchange copies)	0	0
(3) Paid Distribution Outside the Mails Including Sales Through Dealers and Carriers, Street Vendors, Counter Sales, and Other Paid Distribution Outside USPS®	671	636
(4) Paid Distribution by Other Classes of Mail Through the USPS (e.g., First-Class Mail®)	0	0
c. Total Paid Distribution (Sum of 15b (1), (2), (3), and (4))	3872	3832
d. Free or Nominal Rate Distribution (By Mail and Outside the Mail) (1) Free or Nominal Rate Outside-County Copies included on PS Form 3541	0	0
(2) Free or Nominal Rate In-County Copies included on PS Form 3541	0	0
(3) Free or Nominal Rate Copies Mailed at Other Classes Through the USPS (e.g., First-Class Mail)	0	0
(4) Free or Nominal Rate Distribution Outside the Mail (Carriers or other means)	40	40
e. Total Free or Nominal Rate Distribution (Sum of 15d (1), (2), (3) and (4))	40	40
f. Total Distribution (Sum of 15c and 15e)	3913	3872
g. Copies not Distributed (See Instructions to Publishers #4 (page #3))	542	550
h. Total (Sum of 15f and g)	4455	4422
i. Percent Paid (15c divided by 15f times 100)	98.97	98.97

16. ☐ Total circulation includes electronic copies. Report circulation on PS Form 3526-X worksheet.

17. Publication of Statement of Ownership
☒ If the publication is a general publication, publication of this statement is required. Will be printed in the November issue of this publication. ☐ Publication not required.

18. Signature and Title of Editor, Publisher, Business Manager, or Owner: MANAGING EDITOR — Date: 9/17/2013

I certify that all information furnished on this form is true and complete. I understand that anyone who furnishes false or misleading information on this form or who omits material or information requested on the form may be subject to criminal sanctions (including fines and imprisonment) and/or civil sanctions (including civil penalties).

PS Form 3526, August 2012 (Page 2 of 3)

AJNR

Go Green!

AJNR urges American Society of Neuroradiology members to reduce their environmental footprint by voluntarily suspending their print subscription.

The savings in paper, printing, transportation, and postage not only help members cut down on clutter, but go to fund new electronic enhancements and expanded content.

The digital edition of *AJNR* presents the print version in its entirety, along with extra features including:

- Publication Preview
- Case of the Week
- Podcasts
- Special Collections
- The *AJNR* Blog
- Weekly Poll

It also **reaches subscribers much faster than print**. An **electronic table of contents** will be sent directly to your mailbox to notify you as soon as it publishes.

Readers can **search, reference, and bookmark** current and archived content 24 hours a day on www.ajnr.org, rather than thumb through stacks of accumulated paper issues for articles and images they need.

http://www.ajnr.org/cgi/feedback

ASNR members who wish to opt out of print can do so by using the Feedback form on the *AJNR* Website (**http://www.ajnr.org/cgi/feedback**). Just type "Go Green" in the subject line to stop print and spare our ecosystem.

DOTAREM® (gadoterate meglumine) injection, for intravenous use
Initial U.S. Approval: 2013

BRIEF SUMMARY OF PRESCRIBING INFORMATION
CONSULT PACKAGE INSERT FOR FULL PRESCRIBING INFORMATION

WARNING: NEPHROGENIC SYSTEMIC FIBROSIS (NSF)

Gadolinium-based contrast agents (GBCAs) increase the risk for NSF among patients with impaired elimination of the drugs. Avoid use of GBCAs in these patients unless the diagnostic information is essential and not available with non-contrasted MRI or other modalities. NSF may result in fatal or debilitating fibrosis affecting the skin, muscle and internal organs.

- **The risk for NSF appears highest among patients with:**
  - **Chronic, severe kidney disease (GFR < 30 mL/min/1.73m^2), or**
  - **Acute kidney injury.**
- **Screen patients for acute kidney injury and other conditions that may reduce renal function. For patients at risk for chronically reduced renal function (e.g. age > 60 years, hypertension, diabetes), estimate the glomerular filtration rate (GFR) through laboratory testing (5.1).**
- **For patients at highest risk for NSF, do not exceed the recommended DOTAREM dose and allow a sufficient period of time for elimination of the drug from the body prior to any re-administration *[see Warnings and Precautions (5.1)]*.**

1 INDICATIONS AND USAGE

DOTAREM is a gadolinium-based contrast agent indicated for intravenous use with magnetic resonance imaging (MRI) in brain (intracranial), spine and associated tissues in adult and pediatric patients (2 years of age and older) to detect and visualize areas with disruption of the blood brain barrier (BBB) and/or abnormal vascularity. (1)

4 CONTRAINDICATIONS

History of clinically important hypersensitivity reactions to DOTAREM. (4)

5 WARNINGS AND PRECAUTIONS

5.1 Nephrogenic Systemic Fibrosis

Gadolinium-based contrast agents (GBCAs) increase the risk for nephrogenic systemic fibrosis (NSF) among patients with impaired elimination of the drugs. Avoid use of GBCAs among these patients unless the diagnostic information is essential and not available with non-contrast MRI or other modalities. The GBCA-associated NSF risk appears highest for patients with chronic, severe kidney disease (GFR < 30 mL/min/1.73m^2) as well as patients with acute kidney injury. The risk appears lower for patients with chronic, moderate kidney disease (GFR 30 - 59 mL/min/1.73m^2) and little, if any, for patients with chronic, mild kidney disease (GFR 60 - 89 mL/min/1.73m^2). NSF may result in fatal or debilitating fibrosis affecting the skin, muscle and internal organs. Report any diagnosis of NSF following DOTAREM administration to Guerbet LLC (1-877-729-6679) or FDA (1-800-FDA-1088 or www.fda.gov/medwatch).

Screen patients for acute kidney injury and other conditions that may reduce renal function. Features of acute kidney injury consist of rapid (over hours to days) and usually reversible decrease in kidney function, commonly in the setting of surgery, severe infection, injury or drug-induced kidney toxicity. Serum creatinine levels and estimated GFR may not reliably assess renal function in the setting of acute kidney injury. For patients at risk for chronically reduced renal function (e.g., age > 60 years, diabetes mellitus or chronic hypertension), estimate the GFR through laboratory testing.

Among the factors that may increase the risk for NSF are repeated or higher than recommended doses of a GBCA and the degree of renal impairment at the time of exposure. Record the specific GBCA and the dose administered to a patient. For patients at highest risk for NSF, do not exceed the recommended DOTAREM dose and allow a sufficient period of time for elimination of the drug prior to re-administration. For patients receiving hemodialysis, physicians may consider the prompt initiation of hemodialysis following the administration of a GBCA in order to enhance the contrast agent's elimination. The usefulness of hemodialysis in the prevention of NSF is unknown *[see Dosage and Administration (2) and Clinical Pharmacology (12)]*.

5.2 Hypersensitivity Reactions

Anaphylactic and anaphylactoid reactions have been reported with DOTAREM, involving cardiovascular, respiratory, and/or cutaneous manifestations. Some patients experienced circulatory collapse and died. In most cases, initial symptoms occurred within minutes of DOTAREM administration and resolved with prompt emergency treatment *[see Adverse Reactions (6)]*.

- Before DOTAREM administration, assess all patients for any history of a reaction to contrast media, bronchial asthma and/or allergic disorders. These patients may have an increased risk for a hypersensitivity reaction to DOTAREM.
- Administer DOTAREM only in situations where trained personnel and therapies are promptly available for the treatment of hypersensitivity reactions, including personnel trained in resuscitation.
- During and following DOTAREM administration, observe patients for signs and symptoms of hypersensitivity reactions.

5.3 Acute Kidney Injury

In patients with chronically reduced renal function, acute kidney injury requiring dialysis has occurred with the use of GBCAs. The risk of acute kidney injury may increase with increasing dose of the contrast agent; administer the lowest dose necessary for adequate imaging. Screen all patients for renal impairment by obtaining a history and/or laboratory tests. Consider follow-up renal function assessments for patients with a history of renal dysfunction.

5.4 Extravasation and Injection Site Reactions

Ensure catheter and venous patency before the injection of DOTAREM. Extravasation into tissues during DOTAREM administration may result in tissue irritation *[see Nonclinical Toxicology (13.2)]*.

6 ADVERSE REACTIONS

GBCAs have been associated with a risk for NSF *[see Warnings and Precautions (5.1)]*. NSF has not been reported in patients with a clear history of exposure to DOTAREM alone. For hypersensitivity reactions and acute kidney injury see Warnings and Precautions *(5.2) and (5.3)*.

6.1 Clinical Studies Experience

Because clinical trials are conducted under widely varying conditions, adverse reaction rates observed in the clinical trials of a drug cannot be directly compared to rates in the clinical trials of another drug and may not reflect the rates observed in clinical practice.

The data described below reflect DOTAREM exposure in 2813 patients, representing 2672 adults and 141 pediatric patients. Overall, 55% of the patients were men. In clinical trials where ethnicity was recorded the ethnic distribution was 74% Caucasian, 12% Asian, 4% Black, and 10% others. The average age was 53 years (range from 0.1 to 97 years).

Overall, 3.9% of patients reported at least one adverse reaction, primarily occurring immediately or several days following DOTAREM administration. Most adverse reactions were mild or moderate in severity and transient in nature.

Table 1 lists adverse reactions that occurred in ≥ 0.2% patients who received DOTAREM.

Table 1: Adverse Reactions in Clinical Trials

Reaction	Rate (%) n = 2813
Nausea	0.6%
Headache	0.5%
Injection Site Pain	0.4%
Injection Site Coldness	0.2%
Burning Sensation	0.2%

Adverse reactions that occurred with a frequency < 0.2% in patients who received DOTAREM include: feeling cold, rash, somnolence, fatigue, dizziness, vomiting, pruritus, paresthesia, dysgeusia, pain in extremity, anxiety, hypertension, palpitations, oropharyngeal discomfort, serum creatinine increased and injection site reactions, including site inflammation, extravasation, pruritus, and warmth.

Adverse Reactions in Pediatric Patients

During clinical trials, 141 pediatric patients (7 aged < 24 months, 33 aged 2 - 5 years, 58 aged 6 - 11 years and 43 aged 12 -17) received DOTAREM. Overall, 6 pediatric patients (4.3%) reported at least one adverse reaction following DOTAREM administration. The most frequently reported adverse reaction was headache (1.5%). Most adverse events were mild in severity and transient in nature, and all patients recovered without treatment.

6.2 Postmarketing Experience

The following additional adverse reactions have been identified during postmarketing use of DOTAREM. Because these reactions are reported voluntarily from a population of uncertain size, it is not always possible to reliably estimate their frequency or establish a causal relationship to drug exposure.

- bradycardia, tachycardia, arrhythmia
- hypersensitivity / anaphylactoid reactions including cardiac arrest, respiratory arrest, cyanosis, pharyngeal edema, laryngospasm, bronchospasm, angioedema, conjunctivitis, ocular hyperemia, eyelid edema, lacrimation increased, hyperhidrosis, urticaria
- coma, convulsion, syncope, presyncope, parosmia, tremor
- muscle contracture, muscle weakness
- diarrhea, salivary hypersecretion
- malaise, fever
- NSF, in patients whose reports were confounded by the receipt of other GBCAs or in situations where receipt of other GBCAs could not be ruled out. No unconfounded cases of NSF have been reported with DOTAREM.
- superficial phlebitis

7 DRUG INTERACTIONS

DOTAREM does not interfere with serum and plasma calcium measurements determined by colorimetric assays. Specific drug interaction studies with DOTAREM have not been conducted.

8 USE IN SPECIFIC POPULATIONS

8.1 Pregnancy

Pregnancy Category C

There are no adequate and well-controlled studies with DOTAREM conducted in pregnant women. Limited published human data on exposure to other GBCAs during pregnancy did not show adverse effects in exposed neonates. No effects on embryo fetal development were observed in rats or rabbits at doses up to 10 mmol/kg/day in rats or 3 mmol/kg/day in rabbits. The doses in rats and rabbits were respectively 16 and 10 times the recommended human dose based on body surface area. DOTAREM should be used during pregnancy only if the potential benefit justifies the potential risk to the fetus.

While it is unknown if DOTAREM crosses the human placenta, other GBCAs do cross the placenta in humans and result in fetal exposure.

Reproductive and developmental toxicity studies were conducted with gadoterate meglumine in rats and rabbits. Gadoterate meglumine was administered intravenously in doses of 0, 2, 4 and 10 mmol/kg/day (or 3.2, 6.5 and 16.2 times the recommended human dose based on body surface area) to female rats for 14 days before mating throughout the mating period and until gestation day (GD) 17. Pregnant rabbits were intravenously administered gadoterate meglumine at the dose levels of 0, 1, 3 and 7 mmol/kg/day (or 3.3, 10 and 23 times the human doses based on body surface area) from GD6 to GD19. No effects on embryo fetal development were observed in rats or rabbits at doses up to 10 mmol/kg/day in rats or 3 mmol/kg/day in rabbits. Maternal toxicity was observed in rats at 10 mmol/kg/day (or 16 times the human dose based on body surface area) and in rabbits at 7 mmol/kg/day (23 times the human dose based on body surface area).

8.3 Nursing Mothers

It is not known whether DOTAREM is excreted in human milk. Limited case reports on use of GBCAs in nursing mothers indicate that 0.01 to 0.04% of the maternal gadolinium dose is excreted in human breast milk. Because many drugs are excreted in human milk, exercise caution when DOTAREM is administered to a nursing woman. Nonclinical data show that gadoterate meglumine is excreted into breast milk in very small amounts (< 0.1% of the dose intravenously administered) and absorption via the gastrointestinal tract is poor.

8.4 Pediatric Use

The safety and efficacy of DOTAREM at a single dose of 0.1 mmol/kg have been established in pediatric patients from 2 to 17 years of age. No dosage adjustment according to age is necessary in this population *[See Dosage and Administration (2.1) and Clinical Studies (14)]*. The safety and efficacy of DOTAREM have not been established in pediatric patients below 2 years of age. GFR does not reach adult levels until 1 year of age *[see Warnings and Precautions (5.1)]*.

8.5 Geriatric Use

In clinical studies of DOTAREM, 900 patients were 65 years of age and over, and 312 patients were 75 years of age and over. No overall differences in safety or efficacy were observed between these subjects and younger subjects. In general, use of DOTAREM in elderly patients should be cautious, reflecting the greater frequency of impaired renal function and concomitant disease or other drug therapy. No age-related dosage adjustment is necessary.

8.6 Renal Impairment

No DOTAREM dosage adjustment is recommended for patients with renal impairment. Gadoterate meglumine can be removed from the body by hemodialysis *[see Warnings and Precautions (5.1) and Clinical Pharmacology (12.3)]*.

10 OVERDOSAGE

DOTAREM administered to healthy volunteers and to patients at cumulative doses up to 0.3 mmol/kg was tolerated in a manner similar to lower doses. Adverse reactions to overdosage with DOTAREM have not been reported. Gadoterate meglumine can be removed from the body by hemodialysis *[See Clinical Pharmacology (12.3)]*.

13 NONCLINICAL TOXICOLOGY

13.1 Carcinogenesis, Mutagenesis, Impairment of Fertility

Long-term animal studies have not been performed to evaluate the carcinogenic potential of gadoterate meglumine.

Gadoterate meglumine did not demonstrate mutagenic potential in *in vitro* bacterial reverse mutation assays (Ames test) using Salmonella typhimurium, in an *in vitro* chromosome aberration assay in Chinese hamster ovary cells, in an *in vitro* gene mutation assay in Chinese hamster lung cells, nor in an *in vivo* mouse micronucleus assay.

No impairment of male or female fertility and reproductive performance was observed in rats after intravenous administration of gadoterate meglumine at the maximum tested dose of 10 mmol/kg/day (16 times the maximum human dose based on surface area), given during more than 9 weeks in males and more than 4 weeks in females. Sperm counts and sperm motility were not adversely affected by treatment with the drug.

13.2 Animal Toxicology and/or Pharmacology

Local intolerance reactions, including moderate irritation associated with infiltration of inflammatory cells were observed after perivenous injection in rabbits suggesting the possibility of local irritation if the contrast medium leaks around the veins in a clinical setting *[see Warnings and Precautions (5.4)]*.

17 PATIENT COUNSELING INFORMATION

17.1 Nephrogenic Systemic Fibrosis

Instruct patients to inform their healthcare provider if they:

- have a history of kidney disease, or
- have recently received a GBCA.

GBCAs increase the risk for NSF among patients with impaired elimination of the drugs. To counsel patients at risk for NSF:

- Describe the clinical manifestations of NSF.
- Describe procedures to screen for the detection of renal impairment.

Instruct the patients to contact their physician if they develop signs or symptoms of NSF following DOTAREM administration, such as burning, itching, swelling, scaling, hardening and tightening of the skin; red or dark patches on the skin; stiffness in joints with trouble moving, bending or straightening the arms, hands, legs or feet; pain in the hip bones or ribs; or muscle weakness.

17.2 Common Adverse Reactions

Inform patients that they may experience:

- Reactions along the venous injection site, such as mild and transient burning or pain or feeling of warmth or coldness at the injection site.
- Side effects of headache, nausea, abnormal taste and feeling hot.

17.3 General Precautions

Instruct patients receiving DOTAREM to inform their physician if they:

- Are pregnant or breastfeeding.
- Have a history of allergic reaction to contrast media, bronchial asthma or allergy.
- Are taking any medications.

Rx Only

Guerbet LLC
120 W 7th Street. Suite 108
Bloomington, IN 47404

Pre-filled syringes manufactured by Catalent, Belgium for Guerbet
Vials manufactured by Recipharm, France for Guerbet

GU06131043
Revised 06/2013

DOTAREM®
(gadoterate meglumine) Injection

Macrocyclic and Ionic...

DOTAREM

...There is only One.

The first and only macrocyclic and ionic gadolinium agent in its class.[1]

Visit us at **RSNA 2013 Booth #2535**
South Building, Hall A

Global clinical experience with over **37 million doses** administered outside the US.[2]

INDICATION[1]

DOTAREM is a gadolinium-based contrast agent indicated for intravenous use with magnetic resonance imaging (MRI) in brain (intracranial), spine and associated tissues in adult and pediatric patients (2 years of age and older) to detect and visualize areas with disruption of the blood brain barrier (BBB) and/or abnormal vascularity.

IMPORTANT SAFETY INFORMATION[1]

WARNING: NEPHROGENIC SYSTEMIC FIBROSIS (NSF)

Gadolinium-based contrast agents (GBCAs) increase the risk for NSF among patients with impaired elimination of the drugs. Avoid use of GBCAs in these patients unless the diagnostic information is essential and not available with non-contrasted MRI or other modalities. NSF may result in fatal or debilitating fibrosis affecting the skin, muscle and internal organs.

- **The risk for NSF appears highest among patients with:**
  - **Chronic, severe kidney disease (GFR < 30 mL/min/1.73m^2), or**
  - **Acute kidney injury.**
- **Screen patients for acute kidney injury and other conditions that may reduce renal function. For patients at risk for chronically reduced renal function (e.g. age > 60 years, hypertension, diabetes), estimate the glomerular filtration rate (GFR) through laboratory testing (5.1).**
- **For patients at highest risk for NSF, do not exceed the recommended DOTAREM dose and allow a sufficient period of time for elimination of the drug from the body prior to any re-administration (5.1).**

Contraindicated in patients with a history of clinically important hypersensitivity reactions to DOTAREM.

The possibility of serious or life-threatening anaphylactoid/anaphylactic reactions with cardiovascular, respiratory or cutaneous manifestations, ranging from mild to severe, including death, should be considered. Monitor patients closely for need of emergency cardiorespiratory support.

In patients with chronically reduced renal function, acute kidney injury requiring dialysis has occurred with the use of GBCAs. The risk of acute kidney injury may increase with increasing dose of the contrast agent; administer the lowest dose necessary for adequate imaging. Screen all patients for renal impairment by obtaining a history and/or laboratory tests. Consider follow-up renal function assessments for patients with a history of renal dysfunction.

The most common adverse reactions associated with DOTAREM in clinical studies were nausea, headache, injection site pain, injection site coldness, and burning sensation.

For more information about DOTAREM, including full Boxed WARNING, please see the Full Prescribing Information.

Please see adjacent Brief Summary of Prescribing Information.

DOTAREM is a registered trademark of Guerbet and is available by prescription only.

GU09131071

References: 1. Dotarem [package insert]. Bloomington, IN: Guerbet LLC; 2013. **2.** Data on file, Guerbet LLC.

www.guerbet-us.com

Guerbet
Contrast for Life